Technische Universität München

TUM School of Natural Sciences

How Light Scalars Change the Stellar Landscape

Konstantin F. Springmann

Vollständiger Abdruck der von der TUM School of Natural Sciences der Technischen Universität München zur Erlangung des akademischen Grades eines

Doktors der Naturwissenschaften

genehmigten Dissertation.

Vorsitz:		Prof. Dr. Laura Fabbietti
Prüfer*innen der Dissertation:	1.	Prof. Dr. Andreas Weiler
	2.	Prof. Dr. Björn Garbrecht

Die Dissertation wurde am 23.08.2023 bei der Technischen Universität München eingereicht und durch die TUM School of Natural Sciences am 04.10.2023 angenommen.

Technische Universität München

How Light Scalars Change the Stellar Landscape

Dissertation

by

Konstantin F. Springmann

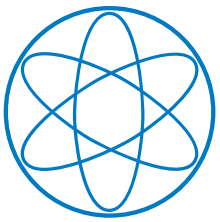

TUM School of Natural Sciences, T75

Für Hanna und Beate

How Light Scalars Change the Stellar Landscape

Wie leichte Skalarfelder die stellare Landschaft verändern

Konstantin F. Springmann

Abstract

Light scalar fields are the essence of many well-motivated theories beyond the Standard Model of particle physics. In this thesis, we study the rich phenomenology of the interplay between these fields and the finite baryon density present in astrophysical environments such as stars and supernovae. The emerging phenomena range from changes in QCD axion couplings to phase transitions from stars to changing the stellar landscape. Compatibility with observations allows us to put stringent constraints on such models.

Zusammenfassung

Leichte Skalarfelder sind die Essenz vieler motivierter Theorien, die über das Standardmodell der Teilchenphysik hinausgehen. In dieser Dissertation untersuchen wir die reichhaltige Phänomenologie des Zusammenspiels zwischen diesen Feldern und der endlichen Baryonendichte, die in astrophysikalischen Umgebungen wie Sternen und Supernovae vorhanden ist. Die aufkommenden Phänomene reichen von Veränderungen in QCD-Axionkopplungen über Phasenübergänge durch Sterne bis hin zu Veränderungen der stellaren Landschaft. Die Kompatibilität mit Beobachtungen ermöglicht es, solchen Modellen strenge Einschränkungen aufzuerlegen.

Contents

Chapter 1

Introduction

The discovery of the Higgs boson in 2012 at the LHC [1,2] is one of the crowning achievements in modern physics. It constitutes the last missing piece in the complete and consistent description of all known forces and particles of nature, the Standard Model of Particle Physics (SM), and concludes the monumental theoretical as well as experimental effort that made sense of the 'particle zoo' in the 1960s. The spontaneous symmetry breaking of the Higgs gives mass to the electroweak (EW) gauge bosons and leptons and explains the short range of EW interactions. The Higgs also addresses the unitarity violation in the perturbative scattering of massive gauge bosons [3].

However, the SM including the Higgs boson, despite its amazing success, together with the non-observation of new physics around the EW scale, fails to answer many longstanding theoretical questions. The mass of the Higgs boson is sensitive to ultra-violet (UV) radiative corrections and should therefore be orders of magnitude above its measured value, a problem commonly referred to as the EW Hierarchy Problem. None of the proposed solutions beyond the SM (BSM) with symmetry-based mechanisms, like Supersymmetry or Composite Higgs, were found at the LHC.

But this is not the only problem the SM cannot address. There is compelling evidence that SM matter only constitutes a small fraction of the matter abundance in the universe. The lack of a dark matter (DM) candidate is another shortcoming of the SM. Furthermore, the Cosmological Constant (CC) comes with another Hierarchy Problem similar to the EW Hierarchy Problem: It is not protected from UV contributions and should therefore be much larger than the observed value.

Continuing the list of shortcomings of the SM, quantum chromodynamics (QCD), the theory of strong interactions in the SM, is invariant under simultaneous Charge Conjugation and Parity $\mathcal{CP}$ (or equivalently Time Reversal $\mathcal{T}$) transformations, a problem known as the Strong $\mathcal{CP}$ Problem. An alternative formulation of the problem is the question of why $\bar{\theta}$-parameter is so extremely small, measured via the electric dipole moment of the neutron to be $\left|\bar{\theta}\right| < 10^{-10}$ [4]. Given that the SM does violate $\mathcal{CP}$ in the EW sector this is in stark contrast to the order one value one would expect from an effective field theory (EFT) point of view.

The above-mentioned issues clearly call for the necessity for BSM physics and suggest interpreting the SM as an EFT which needs to be replaced at energy scales above some cut-off. Very often, light scalar fields give compelling solutions to these problems. Perhaps the most motivated candidate is the QCD axion which can solve the DM as well as the Strong $\mathcal{CP}$ Problem. The idea is to promote the $\bar{\theta}$-parameter to a dynamical field that gets a mass around the scale where QCD confines and thereby dynamically relax $\bar{\theta}$ to zero. The original works by Peccei, Quinn, Weinberg and Wilczek (PQWW) [5–8] coupled the QCD axion decay constant to the

EW scale which sets the coupling strength to SM particles and was hence ruled out soon after. Invisible QCD axion models are straightforward generalizations of the original PQWW axion but with much larger decay constants and correspondingly weaker couplings to the SM, while solving both the DM as well as the Strong $\mathcal{CP}$ Problem.

Light scalar fields can also address the Hierarchy Problems of the SM. Instead of relying on symmetry, the dynamical evolution of light scalars scans the problematic parameter during the evolution of the early universe. A light scalar field can scan the magnitude of the Cosmological Constant during the evolution of the universe, leading to a small observed value as first brought up in [9]. The relaxion [10] scans the Higgs mass parameter during inflation while a backreaction mechanism, in the simplest realization QCD, stops the evolution around the origin.

In this thesis we study the phenomenology of such light scalar and pseudo-scalar particles and their interaction with SM matter, focusing on astrophysical environments such as neutron stars and supernovae.

We start Chap. 2 by introducing the Strong $\mathcal{CP}$ Problem and the QCD axion as its solution. We further generalize to axion-like particles (ALPs). In particular, in Sec. 2.1 we review the vacuum structure of Yang-Mills theories, where we see that non-perturbative topological terms contribute to the theory. In Sec. 2.2 we see how these non-topological terms give rise to experimentally measurable quantities in the presence of fermions. In order to see that we review the axial anomaly in QCD which naturally brings us to the formulation of the Strong $\mathcal{CP}$ Problem. Sec. 2.3 is devoted to the QCD axion solution to the Strong $\mathcal{CP}$ Problem. We discuss both the original PQWW axion as well as two benchmark models of invisible axions in the UV. In Sec. 2.4 we derive the effective theory of the QCD axion at low energies i.e. the infrared (IR) with the use of chiral perturbation theory (ChPT) and precisely determine its couplings to SM matter, focusing on the couplings to nucleons. In order for the effective theory for nucleons to be valid they have to be non-relativistic which leads us to explore heavy baryon chiral perturbation theory (HBChPT) with the QCD axion. In Sec. 2.5 we review an ALP which behaves similarly to the QCD axion except that its mass can be orders of magnitudes below the vanilla prediction. We conclude the chapter with a discussion on bounds on axions from astrophysical environments such as stellar remnants and supernovae in Sec. 2.6.

In Chap. 3 we review the landscape of stellar remnants. In Sec. 3.1 we review the physics of White Dwarf (WD) stars and discuss various refinements of their equation of state (EOS), while Sec. 3.2 is devoted to Neutron Star (NS) physics. We discuss the difficulties that arise in determining the NS EOS, such as the potential shortcomings of the SM i.e. the hyperon puzzle.

Next up, in Chap. 4 we study the effect of finite baryonic density on the QCD axion-nucleon coupling. We start in Sec. 4.1 to review HBChPT at finite density by deriving the nucleon propagator in a finite density background using real-time thermal field theory. In Sec. 4.2 we calculate the density contributions to the QCD axion-nucleon vertex up to next-to-next-to-leading ($\mathrm{N^2LO}$) in the power counting scheme of chiral perturbation theory. We show the results for two benchmark QCD axion models and finish the chapter in Sec. 4.3 with a discussion on the implication for stellar bounds from Supernova (SN) and NS cooling.

In Chap. 5 we study the possibility that the QCD axion develops a condensate at baryonic densities such as found within NSs. We start with a review of quantum field theories with a chemical potential, review the basics of meson condensation and study the QCD axion potential with $N_f = 2$ light flavors in the presence of a pion condensate in Sec. 5.1. In Sec. 5.2 we extend the study of the QCD axion potential at finite baryonic densities to $N_f = 3$ light flavors and entertain the possibility of kaon condensation which might trigger condensation of the QCD axion. In Sec. 5.3 we go to asymptotic densities where QCD is in a color-flavor-locked (CFL) phase and explore the potential of QCD axion in this phase, finding that condensation is possible.

In Chap. 6 we study the backreaction, neglected in Chap. 5, that scalar condensation induces on the stellar object and find that scalar condensate significantly change the stellar landscape. In Sec. 6.1 we study how light QCD axions change the stellar composition of WD stars. We find that the axion triggers an instability in the EOS of the WD that translates to a gap in the mass radius ($M - R$) curve. The confrontation of the modified $M - R$ relation with observational data is not compatible with large parts of unexplored axion parameter space, allowing us to set stringent constraints. In Sec. 6.2 we show how light scalar fields change the stellar composition of NSs. Employing a simple free Fermi gas we show that the sourcing of light scalars can both stiffen and soften the EOS of NSs depending on the parameters of the model. In particular, we study QCD axions, lighter variations thereof as well as scalars linearly and quadratically coupled to nucleons.

In Chap. 7 we study density induced instabilities of scalar fields with meta-stable minima in vacuum. In Sec. 7.1 we find that in such theories the scalar bubble does not stay confined to the compact object, as previously in Chap. 6, but might in fact escape and permeate indefinitely throughout the universe. We analytically determine (and verify numerically) conditions for such a bubble to escape the object for a simple two minimum potential with a $\mathcal{Z}_2$ symmetry $\phi \to -\phi$ that is explicitly broken by a linear term. These late-time phase transitions, seeded by stars, come with a change of the CC and early vs. late-time measurements thereof allow us to place bounds in the parameter space of these models. In Sec. 7.2 we formulate the Higgs Hierarchy problem and introduce the relaxion in Sec. 7.3. Relaxion models exactly satisfy the conditions needed for such a phase transition to be triggered: the field always stops in a meta-stable minimum. We use our density effects to destabilize this minimum and investigate under which conditions a phase transition in the entire universe is triggered with our findings from Sec. 7.1. For several benchmark relaxion models, this allows us to set stringent bounds from forbidden late-time phase transitions.

Finally, we conclude in Chap. 8, where we summarize our main results and discuss future directions.

This thesis is largely based on the following publications

[11] R. Balkin, J. Serra, K. Springmann, and A. Weiler, *The QCD axion at finite density*, JHEP **07**, 221 (2020), [arXiv:2003.04903].

[12] R. Balkin, J. Serra, K. Springmann, S. Stelzl and A. Weiler, *Runaway relaxion from finite density*, JHEP **06**, 023 (2022), [arXiv:2106.11320].

[13] R. Balkin, J. Serra, K. Springmann, S. Stelzl and A. Weiler, *Density induced vacuum instability*, SciPost Phys. **14**, 4 (2023) [arXiv:2105.13354].

[14] R. Balkin, J. Serra, K. Springmann, S. Stelzl and A. Weiler, *White dwarfs as a probe of light QCD axions*, [arXiv:2211.02661].

[15] R. Balkin, J. Serra, K. Springmann, S. Stelzl and A. Weiler, *Heavy neutron stars from light scalars*, [arXiv:2307.14418].

and work in progress

[16] K. Springmann, M. Stadlbauer, S. Stelzl and A. Weiler, *QCD axion couplings at finite density*, in preparation.

[17] R. Balkin, K. Bartnick, F. Jung, K. Springmann, S. Stelzl and A. Weiler, *Stellar remnants as a probe of non-derivatively coupled scalars*, in preparation.

In particular, some figures contained in this thesis have previously appeared or will soon appear in one of these articles.

Chapter 2

The QCD Axion and ALPs

In this chapter we introduce the strong $\mathcal{CP}$ puzzle and present the QCD axion as a solution. The foundation of the strong $\mathcal{CP}$ puzzle is the non-trivial vacuum structure of QCD, which we will discuss in Sec. 2.1. Expanding on that knowledge, we formulate the strong $\mathcal{CP}$ puzzle in Sec. 2.2 and introduce the QCD axion as a solution in Sec. 2.3. In Sec. 2.4 we derive its couplings to matter within ChPT and discuss astrophysical bounds. In Sec. 2.5 we explore a version of the QCD axion with seemingly fined tuned mass but the same couplings as the ordinary QCD axion.

2.1 The Yang-Mills Vacuum

The discovery of instanton solutions in Euclidean Yang-Mills theories by Belavin, Polyakov, Schwarz, and Tyupkin [18] implies the existence of a non-trivial vacuum structure discovered in [19, 20] and allows to interpret instantons as tunneling solutions between energy-degenerate vacuum states. Since this lies at the heart of the strong $\mathcal{CP}$ problem, let us consider a pure Yang-Mills theory for the gauge group $SU(N)$. Note, however, that it is straightforward to generalize the following discussion to arbitrary non-abelian groups. The Lagrangian reads

$$\mathcal{L}_{\text{YM}} = -\frac{1}{4} G^a_{\mu\nu} G^{a,\mu\nu}, \tag{2.1}$$

where $G^a_{\mu\nu} = \partial_\mu \phi^a_\nu - \partial_\nu A^a_\mu + g f^{abc} A^b_\mu A^c_\nu$ is the gluon field strength tensor with A^a_μ in the adjoint representation of $SU(N)$, g the gauge coupling and f^{abc} the corresponding structure constants. In what follows it is useful to switch to temporal gauge $A_0 = 0$, such that we can write down the Hamiltonian

$$\mathcal{H} = \frac{1}{2} \int d^3x \left(E^2 + B^2 \right), \tag{2.2}$$

where $E^2 = \mathbf{E}^a \cdot \mathbf{E}^a$ with $\mathbf{E}^a = \dot{\mathbf{A}}^a$ and $B^2 = \mathbf{B}^a \cdot \mathbf{B}^a$ are the squares of chromoelectric and chromomagnetic fields, respectively. First, we note that the above Hamiltonian does not fix Gauss law but has to be imposed by hand on the Hilbert space of the theory. Second, we note that picking the temporal gauge leaves us free to perform time independent gauge transformations. Under a generic, time independent gauge transformation $U(\mathbf{x}) \in SU(N)$ the gauge fields transform as

$$A_i(\mathbf{x}) \to A'_i(\mathbf{x}) = U(\mathbf{x}) A_i(\mathbf{x}) U^{-1}(\mathbf{x}) + \frac{i}{g} U(\mathbf{x}) \partial_i U^{-1}(\mathbf{x}), \tag{2.3}$$

where we defined $A_i = A_i^a T^a$ with T^a a $SU(N)$ generator. As is clear from Eq. (2.2), the minimum energy configuration or vacuum has $A_i(\mathbf{x}) = 0$ but can still be a non-trivial pure gauge configuration of the form

$$A_i(\mathbf{x})|_{\text{vac}} = \frac{i}{g} U(\mathbf{x}) \partial_i U^{-1}(\mathbf{x}). \tag{2.4}$$

We aim to study local effects and therefore require

$$U(\mathbf{x}) \to 1 \quad \text{for} \quad |\mathbf{x}| \to \infty. \tag{2.5}$$

This effectively compactifies our three-dimensional space at $|x| \to \infty$ and we note that this is topologically equivalent to a three sphere $S^3_{\mathbb{R}}$. Let us work out the details for $N = 2$ which becomes particularly simple since $SU(2)$ is also topologically equivalent (or diffeomorphic) to $S^3_{SU(2)}$. Mathematically, the gauge transformation $U(\mathbf{x})$ constitutes a mapping from $S^3_{\mathbb{R}} \to S^3_{SU(2)}$, which fall into equivalence classes called elements of the homotopy group, which for $SU(2)$ gives [21]

$$\pi_3(S^3) = \mathbb{Z}. \tag{2.6}$$

What this simply means is that the continuous map of $S^3_{\mathbb{R}} \to S^3_{SU(2)}$ depends on how many times the sphere in group space is covered while $\mathbf{x}$ is wound once around the coordinate sphere. Therefore, each function $U(\mathbf{x})$ depends on the number of windings $n[U(\mathbf{x})]$ which is given by

$$n[U(\mathbf{x})] = \frac{1}{24\pi^2} \epsilon^{ijk} \int d^3x \text{Tr} \left[U(\partial_i U^{-1}) U(\partial_j U^{-1}) U(\partial_k U^{-1}) \right]. \tag{2.7}$$

Note that, winding is additive $n[U_1 U_2] = n[U_1] + n[U_2]$ as one would naively expect. We continue by defining a gauge dependent Chern-Simons current

$$j^\mu_A = \frac{g^2}{16\pi^2} \epsilon^{\mu\nu\rho\sigma} \text{Tr} \left[A_\nu G_{\rho\sigma} + \frac{2ig}{3} A_\nu A_\rho A_\sigma \right] \tag{2.8}$$

whose divergence gives the gauge invariant contribution

$$\partial_\mu j^\mu_A = \frac{g^2}{16\pi^2} \text{Tr}\, G_{\mu\nu} \tilde{G}^{\mu\nu}, \tag{2.9}$$

where $\tilde{G}_{\mu\nu} = \epsilon_{\mu\nu\rho\sigma} G^{\rho\sigma}/2$ is the Hodge dual to the gluon field strength tensor. The associated topological charge Q_ϕ is not conserved since $\partial_\mu j^\mu_A \neq 0$ and given by

$$Q_\phi = \int d^3x j^0_A = \frac{g^2}{16\pi^2} \int d^3x \epsilon^{ijk} \text{Tr} \left[A_i G_{jk} + \frac{2ig}{3} A_i A_j A_k \right]. \tag{2.10}$$

Consider again zero energy configurations $A_i = \frac{i}{g} U \partial_i U^{-1}$, for which $G_{jk} = 0$, we find a connection between the winding number and the (unconserved) charge associated with the Chern-Simons current, namely

$$Q_\phi = n[U(\mathbf{x})]. \tag{2.11}$$

Therefore, we have seen that there exist degenerate vacua, classified by their winding number or topological charge, which cannot be transformed into each other by continuous gauge transformations. The fact that they are not continuously deformable into each other implies that one cannot find a set of infinitesimal gauge transformations that rotate them into each other and therefore they have to be treated as being separated by energy barriers. Hence, topologically

distinct vacua are classically stable, however, there exist field configurations that interpolate between degenerate minima. Consider a finite energy solution that describes such a transition $A_\mu(t, \mathbf{x})$, then indeed Q_ϕ is not conserved

$$\frac{g^2}{16\pi^2}\int d^4x \mathrm{Tr}\, G_{\mu\nu}\tilde{G}^{\mu\nu} = \int d^3x \left(j_A^0\big|_{t_2} - j_A^0\big|_{t_1}\right) = Q_\phi^{(2)} - Q_\phi^{(1)} = n_2 - n_1, \tag{2.12}$$

where the gradient terms vanish as $\partial_i A_i \to 0$ for $|x| \to \infty$. These field configurations are perfectly valid solutions to the Euclidean equation of motion, have finite energy, and are the aforementioned instantons that can be interpreted as tunneling solutions between vacua of different topological charges.

The presence of instantons changes the interpretation of the vacuum. Previously, we classified a degenerate vacuum $|n\rangle$ of the system by the number of windings, which can now be accessed by tunneling processes. As a consequence we should define the vacuum as a superposition of all winding numbers, usually called the θ-vacuum (the $|n\rangle$ states are sometimes called pre-vacua)

$$|\theta\rangle = \sum_{n=-\infty}^{\infty} e^{-in\theta}\,|n\rangle\,, \tag{2.13}$$

where θ is an angle, which is a physical parameter. Universes with different values of θ cannot be accessed

$$\langle\theta'|\, e^{-iHt}\,|\theta\rangle = \sum_{n_1,n_2} e^{in_2(\theta'-\theta)} e^{i\theta(n_2-n_1)}\,\langle n_2|\, e^{-iHt}\,|n_1\rangle = \delta(\theta'-\theta)\sum_{\Delta n} e^{i\Delta n\theta}\,\langle \Delta n|\, e^{-iHt}\,|0\rangle\,, \tag{2.14}$$

where we used the fact that transition amplitudes correspond to large energy processes and that the Hamiltonian commutes with such operators. The last expression can be pleasingly rewritten in terms of a path integral

$$\begin{aligned}\sum_n e^{in\theta}\,\langle n|\, e^{-iHt}\,|0\rangle &= \sum_n e^{in\theta}\int [\mathcal{D}A_\mu]_n \exp\left\{ i\int d^4x \mathcal{L}\,[A_\mu]\right\} \\ &= \int \mathcal{D}A_\mu \exp\left\{ i\int d^4x\mathcal{L}\,[A_\mu] + \frac{\theta g^2}{16\pi^2}\mathrm{Tr}\, G_{\mu\nu}\tilde{G}^{\mu\nu}\right\}.\end{aligned} \tag{2.15}$$

Therefore, we conclude that for Yang-Mills theories, even though not arising in perturbation theory, topological non-trivial configurations are important and that one should therefore work with the modified Lagrangian

$$\mathcal{L}_{\mathrm{YM}} = -\frac{1}{4}\mathrm{Tr}\, G_{\mu\nu}G^{\mu\nu} + \frac{\theta g^2}{16\pi^2}\mathrm{Tr}\, G_{\mu\nu}\tilde{G}^{\mu\nu}, \tag{2.16}$$

where the second term is sometimes called θ-term. Importantly, in theories involving Fermions, it leads to physical effects which we will explore in the next section.

2.2 Anomalies and the Strong $\mathcal{CP}$ Problem

Now that we have established the necessity to include the topological θ-term, let us explore its implications for QCD, i.e. the case of the color gauge group $SU(3)$. First of all, we note that our new term violates $\mathcal{CP}$. In order to understand this fact it is useful to write $G\tilde{G}$ in terms of chromoelectric and chromomagnetic fields, $G\tilde{G} \sim \mathbf{E}^a \cdot \mathbf{B}^a$. While $\mathbf{E}^a$ stays invariant under

time reversal $\mathcal{T}$, $\mathbf{B}^a \to -\mathbf{B}^a$. Using the $\mathcal{CPT}$ theorem we conclude that the θ-term violates $\mathcal{CP}$. QCD also involves N_f fermions q_i in the fundamental representation of $SU(3)$

$$\mathcal{L} \supset i\bar{q}\not{D}q - (\bar{q}_L M_q q_R + \text{h.c.}) = \bar{q}\left(i\not{D} - m_q e^{i\gamma_5\theta_q}\right)q, \tag{2.17}$$

where $D_\mu = \partial_\mu - igA^a_\mu T^a$, $M_q = m_q e^{i\theta_q}$ is the quark mass matrix and θ_q a $\mathcal{CP}$ violating flavor matrix. In the limit $m_q \to 0$ the theory is invariant under the symmetry group

$$U(N_f)_L \times U(N_f)_R = SU(N_f)_L \times SU(N_f)_R \times U(1)_L \times U(1)_R, \tag{2.18}$$

at the classical level. Of particular interest are rotations of the global axial symmetry group $U(1)_A = U(1)_{L-R}$ which are explicitly broken at the classical level by the quark masses as can be seen by considering

$$U(1)_A : \quad q \to e^{i\gamma_5\alpha Q_\phi}q, \tag{2.19}$$

where Q_ϕ is an arbitrary $N_f \times N_f$ matrix in flavor space. The above transformation generates a non-vanishing divergence in the associated axial current j^μ_5 at the classical level

$$\partial_\mu j^\mu_5 = 2im_q\bar{q}\gamma_5 Q_\phi q. \tag{2.20}$$

However, this is not the only source of explicit breaking since $U(1)_A$ is also broken at the quantum level by the chiral Adler-Bell-Jackiw anomaly [22, 23]. The Adler-Bell-Jackiw anomaly is also the solution to the $U(1)_A$ or so-called 'missing meson' problem. In $N_f = 3$ the spontaneous breakdown of the global symmetry to the diagonal subgroup $U(3)_L \times U(3)_R \to U(3)_{L+R}$ due to confinement should give rise to $8 + 1 = 9$ pNGBs with masses much lighter than the breaking scale. However, the η', the would-be pNGB has a mass that lies close to the cut-off of the effective theory which can be directly linked to the presence of non-perturbative effects [24]. After this short digression, we realize that we should write the divergence of the axial current as

$$\partial_\mu j^\mu_5 = 2im_q\bar{q}\gamma_5 Q_\phi q + \frac{g^2}{8\pi^2}\text{Tr}[Q_\phi]\text{Tr}\, G_{\mu\nu}\tilde{G}^{\mu\nu}, \tag{2.21}$$

which includes a piece explicitly breaking the $U(1)_A$ by the topology of the QCD vacuum. The breaking due to quantum effects can also neatly be understood as the transformation of the fermion measure in the path integral which is also called Fujikawa method [25]. Now, under a global axial $U(1)_A$ transformation on the quark fields Eq. (2.19) the QCD Lagrangian transforms as

$$\begin{aligned}\mathcal{L} &\supset \bar{q}\left(i\not{D} - m_q e^{i\gamma_5\theta_q}\right)q + \frac{\theta g^2}{16\pi^2}\text{Tr}\, G_{\mu\nu}\tilde{G}^{\mu\nu} \\ &\to \bar{q}\left(i\not{D} - m_q e^{i\gamma_5(\theta_q + 2\alpha Q_\phi)}\right)q + \frac{g^2}{16\pi^2}\left(\theta + 2\alpha\text{Tr}[Q_\phi]\right)\text{Tr}\, G_{\mu\nu}\tilde{G}^{\mu\nu}.\end{aligned} \tag{2.22}$$

Now several remarks are in order. The first is to observe that with the appropriate rotation we can completely remove the topological θ term from the Lagrangian and move the θ parameter effectively into the quark masses. This has the important consequence that if one of the quark masses were zero, one could remove the θ dependence completely and it would not generate any physical effects. We also note that due to axial transformations only the linear combination

$$\bar{\theta} = \theta - \text{Arg}\,\text{Det}\, M_q, \tag{2.23}$$

where $\text{Arg}\,\text{Det}\, M_q = \text{Tr}[\theta_q]$ is physical, i.e. basis independent. Now that we know the physical parameter that measures $\mathcal{CP}$ violation in the strong interaction, we need to find an observable

that we can measure. We remove $\mathcal{L}_\theta$ from the QCD Lagrangian by an axial rotation on the quark fields, and assuming $\bar{\theta} \ll 1$ we obtain a $\mathcal{CP}$ violating operator for $N_f = 3$ flavors [26]

$$\mathcal{O}_{\mathcal{CP}} = i\bar{\theta}\frac{m_u m_d m_s}{m_u m_d + m_u m_s + m_d m_s}\sum_{q=u,d,s}\bar{q}\gamma_5 q. \tag{2.24}$$

which contributes to an electric dipole moment of the neutron (nEDM) d_n (see e.g. Refs. [27–29]). The nEDM is defined via the non-relativistic Hamiltonian

$$\mathcal{H} = -d_n \mathbf{E}\cdot\hat{S} \tag{2.25}$$

where the current best experimental bound is [4]

$$|d_n^{\text{exp}}| < 1.8\cdot 10^{-26}\, e\,\text{cm}\ \ (90\%\,\text{CL}). \tag{2.26}$$

One can write Eq. (2.25) in terms of a Lorentz covariant Lagrangian

$$\mathcal{L} = -\frac{i}{2}d_n \bar{n}\sigma_{\mu\nu}\gamma_5 n F^{\mu\nu}. \tag{2.27}$$

The actual calculation of the nEDM can be done via different techniques, i.e. chiral perturbation theory, QCD sum rules, on the lattice, holography, which all show an overall agreement. As usual, however, one can understand the order of magnitude by simple NDA. The dipole is a dimension 5 operator which is naively suppressed by one order of m_n. However, in order to contribute to the nEDM we need a quark mass insertion and therefore find the scaling

$$\mathcal{L} \sim \frac{e}{16\pi^2}\frac{i m_q \sin\bar{\theta}}{m_n^2}\bar{n}\sigma_{\mu\nu}\gamma_5 n F^{\mu\nu} \simeq \bar{\theta}\frac{e}{16\pi^2}\frac{i m_q}{m_n^2}\bar{n}\sigma_{\mu\nu}\gamma_5 n F^{\mu\nu}, \tag{2.28}$$

which implies that the contribution to the nEDM is

$$|d_n| \sim \bar{\theta}\frac{e}{8\pi^2}\frac{m_q}{m_n^2} \simeq 10^{-4}\,\bar{\theta}\,e\,\text{GeV}^{-1}. \tag{2.29}$$

This already gives a good feeling for the smallness of $\bar{\theta}$ but using a precise sum rule calculation [30] one obtains a bound

$$|\bar{\theta}| < 10^{-10}. \tag{2.30}$$

The puzzling smallness of $\bar{\theta}$ is what is called the strong $\mathcal{CP}$ problem. The parameter $\bar{\theta}$ could take any value from 0 to π and according to the EFT paradigm should rather be $\sim \mathcal{O}(1)$ than this small. The strong $\mathcal{CP}$ problem hence begs for a natural explanation of why the $\bar{\theta}$-parameter is so small. One could of course naively argue that the smallness of $\bar{\theta}$ is not a naturalness problem because if $\bar{\theta} \to 0$ then $\mathcal{CP}$ is conserved in the strong sector and the theory would be considered technically natural. However, if we remember that we actually deal with the linear combination $\bar{\theta} = \theta - \text{Arg}\,\text{Det}\,M_q$, where the second term comes from the $\mathcal{CP}$ violating phases in the quark mass matrix and that $\mathcal{CP}$ is actually violated in the weak sector of the SM, then the smallness of $\bar{\theta}$ implies a cancellation of two terms that a priori have nothing to do with each other.

We would also like to argue that similar problems for the electroweak sector do not appear since the corresponding angle can always be made unphysical by the appropriate rotation. Imagine the operator from the weak sector $\sim \theta_w\,\text{Tr}\,W\tilde{W}$. Due to the chiral nature of $SU(2)_L$ we can first remove the topological term from the Lagrangian by performing an axial rotation on the left-handed fields. But then we can remove the phase simply by performing a rotation on the right-handed fields without re-introducing the topological term.

One of the easiest solutions to the strong $\mathcal{CP}$ problem would be to set one of the quark masses to zero. In this case, we could rotate $\bar{\theta}$ into the phase of the massless quark thereby removing it from any physical observable. However, lattice simulations seem to suggest that none of the light quark masses are compatible with zero within the SM [31].

While there exist many different approaches to the strong $\mathcal{CP}$ problem we will in the following focus on a particularly thrilling and simple approach that promotes the constant $\bar{\theta}$ to a dynamical field $\phi(x)$ called the axion.

2.3 The QCD axion

The basic idea behind the axion solution to the strong $\mathcal{CP}$ problem relies on the observation that the QCD vacuum energy depends on $\bar{\theta}$. In ChPT, taking $N_f = 2$ one can calculate the energy density explicitly to find [32]

$$\varepsilon(\bar{\theta}) = -m_\pi^2 f_\pi^2 \left(\sqrt{1 - \frac{4 m_u m_d}{(m_u + m_d)^2} \sin^2\left(\frac{\bar{\theta}}{2}\right)} - 1 \right), \tag{2.31}$$

where m_π, f_π are the mass and decay constant of the pion and m_u, m_d the up- and down-quark mass respectively. Note that one can also calculate the energy density using a dilute instanton gas approximation, which yields a similar periodic result, see Ref. [33]. In any case, we can make the important observation that the the energy density is minimum if $\bar{\theta} = 0$. This was proven by Vafa and Witten in Ref. [34]. Note that the proof does not rely on the explicit evaluated form of the energy density. Thus if $\bar{\theta}$ was a dynamical variable, it would naturally be relaxed to $\bar{\theta} = 0$ which is exactly what the QCD axion exploits.

The mechanism that first realized this idea was introduced by Peccei and Quinn [5, 6] and who introduced an additional axial $U(1)_{\text{PQ}}$ symmetry which effectively allowed to shift the $\bar{\theta}$ by an arbitrary phase which they set to cancel $\bar{\theta}$. It was later realized by Weinberg and Wilczek [7,8] that the $U(1)_{\text{PQ}}$ symmetry, despite being explicitly broken by non-topological effects, is broken spontaneously, giving rise to a pNGB, the PQWW QCD axion $\phi(x)$. The axion transforms under $U(1)_{\text{PQ}}$ as

$$\phi \to \phi - \alpha f_\phi, \tag{2.32}$$

where f_ϕ is the axion decay constant and couples due to the $U(1)_{\text{PQ}}$ -QCD anomaly as

$$\mathcal{L}_\phi = \left(\frac{\phi}{f_\phi} + \bar{\theta} \right) \frac{g^2}{16\pi^2} \text{Tr}\, G_{\mu\nu} \tilde{G}^{\mu\nu}. \tag{2.33}$$

The shift symmetry can be used to eliminate $\bar{\theta}$ from Eq. (2.33) in the UV. In the IR, i.e. below the QCD phase transition, instanton effects break the shift symmetry and give rise to a potential for the QCD axion, which takes exactly the (generalized) form of Eq. (2.31) but with $\bar{\theta} \to \phi(x)/f_\phi$

$$V(\phi) = -m_\pi^2 f_\pi^2 \left(\sqrt{1 - \frac{4 m_u m_d}{(m_u + m_d)^2} \sin^2\left(\frac{\phi}{2 f_\phi}\right)} - 1 \right), \tag{2.34}$$

which is minimized at $\langle \phi \rangle = 0$ therefore dynamically solving the strong $\mathcal{CP}$ problem and predicting the existence of a light new scalar with mass

$$m_\phi^2 = \frac{m_u m_d}{(m_u + m_d)^2} \frac{m_\pi^2 f_\pi^2}{f_\phi^2}. \tag{2.35}$$

The early realization by Peccei, Quinn, Weinberg, and Wilczek (PQWW) tied the breaking of $U(1)_{\rm PQ}$ to the spontaneous symmetry breaking of the electroweak sector in a two Higgs doublet model where the anomaly is generated by SM quarks charged under $U(1)_{\rm PQ}$. Since the breaking is fixed at the electroweak scale $f_\phi \simeq v_{\rm EW} \simeq 246\,\text{GeV}$, which sets the interaction scale with SM particles as well as implying $m_\phi \simeq 20\,\text{keV}$, laboratory searches quickly excluded the PQWW axion, see Ref. [29] and references therein.

Even though the original PQWW axion was soon ruled out it is straightforward to generalize the original idea and tie the $U(1)_{\rm PQ}$ breaking to a higher scale. Since the couplings to SM particles are now much suppressed by a large scale they can easily evade most laboratory bounds and are sometimes called invisible axion models.

Before discussing the effective axion Lagrangian in the IR we now move on to discuss explicit realizations of benchmark invisible QCD axion models. UV completions can broadly be divided into two groups classified by how the QCD anomaly of the $U(1)_{\rm PQ}$ is realized. Models, where SM quarks carry the anomaly, are called Dine-Fischler-Srenicki-Zhitnitsky (DSFZ) [35,36], while models where the QCD anomaly is carried by additional colored fermions are called Kim-Shifman-Vainshtein-Zakharov (KSVZ) [37, 38] type.

2.3.1 KSVZ axion

In KSVZ axion models [37, 38] the QCD anomaly is carried by additional vector-like fermions in the fundamental of $SU(3)_c$ and singlet under $SU(2)_L$ $\mathcal{Q} = \mathcal{Q}_L + \mathcal{Q}_R$. In addition, the SM is also extended by a complex SM singlet scalar Φ. For a massless fermion the KSVZ Lagrangian

$$\mathcal{L}_{\rm KSVZ} = |\partial_\mu \Phi|^2 + \bar{\mathcal{Q}} i \not{D} \mathcal{Q} - (y_\mathcal{Q} \Phi \mathcal{Q}_L \mathcal{Q}_R + \text{h.c.}) - V(\Phi) \tag{2.36}$$

with the potential

$$V(\Phi) = \lambda \left(|\Phi|^2 - \frac{v_\phi^2}{2} \right)^2 \tag{2.37}$$

is invariant under the $U(1)_{\rm PQ}$ symmetry

$$\Phi \to e^{i\alpha} \Phi, \quad \mathcal{Q}_L \to e^{i\alpha/2} \mathcal{Q}_L, \quad \mathcal{Q}_R \to e^{-i\alpha/2} \mathcal{Q}_R. \tag{2.38}$$

One can impose that $\mathcal{Q}$ stays massless by a discrete gauge symmetry [37]: $\mathcal{Q}_L \to -\mathcal{Q}_L$, $\mathcal{Q}_R \to -\mathcal{Q}_R$. The potential Eq. (2.37) features a spontaneous symmetry breaking at the scale v_ϕ and decomposing the complex scalar field into an angle and a radial mode

$$\Phi = \frac{1}{\sqrt{2}} (v_\Phi + r_\Phi) e^{i\phi/v_\Phi} \tag{2.39}$$

we find that the axion ϕ appears as the (at tree level massless) GB of the $U(1)_{\rm PQ}$, while both the radial mode r_ϕ and the fermion pick up a mass of the order $\sim v_\Phi$. To be precise $m_{r_\phi} = \sqrt{2\lambda} v_\Phi$ and $m_\mathcal{Q} = y_\mathcal{Q} v_\Phi / \sqrt{2}$. It is the mass term of the fermion

$$\mathcal{L}_{\rm KSVZ} \supset -m_\mathcal{Q} \bar{\mathcal{Q}}_L \mathcal{Q}_R e^{i\phi/v_\Phi} + \text{h.c.}, \tag{2.40}$$

that both, gives rise to the topological term by a (axion) field dependent axial $U(1)_{\rm PQ}$ transformation

$$\mathcal{Q} \to e^{-i\gamma_5 \phi/2v_\Phi} \mathcal{Q} \quad \to \quad \delta\mathcal{L}_{\rm KSVZ} = \frac{g^2}{16\pi^2} \frac{\phi}{v_\Phi} \text{Tr}\, G\tilde{G}. \tag{2.41}$$

and removes the interaction via the mass term with the fermion. Here we can identify $v_\Phi = f_\phi$ and note that we can use the axion shift symmetry to remove the $\bar{\theta}$ angle, solving the strong $\mathcal{CP}$

problem. We also generate an axial current interaction with the fermion $\sim \partial_\mu\phi\bar{Q}\gamma^\mu\gamma_5 Q$ because we performed a field dependent transformation. This interaction is however meaningless because $\mathcal{Q}$ is static below v_Φ. Moreover, we note that the only interaction of the KSVZ axion to SM particles is via the operator $\phi \mathrm{Tr}\, G\tilde{G}$, which is in some sense a model independent contribution for QCD axions.

2.3.2 DSFZ axion

The DSFZ axion [35,36] is a simple extension of the PQWW axion by a complex SM scalar scalar field Φ that allows to decouple the PQ breaking scale from the EW scale. As the PQWW it includes two Higgs doublets $H_u \sim (1,2,-\frac{1}{2})$ and $H_d \sim (1,2,+\frac{1}{2})$ and we can write the potential as

$$\begin{aligned} V_{\mathrm{DSFZ}}(H_u,H_d,\Phi) \supset\, & c_1|H_u|^2|H_d|^2 + (c_2|H_u|^2 + c_3|H_d|^2)|\Phi|^2 + c_4\left[H_u H_d \Phi^{\dagger 2} + \mathrm{h.c.}\right] \\ & + c_5|H_u H_d|^2 + c_6|H_u\tilde{H}_d|^2 \end{aligned} \tag{2.42}$$

The above potential contains all terms allowed by gauge symmetry and a non-hermitian operator which explicitly breaks the re-shuffling symmetry of the three scalar fields into two independent $U(1)$'s, to be identified with hypercharge and the PQ symmetry

$$U(1)_{H_u} \times U(1)_{H_d} \times U(1)_\Phi \to U(1)_Y \times U(1)_{\mathrm{PQ}}. \tag{2.43}$$

The interactions to the SM fermions (we couple equally to all three generations of SM fermions) divides the DSFZ model into type-I and type-II with the difference that either we couple H_d or $\tilde{H}_u = i\sigma_2 H_u^{*t}$ to SM leptons while the quark couplings are identical

$$\text{DSFZ-I:} \quad \mathcal{L}_Y = -y_U \bar{Q}_L u_R H_u - y_D \bar{Q}_L d_R H_d - y_E \bar{\ell}_L e_R H_d + \mathrm{h.c.} \tag{2.44a}$$

$$\text{DSFZ-II:} \quad \mathcal{L}_Y = -y_U \bar{Q}_L u_R H_u - y_D \bar{Q}_L d_R H_d - y_E \bar{\ell}_L e_R \tilde{H}_u + \mathrm{h.c.} \tag{2.44b}$$

We chose our potential Eq. (2.42) such that all scalars pick up a VEV

$$H_u \supset \frac{v_u}{2} e^{i\phi_d/v_u}\begin{pmatrix}1\\0\end{pmatrix}, \quad H_d \supset \frac{v_d}{2} e^{i\phi_d/v_d}\begin{pmatrix}0\\1\end{pmatrix}, \quad \Phi \supset \frac{v_\Phi}{\sqrt{2}} e^{i\phi_\Phi/v_\Phi}, \tag{2.45}$$

where we neglected EM charged angles and radial modes. The physical axion is the linear combination that appears in front of the PQ current, which, neglecting fermion interactions, one can write as

$$\begin{aligned} J_\mu^{\mathrm{PQ}} \supset & - X_\Phi \Phi^\dagger i\overset{\leftrightarrow}{\partial}_\mu \Phi - X_{H_u} H_u^\dagger i\overset{\leftrightarrow}{\partial}_\mu H_u - X_{H_d} H_d^\dagger i\overset{\leftrightarrow}{\partial}_\mu H_d \\ = & \sum_{i=\Phi,u,d} X_i v_i \partial_\mu \phi_i, \end{aligned} \tag{2.46}$$

where $X_{H_{u,d}} = X_{u,d}$ for convenience. Therefore, the axion field is defined as

$$\phi = \frac{1}{v_\phi}\sum_i X_i v_i \phi_i, \quad v_\phi^2 = \sum_i X_i^2 v_i^2, \tag{2.47}$$

such that under a PQ transformation $\phi_i \to \phi_i + \alpha X_i v_i$ the axion transforms as $\phi \to \phi + \alpha v_\phi$. PQ charges X_i are now determined by requiring that $H_u H_d \Phi^{\dagger 2}$ stays invariant which gives $X_u + X_d - 2X_\Phi = 0$ and the orthogonality between J_μ^{PQ} with the corresponding contribution to

the hypercharge current $J_\mu^Y = \sum_i Y_i v_u \phi_i$, which prevents axion mixing into Z-bosons and give $X_d/X_u = v_u^2/v_d^2$. Now we can fix the PQ charges to

$$X_\Phi = 1, \quad X_u = 2\cos^2\beta, \quad X_u = 2\sin^2\beta, \tag{2.48}$$

where $\tan\beta = v_u/v_d$ or $\sin\beta = v_u/v_{\rm EW}$. Therefore,

$$v_\phi^2 = v_\Phi^2 + v_{\rm EW}^2 \sin^2(2\beta) \simeq v_\Phi^2, \tag{2.49}$$

where we used that $v_\Phi \gg v_{\rm EW}^2$. In terms of the axion field the Yukawa sector for type-I DSFZ models Eq. (2.44a) becomes

$$\mathcal{L}_{\rm DSFZ} \supset -m_u \bar{u}_L u_R e^{iX_u\phi/v_\phi} - m_d \bar{d}_L d_R e^{iX_d\phi/v_\phi} - m_\Psi \bar{\Psi}_L \Psi_R e^{iX_d\phi/v_\phi} + \text{h.c.} \tag{2.50}$$

from which we can remove the axion by appropriate field redefinitions. Unlike the KSVZ axion, we now generate both a $G\tilde{G}$ and a $F\tilde{F}$ term because of the QCD and EM anomalies with coefficients N and E respectively and one obtains

$$\begin{aligned} N &= \sum_{i=u,d} N_i = N_g\left(\frac{1}{2}X_u + \frac{1}{2}X_d\right) = 3, \\ E &= \sum_{i=u,d} N_i = N_g\left(3\left(\frac{2}{3}\right)^2 X_u + 3\left(-\frac{1}{3}\right)^2 X_d + (-1)^2)X_d\right) = 8, \end{aligned} \tag{2.51}$$

with $N_g = 3$ the number of SM fermion generations. Therefore, upon defining $f_\phi = v_\phi/2N$ we find the topological part of the DSFZ-I Lagrangian to be

$$\delta\mathcal{L}_{\rm DSFZ} = \frac{g^2}{16\pi^2}\frac{\phi}{f_\phi}\text{Tr}\, G\tilde{G} + \frac{e^2}{16\pi^2}\frac{E}{N}\frac{\phi}{f_\phi}\text{Tr}\, F\tilde{F}. \tag{2.52}$$

As we have already seen for the KSVZ axion, the field dependent PQ transformation does not leave invariant the fermion kinetic term such that we generate the following derivative couplings in this case to SM fermions that cannot be neglected

$$\delta\mathcal{L}_{\partial\Psi} = \frac{1}{3}\frac{\partial_\mu\phi}{2f_\phi}\left[\cos^2\beta\,\bar{u}\gamma^\mu\gamma_5 u + \sin^2\beta\,\bar{d}\gamma^\mu\gamma_5 d + \sin^2\beta\,\bar{e}\gamma^\mu\gamma_5 e\right]. \tag{2.53}$$

The analysis is straight forward for DSFZ-II models and simply involves the change $X_d \to -X_u$ and yields $E = 2$. Lastly, for DSFZ models it is important to determine the allowed range of $\tan\beta = v_u/v_d$ which is limited among other things by loss of perturbativity in top and bottom quark Yukawas and one finds [29] $\tan\beta \in [0.25, 170]$.

2.4 QCD axion couplings

2.4.1 From the UV...

Now that we have seen explicit realizations of the QCD axion in the UV we can write down without loss of generality an effective model-dependent axion Lagrangian valid at energies below the PQ breaking scale v_ϕ and the electroweak scale $v_{\rm EW}$ at leading order in $1/f_\phi$ [32]

$$\begin{aligned} \mathcal{L} &= \mathcal{L}_{\rm QCD,0} - (\bar{q}_L M_q q_R + \text{h.c.}) \\ &\quad + \frac{1}{2}(\partial_\mu\phi)^2 + \frac{g^2}{16\pi^2}\frac{\phi}{f_\phi}\text{Tr}\, G\tilde{G} + \frac{1}{4}\phi g^0_{\phi\gamma\gamma}\text{Tr}\, F\tilde{F} + \frac{\partial_\mu\phi}{2f_\phi}J^\mu_{\rm PQ,0}, \end{aligned} \tag{2.54}$$

with

$$\mathcal{L}_{\text{QCD},0} = -\frac{1}{4}\text{Tr}\, G^{\mu\nu}G_{\mu\nu} + i\bar{q}\not{D}q,, \tag{2.55a}$$

$$J^{\mu}_{\text{PQ},0} = \sum_q c^0_q \bar{q}\gamma^{\mu}\gamma_5 q,, \tag{2.55b}$$

$$g^0_{\phi\gamma\gamma} = \frac{e^2}{4\pi^2 f_\phi}\frac{E}{N}, \tag{2.55c}$$

where c^0_q are model dependent constants (for KSVZ type models $c^0_q = 0$, while *e.g.* for DSFZ-I $c^0_u = \frac{1}{3}\cos^2\beta$) and E/N is the ratio of the EM and the color anomaly (for KSVZ type models $E/N = 0$, while *e.g.* for DSFZ-I $E/N = 8/3$). We have here used the shift-symmetry to remove the QCD $\bar{\theta}$ angle.

In the limit of vanishing quark masses, the Lagrangian in Eq. (2.54) is invariant under global chiral transformations of

$$U(N_f)_L \times U(N_f)_R = SU(N_f)_L \times SU(N_f)_R \times U(1)_V \times U(1)_A \tag{2.56}$$

modulo the fact that $U(1)_A$ is explicitly broken at the quantum level by the QCD anomaly. It is convenient to change basis by the axial quark field redefinition

$$q \to e^{i\gamma_5 \frac{\phi}{2f_\phi}Q_\phi} q, \tag{2.57}$$

where Q_ϕ is an arbitrary flavor matrix modulo the constraint that $\text{Tr}Q_\phi = 1$, such that Eq. (2.54) now reads

$$\mathcal{L} = \mathcal{L}_{\text{QCD},0} - (\bar{q}_L M_\phi q_R + \text{h.c.}) + \frac{1}{2}(\partial_\mu\phi)^2 + \frac{1}{4}\phi g_{\phi\gamma\gamma}\text{Tr}\, F\tilde{F} + \frac{\partial_\mu\phi}{2f_\phi}J^{\mu}_{\text{PQ}}, \tag{2.58}$$

with taking $N_f = 2$

$$J^{\mu}_{\text{PQ}} = J^{\mu}_{\text{PQ},0} - \bar{q}\gamma^{\mu}\gamma_5 Q_\phi q, \tag{2.59a}$$

$$g_{\phi\gamma\gamma} = \frac{e^2}{4\pi^2 f_\phi}\left[\frac{E}{N} - 6\text{Tr}\,\left(Q_\phi Q^2\right)\right], \tag{2.59b}$$

$$M_\phi = e^{i\frac{\phi}{2f_\phi}} M_q e^{i\frac{\phi}{2f_\phi}}, \quad M_q = \text{diag}\,(m_u, m_d)\,, \quad Q = \text{diag}\,(2/3, -1/3)\,. \tag{2.59c}$$

In the following we will focus on couplings of the QCD axion to quarks, and in the IR to nucleons and pions and we neglect the photon coupling. At lower energies around the QCD scale, a quark condensate develops and QCD becomes strongly coupled. The effective theory below the QCD scale is described by chiral perturbation theory ChPT which will be the topic of the next subsection. Since ChPT is the effective theory of pions it is useful to find a basis in which the axion does not mix with the neutral pion (at tree level), which (in hindsight) is ensured by a particular choice of [32]

$$Q_\phi = \frac{M_q^{-1}}{\text{Tr}\, M_q^{-1}} = \frac{\text{diag}[1, z]}{1+z}, \quad z \equiv \frac{m_u}{m_d} \simeq 0.48. \tag{2.60}$$

Using the Fierz identity $(\sigma^a)_{ij}(\sigma^a)_{kl} = 2\delta_{il}\delta_{kj} - \delta_{ij}\delta_{kl}$ the PQ current separates into a isoscalar and isovector piece

$$J^{\mu}_{\text{PQ}} = \bar{q}\gamma^{\mu}\gamma_5\left(c_{u+d}\mathbb{1} + c_{u-d}\tau_3\right)q, \tag{2.61}$$

with

$$c_{u-d} = \frac{1}{2}\left(c_u^0 - c_d^0 - \frac{1-z}{1+z}\right), \tag{2.62a}$$

$$c_{u+d} = \frac{1}{2}\left(c_u^0 + c_d^0 - 1\right). \tag{2.62b}$$

This is handy for the construction of the effective theory, which we show in detail in App. A. In regard to the construction it is furthermore useful to map the axion Lagrangian Eq. (2.58) with PQ current Eq. (2.61) to a general QCD Lagrangian with external local sources. In general the QCD Lagrangian containing external fields takes the form [39, 40]

$$\mathcal{L}_{\text{ext}} = \bar{q}_L \gamma^\mu \left(\ell_\mu + \ell_\mu^s\right) q_L + \bar{q}_R \gamma^\mu \left(r_\mu + r_\mu^s\right) q_R - \bar{q}_L \left(s - ip\right) q_R - \bar{q}_R \left(s + ip\right) q_L, \tag{2.63}$$

where s and p are scalar and pseudo-scalar sources while $\ell_\mu^{(s)}$ and $r_\mu^{(s)}$ are left- and right-handed isovector (isoscalar) vector parity eigenstates respectively. They are related to isovector (isoscalar) vector and axial-vector sources by

$$\begin{aligned} v_\mu^{(s)} &= \frac{1}{2}\left(r_\mu^{(s)} + \ell_\mu^{(s)}\right), \\ a_\mu^{(s)} &= \frac{1}{2}\left(r_\mu^{(s)} - \ell_\mu^{(s)}\right). \end{aligned} \tag{2.64}$$

This permits the mapping

$$\begin{aligned} v_\mu &= v_\mu^s = 0, \\ a_\mu &= c_{u-d}\frac{\partial_\mu \phi}{2f_\phi}\tau_3, \\ a_\mu^s &= c_{u+d}\frac{\partial_\mu \phi}{2f_\phi}\mathbb{1}, \\ s &= \operatorname{Re} M_\phi = M_q \cos\left(\frac{\phi}{f_\phi}Q_\phi\right), \\ p &= -\operatorname{Im} M_\phi = -M_q \sin\left(\frac{\phi}{f_\phi}Q_\phi\right). \end{aligned} \tag{2.65}$$

Therefore, adding the axion to QCD can be thought of as adding the four external fields $\left\{s, p, a_\mu, a_\mu^s\right\}$ to the QCD Lagrangian. It is at this point that we can fully appreciate the change of basis performed in Eq. (2.57) which effectively allowed us to write all derivative couplings as external sources while the only shift-symmetry breaking couplings are captured in the axion-dressed quark masses M_ϕ. Next we discuss the effective theory of the axion with IR QCD degrees of freedom.

2.4.2 . . . to the IR. . .

Around the QCD scale, $\Lambda_{\text{QCD}} \simeq 0.1\,\text{GeV}$, a quark condensate develops $\langle \bar{q}_R q_L + \text{h.c.}\rangle \neq 0$ in consequence of QCD becoming strongly coupled. This spontaneously breaks down the global symmetry of Eq. (2.56) to its diagonal subgroub

$$SU(2)_L \times SU(2)_R \times U(1)_V \to SU(2)_{L+R} \times U(1)_V, \tag{2.66}$$

which again for $N_f = 2$ gives rise to (not counting the anomalous $U(1)_A$) three pNGB's called pions, whose effective theory can be described by chiral perturbation theory ChPT, i.e. a systematic expansion in pion momenta over a cut-off scale p/Λ_χ, compatible with the underlying

symmetries. The cut-off scale of ChPT is roughly given by the next higher resonance in the theory i.e. for $N_f = 2$ it would correspond to the kaon mass $\Lambda_\chi = m_K \simeq 495\,\text{MeV}$ or for $N_f = 3$ the ρ meson $\Lambda_\chi = m_\rho \simeq 775\,\text{MeV}$ [41]. There exists a general framework to construct the full theory below a symmetry breaking scale, developed by Callan-Coleman-Wess-Zumino (CCWZ) [42, 43], which can be used to describe the effective dynamics of fluctuations around the chiral condensate. We do not review the subject of CCWZ construction in generality here but refer the reader to the recent review Ref. [44]. Pions are captured in the unitary 2×2 flavor matrix

$$U = e^{i\frac{\Pi}{f_\pi}}, \quad \Pi = \pi^a \tau^a = \begin{pmatrix} \pi^0 & \sqrt{2}\pi^+ \\ \sqrt{2}\pi^- & -\pi^0 \end{pmatrix}, \tag{2.67}$$

with the pion decay constant $f_\pi \simeq 93\,\text{MeV}$ and τ^a the Pauli matrices. We find the covariant derivative for the pion field to be

$$\nabla_\mu U = \partial_\mu U - i\{a_\mu, U\} - 2ia_\mu^s U, \tag{2.68}$$

which is one of the fundamental building blocks of the effective axion-pion theory. Another spurion in the pion sector can be defined as

$$\chi = 2BM_\phi^\dagger = 2B(s + ip), \tag{2.69}$$

where B is a constant related to the chiral condensate. Out of these, the only non-trivial, hermitian, $\mathcal{C}$ and $\mathcal{P}$ invariant scalars under Lorentz are collected in the Lagrangian

$$\mathcal{L}_{\pi\pi} = \mathcal{L}_{\pi\pi}^{(2)} + \ldots, \tag{2.70a}$$

$$\mathcal{L}_{\pi\pi}^{(2)} = \frac{f_\pi^2}{4}\text{Tr}\Big[\nabla_\mu U(\nabla^\mu U)^\dagger + \Big(\chi U^\dagger + \chi^\dagger U\Big)\Big]. \tag{2.70b}$$

Higher order pion terms are not needed for our analysis, however, writing down the Lagrangian including the axion is straightforward.

Note that another choice for the arbitrary flavor matrix $Q_\phi \sim \mathbb{1}$, does not remove the tree level mixing with the neutral pion, but instead allows to calculate the axion potential from the Lagrangian Eq. (2.70b) once pions are integrated out [32]. With some algebra one finds

$$V(\phi, \pi^0) = -m_\pi^2 f_\pi^2 \sqrt{1 - \frac{4m_u m_d}{(m_u + m_d)^2}\sin^2\left(\frac{\phi}{2f_\phi}\right)}\cos\left(\frac{\pi_0}{f_\pi} - \varphi\right), \tag{2.71}$$

with

$$\tan\varphi = \frac{m_u - m_d}{m_u + m_d}\tan\left(\frac{\phi}{2f_\phi}\right), \tag{2.72}$$

which is minimum for $\langle\pi^0\rangle = f_\pi\varphi$, such that one exactly recovers the potential for the axion we have already seen in Eq. (2.34).

Next up we want to include baryons to our theory. While the inclusion of baryons in the effective relativistic theory spoils the systematic expansion in loop momenta due to the introduction of a heavy mass scale, it has been pursuit since the late 1960's by [40, 42, 43, 45–47] and others. For recent reviews we refer to Refs. [41, 48, 49]. This problem can however be circumvented by going to the ultra non-relativistic limit in which the heavy nucleon can effectively be integrated out up small residual momenta. This limit is known has the heavy baryon limit of chiral perturbation theory (HBChPT). We combine the proton (p) and neutron (n) in the isospin doublet

$$\Psi = \begin{pmatrix} p \\ n \end{pmatrix}, \tag{2.73}$$

which transforms non-linearly under chiral transformations. Note that the isospin doublet Ψ transforms as a pure vector quantity, for details see App. A. Since Ψ is a singlet under axial transformations, the presence of an external axial source, as it is the case for the axion (see Eq. (2.65)), does not change its transformation behaviour. Especially, while the covariant derivative of the pion fields got modified, the covariant derivative for the nucleon field is a pure vector quantity and we find

$$\begin{aligned} D_\mu \Psi &= (\partial_\mu + \Gamma_\mu)\,\Psi, \\ \Gamma_\mu &= \frac{1}{2}\left[u^\dagger(\partial_\mu - i r_\mu)u + u(\partial_\mu - i\ell_\mu)u^\dagger\right], \end{aligned} \tag{2.74}$$

where Γ_μ is the chiral connection and we defined

$$u = \sqrt{U}. \tag{2.75}$$

One can construct a corresponding hermitian isovector axial vector object containing one derivative, called the vielbein

$$u_\mu = i\left[u^\dagger(\partial_\mu - i r_\mu)u - u(\partial_\mu - i\ell_\mu)u^\dagger\right] = i u^\dagger\left(\partial_\mu U - i r_\mu U + i U \ell_\mu\right) u^\dagger. \tag{2.76}$$

Furthermore we need a non-linearly transforming analog to the field χ, which is constructed from the hermitian and anti-hermitian combinations

$$\chi_\pm = u^\dagger \chi u^\dagger \pm u \chi^\dagger u. \tag{2.77}$$

At first chiral order $O(p)$ we find the relativistic pion nucleon Lagrangian invariant under chiral symmetries $\mathcal{C}$ and $\mathcal{P}$, including the axion to be

$$\mathcal{L}_{\pi N}^{(1)} = \bar{\Psi}\left(i\not{D} - m_N + \frac{g_A}{2}\not{u}\gamma_5 + \frac{g_0}{2}\not{\hat{u}}\gamma_5\right)\Psi. \tag{2.78}$$

At the next higher chiral order $O(p^2)$ we find the most general Lagrangian to be

$$\begin{aligned} \mathcal{L}_{\pi N}^{(2)} = \bar{\Psi}\Bigg[& c_1 \langle \chi_+ \rangle - \left(\frac{c_2}{8m_N^2}\langle u_\mu u_\nu\rangle D^{\mu\nu} + \text{h.c.}\right) + \frac{c_3}{2} u\cdot u + c_4 \frac{i}{4}\left[u_\mu, u_\nu\right]\sigma^{\mu\nu} \\ & + c_5 \tilde{\chi}_+ - \left(\frac{c_8}{8m_N^2}\langle \hat{u}_\mu u_\nu\rangle D^{\mu\nu} + \text{h.c.}\right) + \frac{c_9}{2}\hat{u}\cdot u\Bigg]\Psi, \end{aligned} \tag{2.79}$$

where $\langle X\rangle$ denotes the flavor trace and $\tilde{X} = X - \langle X\rangle/2$ singles out the isovector piece. Note that we dropped all $1/f_\phi^2$ terms, and used $\propto [\hat{u}_\mu, u_\nu] \sim \partial_\mu\phi\partial_\nu\pi^a\,[\mathbb{1}, \tau^a] = 0$, as well as $\propto [\hat{u}, \hat{u}] = 0$ to eliminate terms. Note that $c_{6,7}$ are terms proportional to the EM field strength tensor, which we do not include here.

The relativistic treatment of nucleons in the effective theory is not really sensible since the underlying momentum expansion breaks down and is dealt with in HBChPT, which is the topic of the next subsection.

2.4.3 ... to HBChPT

The introduction of baryons is not as straight forward since their mass lies at the cut-off of the effective theory. To circumvent this problem, we perform a double expansion in residual nucleon momenta k/m_N and k/Λ_χ, defined in Eq. (2.80). The resulting effective theory is called HBChPT (see e.g. [41, 48, 49] for reviews). Power counting in HBChPT, developed in [50–53], is

complicated by the fact that both $i\partial_t\Psi \sim m_N\Psi$ are quantities of $\mathcal{O}(1)$, i.e. $m_N \sim \Lambda_\chi$. We split the nucleon momentum into a piece proportional to its mass and the small residual momentum k^μ, which was first done in the context of heavy quark effective field theory [54] but can be written in the same way for nucleons as [55, 56]

$$p^\mu = m_N v^\mu + k^\mu, \tag{2.80}$$

where we choose $v^\mu = (1, \mathbf{0})^T$ such that $v \cdot k \ll m_N$. We split Ψ into velocity dependent heavy and light components and integrate out the heavy component (see again Refs. [48, 49] for pedagogical reviews). The light component can then be organised in terms of the small quantity $(i\partial_t - m_N)\Psi$, which is of order $O(k)$. The chiral order ν of the expansion, defined as $(k/\Lambda_\chi)^\nu$, for each Feynman diagram with two external nucleons is given by

$$\nu = 2L + \sum V_i \Delta_i, \quad \Delta_i = d_i + \frac{1}{2}n_i - 2, \tag{2.81}$$

where L is the number of loops and Δ_i is the order of each vertex, appearing V_i times in the diagram. Here n_i denotes the number of nucleon lines attached to each vertex with index i, d_i the number of derivatives or m_π insertions in the i^{th} vertex. The detailed derivation of this result can also be found in App. A.6.

At leading order in the chiral and non-relativistic expansion, the pion nucleon Lagrangian Eq. (2.78) including the axion becomes

$$\hat{\mathcal{L}}^{(1)}_{\pi N} = \bar{N}\left(iv\cdot D + g_A S\cdot u + g_0 S\cdot \hat{u}\right) N, \tag{2.82}$$

where $S^\mu = \frac{i}{2}\gamma_5\sigma^{\mu\nu}v_\nu$ denotes the nucleon spin operator.

The second order Lagrangian consists of a piece from Eq. (2.79) and relativistic $1/m_N$ corrections from Eq. (2.82). We find the chiral and non-relativistic expansion the pion nucleon Lagrangian invariant under $\mathcal{C}$ and $\mathcal{P}$ including the axion to be

$$\begin{aligned}\hat{\mathcal{L}}^{(2)}_{\pi N} =& \bar{N}\left[-\frac{1}{2m_N}\left(D^2 - (v\cdot D)^2 + ig_A\{S\cdot D, v\cdot u\} + ig_0\{S\cdot D, v\cdot \hat{u}\}\right)\right.\\ &+ \hat{c}_1\langle\chi_+\rangle + \frac{\hat{c}_2}{2}(v\cdot u)^2 + \hat{c}_3(u\cdot u) + \frac{\hat{c}_4}{2}i\epsilon^{\mu\nu\rho\sigma}[u_\mu, u_\nu]v_\rho S_\sigma\\ &\left.+ \hat{c}_5\tilde{\chi}_+ + \frac{\hat{c}_8}{4}(v\cdot u)(v\cdot\hat{u}) + \hat{c}_9(u\cdot\hat{u})\right] N,\end{aligned} \tag{2.83}$$

where some of the constants $\hat{c}_i$ include relativistic $1/m_N$ corrections,

$$\begin{aligned}&\hat{c}_1 = c_1, \quad \hat{c}_2 = c_2 - \frac{g_A^2}{4m_N}, \quad \hat{c}_3 = c_3, \quad \hat{c}_4 = c_4 + \frac{1}{4m_N},\\ &\hat{c}_5 = c_5, \quad \hat{c}_8 = c_8 - \frac{g_A g_0}{m_N}, \quad \hat{c}_9 = c_9.\end{aligned} \tag{2.84}$$

It is straight forward but increasingly more tedious to include higher order corrections. All relevant couplings can now be calculated by expanding the fundamental building blocks,

$$u = \mathbb{1} + i\frac{\pi^a\tau^a}{2f_\pi} - \frac{\pi^a\pi^b\tau^a\tau^b}{8f_\pi^2} + \ldots, \tag{2.85}$$

and keeping relevant terms we find

$$\hat{u}_\mu = c_{u+d}\left(\frac{\partial_\mu\phi}{f_\phi}\right)\mathbb{1} + \ldots, \tag{2.86a}$$

$$u_\mu = -\left(\frac{\partial_\mu \pi^a}{f_\pi}\right)\tau^a + c_{u-d}\left(\frac{\partial_\mu \phi}{f_\phi}\right)\tau_3 + c_{u-d}\left(\frac{\pi^a \pi^b \partial_\mu \phi}{2 f_\phi f_\pi^2}\right)\left(\tau^b \delta^{3a} - \tau^3 \delta^{ab}\right) + \dots, \tag{2.86b}$$

$$D_\mu = \partial_\mu + i c_{u-d}\left(\frac{\pi^a \partial_\mu \phi}{2 f_\pi f_\phi}\right)\epsilon^{ab3}\tau^b + \dots, \tag{2.86c}$$

$$\widetilde{\chi}_+ = m_\pi^2 \left(\frac{4 m_u m_d}{(m_u + m_d)^2}\right)\left(\frac{\pi^a \phi}{f_\pi f_\phi}\right)\tau^a + \dots\ . \tag{2.86d}$$

Note that we are neglecting the contribution $D_\mu \propto \pi^a \pi^b$, since it is kinematically suppressed for the processes we will consider in later chapters.

For later calculations of the density corrections to the axion nucleon coupling Lagrangians including more than two nucleons are also relevant. One finds these nucleon contact interactions at LO and NLO to be

$$\hat{\mathcal{L}}^{(1)}_{NN} = -\frac{1}{2} C_S (\bar{N}N)(\bar{N}N) + 2 C_T (\bar{N}SN)\cdot(\bar{N}SN), \tag{2.87a}$$

$$\hat{\mathcal{L}}^{(2)}_{\pi NN} = \frac{c_D}{2 f_\pi^2 \Lambda_\chi}(\bar{N}N)\left(\bar{N}\, S\cdot u\, N\right) + \frac{\tilde{c}_D}{2 f_\pi^2 \Lambda_\chi}(\bar{N}N)\left(\bar{N}\, S\cdot \hat{u}\, N\right). \tag{2.87b}$$

They are explicitly constructed in App. A.5

Axion nucleon couplings to leading order

The leading order axion-nucleon coupling, according to Eq. (2.82), reads

$$\hat{\mathcal{L}}^{(1)}_{\pi N} \supset \left(\frac{\partial_\mu \phi}{f_\phi}\right)\bar{N}\left(g_A c_{u-d}\tau^3 + g_0 c_{u+d}\mathbb{1}\right) S^\mu N, \tag{2.88}$$

which leads to the Feynman rule of the tree level ($\Delta_i = 0$, see Eq. (2.81)) axion-nucleon vertex within the HBChPT approximation,

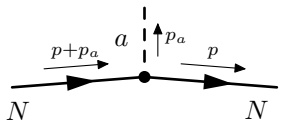

$$= \quad -\frac{1}{f_\phi}\left(g_A c_{u-d}\tau^3 + g_0 c_{u+d}\mathbb{1}\right) S\cdot p_\phi. \tag{2.89}$$

We define

$$\mathrm{Diag}(c_p, c_q)_0 \equiv g_A c_{u-d}\tau^3 + g_0 c_{u+d}\mathbb{1}, \tag{2.90}$$

and with $c^0_{u-d} = (c^0_u - c^0_d)/2$ and $c^0_{u+d} = (c^0_u + c^0_d)/2$ and the constants in Table 2.1 this leads to

$$\begin{aligned}(c_p)_0 &= -0.437(37) + 0.847(50)c^0_u - 0.407(34)c^0_d,\\ (c_n)_0 &= -0.002(30) - 0.407(34)c^0_u + 0.847(50)c^0_d,\end{aligned} \tag{2.91}$$

which for KSVZ axion models ($c^0_q = 0$) yields

$$(c_p)^{\mathrm{KSVZ}}_0 = -0.437(37), \quad (c_n)^{\mathrm{KSVZ}}_0 = -0.002(30), \tag{2.92}$$

while for the DFSZ axion ($c^0_u = \sin^2\beta/3$, $c^0_d = 1 - c^0_u$) we find

$$\begin{aligned}(c_p)^{\mathrm{DFSZ}}_0 &= -0.573(35) + 0.418(20)\sin^2\beta,\\ (c_n)^{\mathrm{DFSZ}}_0 &= +0.280(25) - 0.418(20)\sin^2\beta.\end{aligned} \tag{2.93}$$

Note, that for the QCD axion the value of c_n is smaller than expected due to an accidental cancellation and even compatible with zero. This makes it difficult to constrain KSVZ axion couplings to neutrons from supernovae, see *e.g.* [57], and significantly weakens the bound from neutron star cooling (see *e.g.* [58, 59] or the discussion in [60]).

constant	value(uncertainty)
Δu	0.847(50)
Δd	−0.407(34)
m_u	2.27(9) MeV
m_d	4.67(9) MeV
m_π	136.10(1.82) MeV
z	0.485(19)
$\mathring{m}_N$	872.6(3.1) MeV
$\bar{d}_{16}$	0.4(1.3) GeV^{-2}
d_{18}	−0.44(24) GeV^{-2}
$\hat{c}_1$	0.89(6) GeV^{-1}
$\hat{c}_3$	−5.54(6) GeV^{-1}
$\hat{c}_4$	4.17(4) GeV^{-1}
$\hat{c}_5$	−0.09(1) GeV^{-1}
c_D	−0.85(2.15) GeV^{-1}

Table 2.1: Numerical values chosen for the constants. The constants $\bar{d}_{16}$ and d_{18} are taken from Ref. [61]. The constants $\hat{c}_1$, $\hat{c}_3$, $\hat{c}_4$ are taken from [62], where for $\hat{c}_4$ we included an additional term $\Lambda_\chi/4\mathring{m}_N$ (see App. A.3), $\hat{c}_5$ is taken from [63], while the central value of c_D is taken from [64].

Axion nucleon couplings at higher orders

Higher order corrections start with a single tree level $\nu = 1$ diagram, containing only contributions from relativistic corrections to the leading order Lagrangian, resulting in

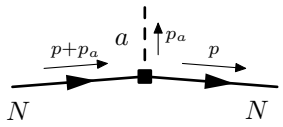

$$= -\frac{1}{2f_\phi m_N}\left(g_A c_{u-d}\tau^3 + g_0 c_{u+d}\mathbb{1}\right) \times (\omega_\phi - \omega_p)\,(S\cdot p_\phi + 2S\cdot p)\,, \tag{2.94}$$

where we defined $\omega_p \equiv -v\cdot p$ and $\omega_\phi \equiv -v\cdot(p+p_\phi)$.

At chiral order $\nu = 2$, one loop corrections start contributing and are renormalized by corresponding tree level terms from $\hat{\mathcal{L}}^{(3)}_{\pi N}$. Omitting axion loops, all relevant, i.e. non-zero $\nu = 2$ diagrams have been calculated in [61] and are shown in Fig. 2.1.

The result can be written as

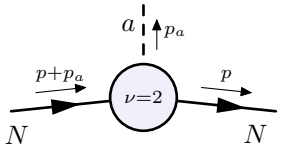

$$= -\frac{1}{f_\phi}\mathcal{A}^{(\nu=2)} S\cdot p_\phi - \frac{1}{f_\phi}\mathcal{B}^{(\nu=2)} S\cdot p, \tag{2.95}$$

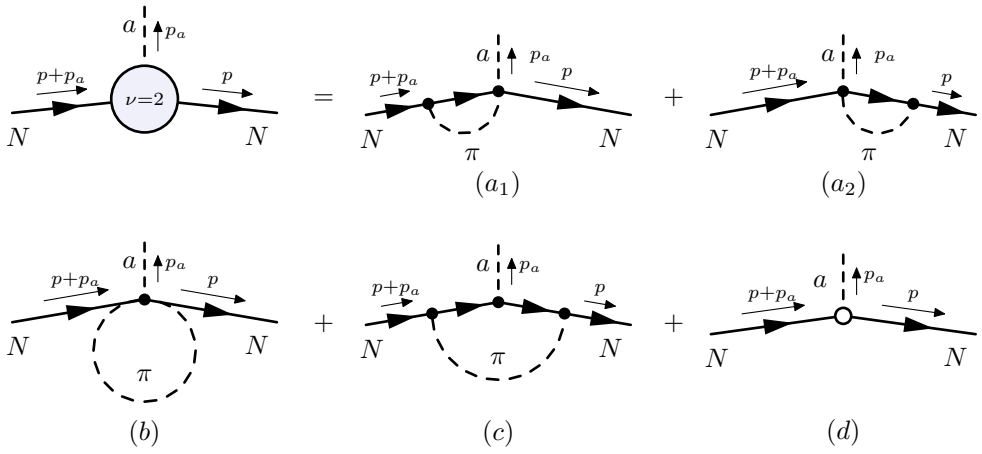

Figure 2.1: Non-zero corrections to the axion nucleon vertex at chiral order $\nu = 2$. Filled dots $(a), \ldots, (c)$ denote $\Delta_i = 0$ vertices according to Eq. (2.81). The empty circle (d) denotes tree level contributions from $\hat{\mathcal{L}}^{(3)}_{\pi N}$ needed to renormalize the previous diagrams, see [61].

with

$$\begin{aligned}\mathcal{A}^{(\nu=2)} = &-\frac{1}{4m_N^2}\left(g_A c_{u-d}\tau^3 + g_0 c_{u+d}\mathbb{1}\right)\left(\omega_p^2 - \omega_\phi^2 + \omega_p\omega_\phi - p^2\right)\\ &-\frac{1}{6}\left(-g_A c_{u-d}\tau_3 + 3g_0 c_{u+d}\mathbb{1}\right)\left(\frac{g_A}{4\pi f_\pi}\right)^2\left[m_\pi^2 + \frac{1}{\omega_\phi - \omega_p}\right.\\ &\left.\times\left(\omega_p^3 - \omega_\phi^3 + 2\left[\left(m_\pi^2 - \omega_\phi^2\right)^{\frac{3}{2}}\arccos\frac{\omega_\phi}{m_\pi} - \left(m_\pi^2 - \omega_p^2\right)^{\frac{3}{2}}\arccos\frac{\omega_p}{m_\pi}\right]\right)\right]\\ &+4m_\pi^2\left[\left(\bar{d}_{16}\tau_3 + d_{17}\frac{m_u - m_d}{m_u + m_d}\right)c_{u-d} + \bar{d}_{16}^{u+d}c_{u+d} - \left(d_{18} + 2d_{19}\right)\frac{m_u m_d}{\left(m_u + m_d\right)^2}\right],\end{aligned} \tag{2.96}$$

and

$$\mathcal{B}^{(\nu=2)} = \frac{1}{4m_N^2}\left(g_A c_{u-d}\tau^3 + g_0 c_{u+d}\mathbb{1}\right)\left[2\left(\omega_\phi^2 - \omega_p^2\right) + \left((p+p_\phi)^2 - p^2\right)\right]. \tag{2.97}$$

We are now in the position to go one order higher. While the next order is of course naively suppressed, it is well known that the low energy constants $\hat{c}_{3/4}$ are larger than the naive power counting expectation. The coupling constants $\hat{c}_{3/4}$ are enhanced by resonances, mostly due to the low-lying $\Delta(1232)$ resonance, which lies about ~ 300 MeV above the nucleon mass (see e.g. [41, 48, 49]). Therefore, including the diagrams with enhanced couplings captures the dominant effects of the next order without calculating all diagrams at $\nu = 3$. The relevant diagrams and corresponding tree-level diagrams that are necessary for their renormalization are shown in Fig. 2.2. Note that the analogous isoscalar diagrams, which are generated by $\hat{c}_9$, are not enhanced by the Δ resonance and thus dropped. The result can again be written in terms of a form factor

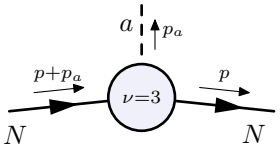

$$= \quad -\frac{1}{f_\phi}\mathcal{A}^{(\nu=3)}S\cdot p_\phi, \tag{2.98}$$

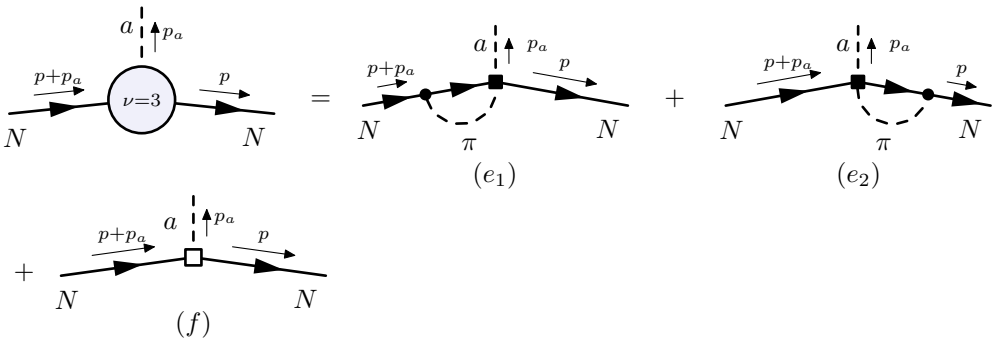

Figure 2.2: Non-zero corrections to the axion nucleon vertex at chiral order $\nu = 3$. Filled squares (e) denote $\Delta_i = 1$, filled circles denote $\Delta_i = 0$ vertices according to Eq. (2.81). The empty square (f) denotes tree level contributions from $\hat{\mathcal{L}}^{(4)}_{\pi N}$ needed to renormalize the previous diagrams.

where

$$\begin{aligned}\mathcal{A}^{(\nu=3)} = &-\frac{2g_A}{3\left(4\pi f_\pi\right)^2}\left(\hat{c}_3-2\hat{c}_4\right)c_{u-d}\tau^3\Big[m_\pi^2\left(\omega_\phi+\omega_p\right)-\left(\omega_\phi^3+\omega_p^3\right)\\ &-4\left(m_\pi^2-\omega_\phi^2\right)^{3/2}\cos^{-1}\left(\frac{-\omega_\phi}{m_\pi}\right)-4\left(m_\pi^2-\omega_p^2\right)^{3/2}\cos^{-1}\left(\frac{-\omega_p}{m_\pi}\right)\Big].\end{aligned} \tag{2.99}$$

In order to arrive at this result, we properly subtracted the divergent piece

$$\frac{2g_A}{3f_\pi^2}\left(\hat{c}_3-2\hat{c}_4\right)c_{u-d}\tau^3\Lambda(\lambda)\left(6m_\pi^2\left(\omega_\phi+\omega_p\right)-4\left(\omega_\phi^3+\omega_p^3\right)\right), \tag{2.100}$$

where $\Lambda(\lambda)$ collects the scale dependent and divergent pieces in dimensional regularization. The isovector divergent parts are renormalized by the appropriate $\Delta_i = 4$ operators found in [65]. Note that divergent isoscalar parts are renormalized analogously by introducing corresponding operators and couplings. To be precise, in the same notation, they are given by

$$e_{117}(\lambda)\bar{N}\left(\langle\chi_+\rangle\, S\cdot u\; iv\cdot D+\text{h.c.}\right)N, \tag{2.101a}$$

$$e_{193}(\lambda)\bar{N}\left(S\cdot u\; i(v\cdot D)^3+\text{h.c.}\right)N, \tag{2.101b}$$

which give rise to the following tree level contributions

$$\frac{4e_{117}}{f_\phi}c_{u-d}\tau^3 m_\pi^2\left(\omega_\phi+\omega_p\right)S\cdot p_\phi, \tag{2.102a}$$

$$-\frac{e_{193}}{f_\phi}c_{u-d}\tau^3\left(\omega_\phi^3+\omega_p^3\right)S\cdot p_\phi. \tag{2.102b}$$

As one can easily check this renormalizes the loop contribution if the beta functions

$$e_i(\lambda)=\bar{e}_i+\frac{\beta_i}{f_\pi^2}\Lambda(\lambda), \tag{2.103}$$

have the following property

$$\beta_{117}\supset g_A\left(\hat{c}_3-2\hat{c}_4\right), \tag{2.104a}$$

$$\beta_{193} \supset \frac{8 g_A}{3} \left(\hat{c}_3 - 2\hat{c}_4\right), \tag{2.104b}$$

which exactly agrees with [65]. A priori there are finite pieces which however are zero for operators that can be eliminated by an appropriate field redefinition (proportional to $v \cdot D$) as established in [66]. Therefore, no finite pieces are generated.

Let us now evaluate the axion coupling to protons and neutrons at N^{3}LO in the limit of small nucleon momenta, $p \to 0$. We take the relevant constants from [11, 61, 67], which are summarized in Table 2.1 in App. A. In analogy to [61], we assume that the undetermined low-energy constants $\bar{d}_{16}^{u+d}$, d_{17}, and d_{19} are natural to consist of a superposition of two normal distributions of $d_i = \pm 0.5(5)$ GeV^{-2}. The model dependent result is

$$\begin{aligned} (c_p)_0 =& -0.390(54) + 0.725(73) c_u^0 - 0.280(65) c_d^0, \\ (c_n)_0 =& -0.041(50) - 0.280(65) c_u^0 + 0.725(73) c_d^0, \end{aligned} \tag{2.105}$$

which for the KSVZ axion therefore gives

$$(c_p)_0^{\text{KSVZ}} = -0.390(54), \quad (c_n)_0^{\text{KSVZ}} = -0.041(50). \tag{2.106}$$

Note that while the coupling of the KSVZ axion to nucleons is still compatible with zero its central value shifted by one order of magnitude. For the DFSZ axion we find

$$\begin{aligned} (c_p)_0^{\text{DFSZ}} =& -0.482(55) + 0.355(37) \sin^2\beta, \\ (c_n)_0^{\text{DFSZ}} =& +0.201(51) - 0.335(37) \sin^2\beta. \end{aligned} \tag{2.107}$$

Finally we would like to note that the inclusion of the strange quark mass, which is not consistent if one calculates with $N_f = 2$ does not change the central value by much in the above calculation.

2.5 Lighter QCD Axions

The QCD axion is extremely predictive as it generically couples to SM particles (minimally to quarks) with couplings and mass both set by the axion decay constant. As a solution to the strong $\mathcal{CP}$ problem it is extremely sensitive to other sources of $U(1)_{\text{PQ}}$ breaking since this would show up in the nEDM measurement, a circumstance known as the axion quality problem, see *e.g.* [68–71]. Therefore, in order to relax the relation between the axion mass m_ϕ and its decay constant f_ϕ, see Eq. (2.35), one has to be careful not to introduce sources of $U(1)_{\text{PQ}}$ breaking which would re-introduce the strong $\mathcal{CP}$ problem.

While there is a plentitude of models that enhance the axion mass, see Sec. 6.7 in Ref. [29] and references therein, it is rather hard to find natural models that modify the $m_\phi - f_\phi$ relation in the opposite direction, i.e. that give rise to lighter than expected QCD axions. Indeed, up to now there exist very few natural models with lighter than expected QCD axion mass, in fact there seem to be only two.

In Ref. [72] the QCD axion is placed in the bulk of some large extra dimension, whose compactification scale sets the QCD axion mass thereby decoupling the $m_\phi - f_\phi$ relation. However, there are strong bounds on the compactification radius such that the mechanism is only viable for axion decay constants $f_\phi \lesssim 3 \cdot 10^9$ GeV.

Another symmetry based mechanism was proposed in Ref. [73] (see also Ref. [74] for details on $\mathcal{O}(1)$ numbers and Ref. [75] for phenomenological implications). The mechanism relies on

a $\mathcal{Z}_N$ symmetry that links N exact copies of the SM via the non-linear transformation on the axion field

$$\begin{aligned} \mathcal{Z}_N: \quad & \mathrm{SM}_k \longrightarrow \mathrm{SM}_{k+1(\mathrm{mod}\, N)} \\ & \phi \longrightarrow \phi + \frac{2\pi k}{N} f_\phi, \end{aligned} \tag{2.108}$$

with $k = 0, \ldots, N-1$. One of the N mirror copies describes our SM while the remaining ones are identical copies except that the θ angle is shifted by $2\pi/N$ w.r.t. the previous copy. Each copy contributes to the QCD axion potential and one finds that the summed up potential has the exact same shape as the standard QCD axion Eq. (2.34) but with decreased amplitude, which can be parameterized by a small quantity ϵ, such that the axion potential can be written as

$$V(\phi) = -\epsilon m_\pi^2 f_\pi^2 \left(\sqrt{1 - \frac{4 m_u m_d}{(m_u + m_d)^2} \sin^2\left(\frac{\phi}{2 f_\phi}\right)} - 1 \right), \tag{2.109}$$

The parameter ϵ is related to the number of SM copies, we refer for a detailed discussion to Ref. [74] and content our selfs here with stating the reduced QCD axion mass in the large N limit

$$m_\phi^2 \simeq \frac{m_\pi^2 f_\pi^2}{f_\phi^2} \sqrt{\frac{1-z}{1+z}} N^{3/2} z^N, \tag{2.110}$$

where z is again the ratio of the up- and down quark, see Eq. (2.60), and the simple observation that ϵ is related to N up to $\mathcal{O}(1)$ numbers (in the large N limit)

$$\epsilon \simeq N^{3/2} z^N. \tag{2.111}$$

We would like to stress that while in these model the QCD axion mass is effectively lighter depending on the number of copies, all couplings to SM particles are identical to benchmark QCD axion models. These models can give rise to spectacular phenomenological signatures as we will show in later chapters.

2.6 Astrophysical limits on the QCD axion

While there exist many ways to search for the QCD axion and variations thereof with terrestrial experiments, see *e.g.* Ref. [29] and Ref. [76] for up-to-date bounds, some of the strongest bounds come from astrophysical systems. In particular, the bound from the Supernova 1987A (SN 1987A) and bounds from NS cooling are among the most restrictive limits on the axion decay constant and especially its coupling to protons and neutrons. In this section, we review the current status of these bounds. For bounds from other astrophysical systems, such as the Sun, WD and Red Giant (RG) cooling, we refer to [77–80] and Refs. [29, 81] for reviews.

The SN 1987A is the only SN that was ever observed with modern instruments. Several observatories detected a neutrino burst with $\sim O(10)$ neutrinos during a time of $\sim O(10)$ seconds [82–84]. The duration of the SN process depends on the cooling mechanism which agrees to very good approximation with the observed neutrinos. In particular, there exist self-consistent three-dimensional Core Collapse Supernova (CCSN) which agree to good approximation with the observed signal [85]. Therefore, any additional source of energy depletion, such as light particles like the QCD axion would modify the neutrino burst duration. A bound can be extracted by requiring that the new light particle should have a cooling rate that lies below the neutrino cooling rate which is roughly $2 \times 10^{52}\,\mathrm{erg\,s^{-1}}$, with a typical SN temperature $T \sim 30\,\mathrm{MeV}$ and baryon energy density $\varepsilon \sim 10^{14}\,\mathrm{g\,cm^{-3}}$ [78]. The axion is emitted during the SN dominantly via

axion-nucleon bremsstrahlung, first calculated in Ref. [86] at tree-level for the one pion exchange. Assuming that the pion is massless (and other simplifacations), this yields a bound for a KSVZ-type QCD axion of $m_\phi \lesssim 16\text{meV}$ or $f_\phi \gtrsim 4\times 10^8\,\text{GeV}$ [87] due to the unobservation of neutrinos from SN 1987A. The bound has a lower limit since KSVZ-type axions with $f_\phi \lesssim 2\times 10^6\,\text{GeV}$ would have a mean free path that lies within the dynamical SN radius, i.e. such axions would effectively be trapped within the remnant.

More recently, these bounds have been reexamined including corrections beyond the one pion exchange in Ref. [57]. Specifically, the authors include a non-zero pion mass, two pion exchanges by means of the inclusion of a rho meson, an effective (density dependent) nucleon mass, and nucleon multiple scatterings have been considered. The authors find $\mathcal{O}(1)$ deviations in the bound, in particular

$$g_{\phi n}^2 + 0.61 g_{\phi p}^2 + 0.53 g_{\phi n} g_{\phi p} \lesssim 8.26\times 10^{-19}, \tag{2.112}$$

where

$$g_{\phi i} = (c_i)_0 \frac{m_N}{f_\phi} \tag{2.113}$$

and $(c_i)_0$ with $i = p, n$ are here taken to be the leading order axion-nucleon couplings, see Eq. (2.91). This corresponds to

$$m_\phi \lesssim 5.67\,\text{meV}\left[(c_n)_0^2 + 0.61(c_p)_0^2 + 0.53(c_n)_0(c_p)_0\right]^{-1/2}. \tag{2.114}$$

These bounds are, however, subject to large uncertainties since we have only observed one single SN, and our present understanding of nuclear matter at large densities as well as the underlying non-perturbative dynamics of the SN is very poor. Therefore, these bounds can only be trusted up to $\mathcal{O}(1)-O(10)$ factors. Nevertheless, we will present in Chap. 4 a revisited analysis including improved axion nucleon couplings due to vacuum loop corrections as well as finite density effects in a systematic fashion.

We would like to note that the above bound on the QCD axion from SNe is model dependent. It relies on UV couplings from the axial $U(1)_A$ PQ current, see Eq. (2.61). In particular, so-called astrophobic axions [88] can easily avoid these types of bounds. However, as long as one is interested in solving the strong $\mathcal{CP}$ problem, there is a model independent bound arising from the coupling of the axion to the neutron electric dipole moment [89], which in this scenario only arises from the topological coupling to gluons, see Eq. (2.33). Of course, if one is not interested in solving the strong $\mathcal{CP}$ problem there can be other contributions to the nEDM such that also this coupling is model dependent. For now we focus on the scenario where we want to solve the strong $\mathcal{CP}$ problem. Following the same reasoning as in the previous section but with the coupling to the nEDM, see Eq. (2.28),

$$\mathcal{L}_{\phi,\text{nEDM}} = -\frac{i}{2}\frac{C_{aN\gamma}}{m_N f_\phi}\phi\bar{N}\gamma_5\sigma_{\mu\nu}NF^{\mu\nu} \tag{2.115}$$

where $C_{aN\gamma} = 0.0033(15)$ is taken from Ref. [90], the authors of Ref. [89] find the weaker bound

$$f_\phi > 5.56\times 10^5\,\text{GeV} \quad \text{or} \quad m_\phi < 10.5\,\text{eV}, \tag{2.116}$$

compared to the model dependent coupling to the nucleon spin.

The observation of NS cooling can provide similar bounds on the QCD axion and ALPs and provide information on the axion-nucleon couplings, see *e.g.* [91–95] and [96]. There are roughly two interesting astrophysical systems that provide bounds on the axion-nucleon coupling. The

first is the SN remnant Cassiopeia A (Cas A), where an anomalously fast cooling rate has been detected. This rapid cooling rate could be explained within the SM [97–99], however, Ref. [93] analyzed the cooling in the presence of the axion and obtained the bound

$$g_{\phi p}^2 + 1.6 g_{\phi n}^2 < 1 \times 10^{-18}, \tag{2.117}$$

while Refs. [92, 95] put the more conservative bound

$$g_{\phi p}^2 < (1-6) \times 10^{-17}, \quad \text{or} \quad f_\phi > (5-7) \times 10^7 \,\text{GeV}. \tag{2.118}$$

Yet another, more involved process where axions arise during the breaking and re-formation of neutron triplet Cooper pairs requires a coupling (or mass) [99]

$$g_{\phi n}^2 < (1.4 \pm 0.5) 10^{-19}, \quad \text{or} \quad (c_n)_0 m_\phi = (2.3 \pm 0.4) \text{meV}. \tag{2.119}$$

Alternatively, another young neutron star within the supernova remnant HESS J1731-347 was examined in Ref. [94], which lead to a limitation of

$$g_{\phi n}^2 < 7.7 \times 10^{-20}. \tag{2.120}$$

Note that the bounds from NS cooling depend sensitively on the axion-neutron coupling which at leading order (and also at higher orders) is compatible with zero within the uncertainty, which makes it difficult to place robust bounds.

We would like to conclude this section with the comment that astrophysical systems and phenomena such as SN and NSs provide excellent laboratories to test physics beyond the Standard Model (SM). In the following chapters, we will study the implications of light new physics in the context of these systems in more detail.

Chapter 3

White Dwarfs and Neutron Stars

Astrophysical environments offer great laboratories to test physics beyond the SM. As discussed in Sec. 2.6, SNe and NS cooling provide some of the strongest bounds on the QCD axion and ALPs, but also WDs, RGs and Sun-like stars provide excellent probes of new physics. While the physics of WDs, RGs and Sun-like stars is mostly understood, which implies that robust bounds on new physics models can be placed, SNe and NSs are much less understood. In particular, the explosion mechanism of SNe has only recently been simulated self-consistently and with three space dimensions [100], while the EOS of NSs is still poorly understood. This is due to large uncertainties on the experimental side as well as the difficulties that arise when calculating the EOS of nuclear matter at supra-nuclear densities, see *e.g.* Ref. [101, 102].

In this chapter we briefly review the underlying physics of NSs and WDs without the inclusion of new physics, whose exciting effects on such systems will be explored later on.

All stars need some source of pressure to prevent gravity from collapsing it to a black hole. For stars like our Sun, i.e. main sequence stars, this source of pressure comes from the energy release in nuclear fusion and is therefore thermal. For degenerate stars, such as WDs and NSs, the source of pressure is instead Fermi degeneracy pressure. The equations that describe the equilibrium between gravitational and matter pressure were derived by Tolman-Oppenheimer-Volkoff (TOV), see *e.g.* Refs. [103–105] for pedagogical introductions,

$$\begin{aligned} p' &= -\frac{GM\varepsilon}{r^2}\left[1+\frac{p}{\varepsilon}\right]\left[1-\frac{2GM}{r}\right]^{-1}\left[1+\frac{4\pi r^3 p}{M}\right], \\ M' &= 4\pi r^2 \varepsilon, \end{aligned} \tag{3.1}$$

where $G = 1/M_{\rm P}^2$ is Newtons constant, $M(r)$ the enclosed mass and all derivatives are taken with respect to the radial coordinate. This system of coupled differential equations can be integrated provided an EOS in some form, *e.g.* $p = p(\varepsilon)$, and the boundary conditions $p(0) = p_0, p'(r) = 0, M(0) = 0$ until the radius that defines the edge of the object defined by $p(R) = 0$ is reached. The enclosed gravitational mass is then given by $M(R)$. Varying the initial pressure p_0, or energy density ε_0, we find a family of solutions that can be displayed as a curve in the $M - R$ diagram of the star, see *e.g.* Fig. 3.1 for the $M - R$ curve of WDs for different compositions. Each point on the $M - R$ curve corresponds to an equilibrium configuration and increasing the central energy density ε_0 moves points towards smaller and more massive configurations until a maximum is reached. The maximum can be explained by noticing that an equilibrium configuration does not imply stability. In fact it can be shown that the criterium of stability implies $\partial M(\varepsilon_0)/\partial\varepsilon_0 > 0$, where we assumed microscopic stabilty i.e. a positive squared sound speed $c_s^2 = \partial p/\partial\varepsilon > 0$.

3.1 White Dwarfs

Main sequence stars use the thermal energy released in nuclear fusion processes, starting with hydrogen, to counterbalance gravitational collapse. Once most of the burning element is depleted, the star collapses and heats up until the next stable fusion process stops further collapse. For progenitor stars with masses of $\sim 8M_\odot$ and below, this process will stop at relatively light nuclei. In this scenario, the stellar remnant is called a white dwarf (WD) [104, 105]. Its mass comes mostly from positively charged nuclei while the pressure to balance gravitational collapse comes to good approximation from a degenerate gas of electrons.

Before discussing the EOS, numeric solutions from the TOV equations and compatibility with data, see Fig. 3.1, we would like to show a very simple naive dimensional analysis (NDA) estimate to get a feeling about the parametric scaling of WD masses and radii. For this purpose we compare the energy of a degenerate free Fermi gas of electrons $E_{\rm Fermi} \sim N m_e$, where N is the electron number within the WD, i.e. $\rho_e = N/R_{\rm WD}^3$, to the gravitational energy in collapsing nuclei $E_{\rm grav} \sim M_{\rm WD}^2/(M_{\rm P}^2 R_{\rm WD})$. Neglecting signs as well as $\mathcal{O}(1)$ numbers and using $M_{\rm WD} \sim N m_N$, where we implied charge neutrality, and $\rho_e \sim m_e^3$, we find

$$M_{\rm WD} \sim \frac{M_{\rm P}^3}{m_N^2} \sim \mathcal{O}(1)\, M_\odot, \quad R_{\rm WD} \sim \frac{M_{\rm P}}{m_e m_N} \sim \mathcal{O}(1)\, 10^4\,{\rm km}. \tag{3.2}$$

The estimation for the mass corresponds to the Chandrasekhar limit which is an estimate for the maximal mass a WD can support. To be precise one finds $M_{\rm Ch} \simeq 1.4\, M_\odot$ [106]. We will now confirm these rough estimates with the numerical solutions to the free Fermi gas EOS.

We denote the non-relativistic nuclei by ψ, with energy density $\varepsilon_\psi = Y_e m_N \rho_\psi$, where $Y_e = A/Z$ is the ratio of the mass number over the atomic number, ρ_ψ is the number density of nuclei and m_N the nucleon mass. The pressure is dominated by the electron contribution, $p = p_e + p_\psi \simeq p_e$, while the nuclei constitute most of the energy density, $\varepsilon = \varepsilon_e + \varepsilon_\psi \simeq \varepsilon_\psi$. Imposing charge neutrality, $\rho_\psi = \rho_e \equiv \rho$, we can relate the electron Fermi momentum to the energy density as $k_F = (3\pi^2 \varepsilon_\psi / Y_e m_N)^{1/3}$, and find the EOS to be

$$p(\varepsilon) = \frac{2}{3} \int_0^{k_F(\varepsilon)} \frac{{\rm d}^3 k}{(2\pi)^3} \frac{k^2}{\sqrt{k^2 + m_e^2}}. \tag{3.3}$$

We work in the limit $T \to 0$, which is justified since $T/\mu_e \ll 1$ for typical WDs, where μ_e is the electron chemical potential. Temperature shifts the $M - R$ relation up to higher masses [112, 114–116], an effect most relevant for the largest and most dilute WDs. This can be understood as an additional thermal pressure source, effectively stiffening the EOS. Due to the high electron degeneracy and the small luminosity given by WDs relatively small radii the interior is is thermally highly conductive which allows to approximate the temperature as constant in the bulk of the star. In the dilute outer layers where electrons become less degenerate, conductivity is lost and temperature transport equations have to be solved [117]. This is left as a future exercise. The ratio $Y_e = A/Z$ is set by the composition of the star, which for light nuclei, ranging from helium ^{4}He to magnesium ^{24}Mg, is well-approximated by $Y_e \simeq 2$. Note however that a $\sim 10\%$ change in the ratio ($Y_e \simeq 2.15$ for ^{56}Fe) changes the maximal mass appreciably since it softens the EOS, see Fig. 3.1. With the EOS at hand we can solve the set of equations that describes the balance between the electron degeneracy pressure and gravity, the TOV equations, see Eq. (3.1). In Fig. 3.1 we show the $M - R$ curve, i.e. the enclosed gravitational mass of the star as function of its radius R. The upper black line corresponds to a composition of $Y_e = 2$, which is realized for ^{4}He, while the lower line corresponds to $Y_e = 2.15$, which would roughly correspond to a ^{56}Fe dominated composition. Each point on the black lines and within the gray

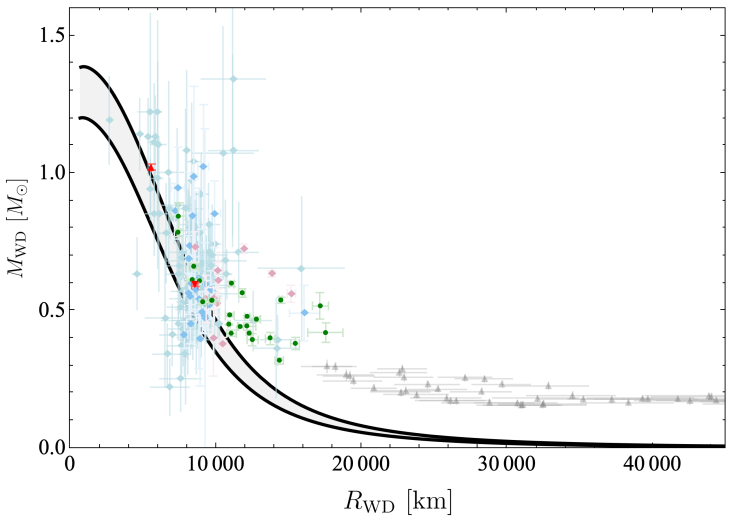

Figure 3.1: Stellar equilibrium configurations for the $T \to 0$ WD EOS, see Eq. (3.3). Top black line corresponds to the composition $Y_e = 2$ common for light elements such as ^{4}He, while the bottom line corresponds to $Y_e = 2.15$ which would correspond to ^{56}Fe. Configurations with intermediate Y_e are shaded in gray. Data points are taken from [107] (turquoise), [108] (blue), [109] (pink), [110, 111] (red), [112] (green) and [113] (gray).

shaded region corresponds to an equilibrium solution to the TOV equations in the $T \to 0$ limit. Configurations that lie on a branch with $\partial M/\partial R > 0$ are instable, see Refs. [103–105]. There are large data sets available containing masses and radii of WDs (see e.g. [107–113, 118–124]). However, not all of these data-sets can be used to probe the M - R relation. In some catalogs, (see [118–122]), the M - R relation is used as an input to significantly reduce observational error. On the other hand, there are sets (e.g. [107–113, 123, 124]) that systematically test the M - R relation using observational data. While in [112] the determination of the mass and radius is completely independent of WD models, most other works depend on an atmospheric model to determine the radius. Nevertheless we show them in Fig. 3.1.

The data of measured WD masses and radii is scattered broadly between radii of (5000 − 40000 km), which matches reasonably well with the free Fermi gas description. The notable deviation in mass found at large radii in Fig. 3.1 is due to finite temperature effects; μ_e (electron chemical potential) in these dilute stars is typically smaller, increasing the relevance of T/μ_e corrections. Finite temperature effects lead to modifications of the EOS and to a slight modification of masses and radii, but importantly they predict a continuous M - R curve.

Finally we would like to mention that the EOS of WDs can be furhter enhanced by taking into account crystallization, pyconuclear reactions and other nuclear reactions [104, 105, 117]. They are however subdominant compared to the simple electron degeneracy picture and can safely be neglected.

3.2 Neutron Stars

We have seen that an instability occurs for the smallest and heaviest WDs. However, there exists a stable branch of even smaller objects with roughly the same mass, so-called neutron stars (NSs). NSs are the densest astrophysical objects that are not yet black holes, (see e.g. [101, 102] for recent reviews). While WDs consist of nuclei, the densities in NSs are so large that nuclei effectively dissolve into nucleons, i.e. neutrons and protons. The precise constitution of NSs is

still subject to active research since theoretical predictions for the EOS of NSs are hampered by the fact that QCD becomes strongly coupled at typical NS densities, roughly $\rho \sim 0.16\,\mathrm{fm}^{-3}$, and numerical modelling on the lattice is not possible due to the infamous fermion sign problem [125]. This implies that $\mathcal{O}(1)$ uncertainties are unavoidable when dealing with systems at these large densities.

The name neutron star historically came about because it was believed that the system minimizes its energy by the inverse β-decay, $p + e^- \to n + \nu_e$, with the neutrinos escaping the object such that energy density and pressure is given by neutrons. Indeed, we can perform a similar NDA estimate as for WDs, but with $E_{\mathrm{Fermi}} \simeq N m_N$ and $\rho \simeq m_N^3$, to find

$$M_{\mathrm{NS}} \sim \frac{M_{\mathrm{P}}^3}{m_N^2} \sim \mathcal{O}(1)\, M_\odot, \quad R_{\mathrm{NS}} \sim \frac{m_e}{m_N} R_{\mathrm{WD}} \sim \frac{M_{\mathrm{P}}}{m_N^2} \sim \mathcal{O}(1)\, 10\,\mathrm{km}, \tag{3.4}$$

which indeed gives the right idea: NSs are solar mass objects with a radii of about $R \sim 10\,\mathrm{km}$. We can easily calculate the Schwarzschild radius for such an object $2GM \sim 3\,\mathrm{km}$, which shows that these objects are extremely compact.

Therefore, a rough approximation for the EOS of a neutron star is to consider a free Fermi gas of degenerate neutrons. The derivation of the EOS is even simpler as in the case for WDs since there is only one neutral constituents and it does not have an analog for the varying nuclear composition Y_e. The energy density and pressure are given by

$$\varepsilon(\rho) = 2 \int^{k_F(\rho)} \frac{\mathrm{d}^3 k}{(2\pi)^3} \sqrt{\mathbf{k}^2 + m_N^2}, \tag{3.5a}$$

$$p(\rho) = \frac{2}{3} \int^{k_F(\rho)} \frac{\mathrm{d}^3 k}{(2\pi)^3} \frac{k^2}{\sqrt{\mathbf{k}^2 + m_N^2}}, \tag{3.5b}$$

with the one-to-one relation between Fermi momentum and number density $k_F = (3\pi^2\rho)^{1/3}$. The EOS $p(\varepsilon)$ can now numerically be found for all densities. Before discussing the solutions to the TOV equations there are two limits in which the EOS takes a simple analytical form, namely the non-relativistic (NR) $k_F \ll m_N$ and the ultra-relativistic (UR) limit $k_F \gg m_N$ with EOSs respectively

$$p^{\mathrm{NR}}(\varepsilon) \simeq \frac{(3\pi^2)^{2/3}}{5} \frac{\varepsilon^{5/3}}{m_N^{8/3}} \left[1 + \mathcal{O}\left(\frac{\varepsilon^{2/3}}{m_N^{8/3}}\right)\right], \qquad k_F = \left(3\pi^2 \varepsilon / m_N\right)^{1/3} \tag{3.6a}$$

$$p^{\mathrm{UR}}(\varepsilon) \simeq \frac{1}{3}\varepsilon \left[1 + \mathcal{O}\left(\frac{m_N^2}{\sqrt{\varepsilon}}\right)\right], \qquad k_F = \left(4\pi^2 \varepsilon\right)^{1/4}. \tag{3.6b}$$

As for WDs, we find the $M-R$ curve of equilibrium configurations by solving the TOV equations Eq. (3.1) with the full free Fermi EOS Eq. (3.5) for different central energy densities $\varepsilon(r=0)$ or equivalently pressures $p(r=0)$. The result is also shown as the left branch in Fig. 3.2.

We want to stress that the free Fermi gas EOS is a very simplistic model for a neutron star and cannot explain most of its observed properties. Maybe most prominantly, it cannot account for measured maximal masses of NSs i.e. the maximal mass of the free Fermi gas EOS is $M_{\mathrm{max}} \sim 0.7 M_\odot$, clearly in contradiction with observations of neutrons stars with masses above $2M_\odot$ [126]. The free Fermi gas EOS should therefore be seen as a substantial simplification which however captures the main properties up to $\mathcal{O}(1)$ factors. However, similar arguments can also be brought up for more sophisticated EOSs. In particular, other baryonic components other than neutrons may be present within NSs such as pions, kaons, meson condensates [127]

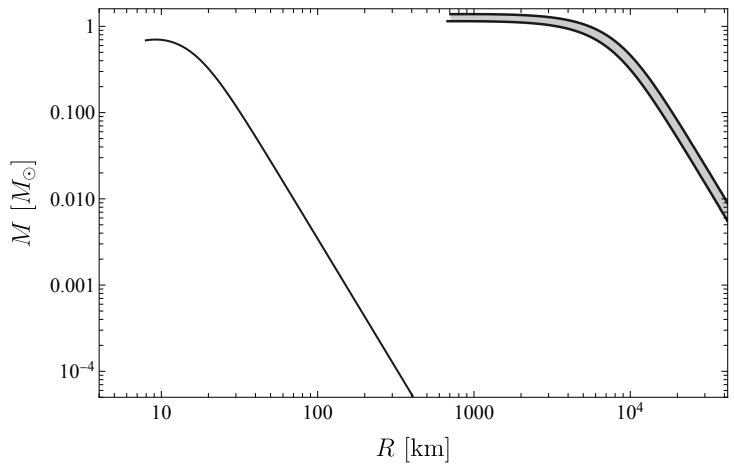

Figure 3.2: Equilibrium configurations of stellar remnants: the stellar landscape. Right branch: Same as Fig. 3.1. Left branch: Free Fermi gas of neutrons in the $T \to 0$ limit.

(also see [128] for a recent review) and hyperons [129] which would not be surprising as they are the right degrees of freedom to describe nuclear physics at the relevant energies [104]. However, the inclusion of these degrees of freedom within the SM usually leads to softer EOSs supporting less massive objects and therefore seems to be ruled out, a question referred to as the hyperon puzzle, see *e.g.* Ref. [130]. Furthermore, NSs are believed to exhibit phases of superfluidity [131], crystalline structures [132], strong first order phase transitions to deconfined phases of quark gluon matter within the star [133, 134]. It is important to note that all the effects mentioned above tend to soften the EOS, leading to less massive objects which seems to be disfavoured by data.

Indeed, existing catalogs feature many measured NS masses from binary pulsar systems, using data obtained from X-ray emissions on their surfaces, i.e. Shapiro delay [135]. The key finding is that neutron stars can have masses of at least two solar masses and excitingly even higher than that. The most prominent instance of this fact is the binary NS merger GW170817 detected in GWs by LIGO and Virgo [136] along with an electromagnetic counterpart (GRB 170817A) detected by Fermi gamma-ray telescope [137] which, among many other physics results, led to constraints on NS radii, maximal mass, and EOS, see e.g. [138–141]. This is promising in light of the many more NS-NS as well as NS-BH (black hole) mergers that the current network of GW detectors is expected to detect [142]. The current stellar remnant catalog [143–145] will also be significantly expanded by third-generation GW observatories [146, 147]. Another interesting result is the merger event GW190814 [148], which measured one of the progenitors to be a stellar remnant with a mass of approximately $2.6 M_\odot$. This could be the heaviest NS or the lightest BH discovered to date. While a distinction between NSs and BHs from GW data alone is non-trivial, see e.g. [149, 150], this event poses a challenge to the expected lower mass gap between NSs and BHs [151–158]. Furthermore, pulsars like PSR J0348+0432 have a mass of $(2.01 \pm 0.04)\, M_\odot$ [159], while PSR J1614-2230 has a mass of $(1.97 \pm 0.04)\, M_\odot$ [160]. Excitingly, there are hints of even more massive neutron stars, as seen in PSR J2215+5135 with a mass of $(2.27 + 0.17 - 0.15)\, M_\odot$ [161] and MSP J0740+6620 with a mass of $(2.17 + 0.10 - 0.09)\, M_\odot$ [126]. These recent discoveries push the boundaries of our understanding of NS EOSs and are particularly hard to explain with SM physics alone.

Determining the radii of neutron stars through observations has proven to be a challenging task due to various factors, such as uncertainties in crust modelling [162], interstellar medium

absorption, and stellar distance [163]. To address this, new generations of X-ray missions, in particular NICER [164], are focused on measuring neutron star radii, leading to constraints in the range of approximately $R \approx (9.9 - 11.3)\,\mathrm{km}$ for more than a dozen neutron stars.

Simultaneously measuring both the mass and radius of the same neutron star is difficult, yet it can be important for constraining the EOS and gravity theories [165–167]. However, alternative observational approaches can also provide valuable insights such as neutron star moment of inertia measurements [168] and the analysis of gravitational wave and gamma-ray burst data from binary neutron star mergers *e.g.* LIGO [138] (see also [169,170]) offer possibilities to infer constrains on tidal deformability and eventually the EOS [171, 172].

As should be clear from the above discussion, the precise composition of NSs is still an open question. However, the simple EOS obtained by a free Fermi gas of degenerate neutrons captures main features of NSs while it is safe to say that it is not describing the entire story. Nevertheless we will use this simple EOS to study effects of beyond the Standard Model (BSM) physics on the stellar structure of WDs and NSs in following chapters.

Lastly, we would like to comment on other approaches for more realistic NS EOSs that are slightly more involved and allow to capture effects of interactions in the dense nuclear medium. We know that at sufficiently low energies or equivalently densities ChPT is perturbative. It is indeed possible to derive the properties of nuclear matter, i.e. symmetric nuclear matter, mixed matter as well as pure neutron matter, which even reproduces non-trivial results such as the correct binding energy of symmetric nuclear matter and compressibility [173, 174]. In addition to the non-interacting pressure and energy density, interacting contributions can be calculated systematically by summing over Hartree and Fock diagrams ordered in powers of k_F/m_π, making use of QFT at finite chemical potential and temperature in the real-time formalism [175]. In the chiral limit, saturation simply arises due to two-pion exchange with the interplay of an attractive k_F^3-term and a repulsive k_F^4-term. Another, more empirical approach is relativistic mean field (RMF) theory, see [105] for a pedagogical introduction. Relativistic nucleon fields interact via exchange of scalar, pseudo-scalar and vector mesons, which are set to their mean values determined by minimizing the energy of the system. Couplings and masses of the meson fields are then fitted to reproduce measured properties of bulk nuclear matter. There are many more empirical approaches to NS EOSs such as many body approaches or skyrme models, which will not be covered in this thesis. For recent review about these topics see *e.g.* Ref. [154].

Chapter 4

Couplings of the QCD Axion to Nucleons at Finite Density

As discussed in Sec. 2.6, astrophysical environments provide great testbeds for new physics, especially in the context of the QCD axion and ALPs. In particular some of the most stringent bounds come from core-collapse supernovae [57, 87, 89] and neutron star cooling [91–94]. While the derived bounds make use of the vacuum couplings of the QCD axion to nuclear matter at all densities, it is well known that couplings generally become density dependent within the medium. For example, it has been shown that the axial pion nucleon coupling g_A is quenched as a function of the baryon density in Gamov-Teller transitions [176]. The density dependence of the axion coupling to nucleon spin has been estimated for the first time in [11], where an order $\mathcal{O}(10)$ modification of the axion neutron coupling has been found at around saturation density due to an accidental cancellation of this coupling in vacuum. The coupling to the proton changes by $\mathcal{O}(1)$ at saturation density. In this Chapter, we systematically calculate the axion coupling at finite baryon density in HBChPT and use the obtained density dependent couplings in the calculation of the emitted energy during supernovae leading to a weaker bound.

We start this Chapter by extending the discussion on HBChPT from Sec. 2.4.3 to finite density. In particular, we review the basics of real-time thermal field theory in Sec. 4.1.1 and derive the nucleon propagator at finite density. Using the power counting scheme mentioned in Sec. 2.4.3 and reviewed in detail in App. A.6, we systematically calculate finite density corrections to the axion-nucleon vertex up to $\mathrm{N^2LO}$ and even include contributions that are enhanced due to the low-lying Δ-resonance from $\mathrm{N^3LO}$ in Sec. 4.2. An explicit construction of the $\mathrm{N^2LO}$ Lagrangian including the axion can be found in App. A. Eventually, we discuss the effect of moderate temperatures, relevant in supernovae. In Sec. 4.3 we comment on the relevance of the deformations of the couplings on astrophysical bounds on the QCD axion.

The content of this chapter is based on work in progress [16].

4.1 Heavy Baryon Chiral Perturbation Theory at Finite Density

We have introduced HBChPT in vacuum already in Sec. 2.4.3. We review some basics about field theory at finite temperature and chemical potential in the real time formalism closely following Ref. [175, 177] in order to derive the nucleon propagator at finite temperature and chemical potential. In the limit of zero temperature the propagator takes a particularly simple form. These techniques have also been applied within ChPT, e.g. in the context of the nucleon potential [178] or as already mentioned in the context of the EOS of nuclear matter [173, 174]. For a general introduction to finite temperature quantum field theory we refer to *e.g.* [179].

4.1.1 Propagators in Real-Time Thermal Field Theory

We summarize the derivation of propagators in thermal field theory for bosons and fermions in real-time thermal field theory following closely [175,177]. The grand canonical potential density is related to the pressure density and partition function as

$$\Omega = -P = -\frac{1}{\beta V} \ln Z[0], \tag{4.1}$$

where $Z[0] = \exp(-\beta V \Omega)$, $\beta = T^{-1}$. At finite temperature and/or chemical potential the partition function can be constructed as a path integral by extending the time integration to the imaginary plane from $[t_0, t_0 - i\beta]$ with $t_0 \in \mathbb{R}$. This can easily be understood as one is generally interested in calculating expectation values of the form

$$\mathrm{Tr}\left[e^{-\beta(\hat{H}-\mu\hat{N})} T \exp\left(i \int_{-t_0}^{t_0} dt \int d^3x \; j(x)\phi(x)\right)\right], \tag{4.2}$$

where T is the ordinary time ordering operator. Note that even though for a real scalar there is a conserved charge in the non-relativistic limit or in the free case, in the following we take $\mu = 0$ for simplicity. Importantly, the contour in the complex plane that reaches from t_0 to $t_0 - i\beta$ is to some extent arbitrary, which, depending on the chosen contour, allows to calculate real-time Green's functions or time independent quantities. Let us for simplicity consider the path integral representation of the partition function of a scalar field ϕ depending on the contour $\mathcal{C}$,

$$\begin{aligned} Z[j] &= \mathcal{N} \int \mathcal{D}\phi \exp\left(i \int_{\mathcal{C}} d^4x \left(\mathcal{L}_0 + \mathcal{L}_I + \phi j\right)\right) \\ &= Z_0 \exp\left\{i \int_{\mathcal{C}} d^4x \mathcal{L}_I \left(\frac{\delta}{i\delta j(x)}\right)\right\} \exp\left\{-\frac{i}{2} \int_{\mathcal{C}} d^4y \int_{\mathcal{C}} d^4z \; j(y) \Delta_0^{(c)}(y-z) j(z)\right\}, \end{aligned} \tag{4.3}$$

where $\mathcal{L}_0$ and $\mathcal{L}_I$ are the free Lagrangian and some self-interaction Lagrangian and j a source current. We imposed the periodic boundary conditions $\phi(t_0) = \phi(t_0 - i\beta)$ and the contour independent normalization

$$Z_0 = \mathcal{N} \int \mathcal{D}\phi \exp\left(i \int_{\mathcal{C}} d^4x \mathcal{L}_0\right), \tag{4.4}$$

is subject to the same boundary conditions. This so far resembles the usual vacuum QFT expression, except for the free contour dependent propagator

$$i\Delta_0^{(c)}(x - x') = \int \frac{d^4k}{(2\pi)^4} e^{-ik\cdot(x-x')} \rho_0(k) \left[\theta_c(t - t') + n_B(k_0)\right], \tag{4.5}$$

where θ_c imposes contour ordering, the Bose-Einstein distribution

$$n_B(\beta, \omega) = \frac{1}{e^{\beta\omega} - 1} \tag{4.6}$$

and the spectral density is

$$\rho_0(k) = 2\pi \left[\theta(k_0) - \theta(-k_0)\right] \delta(k^2 - m^2) = i \left[\theta(k_0) - \theta(-k_0)\right] \left[\Delta_{0F}(k) - \Delta_{0F}(k)^\dagger\right], \tag{4.7}$$

with

$$\Delta_{0F}(k) = \frac{1}{k^2 - m^2 + i\epsilon}. \tag{4.8}$$

We now consider a contour $\mathcal{C} = \mathcal{C}_1 \cap \mathcal{C}_2 \cap \mathcal{C}_3$, where $\mathcal{C}_1$ lies on the real axis from t_0 to t_f, then $\mathcal{C}_3$ going from t_f to $t_f - i\beta$ and then $\mathcal{C}_2$ from $t_f - i\beta$ to $t_0 - i\beta$, with $t_0 < t_f \in \mathbb{R}$ and in the limit $t_0 \to -\infty$ and $t_f \to +\infty$. In this case the generating functional it can be shown that the generating functional factorizes into two pieces, the contour $\mathcal{C}_1 \cap \mathcal{C}_2$, i.e. the union of the two horizontal lines, and the vertical Matsubara contour [1]

$$\lim_{t_0 \to -\infty} \lim_{t_f \to \infty} Z[j] = Z_{12}[j] Z_M[j]. \tag{4.9}$$

Note that in the $j \to 0$ limit Z_M has to contain the normalization factor Z_0 in order to reproduce the usual partition function and therefore $Z_{12}[0] = 1$.

Now we can focus on Z_{12} and derive explicitly the free propagator. We start by writing

$$\begin{aligned} &\exp\left\{ i \int_{\mathcal{C}_1 \mathcal{C}_2} d^4x \; \mathcal{L}_I \left(\frac{\delta}{i\delta j(x)} \right) \right\} \\ &\qquad = \exp\left\{ i \int_{-\infty}^{\infty} dt \int d^3x \left[\mathcal{L}_I \left(\frac{\delta}{i\delta j_1(x)} \right) - \mathcal{L}_I \left(\frac{\delta}{i\delta j_2(x)} \right) \right] \right\}, \end{aligned} \tag{4.10}$$

where the minus in the second term comes from the time flowing in the opposite direction and where

$$j_1(t, \boldsymbol{x}) = j(t, \boldsymbol{x}), \quad j_2(t, \boldsymbol{x}) = j(t - i\beta, \boldsymbol{x}). \tag{4.11}$$

We can then write the real-time propagator as

$$i\Delta_0^{(rs)}(x - x') = \int \frac{d^4k}{(2\pi)^4} e^{-ik\cdot(x-x')} i\Delta_0^{(rs)}(k), \tag{4.12}$$

which we can write in matrix form as

$$\begin{aligned} \boldsymbol{\Delta}_0(k) &\equiv \boldsymbol{\Delta}_{0F}(k) + \boldsymbol{\Delta}_{0T}(k) \\ &= \begin{pmatrix} \Delta_{0F}(k) & \\ & -\Delta_{0F}^{\dagger}(k) \end{pmatrix} - 2\pi i \delta(k^2 - m^2) \sinh\Theta(k) \begin{pmatrix} \sinh\Theta(k) & \cosh\Theta(k) \\ \cosh\Theta(k) & \sinh\Theta(k) \end{pmatrix}, \end{aligned} \tag{4.13}$$

where $\sinh\Theta(k) = \sqrt{n_B(k_0)} = (\exp(\beta k_0) - 1)^{-1/2}$. Importantly, in the limit $\beta \to \infty$, we find

$$\boldsymbol{\Delta}_0(k) = \boldsymbol{\Delta}_{0F}(k), \tag{4.14}$$

which implies that we recover the usual vacuum propagator on the real time axis $\mathcal{C}_1$ which corresponds to the 11-component of $\boldsymbol{\Delta}_0(k)$. Additionally, we note that type-1 and type-2 fields decouple.

We can formally solve the generating functional and find

$$\begin{aligned} Z[j] &= \exp\left\{ i \int_{-\infty}^{\infty} dt \int d^3x \left[\mathcal{L}_I \left(\frac{\delta}{i\delta j_1(x)} \right) - \mathcal{L}_I \left(\frac{\delta}{i\delta j_2(x)} \right) \right] \right\} \\ &\quad \times \exp\left\{ -\frac{i}{2} \int d^4y \int d^4z \; j_r(y) \Delta_0^{(rs)}(y - z) j_s(z) \right\} \\ &= \int \mathcal{D}\phi_1 \mathcal{D}\phi_2 \exp\left\{ i \int d^4x \left[\phi_r (\Delta_0^{(rs)})^{-1} \phi_s + \mathcal{L}_I(\phi_1) - \mathcal{L}_I(\phi_2) + j_r \phi_r \right] \right\}, \end{aligned} \tag{4.15}$$

where the second line is the path integral interpretation of the generating functional and $r, s = 1, 2$ is summed over. With that, we can calculate real-time Green's functions using the usual

[1] It can be shown that the imaginary time formalism is independent on the origin from the contour.

Feynman rules with slight modifications. Vertices have the same rules as in vacuum on $\mathcal{C}_1$ and a relative minus on $\mathcal{C}_2$. Propagators are either purely on $\mathcal{C}_{1,2}$, i.e. the diagonal components of Eq. (4.13) while the off-diagonal elements mix the two.

For fermions the picture is analogous and can be generalized to include a finite chemical potential μ (see also Sec. 5.1) such that the thermal propagator is [175, 177]

$$\begin{aligned}\boldsymbol{G}_0(k) &\equiv \boldsymbol{G}_{0F}(k) + \boldsymbol{G}_{0T}(k) \\ &= \begin{pmatrix} G_{0F}(k) & \\ & -G_{0F}^\dagger(k) \end{pmatrix} + 2\pi i \,(\not{k} + M)\,\delta(k^2 - M^2)\sin\Theta(k) \begin{pmatrix} \sin\Theta(k) & \cos\Theta(k) \\ \cos\Theta(k) & \sin\Theta(k) \end{pmatrix},\end{aligned} \tag{4.16}$$

where

$$G_{0F}(k) = \frac{(\not{k} + M)}{k^2 - M^2 + i\epsilon}, \tag{4.17}$$

and $\sin\Theta(k) = \sqrt{n_F(\beta, k_0)} = (\exp(\beta(k_0 - \mu)) + 1)^{-1/2}$. As for the bosonic case, in the $\beta \to \infty$ and $\mu \to 0$ the propagator becomes

$$\boldsymbol{G}_0(k) = \boldsymbol{G}_{0F}, \tag{4.18}$$

while in the $\beta \to \infty$ but $\mu \neq 0$ we find the propagator

$$\boldsymbol{G}_0(k) = \begin{pmatrix} G_{0F}(k) & \\ & -G_{0F}^\dagger(k) \end{pmatrix} + 2\pi i \,(\not{k} + M)\,\delta(k^2 - M^2) \begin{pmatrix} \Theta(k_F - |\boldsymbol{k}|) & \\ & \Theta(k_F - |\boldsymbol{k}|) \end{pmatrix}, \tag{4.19}$$

with the Fermi momentum $k_F^2 = M^2 - \mu^2$. Importantly, type-1 and type-2 fields are again completely decoupled.

Therefore, considering the 11-component only ($\boldsymbol{G}_0^{11} \equiv G_0$) and taking heavy baryon limit at leading order we find the non-relativistic nucleon propagator for symmetric nuclear matter ($\mu_p = \mu_n = \mu$) at finite temperature to be[2]

$$iG_0(k, \beta) = \frac{i}{k^0 + i\epsilon} - 2\pi \left[\delta(k^0 - \frac{\boldsymbol{k}^2}{2M})\theta(\omega) n_F(\beta, \omega) + \delta(\omega + M)\theta(-\omega) n_F(-\beta, \omega)\right], \tag{4.20}$$

where $\omega \simeq M + k^0$. Note that it is straight forward to extend this result to asymmetric nuclear matter, as is needed in order to describe neutron star matter. Also note that the momentum k_μ is the residual momentum defined in Eq. (2.80). The first term in equation (4.20) is the free vacuum propagator, while the second term accounts for the filled Fermi sea of nucleons and is sometimes called medium insertion. In the zero temperature limit, this simplifies to

$$iG(p) = \frac{i}{k^0 + i\epsilon} - 2\pi\delta(k^0)\theta(p^0)\theta(k_F - |\boldsymbol{k}|). \tag{4.21}$$

It is the medium insertion of this propagator that gives rise to a systematic expansion in $k_F/\Lambda_\chi \sim \rho^{1/3}/\Lambda_\chi$ which allows to calculate the effective density dependence of axion couplings. Using the power counting scheme derived in App. A.6, we proceed with the calculation of density corrections to the axion-nucleon vertex.

[2]Note that at finite temperature there could in principle be a contribution due to thermal ghosts, i.e. loop contributions involving type-2 fields. However for all calculations done in this work they do not play a role.

4.2 The Axion-Nucleon Vertex at Finite Density

With the nucleon propagator at finite density at hand (Eq. (4.21)) we are in the position to construct the density corrections to the axion-nucleon vertex. For each usual vacuum loop diagram we investigated in Sec. 2.4.3 there is a corresponding diagram with a density insertion for the nucleon in the loop [178]. This implies that density corrections start contributing at chiral order $\nu = 2$, according to Eq. (2.81).

As in Sec. 2.4 we omit axion loops as they are suppressed by at least $1/f_\phi$ and only show diagrams that are non-zero. In Fig. 4.1 we show the non-trivial leading order ($\nu = 2$) corrections to the nucleon axion vertex with a density insertion respectively. The density insertion is marked by the double-dashed nucleon line. The vertices at this order come from the LO Lagrangian Eq. (2.82) while the loop with including one density insertion raises the chiral order of the diagram to $\nu = 2$. Note that one can draw diagrams involving contact interactions from the LO Lagrangian Eq. (2.87a) which however evaluate to zero, as shown in App. A.8.2. The result can

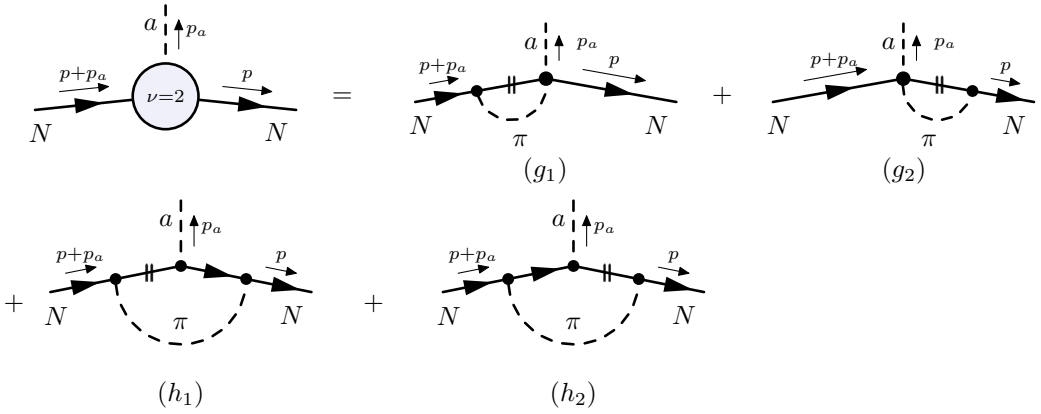

Figure 4.1: ($a = \phi$) Non-zero corrections to the axion nucleon vertex at finite density at chiral order $\nu = 2$. Filled dotes denote $\Delta = 0$ vertices according to Eq. (2.81). The nucleon propagator marked by the double dash implies a density insertion, i.e. second term in Eq. (4.21).

be written though of as form factors in analogy to the vacuum results

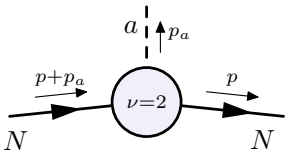

$$= \quad -\frac{1}{f_\phi}\mathcal{A}_n^{(\nu=2)} S\cdot p_\phi - \frac{1}{f_\phi}\mathcal{B}_n^{(\nu=2)} S\cdot p, \tag{4.22}$$

where the form factors are given by

$$\mathcal{A}_n^{(\nu=2)} = F_1(p, k_F^{p/n}, p_\phi)\tau^3 + F_2(p, k_F^{p/n}, p_\phi)\mathbb{1}, \tag{4.23}$$

and

$$\mathcal{B}_n^{(\nu=2)} = F_3(p, k_F^{p/n}, p_\phi)\tau^3 + F_4(p, k_F^{p/n}, p_\phi)\mathbb{1}, \tag{4.24}$$

where the functions $F_i(p, k_F^{p/n}, p_\phi)$ are given in App. A.9.

At next to leading order the relevant diagrams are shown in Fig. 4.2. We find all diagrams at this order by keeping one loop and switching one vertex to a $\Delta = 1$ vertex from the NLO Lagrangian Eq. (2.82). Here it is important to note that only the constants $\hat{c}_{3/4}$ are dom-

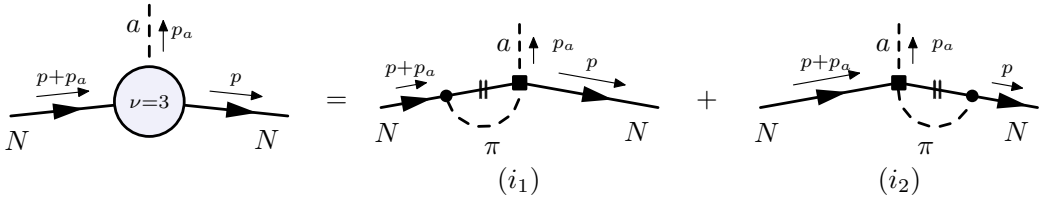

Figure 4.2: ($a = \phi$) Non-zero corrections to the axion nucleon vertex at finite density at chiral order $\nu = 3$. Filled squares denote $\Delta = 1$, filled circles denote $\Delta = 0$ vertices according to Eq. (2.81). The nucleon propagator marked by the double dash implies a density insertion, i.e. the second term in Eq. (4.21).

inant compared to the remaining LECs since they are effectively enhanced by the low-lying Δ-resonance. While the constants $\hat{c}_{1/5/9}$ are order one (but not enhanced) the LECs $\hat{c}_{2/8}$ are even kinematically suppressed since they scale as $v \cdot k \sim k^2/m_N$, see App. A.6. Here we neglect all LECs that are not enhanced. The explicit calculation of the relevant diagrams at $\nu = 3$ is shown in App. A.8.2. Again written as form factors they evaluate to

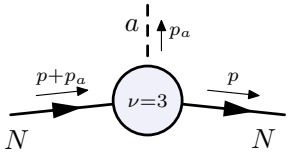

$$= -\frac{1}{f_\phi}\mathcal{A}_n^{(\nu=3)} S\cdot p_\phi - \frac{1}{f_\phi}\mathcal{B}_n^{(\nu=3)} S\cdot p, \tag{4.25}$$

with

$$\begin{aligned}\mathcal{A}_n^{(\nu=3)} = g_A c_{u-d}\Bigg[&\Big(\hat{c}_3 F_5(p,k_F^{p/n},p_\phi) + \hat{c}_4 F_6(p,k_F^{p/n},p_\phi)\Big)\tau^3 \\ &+ \Big(\hat{c}_3 F_7(p,k_F^{p/n},p_\phi) + \hat{c}_4 F_8(p,k_F^{p/n},p_\phi)\Big)\mathbb{1}\Bigg],\end{aligned} \tag{4.26}$$

and

$$\begin{aligned}\mathcal{B}_n^{(\nu=3)} = g_A c_{u-d}\Bigg[&\Big(\hat{c}_3 F_9(p,k_F^{p/n},p_\phi) + \hat{c}_4 F_{10}(p,k_F^{p/n},p_\phi)\Big)\tau^3 \\ &+ \Big(\hat{c}_3 F_{11}(p,k_F^{p/n},p_\phi) + \hat{c}_4 F_{12}(p,k_F^{p/n},p_\phi)\Big)\mathbb{1}\Bigg],\end{aligned} \tag{4.27}$$

where again the functions $F_i(p,k_F^{p/n},p_\phi)$ can be found in App. A.9.

We perform the calculation for the vertices (h_1) and (h_2) in isospin symmetric matter explicitly here to give some intuition and refer to App. A.8.2 for the details of the remaining calculations. Upon defining

$$c_N = \mathrm{Diag}\,(c_p, c_n) = g_A c_{u-d}\tau^3 + g_0 c_{u+d}\mathbb{1}, \tag{4.28a}$$

$$\hat{c}_N = -g_A c_{u-d}\tau_3 + 3 g_0 c_{u+d}\mathbb{1}, \tag{4.28b}$$

the ansatz for the loop integral for (h_1) and (h_2) reads

$$\begin{aligned}&\int \frac{d^4k}{(2\pi)^4}\left[-\frac{g_A}{2f_\pi}\boldsymbol{\sigma}\cdot(\boldsymbol{k}-\boldsymbol{p})\tau^a\right]\left[\frac{i}{k^0} - 2\pi\delta(k^0)\theta(k_F-|\boldsymbol{k}|)\right]\left[\frac{c_N}{2f_\phi}\boldsymbol{\sigma}\cdot\boldsymbol{p}_\phi\right]\times \\ &\times\left[\frac{i}{k^0+p_\phi^0} - 2\pi\delta(k^0+p_\phi^0)\theta(k_F-|\boldsymbol{k}+\boldsymbol{p}_\phi|)\right]\left[\frac{g_A}{2f_\pi}\boldsymbol{\sigma}\cdot(\boldsymbol{k}-\boldsymbol{p})\tau^b\right]\left[\frac{-i\delta^{ab}}{m_\pi^2-(k-p)^2}\right].\end{aligned} \tag{4.29}$$

Taking care of the spin as well as the isospin structures and only keeping the density dependent part (we already calculated the vacuum loop in Sec. 2.4.3) leaves us after simplifying and evaluating the k^0 integrals with

$$(h_1)+(h_2)=\left(\frac{g_A^2\hat{c}_N}{8f_\pi^2 f_\phi}\right)\frac{1}{p_\phi^0}\int_0^{k_F}\frac{d^3k}{(2\pi)^3}\left\{\left[\frac{2\boldsymbol{\sigma}\cdot(\boldsymbol{k}-\boldsymbol{p})\boldsymbol{p}_\phi\cdot(\boldsymbol{k}-\boldsymbol{p})-\boldsymbol{\sigma}\cdot\boldsymbol{p}_\phi(\boldsymbol{k}-\boldsymbol{p})^2}{\tilde{m}_\pi^2+(\boldsymbol{k}-\boldsymbol{p})}\right]\right.$$
$$\left.-\left[\frac{2\boldsymbol{\sigma}\cdot(\boldsymbol{k}-\boldsymbol{p}-\boldsymbol{p}_\phi)\boldsymbol{p}_\phi\cdot(\boldsymbol{k}-\boldsymbol{p}-\boldsymbol{p}_\phi)-\boldsymbol{\sigma}\cdot\boldsymbol{p}_\phi(\boldsymbol{k}-\boldsymbol{p}-\boldsymbol{p}_\phi)^2}{\tilde{m}_\pi^2+(\boldsymbol{k}-\boldsymbol{p}-\boldsymbol{p}_\phi)^2}\right]\right\}, \tag{4.30}$$

where we used that $m_\pi^2-(k-p_\phi)^2=m_\pi^2-(k_0^2+2k_0p_\phi^0+p_{\phi0}^2)+(\boldsymbol{k}-\boldsymbol{p}_\phi)^2=\tilde{m}_\pi^2+(\boldsymbol{k}-\boldsymbol{p}_\phi)^2$, since $k_0\sim\boldsymbol{k}^2/2m_N\ll|\boldsymbol{k}|$ and defined $\tilde{m}_\pi^2=m_\pi^2-(p_\phi^0)^2$. With the help of the standard integrals defined in App. A.9 we can write the result as

$$(h_1)+(h_2)=-\left(\frac{g_A^2\hat{c}_N}{8f_\pi^2 f_\phi}\right)\frac{1}{|\boldsymbol{p}_\phi|}\Big[2\left(I_1(\tilde{m}_\pi,p+p_\phi,p_\phi)-I_1(m_\pi,p,p_\phi)\right)$$
$$-\boldsymbol{\sigma}\cdot\boldsymbol{p}_\phi\left(I_2(\tilde{m}_\pi,p+p_\phi)-I_2(m_\pi,p)\right)\Big]. \tag{4.31}$$

In the same manner we can calculate all density loops of the diagrams shown in Figs. 4.1 and 4.2 for arbitrary matter configurations. We do so in appendix A.8.2, where we calculate the relevant quantities to evaluate the density corrections in arbitrary mixed matter. We calculate the loops using the propagator Eq. (4.21) as well as with the replacement of the density insertion

$$-2\pi\delta\left(k_0\right)\theta\left(k_F-|\boldsymbol{k}|\right)\to-2\pi\delta\left(k_0\right)\theta\left(k_F-|\boldsymbol{k}|\right)\tau^3, \tag{4.32}$$

since arbitrarily mixed matter is suitably described by the propagator

$$iG(p)=\frac{i}{k^0+i\epsilon}-2\pi\delta(k^0)\theta(p^0)\left[\frac{1+\tau^3}{2}\theta\left(k_F^p-|\boldsymbol{k}|\right)+\frac{1-\tau^3}{2}\theta\left(k_F^n-|\boldsymbol{k}|\right)\right]. \tag{4.33}$$

With that we conclude the section of the density corrections to the axion-nucleon vertex and continue discussing the reuslts for the effective couplings.

4.2.1 Density Dependence

We can summarize the results from the previous sections in the following equation

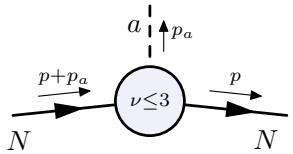

$$=\quad-\frac{1}{f_\phi}\mathcal{A}^{(\nu\leq3)}(p,k_F^{p/n},p_\phi)\,S\cdot p_\phi-\frac{1}{f_\phi}\mathcal{B}^{(\nu\leq3)}(p,k_F^{p/n},p_\phi)\,S\cdot p, \tag{4.34}$$

where the effective axion nucleon vertex is written in terms of form factors $\mathcal{A}$ and $\mathcal{B}$ which consist of isovector and isoscalar contributions and include renormalized vacuum loops and contributions due to loops with density insertions up to $\nu=3$.

At this point, we would like to note that the above result obviously is model dependent since it explicitly depends on the PQ charges in the UV. Furthermore, for the benchmark QCD axion models considered in this thesis, namely KSVZ and DSFZ we found at leading order in Sec. 2.4.3 that $\mathcal{A}^{(\nu=0)}=c_N$ and $\mathcal{B}^{(\nu=0)}=0$. Similarly, for the full result, we find that the contribution

due to $\mathcal{B}^{(\nu\leq 3)}$ is basically negligible compared to $\mathcal{A}^{(\nu\leq 3)}$ for all models under consideration. For bulk nuclear matter the magnitude of nucleon momenta are expected to be close to the Fermi momentum $|\boldsymbol{p}| \sim k_F$. To good approximation, the momentum of the axion is small compared to the momenta of the nucleons i.e. $|\boldsymbol{p}_\phi| \ll k_F \sim p$. Neglecting the contribution due to $\mathcal{B}^{(\nu\leq 3)}$ we can write the density dependent axion-nucleon coupling as a matrix in isospin space in analogy to the LO tree level coupling (see Eq. (2.90))

$$\text{Diag}\left(c_p, c_n\right)_{\rho_n,\rho_p} \simeq \mathcal{A}(\rho_n, \rho_p), \tag{4.35}$$

where $\rho_N = \left(k_F^N\right)^3/3\pi^2$ with $N = n, p$ is the number density of proton and neutron respectively such that the total baryon density is $\rho = \rho_n + \rho_p$.

Before discussing the density dependence as well as the higher order vacuum loop contributions of the axion-nucleon coupling for the benchmark QCD axion models namely the KSVZ and the DFSZ axion, we would like to mention that we treat all unknown LECs, mostly isoscalar couplings, as in Sec. 2.4.3 as the superposition of two normal distributions. In addition, we take into account the error due to the uncertainty of the ChPT expansion. We explicitly checked that the difference between the density corrections at $\nu = 2$ and the next higher order is given by the constant $\pm\, c \times \frac{k_F^3}{(4\pi f_\pi)^2 \Lambda_\chi}$ with $c \sim 5$, neglecting its k_F dependence. We then extrapolate this difference to higher orders such that the ChPT uncertainty is roughly given by

$$\pm\, c \sum_i \frac{k_F^{i+3}}{(4\pi f_\pi)^2 \Lambda_\chi^{i+1}}. \tag{4.36}$$

KSVZ axion

For the KSVZ axion the UV couplings to the PQ current are set to zero, $c^0_{u-d} = c^0_{u+d} = 0$. We show the axion-proton and axion-neutron coupling in for isospin symmetric nuclear matter ($\rho_n = \rho_p = \rho/2$) in Fig. 4.3 and Fig. 4.4 respectively. The left panel in both Figures shows the full contribution, dominated by the form factor $\mathcal{A}^{(\nu\leq 3)}$ while the right panel shows the contribution due to $(\mathcal{B}^{(\nu\leq 3)}\,|\boldsymbol{p}|)/(|\boldsymbol{p}_\phi|)$ which in both cases is at least one order of magnitude suppressed.

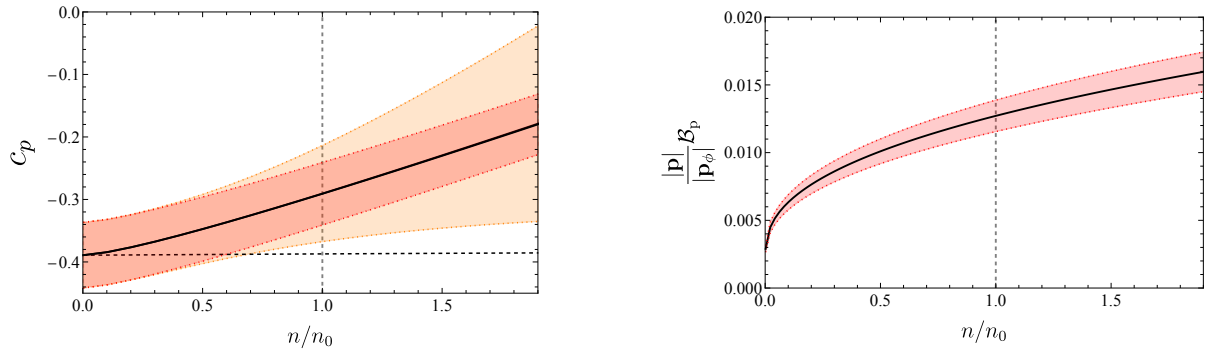

Figure 4.3: Density dependence of the KSVZ axion-proton couplings in isospin symmetric nuclear matter as a function of density in units of nuclear saturation density ρ_0 ($\rho = n$ in the plot). (Left panel) Full contribution. (Right panel) Contribution due to the subleading form factor $\mathcal{B}^{(\nu\leq 3)}$. The shaded region represents the error bars resulting from the uncertainties of the constants given in Table 2.1 as well as the error emerging from higher order terms in the chiral expansion.

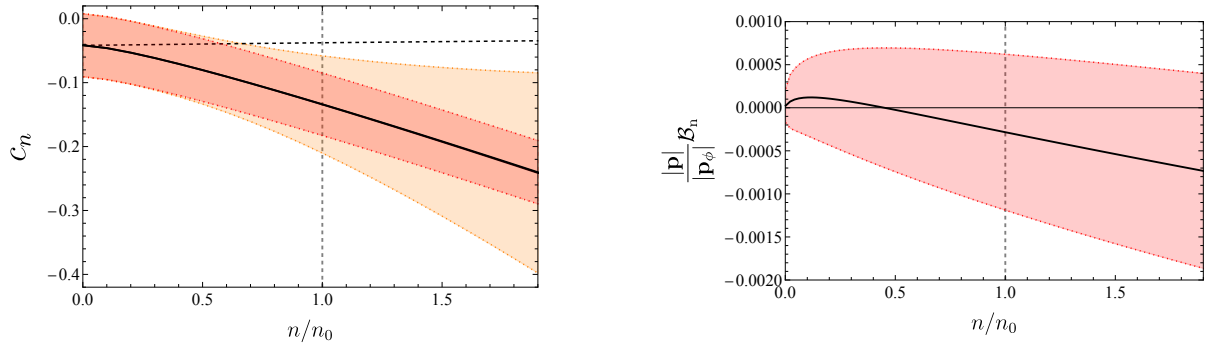

Figure 4.4: Density dependence of the KSVZ axion-neutron couplings in isospin symmetric nuclear matter as a function of density in units of nuclear saturation density ρ_0 ($\rho = n$ in the plot). (Left panel) Full contribution. (Right panel) Contribution due to the subleading form factor $\mathcal{B}^{(\nu\leq 3)}$. The shaded region represents the error bars resulting from the uncertainties of the constants given in Table 2.1 as well as the error emerging from higher order terms in the chiral expansion.

For densities around nuclear saturation density $\rho_0 \simeq 0.16\,\text{fm}^{-3}$, we find

$$(c_p)^{\text{KSVZ}}_{\rho_0} = -0.283(64), \quad (c_n)^{\text{KSVZ}}_{\rho_0} = -0.141(63). \tag{4.37}$$

Let us compare this result to the LO tree level coupling we found previously (see Eq. (2.92)). While for the proton there is an order one difference in the mean-value, the coupling of the neutron changes by two orders of magnitude at nuclear saturation density. This is one of the main results of this part of the thesis and confirms the first estimate of [11] who found that neutron-axion coupling is suppressed by an accidental cancellation between $z = m_u/m_d \approx 1/2$ and the ratio of matrix elements in vacuum $\Delta u/\Delta d = (g_0^{ud} + g_A)/(g_0^{ud} - g_A) \approx -2$,

$$\left(\frac{c_n}{c_p}\right)^{\text{KSVZ}}_0 \propto \frac{1 + z(\Delta u/\Delta d)_0}{(\Delta u/\Delta d)_0 + z} \approx 7.6 \times 10^{-2}\,, \tag{4.38}$$

neglecting RGE and other subleading effects such as $m_{u,d}/m_s$ corrections. We would like to stress here however that the value of c_n at LO tree-level depends sensitively on the constants chosen which is why the effect found here is even more severe i.e. a change by two orders of magnitude.

For pure neutron matter ($\rho_n = \rho$) we show the density dependence of the axion-proton and axion-neutron coupling in Fig. 4.5 and Fig. 4.6 up ρ_0 because Fermi momenta of pure neutron matter at these densities correspond to Fermi momenta of symmetric matter at $\rho = 2\rho_0$. Similarly as to symmetric nuclear matter the contribution from $\mathcal{B}^{(\nu\leq 3)}$ is negligible as can be seen in the left panels of Fig. 4.5 and Fig. 4.6. At nuclear saturation density we find the axion-nucleon couplings to be

$$(c_p)^{\text{KSVZ}}_{\rho_0} = -0.258(66), \quad (c_n)^{\text{KSVZ}}_{\rho_0} = -0.143(73), \tag{4.39}$$

where a similar trend for axion-proton and axion-neutron coupling is found. This just shows that our result does not depend much on isospin asymmetry which would be important for *e.g.* NS cooling.

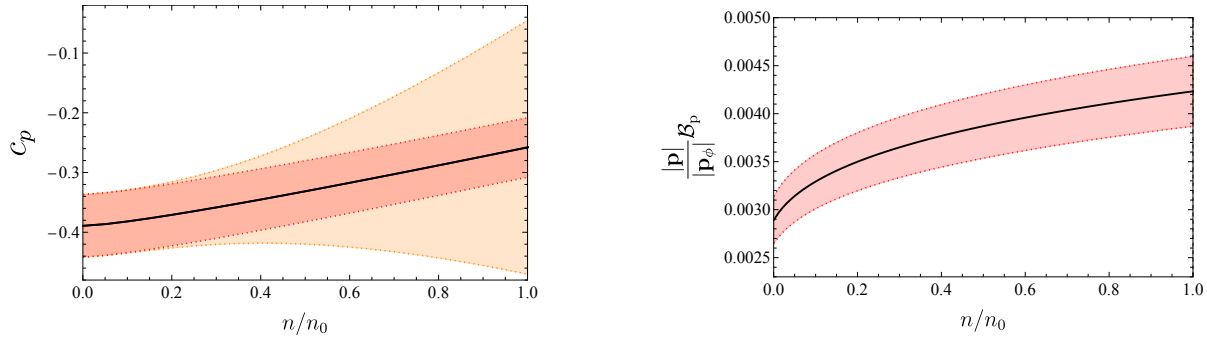

Figure 4.5: Density dependence of the KSVZ axion-proton couplings in pure neutron matter as a function of density in units of nuclear saturation density ρ_0 ($\rho = n$ in the plot). (Left panel) Full contribution. (Right panel) Contribution due to the subleading form factor $\mathcal{B}^{(\nu\leq 3)}$. The shaded region represents the error bars resulting from the uncertainties of the constants given in Table 2.1 as well as the error emerging from higher order terms in the chiral expansion.

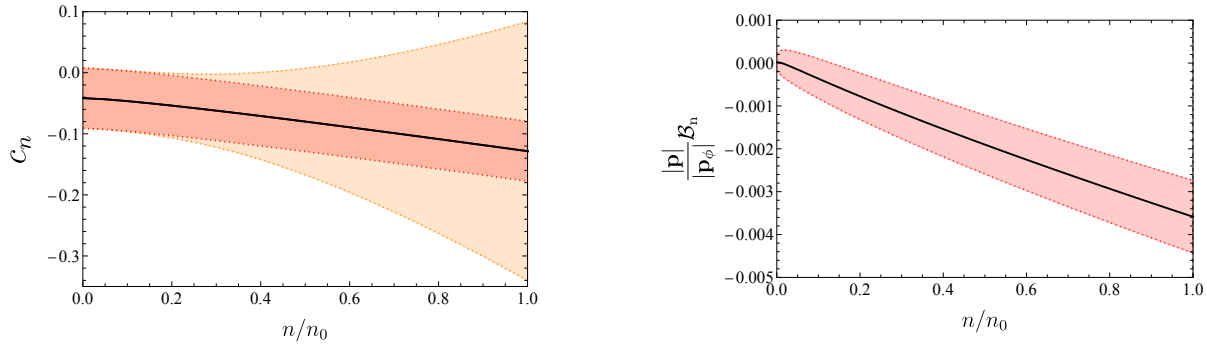

Figure 4.6: Density dependence of the KSVZ axion-proton couplings in isospin symmetric nuclear matter as a function of density in units of nuclear saturation density ρ_0 ($\rho = n$ in the plot). (Left panel) Full contribution. (Right panel) Contribution due to the subleading form factor $\mathcal{B}^{(\nu\leq 3)}$. The shaded region represents the error bars resulting from the uncertainties of the constants given in Table 2.1 as well as the error emerging from higher order terms in the chiral expansion.

DFSZ axion

Next we consider the DFSZ axion model with $c_u^0 = \sin^2\beta/3$, $c_d^0 = 1 - c_u^0$, where β is related to the vevs of the Higgs fields in the UV theory. We consider the case of symmetric nuclear matter for three benchmark points $\sin^2\beta = \{0, 1/2, 1\}$ and show the density dependence of the axion-proton (left panel) and axion-neutron (right panel) couplings in Fig. 4.7, Fig. 4.8 and Fig. 4.9. Evaluating the couplings for each of them at nuclear saturation density we find

$$\begin{aligned}
\sin^2\beta = 0: &\quad (c_p)_{\rho_0}^{\mathrm{DFSZ}} = -0.279(68), \quad (c_n)_{\rho_0}^{\mathrm{DFSZ}} = 0.001(66), \\
\sin^2\beta = 1/2: &\quad (c_p)_{\rho_0}^{\mathrm{DFSZ}} = -0.210(51), \quad (c_n)_{\rho_0}^{\mathrm{DFSZ}} = -0.068(50), \\
\sin^2\beta = 1: &\quad (c_p)_{\rho_0}^{\mathrm{DFSZ}} = -0.142(43), \quad (c_n)_{\rho_0}^{\mathrm{DFSZ}} = -0.136(43).
\end{aligned} \tag{4.40}$$

We want to note that we again find a strong dependence on the axion-neutron coupling for DSFZ-type models, except for the case in which $\sin^2\beta = 1$.

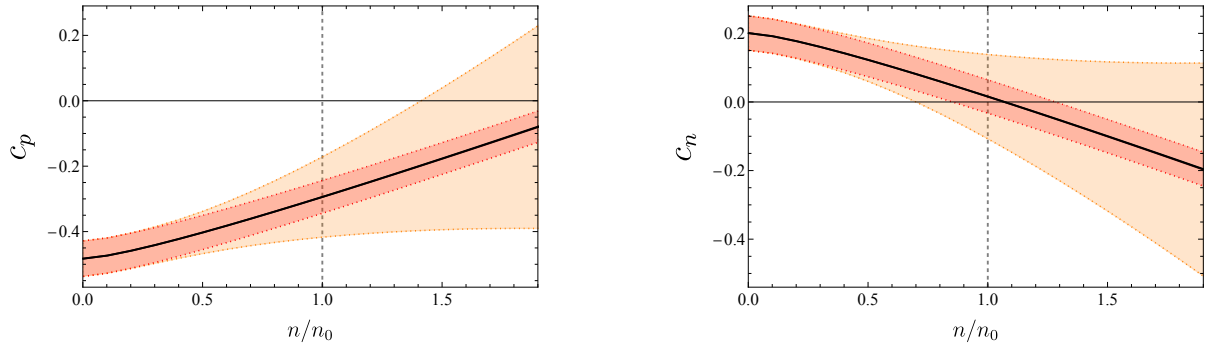

Figure 4.7: Density dependence of the DFSZ axion-nucleon couplings with $\sin^2\beta = 0$ in symmetric nuclear matter as a function of density in units of nuclear saturation density ρ_0. The shaded region represents the error bars resulting from the uncertainties of the constants given in as well as the error emerging from higher order terms in the chiral expansion.

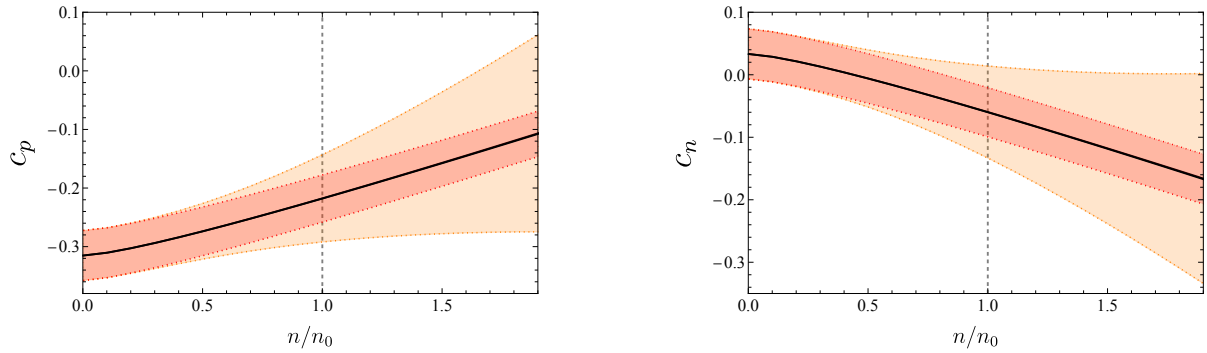

Figure 4.8: Density dependence of the DFSZ axion-nucleon couplings with $\sin^2\beta = 1/2$ in symmetric nuclear matter as a function of density in units of nuclear saturation density ρ_0. The shaded region represents the error bars resulting from the uncertainties of the constants given in as well as the error emerging from higher order terms in the chiral expansion.

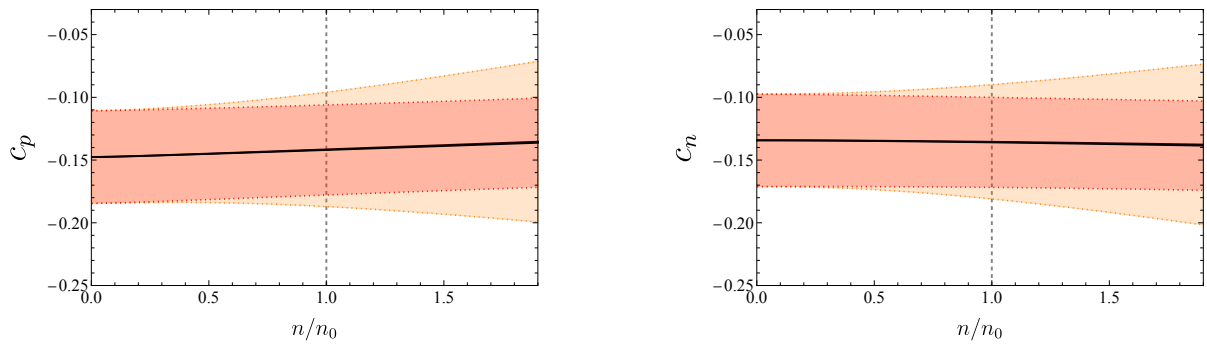

Figure 4.9: Density dependence of the DFSZ axion-nucleon couplings with $\sin^2\beta = 1$ in symmetric nuclear matter as a function of density in units of nuclear saturation density ρ_0. The shaded region represents the error bars resulting from the uncertainties of the constants given in as well as the error emerging from higher order terms in the chiral expansion.

4.3 Implications on Stellar Bounds on Axions

As we have seen, finite density effects significantly affect the QCD axion-nucleon coupling in typical conditions of supernovae and neutron stars. With these at hand, we re-evaluate the bounds on a KSVZ-type QCD axion and an astrophobic QCD axion from supernova and neutron star cooling. While we find an order one change in the total emitted energy due to axions during the SN for KSVZ-type QCD axion, we find for astrophobic axions that the model-independent couplings originating from the topological term, see Eq. (2.54), allows to probe unexplored axion parameter space.

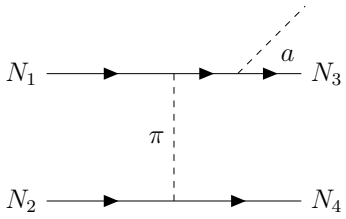

Figure 4.10: ($a = \phi$) The one-pion-exchange diagram with an external axion at leading order.

The dominant process for axion production in these environments is the nucleon Bremsstrahlung process [57, 86, 87], but also see [180–182] for the alternative process $p\,\pi^- \to n\,\phi$ that since recently is believed to play a significant role [183]. At leading order, the Bremsstrahlung process is given by the one-pion exchange, shown in Fig. 4.10. The total process includes eight diagrams which are generated by attaching the axion to different legs and by considering t- and u-channels. A systematic calculation of the nucleon Bremsstrahlung should go beyond the naive one-pion exchange since at the relevant densities within SNe and NSs higher order terms, i.e. two-pion exchange contributions, nucleon re-scatterings and other nuclear physics effects become important [57]. In the literature, one can find many empirical approaches to this problem, but what is, however, lacking so far is a systematic calculation of relevant nuclear physics effects. While such a systematic calculation at finite density keeping all errors under control is a long-term goal, we want to systematically calculate the emissivity from the one-pion-exchange diagram with the density dependent vertex, as shown in Fig. 4.11, which takes the first step towards such a systematic analysis. The axion emissivity $\dot{\epsilon}_\phi$ is the amount of energy emitted by axions per volume

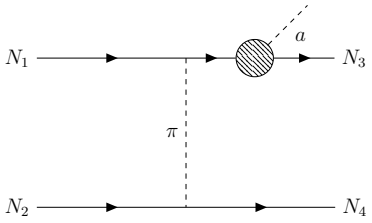

Figure 4.11: ($a = \phi$) The one-pion-exchange diagram with an external axion.

of a stellar object (in our case, the SN) and time. It is given in units of Energy/(Volume $\times$ Time)

and is defined as [86]

$$\dot{\epsilon}_\phi = \int d\Pi_1 d\Pi_2 d\Pi_3 d\Pi_4 d\Pi_\phi (2\pi)^4 S|M|^2 \delta^{(4)} \left(\sum_i p_i\right) E_\phi f_1 f_2 \left(1-f_3\right)\left(1-f_4\right), \tag{4.41}$$

with $d\Pi_i = d^3p_i/(2\pi)^3 2E_i$ and $f_i = n_F(\beta, E_i)$. $E_i = \sqrt{m_N^2 + \boldsymbol{p}_i^2}$ is the energy of the particle, which we can take in the non-relativistic limit to be

$$E_i^{-1} = (m_N^2 + \boldsymbol{p}_i^2)^{-\frac{1}{2}} \simeq \frac{1}{m_N}\left(1 - \frac{\boldsymbol{p}_i^2}{2m_N}\right) = \frac{1}{m_N} + \mathcal{O}\left(\frac{\boldsymbol{p}_i^2}{m_N^3}\right), \tag{4.42}$$

to rewrite $d\Pi_i \simeq d^3p_i/((2\pi)^3 2m_N)$ for the nucleons. $|M|^2$ is the amplitude of the Bremsstrahlungs process under consideration, which at LO is straightforward to evaluate [86].

We show the axion-nucleon Bremsstrahlung process with the density dependent vertex from the previous section in Fig. 4.11. The evaluation of the amplitude squared is done in analogy to the LO result, see Ref. [86]. For a systematic expansion of the emissivity, we expand $|M|^2$ to $\mathcal{O}(k_F^3)$. With the density dependence of the axion-nucleon coupling at hand, we can see that the finite density contribution lifts the cancellation of the axion-neutron coupling in vacuum. As discussed previously, the change in the axion-proton coupling is not as dramatic but still $\mathcal{O}(1)$. We have no reason to believe that including higher order terms will re-introduce this accidental cancellation which would correspond to a huge amount of tuning. Therefore, to get an idea of the typical size we expect at finite density, we also keep the terms that are formally higher order.

Making use of the core-collapse SN profiles assuming an $18.6\,M_\odot$ progenitor mass from [184], also used in [185], we perform the integration of the emissivity Eq. (4.41) over the density-dependent amplitude squared for a KSVZ axion as well as for astrophysics axions.

KSVZ Axion

For the emissivity, we include the statistics due to the uncertainty of the LECs. Drawing the values from the superposition of two normal distributions with mean value $\pm 0.5\text{GeV}^{-1}$ and standard deviation 0.5GeV^{-1}, as explained Sec. 2.4.3, we integrated the emissivity 10^3 times which led to sufficient convergence. It is ongoing work to include the uncertainties due to the expansion in ChPT. Naively, due to the large densities found during the SN, this should be the main source of uncertainty. The result, with the axion decay constant, factored out and evaluated at different time steps can be seen in Fig. 4.12. The shaded bands come from the 1σ uncertainties due to the LECs. We would like to note that for the tree-level vacuum couplings, we recover a similar result as [57], at $t = 1\,\text{s}$ and $r = 1\,\text{km}$ we find

$$\dot{\varepsilon}_\phi \simeq 3 \times 10^{33}\ \text{erg s}^{-1}\,\text{cm}^{-3} \left(\frac{10^9\,\text{GeV}}{f_\phi}\right)^2. \tag{4.43}$$

We observe that while there is half an order of magnitude difference at early times, this difference decreases with later times.

Integrating over the volume gives the luminosity

$$L_\phi = 4\pi \int dr\, r^2\, \dot{\varepsilon}_\phi(r,t). \tag{4.44}$$

The result for a KSVZ axion with tree-level coupling (black) and loop- plus density-corrected coupling (red) is shown in Fig. 4.13 together with the error bars originating from the uncertainties

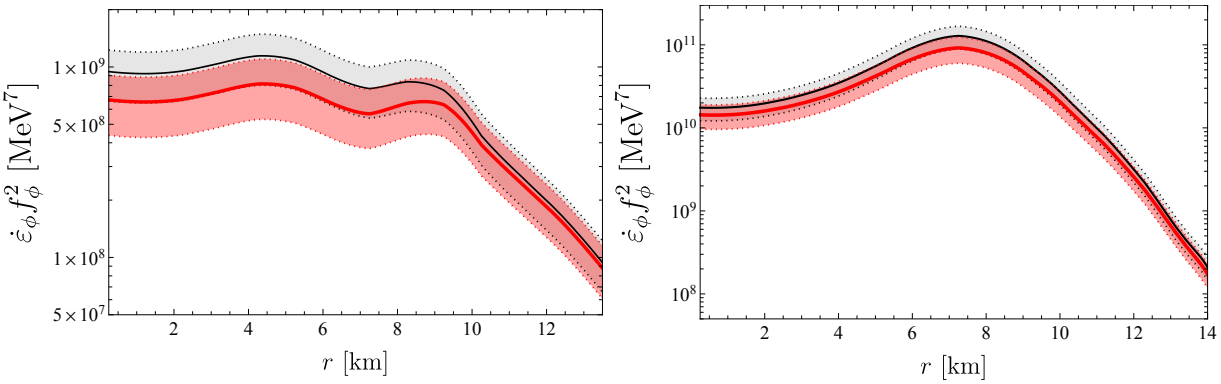

Figure 4.12: Emissivity due to the QCD axion for tree-level vacuum vertex (black) and density-dependent vertex including vacuum loops up to N^{3}LO. We take into account the uncertainties due to low-energy constants. The solid line corresponds to the mean value, while dotted lines and shaded areas correspond to 1σ uncertainties. The left panel is evaluated for $t = 0.1\,\mathrm{s}$ while the right panel shows the emissivities at $t = 1\,\mathrm{s}$.

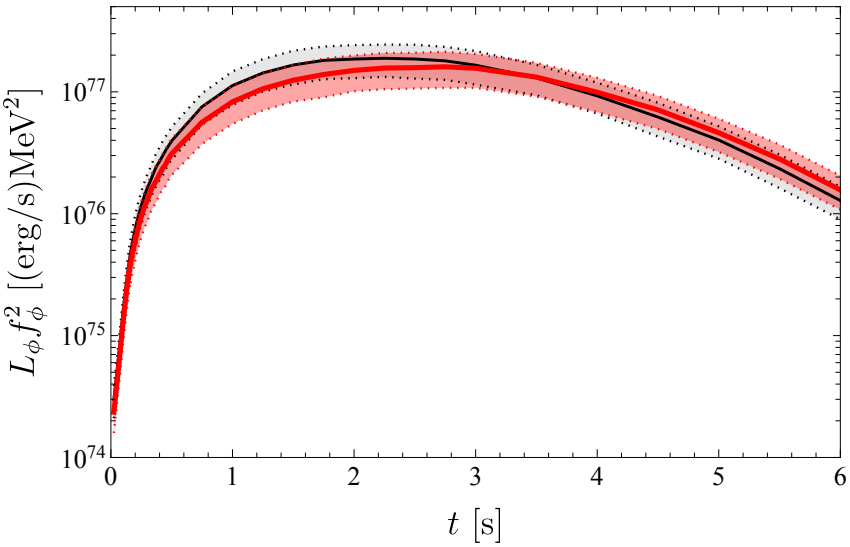

Figure 4.13: Luminosity for the KSVZ axion for tree-level vacuum vertex (black) and density-dependent vertex including dominant (i.e. resonance enhanced) vacuum loops up to N^{3}LO. We take into account the uncertainties due to low-energy constants. The solid line corresponds to the mean value, while dotted lines and shaded areas correspond to 1σ uncertainties.

in the LECs. As can be seen, the difference is not dramatic. While the luminosity, evaluated with the tree-level vacuum couplings, dominates at early times ($t < 3.3\,\mathrm{s}$), the luminosity with the full density- and loop-corrected vertex dominates at later times. This seems to be due to an interplay of the opposite behavior of proton and neutron couplings with density. Eventually, we are interested in the total energy released in axions during the SN, which is given by integrating the luminosity over time. We find a $\sim 10\%$ reduction in the total energy when integrating the luminosity over $t = 6\,\mathrm{s}$

$$E_{\mathrm{corrected}} \simeq 0.9\, E_{\mathrm{tree}} \tag{4.45}$$

While this is certainly not a dramatic effect, it changes the axion SN bound by an order one factor and should be included in state-of-the-art calculations. Furthermore it is important to

quantify the uncertainty in the luminosity since this directly translates to the uncertainty in the axion SN bound. It is ongoing work to calculate the luminosity for later times, including the error due to ChPT uncertainty and different SN EOSs, and re-do the entire analysis for DSFZ-type QCD axions.

Astrophobic Axions

As discussed in Sec. 2.6, astrophobic axions [88] avoid bounds as the one due to the model-dependent coupling to spin by tuning the relevant coupling. Therefore, in order to probe these models, one has to rely on model-independent couplings in the sense that they arise from the topological term in the UV alone, see Eq. (2.54). This line of reasoning has been pursued in light of the effect of the model-independent nEDM portal on SN [89], as discussed in Sec. 2.6.

In this subsection, we are going to show that a stronger bound can be obtained by considering higher-order couplings in the chiral expansion. As expected and explicitly seen in Eq. (2.65), the model dependence of the PQ current is inherited by all shift-symmetric couplings i.e. proportional to the axion gradient, while shift-symmetry breaking couplings are completely generic and come from $\phi G\tilde{G}$ alone. In terms of IR constants, at $\nu = 3$ these are $\hat{c}_1$ and $\hat{c}_5$. The larger $\hat{c}_1$ gives rise to the isospin symmetric part of the nucleon sigma term and is proportional to the external scalar source $s \sim \cos\phi$, see Eq. (2.65). This implies that $\hat{c}_1$ always comes with a $1/f_\phi^2$ suppression and can therefore be safely neglected. However, the smaller $\hat{c}_5$, which gives rise to the isospin-breaking coupling, is proportional to the pseudo-scalar source $p \sim \sin\phi$.

We repeat the same SN integration as for the KSVZ-type axion but now set all couplings to zero except the model-independent $\hat{c}_5$ coupling. The luminosity for this scenario (red curve) compared to the tree-level result for a KSVZ axion from before (black) is shown in Fig. 4.14.

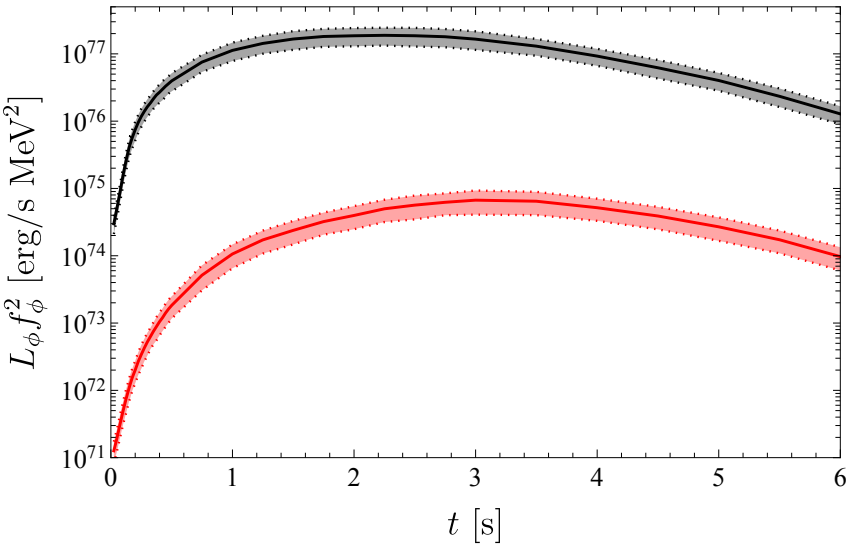

Figure 4.14: Luminosity for the KSVZ axion for tree-level vacuum vertex (black) and density-dependent vertex for astrophobic axions including only the coupling $\hat{c}_5$. We take into account the uncertainties due to low-energy constants. The solid line corresponds to the mean value, while dotted lines and shaded areas correspond to 1σ uncertainties.

While the shape changes only slightly, a decrease in the overall luminosity by three orders of magnitude is clearly visible. Following the rationale of [57], that is, to evaluate the the

luminosity at $t = 1\,\mathrm{s}$, which has to be smaller than $L_\phi(t = 1\,\mathrm{s}) < L_\nu \simeq 2 \times 10^{52}\,\mathrm{erg\,s^{-1}}$ we find

$$f_\phi > (8.5\ - 5.7) \times 10^7\,\mathrm{GeV}, \tag{4.46}$$

which is about two orders of magnitude stronger than the bound found by [89], see also Eq. (2.116). It is work in progress to include the errors due to ChPT uncertainty and check whether axion-nucleon spin couplings due to higher numbers of flavors for astrophobic axions strengthen this bound. As explained previously though, this is the conservative model-independent contribution that automatically arises for a QCD axion and cannot be tuned away without re-introducing the strong $\mathcal{CP}$ problem.

Chapter 5

The QCD Axion at Finite Density

In this chapter we show how the properties of the QCD axion change in systems at finite baryonic density, such as neutron stars and supernovae. At densities moderately higher than nuclear saturation density, if realized, meson (kaon) condensation can lead to axion condensation. We also study the axion potential at asymptotically large densities, where we find that the color-superconducting phase of QCD can lead to axion condensation and that the mass of the axion is generically several orders of magnitude smaller than in vacuum due to the suppressed instantons. QCD Axion condensation could therefore occur within the densest objects in our universe i.e. neutron stars. If the star is large enough, formation of an axion condensate can be thought of as an axion bubble that stays confined to or within the star depending on the scalar mass. Equivalently, the star can be thought of as sourcing the QCD axion. Several phenomenological consequences of the axion being sourced by neutron stars are discussed, such as its contribution to their total mass or axion-photon conversion in the magnetosphere. We would like to highlight that such a possibility was first considered in [186] for a exceptionally light QCD axion whose mass is below the expected value of $\sim \Lambda_{\rm QCD}^2/f_\phi$ (cf. Sec. 2.5).

The chapter is organized as follows. We start by review the effects of chemical potentials in quantum field theory in Sec. 5.1, where we discuss a toy model of meson condensation as well as a the implications of meson condensation on the QCD axion potential for $N_f = 2$ flavors. In Sec. 5.2 we show how general properties of the QCD axion potential change at finite baryonic densities with the focus of densities around saturation and extend the discussion of Sec. 5.1 to $N_f = 3$. In Sec. 5.3 we discuss QCD at asymptotic densities in the color-flavor-locked phase and its implications on the QCD axion potential and end the chapter with a discussion on the phenomenology of an axion condensate in the context of NSs in Sec. 5.4.

All figures and large parts of the text of this chapter are taken from [11].

5.1 Chemical potential in quantum field theory

Introducing a chemical potential in quantum field theory is a generalization of the procedure in statistical mechanics. One defines a new operator corresponding to the thermodynamic Landau free energy, the grand thermodynamic potential density, as we have seen in Sec. 4.1.1

$$\Omega = \mathcal{H} - \mu_i j_i^0 \,, \tag{5.1}$$

with $\mathcal{H}$ the Hamiltonian density, j_i^0 the conserved charge density associated with a given global symmetry of the system (i.e. the temporal component of the conserved current), and μ_i the

corresponding chemical potential. [1] From the path integral representation of the partition function (see Eq. (4.3) for a real scalar field or Ref. [187] for a pedagogical introduction), one arrives at the following prescription: the temporal derivative of each field transforming under the global symmetry in question is shifted by

$$\partial_0 \to \partial_0 + i\mu_i T_i^{\mathcal{R}}\,, \tag{5.2}$$

with $T_i^{\mathcal{R}}$ the generator of the global symmetry in the appropriate representation $\mathcal{R}$. Chemical potential therefore acts as a source for the temporal component of the corresponding conserved current, much like a background gauge field potential. Since it singles out the time direction, the chemical potential breaks the Lorentz symmetry down to its $SO(3)$ subgroup of spatial rotations. Charge conjugation symmetry (C), under which $j_i^0 \to -j_i^0$, is also broken, while parity (P) and time-reserval (T) are preserved – CP and CPT are thus broken. If part of a non-abelian group, a chemical potential also breaks the global symmetry by singling out a specific direction in generator space, namely $\mu_i T_i$, which defines an unbroken $U(1)$ subgroup.

5.1.1 $U(1)$ toy model

A simple toy model that illustrates the main effect of the chemical potential is a complex scalar theory with a global $U(1)$ symmetry [188, 189]. After using the prescription of Eq. (5.2), one finds the following Lagrangian

$$\mathcal{L}(\mu) = \partial_\mu\phi^*\partial^\mu\phi + i\mu(\phi\partial_0\phi^* - \phi^*\partial_0\phi) - (m^2-\mu^2)|\phi|^2 - \lambda|\phi|^4\,. \tag{5.3}$$

For $m^2 > \mu^2$, the field expectation value is trivial, $\langle\phi\rangle = 0$, and respects the global $U(1)$ symmetry. The two propagating degrees of freedom have different dispersion relations

$$\omega_\phi(\boldsymbol{k}) = \sqrt{k^2+m^2} - \mu\,, \quad \omega_{\phi^*}(\boldsymbol{k}) = \sqrt{k^2+m^2} + \mu\,. \tag{5.4}$$

The appearance of the chemical potential breaks C symmetry, which appears as a $\phi \leftrightarrow \phi^*$ exchange symmetry in the $\mu = 0$ theory – therefore μ can be treated as a spurion transforming as $\mu \to -\mu$.

Above the threshold $|\mu| > m$, the global $U(1)$ is spontaneously broken by the expectation value and the theory describes a Bose-Einstein condensate (BEC) phase. In contrast to the *ideal* ($\lambda = 0$) ultra-relativisitic Bose gas [188], in the *interacting* theory (with $\lambda > 0$) the chemical potential can be larger than m [189], without leading to any inconsistencies. Note, that our fundamental potential being the Landau free energy Ω, the fixed thermodynamical parameter is μ, which sets the effective energies of the particles in the system due to a coupling to the "particle bath". This allows the flow of particles in and out of the system, implying that the charge density, $\rho_\phi - \rho_{\phi^*}$, is a derived quantity set by μ.[2] As we show below, for $|\mu| > m$, the $T = 0$ system contains non vanishing charge density in the form of the BEC. One can interpret

[1] We recall that the grand-canonical density matrix is given by $\hat{\rho} = \exp\left[-\beta(H - \mu_i Q_i)\right]$, with $\beta = 1/T$ (T is the temperature), H the Hamiltonian, and Q_i the conserved charge. The partition function is then $Z(V,T,\mu_i) = \mathrm{Tr}\hat{\rho}$, where V is the volume, eventually taken to infinity. The thermodynamic potential density is $\Omega(T,\mu) = -(T/V)\ln Z = \varepsilon - \mu_i\rho_i = -p$, with ε the energy density, ρ_i the number density, and p the pressure. The grand-canonical average of an operator $\mathcal{O}$ is then $\langle O\rangle_{T,\mu_i} = \mathrm{Tr}[\mathcal{O}\hat{\rho}]/Z$ (with a slight abuse of notation, when clear we will denote ensemble averages simply by $\langle O\rangle$). Then $\rho_i = \langle j_i^0\rangle = -(\partial\Omega/\partial\mu)_T$, while the entropy density is given by $s = -(\partial\Omega/\partial T)_\mu$.

[2] This is in complete analogy to temperature T, with sets the effective energy of particles in the system due to a coupling to a "heat bath". This allows the flow of heat in and out of the system, implying that the entropy of the system is a derived quantity set by T.

this appearance of charge as particles from the "particle bath" being inserted in the ground state of the system.

In the BEC phase, the following parameterization is useful

$$\phi(x) = \frac{1}{\sqrt{2}} e^{i\chi(x)/v}(v + \sigma(x)) \,. \tag{5.5}$$

The classical potential is minimized for $v^2 = \frac{\mu^2 - m^2}{\lambda}$, and we find the following Lagrangian

$$\mathcal{L}(\mu) = \frac{1}{2}\left[(\partial_\mu \chi)^2 \left(1 + \frac{\sigma}{v}\right)^2 + (\partial_\mu \sigma)^2\right] + \mu v \left(1 + \frac{\sigma}{v}\right)^2 \partial_0 \chi - V(\mu) \,, \tag{5.6a}$$

$$V(\mu) = \frac{1}{2} m_\sigma^2 \sigma^2 + \lambda v \sigma^3 + \frac{1}{4}\lambda \sigma^4 - \frac{1}{4}\lambda v^4 \,, \tag{5.6b}$$

with $m_\sigma^2 = 2\lambda v^2 = 2(\mu^2 - m^2)$. The charge density in the condensed phase is non-vanishing in the limit of zero temperature $\beta \equiv 1/T \to \infty$ and infinite volume $V \to \infty$,

$$(\rho_\phi - \rho_{\phi^*})|_{T=0} = \lim_{\beta, V \to \infty} \frac{1}{\beta V} \left(\frac{\partial \ln Z}{\partial \mu}\right)_\beta = -\left(\frac{\partial V}{\partial \mu}\right)\Big|_{\langle\sigma\rangle = 0} = \frac{\mu^3}{\lambda}\left(1 - \frac{m^2}{\mu^2}\right) \,, \tag{5.7}$$

where we used the classical ($\hbar \to 0$) result for the generating functional $\ln Z = -\beta V V(\mu)$ for a homogeneous classical configuration $\langle\sigma\rangle$. By diagonalizing the quadratic field operators in momentum space one finds the dispersion relations for the two propagating degrees of freedom

$$\omega_\pm^2(\boldsymbol{k}) = (3\mu^2 - m^2)\left[1 + \frac{k^2}{3\mu^2 - m^2} \pm \sqrt{1 + \left(\frac{2\mu k}{3\mu^2 - m^2}\right)^2}\right] \,, \tag{5.8}$$

which at zero momentum are

$$\omega_-(\boldsymbol{0}) = 0 \,, \quad \omega_+(\boldsymbol{0}) = \sqrt{6\mu^2 - 2m^2} \,. \tag{5.9}$$

As expected, there is one massless excitation, corresponding to the NGB of the spontaneously broken $U(1)$, and one massive excitation, the radial (or Higgs) mode.

5.1.2 Meson condensation

We review now the importance of a chemical potential in the context of meson condensation in QCD, in particular for the case of two flavors [128, 190–192], and discuss for the first time its effects on the axion potential. This is a simplified version of the more complicated, but plausibly more realistic, scenario of kaon condensation ($N_f = 3$), to be discussed in Sec. 5.2.2.

For $N_f = 2$, the chiral condensate breaking $SU(2)_L \times SU(2)_R \times U(1)_B \times U(1)_A$ spontaneously to $SU(2) \times U(1)_B$ can be parameterized, in full generality, as

$$\begin{gathered} \langle \bar{q}_R q_L \rangle \equiv \langle \bar{q}_R q_L \rangle_0 \, e^{i\alpha} \, U_0 \,, \\ U_0 = \cos\theta \, \mathbb{1}_2 + i \sin\theta \, \hat{n} \cdot \boldsymbol{U} \,, \quad \hat{n} = (\sin\psi \cos\chi, \sin\psi \sin\chi, \cos\psi) \,, \end{gathered} \tag{5.10}$$

where $-\pi/2 \le \theta < \pi/2$,[3] and with the U field transforming as (see also Eq. (A.4))

$$U_0 \to V_R U_0 V_L^\dagger \,. \tag{5.11}$$

[3] The shift $\theta \to \theta + \pi$ can be compensated by shifting $\alpha \to \alpha + \pi$.

In Eq. (5.10), we used the fact that a field transforming as a bi-fundamental under $SU(2)_L \times SU(2)_R$ can be written as a radial mode, here frozen to some constant value $\langle \bar{q}_R q_L \rangle_0$, times a 2-by-2 unitary matrix U_0, which parameterizes the orientation of the ensemble average in the presence of finite μ, which we call the orientation of the expectation value here. [4]

The phase factor $e^{i\alpha}$ is identified with the direction in field space associated with the anomalous axial $U(1)$. A potential for α is generated by non-perturbative effects, whose minimum is at $\alpha = 0$, which we take from this point on. The angles defined in Eq. (5.10) can be related to expectation values of the usual pion fields (at vanishing chemical potential)

$$\theta \equiv \frac{\langle \Pi \rangle}{f_\pi}\,, \quad \frac{1}{\sqrt{2}} \sin\psi e^{\mp i\chi} = \frac{\langle \pi_\pm \rangle}{\langle \Pi \rangle}\,, \quad \cos\psi = \frac{\langle \pi_3 \rangle}{\langle \Pi \rangle}\,, \tag{5.12}$$

where we defined $\sqrt{\langle \pi_i \pi_i \rangle} \equiv \langle \Pi \rangle$. In Dirac notation

$$\langle \bar{q} q \rangle = \frac{1}{2} \langle \bar{q} q \rangle_0 (U_0 + U_0^\dagger)\,, \quad \langle \bar{q} i\gamma_5 q \rangle = \frac{1}{2i} \langle \bar{q} q \rangle_0 (U_0 - U_0^\dagger)\,, \tag{5.13}$$

where we denoted $\langle \bar{q}_R q_L \rangle_0 = \langle \bar{q}_L q_R \rangle_0 \equiv \langle \bar{q} q \rangle_0 / 2$. Therefore CP is broken in the ground state if $U_0 \neq U_0^\dagger$, that is if $\theta \neq 0$.

We wish to study this system at a non-vanishing chemical potential for isospin

$$\hat{\mu} = \mu (T_L^3 + T_R^3)\,, \tag{5.14}$$

and we shall neglect for the remainder of this section isospin breaking due to the quark masses and electromagnetic interactions, making the choice in Eq. (5.14) completely generic. Such a chemical potential is associated with the U_3 rotation of the vector $SU(2)_{L+R}$ subgroup. Therefore, according to Eqs. (5.2), (5.11), we promote the temporal derivative of U_0 to

$$\partial_0 U_0 \to \partial_0 U_0 + i\mu T_L^3 U_0 - i\mu U_0 T_R^3 = \frac{i}{2} \mu [U_3, U_0]\,. \tag{5.15}$$

Note that changing $\hat{\mu} \to \hat{\mu} + \frac{1}{6}\mathbb{1}_2$ in Eq. (5.14) has no effect on Eq. (5.15) and on the following derivation, therefore in this context the isospin chemical potential can be equivalently associated with the chemical potential for electric charge.[5] The resulting potential for the pions and the axion, the latter entering via the quark mass matrix, $M_q = m\mathbb{1}_2$ ($m_u = m_d \equiv m$), as in Eq. (2.59c) (with $Q_\phi = \mathbb{1}_2/2$), is given by

$$V = \frac{f_\pi^2 \mu^2}{16} \mathrm{Tr}[[U_3, U_0][U_3, U_0^\dagger]] + \frac{\langle \bar{q} q \rangle_0}{2} \mathrm{Tr}[U_0 M_q e^{-\frac{i\phi}{2f_\phi}} + U_0^\dagger M_q e^{\frac{i\phi}{2f_\phi}}]\,, \tag{5.16}$$

at leading order in m/Λ_χ and μ/Λ_χ, Λ_χ being the cutoff of the chiral Lagrangian, see the discussion in Sec. 2.4.2. Here we have used that the QCD axion potential in vacuum depends on the quark condensate since we can write using Eq. (2.70b)

$$V_0 = \frac{f_\pi^2}{2} (\mathrm{Tr}[U^\dagger B M_\phi] + \text{h.c.})\,, \tag{5.17}$$

and realizing that

$$B = \frac{m_\pi^2}{2(m_u + m_d)} = -\frac{\langle \bar{q} q \rangle_0}{2 f_\pi^2}, \tag{5.18}$$

[4] $SU(2)_L$ and $SU(2)_R$ are generated by $T_L^a = \frac{1}{2} U^a$ and $T_R^a = \frac{1}{2} U^a$, respectively, where as usual it should be understood that the L and R operators act on different indices and therefore commute.

[5] One can then think of μ as a non-vanishing averaged value for the zero component of the photon field $\mu = \langle A_0 \rangle$, which can be intuitively understood as a classical background electric charge density.

where we used the GOR relation (see Eq. (5.20)) in the last step. We note that the first term arises from the usual kinetic term, $\frac{1}{4}f_\pi^2\mathrm{Tr}[\partial_\mu U_0 \partial^\mu U_0^\dagger]$, after the replacement (5.15). Using Eq. (5.10) we find

$$V = -\frac{1}{2}\mu^2 f_\pi^2 \sin^2\theta \sin^2\psi - m_\pi^2 f_\pi^2 \cos\theta \cos\left(\frac{\phi}{2f_\phi}\right), \tag{5.19}$$

where m_π here is the neutral pion mass in vacuum, which is related to the condensate b; the Gell-Mann-Oakes-Renner (GOR) relation

$$m_\pi^2 f_\pi^2 = -2m\langle\bar{q}q\rangle_0. \tag{5.20}$$

We see that the isospin chemical potential introduces an additional source of explicit symmetry breaking while leaving unbroken the $U(1)_{L+R}$ symmetry defined by the generator in Eq. (5.14). $\hat{\mu}$ explicitly breaks the shift symmetries associated with the would-be NGBs charged under $U(1)_{L+R}$, i.e. the charged pions. Indeed, as discussed above, $U(1)_{L+R}$ is equivalent to the electric charge. Consequently, the first term in Eq. (5.19) is proportional to the expectation value of the charged pions, $\sin^2\theta\sin^2\psi \propto \langle\pi^+\pi^-\rangle$. Since $\hat{\mu}$ commutes with the $U(1)_{L-R}$ associated with the neutral pion, the neutral NGBs are unaffected by the chemical potential and the potential Eq. (5.19) is minimized at $\langle\pi_3\rangle = 0$ ($\psi = \pi/2$) and $\langle\phi\rangle = 0$ as in the $\mu = 0$ vacuum.

The minimum of the potential for any value of μ is then found at

$$\cos\theta = \mathrm{Min}\left[1, \frac{m_\pi^2}{\mu^2}\right]. \tag{5.21}$$

For $|\mu| < m_\pi$, the ground state is the trivial one, $U_0 = 1$, thus its orientation is the same as for $\mu = 0$. For $|\mu| > m_\pi$, pion condensation takes place and the orientation of the expectation value is no longer trivial. We note that in this case χ constitutes a flat direction which, as we confirm later, corresponds to a NGB from the spontaneous breaking of electric charge, $U(1)_{L+R}$. Setting, without loss of generality, $\chi = 0$, we can write the QCD orientation for $|\mu| > m_\pi$ as

$$U_0 = \begin{pmatrix} \cos\theta & i\sin\theta \\ i\sin\theta & \cos\theta \end{pmatrix}. \tag{5.22}$$

At this point we recall that since $\theta \neq 0$, CP is broken by the expectation value, a result of a sufficiently large explicit breaking of CP by the chemical potential in the *charged* pion sector. Instead, CP-invariance in the *neutral* sector is preserved by the charge chemical potential, which leaves the expectation values in that sector untouched. We see now that only if $\langle\pi_3\rangle \neq 0$ ($\psi \neq \pi/2$) could the axion condense, which requires additionally explicit breaking of isospin, i.e. $m_u \neq m_d$.

Having established the Goldstone boson expectation values at finite-density, let us turn our attention to their fluctuations. Since these are associated with the $SU(2)_L \times SU(2)_R$ generators broken by U_0, we define the following rotated generators

$$(T_L^a)_\theta = u_0(T_L^a)u_0^\dagger, \quad (T_R^a)_\theta = u_0^\dagger(T_R^a)u_0, \tag{5.23}$$

where again $u_0 = \sqrt{U_0}$, cf. Eq. (2.75). The broken and unbroken generators are then given by

$$X^a = (T_L^a)_\theta - (T_R^a)_\theta, \quad T^a = (T_L^a)_\theta + (T_R^a)_\theta, \tag{5.24}$$

respectively. The fluctuations around the U_0 ground state can be parameterized as

$$U = u_L U_0 u_R^\dagger = \exp\left[\frac{i\pi^a (T_L^a)_\theta}{f_\pi}\right] U_0 \exp\left[\frac{i\pi^a (T_R^a)_\theta}{f_\pi}\right] = u_0 \exp\left[\frac{i\pi^a U^a}{f_\pi}\right] u_0, \tag{5.25}$$

where, abusing notation, we have written the (pseudo-)NGBs as π^a, like the standard $\theta = 0$ pions. [6]

The dispersion relations for the neutral degrees of freedom, π_0 and the axion, are the same as for vanishing chemical potential. Their masses can be obtained from Eq. (5.16) (with the substitution of U_0 by U),

$$(m^2_{\pi_0})_\theta = m^2_\pi/\cos\theta\,, \quad (m^2_\phi)_\theta = (m^2_\phi)_0\cos\theta\,, \tag{5.26}$$

with $(m^2_\phi)_0$ the mass of the axion in vacuum, Eq. (2.35), and where we note that for $|\mu| > m_\pi$, $(m^2_{\pi_0})_\theta = \mu^2$. The change of the axion mass for $\theta \neq 0$ follows from the fact that, once the mixing with π_3 is eliminated, it has to be proportional to the CP-even combination $\mathrm{Tr}[U_0 + U_0^\dagger] \propto \cos\theta$. The increase in the neutral pion mass can be understood as a result of its repulsive interaction with the charged pions. The dispersion relation for the charged pions is very similar to the $U(1)$ toy model of Sec. 5.1.1. In the uncondensed phase $|\mu| < m_\pi$, their dispersion relations are

$$\omega_{\pi_\pm}(\boldsymbol{k}) = \sqrt{m^2_\pi + k^2} \mp \mu\,. \tag{5.27}$$

Indeed, for the charged states $\pi_\pm \equiv \frac{1}{\sqrt{2}}(\pi_1 \mp i\pi_2)$ we recognize the same mass splitting we found in Eq. (5.4). In the condensed phase $|\mu| > m_\pi$, the remaining $U(1)_{L+R}$ symmetry is spontaneously broken. The effective masses of the charged pions are

$$\omega_{\pi_+}(\mathbf{0}) = 0\,, \quad \omega_{\pi_-}(\mathbf{0}) = \mu\sqrt{1 + \frac{3m^4_\pi}{\mu^4}}\,. \tag{5.28}$$

As in the $U(1)$ toy model, the condensed phase contains one massless Goldstone mode and one massive radial mode. In this phase, the system has a non-vanishing charge density

$$\rho_{\pi_+} - \rho_{\pi_-} = -\left(\frac{\partial V}{\partial \mu}\right)\bigg|_{\pi_i = a = 0} = f^2_\pi \mu\left(1 - \frac{m^4_\pi}{\mu^4}\right)\,. \tag{5.29}$$

The effective masses of the pions and the axion are plotted in Fig. 5.1.

5.2 Nuclear phase

In this section we study how the properties of the axion, mainly its potential and coupling to nucleons, change in systems at finite baryon density, ρ. In particular, our focus here is on densities around nuclear saturation, $\rho \sim \rho_0$, where a description of QCD in terms of hadrons is still meaningful.

For the axion potential, we identify two main effects: 1) the change in the size and, to some degree, flavor orientation of the quark condensates, as measured by the mass of the pions (Sec. 5.2.1), and 2) kaon condensation (Sec. 5.2.2), similar to meson condensation, introduced in Sec. 5.1.2. Both of these effects can be taken into account by a generalization of the axion potential in vacuum.

We therefore generalize the axion potential in vacuum to the density dependent expression

$$V(\rho) = \frac{1}{2}\mathrm{Tr}[\langle\bar{q}q\rangle_\rho \hat{M}_\phi + \mathrm{h.c.}]\,, \quad \hat{M}_\phi = u_0^\dagger u_L^\dagger M_\phi u_R u_0^\dagger \tag{5.30}$$

[6] We note that, given Eq. (5.23) and $T^a_L = \frac{1}{2}U^a$, $T^a_R = \frac{1}{2}U^a$, it follows that $u_L = u_0 \exp\left[\frac{i\pi^a U^a}{2f_\pi}\right] u_0^\dagger$ and $u_R = u_0^\dagger \exp\left[-\frac{i\pi^a U^a}{2f_\pi}\right] u_0$.

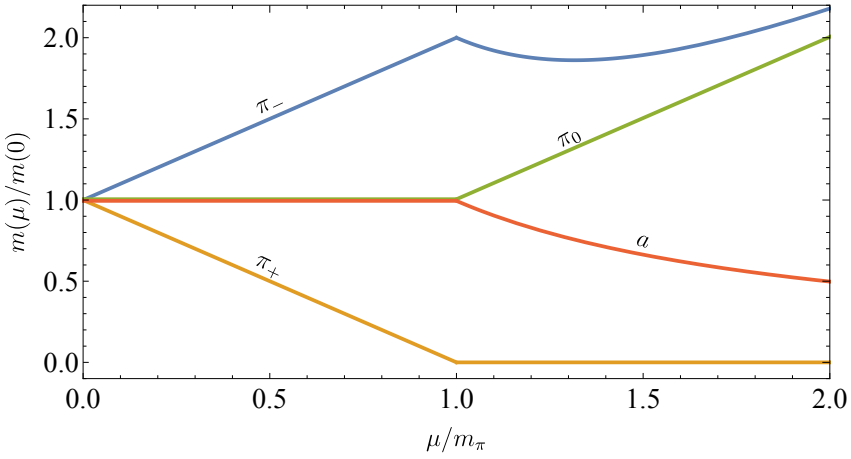

Figure 5.1: Mass spectrum of the vacuum excitations as a function of μ/m_π. The masses are normalized to their respective $\mu = 0$ value. The charged π_+ and π_- modes (orange and blue curves respectively) evolve similarly as the complex ϕ and ϕ^* modes in the $U(1)$ toy model: a linear split in masses in the uncondensed phase, continuously transitioning to a massless Goldstone mode and a massive radial mode in the condensed phase. The masses of the neutral modes, the neutral pion π_0 and the axion $a = \phi$ (green and red curve respectively) are unaffected by the chemical potential in the uncondensed phase. In the condensed phase, m_{π_0} increase linearly with μ, while the axion becomes lighter as μ increases.

with M_ϕ encoding the dependence on the axion as in Eq. (2.59c). $U_0 = u_0^2$ parametrizes the orientation of the QCD ground state that spontaneously breaks $SU(3)_L \times SU(3)_R$ to $SU(3)$ and therefore includes effects of kaon condensation. In vacuum, we have $u_0 = \mathbb{1}_3$ and the unbroken subgroup is the usual $SU(3)_{L+R}$, while in the kaon-condensed phase, we have $u_0 = u_0(\theta)$, with θ controlling the size of the kaon condensate which, as explained below, ultimately depends on the baryon density. $u_{L,R}$ are the Goldstone matrices, given by

$$u_L = e^{i\frac{\pi^a}{2f_\pi}(T_L^a)_\theta} = u_0 \exp\left[\frac{i\pi^a\lambda^a}{2f_\pi}\right] u_0^\dagger\,, \quad u_R = e^{-i\frac{\pi^a}{2f_\pi}(T_R^a)_\theta} = u_0^\dagger \exp\left[-\frac{i\pi^a\lambda^a}{2f_\pi}\right] u_0\,, \tag{5.31}$$

a generalization to $SU(3)_L \times SU(3)_R$ of those in Eq. (5.25). Finally, the quark condensate $\langle\bar{q}q\rangle_\rho$ at finite density becomes a matrix in flavor space,

$$\langle\bar{q}q\rangle_\rho = \mathrm{Diag}[\langle\bar{u}u\rangle_\rho, \langle\bar{d}d\rangle_\rho, \langle\bar{s}s\rangle_\rho]\,, \tag{5.32}$$

The detailed derivation of Eq. (5.30) is given in App. B.2. The result can also be understood in terms of symmetries: $\hat{M}_\phi$ is a spurion that has been dressed by the Goldstones and projected into the $SU(3)_{L+R}$ subgroup. Therefore, it transforms as $\hat{M}_\phi \to V\hat{M}_\phi V^\dagger$, where V is an $SU(3)_{L+R}$ transformation. $\langle\bar{q}q\rangle_\rho$ transforms in the same way, since it is the result of a non-vanishing expectation value of the temporal component of the baryonic current, $\rho = \langle j_B^0\rangle$. [7]

Before going into the details, several general comments about our treatment of the nuclear medium are in order. To describe the state of the system, we will work directly in terms of baryon densities, ρ_p and ρ_n considering only protons and neutrons, respectively. In practice, our independent parameters are the total baryonic density, $\rho = \rho_p + \rho_n$, and the proton fraction,

[7] When the quark condensate is trivial, $\langle\bar{q}q\rangle_\rho \propto \mathbb{1}_3$, we recover $V(\rho) \propto \mathrm{Tr}[U^\dagger M_\phi + \text{h.c.}]$. Instead, when the ground state is trivial, $U_0 = \mathbb{1}_3$, the change in condensates effectively amounts to $m_q \to m_q\langle\bar{q}q\rangle_\rho/\langle\bar{q}q\rangle_0$.

ρ_p/ρ. This will be more convenient than introducing the corresponding chemical potentials, because our analysis is limited to linear order in ρ, i.e. we work in the mean-field or Hartree approximation, where e.g. $\rho_p \approx \langle \bar{p}\gamma_0 p\rangle_{T,\mu_i}$ (and in fact $\rho_p \approx \langle \bar{p}p\rangle_{T,\mu_i}$ in the non-relativistic limit) – higher-order corrections generically being beyond perturbative control when relevant. Besides, the relative fraction of protons and neutrons is, as shown below, relevant only in our discussion of kaon condensation. There, the chemical potential for electric charge, μ, will also be required to properly describe the system, along with the condition of charge neutrality.

5.2.1 Quark condensates

We first discuss how the quark condensate changes at finite baryonic density, since this is the most robust effect from the point of view of perturbative control. We derive the implications for the axion mass, which were first noted in [186]. The change with density of the quark condensates can be calculated utilizing the Hellmann-Feynman theorem [193]

$$\zeta_{\bar{q}q}(\rho) \equiv \frac{\langle \bar{q}q\rangle_\rho}{\langle \bar{q}q\rangle_0} = 1 + \frac{1}{\langle \bar{q}q\rangle_0}\frac{\partial \Delta E(\rho)}{\partial m_q}\,, \quad q = u,d,s\,. \tag{5.33}$$

$\Delta E(\rho)$ is the energy shift of the QCD ground state due to the finite density background, such that $\Delta E(0) = 0$. It can be decomposed as

$$\Delta E = E^{\text{free}} + E^{\text{int.}}\,, \tag{5.34}$$

where the first term represents the energy shift due to the presence of a non-interacting Fermi gas, while the second term encodes the energy shift due to nuclear interactions. Neglecting these interactions as well as relativistic corrections, we have $\Delta E = \sum_{x=n,p,\ldots} m_x \rho_x$, and we arrive at the so-called linear approximation for the in-medium condensate

$$\zeta_{\bar{q}q}(\rho) = 1 + \frac{1}{\langle \bar{q}q\rangle_0}\sum_x \rho_x \frac{\partial m_x}{\partial m_q}\,, \quad q = u,d,s\,. \tag{5.35}$$

The derivatives $\partial m_x/\partial m_q$ describe the shift in the nucleon mass due to the non-vanishing quark masses. For two nucleons $\{n,p\}$ and three quarks $\{u,d,s\}$, one naively counts six independent shifts. However, due to the $\{p,u\} \leftrightarrow \{n,d\}$ exchange symmetry, only three shifts are independent. Working in the isospin basis for the quark masses, $\bar{m} \equiv \frac{1}{2}(m_u + m_d)$ and $\Delta m \equiv \frac{1}{2}(m_u - m_d)$, the following sigma terms are identified and defined

$$\sigma_{\pi N} \equiv \bar{m}\left(\frac{\partial m_p}{\partial \bar{m}}\right) = \bar{m}\left(\frac{\partial m_n}{\partial \bar{m}}\right)\,, \tag{5.36}$$

$$\tilde{\sigma}_{\pi N} \equiv \Delta m\left(\frac{\partial m_n}{\partial \Delta m}\right) = -\Delta m\left(\frac{\partial m_p}{\partial \Delta m}\right)\,, \tag{5.37}$$

$$\sigma_s \equiv m_s\left(\frac{\partial m_p}{\partial m_s}\right) = m_s\left(\frac{\partial m_n}{\partial m_s}\right)\,, \tag{5.38}$$

such that

$$m_n = \mathring{m}_N + \sigma_{\pi N} + \tilde{\sigma}_{\pi N} + \sigma_s\,, \tag{5.39}$$

$$m_p = \mathring{m}_N + \sigma_{\pi N} - \tilde{\sigma}_{\pi N} + \sigma_s\,. \tag{5.40}$$

with $\mathring{m}_N$ the baryon mass in the chiral limit given in Table 2.1, $m_q \to 0$. We note that the sigma terms can be expressed in terms of the parameters of the $N_f = 3$ chiral Lagrangian

for baryons, see Eq. (B.50) in App. B.2. The $\sigma_{\pi N}$ and σ_s terms have been extracted from pion-nucleon and kaon-nucleon scattering experiments, as well as from lattice simulations by calculating the mass shifts of the nucleons. There are ongoing efforts aimed at the determination of the precise values of these sigma terms. A summary of latest results [194] shows that their current values are scattered over a fairly wide range, with some tension between experimental and lattice results. In this work we use the conservative estimates $\sigma_{\pi N} = 45 \pm 15\,\mathrm{MeV}$ and $\sigma_s = 30\,\mathrm{MeV}$. The other sigma term is extracted from the $p - n$ non-electromagnetic mass splitting $2\tilde{\sigma}_{\pi N} = (m_n - m_p)^{\text{non-EM}} = 2 \pm 0.3\,\mathrm{MeV}$ [39]. Using the GOR relation in Eq. (5.20), we rewrite the ratios $\langle\bar{q}q\rangle_\rho/\langle\bar{q}q\rangle_0$ as

$$\zeta_{\bar{u}u}(\rho) = 1 - b_1\frac{\rho}{\rho_0} + b_2\left[2\frac{\rho_p}{n} - 1\right]\frac{\rho}{\rho_0}\,, \tag{5.41a}$$

$$\zeta_{\bar{d}d}(\rho) = 1 - b_1\frac{\rho}{\rho_0} - b_2\left[2\frac{\rho_p}{n} - 1\right]\frac{\rho}{\rho_0}\,, \tag{5.41b}$$

$$\zeta_{\bar{s}s}(\rho) = 1 - b_3\frac{\rho}{\rho_0}\,, \tag{5.41c}$$

with

$$b_1 \equiv \frac{\sigma_{\pi N}\rho_0}{m_\pi^2 f_\pi^2} = 3.5\times10^{-1}\left(\frac{\sigma_{\pi N}}{45\ \mathrm{MeV}}\right)\,, \tag{5.42a}$$

$$b_2 \equiv \frac{\tilde{\sigma}_{\pi N}\rho_0}{m_\pi^2 f_\pi^2}\frac{\bar{m}}{\Delta m} = -2.2\times10^{-2}\left(\frac{\tilde{\sigma}_{\pi N}}{1\ \mathrm{MeV}}\right)\,, \tag{5.42b}$$

$$b_3 \equiv \frac{\sigma_s\rho_0}{m_\pi^2 f_\pi^2}\frac{2\bar{m}}{m_s} = 1.7\times10^{-2}\left(\frac{\sigma_s}{30\ \mathrm{MeV}}\right)\,. \tag{5.42c}$$

Clearly the $\langle\bar{s}s\rangle_\rho$ condensate is only weakly affected by the nucleonic background. Therefore, as in vacuum, its contribution to the axion mass will be subleading, being suppressed by $m_{u,d}/m_s$. Additionally, $\langle\bar{u}u\rangle_\rho \approx \langle\bar{d}d\rangle_\rho$ up to the small isospin breaking correction [195], which we neglect. From Eq. (5.30) with $u_0 = \mathbb{1}_3$ and after taking care of axion-pion mixing we reproduce the axion mass at finite density found in [186]

$$(m_\phi)_\rho^2 = (m_\phi)_0^2\langle\bar{u}u\rangle_\rho \approx (m_\phi)_0^2\left(1 - b_1\,\frac{\rho}{\rho_0}\right)\,, \tag{5.43}$$

where m_π here is the neutral pion mass in vacuum, Eq. (5.20). In this regard, we note that at the linear order in density the same correction as the axion enters the neutral pion mass in medium, i.e. $(m_\pi)_\rho^2 = m_\pi^2\langle\bar{u}u\rangle_\rho$. This is why for the remainder of this section, we shall only consider $\rho < \rho_c \equiv \rho_0/b_1 \approx 2.8\,\rho_0\,(45\,\mathrm{MeV}/\sigma_{\pi N})$, with ρ_c being the critical density at which one naively expects chiral symmetry restoration in the linear approximation.

At this point, let us turn our attention to the corrections to the linear, non-relativistic approximation we have considered. This will allow us to estimate the densities up to which our leading result is under perturbative control and can therefore be trusted. First, the energy of a degenerate (zero temperature) ideal Fermi gas receives relativistic corrections. In the fully relativistic limit, the free part of the energy for a fermion x is given by

$$E_x^{\text{free}} = 2\int^{k_F^x}\frac{\mathrm{d}^3k}{(2\pi)^3}\sqrt{k^2 + m_x^2} = m_x\rho_x F(k_F^x/m_x)\,, \tag{5.44}$$

$$F(q) = \frac{3q\sqrt{q^2+1}\,\left(2q^2+1\right) - 3\sinh^{-1}(q)}{8q^3} = 1 + \frac{3q^2}{10} + \mathcal{O}(q^4)\,, \tag{5.45}$$

where k_F^x is the Fermi momentum, $k_F^x = \sqrt{m_x^2 - \mu_x^2}$, which determines the number density,

$$\rho_x = 2 \int^{|\boldsymbol{k}| \leq k_F^x} \frac{\mathrm{d}^3 k}{(2\pi)^3} = \frac{(k_F^x)^3}{3\pi^2} \,. \tag{5.46}$$

Therefore, relativistic corrections, of $\mathcal{O}((k_F^x/m_x)^2)$, become important at large densities. When this happens, corrections to the QCD ground state energy Eq. (5.34) from nucleon interactions become important as well. These are predominantly due to pion exchange, but also from four-baryon contact interactions. It is clear that the latter become important when $\rho_x/\Lambda_\chi f_\pi^2$ becomes order one. Given Eq. (5.46), this is also the place where ChPT is beyond control, $k_F^x \sim \Lambda_\chi$, e.g. the pion-exchange contribution to the energy is not predictable. In addition, since the cutoff of ChPT Λ_χ is numerically close to $m_p \approx m_n$, relativistic corrections are approximately controlled by the same expansion parameter,

$$\frac{k_F^2}{\Lambda_\chi^2} \approx \frac{(3\pi^2\rho/2)^{2/3}}{\Lambda_\chi} \approx (15\,\%) \left(\frac{\rho}{\rho_0}\right)^{2/3} \left(\frac{700\,\mathrm{MeV}}{\Lambda_\chi}\right)^2 , \tag{5.47}$$

where we took $k_F = k_F^p \sim k_F^n$. Ultimately the best way to asses the validity of our linear approximation is to explicitly compute the relevant NLO corrections. The interaction energy $E^{\text{int.}}$ has been calculated by summing the so-called Hugenholtz diagrams, which are connected bubble diagrams describing ground-state to ground-state transitions [173]. The resulting higher-order finite density effects on the quark condensates have been obtained in ChPT for symmetric nuclear matter [196, 197] and pure neutron matter [198, 199]. These authors have indeed found $O(1)$ deviations from the linear approximation for densities somewhat above nuclear saturation. Specifically, nucleon interactions seem to ameliorate the linear decrease of $\langle \bar{u}u \rangle_\rho \approx \langle \bar{d}d \rangle_\rho$ in Eq. (5.41), such that already at $\rho \approx 2\rho_0$, the condensates are only at approximately 60 % of their vacuum value, as opposed to the 15 % predicted by the linear approximation, and in fact start increasing with density [196]. This then implies that a more realistic prediction of the axion mass in dense symmetric nuclear matter is

$$(m_\phi)^2_{n \lesssim 2\rho_0} \gtrsim 0.6\, (m_\phi)_0^2 \,. \tag{5.48}$$

while for larger densities $\rho \gtrsim 2_0 \sim \rho_c$ it becomes difficult to trust the results of ChPT.

Therefore, the determination of the quark condensates and the axion mass at densities significantly beyond nuclear saturation remains an open and difficult theoretical problem. Importantly, realistic lattice simulations at finite density are currently not feasible due to so-called sign problem. In addition, at such high densities other issues arise (ultimately related to the problem of perturbativity), such as the "hyperon puzzle", which concerns the appearance, or absence, of hyperons, see e.g. [200] and references therein. In the next section we will focus our attention instead on another effect of strangeness, potentially much more relevant for the fate of the axion at finite density.

5.2.2 Kaon condensation

In the previous section we assumed that the vacuum of QCD is trivially oriented and CP-preserving, or equivalently that none of the mesons acquire a non-trivial expectation value. This might, however, not be the case in dense matter. It has been hypothesized [201] that above certain baryonic densities it becomes energetically possible for the strangeness changing process of a neutron splitting into a proton and a scalar K^- meson, and vice versa, to take place

$$n \leftrightarrow p^+ + K^- \,, \tag{5.49}$$

The reason being the low in-medium kaon mass, which eventually leads to the formation of a K^- condensate. This process takes place along with, and even becomes favored over, the usual neutron β-decay, $n \to p^+ + e^- + \bar{\nu}_e$, and inverse β-decay, $p^+ + e^- \to n + \nu_e$, because of the high price of occupying the increasingly energetic Fermi surface of the electrons. Because of this fact, also the processes $e^- \leftrightarrow K^- + \nu_e$ and $e^- \leftrightarrow \mu^- + \bar{\nu}_\mu + \nu_e$, $\mu^- \leftrightarrow e^- + \nu_\mu + \bar{\nu}_e$ reach β-equilibrium [202]. On the other hand, the formation of a pion (π^-) condensate ($n \leftrightarrow p^+ + \pi^-$) seems to be disfavored, as we shall discuss below.

Motivated by these arguments, we shall now entertain the possibility of kaon condensation and derive its effects on the axion potential. Several important comments and some caveats are however in order. We consider this scenario because of the thrilling possibility of leading to axion condensation, even though it takes place – if it takes place at all – at densities where a perturbative expansion is questionable, $\rho \gtrsim 2\rho_0$. Because of the inherent uncertainties at such densities, our conclusions will be *qualitative* rather than quantitive. Indeed, similar to our discussion at the end of the previous section on the quark condensates and their finite density corrections beyond the linear approximation, kaon condensation cannot be simply described by the leading order terms in ChPT. In particular, nucleon self-interactions and interactions with pions need to be considered in order to capture the full complexity of this strongly interacting system [203] – for instance, the latter are the reason behind the fact that K^- condensation is more likely than π^- condensation. Our working assumption is that all the processes above (neglecting the pions) are in equilibrium, which implies a set of equations relating the chemical potentials of the particle species involved,

$$\mu_\mu = \mu_e = \mu_{K^-} = \mu\,, \quad \mu_p - \mu_n = \mu\,, \tag{5.50}$$

where μ is the chemical potential associated with (positive) electric charge. For convenience, we work directly with muon and electron densities, ρ_μ and ρ_e respectively, both of which are determined by μ as they follow from an ideal Fermi gas. The size of the kaon condensate, θ, is determined, as in the simple example of meson condensation discussed in Sec. 5.1.2, by the minimization of the scalar potential, which of course also determines if the axion condenses or not. Finally, due to the importance of nuclear interactions, the densities of protons and neutrons, or equivalently the total baryon density ρ and the proton fraction ρ_p/ρ, are not determined by μ. Instead, we enforce the condition of (electric) charge neutrality $\rho_{\rm EM} = 0$, and present our results in terms of ρ and ρ_p/ρ.

An additional important final comment regards the implications of kaon condensation on the NS equation of state (EOS), see also the discussion in Sec. 3.2. It has been argued that the inclusion of kaon condensation generically leads to a softer EOS [202, 204], which usually cannot sustain a large NS mass. This is in conflict with the most massive NSs observed, with masses around $2M_\odot$ [159, 205]. This is the main reason why kaon condensation is currently considered an "exotic" possibility. However, axion effects can in fact harden the EOS [15] and reopen this window. Also, kaon condensation is in fact related to another issue, namely the hyperon puzzle [206]. The appearance of hyperons also tends to soften the EOS, resulting in a similar apparent conflict with the observation of massive NSs. Therefore, although the appearance of strangeness seems to be in tension with observations, we think it would be premature to definitively exclude the possibility of kaon condensation at this point, especially in the presence of new physics.

Let us consider then the possibility that kaon condensation occurs in nuclear matter and qualitatively examine its effects on the axion potential. Once the chemical potential for electric

charge μ is introduced, the dispersion relations for the $K^\pm$ modes are given by

$$\omega_{K^\pm}(\boldsymbol{k}) = \sqrt{\left(m^2_{K^\pm}\right)_\rho + k^2} \pm \mu\,, \tag{5.51}$$

with the kaon effective in-medium mass

$$\left(m^2_{K^\pm}\right)_\rho = \frac{1}{f_\pi^2}\left(-\frac{\langle \bar{u}u + \bar{s}s\rangle_\rho}{2} m_s - \frac{1}{2}(\rho + \rho_p)\,\mu\right)\,. \tag{5.52}$$

The first term in Eq. (5.52) is the usual kaon mass to leading order in m_s, with the inclusion of the finite density corrections to the relevant quark condensate, which in the linear approximation are given by

$$-\frac{\langle \bar{u}u + \bar{s}s\rangle_\rho}{2f_\pi^2}\, m_s = m_K^2\left(1 - \frac{1}{2}\left[b_1 - b_2\left(\frac{2\,\rho_p}{\rho} - 1\right) + b_3\right]\frac{\rho}{\rho_0}\right)\,, \tag{5.53}$$

where $m_K^2 = -m_s\langle\bar{q}q\rangle_0/f_\pi^2$, the neutral kaon mass in vacuum, neglecting $O(m_{u,d}/m_s)$ terms. The second term in Eq. (5.52) is a mass correction induced by the baryonic background, due to the model-independent s-wave interactions of the baryons with the mesons, arising from the baryon kinetic term,

$$(\mathcal{L}_B)_\rho = i\mathrm{Tr}[\bar{B}\gamma^\mu D_\mu B] \supset -\mu\mathrm{Tr}[\bar{B}\gamma^0[\hat{Q}_e, B]]\,,\ \hat{Q}_e = \tfrac{1}{2}\left(u_0^\dagger u_L^\dagger Q_e u_L u_0 + u_0 u_R^\dagger Q_e u_R u_0^\dagger\right) \tag{5.54}$$

as it follows from the covariant derivative of ChPT, $D_\mu B = \partial_\mu B + [e_\mu, B]$ with the chiral connection $e_\mu = \frac{1}{2}(u_0^\dagger u_L^\dagger \partial_\mu u_L u_0 + u_0 u_R^\dagger \partial_\mu u_R u_0^\dagger)$ (see App. A.3 for the $N_f = 2$ case), upon introducing the charge chemical potential, $\partial_0 \to \partial_0 + i\mu Q_e$ with $Q_e = \mathrm{Diag}[2/3, -1/3, -1.3]$, see App. B.2 for the details. Note that since $b_2 \ll b_1$, the effective kaon mass decreases with density, and condensation is expected to occur when [8]

$$\omega_{K^-}(0) = \left(m_{K^\pm}\right)_\rho - \mu = 0 \tag{5.56}$$

Kaon condensation is introduced by allowing the kaon field to take a non-trivial average value, $\langle\sqrt{2}K^\pm/f_\pi\rangle$, or equivalently, in our notation, reorienting the QCD ground state in medium [202],

$$U_0 = \begin{pmatrix} \cos\theta & 0 & i\sin\theta \\ 0 & 1 & 0 \\ i\sin\theta & 0 & \cos\theta \end{pmatrix}\,. \tag{5.57}$$

The ground state orientation is determined by the static Lagrangian after setting all the fluctuations to zero. Neglecting for the time being the axion, we find a similar potential to Eq. (5.19)

$$V(\theta) = -\frac{1}{2}\mu^2 f_\pi^2 \sin^2\theta - f_\pi^2 (m^2_{K^\pm})_\rho \cos\theta\,. \tag{5.58}$$

[8] It is illustrative to also consider the pion effective in-medium mass,

$$\left(m^2_{\pi^\pm}\right)_\rho = \frac{1}{f_\pi^2}\left(-\langle\bar{u}u + \bar{d}d\rangle_\rho \bar{m} + \frac{1}{2}(\rho - 2\rho_p)\mu\right)\,, \tag{5.55}$$

since it shows that, due to the second term and contrary to the kaon, the charge pion becomes heavier with increasing density, at least for a neutron rich background $\rho_p/\rho < 1/2$ [207]. The argument against pion condensation becomes even stronger when considering higher order terms in ChPT [195], as we discussed at the end of Sec. 5.2.1 – these additional corrections even make the pion mass increase with density for $\rho \approx 2\rho_0$, even in symmetric nuclear matter, $\rho_p/\rho = 1/2$.

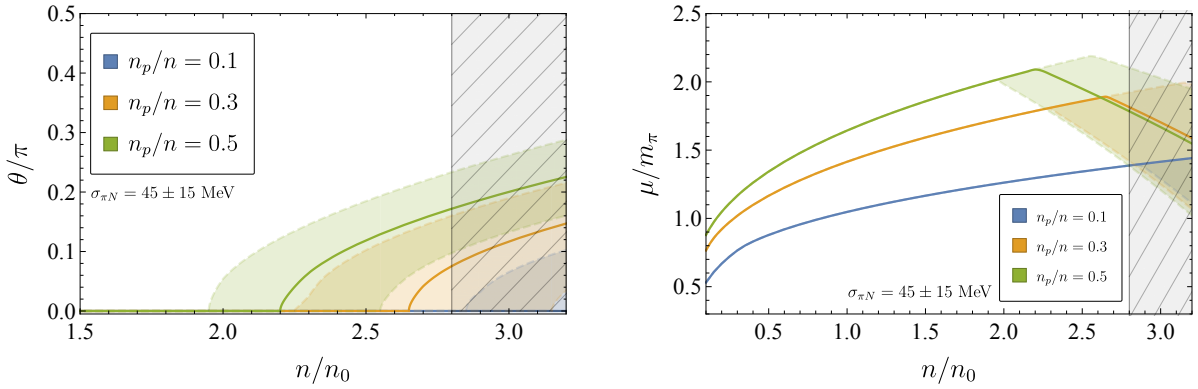

Figure 5.2: The ground state orientation angle θ (left panel) and the chemical potential μ in units of pion mass (right panel) as function of baryon density ρ ($n = \rho$ in the plot) for fixed values of proton fraction ρ_p/ρ. The blue, orange and green curves correspond to $\rho_p/\rho = 0.1$, 0.3 and 0.5, respectively. The solid curves correspond to the numerical solution using the central value of $\sigma_{\pi N} = 45 \pm 15\,\text{MeV}$, while the bands are obtained by the corresponding 1σ variation. The gray slashed region corresponds to $\rho > \rho_c \approx 2.8\,\rho_0$ where the quark condensate $\langle \bar{u}u \rangle_\rho$ changes sign (for the central value of $\sigma_{\pi N}$).

Minimizing $V(\theta)$ leads to the condition

$$\cos\theta = \text{Min}\left[1, \frac{(m^2_{K^\pm})_\rho}{\mu^2}\right], \tag{5.59}$$

which can be used to determined $\theta = \theta(\mu, \rho, \rho_p/\rho)$. The requirement of electrical neutrality, $\rho_{\text{EM}} = -\langle \partial\mathcal{L}/\partial\mu \rangle = 0$, leads to

$$-f_\pi^2 \mu \sin^2\theta + \cos\theta\,\rho_p - \sin^2(\theta/2)\,\rho_n - \rho_e(\mu) - \rho_\mu(\mu) = 0\,, \tag{5.60}$$

where we included the lepton charge densities, given by

$$\rho_l(\mu) = \Theta(|\mu| - m_l)\,\text{Sign}(\mu)\,\frac{(\mu^2 - m_l^2)^{3/2}}{3\pi^2}\,, \quad l = e, \mu\,. \tag{5.61}$$

Solving (numerically) the coupled Eqs. (5.59), (5.60), one can determine the values of $\{\theta, \mu\}$ as a function of $\{\rho, \rho_p/\rho\}$. In Fig. 5.2 we show the results for θ and μ as a function of baryon density for different values of the proton fraction, while in Fig. 5.4 we plot the region (blue) in the $\{\rho, \rho_p/\rho\}$ plane where $\theta \neq 0$, namely where the system is in the kaon-condensed phase. The evolution for given $\{\rho, \rho_p/\rho\}$ can be understood as follows: for a fixed proton fraction ρ_p/ρ, as ρ increases the amount of positive charge due to the protons increases as well, and more leptons are required to satisfy the neutrality condition, leading to an increase in μ. This increase in μ drives the effective mass of the kaon, Eq. (5.52), further down (on top of the decrease in $\langle \bar{u}u \rangle$ at finite density), until eventually the threshold condition for kaon condensation is met, $\mu = (m_{K^\pm})_\rho$, and a further increase in the proton density can be compensated by inserting K^- particles in the ground state.

Even though we keep them undetermined, let us briefly comment at this point on how the proton fraction could be determined in terms of the total density. Since the interaction energy of nuclear matter also depends on the proton fraction, $E^{\text{int.}} = \rho\, E^{\text{int.}}(\rho, \rho_p)$, one could enforce that the total energy density is minimal with respect to ρ_p/ρ, which would lead to the constraint [202],

$$c_4 \sin^2(\theta/2) + \mu \cos^2(\theta/2) + \frac{\partial E^{\text{int.}}(\rho, \rho_p)}{\partial(\rho_p/\rho)} = 0\,, \tag{5.62}$$

where $c_4 \equiv (2b_2 f_\pi^2 m_K^2)/\rho_0 \sim 49\,\mathrm{MeV}$.

After determining the ground state orientation, let us examine the consequences on the axion potential. The pseudo-NGB potential, after reintroducing the fluctuations we are mainly interested in, namely the neutral mesons π_0, η and the axion, is given by

$$V(\pi_0, \eta, \phi) = \frac{f_\pi^2 \mu^2}{4} \mathrm{Tr}[[Q_e, U][Q_e, U^\dagger]] + \frac{1}{2} \mathrm{Tr}[\langle \bar{q} q \rangle_\rho \hat{M}_\phi + \mathrm{h.c.}] \tag{5.63}$$

with $\hat{M}_\phi$ given in Eq. (5.30) and

$$U = u_L U_0 u_R^\dagger = u_0 \exp\left[\frac{i\pi^a \lambda^a}{f_\pi}\right] u_0 \,. \tag{5.64}$$

Note this potential is similar to that discussed in Sec. 5.1.2 in the context of meson condensation, with the additional relevant feature of the density dependent quark condensates, in particular their decrease with density, $\zeta_{\bar{u}u} \approx \zeta_{\bar{d}d} \approx 1 - b_1(\rho/\rho_0)$. The three mass eigenstates, corresponding to mixtures of π_3, η and a, have the following masses in the isospin symmetric limit $\Delta m = 0$ and at leading order in θ and $\bar{m}/m_s$, [9]

$$(m_{\pi_0}^2)_{\rho,\theta} \approx m_\pi^2 \, \zeta_{\bar{u}u} \left[1 + \frac{1}{8}\left(\frac{2\mu^2}{m_\pi^2 \zeta_{\bar{u}u}} - \frac{m_s}{\bar{m}}\right)\theta^2\right] , \tag{5.65}$$

$$(m_\eta^2)_{\rho,\theta} \approx m_\eta^2 \left[1 - \frac{1}{4}\left(1 + \frac{\zeta_{\bar{u}u}}{4}\right)\theta^2\right] , \tag{5.66}$$

$$(m_\phi^2)_{\rho,\theta} \approx (m_a^2)_0 \, \zeta_{\bar{u}u} \left[1 - \frac{1}{8}\left(1 + \frac{1}{\zeta_{\bar{u}u}}\right)\theta^2\right] . \tag{5.67}$$

with m_π and m_η the masses in vacuum, respectively Eq. (5.20) and $m_\eta^2 = -4 m_s \langle \bar{q} q \rangle_0 / 3 f_\pi^2$ neglecting $O(m_{u,d}/m_s)$ terms. Note that only the neutral pion mass depends on the charge chemical potential, and that such dependence enters along with kaon condensation. The effect of a non-vanishing θ on $(m_{\pi_0}^2)_{\rho,\theta}$ therefore depends on the relative size of $m_s/\bar{m} \approx 27$ and $2\mu^2/(m_\pi^2 \zeta_{\bar{u}u})$, which enter with opposite signs. Note in this regard that while we use the leading order result for the quark condensate ratio $\zeta_{\bar{u}u}$, we did not perform an expansion in density. This is because, as we advanced at the beginning of this section and as explicitly shown in Fig. 5.2, when kaon condensation sets in we have $\rho/\rho_0 > 1$. Then, when $m_s/\bar{m} > 2\mu^2/m_\pi^2 \zeta_{\bar{u}u}$, the coefficient of θ is negative and π_0 becomes lighter as kaon condensation sets in. Such a decrease could potentially lead to an instability and CP violation in the neutral sector. However, in the opposite case, when $m_s/\bar{m} < 2\mu^2/(m_\pi^2 \zeta_{\bar{u}u})$, which occurs at larger densities where $\zeta_{\bar{u}u}$ is small and μ/m_π large (see Fig. 5.2), the coefficient of θ is positive and π_0 becomes heavier in the kaon-condensed phase. As opposed to the π_0, the η mass depends only weakly on θ. In Fig. 5.3 we plot the numerical result for $(m_{\pi_0}^2)_{\rho,\theta}$ as a function of density for fixed values of proton fraction, using the numerical results for $\theta(\rho)$ and $\mu(\rho)$ displayed in Fig. 5.2. We find that the μ^2 contribution leads to an increase in the mass of the neutral pion, similar to the effect of pion condensation in the simplified case discussed in Sec. 5.1.2. Finally, the axion mass is independent of μ and decreases with the size of the kaon condensate. Interestingly, the negative coefficient of θ^2 is enhanced as density increases, since then $\zeta_{\bar{u}u}$ becomes smaller. As shown in Fig. 5.4, this behavior eventually results in axion condensation at large densities, yet before the quark condensate vanishes. In this phase CP is thus spontaneously broken in the neutral sector.

[9] The calculation of the axion mass is simplified by choosing a particular θ-dependent Q_ϕ matrix which removes the tree-level mixing between the axion and π_0 and η, see App. B.3 for more details.

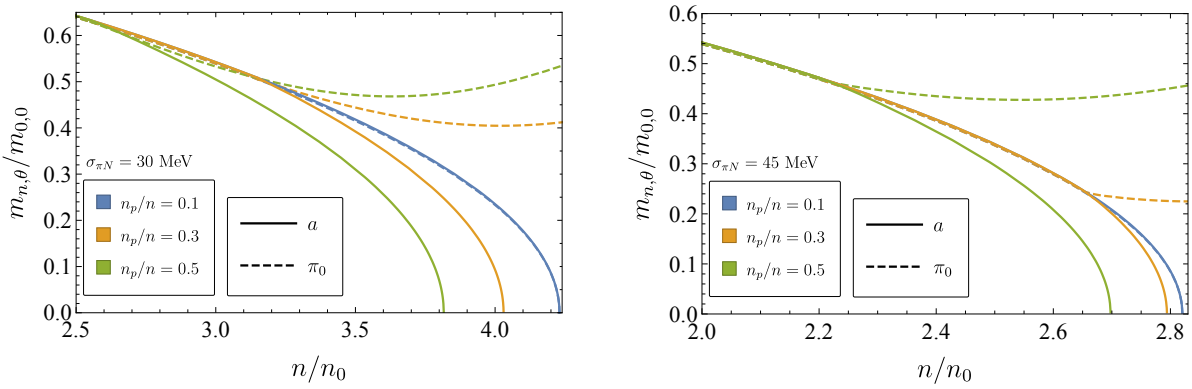

Figure 5.3: Numerical result for the neutral pion (dashed line) and axion (solid line) masses normalized to their $\rho = \theta = 0$ values as a function of density ρ/ρ_0 ($n = \rho$ and $a = \phi$ in the plot) for $\sigma_{\pi N} = 30\,\text{MeV}$ (left panel) and $\sigma_{\pi N} = 45\,\text{MeV}$ (right panel). The blue, orange and green curves correspond to fixed values of the proton fraction $\rho_p/\rho = 0.1$, 0.3 and 0.5, respectively. We consider densities in the region $\rho < \rho_c \equiv \rho_0/b_1 \approx 2.8\rho_0\,(45\,\text{MeV}/\sigma_{\pi N})$ for the corresponding values of $\sigma_{\pi N}$. The effect of kaon condensation is to eventually increase the neutral pion mass, while the axion becomes lighter and even massless at some density below ρ_c. Above this density the axion field is therefore unstable around $\langle\phi\rangle = 0$ and axion condensation is expected to occur.

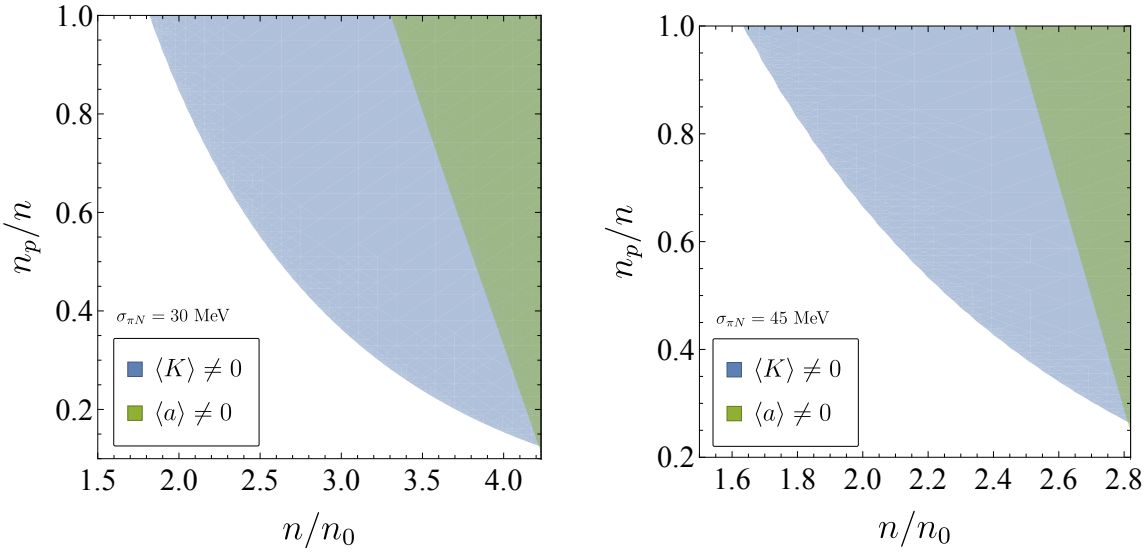

Figure 5.4: Phase diagram in the plane of baryon density ρ/ρ_0 ($n = \rho$ and $a = \phi$ in the plot) and proton fraction ρ_p/ρ based on the numerical solution of Eqs. (5.59), (5.60) for $\sigma_{\pi N} = 30\,\text{MeV}$ (left panel) and $\sigma_{\pi N} = 45\,\text{MeV}$ (right panel). The blue region marks the kaon-condensed phase, while the green region marks the axion-condensed phase. We consider densities in the region $\rho < \rho_c$ for the corresponding values of $\sigma_{\pi N}$.

Lastly, we note that one should be wary of the fact that for the quark condensates we included only density corrections at linear order and disregarded higher order corrections. As discussed at the end of the previous section, for densities $\rho \sim \rho_c$, these corrections are in fact important. In this regard, we would like to stress the fact that while our results might not be trustable at the quantitative level, this does not necessarily make an axion-condensed phase less likely.

First, let us note that qualitatively we expect $(m_\phi^2)_{\rho,\theta}$ to decrease with ρ even when considering higher-order corrections to $\zeta_{\bar{u}u}(\rho)$. Second, to further support our claim, let us consider the limit of maximal kaon condensation, i.e. $\theta \to \pi/2$, where

$$(m_\phi^2)_{\rho,\pi/2} \approx (m_\phi^2)_0(\zeta_{\bar{u}u} - \zeta_{\bar{s}s}) \approx -(m_\phi^2)_0\, b_1\, \frac{\rho}{\rho_0}\,. \tag{5.68}$$

If one ignores the density dependence of the condensates by taking $b_1 = 0$, this result is consistent with the naive expectation of a vanishing axion mass for $\cos\theta \to 0$, since $(m_\phi^2)_\theta \propto \mathrm{Tr}[U_0 + U_0^\dagger] \propto \cos\theta$, as we showed in Sec. 5.1.2. However, as discussed in Sec. 5.2.1, a background of protons and neutrons makes $\zeta_{\bar{u}u} < \zeta_{\bar{s}s} \approx 1$, in other words $b_1 > 0$, this implies a negative axion mass for large kaon condensates, where it becomes energetically favorable for the axion field to develop a non-vanishing expectation value.

5.3 CFL phase

In this section we make a jump to asymptotically large baryon densities, or equivalently large quark chemical potentials, $\mu_q \gg \Lambda_\chi$ ($\mu_q \equiv \mu_u = \mu_d = \mu_s$). At such high densities, two quark around the highly energetic Fermi surface interact weakly via tree-level gluon exchange, interactions which can be effectively parametrized below the Fermi momentum by 4-Fermi operators. Such operators, when in the attractive color $\bar{\mathbf{3}}$ channel, become relevant for back-to-back scattering as one approaches the Fermi surface (see e.g. [208,209]), leading to the formation of diquark pairs and ultimately to color superconductivity [210–213], see also [214] for a comprehensive review. Such a diquark pairing manifests itself in the form of a diquark condensate $\langle q_L C q_L\rangle$, which leads to the color-flavor-locked symmetry breaking pattern

$$SU(3)_c \times SU(N_f)_L \times SU(N_f)_R \times U(1)_B \times U(1)_A \to SU(N_f)_{L+R+c}\,. \tag{5.69}$$

The condensates are given by [214]

$$\langle q_L^{ia} C q_L^{jb}\rangle = \left(\epsilon^{abc}\epsilon^{ijk}\langle\Delta_L^{\bar{3}}\rangle_{kc} + \langle\Delta_L^{6}\rangle^{ij,ab}\right)\frac{3\sqrt{2}\pi}{g_s}\frac{\mu_q^2}{2\pi}\,, \tag{5.70}$$

$$\langle q_R^{\bar{i}a} C q_R^{\bar{j}b}\rangle = \left(\epsilon^{abc}\epsilon^{\bar{i}\bar{j}\bar{k}}\langle\Delta_R^{\bar{3}}\rangle_{\bar{k}c} + \langle\Delta_R^{6}\rangle^{\bar{i}\bar{j},ab}\right)\frac{3\sqrt{2}\pi}{g_s}\frac{\mu_q^2}{2\pi}\,, \tag{5.71}$$

where i,j,k are $SU(3)_L$ indices, $\bar{i},\bar{j},\bar{k}$ are $SU(3)_R$ indices, and a,b,c are $SU(3)_c$ indices, upper (lower) if in the (anti-)fundamental. The representations under the unbroken symmetries in (5.69) of the scalar field matrices above are

$$\Delta_L^{\bar{3}} : (\bar{\mathbf{3}},\bar{\mathbf{3}},\mathbf{1})_{+2,+2}\,, \quad \Delta_L^{6} : (\mathbf{6},\mathbf{6},\mathbf{1})_{+2,+2}\,, \tag{5.72}$$

$$\Delta_R^{\bar{3}} : (\bar{\mathbf{3}},\mathbf{1},\bar{\mathbf{3}})_{+2,-2}\,, \quad \Delta_R^{6} : (\mathbf{6},\mathbf{1},\mathbf{6})_{+2,-2}\,, \tag{5.73}$$

while their expectation values, proportional to the gap parameters Δ_3 and Δ_6, are

$$\langle\Delta_L^{\bar{3}}\rangle_{kc} = \delta_{kc}\Delta_3\,, \quad \langle\Delta_L^{6}\rangle^{ij,ab} = (\delta^{ia}\delta^{jb} + \delta^{ja}\delta^{ib})\Delta_6\,, \tag{5.74}$$

$$\langle\Delta_R^{\bar{3}}\rangle_{\bar{k}c} = -\delta_{\bar{k}c}\Delta_3\,, \quad \langle\Delta_R^{6}\rangle^{\bar{i}\bar{j},ab} = -(\delta^{\bar{i}a}\delta^{\bar{j}b} + \delta^{\bar{j}a}\delta^{\bar{i}b})\Delta_6\,. \tag{5.75}$$

We parametrize the low-energy fluctuations of the ground state, i.e. the NGBs associated with the symmetry breaking pattern (5.69) as

$$\Delta_L^{\bar{3}} = u_L^\dagger\langle\Delta_L^{\bar{3}}\rangle \exp\left[2i\left(\frac{\eta'}{f_{\eta'}} + \frac{H}{f_H}\right)\right]\,, \tag{5.76}$$

$$\Delta_R^{\bar{3}} = u_R^\dagger \langle \Delta_R^{\bar{3}} \rangle \exp\left[2i\left(-\frac{\eta'}{f_{\eta'}} + \frac{H}{f_H}\right)\right], \tag{5.77}$$

$$\Delta_L^6 = u_L^T \langle \Delta_L^6 \rangle u_L \exp\left[2i\left(\frac{\eta'}{f_{\eta'}} + \frac{H}{f_H}\right)\right], \tag{5.78}$$

$$\Delta_R^6 = u_R^T \langle \Delta_R^6 \rangle u_R \exp\left[2i\left(-\frac{\eta'}{f_{\eta'}} + \frac{H}{f_H}\right)\right], \tag{5.79}$$

where

$$u_L = u_R^\dagger = \exp\left[\frac{i\pi^a \lambda^a}{2f_\pi}\right]. \tag{5.80}$$

The η' and H are the NGBs associated with the spontaneous breaking of $U(1)_A$ and $U(1)_B$, respectively. The NGBs associated with the breaking of color have been removed, since they are "eaten" by the gluons (unitary gauge). The rest of the NGBs, formally equivalent to those of the standard QCD chiral Lagrangian, are contained in the $u_{L,R}$ matrices, which are used to construct the following linearly-transforming color-neutral Goldstone matrix

$$U \equiv u_L u_R^\dagger : (\mathbf{1}, \mathbf{3}, \bar{\mathbf{3}})_{0,0}\,. \tag{5.81}$$

5.3.1 Kinetic terms

The kinetic terms in the CFL phase are given by

$$\mathcal{L}_{\text{kin.}}^{\text{CFL}} = \frac{f_\pi^2}{4}\eta_U^{\mu\nu}\text{Tr}[D_\mu U D_\nu U^\dagger] + \frac{1}{2}\eta_{\eta'}^{\mu\nu}\partial_\mu\eta'\partial_\nu\eta' + \frac{1}{2}\eta_H^{\mu\nu}\partial_\mu H\partial_\nu H\,, \tag{5.82}$$

with

$$\eta_\varphi^{\mu\nu} = \text{Diag}[1, -v_\varphi^2, -v_\varphi^2, -v_\varphi^2]\,, \quad \varphi = U, \eta', H\,. \tag{5.83}$$

We recall that the introduction of chemical potential breaks Lorentz symmetry down to spatial rotations, and the low-energy excitations, even if massless, propagate sub-luminally. These velocities, as well as the decay constants, can be calculated by matching the UV microscopic theory [215] to the effective low-energy theory [216, 217], [10]

$$f_\pi^2 = \frac{21 - 8\ln 2}{18}\frac{\mu_q^2}{2\pi^2}\,, \quad f_{\eta',H}^2 = 18\frac{\mu_q^2}{2\pi^2}\,, \quad v_{U,\eta',H}^2 = 1/3\,. \tag{5.84}$$

The U field gets a dynamically induced chemical potential due to the non-vanishing quark masses [219]

$$D_0 U = \partial_0 U + i\mu_L^{\text{eff}} U - iU\mu_R^{\text{eff}}\,, \tag{5.85}$$

with

$$\mu_L^{\text{eff}} = (\mu_R^{\text{eff}})^\dagger = \frac{M_q M_q^\dagger}{2\mu_q}\,. \tag{5.86}$$

Note that even if we choose a basis in which the axion enters the CFL effective Lagrangian via an axion-dependent quark mass matrix M_ϕ, as in Eq. (2.59c), it will not appear in such an effective chemical potential, since we can restrict ourselves to diagonal Q_ϕ matrices. In any case, for the analysis of the axion potential in the CFL phase, it will be more convenient to work in a basis where the axion is coupled to gluons, since a perturbative instanton expansion exists, being the gluons heavy and weakly coupled.

[10] As mentioned above, the gluons, with electric and magnetic masses $m_D^2 = g_s^2 f_\pi^2$ and $m_M^2 = v_\varphi^2 m_D^2$ respectively, are heavy and integrated out [218].

5.3.2 Mass Terms

Given the spurionic transformation properties of the quark mass M_q see Eq. (A.8) in App. A.2, the leading order terms preserving the global symmetries in (5.69) are

$$V_{M_q}^{\rm CFL} = A_1 \epsilon^{ijk} \epsilon_{\bar{i}\bar{j}\bar{k}} \left([\Delta_L^{\bar{3}\dagger} \Delta_R^{\bar{3}}]_i{}^{\bar{i}} M_j{}^{\bar{j}} M_k{}^{\bar{k}} + \text{h.c.} \right) - \frac{A_2}{2} \left([\Delta_L^{6\dagger} \Delta_R^{6}]^{ij}_{\bar{i}\bar{j}} M_i{}^{\bar{i}} M_j{}^{\bar{j}} + \text{h.c.} \right). \tag{5.87}$$

Note that this potential respects $U(1)_A$ and it is generated perturbatively. Contrary to QCD in vacuum, the axial symmetry thus dictates that the leading order terms in the scalar potential are $O(M_q^2)$. Using Eqs. (5.74) - (5.79) one finds [216] [11]

$$\begin{aligned} V_{M_q}^{\rm CFL} = &- A_1 \Delta_3^2 \left[e^{-4i\eta'/f_{\eta'}} \left(\text{Tr}[U^\dagger M_q] \text{Tr}[U^\dagger M_q] - \text{Tr}[U^\dagger M_q U^\dagger M_q] \right) + \text{h.c.} \right] \\ &+ A_2 \Delta_6^2 \left[e^{-4i\eta'/f_{\eta'}} \left(\text{Tr}[U^\dagger M_q] \text{Tr}[U^\dagger M_q] + \text{Tr}[U^\dagger M_q U^\dagger M_q] \right) + \text{h.c.} \right]. \end{aligned} \tag{5.88}$$

The coefficients can be computed by appropriately matching to the UV theory [216, 217, 220],

$$A_1 = 2A_2 = \frac{3}{4\pi^2}. \tag{5.89}$$

Importantly, these two coefficients enter with opposite signs in Eq. (5.87). This is due to the fact that while the color $\bar{\mathbf{3}}$ channel is attractive and lowers the total energy of the system, the color $\mathbf{6}$ channel is repulsive and increases it. As a result, one finds that $\Delta_6 = 0$ at the classical level. However, since $\langle \Delta_{L,R}^6 \rangle$ does not break any additional symmetries compared to $\langle \Delta_{L,R}^{\bar{3}} \rangle$, there is nothing preventing it from being generated at the quantum level in the presence of a non-vanishing Δ_3. Indeed, a perturbative calculation yields [221]

$$\Delta_6^2 = \alpha_s \frac{\ln^2 2}{162\pi} \Delta_3^2, \tag{5.90}$$

where $\alpha_s = g_s^2/4\pi$. Δ_3 itself can be calculated using the so-called gap equation, in particular in the CFL phase with $N_f = 3$ [214]

$$\Delta_3 = 512\pi^4 (2/3)^{5/2} e^{-\frac{\pi^2+4}{8}} 2^{-1/3} \frac{\mu_q}{g_s^5} \exp\left(-\frac{3\pi^2}{\sqrt{2} g_s} \right). \tag{5.91}$$

The reason for considering the contribution of the condensate Δ_6 to the potential, even though it is suppressed with respect to Δ_3, comes from the hierarchy in the quark masses. Indeed, one finds e.g. contributions from both condensates to the masses of the mesons, of order [222],

$$\Delta_3 m_{u,d}^2 \sim \Delta_6 m_s^2. \tag{5.92}$$

The similarity of these two contributions, along with the fact that the coefficients of the respective operators (in Eq. (5.89)) come with opposite signs, can lead to non-trivial vacuum structures, as we review below.

Finally, we note that although at $O(M_q M_q^\dagger)$ there exist other operators which could be considered along with those in Eq. (5.87), $\text{Tr}[M_q U^\dagger M_q^\dagger U]$ and $\text{Tr}[M_q U^\dagger] \text{Tr}[M_q^\dagger U]$, these are not generated at the order we are interested in [216].

[11] The first term in Eq. (5.87) can also be written as $-2A_1\Delta_3^2(e^{4i\eta'/f_{\eta'}} \text{Tr}[\tilde{M}_q U] + \text{h.c.})$, where $\tilde{M}_q = \det[M_q] M_q^{-1} = (\bar{m} m_s, \bar{m} m_s, \bar{m}^2)$.

5.3.3 Non-perturbative Terms

Instantons explicitly break the $U(1)$ axial symmetry of QCD, also in the CFL phase [223]. At leading order in the gap parameters, one finds the following term generated via a single t'-Hooft vertex

$$V^{\text{CFL}}_{\text{1-inst.}} = A_3 \left([\Delta^{\bar{3}\dagger}_L \Delta^{\bar{3}}_R]_i{}^{\bar{i}} [M_q^\dagger]^i{}_{\bar{i}} + \text{h.c.} \right) = -A_3 \Delta_3^2 \, \text{Tr}[e^{-4i\eta'/f_{\eta'}} U M_q^\dagger + \text{h.c.}] \,. \tag{5.93}$$

The coefficient A_3 can be calculated reliably at large chemical potentials due to the screening of gluons for instantons of size $\rho \gtrsim 1/\mu_q \ll 1/\Lambda_{\text{QCD}}$, where $\Lambda_{\text{QCD}} \approx 250\,\text{MeV}$ is the QCD scale parameter,

$$A_3 = c\,(6\pi)^3 \, \frac{\Lambda^9_{\text{QCD}}}{3\alpha_s^7 \mu_q^8} \,, \tag{5.94}$$

with $c = 0.155$ [214, 223]. Given that the operator in Eq. (5.93) matches the leading term in the meson potential of the chiral Lagrangian at zero density, Eq. (5.17), its coefficient can be mapped to the value of the standard quark condensate in the CFL phase

$$\frac{\langle \bar{q} q \rangle^{\text{CFL}}_\rho}{\langle \bar{q} q \rangle_0} = \frac{A_3 \Delta_3^2}{\langle \bar{q} q \rangle_0} \sim 1 \times 10^{-5} \left(\frac{\Delta_3}{50\,\text{MeV}} \right)^2 \left(\frac{\pi}{\alpha_s} \right)^7 \left(\frac{500\ \text{MeV}}{\mu_q} \right)^8 \left(\frac{\Lambda_{\text{QCD}}}{250\,\text{MeV}} \right)^9 , \tag{5.95}$$

where we set the chemical potential to a value expected to be realized in the core of a NS, noting that α_s is to be evaluated at the scale μ_q and that Δ_3 depends on both α_s and μ_q. Due to the limited reliability of the perturbative result at such chemical potentials (see the discussion below), as well as to the strong dependence on Λ_{QCD}, it is clear that one cannot make a robust prediction regarding the value of the quark condensate at realistic densities, yet a strong suppression of $\langle \bar{q} q \rangle$ remains the most plausible outcome.

A higher-order operator that contributes to the mass of the η' in the chiral limit appears at the two-instanton level,

$$V^{\text{CFL}}_{\text{2-inst.}} = \frac{1}{\Lambda^2} \left(\det[\Delta^{\bar{3}\dagger}_L \Delta^{\bar{3}}_R] + \text{h.c.} \right) = -\frac{2\Delta_3^6}{\Lambda^2} \cos\left(\frac{12\eta'}{f_{\eta'}} \right) . \tag{5.96}$$

Note this term matches the would-be leading potential for the standard η' in vacuum.

Before moving to the discussion of the axion potential in the CFL phase, let us note that the matching procedure by which the coefficients of the effective CFL Lagrangian are extracted from the microscopic theory relies on perturbative calculations that have been found to be under control for $g_s \lesssim 0.8$ [224]. Such a small coupling corresponds to very high quark chemical potentials, $\mu_q \gtrsim 10^8\,\text{MeV}$, five orders of magnitude higher than those expected at the cores of dense NSs, where $\mu_q \sim 500\,\text{MeV}$. Still, a quantitative but more importantly a qualitative understanding of the CFL phase and of the corresponding axion potential provides a solid ground from which to extrapolate to lower chemical potentials and thus to realistic densities. In fact, the qualitative features and basic symmetry structure of the CFL phase should hold down to $\mu \sim m_s^2/\Delta_3 \approx 180\,\text{MeV}\,(50\,\text{MeV}/\Delta_3)$ [214].

5.3.4 Axion potential

In view of the previous discussion, in the following we examine the different axion potentials that arise by considering different hierarchies between the coefficients of the CFL operators.

Non-perturbative dominance

In this case we assume that the non-perturbative contributions to the potential dominate over the mass terms, that is $V^{\text{CFL}}_{\text{1-inst.}}, V^{\text{CFL}}_{\text{2-inst.}} \gg V^{\text{CFL}}_{M}$. Nevertheless, we still consider there exists a weak-coupling expansion, in the sense that the one-instanton contribution dominates over the two-instanton one, that is

$$e^{-S_I} \gg e^{-2S_I} \sim e^{-S_{II}}\,, \tag{5.97}$$

with S_I, S_{II} the action of the one- and two-instanton solutions, respectively. Given that the CFL operators in Eq. (5.87) are of order $V^{\text{CFL}}_{M} \sim \bar{m} m_s \Delta_3^2$, where here and in the following we neglect $\Delta m = \frac{1}{2}(m_u - m_d)$, our hierarchy of potentials implies $\bar{m} A_3 \gg \Delta_3^4/\Lambda^2 \gg \bar{m} m_s$. In this case the potential, including the axion, reads

$$V^{\text{CFL}}_{\text{1+2-inst.}} = -A_3 \Delta_3^2 \,\text{Tr}[e^{i(\phi/f_\phi + 4\eta'/f_{\eta'})} U^\dagger M_q + \text{h.c.}] + \frac{\Delta_3^6}{\Lambda^2}(e^{i(2\phi/f_\phi + 12\eta'/f_{\eta'})} + \text{h.c.})\,. \tag{5.98}$$

After a field redefinition $\eta' \to \eta' - (f_{\eta'}/4f_\phi)\phi$, this is found to be the same as in the vacuum chiral Lagrangian with a light η', which is minimized at the trivial vacuum, $\langle \eta' \rangle = \langle \phi \rangle = 0$ in particular. The axion mass can be calculated by integrating out the mesons as we did in zero density. The details of this derivation can be found in App. B.1. We find that the axion mass is suppressed with respect to its vacuum value by

$$\frac{(m_\phi^2)^{\text{NP}}_{\text{CFL}}}{(m_\phi^2)_0} = \frac{8\Delta_3^6}{(m_\pi^2 f_\pi^2)_0 \Lambda^2} \sim 3 \times 10^{-3} \left(\frac{\Delta_3}{50\,\text{MeV}}\right)^6 \left(\frac{500\,\text{MeV}}{\Lambda}\right)^2\,. \tag{5.99}$$

Perturbative dominance

Let us now consider the hierarchy $V^{\text{CFL}}_{M} \gg V^{\text{CFL}}_{\text{1-inst.}} \gg V^{\text{CFL}}_{\text{2-inst.}}$. One should first note that if the instanton terms are set to zero, the axion is massless, as can be immediately seen by using the basis defined by $Q_\phi = 0$ in Eq. (2.57); we use such a basis in the following. We write the potential in terms of the variables

$$\langle 4\eta'/f_{\eta'} \rangle \equiv \alpha\,, \quad \langle \phi/f_\phi \rangle \equiv \beta\,, \tag{5.100}$$

and use the ansatz [222]

$$\langle U \rangle = \text{Diag}[e^{-i\varphi}, e^{-i\varphi}, e^{2i\varphi}] \begin{pmatrix} 1 & 0 & 0 \\ 0 & \cos\theta & i\sin\theta \\ 0 & i\sin\theta & \cos\theta \end{pmatrix}\,, \tag{5.101}$$

where the angles φ and θ correspond to the expectation values $\langle \eta/\sqrt{3}f_\pi \rangle$ and $\langle K_0/f_\pi \rangle$, respectively. In this basis the meson potential is given by

$$V^{\text{CFL}}_{\text{pert.,LO}} = -\frac{f_\pi^2 m_s^4}{8\mu_q^2}\sin^2\theta - 4A_1\Delta_3^2 \bar{m} m_s(\cos\theta + 1)\cos(\alpha - \varphi)\,, \tag{5.102a}$$

$$V^{\text{CFL}}_{\text{pert.,NLO}} = -4A_1\Delta_3^2\bar{m}^2\cos\theta\cos(\alpha + 2\varphi) + 4A_2\Delta_6^2 m_s^2\cos^2\theta\cos(\alpha - 4\varphi)\,, \tag{5.102b}$$

$$V^{\text{CFL}}_{\text{1-inst.}} = -2A_3\Delta_3^2 m_s\cos\theta\cos(\alpha + \beta + 2\varphi)\,. \tag{5.102c}$$

where we separated LO terms of $O(\bar{m}m_s\Delta_3^2)$, from NLO terms of $O(\bar{m}^2\Delta_3^2 \sim m_s^2\Delta_6^2)$, and instanton-generated terms. [12] Minizing the LO potential $V^{\rm CFL}_{\rm pert.,LO}$ with respect to φ and θ yields

$$\varphi = \alpha \tag{5.103}$$

$$\cos\theta = \text{Min}\left[1, \frac{16A_1\Delta_3^2\bar{m}}{m_s^3}\left(\frac{\mu_q}{f_\pi}\right)^2\right] \tag{5.104}$$

The solution $\varphi = \alpha$ implies that the minimization of the NLO potential $V^{\rm CFL}_{\rm pert.,NLO}$ with respect to α is found at

$$\cos 3\alpha = \text{Sign}[A_1\Delta_3^2\bar{m}^2 - A_2\Delta_6^2 m_s^2\cos\theta]\,. \tag{5.105}$$

Eqs. (5.104), (5.105) match the the results of [222]. Lastly, the instanton potential is minimized with respect to β at

$$\cos\beta = \text{Sign}\left[\cos(3\alpha)\right]\,. \tag{5.106}$$

Therefore, one finds that the the axion is aligned with the η', such that

$$\langle\phi/f_\phi\rangle = \begin{cases} 0\,, & A_1\Delta_3^2\bar{m}^2 > A_2\Delta_6^2 m_s^2\cos\theta \\ \pi\,, & A_1\Delta_3^2\bar{m}^2 < A_2\Delta_6^2 m_s^2\cos\theta \end{cases}\,, \tag{5.107}$$

while the axion mass, neglecting mixing with η' and normalized to its vacuum value, is given by

$$\frac{(m_\phi^2)_{\rm CFL}}{(m_\phi^2)_0} = \frac{8A_3\Delta_3^2 m_s\cos\theta}{(m_\pi^2 f_\pi^2)_0} \sim 7\times 10^{-4}\left(\frac{\Delta_3}{50\,\text{MeV}}\right)^2\left(\frac{A_3}{4\times 10^{-4}\,\text{MeV}}\right)\left(\frac{\cos\theta}{1}\right)\,. \tag{5.108}$$

where we evaluated A_3 in Eq. (5.94) at $\mu_q = 1$GeV, $\Lambda_{\rm QCD} = 250\,$MeV and $\alpha_s = \pi$. We therefore find that the axion can develop a non-vanishing expectation value in the CFL phase also, when the kaon condensate is large. Up to uncertainties associated with the value of A_3, the axion is significantly lighter than in vacuum.

5.4 Axion sourcing observables

We briefly discuss in this section the potentially observable consequences of a non-vanishing axion condensate in NSs, where the largest baryonic densities among the stars are found. We defer to future work a more in-depth analysis of the corresponding phenomenology [15], as well as the study of the implications of the change in the axion-nucleon couplings with density, the latter particularly relevant for supernovae and NS cooling.

For simplicity, let us consider the following toy model, namely a stepwise radius-dependent axion potential

$$V(\phi, r) = \begin{cases} f_\phi^2(m_\phi^2)_{\rm in}\left[\cos(\phi/f_\phi) - 1\right] & r < r_c \\ -f_\phi^2(m_\phi^2)_{\rm out}\left[\cos(\phi/f_\phi) - 1\right] & r > r_c \end{cases}\,, \quad f_\phi^2(m_\phi^2)_{\rm out} \sim m_\pi^2 f_\pi^2\,, \tag{5.109}$$

where m_π and f_π are the vacuum values and we have fixed the constants such that in the decoupling limit $f_\phi \to \infty$, the potential vanishes. The potential grossly captures the effect of

[12] We should note at this point that we did not include the neutral pion π_0 in our analysis because the corresponding first term in Eq. (5.102a), which destabilizes the potential at the origin of field space for K^0, vanishes for π_0.

matter on the axion potential, i.e. at a critical radius r_c, which is of the order of the NS radius R, the axion field gets destabilized and the minimum of the potential is located at $\langle \phi/f_\phi \rangle = \pi$. The field equation can be solved numerically and one finds the intuitive result based on energy conservation, i.e. for the axion to get sourced the gain in potential energy needs to be enough to compensate for the gradient energy that comes with the change in field value, $\Delta V \sim (\Delta a/R)^2$, which occurs when the object is large enough compared to the de Broglie wavelength of the field inside the object [186], namely

$$(m_\phi)_{\rm in}^{-1} \lesssim r_c \sim R\,. \tag{5.110}$$

Let us assume this is the case for the rest of the discussion, keeping in mind that the axion mass decreases with baryon density and that in vacuum $(m_\phi)_{\rm out}^{-1} \sim 16\,{\rm km}\,(f_\phi/10^{18}{\rm GeV})$. The typical field configuration of the sourced axion is roughly

$$\frac{\phi(r)}{\pi f_\phi} = \begin{cases} 1\,, & r < r_c \\ \frac{r_c}{r} e^{-(m_\phi)_{\rm out}(r-r_c)}\,, & r > r_c \end{cases}\,. \tag{5.111}$$

In Fig. 5.5 we depict the typical field configurations of the axion sourcing, highlighting in grey the possible observable implication, to be discussed in turn below.

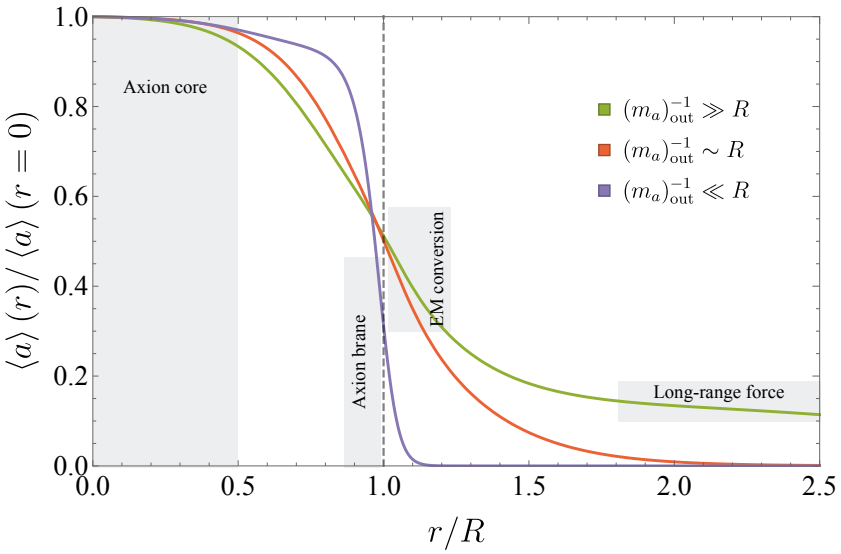

Figure 5.5: ($a = \phi$) Sketch of the typical field configurations of a sourced axion field, see the discussion in the main text.

5.4.1 Free (vacuum) energy

The first potentially observable implication is associated with the shift in potential energy density inside the NS,

$$\Delta V \sim -2 f_\phi^2 (m_\phi^2)_{\rm in}, \tag{5.112}$$

as a result of the axion sourcing. This effect is independent of the field configuration outside the core of the NS, namely it is independent of $\left(m_\phi^2\right)_{\rm out}$. Such an energy density shift can be of considerable size compared to the energy density inside a NS, $\rho_0 \approx m_n \rho_0 \approx (190\,{\rm MeV})^4$.

Indeed, if the axion is sourced at relatively low baryon densities, as in the kaon condensed phase (Sec. 5.2.2), one expects $\Delta V \sim m_\pi^2 f_\pi^2$, which is indeed not significantly below ρ_0 or the energy change due to kaon condensation, of $O(m_K^2 f_\pi^2)$. Instead, if axion sourcing happens in the CFL phase (Sec. 5.3), this effect is expected to be suppressed by a few orders of magnitude, see Eq. (5.108), and therefore likely negligible.

A NS with a core of "vacuum energy" was considered as a generic scenario in [225, 226], in the context of exotic QCD phases. It was found that the energy shift inside the NS leads to a significant change in the mass-radius relation of NSs, as well as to changes of the so-called chirp mass, one of main the gravitational wave observables of compact binary mergers. Such a shift has been discussed in Ref. [15].

5.4.2 Axion-EM conversion

Next we consider the interplay between the EM fields of rotating NSs (i.e. pulsars), which are the strongest found in the Universe, and the axion, in particular when

$$(m_\phi)_{\rm out}^{-1} \gtrsim R\,, \tag{5.113}$$

such that the sourced axion field is still non-negligible in the close surroundings of the NS.

The axion and the classical EM fields form a coupled system, as seen from the generalized form of the Maxwell equations

$$\boldsymbol{\nabla}\cdot\mathbf{E} = g_{\phi\gamma\gamma}\,\mathbf{B}\cdot(\boldsymbol{\nabla}\phi)\,, \tag{5.114a}$$

$$\boldsymbol{\nabla}\times\mathbf{B} = \frac{\partial\mathbf{E}}{\partial t} + g_{\phi\gamma\gamma}\left[\mathbf{E}\times\boldsymbol{\nabla}\phi - \mathbf{B}\dot{\phi}\right]\,, \tag{5.114b}$$

$$\Box\phi = g_{\phi\gamma\gamma}(\mathbf{E}\cdot\mathbf{B}) - \frac{\partial V}{\partial\phi} = g_{\phi\gamma\gamma}(\mathbf{E}\cdot\mathbf{B}) - (m_\phi^2)_{\rm out}\phi + O(\phi^2)\,, \tag{5.114c}$$

where the last line is the axion equation of motion. The interplay between the axion and the EM field of pulsars has been actively investigated before, see e.g. [227–230] for recent works on the subject, although the effects we consider here, associated with a large classical axion field configuration also sourced by the NS, are novel. Assuming the conventional rotating dipole model, one finds that at the surface of the NS

$$B_{\rm dipole}(R) \sim B_* \sim 10^{14}\,{\rm G} \sim\ {\rm MeV}^2\,, \tag{5.115}$$

$$E_{\rm dipole}(R) \sim R\Omega B_* \sim 10^{-3}\left(\frac{R}{10\,{\rm km}}\right)\left(\frac{\Omega}{100\,{\rm Hz}}\right)B_*\,, \tag{5.116}$$

with Ω the angular velocity of the NS. Even with such large EM fields, we may still neglect the effects of the axion-photon coupling on the axion dynamics, since

$$\frac{g_{\phi\gamma\gamma}(\mathbf{E}\cdot\mathbf{B})}{(m_\phi^2)_{\rm out}\langle\phi(r)\rangle} \sim \frac{\alpha_{\rm EM}R\Omega B_*^2}{m_\pi^2 f_\pi^2} \sim 10^{-13}\left(\frac{R}{10\,{\rm km}}\right)\left(\frac{\Omega}{100\,{\rm Hz}}\right)\left(\frac{B_*}{10^{14}\,{\rm G}}\right)^2\,, \tag{5.117}$$

where we used $(m_\phi^2)_{\rm out} \sim m_\pi^2(f_\pi/f_\phi)^2$, $\langle\phi(r)\rangle \sim f_\phi$ and $g_{\phi\gamma\gamma} \sim \alpha_{\rm EM}/f_\phi$. While we can safely assume that the back-reaction of the EM fields on the axion is negligible, it is also important to note that the value of $\langle\phi(r)\rangle$ decreases exponentially outside the NS, see Eq. (5.111), such that one could well imagine a situation where the effect of the $g_{\phi\gamma\gamma}(\mathbf{E}\cdot\mathbf{B})$ term is in fact comparable to the axion mass term. In this case the back-reaction of the EM fields would have to be taken into account, which is an interesting effect to study in the future.

We thus treat the axion field as a rigid source of additional EM fields, which can be simply estimated as

$$\Delta E \sim g_{\phi\gamma\gamma} B_* \langle \phi(r) \rangle \sim \alpha_{\rm EM} B_* \,, \tag{5.118}$$

$$\Delta B \sim g_{\phi\gamma\gamma} R\Omega B_* \langle \phi(r) \rangle \sim \alpha_{\rm EM} R\Omega B_* \,. \tag{5.119}$$

While the magnetic field receives a small correction $\Delta B/B \sim \alpha_{\rm EM} R\Omega \ll 1$, for the electric field

$$\frac{\Delta E}{E} \sim \frac{\alpha_{\rm EM}}{R\Omega} \sim 2 \left(\frac{10\,\text{km}}{R}\right) \left(\frac{100\,\text{Hz}}{\Omega}\right) , \tag{5.120}$$

thus leading to an $O(1)$ enhancement around the surface of the NS. We note that since this correction is large, one could be concerned about whether the system can be treated perturbatively. This is in fact the case, since the higher order terms scale like

$$E \sim R\Omega B_* (1 + \alpha_{\rm EM}^2 + \dots) + \alpha_{\rm EM} B_* (1 + \alpha_{\rm EM}^2 + \dots) \,. \tag{5.121}$$

This means that, apart from the leading $O(\alpha_{\rm EM} B_*)$ correction, further contributions are subleading.

An additional sensitive observable is the dipole radiation output P that is responsible for the spin-down of rotating NSs. In this case we find that $\Delta P/P \sim \alpha_{\rm EM}^2 \ll 1$, namely there is no appreciable addition to the radiated energy due to the axion field.

5.4.3 Long-range force

Lastly, we can consider the case

$$(m_\phi)_{\rm out}^{-1} \gg R \,, \tag{5.122}$$

even though we note that from our previous analysis of the QCD axion at finite density, we expect this regime not to be realized since $(m_\phi)_{\rm out}^{-1} \lesssim (m_\phi)_{\rm in}^{-1} \lesssim R$, where the last condition follows from the requirement of the axion being actually sourced, Eq. (5.110). Therefore we expect the hierarchy $(m_\phi)_{\rm in}^{-1} \lesssim R \ll (m_\phi)_{\rm out}^{-1}$ to arise only in non-standard scenarios, such as the one considered in [186]. If that is indeed the case, the long tails of the axion field configuration lead to a long range force between the NSs, generated by the Yukawa-like potential

$$V \sim \frac{Q_{\rm eff}}{r} e^{-(m_\phi)_{\rm out} r} \,, \tag{5.123}$$

where $Q_{\rm eff} = 4\pi f_\phi R$ plays the role of the effective charge. This could lead to a deformation of the merger wave-form predicted by general relativity in case of NS with opposite-sign charges. A more dramatic effect would be found in the case of a repulsive force from same-sign charges, since in this case at some critical distance the axion force would dominate gravity, which could lead to halt in the merger process [186]. The presence of the axion field can also lead to an additional mechanism of energy loss in NS mergers, in the form of the scalar equivalent of Larmor radiation [231].

Chapter 6

How Light Scalars change the Stellar Landscape

In this Chapter we study how light scalars with a non-dertivative (and hence shift symmetry breaking) coupling to matter change the stellar landscape by triggering a new phase of matter. Such a phase arises due to a sourcing of the scalar triggered by the matter background, similar to the case of the QCD axion [11] as we have discussed in Chap. 5. Here we will study the striking and possible observable effects of such a phase on stellar remnants, namely white dwarf stars and neutron stars. The shift symmetry breaking coupling leads to a reduced mass of the matter field once the light scalar is sourced and provides additional energy density (and resulting gravitational pressure), as mentioned in Sec. 5.4. Under generic conditions, a new ground state of matter emerges, with striking implications for the configuration of stellar remnants. We also find hybrid stellar compositions and stable self-bound objects with sizes as small as the Compton wavelength of the scalar.

Exceptionally light QCD axions naturally come with a non-derivative coupling to nucleons and hence get sourced within white dwarfs. We find that once the axion is sourced the white dwarf's stellar structure is dramatically altered, as we discuss in Sec. 6.1. In particular, the comparison of the resulting mass-radius relationship with data of equation of state independent mass radius measurements allows us to probe large chunks of unexplored axion parameter space. Notably this does not depend on the axion constituting a significant fraction of the dark matter.

In Sec. 6.2 we discuss several realizations of light scalar fields with non-derivative couplings to nucleons: the QCD axion, lighter generalizations thereof and linearly or quadratically coupled scalar fields which we show to be effectively equivalent to a class of scalar-tensor modification of gravity. We find that neutron stars generically can either be in the new ground state phase or a coexistence phase leading to a hybrid star configuration. Notably, neutron stars in the new ground state can be significantly heavier than QCD equations of state currently predict. In the limit where gravity is negligible, we also find stable self-bound objects with sizes as small as the Compton wavelength of the scalar.

All figures and large parts of the text of this chapter are taken from [14] an [15].

6.1 White Dwarfs as a Probe of Light QCD Axions

As we have seen in Chap. 3 the EOS of WD is well understood within the SM which turns WDs into an excellent probe of BSM physics. In this section we exploit this fact in order to study the validity of lighter than expected QCD axion models, see Sec. 2.5. The existence of such a light QCD axion would imply a dramatically different EOS for WD, no longer compatible with data

from mass and radius measurements of WDs. This allows us to probe large parts of unexplored parameter space.

6.1.1 The axion WD system: a new ground state

In the presence of the axion, the full system is described by a free Fermi gas of electrons, an ideal gas of nuclei with a ϕ-dependent mass [1], $m^*_\psi(\phi) = 2m^*_N(\phi)$, the gravitational field $g_{\mu\nu}$, and the axion ϕ. The gravitational field is sourced by an energy-momentum tensor

$$T_{\mu\nu} = T^{\psi\phi}_{\mu\nu} + T^{\rm grad}_{\mu\nu}. \tag{6.1}$$

The first term takes the form of an ideal fluid, $T^{\psi\phi}_{\mu\nu} = \text{Diag}\left(\varepsilon, -p, -p, -p\right)$, with

$$p(\phi,\rho) = \frac{2}{3}\int_0^{k_F(\rho)} \frac{\mathrm{d}^3k}{(2\pi)^3}\frac{k^2}{\sqrt{k^2+m_e^2}} - V(\phi), \tag{6.2}$$

$$\varepsilon(\phi,\rho) = m^*_\psi(\phi)\rho + \varepsilon_e(\rho) + V(\phi), \tag{6.3}$$

where we neglected the sub-leading contributions to the pressure $p_\psi(\phi,\rho) \ll p_e(\rho)$. The second term in Eq. (6.1) contains the contribution of the axion gradient

$$(T^{\rm grad})^\mu{}_\nu = \frac{(\phi')^2}{2}\left[1-\frac{2GM}{r}\right](\delta^\mu_\nu - 2\delta^\mu_r\delta^r_\nu). \tag{6.4}$$

Using Einstein's equations and the scalar equations of motion, we find the following set of coupled differential equations (see App. C.1 for an explicit derivation)

$$\phi''\left[1-\frac{2GM}{r}\right] + \frac{2}{r}\phi'\left[1-\frac{GM}{r}-2\pi Gr^2(\varepsilon-p)\right] = \frac{\partial V}{\partial\phi} + \rho\frac{\partial m^*_\psi(\phi)}{\partial\phi} \equiv U(\phi,\rho), \tag{6.5a}$$

$$p' = -\frac{GM\varepsilon}{r^2}\left[1+\frac{p}{\varepsilon}\right]\left[1-\frac{2GM}{r}\right]^{-1}\left[1+\frac{4\pi r^3}{M}\left(p+\frac{(\phi')^2}{2}\left\{1-\frac{2GM}{r}\right\}\right)\right] - \phi' U(\phi,\rho), \tag{6.5b}$$

$$M' = 4\pi r^2\left[\varepsilon + \frac{1}{2}\left(1-\frac{2GM}{r}\right)(\phi')^2\right]. \tag{6.5c}$$

Eq. (6.5a) is the static axion equation of motion coupled to gravity, while Eqs. (6.5b) and (6.5c) are the TOV equations in the presence of an axion. Note that, we recover the ordinary TOV equations, Eq. (3.1), in the limit $\phi = 0$. While it is possible to numerically solve Eq. (6.5) using the shooting method, there exists a limit in which these equations simplify dramatically.

The displacement of the axion at sufficiently high densities costs gradient energy and therefore it only occurs if balanced by the gain in potential energy. This leads to the typical scale on which the axion is displaced

$$\lambda_\phi(\rho) \simeq \frac{\pi f_\phi}{\sqrt{2(\delta m_N\rho - \epsilon m_\pi^2 f_\pi^2)}}, \tag{6.6}$$

to be evaluated at typical WD densities.

For $R_{\rm WD} \gg \lambda_\phi$, the field essentially tracks the minimum of the effective in-density potential on stellar scales and is given by the solution to

$$U(\phi,\rho) = 0. \tag{6.7}$$

[1] The interesting case of a scalar coupled non-derivatively to electrons inducing a ϕ dependent mass $m^*_e(\phi)$ is left for a separate publication [17]

At the same time, the gradient terms in Eqs. (6.5b) and (6.5c) are confined to a small transition shell, where the field does not follow its minimum. However, this localized contribution is negligible as long as $\frac{\lambda_\phi}{R_{\rm WD}}\frac{\delta m_N}{m_N} \ll 1$, which is trivially fulfilled in this case.

Therefore, for large systems we can neglect the axion gradient $\phi' \simeq 0$. As a result, Eq. (6.5) decouples to give the regular TOV equations, Eq. (3.1), in addition to Eq. (6.7). Note that the latter is the same condition as the minimization of the energy density $\varepsilon(\phi, \rho)$ with respect to ϕ. Solutions $\phi(\rho)$ describe a thermodynamically stable EOS used to solve the regular TOV equations.

Interestingly, if the axion is destabilized in a WD, the energy per particle of the light nuclei $\varepsilon(\rho)/\rho$ is not minimized when the nuclei are infinitely separated ($\rho \to 0$), but rather at some finite density ρ^*, which can be found numerically. This implies the existence of an energetically favored state of matter at ρ^*, where the axion is at $\langle\phi\rangle = \pm\pi f_\phi$. This new ground state is in fact reminiscent to strange quark matter [232]. Note that the density of the new ground state is slightly larger than the density at which the destabilization occurs, $\rho^* > \rho_c \equiv \epsilon\, m_\pi^2 f_\pi^2 / 2\sigma_N$.

For low densities $\rho < \rho_c$, matter is in a meta-stable state where the classical sourcing of the axion is not preferable. Once $\langle\phi\rangle = \pm\pi f_\phi$, there is a range $\rho_c < \rho < \rho^*$, where the energy per particle decreases $\partial_\rho(\varepsilon(\rho)/\rho) < 0$, implying a negative pressure. At densities slightly above ρ_c, the total pressure turns negative due to the onset of the the axion potential $p = p_e - V < 0$. As ρ increases, V stays constant while p_e increases, until finally the system stabilizes at $p = p_e(\rho^*) - V = 0$, see Fig. 6.1. In this unstable phase the system contracts until it stabilizes in the new ground state.

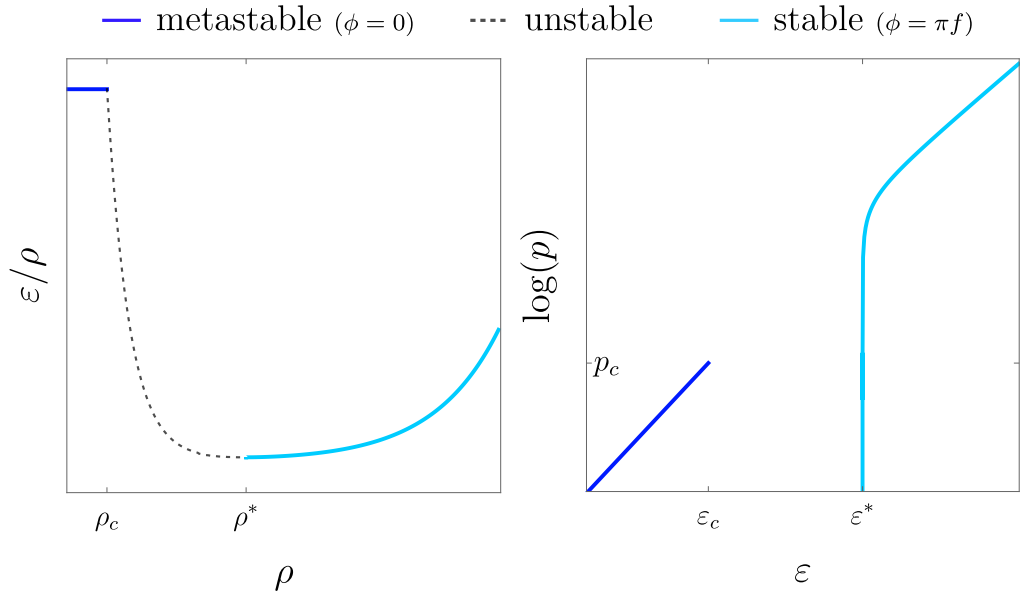

Figure 6.1: The energy per particle ε/ρ as a function of number density (left) and the EOS (right). At low densities $\rho < \rho_c$, the system is in its meta-stable $\phi = 0$ phase (dark blue). For $\rho_c < \rho < \rho^*$, the system is unstable i.e. $p < 0$ (dashed line in left panel). At larger densities $\rho^* < \rho$, the system is in its $\phi = \pm\pi f_\phi$ phase (light blue), with a new ground state at ε^* where $p = 0$.

This instability leads to a *gap* in the predicted M - R relationship as seen in Fig. 6.2. The position of this gap is ϵ dependent; the smaller ϵ is, the more the gap is shifted towards small masses and large radii. We use the position of this gap to probe the existence of light QCD axions.

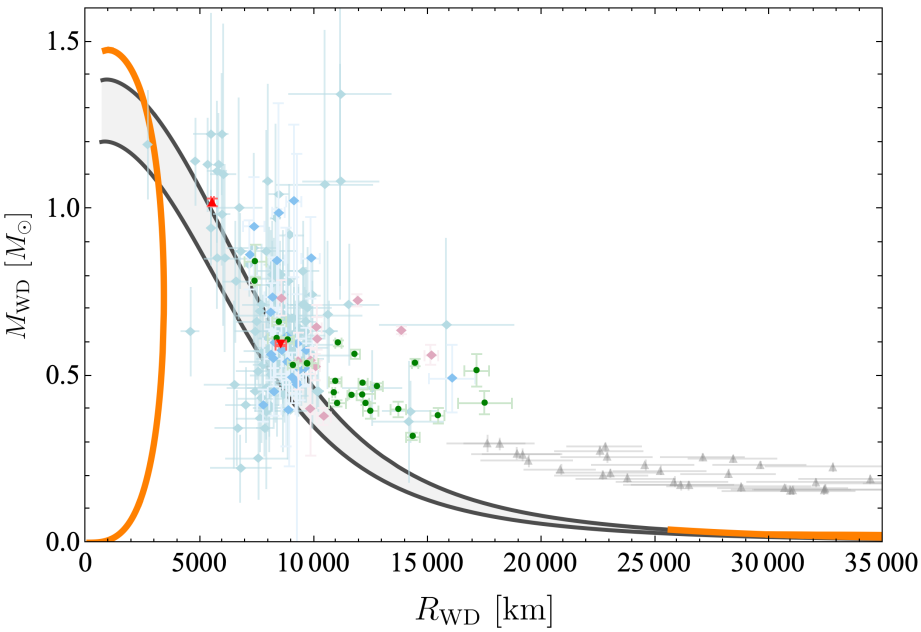

Figure 6.2: White dwarf M - R relation with light QCD axions. Free Fermi gas of nuclei and electrons without an axion (black). The upper and lower bands correspond to the constitutions of light and more heavy nuclei, i.e. ^{4}He which corresponds to $Y_e = 2$ and ^{56}Fe corresponding to $Y_e = 2.15$ respectively, while the gray shaded area corresponds to intermediate values. In orange we show the two branches with an axion for $\epsilon = 10^{-11}$ in the limit $R_{\rm WD} \gg \lambda_\phi$ for $Y_e = 2$. The meta-stable branch follows the free Fermi gas line at large radii, while the new ground state phase has much smaller radii. Data points are taken from [107] (turquoise), [108] (blue), [109] (pink), [110, 111] (red), [112] (green) and [113] (gray). One can clearly see the gap in the predicted M - R relation that is incompatible with data.

Note that the simplified discussion above is only valid for $R_{\rm WD} \gg \lambda_\phi$. For $R_{\rm WD} \sim \lambda_\phi$ we numerically solve the full coupled system in Eq. (6.5) and find that for large values of the axion decay constant, f_ϕ, and small ϵ, the position of the gap is ϵ independent. This is understood as follows: on the stable branch, the gradient pressure, which is controlled by f_ϕ, is relevant. If gravity is subdominant, this pressure fixes the central density of the star, $\rho(r = 0) > \rho^*$. The maximal radius is then achieved when the gravitational pressure equals the gradient pressure. For the meta-stable branch, the minimum radius is set by $R \sim \lim_{\epsilon \to 0} \lambda_\phi$.

Finally, in the limit $R_{\rm WD} \ll \lambda_\phi$, the gradient energy is so large that the field cannot move away from its in-vacuum minimum and therefore has no influence on the structure of WDs.

6.1.2 Confrontation with Observational Data

There are large data sets available containing masses and radii of WDs (see e.g. [107–113, 118–124]). However, not all of these data-sets can be used to probe the M - R relation. In some catalogs, (see [118–122]), the M - R relation is used as an input to significantly reduce observational error. On the other hand, there are sets (e.g. [107–113, 123, 124]) that systematically test the M - R relation using observational data. While in [112] the determination of the mass and radius is completely independent of WD models, most other works depend on an atmospheric model to determine the radius. Nevertheless, we combine the data sets [107–113] and show them in Fig. 6.2.

The data of measured WD masses and radii is scattered broadly between radii of (5000 − 40000 km), which matches reasonably well with the free Fermi gas description. The notable deviation in mass found at large radii in Fig. 6.2 is due to finite temperature effects; μ_e in these dilute stars is typically smaller, increasing the relevance of T/μ_e corrections. Finite temperature effects lead to modifications of the EOS and to a slight modification of masses and radii, but still predict a continuous M - R curve. The same holds for other well-known corrections to the EOS, such as different compositions, electrostatic corrections, or nuclear reactions, see e.g. Refs. [104, 233]. While nuclear reactions change in the sourced phase e.g. due to a different mass of the pions, this has negligible effect on the static structure of white dwarfs [234] [2].

We perform a simplified statistical analysis to determine the compatibility of the observed WD radii with a gapped radius distribution hypothesis (marginalizing over mass and neglecting small theory systematics). We summarize here its main results, with the full details given in Sec. 6.1.3 and Sec. 6.1.4. For the purpose of the analysis, we calculate the position of the radius gap as a function of ϵ and f_ϕ, relying both on numerical results, as well as on numerically-verified analytical estimates. In the region $f_\phi \ll 10^9\,\mathrm{GeV}$, finite gradient effects are negligible w.r.t the position of the gap, making it f_ϕ-independent. We are able to exclude at the 2σ level the following interval in ϵ,

$$2 \times 10^{-20} \lesssim \epsilon \lesssim 2 \times 10^{-7} \quad (95\%\ \mathrm{C.L})\,, \tag{6.8}$$

see Fig. (6.3).

The upper limit is set by the smallest, most massive WDs and our analysis effectively excludes all points in the axion parameter space that cannot predict a WD with a radius smaller than around $\sim 4000\,\mathrm{km}$ on the meta-stable branch. The lower limit is sensitive to the largest, extremely low-mass WDs [113]. For even lower values of ϵ, the stable branch covers most of the range of observed radii. In this case, although all the observed WDs are sourcing the scalar field, the gap in radius is relegated to extremely large (and potentially unpopulated) WD radii. Note however that this region in parameter space is already ruled out by requiring that no sourcing occurs in our sun [186]. Conversely, in the region $\epsilon \ll 10^{-20}$, finite gradient effects are dominant w.r.t the position of the gap, making it ϵ-independent. Using solutions of the coupled system, Eq. 6.5, we are able to exclude at the 2σ level the following interval in f_ϕ,

$$5.5 \times 10^9 < f/\mathrm{GeV} < 1.1 \times 10^{16} \quad (95\%\ \mathrm{C.L})\,, \tag{6.9}$$

see Fig. (6.3). The upper value represents the limit in which WDs are not large enough to source the scalar field, i.e. $\lambda_\phi \gtrsim R_{\mathrm{WD}}$. In the region $f_\phi \epsilon^{-1/3} \sim M_{\mathrm{P}}$, in which both gradient and finite ϵ effects are important, we verify numerically that the sourcing stops at lower values of f_ϕ. Similarly to the lower bound on ϵ, the lower bound on f_ϕ is sensitive to the largest, extremely low-mass WDs. We stress again that we do not expect our results to strongly depend on finite temperature effects.

6.1.3 Analytic Estimates for Radius Gap

We define p_0 as the inward pointing pressure at the core of a white dwarf (WD) as a sum of a gravitational and a gradient contributions

$$p_0 \simeq \Delta p_{\mathrm{grav}} + \Delta p_{\mathrm{grad}}\,, \tag{6.10}$$

[2] In this work we take a conservative approach and stay agnostic of the process of formation of the new ground state phase, where the change of nuclear reactions could play a role.

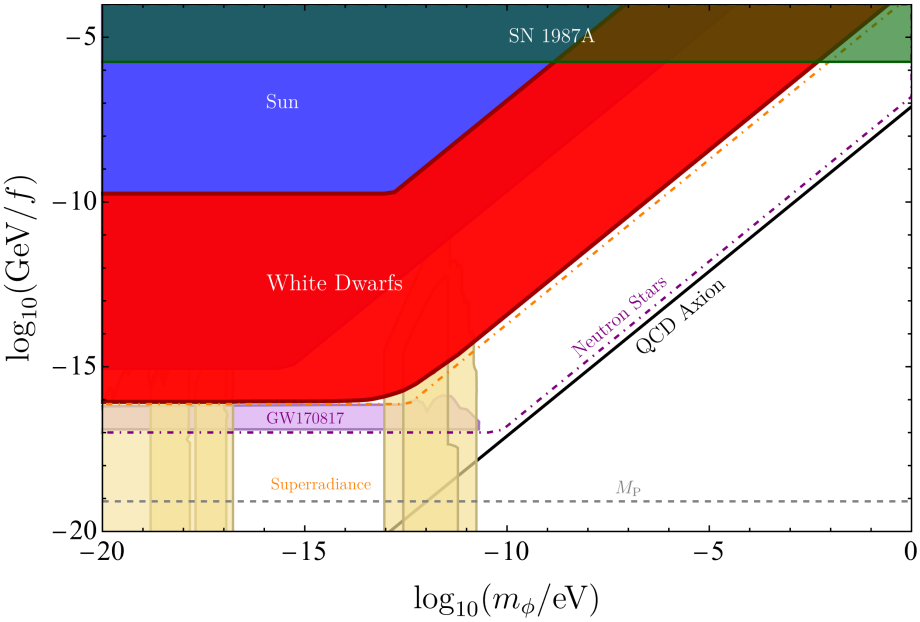

Figure 6.3: Constraints and future projections on the axion parameter space. Exclusions from modifications of the white dwarf M - R relation are shown in red. Note that the WD bound overlaps with bounds from the Sun in large parts of the region (slightly darker red). The observation of WDs close to the Chandrasekhar limit can further probe the parameter space until the orange dashed line. The solid black line shows the QCD axion with $m_\phi f_\phi = m_\pi f_\pi$. For reference, we plot $f_\phi = M_{\rm P}$ in gray. Further bounds originate from the sourcing in the Sun [186] (blue) and the gravitational wave signal of the NS binary GW170817 [235] (violet), which we both adapted at large f_ϕ according to numerically inspired $\mathcal{O}(1)$ factors, the supernova 1987A [89] (green), and black hole superradiance [236] (yellow). We would furthermore like to note that the pulsar bound of [186] goes away once all finite gradient effects are properly taken into account (besides lying within a region that is strongly dependent on the neutron star EOS) [15]. Finally, we show which parameters lead to a new ground state accessible in neutron stars (dot-dashed purple); for more details see [15].

with the gravitational pressure is given by

$$\Delta p_{\rm grav} = \frac{R^2 m_N^2 \rho_0^2}{M_{\rm P}^2}\,, \tag{6.11}$$

where ρ_0 is the number density at the core ($r = 0$). The gradient pressure in the sourced phase (i.e. stars on the stable branch) is given by

$$\Delta p_{\rm grad} = \begin{cases} \frac{f_\phi^2}{R\lambda_\phi} = \frac{f_\phi\sqrt{\delta m_N \rho_R}}{R} & \lambda_\phi \ll R \\ \frac{f_\phi^2}{R^2} & \lambda_\phi \sim R \end{cases}\,, \tag{6.12}$$

where ρ_R is the number density at the edge ($r = R - \lambda_\phi \approx R$) of the WD. The first line in Eq. (6.12) represents the thin wall limit $\lambda_\phi \ll R$, in which the gradient pressure is exerted at a small transition region at the edge of the star. In the last step we use the definition of the in-medium wavelength of Eq. (6.6) assuming a negligible contribution from the scalar potential and neglecting $\mathcal{O}(1)$ factors. The second line in Eq. (6.12) is the opposite regime $\lambda_\phi \sim R$, where the gradient pressure is delocalized and is spread throughout the star. This is the typical edge

case configuration in which the star is barely large enough to source the axion. In the unsourced phase, i.e. stars on the meta-stable branch, $\Delta p_{\rm grad} = 0$. See Ref. [15] for more details on the derivation of Eqs. (6.11) and (6.12).

On the other hand, we define the outwards pressure at the core balancing p_0, see Eq. 6.10, as the contribution of the electron gas and the scalar potential, which can be written analytically in the non-relativistic (NR) and ultra-relativistic (UR) limits as

$$p_0 \simeq -V(\phi) + p_e(\rho_0)\,, \quad p_e(\rho_0) \simeq \begin{cases} \rho_0^{5/3}/m_e & (\text{NR } \rho_0 \ll m_e^3) \\ \rho_0^{4/3} & (\text{UR } \rho_0 \gg m_e^3) \end{cases}\,, \tag{6.13}$$

where in the sourced phase we have by definition $V(\phi) = p_e(\rho_{\rm NGS})$, while in the unsourced phase the scalar potential vanishes $V(\phi) = 0$. Note that in Eqs. (6.11), (6.12) and (6.13), we work at leading order in $\delta m_N/m_N \ll 1$ and neglect $\mathcal{O}(1)$ numerical prefactors.

Negligible gradient regime

Let us start by estimating the minimal radius on the meta-stable branch, which we denote by $R_{\rm min}^{\rm meta}$, and the maximal radius on the stable branch, which we denote by $R_{\rm max}^{\rm stable}$, in the negligible gradient regime, where $\Delta p_{\rm grav} \gg \Delta p_{\rm grad}$. In this limit, $R_{\rm max}^{\rm stable}$ is the radius of the largest approximately constant energy density configurations. Therefore, we estimate it by setting $\rho_0 \approx c\,\rho_{\rm NGS} \approx c\,\epsilon^{3/5}(m_e m_\pi^2 f_\pi^2)^{3/5}$, where $c \sim \mathcal{O}(1)$, and solving for R. The contribution to the pressure from $V(\phi) = p_e(\rho_{\rm NGS})$ is neglected since it is at most of the same order as $p_e(\rho_0)$, and would therefore have at most an $\mathcal{O}(1)$ effect on the final result. We find

$$R_{\rm max}^{\rm stable}(\epsilon) = \frac{M_{\rm P}}{m_N \Lambda_{\rm QCD}} \begin{cases} (\Lambda_{\rm QCD}/m_e)^{3/5}\epsilon^{-1/10} & (\text{NR}) \\ \epsilon^{-1/4} & (\text{UR}) \end{cases}\,, \tag{6.14}$$

where for brevity we denoted $m_\pi^2 f_\pi^2 \equiv \Lambda_{\rm QCD}^4$. We omit the weak dependence on c, which amounts to an $\mathcal{O}(1)$ pre-factor. In the left panel of Fig. (6.4) we compare the analytic estimates to the numeric results. We find that the NR estimation is in excellent agreement with the numerical results for $\epsilon \lesssim 10^{-13}$ (red curve). For larger values of ϵ, the smaller minimal radii on the stable branch correspond to denser configurations, where relativistic corrections become important. Thus, for $\epsilon \gtrsim 10^{-11}$ the UR estimation agrees with the numerical results (red dashed curve).

The edge of the meta-stable branch $R_{\rm min}^{\rm meta}$ is found by taking $\rho_0 \approx \rho_c \approx \epsilon\Lambda_{\rm QCD}^4/(2\sigma_N)$ and solving for R in the NR approximation, resulting in

$$R_{\rm min}^{\rm meta}(\epsilon) = \frac{M_{\rm P}}{m_N \Lambda_{\rm QCD}} \left(\frac{\sigma_N \Lambda_{\rm QCD}^2}{m_e^3}\right)^{1/6} \epsilon^{-1/6} \quad (\text{NR})\,. \tag{6.15}$$

A similar UR approximation is straightforward to derive. However, it is only valid for $R \ll M_{\rm P}/(m_N m_e) \sim 5000\,\text{km}$, which is outside our range of interest. In the left panel of Fig. (6.4), we compare the analytic numerical results of $R_{\rm min}^{\rm meta}(\epsilon)$ to the analytic estimate. We find good agreement in most of the calculated region, namely for $\epsilon \lesssim 10^{-9}$. For larger values, relativistic corrections start becoming important and the UR approximation begins to degrade.

The radius gap in negligible gradient regime is plotted in the right panel of Fig. (6.4) as a function of ϵ. For the purpose of the analysis of Sec. (6.1.4), solid curves indicate the regions where we use our numerical results, while dashed lines indicates regions where extrapolation, based on the verified numerical estimate, is used. The gray region corresponds to the observed radii range of WDs.

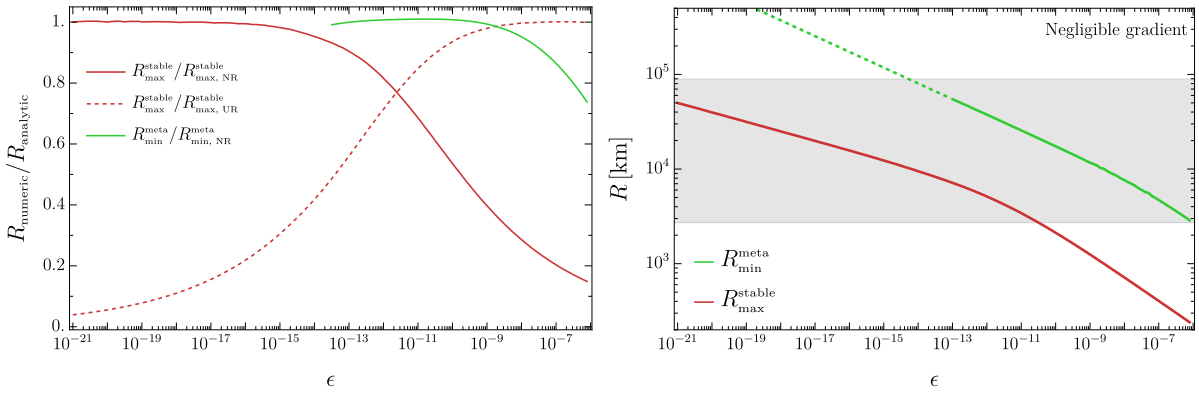

Figure 6.4: Left panel: the ratio between the numerical results and the analytical estimates for the radii which correspond to the edges of the radius gap, as a function of ϵ. In (dashed) red we plot the ratio for $R^{\rm stable}_{\rm max}$ divided by the NR (UR) estimate given in Eq. (6.14). In green we plot the ratio for $R^{\rm meta}_{\rm min}$, divided by the NR estimate give in Eq. (6.15). In all cases we match the $\mathcal{O}(1)$ prefactors to the numerical results. Right panel: the radius gap defined by $R^{\rm stable}_{\rm max}$ (red) and $R^{\rm meta}_{\rm min}$ (green) as a function of ϵ. Solid curves indicate region where numerical results are used while the dashed curve indicates where extrapolation (using the verified analytic estimates) is used. The gray region corresponds to the observed radii range of WDs.

Negligible ϵ regime

In region of parameter space where ϵ is negligibly small (to be determined below), the position of the radius gap is determined by finite gradient effects. On one side, the edge of the meta-stable branch indicates when a region of size λ_ϕ with above-critical density is formed, which leads to an instability. On the other side, the largest configurations on the stable branch are those in which the gravitational pressure begins to dominate over the gradient pressure exerted at the edge of the star [15].

First we find $R^{\rm stable}_{\rm max}$ for lower values of f_ϕ where the thin-wall approximation holds. by taking $\rho_0 = \rho_R \equiv \rho_{\rm eq} > \rho_{\rm NGS}$, where $\rho_{\rm eq}$ is found by solving $\Delta p_{\rm grav}(\rho_{\rm eq}) = \Delta p_{\rm grav}(\rho_{\rm eq})$ for $\rho_{\rm eq}$. We then plug $\rho_{\rm eq}$ into Eq. (6.10), and using the NR approximation of Eq. (6.13) solve for R and find

$$R^{\rm stable}_{\rm max}(f_\phi) = \left(\frac{M_{\rm P}}{m_N}\right)^{7/6} \left(\frac{1}{\delta m_N^{1/12} f_\phi^{1/6} m_e^{3/4}}\right) \quad (\lambda_\phi \ll R)\,, \tag{6.16}$$

where we again neglect the contribution from $V(\phi)$ as an $\mathcal{O}(1)$ correction at most. We compare this estimate with the numerical results in Fig. (6.5) (red curve). We find is is consistent with the numerical results in the region $f_\phi \ll 10^{15}\,{\rm GeV}$. Above these values of f_ϕ, the thin-wall approximation breaks down and $R^{\rm stable}_{\rm max}(f_\phi)$ can be estimated using the $\lambda_\phi \sim R$ expression for $\Delta p_{\rm grad}$ and the UR expression for the electron pressure, which gives us

$$R^{\rm stable}_{\rm max}(f_\phi) = \frac{M_{\rm P}^2}{m_N^2 f_\phi} \quad (\lambda_\phi \lesssim R)\,. \tag{6.17}$$

We find this estimate consistent with the numerical results in the region $f_\phi \gg 10^{15}\,{\rm GeV}$, see dashed curve in Fig. (6.5). The edge of the meta-stable branch $R^{\rm meta}_{\rm min}$ is found by first finding the critical density for which the while size of the star is of the order of the scalar in-medium wavelength, namely by solving $\lambda_\phi(\rho) = f_\phi/\sqrt{\rho\delta m_N} = R$ for ρ and plugging the result in Eq. (6.10)

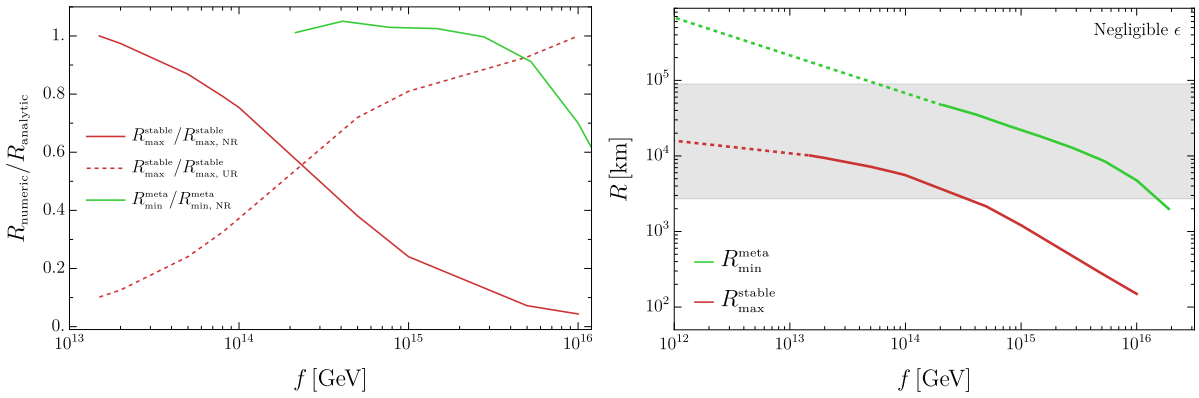

Figure 6.5: Left panel: the ratio between the numerical results and the analytical estimates for the radii which correspond to the edges of the radius gap, as a function of f_ϕ. In red and dashed-red we plot the ratio for $R^{\rm stable}_{\rm max}$ divided by the NR and UR estimates given in Eq. (6.16) and Eq. (6.17), respectively. In green we plot the ratio for $R^{\rm meta}_{\rm min}$, divided by the NR estimate give in Eq. (6.18). In all cases we match the $\mathcal{O}(1)$ prefactors to the numerical results. Right panel: the radius gap defined by $R^{\rm stable}_{\rm max}$ (red) and $R^{\rm meta}_{\rm min}$ (green) as a function of f_ϕ. Solid curves indicate region where numerical results are used while the dashed curve indicates where extrapolations (using the verified analytic estimates) are used. The gray region corresponds to the observed radii range of WDs.

using the NR approximation for the electron gas. We find

$$R^{\rm meta}_{\rm min}(f) = \left(\frac{\delta m_N^{1/2} M_{\rm P}^3}{f_\phi m_e^{3/2} m_N^3}\right)^{1/2} . \tag{6.18}$$

We find this estimate consistent with the numerical results, see green curve in Fig. (6.5). The deviations from the analytical estimate at large value of f_ϕ is expected, since for smaller and denser stars relativistic corrections to the EOS become increasingly larger.

To conclude we note that for the whole $\{\epsilon, f_\phi\}$ plane, we define the maximal radius of the gap as

$$R^{\rm meta}_{\rm min}(\epsilon, f_\phi) = {\rm Min}\left[R^{\rm meta}_{\rm min}(\epsilon), R^{\rm meta}_{\rm min}(f_\phi)\right] , \tag{6.19}$$

where the two radii coincide $R^{\rm meta}_{\rm min}(\epsilon) \sim R^{\rm meta}_{\rm min}(f_\phi)$ around the curve defined by

$$f\epsilon^{-1/3} \approx \frac{\sqrt{\delta m_N}}{\sqrt{m_e m_N}} \left(\frac{\Lambda^4_{\rm QCD}}{\sigma_N}\right)^{1/3} M_{\rm P} \sim M_{\rm P} , \tag{6.20}$$

using the NR estimations for both expressions. This defines (a posteriori) the ranges of validity for the negligible gradient and negligible ϵ approximations for the determination of $R^{\rm meta}_{\rm min}$, e.g. the negligible gradient is a valid approximation in the region of parameter space where $f\epsilon^{-1/3} \ll M_{\rm P}$. Around $f_\phi \epsilon^{-1/3} \sim M_{\rm P}$, we computed a numerical solution using the appropriate $\{\epsilon, f_\phi\}$ values in order to obtain $R^{\rm meta}_{\rm min}(\epsilon, f_\phi)$. In a similar fashion, we define for the whole $\{\epsilon, f_\phi\}$ plane the minimal radius of the gap as

$$R^{\rm stable}_{\rm max}(\epsilon, f_\phi) = {\rm Max}\left[R^{\rm stable}_{\rm max}(\epsilon), R^{\rm stable}_{\rm max}(f_\phi)\right] , \tag{6.21}$$

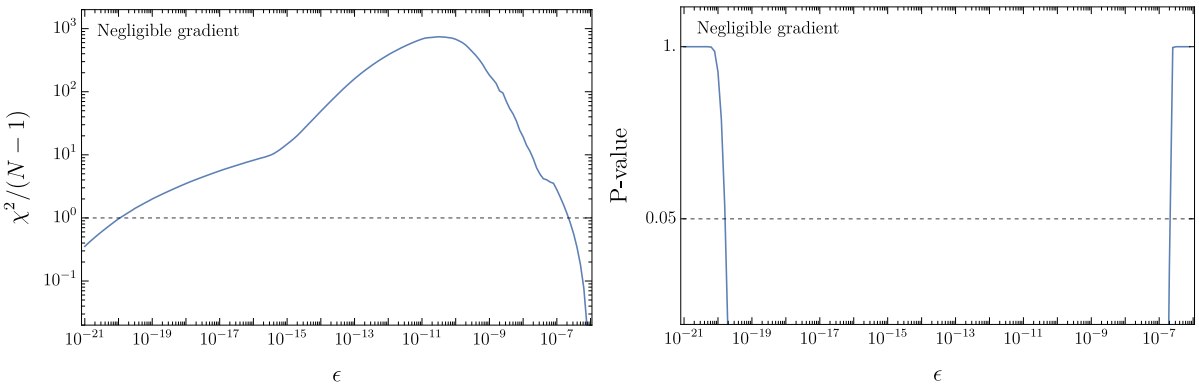

Figure 6.6: Left panel: $\chi(\epsilon)$, as defined Eq. (6.23) in the negligible gradient limit, normalized to the effective number of degrees of freedom $N-1=294$, as a function of ϵ. Right panel: The p-value as a function of ϵ. For reference, we plot the 2σ threshold, equivalent to $p=0.05$, as a gray dashed line.

where the two radii coincide $R^{\rm stable}_{\rm max}(\epsilon) \sim R^{\rm stable}_{\rm max}(f_\phi)$ around the curve defined by

$$f_\phi \epsilon^{-3/5} \approx \frac{\Lambda_{\rm QCD}^{12/5} M_{\rm P}}{\sqrt{\delta m_N} m_e^{9/10} m_N} \sim 20 M_{\rm P}\,, \tag{6.22}$$

using the NR estimations for both expressions. This defines (a posteriori) the ranges of validity for the negligible gradient and negligible ϵ approximations for the determination of $R^{\rm stable}_{\rm max}$.

6.1.4 Statistical analysis and bounds

The goal is to quantitatively determine how compatible are the observed WD radii with a gapped distribution. Our working assumption is that the variance in the observed mass can be explained by varying other important properties of WDs, such as temperature and composition, which for simplicity we kept fixed. Therefore our focus is strictly on the radius distribution, and in order to determine the bounds on ϵ and f_ϕ, we perform a 1D goodness-of-fit test on the radius axis. Given the central values from a combined dataset of $N=295$ observed WD radii $\{r_i\}$ and thier corresponding uncertainties $\{\sigma_i\}$ [107–113], we calculate the sum of squares, which we denote by χ, for each point in the $\{\epsilon, f_\phi\}$ plane

$$\chi(\epsilon, f_\phi) = \sum_{i=1}^{N} \frac{D^2[(r_i), R^{\rm stable}_{\rm max}(\epsilon, f_\phi), R^{\rm meta}_{\rm min}(\epsilon, f_\phi)]}{\sigma_i^2}\,, \tag{6.23}$$

with the distance function

$$D[(r_i), R^{\rm stable}_{\rm max}(\epsilon, f_\phi), R^{\rm meta}_{\rm min}(\epsilon, f_\phi)] = \begin{cases} \min\left[r_i - R^{\rm stable}_{\rm max}(\epsilon, f_\phi), R^{\rm meta}_{\rm min}(\epsilon, f_\phi) - r_i\right] & r_i \in [R^{\rm stable}_{\rm max}(\epsilon, f_\phi), R^{\rm meta}_{\rm min}(\epsilon, f_\phi)] \\ 0 & \text{otherwise} \end{cases}. \tag{6.24}$$

We use the numerically-calculated values for $\{R^{\rm stable}_{\rm max}(\epsilon, f_\phi), R^{\rm meta}_{\rm min}(\epsilon, f_\phi)\}$ where available, and otherwise use the verified analytical estimates as extrapolation, see right panel of Fig. (6.4) and Fig. (6.5). In Fig. (6.6) and Fig. (6.7) we plot the results of our statistical analysis in the negligible gradient and negligible ϵ limits, respectively. In the left panels we plot χ normalized

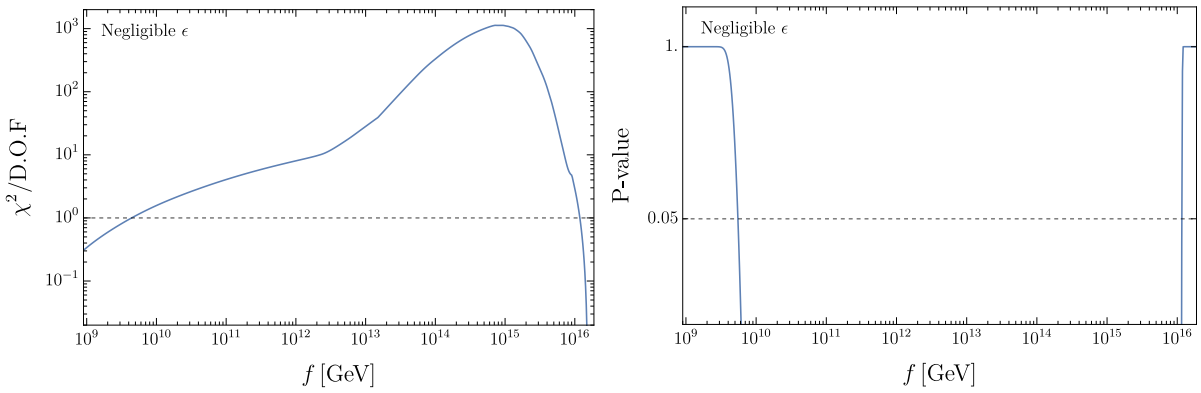

Figure 6.7: Left panel: $\chi(f)$, as defined Eq. (6.23) in the negligible ϵ limit, normalized to the effective number of degrees of freedom $N - 1 = 294$, as a function of f_ϕ. Right panel: The p-value as a function of f_ϕ. For reference, we plot the 2σ threshold, equivalent to $p = 0.05$, as a gray dashed line.

to the effective number of degrees of freedom $N - 1$. As a rough estimate, the range in which $\chi > 1$ is considered incompatible with the gapped radii distribution hypothesis. A more refined statement can be made by calculating the corresponding p-values for each value of ϵ of f_ϕ, shown in the right panel of Fig. (6.6) and Fig. (6.7), respectively. We are able to exclude at the 2σ level the following interval in ϵ

$$2 \times 10^{-20} < \epsilon < 2 \times 10^{-7} \quad (95\% \text{ C.L}) \,. \tag{6.25}$$

We are able to exclude at the 2σ level the following interval in f_ϕ,

$$5.5 \times 10^{9} < f_\phi/\text{GeV} < 1.1 \times 10^{16} \quad (95\% \text{ C.L}) \,. \tag{6.26}$$

6.1.5 Conclusions

The mass-radius relationship of white dwarfs is well-understood and has been observationally tested with increasing accuracy in recent years. We showed how light QCD axions change the structure of WDs, thus predicting the presence of a gap. We used existing data to place novel bounds on their parameter space. We stress that the bounds arising from the existence of a new ground state accessible in white dwarfs, and the corresponding gap in radii, are qualitatively very different than the strategy proposed in Ref. [186], which relies on the change of the properties of nuclei, and the corresponding change in X-ray emission, when a (lighter) QCD axion is displaced to $\theta = \pi$ [234].

The QCD axion generically predicts a non-derivative coupling to nucleons. At finite baryon density this coupling can destabilize the axion from its in-vacuum minimum. If sourced, the non-zero axion expectation value reduces the mass of nucleons. For a large region of the parameter space, this leads to a new ground state of matter, which has less energy per particle than infinitely separated nucleons. If accessible in WDs, this drastically changes their M - R relation. Since the axion is sourced by the WD, this does not rely on the axion contributing to the dark matter relic abundance.

More precise tests of the WD M - R curve using the recent Gaia DR3 are expected in the near future and will further probe the parameter space of light QCD axions.

As a consequence of the new ground state of matter, we predict new small self-bound objects held together by the gradient pressure of the axion. These objects could give rise to novel signatures of exceptionally light QCD axions down to the QCD axion line.

6.2 Heavy Neutron Stars from Light Scalars

As we have discussed in Sec. 3.2, the observation of NSs with masses beyond $2M_\odot$, with GW190814 [148] even hinting at NSs with masses of $2.6M_\odot$, really pushes SM EOSs to their limit. Furthermore, the trend for more complex EOSs within the SM tends towards softer EOS, which makes it even harder to explain such observations.

Interestingly, we find that once light scalar fields get sourced within neutron stars a new ground state of nuclear matter is unlocked which can significantly stiffen the EOS of NSs. Such a scalarization takes place for dense and large enough objects. This translates into an upper bound on the scale M_ϕ which, in analogy to $M_{\rm P}$, controls the strength of the scalar interaction with matter, along with an upper bound on its mass m_ϕ. These conditions in turn imply that the scalar is not significantly sourced, or not sourced at all, by dilute and small systems, nor arbitrarily long-ranged, such that conventional constraints from fifth-force searches and e.g. pulsar timing measurements can be bypassed, even for $M_\phi \ll M_{\rm P}$. Particularly in the context of modified theories of gravity, it has been recognized that scalarized NSs exhibit macroscopic properties, like mass, radius, moment of inertia, etc., different from those predicted in GR with a given equation of state (EOS), see e.g. [237] for a review. However, it has not been fully appreciated until now that, under generic conditions, large deviations in the configuration of compact stars are due to the appearance of a new ground state (NGS) of nuclear matter.

To make the physics as transparent as possible, we carry out our analysis in terms of the EOS of a free Fermi gas of nucleons. The existence of a scalar coupled (non-derivatively) to nucleons, which can be encoded as a scalar-dependent nucleon mass, $m_*(\phi)\bar{\psi}\psi$, brings up two competing effects when the conditions for scalarization are met. On the one hand, the effective mass of the nucleon inside the scalar bubble gets reduced [238], while on the other, the scalar potential $V(\phi)$ acts as additional vacuum energy contributing to the total energy density and pressure, see e.g. [225, 226]. The parameter space is then generically split into two parts: if the potential dominates, a phase transition occurs at some finite density, softening the EOS. Stable configurations are in the form of hybrid stars, with smaller maximal masses compared to the phase where the scalar field is not sourced. In the rest of the parameter space, the reduction of the nucleon mass dominates and a new ground state of matter, with energy per particle smaller than for well-separated neutrons, is found, as we have seen in the context of WDs in Sec. 6.1. Stable configurations are in the form of homogeneously scalarized stars, which can have much larger masses. NSs in this case can be heavier than the maximal mass predicted by standard causal bounds [101, 239–241], which assume a certain low-density behavior consistent with the properties of dilute matter, an invalid assumption when the NGS is present. Small or dilute systems like nuclei or regular stars are in this case meta-stable and long-lived. Other distinctive features of NSs in the NGS are their compactness, which can be larger than in typical NSs yet below that required for a photon sphere, and their minimal rotation period. In addition, since the NGS leads to a branch of NSs disconnected from the standard one predicted in GR, we find instability gaps in radii and self-bound objects as small as the Compton wavelength of the scalar, changing the landscape of stellar remnants.

The Chapter is organized as follows. In Sec. 6.2.1 we start by giving an overview of the different types of models under consideration, explaining the relevant scales and the connection to models of scalarization. In Sec. 6.2.2, we present our simple free Fermi gas description and

the equations governing the full coupled system of gravity plus the scalar. All of our results are described in this section in a model-independent fashion. In Sec. 6.2.2, we discuss the limit where the scalar field gradient can be neglected, in which case it is sensible to define an EOS. After presenting the two qualitatively different types of EOS, we discuss the effects of a finite gradient energy in Sec. 6.2.2. A more quantitative case study in presented in Sec. 6.2.3 for three types of scalar-matter couplings, namely axion-like (Sec. 6.2.3), linear (Sec. 6.2.3), and quadratic (Sec. 6.2.3), while in Sec. 6.2.4 we explicitly work out the equivalence with scalar-tensor theories of gravity. Our conclusions are presented in Sec. 6.2.5. A detailed discussion regarding the limit of negligible gradient energy, which is used extensively throughout this work, is presented in App. C.2. Some useful analytical approximations for constant density objects are given in App. C.3. Finally, in App. C.4 we present the details on a simple scalar model that realizes a large in-density reduction of the nucleon mass via a coupling to gluons.

6.2.1 Decoding scalarization

Before moving on to the bulk of our work, let us briefly discuss the main features of the different classes of scenarios in which a scalarized ground state of matter can be reached. Beyond the scale M_ϕ that sets the strength of the leading coupling to matter and the mass m_ϕ, the scalar theories under consideration can be characterized in general by two other scales, F_ϕ and f_ϕ, which control, respectively, the higher-order interactions of the scalar with matter and its self-interactions,

$$m_*(\phi)/m = 1 - \left(\frac{\phi}{M_\phi}\right)^n \left[1 + O\left(\frac{\phi}{F_\phi}\right)\right] , \quad V(\phi) = \frac{1}{2} m_\phi^2 \phi^2 \left[1 + O\left(\frac{\phi}{f_\phi}\right)\right] . \tag{6.27}$$

where $m_*(\phi)\bar{\psi}\psi$ is the scalar-dependent matter mass. We focus only on linearly ($n = 1$) or quadratically ($n = 2$) coupled scalars, as these two are the most generic cases without or with a parity symmetry $\phi \to -\phi$ in the interaction with matter, respectively. The simplest scenario is when higher-order terms in ϕ can be neglected, namely when $F_\phi, f_\phi \gg M_\phi$. In that case scalarization takes place with $\phi \sim M_\phi$ and $m_*(M_\phi)/m \ll 1$ is approached within the star, a limit in which the scalar field effectively reaches a constant in-medium value. This case, which we denote as *unbounded* m_*, is typical of scalar-tensor theories of the Damour-Esposito-Farèse type [242], where the scalar couples to the trace of the energy-momentum tensor, equal to $m\bar{\psi}\psi$ in the free Fermi gas limit. Factoring in higher ϕ terms, even when $f_\phi < M_\phi$, one can still find unbounded m_* systems where $\phi \sim M_\phi$ in medium, specially at high-enough densities where the scalar dynamics is mainly controlled by $m_*(\phi)$ (with $F_\phi \gg M_\phi$). In this class of scenarios, the main effect of a finite f_ϕ is to set the value of the scalar potential $V(M_\phi)$. Finally, there exists a *bounded* m_* class of theories, in which non-linearities are such that $\phi \sim F_\phi$ or $\phi \sim f_\phi$ inside the star. The typical example is chameleon screening [243] (see also [244]), where non-linear terms in the potential prevent the scalar from reaching in-medium values much beyond $\phi \sim f_\phi \ll M_\phi$. In this paper, we pay more attention to scenarios where non-linearities in the scalar-matter interactions force $\phi \sim F_\phi \ll M_\phi$ inside NSs. This is the case (for $n = 2$) of the QCD axion, if sourced by dense matter [11], and by its generalizations where the axion coupling to gluons is decorrelated from its mass [73, 74, 186]. We will not discuss ($n = 1$) scalar-tensor theories of the Damour-Polyakov type [245] since in that case $m_*(F_\phi) = m$.

Finally, let us note that we are leaving aside theories in which scalarization takes place not because of the interactions with matter but due to the coupling of the scalar to the curvature (i.e. to $R^2_{\mu\nu\rho\sigma}$ at leading order in a derivative expansion) [246–248]. See however [249, 250] for recent theoretical constraints on this type of scenarios.

6.2.2 Scalarized free Fermi gas

Neutron stars are well-described at leading order by a degenerate free Fermi gas coupled to gravity. To study the effects of a scalar field coupled to nucleons, we consider the following Lagrangian, containing a single massive fermion ψ and a single real scalar ϕ, coupled to the gravitational field $g_{\mu\nu}$,

$$\mathcal{L}_{\psi\phi} = \sqrt{-g}\left[\bar{\psi}\left(ie^{\mu}{}_{a}\gamma^{a}D_{\mu} - m_{*}(\phi)\right)\psi + \frac{1}{2}g^{\mu\nu}(\partial_{\mu}\phi)(\partial_{\nu}\phi) - V(\phi)\right], \tag{6.28}$$

where $D_\mu = \partial_\mu - i\omega_\mu$ is the covariant derivative of a fermion field in curved space. ψ and ϕ are coupled via the term $m_*(\phi)\bar{\psi}\psi$, while the self-interactions of ϕ are encoded in the function $V(\phi)$, see Eq. (6.27). Such a coupling to nucleons naturally arises in models where the scalar field couples in the UV to the (light) quarks, or to the gluon field strength, or simply to the trace of the energy-momentum tensor (see Sec. 6.2.4). For convenience, we shall henceforth work with the dimensionless field $\theta \equiv \phi/f$, where we introduce the scale f as the typical scale of the scalar field. This can be conveniently identified with either M_ϕ, F_ϕ, or f_ϕ introduced in Eq. (6.27), depending on the particular realization. We further assume that at zero density (i.e. in the absence of the Fermi gas), the potential $V(\theta)$ is minimized at θ_0 such that

$$\left.\frac{\partial V}{\partial\theta}\right|_{\theta=\theta_0} = 0\,, \quad V(\theta_0) = 0\,, \quad \text{and} \quad m(\theta_0) \equiv m \quad \text{(at zero density)}\,. \tag{6.29}$$

Let us derive the static coupled equations of motion (EOMs) for the fermion, scalar and gravitational fields. Assuming radial symmetry, we use the Schwarzschild metric parametrization,

$$g_{00} = e^{2\nu(r)}\,, \quad g_{rr} = -\left[1 - \frac{2M(r)}{M_{\rm P}^2 r}\right]^{-1} \quad g_{\Theta\Theta} = -r^2\,, \quad g_{\varphi\varphi} = -r^2\sin^2\Theta\,, \tag{6.30}$$

where $M_{\rm P} = G^{-1/2}$ and we choose the metric convention $\eta_{\mu\nu} = \mathrm{Diag}[1, -1, -r^2, -r^2\sin^2\Theta]$. The gravitational field is sourced by an energy-momentum tensor that is the sum of two terms,

$$T^{\mu}{}_{\nu} = (T_{\rm ideal})^{\mu}{}_{\nu} + (T_{\rm grad})^{\mu}{}_{\nu}\,. \tag{6.31}$$

$T_{\rm ideal}$ contains the contributions of the Fermi gas and the scalar potential $V(\theta)$, and has the form of an ideal fluid, i.e. $(T_{\rm ideal})^{\mu}{}_{\nu} = \mathrm{Diag}[\varepsilon, -p, -p, -p]$ with

$$\varepsilon = \varepsilon_\psi(m_*(\theta), \rho) + V(\theta) \quad \text{and} \quad p = p_\psi(m_*(\theta), \rho) - V(\theta)\,. \tag{6.32}$$

The total pressure of the system p as defined above can become negative in regions where the contribution from the potential $V(\theta)$ dominates over the strictly positive pressure of the Fermi gas. Note also that ε_ψ, p_ψ and ε, p separately satisfy the thermodynamic relation $d(\epsilon/\rho) = -pd(1/\rho)$ in the constant θ limit. $(T_{\rm grad})^{\mu}{}_{\nu}$ is proportional to f^2,

$$(T_{\rm grad})^{\mu}{}_{\nu} = f^2(\partial_r\theta)^2\left[\frac{1}{2}\delta^{\mu}_{\nu} - \delta^{\mu}_{r}\delta^{r}_{\nu}\right]\left(1 - \frac{2M}{rM_{\rm P}^2}\right)\,. \tag{6.33}$$

The term in the square brackets describes the gradient energy of the field and has the form of a perfect fluid. The second term deviates from the perfect fluid behavior in the form of additional (anisotropic) pressure. Both terms are proportional to f^2, therefore we expect them to become negligible when f is much smaller than other scales appearing in the EOM, see App. C.2 for a detailed discussion. We have already encountered the three independent EOMs defined by the

Lagrangian $\mathcal{L} = (M_{\rm P}^2/16\pi)\sqrt{-g}R + \mathcal{L}_{\psi\phi}$ in Eq. (6.5), where we introduced the fermion scalar density $\rho_s(m_*(\theta),\rho) \equiv \langle\bar{\psi}\psi\rangle$. Eq. (6.5a) is the generalized form of the scalar EOM. It contains the coupling to gravity, which deforms the derivatives on the LHS. The scalar self-interactions are encoded in the first term in parenthesis on the RHS. The scalar interaction with the nucleons is given by the second term in parenthesis on the RHS. The last two equations are the generalized Tolman-Oppenheimer-Volkoff (TOV) equations [251,252]. Eq. (6.5b) dictates how the total pressure is balanced by the gravitational force and an additional new scalar force. Eq. (6.5c) is associated with the enclosed mass $M(r)$, found by integrating over the energy density associated with the Fermi gas, the scalar potential, as well as a contribution from the scalar gradient. There are in principle two additional EOMs which we do not present. The EOM for the fermion field is implicitly used in the expression for the energy and pressure of the Fermi gas.[3] The equation of motion for the temporal component of the metric $\nu(r)$ can be solved separately since $\nu(r)$ and its derivatives do not appear in any of the other equations. The combination of all EOMs imply by construction energy-momentum conservation, i.e. $\partial_{;\mu}T^{\mu\nu} = 0$, which is equivalent to the so-called hydrostatic equilibrium condition [103].

The derivation so far has been independent of the properties of the Fermi gas. For concreteness, from this point on we consider the simple case of a free Fermi gas (see *e.g.* [105])

$$\varepsilon_\psi(m_*(\theta),\rho) = 2\int^{k_F(\rho)} \frac{\mathrm{d}^3k}{(2\pi)^3}\sqrt{\mathbf{k}^2 + m_*^2(\theta)}\,, \tag{6.34a}$$

$$p_\psi(m_*(\theta),\rho) = \frac{2}{3}\int^{k_F(\rho)} \frac{\mathrm{d}^3k}{(2\pi)^3}\frac{k^2}{\sqrt{\mathbf{k}^2 + m_*^2(\theta)}}\,, \tag{6.34b}$$

$$\rho_s(m_*(\theta),\rho) = (\varepsilon_\psi - 3p_\psi)/m_*(\theta)\,. \tag{6.34c}$$

The Fermi momentum k_F and the number density ρ are related as usual by $k_F(\rho) = (3\pi^2\rho)^{1/3}$. The scalar interactions are implied by the θ-dependent fermion mass. The θ field itself would eventually be an r-dependent background field, reminiscent of a mean-field approximation. [4] In later stages, changing variables to the chemical potential μ would prove helpful since it must be a continuous parameter in any static solution where chemical equilibrium is assumed. This change of variables is done by identifying the Fermi energy with the chemical potential, namely $k_F(\mu) = \sqrt{\mu^2 - m_*^2(\theta)}\Theta(\mu - m_*(\theta))$. From this definition it should be understood that, for a given θ, for values of μ below the mass threshold $m_*(\theta)$ the total energy and pressure of the system are μ-independent and originate only from the scalar field, i.e. $\varepsilon \to V(\theta)$ and $p \to -V(\theta)$.

The fermion field ψ describes nuclear matter in its simplest form: pure non-interacting neutrons, believed to be the main component in NSs and provide the dominant source of energy density in the non-relativistic limit. Such a description leaves out important ingredients such as additional particles (protons, electrons, muons) and interactions, namely the electroweak and nuclear forces. The latter plays a critical role, as nuclear interactions become increasingly

[3] Note that one should solve the fermion EOM in flat space, such that the microscopic properties of the fermion gas are independent of the gravitational field; one can always choose a reference frame which is flat at the characteristic scales of the Fermi gas.

[4] By using the mean-field approach we are treating the scalar very much like the gravitational field. In particular, we neglect interactions associated with *e.g.* single scalar exchanges, even if these are possible for background values of θ for which $\partial m_*(\theta)/\partial\theta \neq 0$. However, we expect this force (which may be effectively long range for light scalar masses) to be suppressed by the small effective coupling $\sim m/M_\phi \ll 1$ and therefore irrelevant for the thermodynamic properties of the system of fermions. It is also implicitly understood that the scalar is light enough to coherently couple to the Fermi gas, i.e. $m_\phi \lesssim \rho^{1/3}$.

important at high densities. All of these generate $\mathcal{O}(1)$ corrections to the main predictions (*e.g.* maximal mass of the bound object), which rely on the balance of all relevant forces. Nevertheless, the pure neutron gas model is useful when extracting order-of-magnitude effects due to physics beyond the SM, and thanks to its simplicity it allows a clear identification of the physical processes behind those effects. In addition, the formalism outlined above can be extended to different models of interacting and non-interacting Fermi gases, or adapted to the phase of matter in white dwarfs [14].[5]

The coupled system Eq. (3.1) can in principle be numerically solved by specifying the initial conditions $p(0)$ and $\theta(0)$, with the remaining initial conditions $\theta'(0) = M'(0) = 0$ dictated by radial symmetry. In practice, however, finding valid static solutions for Eq. (6.5a) is challenging. This can be understood by the classic intuition provided by Coleman [253]. Static solutions of the scalar EOM are analogous to classical one-dimensional trajectories in an inverted potential, where the radial direction plays the role of time. In this picture, a valid static solution is one which connects one maximum of the potential to another, with the tail of the scalar profile staying exponentially close to θ_0 for arbitrarily large values of r. These type of trajectories are inherently chaotic, given that small variations to the initial condition would cause either an over- or an under-shoot.[6] Thus, viable static solutions of Eq. (6.5a) typically require to tune the initial condition $\theta(0)$. This issue can be avoided in case Eq. (6.5a) is solved in isolation by adding a fictitious friction term [186]. However, this requires neglecting the back-reaction of the scalar field on the density profile, which is precisely the effect we are after. Therefore, our numerical solutions of Eq. (3.1) are based on an automatized shooting method, which tunes the value $\theta(0)$ for a fixed $p(0)$ until a viable static solution is found.

Equation of state: the negligible gradient limit Finding a solution to the coupled system Eq. (3.1) is significantly simpler if there is a separation between the typical length scale of the scalar field λ_ϕ and the NS radius R,

$$\lambda_\phi \equiv f/\Lambda_{\rm eff}^2 \ll R\,. \tag{6.35}$$

We refer to this particularly simple limit as the negligible gradient limit, in which all $\theta'(r)$ and $\theta''(r)$ terms in Eq. (3.1) can be neglected. The detailed derivation of this limit from a dimensional analysis of Eq. (6.5a) is presented in App. C.2. $\Lambda_{\rm eff}^2$ is a scale typically associated with either the potential term $\sqrt{\partial V(\theta)/\partial\theta}$ or the Fermi gas term $\sqrt{\rho_s|\partial m_*(\theta)/\partial\theta|}$. For a NS this limit roughly translates into $f/M_{\rm P} \ll \Lambda_{\rm eff}^2/m^2$.

In this limit, solutions to the system can be found in terms of standard thermodynamic quantities. The value of the scalar field at a given number density ρ or chemical potential μ is then determined either by minimizing the total energy $\varepsilon(\theta,\rho)$ or the grand canonical potential $\Omega(\theta,\mu) \equiv \varepsilon - \mu\rho = -p(\theta,\mu)$ w.r.t. θ

$$\left.\frac{\partial\varepsilon(\theta,\rho)}{\partial\theta}\right|_\rho = \left.\frac{\partial\Omega(\theta,\mu)}{\partial\theta}\right|_\mu = \frac{\partial V}{\partial\theta} + \rho_s\frac{\partial m_*(\theta)}{\partial\theta} = 0\,. \tag{6.36}$$

[5] In this regard, we note that the nuclear force, mediated at leading order by pion exchange, could change in a scalarized system, via a θ-dependent pion mass and interactions. We leave the detailed discussion of the impact of a sourced scalar on nuclear physics for a future publication, see for instance [234].

[6] One important difference w.r.t. [253] is that in our scenario the explicit radial dependence of the effective scalar potential, through the pressure dependence of $\rho_s(\theta(r), p(r))$, translates into a time-dependent potential in the classical trajectory analogy. This leads to a violation of energy conservation that could complicate the over-/under-shooting argument. However, since pressure is always continuous, this dependence can be neglected in small regions where p can be treated as constant.

Here $\rho_s = \partial\varepsilon_\psi/\partial m_*|_\rho = -\partial p_\psi/\partial m_*|_\mu$ depends on the chosen free variable, namely either ρ or μ. Eq. (6.36) defines the microscopic EOS, along with $\partial\varepsilon/\partial\rho|_\theta = \mu$ and $\partial\Omega/\partial\mu|_\theta = \rho$. Unsurprisingly, Eq. (6.36) is the scalar EOM in the limit where the scalar derivatives are negligible, i.e. Eq. (6.5a) with its LHS set to zero. For Eq. (6.36) to have non-trivial solutions, i.e. for scalarization to take place, there must be a region where the two terms appearing in it are comparable. The condition $\rho_s \partial m_*/\partial\theta \sim \partial V/\partial\theta$ implies that the compact object must be dense enough for non-trivial solutions to exist. This condition, along with the largeness condition of Eq. (6.35), are essentially the same conditions discussed in the context of scalar sourcing at finite density in Refs. [13, 254].

Solutions of Eq. (6.36) are of the form $\theta(\mu)$ (or $\theta(\rho)$). This allows us to express the total energy density and pressure of the system in terms of a single independent variable, *e.g.* the chemical potential, such that $\varepsilon(\mu) = \varepsilon(\theta(\mu), \mu)$ and $p(\mu) = p(\theta(\mu), \mu)$. By constructing the EOS using μ as the free parameter, the preferred phase (with maximal pressure) is always selected and the procedure outlined above produces the thermodynamically stable EOS. This ensures the continuity of μ and p across a phase transition boundary, which is required for chemical and mechanical stability.[7] At this point one can readily construct the effective EOS, i.e. $\varepsilon(p)$, and numerically solve the usual TOV equations, see Eq. (3.1), given the initial condition $M(0) = 0$ and some internal pressure $p(0)$.

Let us get a qualitative understanding on how the effective mass of the fermion $m_*(\theta)$ would change at increased densities in light of Eq. (6.36). As we infinitesimally increase ρ_s (i.e. increasing $\rho \simeq \rho_s$ in the non-relativistic limit), Eq. (6.36) can only be satisfied if $\partial m_*/\partial\theta < 0$, namely if the mass of the fermion decreases. In other words, the increase in $V(\theta)$ due to the deviation from θ_0 would be compensated by the decrease in the energy of the Fermi gas.[8] Indeed, for a fixed number density ρ, a Fermi gas has less energy when the mass of the fermion is decreased. Thus, we find that solutions of Eq. (6.36) always satisfy the upper bound $m_*(\theta) \leq m_*(\theta_0) \equiv m$ at all densities. It is also useful to consider the opposite regime of very high densities, where we identify two types of solutions for Eq. (6.36). The first type is relevant if there exists a θ_∞ for which $m_*(\theta_\infty) = 0$. Then, Eq. (6.36) is solved at arbitrary high densities along a curve in the $\{\theta, \rho\}$ plane defined by

$$\rho_s(\theta, \rho) = \left| \frac{\partial V/\partial\theta}{\partial m_*(\theta)/\partial\theta} \right|_{\theta=\theta_\infty} \equiv \rho_{s,\infty} = \text{const.} \tag{6.37}$$

In the ultra-relativistic approximation $\rho_s(\theta, \rho) \sim \rho^{2/3} m_*(\theta)$, therefore the condition above is satisfied by $m_*(\theta) \sim \rho_{s,\infty}/\rho^{2/3}$, which is achieved by taking θ close enough to θ_∞ for $\rho \gg \rho_{s,\infty}$. Therefore, in this type of unbounded solution, $m_*(\theta)$ remains positive and approaches 0 from above as the density is increased. This implies that the effective mass of the fermion can be much smaller than its zero density value m at high enough densities.

If $m_*(\theta)$ is bounded from below and does not cross 0, we find the second type of solution: the asymptotic value of θ at high densities would then be θ_∞ for which the first derivative vanishes, namely $(\partial m_*(\theta)/\partial\theta)|_{\theta=\theta_\infty} = 0$. This can be easily understood as the solution of Eq. (6.36) in the limit where the contribution from $\partial V(\theta)/\partial\theta$ is negligible and $\rho_s \neq 0$. In this type of solution, $m_*(\theta)$ remains positive and approaches $m_*(\theta_\infty)$ from above as the density is increased. Depending on the function $m_*(\theta)$, both $m_*(\theta_\infty) \lesssim m$ and $m_*(\theta_\infty) \ll m$ are possible. The scalar

[7] As we discuss extensively below, there can exist a meta-stable, potentially long-lived, branch of the EOS. In this case, it is necessary to use ρ as the free parameter.

[8] For concreteness, we use $\varepsilon(\theta, \rho)$ as the relevant quantity for this particular discussion, but similar arguments can be made using $\Omega(\theta, \mu)$.

density ρ_s increases as ρ increases while the mass is fixed, which implies that $\theta(\rho) \to \theta_\infty$ at high densities, making this solution self-consistent. In both cases discussed above, we find that any solution of Eq. (6.36) satisfies also the lower bound $m_*(\theta) > 0$ at all densities.

What kind of EOS can we expect? To answer this question, let us first discuss the qualitative effects of the scalar field. The first effect we can consider is the reduction of the mass of ψ. This has the generic effect of stiffening the EOS, which can be seen easily *e.g.* in the non-relativistic approximation (neglecting $V(\theta)$, $p \simeq p_\psi$),

$$p_\psi^{\rm NR} \propto \varepsilon_\psi^{\rm NR} \left(\frac{\varepsilon_\psi^{\rm NR}}{m_*^4(\theta)} \right)^{2/3} \quad \to \quad \frac{\partial p_\psi^{\rm NR}}{\partial m_*(\theta)} < 0 \,. \tag{6.38}$$

A reduction of the mass, therefore, leads to a larger pressure for a fixed energy density, i.e. to a stiffer EOS that can support a larger total mass for a given radius. On the other hand, the additional contribution of $V(\theta)$ would generically lead to a softening of the EOS state. Again *e.g.* in the non-relativistic approximation,

$$p^{\rm NR} \simeq c\, m_*^{-8/3} \big(\varepsilon^{\rm NR} - V(\theta)\big)^{5/3} - V(\theta) \quad \to \quad \frac{\partial p^{\rm NR}}{\partial V(\theta)} < 0 \,, \tag{6.39}$$

where c is a numerical constant. An increase in $V(\theta)$ leads to smaller pressure for a fixed energy density, therefore to a softer EOS.

These two competing effects split the parameter space of any model into two qualitatively different regions. First, a coexistence (CE) region, in which a phase of matter, with $\theta = \theta^{\rm CE} \neq \theta_0$, is accessible above a certain critical pressure. In this case, for internal pressures above the critical pressure, the bound object can be described as a hybrid star, with a core in one phase ($\theta \simeq \theta^{\rm CE}$) and a crust in another ($\theta \simeq \theta_0$). Below that critical pressure, only the low-density phase is present. Such phase transitions typically soften the EOS, and the resulting hybrid stars are less massive in comparison to stars made of matter in their low-density phase.

We dub the rest of the parameter space the new ground state (NGS) region. As the name suggests, at high enough densities matter can transition to a new, stable ground state with $\theta = \theta^{\rm NGS}$. Stars could be totally stable only in this new phase, while dilute stars (with $\theta \simeq \theta_0$) can be long-lived until a fluctuation causes them to transition to the stable phase. Importantly, the EOS for the new ground state could be stiffer in comparison to the low-density (meta-stable) phase and therefore may support bound objects with larger masses. The NGS region shares some similarities with strange stars [232, 255, 256].

To better define the CE and NGS regions, let us denote our parameter space as $\boldsymbol{\alpha} = \{\alpha_i\}$, namely the space of parameters (couplings and scales) that fix the $m_*(\theta)$ and $V(\theta)$ functions, see Eq. (6.27). The two regions can be easily identified in terms of preferred phases. In this case, it is useful to pick μ as the independent variable, where the preferred phase is the one with maximal pressure.

Coexistence region This region in parameter space is defined by $p(\theta, \mu; \boldsymbol{\alpha}) < 0$ for all values of $\theta \neq \theta_0$ and for $0 < \mu < m$. This means that the θ_0 phase is preferred around the $\mu \gtrsim m$ threshold (since by definition $p(\theta_0, \mu) = 0$ in the region $0 < \mu < m$). A phase transition may then occur at some critical $\mu_c^{\rm CE}(\boldsymbol{\alpha}) > m$, see the blue curve in Fig. 6.8. Although this transition is always continuous in (p, μ), it could either be smooth or first-order in (ε, ρ). In the latter case, there is a discontinuity (i.e. "jump"), like the one shown in Fig. 6.9. Phase transitions typically

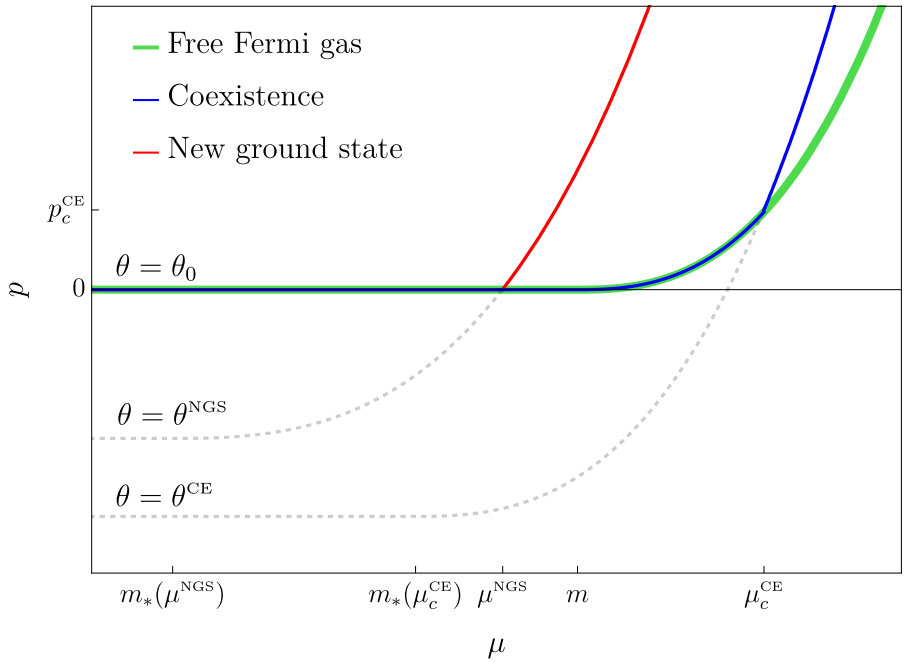

Figure 6.8: Pressure as a function of chemical potential. The thick, green curve describes a free Fermi gas. The blue curve describes a first-order phase transition from θ_0 to some θ^{CE}, typical in the CE region of parameter space. The phase transition occurs at a critical chemical potential μ_c^{CE} where the pressure of both phases are equal, denoted here by p_c^{CE}. The red curve describes the NGS, with $\theta = \theta^{\mathrm{NGS}}$ starting at the $p = 0$ point at non-zero $\mu^{\mathrm{NGS}} < m$. This plot demonstrates how the intersection point between the $\theta \neq \theta_0$ curves and the $\theta = \theta_0$ thick green curve, which is controlled by the properties of $m_*(\theta)$ and $V(\theta)$, determine whether a certain parameter point belongs to the CE or the NGS region.

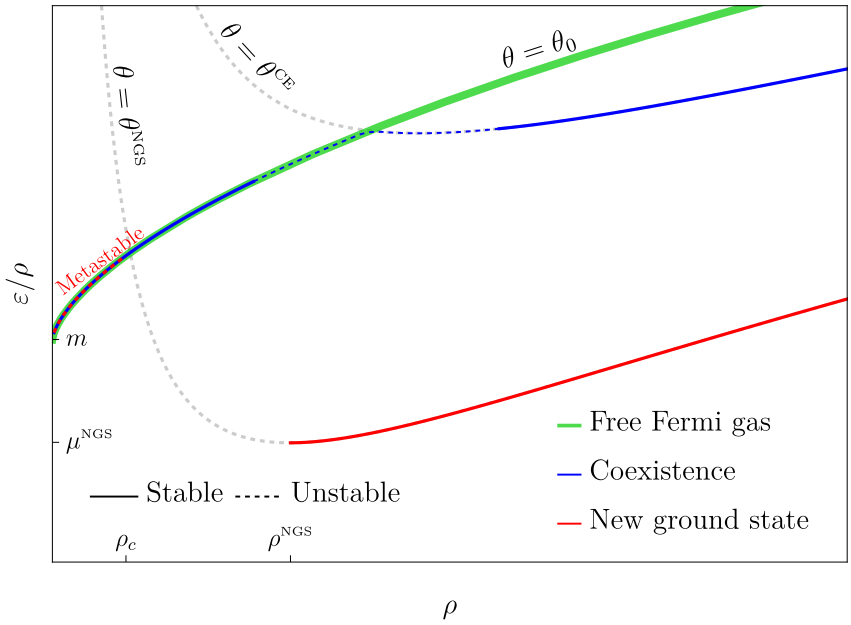

Figure 6.9: The binding energy ε/ρ as a function of number density ρ. The thick, green curve describes a free Fermi gas. The blue curve describes a first-order phase transition typical in the CE region of parameter space. The transition is accompanied by a discontinuity in ε and ρ, in the region plotted here as the dashed blue line. The phases at the edges of the dashed blue line have the same pressure. Both the thick green and the blue curves share the same ground state at $\rho \to 0$, where the binding energy is simply the rest mass m. The red curve describes the binding energy of the NGS. An absolutely stable branch is defined for $\rho \geq \rho^{\rm NGS}$, with the NGS at $\rho^{\rm NGS}$. A meta-stable branch equivalent to a free Fermi gas in found at $\rho < \rho_c$. The region $\rho_c < \rho < \rho^{\rm NGS}$ is completely unstable.

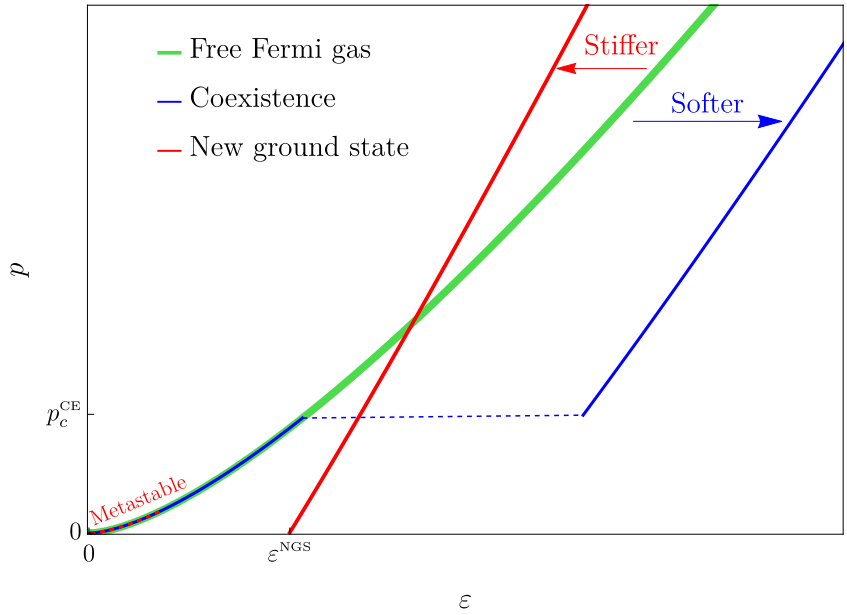

Figure 6.10: Pressure as a function of energy density for the various regions discussed in the text. The thick, green curve describes a free Fermi gas. The blue curve describes a first-order phase transition, typical in the CE region of parameter space. While the pressure is continuous across the phase transition, which takes place at p_c^{CE}, the energy density is discontinuous, shown as the dashed blue line. Such a jump leads to a softer EOS, at least in some finite region. The red curve describes the NGS, characterized by vanishing pressure at some finite energy density $\varepsilon^{\mathrm{NGS}}$. This EOS can be stiffer than the θ_0 phase at high densities. There is typically also a meta-stable branch at low energy densities, equivalent to the free Fermi gas, shown here as the dashed red curve.

lead to a softening of the equation of state, see Fig. 6.10. We also note that one can classify three types of possible phase transitions, depending on whether the low- and high-density phases are non-relativistic (NR) or ultra-relativistic (UR). A noticeable effect arises only when at least one of the phases is NR, such that the nucleon mass plays a role, therefore only in NR $\to$ NR and NR $\to$ UR transitions. The third possible transition, UR $\to$ UR, occurs when the mass is irrelevant, and therefore changing its value does not affect the EOS. Note that the UR $\to$ NR transition is not possible; as argued above, the mass of the fermion in the high-density phase is never larger.

New ground state region The NGS region of parameter space is defined by demanding that there exists a solution of $p(\theta^{\rm NGS}, \mu; \boldsymbol{\alpha}) = 0$ at a chemical potential $\mu^{\rm NGS}(\boldsymbol{\alpha})$ satisfying $m_*(\theta^{\rm NGS}) < \mu^{\rm NGS} < m$, with $\theta^{\rm NGS}(\mu, \boldsymbol{\alpha})$ the solution of Eq. (6.36). This is shown by the red curve in Fig. 6.8. In order to see that there is indeed a new ground state of the system, it is useful to switch and use the number density ρ as a free parameter. The condition above implies, according to the first law of thermodynamics,

$$p(\mu^{\rm NGS}) = (\rho^{\rm NGS})^2 \frac{\partial(\varepsilon/\rho)}{\partial\rho}\bigg|_{\rho=\rho^{\rm NGS}} = \mu^{\rm NGS}\rho^{\rm NGS} - \varepsilon^{\rm NGS} = 0\,, \tag{6.40}$$

where $\varepsilon^{\rm NGS} = \varepsilon(\theta^{\rm NGS}, \rho^{\rm NGS})$ and $\rho^{\rm NGS} = k_F^3(\mu^{\rm NGS})/3\pi^2$, with $k_F^2(\mu^{\rm NGS}) = (\mu^{\rm NGS})^2 - m_*^2(\theta^{\rm NGS})$ and $\theta^{\rm NGS}(\boldsymbol{\alpha})$ evaluated at $\mu^{\rm NGS}$. From this condition we learn two things,

1. There is a minimum of the function ε/ρ at $\rho = \rho^{\rm NGS}$.
2. The value of the function at that minimum is $\frac{\varepsilon^{\rm NGS}}{\rho^{\rm NGS}} = \mu^{\rm NGS} < m$.

This new and deeper minimum is shown in Fig. 6.9. We find that the function describing the energy per particle, namely ε/ρ, has a global minimum at $\rho^{\rm NGS}$, which is lower than the minimum at $\rho = 0$, since $\lim_{\rho\to 0}\varepsilon(\theta_0, \rho)/\rho = m$. This implies the existence of a new ground state for matter with $\theta^{\rm NGS} = \theta(\rho^{\rm NGS})$. This is analogous to the effect of the nuclear force in nuclear matter. The short-distance repulsion and long-distance attraction are balanced at nuclear saturation density $\rho_0 \approx 0.15$ fm^{-3}, i.e. the density of nuclei, which are the ground states of nuclear matter. In the presence of the NGS, the EOS has a stable branch that reaches $p = 0$ at some non-vanishing number density $\rho^{\rm NGS}$ or energy density $\varepsilon^{\rm NGS}$, see Fig. 6.10. Importantly for our discussion, the EOS of this new phase could be stiffer than the θ_0 phase, and therefore can potentially support bound objects of larger mass. Since the NGS is not continuously connected to the θ_0 phase, matter below some critical density $\rho < \rho_c$ is meta-stable, see Fig. 6.9. Given a system at sub-critical density, any density fluctuation large enough to overcome the potential barrier can cause a phase transition, as long as its spatial extent is large compared to λ_ϕ, even if small compared to the size of the system (due to the negligible gradient limit formulated, see Eq. (6.35)). The region $\rho_c < \rho < \rho^{\rm NGS}$ corresponds to negative total pressure and is therefore completely unstable.[9]

Let us now focus on the NGS, and take the contribution coming from $V(\theta)$ to be negligible. Furthermore, let us assume that the effective fermion mass remains approximately constant in the NGS; this would be the case in models where $m_*(\theta)$ is positive and bounded from below at some $\theta = \theta_\infty$ (see discussion below Eq. (6.37)). Thus, if the total effect of the scalar interactions

[9] We should note that for $m_*(\theta)$ linear in θ ($n = 1$ in Eq. (6.27)) there exists another (hydrodynamical) instability due to an imaginary speed of sound $c_s^2 = \partial p/\partial\varepsilon < 0$ [257]. This is absent for $m_*(\theta)$ quadratic in θ ($n = 2$ in Eq. (6.27)) since θ_0 is not continuously connected to $\theta^{\rm CE}$ (nor to $\theta^{\rm NGS}$) as one varies ρ.

can be described as simply reducing the mass of the fermion to some density-independent value $m_*(\theta_\infty) < m$, the maximal mass and corresponding radius of a star composed of matter in this new phase can be easily calculated using the standard TOV equations, to find

$$M_{\rm max} \approx (0.7\ M_\odot) \left(\frac{m_N}{m_*(\theta_\infty)}\right)^2 , \quad R(M_{\rm max}) \approx (9.3\ {\rm km}) \left(\frac{m_N}{m_*(\theta_\infty)}\right)^2 , \tag{6.41}$$

where we have set $m = m_N$, with $m_N \approx 939$ MeV the neutron mass. Clearly, a reduced fermion mass has a strong effect on the NS maximal mass, as well as on the corresponding radius. This effect is potentially much larger than the usual $\mathcal{O}(1)$ effect one gets by using different EOSs, which model dense matter using different approaches (see *e.g.* [101, 152]).

On the other hand, the inclusion of the scalar self-interactions encoded in $V(\theta)$ would generically have the opposite effect and drive the maximal mass to lower values compared to the simple case above. Indeed, in the regime where the reduction in the fermion mass is so large that the Fermi gas becomes ultra-relativistic, $m_*(\theta_\infty)$ ceases to play a relevant role in the EOS in comparison with (a fixed) $V(\theta_\infty)$. The EOS then takes a particularly simple form $\varepsilon \simeq 3p + 4V(\theta_\infty)$, and we find

$$M_{\rm max} \approx (1.1 M_\odot) \left(\frac{(0.2\ {\rm GeV})^4}{V(\theta_\infty)}\right)^{1/2} , \quad R(M_{\rm max}) \approx (5.8\ {\rm km}) \left(\frac{(0.2\ {\rm GeV})^4}{V(\theta_\infty)}\right)^{1/2} . \tag{6.42}$$

While the maximal mass is of particular interest given its constraining power from single NS observations, other macroscopic parameters such as compactness, $C \equiv GM/R$, are of special relevance for what regards the sensitivity of GW observatories such as LIGO, see *e.g.* [**?**]. When the main effect of the scalar field is just the reduction of the neutron mass, the compactness is approximately the same as for the free Fermi gas, i.e. $C \simeq 0.11$, see Eq. (6.41). The compactness is larger if the scalar potential also plays a role, and it is maximal in the ultra-relativistic limit, where it takes the value $C \simeq 0.27$, see Eq. (6.42). We have explicitly checked that these two values delimit, to good approximation, the range of compactness of the heaviest NSs in the NGS, i.e.

$$0.11 \lesssim C \lesssim 0.27 , \tag{6.43}$$

and that such a range is fully covered independently of the NS maximum mass, see Fig. 6.11. Therefore, while the maximal compactness is below that required for the existence of a photon sphere, $C < 1/3$, it is larger than that of standard NSs with realistic EOSs, whose compactness does not typically exceed $C \lesssim 0.23$, see *e.g.* [101, 154].

An important consequence of the above discussion regards the causal bounds on the maximal NS mass and compactness. Bounds on the maximal mass of NSs, independent of their radius, were originally derived by Nauenberg and Chapline [239] as well as by Rhoades and Ruffini [240], based on the causality requirement that the speed of sound be smaller than the speed of light, $c_s < 1$. These bounds can be understood taking the maximally-compact EOS, namely $p = \varepsilon - \varepsilon_c$ for $\varepsilon > \varepsilon_c$, and $p = 0$ otherwise, from which one finds the bound $M \lesssim 4.1 M_\odot \sqrt{\varepsilon_0/\varepsilon_c}$ with $\varepsilon_0 = m_N \rho_0 \approx 150\,{\rm MeV\,fm^{-3}}$ the nuclear saturation energy density [101, 258]. Given our understanding of matter around nuclear density ρ_0, for $\varepsilon_c \simeq 2\varepsilon_0$ this approximately reproduces the original bounds on the maximal NS mass, $M_{\rm max} \simeq 3 M_\odot$. This seems to be in contradiction, for example, with our simple estimate in Eq. (6.41). However, this causal bound is clearly based on our assumed understanding of matter at $\rho \lesssim \rho_0$. In the presence of light scalars coupled to nucleons, nuclear matter as we know it in nuclei may be only metastable (see Sec. 6.2.2), and the NGS energy density may in fact be lower than ε_0, allowing for a larger maximal NS mass.

Bounds on the maximal compactness of NSs are instead not violated by stars in the NGS. These include the ε_c-independent causal upper bound from the maximally-compact EOS just discussed, $C \lesssim 0.35$ [101, 259, 260], as well as Buchdahl's limit $C \leqslant 4/9$, which ensures the finiteness of the pressure inside the NS [103, 261].

Another observable to consider in the context of NSs in the NGS is the rotation frequency of pulsars, which is very slowly varying in time and precisely measured, see *e.g.* [262]. Due to their resemblance at the macroscopic level, it is worth commenting on the rotation periods of strange stars. In Ref. [263] it was shown that the maximal rotation frequency of strange stars can be mildly larger than standard NSs for the same masses and radii, by a factor $\lesssim 10\%$. The fact that strange stars have the potential to rotate faster also impacts the causal bounds on the rotation periods, which are typically slightly weaker compared to standard NSs [105, 258, 260].

Besides rotation periods, it would be interesting to further explore other related observables such as the moment of inertia and the spin-induced quadrupole moment [264, 265], see also e.g. [105]. These observables have been studied mostly in the context of scalar-tensor modifications of gravity [266–269]. Their importance goes beyond the characterization of the macroscopic properties of NSs in that the moment of inertia and quadrupole in GR are found to be related in a way that weakly depends on the EOS [270, 271]. These universal relations, also known as I-Love-Q relations, also involve tidal Love numbers such as the tidal deformability [272], which parametrizes the quadrupole response of a star to the gravitational field of a companion object. Strange stars have been found to exhibit much larger tidal deformabilities than normal NSs [273], yet the universal relations have been shown to hold regardless, see e.g. [274]. Perhaps the stronger indication that this set of observables is likely different for NSs in the NGS than for standard NSs is that departures from the I-Love-Q relations are typically significant in scalar-tensor theories, as reviewed in [237].

Finite gradient effects

Meta-stability The negligible gradient limit ($f/M_{\rm P} \ll \Lambda_{\rm eff}^2/m^2$) is useful and applicable when considering bound objects that are much larger than the effective wavelength of the scalar field, see Eq. (6.35). For objects whose size R satisfies the opposite condition

$$R \ll \lambda_\phi \,, \tag{6.44}$$

the cost in gradient energy outweighs the in-medium gain in potential energy, such that the energetically favorable configuration remains $\theta = \theta_0$. This limit has an important implication: the new stable phase of matter is not accessible in small systems, even if these are dense enough. For instance, considering a low value of the scalar decay constant, *e.g.* $f = 10^3$ GeV, and taking a conservative estimate $\Lambda_{\rm eff}^2 \sim (1\ {\rm GeV})^2$ (which is relevant for nuclei and NSs), we find that the effective wavelength is $\lambda_\phi \sim 200$ fm, two orders of magnitude larger than nuclear radii $\sim 1\ {\rm fm} \times A^{1/3}$, with mass number A. Since most nuclei with $A \sim O(200)$ are already short-lived, it is extremely unlikely that a nucleus with $A \sim 10^6$ is spontaneously formed in small systems. In practice, experimental tests typically bound f to be much higher than considered above, making λ_ϕ much larger and the new phase even less accessible in small systems (the discussion on these model-dependent experimental tests is postponed to Sec. 6.2.3). Therefore, the stability of standard nuclei in light of the absolutely stable scalarized ground state is ensured due to the gradient energy required to displace the scalar field, and it is consistent with the fact that some nuclei are very long-lived, and in fact stable on cosmological scales.

In addition, note that only matter fluctuations whose spatial extent is of the order of λ_ϕ can lead to a transition from the meta-stable phase to the NGS phase. This type of large and dense

regions are expected to appear first in violent events such as stellar collapse (e.g. supernova) and stellar collisions (e.g. binary mergers), which therefore should be the main production mechanisms of matter in its true ground state, see also e.g. the discussion in [237]. Depending on the critical density, the existence of a NGS can affect the formation of main sequence stars as well as stellar remnants such as white dwarfs and NSs. We leave the study of these effects for future investigation and limit ourselves here to the study of time-independent systems.

Finally, we note that in our simple working assumption of a free Fermi gas (of neutrons), every time a clump or nugget of matter in the NGS comes into contact with matter in the metastable low-density phase, it would convert it to the NGS. In the case of strange quark matter [232, 255, 256], this is avoided by adding electrons according to charge neutrality. These form a cloud of size $(\alpha m_e)^{-1}$ around the strange nugget, which itself has a crust of order $\Lambda_{\rm QCD}^{-1}$ (which is also the smallest nugget size). The Coulomb barrier then prevents these objects from converting other nuclei to strange matter. In our case, such a separation of scales is not necessarily present (since $\lambda_\phi \gg \Lambda_{\rm QCD}^{-1}$) and therefore this argument is not applicable. Nevertheless, we expect the abundance of NGS nuggets to be significantly smaller than their strange counterparts due to a suppressed production rate in extreme astrophysical environments by $\sim (\Lambda_{\rm QCD}\lambda_\phi)^{-2}$. Still, we believe a more careful examination of this question is warranted.

Self-bound and constant density objects For all configurations on the stable branch, the total core pressure balances two inward pressure contributions, the gravitational pressure and the pressure from the change in mass due to the scalar field, which we refer to as the gradient pressure. We define self-bound objects (SBOs) as those for which the gravitational contribution is subdominant. They are composed of matter in the NGS, held together by the gradient pressure of the scalar field at the boundary (or crust) of the object, which is typically of size λ_ϕ and where the scalar transitions from $\theta_\infty \to \theta_0$. The opposite limit represents the conventional gravitationally-bound objects, also known as stars. As discussed below, in the NGS branch, both types of objects can have approximately constant energy density profiles. In App. C.3 we provide a detailed analytic treatment of these objects.

SBOs are typically not compact, $GM/R \ll 1$, consistent with the fact that they are well-described by the $M_{\rm P} \to \infty$ limit of the coupled TOV equations,

$$p' = -\theta' \left(\frac{\partial V}{\partial \theta} + \rho_s \frac{\partial m_*}{\partial \theta} \right) , \tag{6.45a}$$

$$\theta'' + \frac{2}{r}\theta' = \frac{1}{f^2} \left(\frac{\partial V}{\partial \theta} + \rho_s \frac{\partial m_*(\theta)}{\partial \theta} \right) . \tag{6.45b}$$

Note that the pressure profile is non-trivial only in regions where $\theta' \neq 0$ and the condition in Eq. (6.36), which defined our microscopic EOS, is not satisfied. The smallest possible SBOs, also known as nuggets, are of size

$$R_{\rm SBO}^{\rm min} \sim \lambda_\phi \, . \tag{6.46}$$

These are the densest of all the SBOs, since for higher densities Eq. (6.45) no longer admits stable solutions. In the $R \gg \lambda_\phi$ limit, the interior of SBOs is well-described by constant internal pressure and energy density, as well as a constant scalar field value. They are held together by the gradient pressure exerted in a small region of size $\lambda_\phi \ll R$, at the edge of the object. For even lower densities, the SBOs become large, reaching the point where gravity can no longer be neglected. Depending on the region of parameter space, SBOs can range many order of magnitude in size $R_{\rm SBO}^{\rm max} \gg R_{\rm SBO}^{\rm min}$. In particular, they can be as large as NSs and with similar

masses. On the other hand, for large values of f, SBOs may not be viable configurations at all. Indeed, the existence of SBOs requires that $R_{\rm SBO}^{\rm max} > R_{\rm SBO}^{\rm min} \sim \lambda_\phi$, which reduces to an upper bound on f

$$f \lesssim \frac{\delta m_*}{1-\delta m_*} M_{\rm P}\,, \tag{6.47}$$

where $\delta m_* = 1 - m_*(\theta_\infty)/m$. For objects of size $R \gtrsim R_{\rm max}^{\rm SBO}$, the gradient pressure and the gravitational pressure are equally important and the full coupled set of equations of Eq. (3.1) must be solved, as discussed just above Sec. 6.2.2.

As the objects in the NGS become more compact (larger and more massive, since ε is approximately constant) gravity can no longer be neglected and eventually dominates. We identify then two distinct limits, depending on the model parameters $\boldsymbol{\alpha}$, here encoded in δm_* and m_* (evaluated at θ_∞), f, and $\varepsilon^{\rm NGS}(\boldsymbol{\alpha})$. In the limit $\delta m_*^{1/2}(m_*^4/\varepsilon^{\rm NGS})(f/M_{\rm P}) \ll 1$, in which SBOs have energy densities close to that of the ground state, $\varepsilon^{\rm NGS}$ (where the EOS is $p \simeq 0$), the smallest gravitationally-bound objects can still be approximated as constant energy density systems. However, their pressure drops away from the core (as opposed to the constant pressure SBOs), at sufficiently low pressures the EOS is probed only in regions where $\varepsilon \simeq \varepsilon^{\rm NGS} \simeq$ const. At large enough core pressures, the approximation of constant energy density breaks down, and any further increase in core pressure leads to a decrease in radius, which is the typical behavior of stars described by a Fermi gas.

On the other hand, for $\delta m_*^{1/2}(m_*^4/\varepsilon^{\rm NGS})(f/M_{\rm P}) \gg 1$, the most massive and largest SBOs have $\varepsilon \gg \varepsilon^{\rm NGS}$ and already probe, by definition, the part of the EOS in which any further increase in pressure leads to stars that are no longer constant density objects. Therefore, when the gravitational pressure becomes relevant, these objects have both decreasing pressure and energy density away from their core.

Following App. C.3, we find that the maximal radius for constant energy density objects in the $\delta m_* \ll 1$ limit is approximately given by

$$R_{\rm const}^{\rm max} \sim \begin{cases} \dfrac{M_{\rm P}}{m_*^{8/6}(\varepsilon^{\rm NGS})^{1/6}} & \delta m_*^{1/2}\left(\dfrac{m_*^4}{\varepsilon^{\rm NGS}}\right)\left(\dfrac{f}{M_{\rm P}}\right) \ll 1 \\ \dfrac{M_{\rm P}^{7/6}}{\delta m_*^{1/12} m_*^2 f^{1/6}} & \delta m_*^{1/2}\left(\dfrac{m_*^4}{\varepsilon^{\rm NGS}}\right)\left(\dfrac{f}{M_{\rm P}}\right) \gg 1 \end{cases}. \tag{6.48}$$

To conclude, let us note that a simple prediction regarding the mass-radius relation can be given for objects in the NGS with densities of order $\rho^{\rm NGS}$; this is the region in the EOS where the energy density becomes almost constant as $p \to 0$, approaching the critical value $\varepsilon \to \varepsilon^{\rm NGS}$. The mass of these constant-density objects is then given simply by the product of the energy density times the volume

$$M/R^3 \simeq \frac{4\pi}{3}\varepsilon^{\rm NGS}\,. \tag{6.49}$$

Their compactness, scaling as $C \propto R^2$, is much smaller than for stars in the NGS, since their radius is much smaller. As we have explained above, as the radius grows the gravitational pressure becomes important and the energy density acquires a non-trivial profile, and one returns to the predictions given in Eq. (6.43).

6.2.3 Case studies

Bounded $m_*(\theta)$ solutions

We begin the analysis with models in which $m_*(\theta)$ is bounded from below and does not cross zero, such that the high-density value of the scalar is θ_∞ defined by $(\partial m_*/\partial\theta)|_{\theta=\theta_\infty} = 0$. We analyze these models in the negligible gradient limit, with the additional assumption that θ jumps from the trivial phase $\theta = \theta_0$ to the $\theta = \theta_\infty$ phase. This is a good approximation if $(\partial m_*/\partial\theta)|_{\theta=\theta_0}$, as well as $(\partial V/\partial\theta)|_{\theta=\theta_\infty}$, are sufficiently small. The first of these conditions has to be fulfilled if the model is not to be excluded by fifth force experiments, and effectively corresponds to taking $n = 2$ in Eq. (6.27). The second condition is only necessary for our model-independent treatment and can easily be violated in explicit models. Then, under these assumptions, the parameter space is reduced to simply $\{m_*(\theta_\infty), V(\theta_\infty)\}$. As described in Sec. 6.2.2, the two phases could either coexist, leading to hybrid star configurations or describe a meta-stable phase and a new absolutely stable phase of matter. The boundary line between the CE region and the NGS region in the $\{m_*(\theta_\infty), V(\theta_\infty)\}$ plane is given by

$$p(\theta_\infty, \mu = m) = p(\theta_0, \mu = m) = 0\,. \tag{6.50}$$

In the CE region, the two phases meet at some critical chemical potential $\mu_c^{\rm CE}$ at equal pressures. In contrast, in the NGS region, it is more convenient to find the meta-stable and stable branches using ρ as a free parameter. The critical number density $\rho_{\rm c}$, which determines the edge of the homogeneous (meta-stable) branch in the CE (NGS) region,[10] is defined by the scalar density in which the second derivative of the effective scalar potential flips sign,

$$\rho_s(\theta_0, \rho_{\rm c}) = -\left(\frac{\partial^2 V/\partial\theta^2}{\partial^2 m_*/\partial\theta^2}\right)\bigg|_{\theta=\theta_0}\,, \tag{6.51}$$

where we have expressed the scalar density in terms of the number density.

The total mass M and radius R of the stars are found by solving Eq. (3.1) numerically and scanning over the parameter space. In Fig. 6.11, we show the contours of constant mass and radius for the most massive stars in the NGS region. For small values of $V(\theta_\infty)$, the constant M and R contours are approximately $V(\theta_\infty)$-independent. The increase in mass and radius of the NGS stars are solely due to a decreased fermion mass. We recover the same scaling as in Eq. (6.41). On the other hand, near the gray region in (the upper-left part of) Fig. 6.11, the NGS becomes ultra-relativistic, thus the EOS is nearly $m_*(\theta_\infty)$-independent, and we recover the scaling of Eq. (6.42). As expected, larger values of $V(\theta_\infty)$ make the EOS softer, resulting in lighter stars.

Let us comment on the gray region in Fig. 6.11. It indicates where we expect the $\theta = \theta_\infty$ approximation to break down. This happens when the scalar density in the $\theta = \theta_\infty$ phase, $\rho_s(\theta_\infty, \mu)$, drops below a value given by

$$\rho_s^\infty = -\left(\frac{\partial V/\partial\theta}{\partial m_*/\partial\theta}\right)\bigg|_{\theta=\theta_\infty}\,. \tag{6.52}$$

The exact position of the boundary of the gray region is in general, model-dependent. That plotted in Fig. 6.11 corresponds to models with $m - m_*(\theta) \propto V(\theta)$ (*e.g.* the QCD axion and its lighter variations, see Secs. 2.3 and 6.2.3), in which $\rho_s^\infty = V(\theta_\infty)/(m - m_*(\theta_\infty))$. In general, this

[10] In general, the homogeneous branch in the CE region also includes a meta-stable part which probes the $\theta = \theta_0$ EOS above the critical pressure determined by the Maxwell construction, $p_c^{\rm CE}$, but below the critical number density.

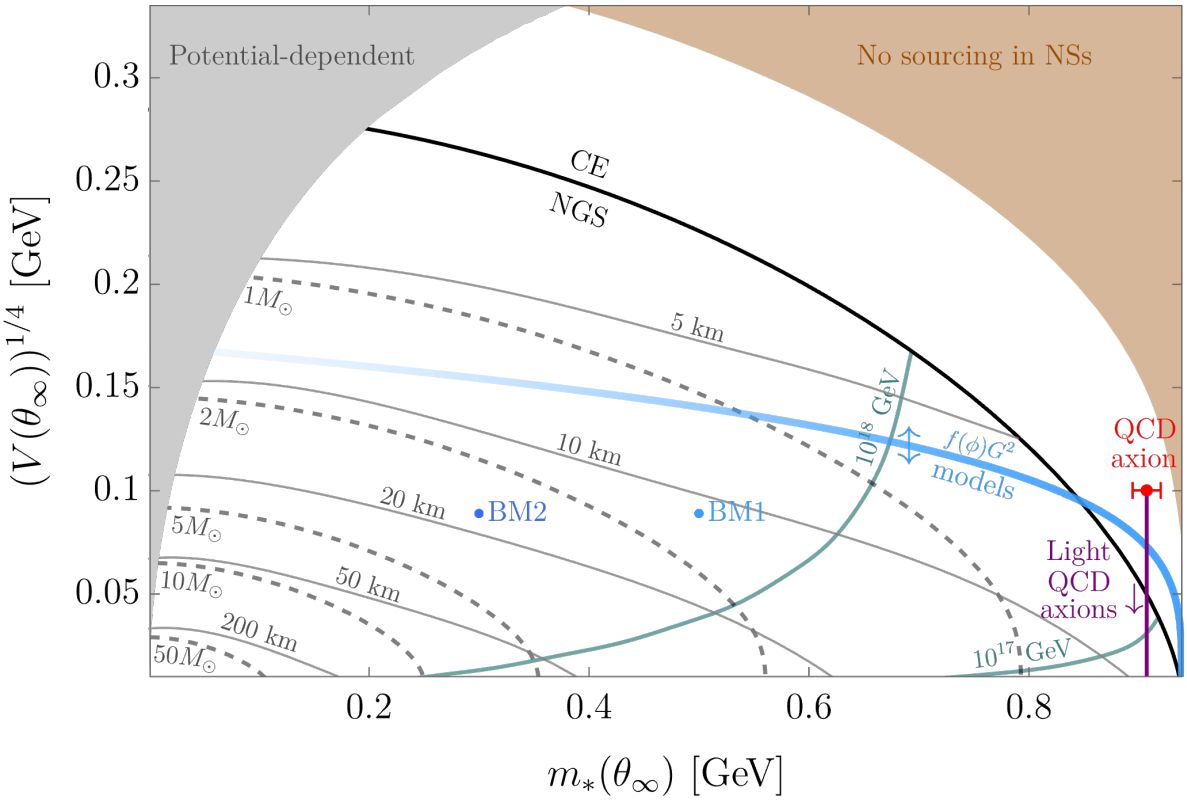

Figure 6.11: The $\{m_*(\theta_\infty), V(\theta_\infty)\}$ parameter space. The black line is the CE-NGS boundary, Eq. (6.50). Curves of constant stellar mass and radius for the most massive configuration allowed by the EOS are shown in dashed and solid gray, respectively. In the gray region, the $\theta = \theta_\infty$ approximation breaks down. In the brown region, neutron stars are not dense enough to source the scalar. We also show where different models that conform to our simplified treatment lie in this plane: the QCD axion (red dot), see Sec. 2.3; light QCD axions (purple line), Sec. 6.2.3; and two generic axion benchmark points (blue dots), Sec. 6.2.3, with $m_*(\theta_\infty) = m_N/2$ and $V(\theta_\infty) = 2 \times (0.075 \text{ GeV})^4$ (BM1) and $m_*(\theta_\infty) = m_N/3$ and $V(\theta_\infty) = 2 \times (0.075 \text{ GeV})^4$ (BM2). The thick-blue line describes a UV completion from a $f(\phi)GG$ interaction that allows for large nucleon couplings. As indicated by the arrows, this model can populate most of the parameter space although with decreasing calculability towards small $m_*(\theta_\infty)$, which we indicate with a decreasing opacity. See App. C.4 for more details. Below the green contours, finite gradient effects become important for the corresponding value of f shown.

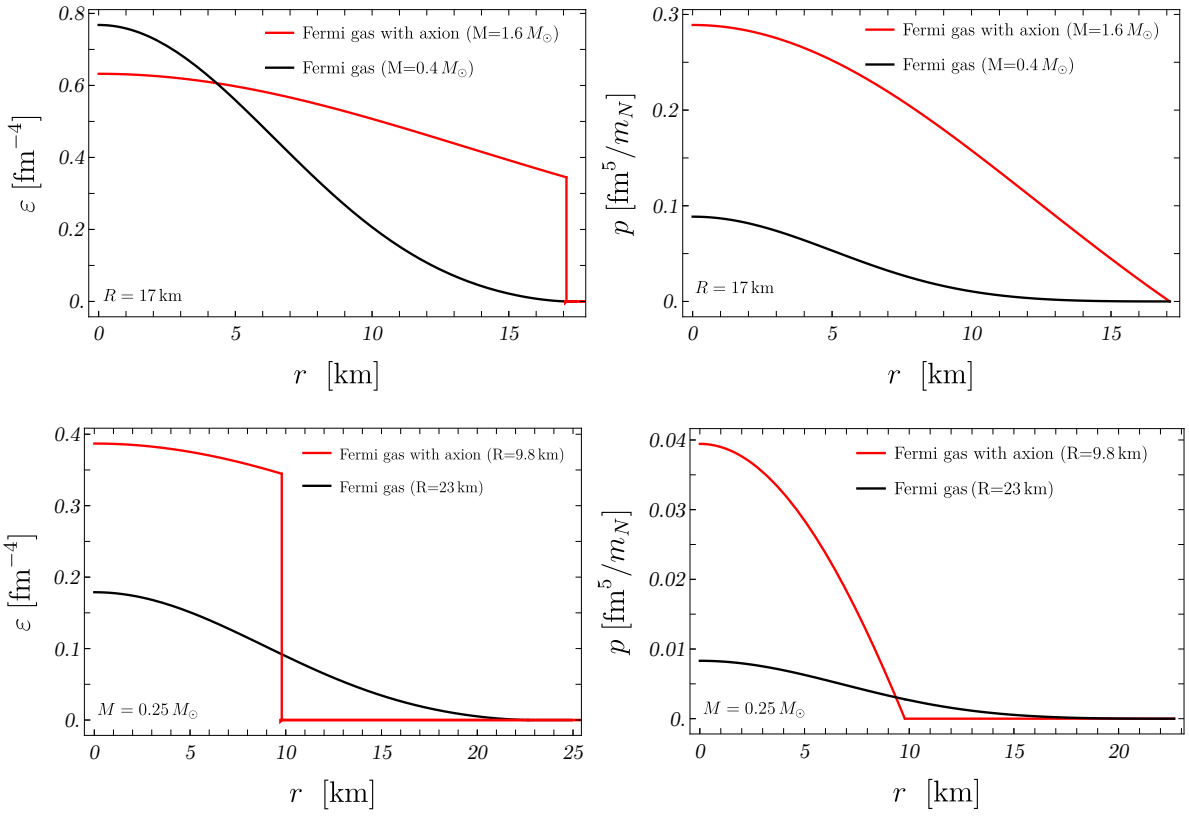

Figure 6.12: Top panel: Energy density (left) and pressure (right) profiles of solutions to the TOV equations. In red a configuration in the BM2 axion model with $R = 17\,\mathrm{km}$ and $M = 1.6\,M_\odot$, and in black the free Fermi gas solution of equal radius and $M = 0.4\,M_\odot$. Bottom panel: Profiles for stars of equal mass, $M = 0.25 M_\odot$, and $R = 9.8\,\mathrm{km}$ and $R = 23\,\mathrm{km}$ for the BM2 benchmark and the free Fermi gas, respectively.

region in which θ does not jump all the way to the point where $\partial m_*/\partial\theta = 0$ depends strongly on the shape of $V(\theta)$ and $m_*(\theta)$ and it has to be determined numerically.

Let us also discuss the validity of the negligible gradient limit, which we have assumed to hold in the discussion above. Finite gradient effects become important as soon as $\lambda_\phi \sim R$, where recall $\lambda_\phi \equiv f/\Lambda_{\rm eff}^2$, see Eq. (6.35). At high densities, we have $\Lambda_{\rm eff}^4 = -\rho_s(\partial m_*/\partial\theta)$ (see Eq. (C.31) and the associated discussion), which we can approximate as $\rho^{\rm NGS}[m - m_*(\theta_\infty)]$. As a result, most of the parameter space in Fig. 6.11 is valid for $f \ll (10^{17} - 10^{18})$ GeV, except for the lower-right corner, as indicated by the green lines. As we show below, finite gradient effects typically suppress the deviations from the ideal Fermi gas, thus the results of Fig. 6.11 represent the maximal effect one can expect from a sourced scalar.

Before moving to the discussion of specifics models with bounded $m_*(\theta)$, it is worth illustrating already here the effects of a sourced scalar field on the configuration of stars in the NGS. In Fig. 6.12 we show in red the energy density and pressure profiles of a representative point in the BM2 axion benchmark (see Fig. 6.11), and compare it with the free Fermi gas solution, in black, of either similar radius (top panel) or similar mass (bottom panel). The emergence of the NGS can be deduced from the behavior of the energy density at the edge of the star, where it does not vanish even though the pressure does. We do not show the scalar profile since for this benchmark $\lambda_\phi \ll R$ and therefore, the transition from θ_∞ to θ_0 is very narrowly localized at the

edge of the star.

The QCD axion

The QCD axion is an elegant solution to the strong CP problem as we have seen in Sec. 2.3 where the QCD $\bar{\theta}$-angle is promoted to a dynamical field. Here we introduce again the relevant properties of the QCD-axion. The Lagrangian at energies above the QCD scale is

$$\mathcal{L}_\phi \supset \frac{1}{2}(\partial\phi)^2 + \frac{g_s^2}{32\pi^2}\frac{\phi}{f}G_{\mu\nu}\tilde{G}^{\mu\nu}. \tag{6.53}$$

Here g_s is the strong coupling constant and $G_{\mu\nu}$ is the gluon field strength. At energies below the QCD confinement scale, a potential for the QCD axion is generated by non-perturbative effects,

$$V(\phi) = -m_\pi^2 f_\pi^2 \left(\sqrt{1 - z_{ud}\sin^2\left(\frac{\phi}{2f}\right)} - 1\right), \tag{6.54}$$

where $z_{ud} = 4m_u m_d/(m_u + m_d)^2$. In vacuum, this potential is minimized at $\langle\phi\rangle = 0$, such that CP is conserved, thus solving the strong CP problem.

A non-derivative coupling of the QCD axion to nucleons (neutrons and protons) is also generated at low energies, giving rise to a scalar-dependent fermion mass, see *e.g.* [11, 234]

$$m_*(\phi) = m_N + \sigma_{\pi N}\left(\sqrt{1 - z_{ud}\sin^2\left(\frac{\phi}{2f}\right)} - 1\right), \tag{6.55}$$

where $\sigma_{\pi N} \approx 50\,\mathrm{MeV}$ is the so-called nucleon sigma term, and we neglected isospin-violating contributions.

Following our definitions in Eq. (6.27), the QCD axion belongs to the case with $n = 2$, i.e. a quadratically coupled scalar, and we can identify

$$M_\phi^2 = \frac{2m_N}{z_{ud}\sigma_{\pi N}}f^2\,, \quad m_\phi^2 = \frac{z_{ud}}{4}\frac{m_\pi^2 f_\pi^2}{f^2}\,, \quad F_\phi = f_\phi = f\,. \tag{6.56}$$

Given that $M_\phi \gg F_\phi, f_\phi$, higher-order terms in ϕ are generically relevant. In addition, it is natural to identify the characteristic scale of the scalar with the axion decay constant f, therefore $f \equiv f$ and $\theta \equiv \phi/f$. The in-vacuum value of the scalar is then $\theta_0 = 0$.

At finite baryon density, one can identify an effective in-medium QCD axion potential, which at leading order in chiral perturbation theory reads [11, 186]

$$V_{\text{eff}}(\phi, \rho_s) = V(\phi) + \rho_s\left[m_*(\phi) - m_N\right] = \left(1 - \frac{\sigma_{\pi N}\rho_s}{m_\pi^2 f_\pi^2}\right)V(\phi)\,. \tag{6.57}$$

This potential is only valid at low densities, below around nuclear saturation, $\rho_s \simeq \rho \lesssim \rho_0$, while the exact form of the potential at high densities is unknown. This means that, for the QCD axion, keeping only the low-density potential is not realistic. Indeed, the critical density for scalarization Eq. (6.51), where $\theta = \theta_0$ becomes unstable, would be given by

$$\rho_s(0, \rho_c) = \frac{m_\pi^2 f_\pi^2}{\sigma_{\pi N}}\,, \tag{6.58}$$

which implies $\rho_c \gg \rho_0$ and therefore beyond perturbative control. In addition, at leading chiral order, the pions become massless at such densities, clearly invalidating our treatment of the axion. Nevertheless, it has been discussed in Chap. 5 (see Ref. [11]) that the sourcing of the QCD

axion could be triggered by Kaon condensation. The latter is a possibility widely considered in the literature, particularly concerning the so-called hyperon puzzle, see *e.g.* [153]. For the rest of this section, we assume that our simple treatment based on an axion-dependent nucleon mass given by Eq. (6.55), and the corresponding effective potential in Eq. (6.57), hold at all relevant densities, keeping in mind that the high-density dynamics of QCD has a critical impact on the possibility that the axion actually leads to scalarized NSs. What we learn is still useful since for a lighter version of the QCD axion, discussed in Sec. 6.2.3, the relevant densities are much lower and, therefore, under perturbative control.

In the negligible gradient limit, the system is minimized at $\theta_\infty = \pi$ for densities $\rho > \rho_c$, which implies

$$m_*(\theta_\infty) = m_N - \sigma_{\pi N}\left(1 - \sqrt{1 - z_{ud}}\right) , \quad V(\theta_\infty) = m_\pi^2 f_\pi^2 \left(1 - \sqrt{1 - z_{ud}}\right) . \tag{6.59}$$

Recall that in this case, the high-density value of the scalar corresponds to $\partial m_*/\partial\theta = 0$, which sets $\langle\phi\rangle = \pi f \ll M_\phi$. This constitutes, therefore, an example of screened scalarization, where the screening is due to higher-order terms in the interaction of the scalar with matter. NSs with a sourced QCD axion belong to the CE region only, see Fig. 6.11. This is because the chemical potential corresponding to the critical density is much larger than m_N; see the discussion in Sec. 6.2.2. Since the QCD axion with $\lambda_\phi \ll R$ is compatible with all the assumptions discussed at the beginning of Sec. 6.2.3, its M-R curve can be calculated given the values of $\{m_*(\theta_\infty), V(\theta_\infty)\}$, see the left panel of Fig. 6.13 (red curve).

Moving beyond the negligible gradient limit, we show the resulting M-R curves, found by solving the full coupled system of Eq. (3.1), in the right panel of Fig. 6.13, for different values of f. As expected, the phase transition from $\theta_0 = 0$ to $\theta_\infty = \pi$ leads to a softening of the EOS and therefore to less massive stars. The larger stars follow the free Fermi gas line, as their densities are sub-critical, i.e. $\rho(r = 0) < \rho_c$. Smaller and denser configurations are hybrid stars, composed of a core in the θ_∞ phase and an exterior region in the θ_0 phase. Two particular features can recognize the effect of the gradient. First, the inner core of the homogeneous stars (on the right branch) can have a region that is above the critical density, as long as this region is smaller than the effective in-medium wavelength of the scalar field $\lambda_\phi \propto f$. Higher values of f trace the Fermi gas line (solid black) until smaller radii and larger masses, at which point a large enough central region is created and it is energetically favorable for the high-density phase to form. Second, for high values of f the start of the hybrid branch consists of configurations where the axion is not fully sourced, i.e. the value of the field does not reach θ_∞ at the core, thus forming a thick-wall bubble. In such configurations, the transition region of the scalar inside the hybrid star occupies a significant fraction of the whole object, which modifies its equilibrium configuration. This explains the visible deviations of the finite f hybrid branches (solid colored lines) compared to the negligible gradient limit (dashed line). However, at higher internal pressures, once the QCD axion is fully sourced, indicating a thin-wall bubble, all the curves in the M-R plane converge, particularly to a similar maximal mass configuration. This is not a surprise, since the existence of a thin wall is tantamount to a negligible gradient, $\lambda_\phi \ll R$.

Lighter QCD axions

In this subsection we review the relevant properties of lighter than expected QCD axions as discussed in Sec. 2.5.

The QCD axion solution to the strong CP problem has been recently extended by relaxing the relation between the potential of the axion and its coupling to the SM [73, 74, 186]. These

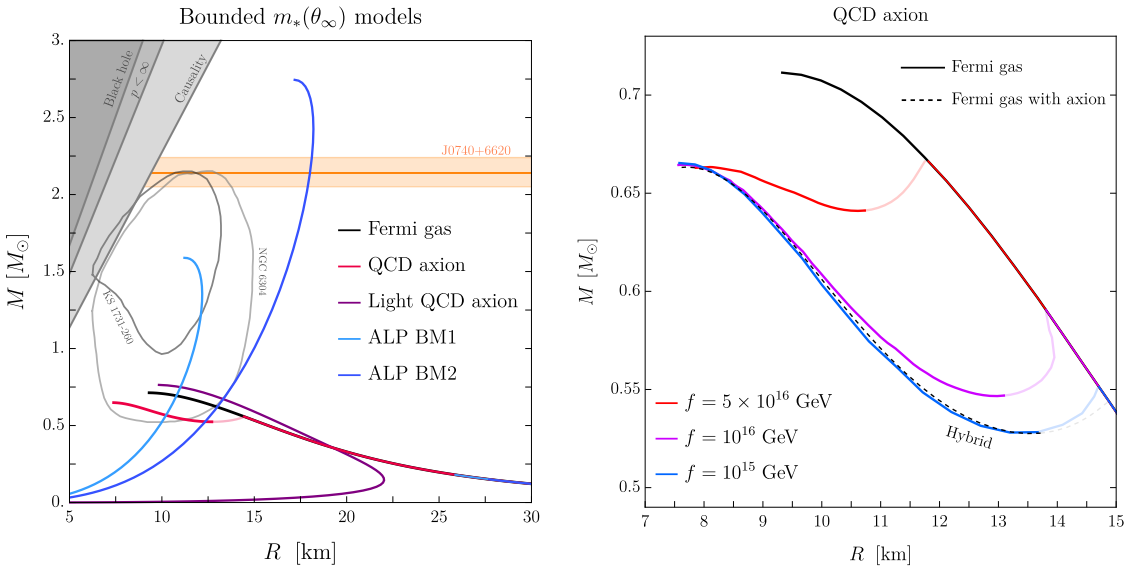

Figure 6.13: Left panel: M-R curves in the negligible gradient limit for several benchmark cases as indicated in the legend, with $\epsilon = 10^{-4}$ for the light QCD axion. Also shown two representative constraints at the 68% confidence level on NS masses and radii, obtained from low-mass X-ray binaries during quiescence (NGC 6304) and thermonuclear bursts (KS 1731-260), taken from [135]. In orange we plot the mass measurement of the millisecond pulsar J0740+6620, taken from [126]. The gray regions are the theoretically excluded regions with $C = GM/R \leqslant 1/2$ (Black hole), Buchdahl's limit $C \leqslant 4/9$ ($p < \infty$), and $C \lesssim 0.35$ (Causality; see the discussion below Eq. (6.43)). Right panel: M-R curves for the QCD axion. The free Fermi gas without the axion (solid black), the negligible gradient limit (dashed black), and including finite gradient effects for $f = \{5 \times 10^{16}, 10^{16}, 10^{15}\}$GeV in (solid) red, purple, and blue respectively. The light-colored curves are unstable configurations.

QCD axions are lighter than usual, a fact that gives rise to novel astrophysical signatures [14, 75, 186, 235].

For our purposes, the only yet key difference w.r.t. the standard QCD axion is a suppressed (in-vacuum) axion potential, which can be parametrized as

$$V(\phi) = -\epsilon m_\pi^2 f_\pi^2 \left(\sqrt{1 - z_{ud} \sin^2\left(\frac{\phi}{2f}\right)} - 1 \right) , \tag{6.60}$$

with $\epsilon < 1$. Conversely, the axion-dependent nucleon mass remains the same, see Eq. (6.55). Therefore, this model can be characterized by the same scales as the QCD axion, Eq. (6.56), except for the scalar mass, which now reads

$$m_\phi^2 = \epsilon \frac{z_{ud}}{4} \frac{m_\pi^2 f_\pi^2}{f^2} . \tag{6.61}$$

As a consequence, the effective potential at finite density is given by

$$V_{\text{eff}}(\phi, \rho_s) = \left(1 - \frac{\sigma_{\pi N} \rho_s}{\epsilon m_\pi^2 f_\pi^2}\right) V(\phi) . \tag{6.62}$$

Due to the relative enhancement of the finite density corrections, the critical density where θ_0 is no longer a minimum is ϵ-suppressed compared to that of the QCD axion,

$$\rho_s(0, \rho_c) = \epsilon \frac{m_\pi^2 f_\pi^2}{\sigma_{\pi N}} . \tag{6.63}$$

This is crucial since, as opposed to the QCD axion, for small enough ϵ the transition to the θ_∞ phase may occur at such low densities that chiral perturbation theory is valid and the pions are heavy ($\rho_c < \rho_0$), making our treatment in terms of a scalar-dependent nucleon mass and Eq. (6.62) a viable approximation. In that case, we can reliably infer that in the "high-density" regime, $\rho > \rho_c$, $\partial m_*/\partial\theta = 0$ sets $\theta_\infty = \pi$ in the negligible gradient limit. While this leads to the same $m_*(\theta_\infty)$ as for the QCD axion, $V(\theta_\infty)$ is ϵ-suppressed,

$$m_*(\theta_\infty) = m_N - \sigma_{\pi N} \left(1 - \sqrt{1 - z_{ud}}\right) , \quad V(\theta_\infty) = \epsilon m_\pi^2 f_\pi^2 \left(1 - \sqrt{1 - z_{ud}}\right) . \tag{6.64}$$

Because of the smaller potential in the scalarized phase, the NGS is now accessible if ϵ is small enough. Since all the parameters in Eq. (6.64) except for ϵ are fixed experimentally ($z_{ud} \approx 0.88$, $m_\pi \approx 135\,\text{MeV}$, $f_\pi \approx 92\,\text{MeV}$), one can phrase the condition for the existence of a NGS, see Eq. (6.50), as the following upper bound

$$\epsilon \lesssim \frac{4\sqrt{2}}{15\pi^2} \frac{m_N^4}{m_\pi^2 f_\pi^2} \left(\frac{\sigma_{\pi N}}{m_N}\right)^{5/2} \left(1 - \sqrt{1 - z_{ud}}\right)^{3/2} \approx 0.07 . \tag{6.65}$$

at leading order in $\sigma_{\pi N}/m_N$ (in the non-relativistic limit). The number density of the axionic (absolutely stable) ground state is given, under the same approximations, by

$$\rho^{\text{NGS}} \sim [m_*(\theta_\infty) V(\theta_\infty)]^{3/5} \sim \left(\epsilon m_N m_\pi^2 f_\pi^2\right)^{3/5} . \tag{6.66}$$

Since the light QCD axion with $\lambda_\phi \ll R$ is compatible with all the assumptions discussed at the beginning of Sec. 6.2.3, its M-R curve can be calculated given the values of $\{m_*(\theta_\infty), V(\theta_\infty)\}$, see the left panel of Fig. 6.13 (purple curve). As expected, since the EOS of the NGS is slightly

stiffer, it leads to slightly more massive stars than the free Fermi gas, enhancing the maximal mass of NSs by $(m_N/m_*(\theta_\infty))^2 - 1 \approx 10\%$.

Moving beyond the negligible gradient limit, we show the resulting M-R curves, found by solving the full coupled system of Eq. (3.1), in the left panel of Fig. 6.14, for different values of f. Let us note that comparing the analytic estimate in C.31 with the end of the meta-stable branch, one finds $\mathcal{O}(1)$ deviations from finite gradient effects. While expected, this has implications for the robustness of bounds on lighter QCD axions derived from GW observations from the NS merger GW170817 [235]; indeed, assuming similar deviations away from the $\lambda_\phi \ll R$ limit for the NSs in the binary, we find a weakening of the bound at large f, precisely where they are relevant, by a factor of a few. Interestingly, we find that the axion halo responsible for the long-range force, which extends much further than the radius of the star (defined by $p_\psi(R) = 0$) contributes negligibly to the mass of the system.

While lighter QCD axions lead to a moderate enhancement of the maximal NS mass, they also lead to other striking signatures. The instability of the EOS at intermediate densities, namely between the critical density and NGS density, leads to a gap in the M-R curve between the meta-stable branch and the stable branch, clearly visible in Fig. 6.14. As explained in Ref. [14], the gap moves to smaller radii for higher values of f. Ideally, once the M-R plane is sufficiently populated with accurately measured masses and radii of NSs, the observation of such a gap would be a smoking-gun signal for this type of BSM physics, since standard QCD EOSs do not predict such gaps. On the other hand, the non-observation of a gap would lead to tight constraints on the parameter space of such models. This rationale has been recently followed in Ref. [14], where the M-R distribution of white dwarfs was used, leading to the experimental bound $\epsilon \lesssim 10^{-8}$, stronger than the bounds from the Earth and the Sun [186]. We stress that the bounds arising from the existence of a NGS accessible in white dwarfs, and the corresponding gap in radii, are qualitatively very different than the strategy proposed in Ref. [186], which relies on the change of the properties of nuclei, and the corresponding change in X-ray emission, when a (lighter) QCD axion is displaced to $\theta = \pi$ [234]. Let us also recall that there are other (weaker) astrophysical and cosmological bounds on f, see [87] as well as [89, 275], which rely on the derivative couplings of axions to the nucleon axial current and the nucleon EDM, which also arise at low energies from Eq. (6.53).

Another interesting prediction associated with lighter QCD axions is the existence of SBOs (see Sec. 6.2.2), with a range of radii that can potentially span many orders of magnitude, from microscopic to a few km, depending on the value of f. At zero temperature, these objects are absolutely stable and cannot decay. We leave the study of the phenomenology of these objects for future work.

Axion-like particles

Motivated by the interesting phenomenological signatures associated with the existence of a new ground state of matter in lighter versions of the QCD axion, in this section, we wish to explore the possibility that a light scalar has a larger (non-derivative) coupling to nucleons while keeping its potential tunable. A possible UV completion of such a scenario, based on a $f(\phi)GG$ interaction above the QCD scale, is presented in App. C.4.

For concreteness, we choose the bounded function $f(\phi) = (1 - \cos(\phi/f))/2$, such that the scalar-dependent nucleon mass and the scalar potential are

$$m_*(\theta) = m_N \left[1 + \frac{g}{2}(\cos\theta - 1)\right], \quad V(\theta) = -\Lambda^4(\cos\theta - 1), \tag{6.67}$$

where $\theta \equiv \phi/f$, the dimensionless factor g parametrizes the reduction of the fermion mass when $\theta \neq \theta_0 = 0$, and the scale Λ sets the overall scale of the potential.

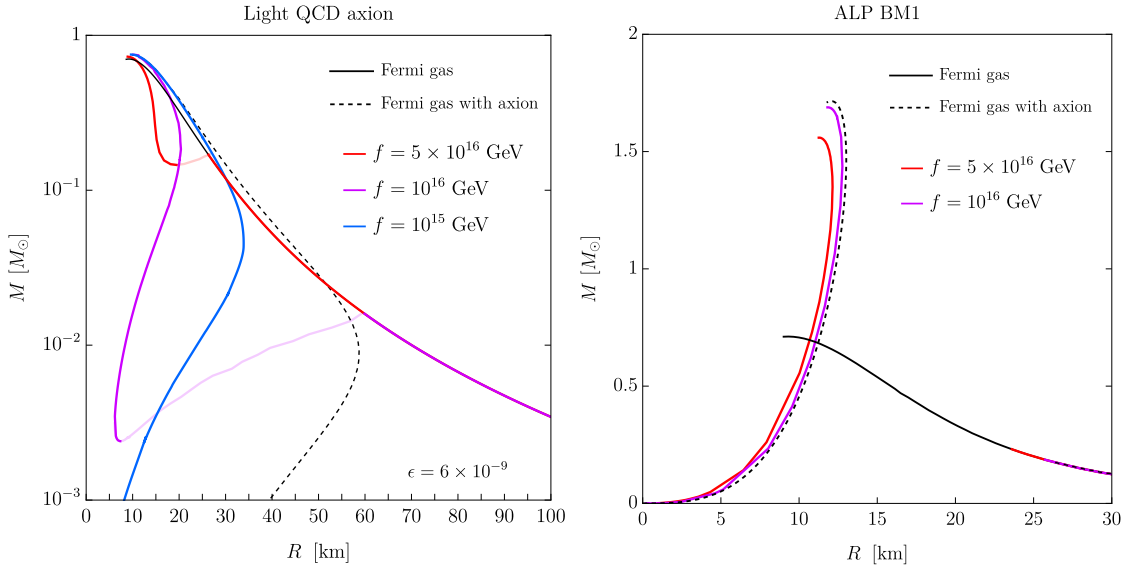

Figure 6.14: Left panel: M-R curves for a light QCD axions with $\epsilon = 6 \times 10^{-9}$. The free fermi gas without axion (solid black), the negligible gradient limit (dashed black), and including finite gradient effects for $f = \{5 \times 10^{16}, 10^{16}, 10^{15}\}$GeV in (solid) red, purple, and blue respectively. The light-colored curves are unstable configurations. Note that the metastable branch for the lowest f is not within the range of the plot. Right panel: M-R curves for the ALP benchmark BM1. The free Fermi gas without axion (solid black), the negligible gradient limit (dashed black), and including finite gradient effects for $f = \{5 \times 10^{16}, 10^{16}\}$GeV in (solid) red and purple, respectively.

Following Eq. (6.27), we further identify $n = 2$ and

$$M_\phi^2 = \frac{4f^2}{g}\,, \quad m_\phi^2 = \frac{\Lambda^4}{f^2}\,, \quad F_\phi = f_\phi = f\,, \tag{6.68}$$

with $M_\phi \gg F_\phi, f_\phi$ when $g \ll 1$.

As in the previous sections, it is illuminating to first consider the negligible gradient limit. At densities above the critical density, implicitly given by

$$\rho_s(0, \rho_c) = \frac{2\Lambda^4}{g m_N}\,, \tag{6.69}$$

the system is minimized at $\theta_\infty = \pi$ for $0 < g < 1$. The (unbounded) case $g \geq 1$ will be discussed in Sec. 6.2.3. For negative g, the scalar field will always stay at $\theta_0 = 0$ since any deviation from the in-vacuum value would result in an increase of the nucleon mass. As for the (light) QCD axion, scalarization is screened if $g \ll 1$ due to higher-order scalar terms in m_*.

We use Eq. (6.67) as a simple parametrization of any bounded-m_* model that can be mapped to any point in Fig. 6.11 according to

$$m_*(\theta_\infty) = m_N(1 - g)\,, \quad V(\theta_\infty) = 2\Lambda^4\,. \tag{6.70}$$

For the sake of exposition, let us derive the condition for the existence of the NGS in two different simple limits. For a non-relativistic Fermi gas, the NGS arises when

$$\Lambda^4 \lesssim \frac{2\sqrt{2}}{15\pi^2} m_N^4 g^{5/2} + O(g^{7/2})\,, \quad \text{(NR)} \tag{6.71}$$

where we expanded in $g \ll 1$. The corresponding ground state number density is given by

$$\rho^{\rm NGS} \sim \left(m_N \Lambda^4\right)^{3/5} + O(g)\,. \quad \text{(NR)} \tag{6.72}$$

Instead, in the ultra-relativistic limit and expanding around $g = 1$, there exists a NGS for

$$\Lambda^4 \lesssim \frac{m_N^4}{24\pi^2} + O((1-g)^2)\,, \quad \text{(UR)} \tag{6.73}$$

with the ground state starting at a density

$$\rho^{\rm NGS} \sim 2\Lambda^3\,, \quad \text{(UR)} \tag{6.74}$$

with no $(1-g)$ corrections at leading UR order. Note that although we have chosen $g \ll 1$ for a NR system and $1 - g \ll 1$ for an UR one, there certainly exist UR configurations with $g \simeq 0$ and NR ones with $g \simeq 1$.

While the simple ALP model defined by Eq. (6.67), in the negligible gradient limit, is a proxy for any model that populates the parameter space $\{m_*(\theta_\infty), V(\theta_\infty)\}$, with the resulting maximal mass and corresponding radii shown in Fig. 6.11, finite gradient effects, on the other hand, are model-dependent; they are sensitive to the particular shape of the scalar potential and the scalar-dependent fermion mass.

To illustrate these finite gradient effects, we consider a benchmark point marked in Fig. 6.11 as BM1. This benchmark is defined by

$$\text{BM1:} \quad g = 0.5\,,\ \Lambda = 0.075\text{GeV}\,, \tag{6.75}$$

where we expect to find meta-stable configurations with densities that are at most of the order of the critical density, in this case

$$\rho_c \approx 0.017\,\text{fm}^{-3} \approx 0.1\rho_0\,. \tag{6.76}$$

The absolutely stable configurations are composed purely of the NGS phase, characterized by number and energy densities similar to those of nuclei

$$\rho^{\rm NGS} \approx 0.17\,\text{fm}^{-3} \approx \rho_0\,, \quad \varepsilon^{\rm NGS} \simeq m_N \rho^{\rm NGS} \approx \varepsilon_0 = 2.5 \times 10^{14}\,\text{g/cm}^3. \tag{6.77}$$

Taking gradient effects into account, we find SBOs with their (numerically computed) minimal and maximal radii given by

$$R_{\rm min}^{\rm SBO} \simeq (25\,\text{m})\left(\frac{f}{10^{15}\text{GeV}}\right), \quad R_{\rm max}^{\rm SBO} \simeq (2.3\,\text{km})\left(\frac{f}{10^{15}\text{GeV}}\right)^{1/3}. \tag{6.78}$$

These values are consistent with the analytical estimates given in App. C.3. For objects with radii larger than $R_{\rm max}^{\rm SBO}$, gravity becomes relevant and eventually dominant over the scalar force. However, as long as the energy density of the object is approximately constant, the mass and radius are related by Eq. (6.49), in this case

$$M \simeq (5 \times 10^{-4} M_\odot)\left(\frac{R}{1\,\text{km}}\right)^3, \tag{6.79}$$

which is independent of f.

In the right panel of Fig. 6.14 we show the M-R curves, found by solving the full coupled system of Eq. (3.1), for $f = \{5 \times 10^{16}, 10^{16}\}$GeV and in the negligible gradient approximation ($f/M_{\rm P} \to 0$). At large radii, we find the low-density meta-stable branch corresponding to the free Fermi gas with no scalarization, while at small radii we find the absolutely stable branch, with a large gap (compared to the typical radius) between them. Note as well that the maximal NS mass with a sourced ALP is much larger than without scalarization. As shown in the left panel of Fig. 6.13, for values of f such that scalar gradients are negligible, the enhancement of the maximal mass is even more pronounced for the benchmark denoted by BM2 (dark blue curve), defined by a larger $g = 2/3$ compared to BM1, with the same Λ. Indeed, in the case of large g, i.e. small $m_*(\theta_\infty)$, this ALP model leads to a large enhancement of the maximal mass of NSs, following Eq. (6.41). This is in contrast to the expected reduction in mass due to the softening of the EOS as a result of additional SM degrees of freedom, *e.g.* hyperons or more exotic possibilities such as meson condensation and first-order phase transitions, see *e.g.* [101,127,152].

Unbounded $m_*(\theta)$ solutions

We now turn to the analysis of models in which $m_*(\theta)$ is unbounded and vanishes asymptotically, i.e. $m_*(\theta = \theta_\infty) = 0$, which defines the high-density value of the scalar θ_∞. As discussed in Sec. 6.2.2, θ approaches θ_∞ at asymptotically large densities, following the curve in Eq. (6.37). At such high densities and whenever scalar gradients can be neglected, the maximal mass and corresponding radius only depend on $V(\theta_\infty)$ and are given by Eq. (6.42), which recall follows from the ultra-relativistic limit of the EOS. In the following, we consider two concrete realizations of such a scenario: linearly- and quadratically-coupled scalar fields, $n = 1$ and 2 in our classification of Sec. 6.2.1.

Linear coupling to matter Let us consider a scalar that couples linearly to nucleons and has a simple quartic potential,

$$m_*(\phi) = m_N \left(1 - \frac{\phi}{M_\phi}\right) \,, \quad V(\phi) = \frac{1}{2} m_\phi^2 \phi^2 + \frac{\lambda}{4}\phi^4 . \tag{6.80}$$

Following Eq. (6.27), we can easily identify the scales that characterize this model, besides its mass m_ϕ and interaction strength with matter $1/M_\phi$,

$$F_\phi \to \infty \,, \quad f_\phi = \sqrt{\frac{2m_\phi^2}{\lambda}} \,. \tag{6.81}$$

In addition, since the high-density limiting value of the scalar field corresponds to a vanishing m_*, it is natural to identify the typical scale of the field as $f \equiv M_\phi$, thus $\theta \equiv \phi/M_\phi$.

Let us start by considering the limit $f_\phi \gg M_\phi$, in which we can neglect the quartic term in the potential for all field excursions, i.e. higher-order terms in ϕ are irrelevant. The stellar structure of this model was recently investigated in Ref. [257]. In the following, we re-derive some of the results and pay special attention to the impact of fifth-force bounds.

A linearly-coupled scalar is always sourced at finite density, leading to a fifth force even between dilute and small objects. Despite this fact, as discussed in Sec. 6.2.2 for the unbounded-m_* case, only when densities are of order $\rho_{s,\infty}$ in Eq. (6.37) we can expect appreciable effects due to the scalar field being significantly displaced from its in-vacuum value, i.e. $\theta \sim \theta_\infty = 1$.

This corresponds to number densities (implicitly) given by

$$\rho_s(\theta \sim \theta_\infty, \rho) \sim \rho_{s,\infty} = \frac{m_\phi^2 M_\phi^2}{m_N}\,, \tag{6.82}$$

and assumes finite gradient effects are negligible, i.e.

$$R \gg \lambda_\phi \sim \frac{M_\phi}{\sqrt{\rho_{s,\infty}|\partial m_*(\theta)/\partial\theta|}} = m_\phi^{-1}, \tag{6.83}$$

following Eq. (C.31) (taking $\bar{\rho}_s \sim \rho_{s,\infty}$ and $\Delta\theta \sim 1$). The parameter space of this model is effectively one-dimensional, since

$$m_* \sim m_N\,, \quad V \sim m_\phi^2 M_\phi^2\,, \tag{6.84}$$

where recall $m_*(\theta_\infty) = 0$, and therefore the dimensionless ratio

$$c \equiv \frac{1}{2}\frac{m_\phi^2 M_\phi^2}{m_N^4}\,. \tag{6.85}$$

suffices to describe the phase of the system. As expected, only for small values of the scalar potential, i.e. of c, there is a NGS (see the discussion around Eq. (6.40)),

$$c \lesssim 0.015 \equiv c^{\rm NGS}\,. \tag{6.86}$$

This transition value between the existence of NGS and the CE region has been found numerically, using the solution of the scalar EOM in the negligible gradient limit, Eq. (6.36). We find agreement with the results of Ref. [257].

In Fig. 6.15, we show where the transition between the NGS and the CE region lies in the $\{m_\phi, M_\phi\}$ plane, and compare it with current fifth-force bounds [276], which exclude the blue-shaded region. We have dashed the CE-NGS boundary line where gradient effects become relevant, and we have cut it off altogether at the edge of the gray-shaded region, where gradient effects are so strong that the field can no longer be significantly sourced. In this region, the scalar has therefore little to no effect on the configuration of NSs.

In this regard, it is important to take into consideration the size of the scalarized NSs in this scenario. Close to the CE-NGS boundary, we find as expected no strong deviations from the standard radii of NSs. In contrast, deep inside the NGS ($c \ll c^{\rm NGS}$), we find

$$M_{\rm max} \sim (0.7\,M_\odot)\sqrt{\frac{c^{\rm NGS}}{c}}\,, \quad R(M_{\rm max}) \sim (9.3\,{\rm km})\sqrt{\frac{c^{\rm NGS}}{c}}\,, \tag{6.87}$$

in agreement with Eq. (6.42). Given that $\lambda_\phi \sim 1/m_\phi$, see Eq. (6.83), and the parametric estimate for the free Fermi gas radius $R \sim M_{\rm P}/m_N^2$, this implies that the negligible gradient approximation is valid as long as $M_\phi \ll \sqrt{c^{\rm NGS}} M_{\rm P} \approx M_{\rm P}/10$.

As can be seen in Fig. 6.15, the parameter space compatible with fifth-force bounds, which extend to $m_\phi \sim \mu{\rm m}^{-1}$ for $M_\phi \sim M_{\rm P}$, is far from the NGS line. Assuming that these bounds can be circumvented, the details of the EOS and stellar structure in this model can be found in Ref. [257]. However, we expect that a situation where any screening takes place on Earth, such that fifth-force bounds are evaded, yet it does not take place on NSs, is far from generic at the very least.

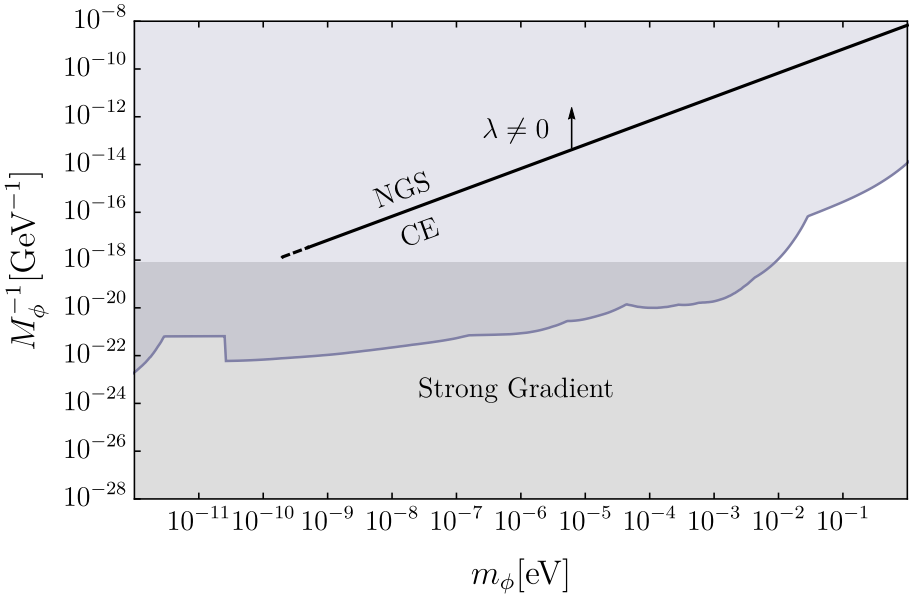

Figure 6.15: Parameter space of the linearly-coupled scalar model. The black line delimits the transition between the NGS (above) and the CE region (below). The arrow indicates that this transition happens at smaller values of M_ϕ for non-negligible λ. These lines become dashed when neglecting gradient effects in NSs ceases to be a good approximation and ends at the gray-shaded region, which indicates a strong gradient where the scalar field has no effect. In light-blue shaded, we plot fifth-force bounds taken from [276], leading to the conclusion that all the interesting parameter space is excluded.

We conclude this section by considering the effect of the quartic term in the scalar potential. As indicated by the black arrow in Fig. 6.15, a non-negligible λ, i.e. $f_\phi \lesssim M_\phi$, would cause the NGS-CE boundary line to shift up. Due to the larger contribution to the energy density and pressure from the potential,

$$V(\theta_\infty) = \frac{1}{2} m_\phi^2 M_\phi^2 \left(1 + \frac{M_\phi^2}{f_\phi^2}\right) , \tag{6.88}$$

a smaller value of M_ϕ is needed to reduce the fermion mass and reach the NGS. Such a conclusion is valid only as long as (scalar) densities are above the new density

$$\rho_{s,\infty}^{(\lambda)} = \rho_{s,\infty} \frac{M_\phi^2}{f_\phi^2} , \tag{6.89}$$

where we have taken $f_\phi \ll M_\phi$ and $\rho_{s,\infty}$ is given in Eq. (6.82). For intermediate densities $\rho_{s,\infty} < \rho < \rho_{s,\infty}^{(\lambda)}$, we effectively have a screened system in which $\langle\phi\rangle \sim f_\phi \ll M_\phi$.

Quadratic coupling to matter Let us consider next a scalar field that couples quadratically to nucleons,

$$m_*(\phi) = m_N \left(1 - \frac{\phi^2}{M_\phi^2}\right) , \quad V(\phi) = \frac{1}{2} m_\phi^2 \phi^2 + \frac{\lambda}{4} \phi^4 . \tag{6.90}$$

Besides the mass m_ϕ and the interaction strength with matter set by $1/M_\phi$, we identify the scales associated with higher-order ϕ terms as in the linear model, see Eq. (6.81). Likewise, the characteristic scale of the field can be conveniently chosen to be $f \equiv M_\phi$, therefore we define $\theta \equiv \phi/M_\phi$.[11]

As in the linear model, we can differentiate between two opposing limits, the mass-dominated regime in which higher-order terms in the scalar potential are irrelevant, $f_\phi^2 \gg M_\phi^2$, and the quartic-dominated regime where instead these control the dynamics, $f_\phi^2 \ll M_\phi^2$. In each of these regions, the parameter space that determines the phase of the system is effectively one-dimensional,

$$c \equiv \frac{1}{2} \frac{m_\phi^2 M_\phi^2}{m_N^4} , \quad \text{or} \quad c_\lambda \equiv c \frac{M_\phi^2}{f_\phi^2} = \frac{\lambda M_\phi^4}{4 m_N^4} , \tag{6.91}$$

for the mass- or quartic-dominated regimes, respectively. They have a clear physical interpretation as the contributions to the scalar potential in the high-density limit, $V(\theta_\infty)$, in units of m_N^4 (recall $m_*(\theta_\infty) = 0$),

$$V(\theta_\infty) = \frac{1}{2} m_\phi^2 M_\phi^2 \left(1 + \frac{M_\phi^2}{f_\phi^2}\right) = m_N^4 \left(c + c_\lambda\right) . \tag{6.92}$$

As in the linear case, the transition values that separate the CE and NGS regions are found numerically (neglecting gradients). The NGS exists if the dimensionless coefficients satisfy the upper bounds

$$c \lesssim 0.0093 \equiv c^{\rm NGS} , \quad \text{and} \quad c_\lambda \lesssim 0.015 \equiv c_\lambda^{\rm NGS} , \tag{6.93}$$

[11] Note that in the $g \gg 1$ limit of the ALP model of Sec. 6.2.3, fields excursion are small ($\theta \ll 1$), thus the ALP model can be mapped to this quadratic model with $m_\phi^2 = \Lambda^4/f^2$, $\lambda = -(\Lambda/f)^4/6$ and $M_\phi^2 = 4f^2/g$.

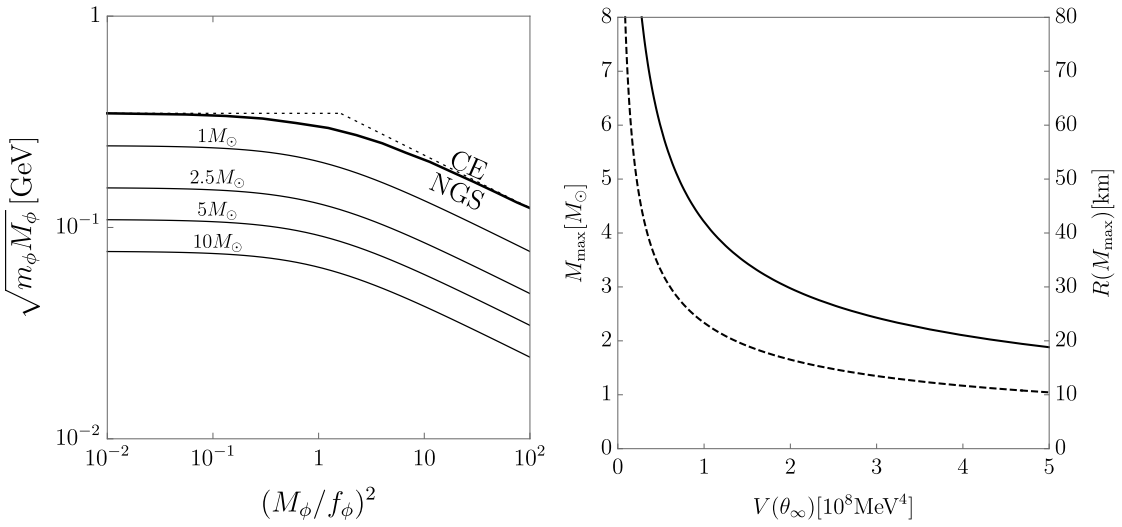

Figure 6.16: Left panel: Parameter space of the quadratic model, with CE above and the NGS below the solid thick line. The dashed line denotes the same NGS-CE boundary but in the $(M_\phi/f_\phi)^2 \ll 1$ or $(M_\phi/f_\phi)^2 \gg 1$ limit. Thin-black: contours of maximal mass, for clarity only up to $10M_\odot$. Right panel: Maximal mass (solid) and corresponding radius (dashed) of NSs as a function of $V(\theta_\infty)$.

for $f_\phi^2 \gg M_\phi^2$ and $f_\phi^2 \ll M_\phi^2$, respectively. This is shown as the dashed line in Fig. 6.16.

If both contributions to the potential are of similar size, i.e. $f_\phi^2 \sim M_\phi^2$, the parameter space is two-dimensional. The boundary between the CE and NGS region is again found numerically and shown as the solid thick line in Fig. 6.16.

The typical densities associated with the NGS can be estimated according to Eq. (6.37). For the mass- or quartic-dominated regions these are given, respectively, by

$$\rho_{s,\infty} = \frac{m_\phi^2 M_\phi^2}{2m_N} = m_N^3 c\,, \quad \text{or} \quad \rho_{s,\infty}^{(\lambda)} = 2\rho_{s,\infty}\frac{M_\phi^2}{f_\phi^2} = 2m_N^3 c_\lambda\,. \tag{6.94}$$

The scalar field approaches $\theta \to \theta_\infty$ asymptotically for densities $\rho \gg \rho_{s,\infty}$ or $\rho \gg \rho_{s,\infty}^{(\lambda)}$, under the assumption that the field gradient is negligible, i.e. $R \gg \lambda_\phi$ with $\lambda_\phi \sim 1/m_\phi$ or $\lambda_\phi \sim f_\phi/(m_\phi M_\phi) \ll 1/m_\phi$ for a negligible or dominant quartic term, respectively.

Let us also note that in this model, as in the bounded models discussed in Sec. 6.2.3 where the scalars also couple quadratically to matter at leading order in ϕ, one can identify a critical density where the in-vacuum value of the scalar, $\theta_0 = 0$, becomes unstable, see Eq. (6.51). We find, as expected, that this is given by $\rho_s(0, \rho_c) = \rho_{s,\infty}$. In addition, in the quartic-dominated regime, i.e. $f_\phi^2 \ll M_\phi^2$, we have $\rho_{s,\infty} \ll \rho_{s,\infty}^{(\lambda)}$. At intermediate densities, $\rho_{s,\infty} < \rho < \rho_{s,\infty}^{(\lambda)}$, the field is destabilized at the origin, $\rho > \rho_c$, thus triggering scalarization, yet $\theta \sim \theta_\infty$ is never reached. In such a case, the scalar is screened, and we effectively have $\langle\phi\rangle \sim f_\phi$ as a limiting value.

Deep inside the NGS region, $\theta \simeq \theta_\infty$, $m_* \ll m_N$, and the maximal star mass and corresponding radius are well approximated by Eq. (6.42), with the only relevant dimensionful parameter given by $V(\theta_\infty)$ in Eq. (6.92). There are $\mathcal{O}(1)$ deviations from these approximations near the NGS-CE boundary, while the deviations are reduced away from the boundary. Numerically,

we find *e.g.* that $\theta^{\rm NGS}$ is $\sim 10\%$ away from θ_∞ for $c \simeq 10c^{\rm NGS}$, while it is only $\sim 1\%$ away for $c \simeq 100c^{\rm NGS}$, where $c^{\rm NGS}$ are given in Eq. (6.93) for the mass- and quartic-dominated regimes. The numerically obtained $M_{\rm max}$ and $R(M_{\rm max})$ are shown in the right panel of Fig. 6.16.

As opposed to the linearly-coupled scalar, this model leads to large NSs masses (and radii), SBOs, and a gap in the M-R curve, without being in tension with current fifth-force bounds (see e.g. [277] for a recent analysis on the experimental tests of the forces mediated by quadratically-coupled scalars). It is worth pointing out that these conclusions rely on the validity of our effective description, Eq. (6.90), at large field excursions, such that higher-order ϕ terms in $m_*(\phi)$ do not play any role. This is a non-trivial requirement on the underlying dynamics, especially since we assume our model to be valid towards small nucleon masses.

Finally, we discuss other potentially relevant bounds on this type of scalars bilinearly coupled to nucleons. First, the astrophysical and cosmological bounds that apply to (light) QCD axions (see end of Sec. 6.2.3), which exhibit as well as quadratic couplings to nuclei, do not generically apply here; these bounds are associated with IR couplings different than those from $m_*(\phi)\bar\psi\psi$, which are predicted from our knowledge of the UV interactions of the scalar above the QCD scale, Eq. (6.53). Therefore, without specifying the interactions of the scalar above $\Lambda_{\rm QCD}$, such type of bounds do not generically apply. An example of a possible UV completion, based on a coupling to the gluon field strength, is provided in App. C.4. Still, robust, general bounds can potentially be derived given only Eq. (6.90). For instance, as show in Ref. [14], a reduction of the nucleon mass has a strong impact on the configuration of white dwarfs, whenever these are large and dense enough to trigger scalarization. It would be interesting to recast such an analysis to constrain the parameter space of the quadratic model. For other interesting directions, see e.g. [278], where a bound due to excessive energy loss in supernovae from pair emission of scalars via $NN \to NN\phi\phi$ was estimated to be $M_\phi \gtrsim 15\,\text{TeV}$. Let us note however that if the scalar is sourced during the supernova, a linear coupling for the ϕ excitation is present and suppressed by $\sim 1/M_\phi$. Accordingly, we estimate the bound from single emission to be $M_\phi \gtrsim 10^7\,\text{TeV}$.

6.2.4 Scalar-tensor theories

Scalar-tensor theories of the type first proposed by Damour and Esposito-Farèse [242] can be equivalently described, as we have done in this paper, via scalar-dependent masses for the (non-interacting) matter fields. In this section, we re-derive this well-known fact in the context of a free Fermi gas. For a recent discussion, see [279].

The action for a conformally coupled scalar field, in the Einstein frame, is given by

$$S = \int d^4x\sqrt{-g}\left[\frac{M_{\rm P}^2}{16\pi^2}R + \frac{1}{2}g^{\mu\nu}\partial_\mu\phi\partial_\nu\phi - V(\phi)\right] + S_m[\Psi, \tilde g_{\mu\nu}]\,, \tag{6.95}$$

with the matter action

$$S_m = \int d^4x\sqrt{-\tilde g}\left[\bar\Psi i\tilde e^\mu{}_a\gamma^a\tilde D_\mu\Psi - m\bar\Psi\Psi\right]\,, \quad \tilde g_{\mu\nu} = A^2(\phi)g_{\mu\nu}\,, \tag{6.96}$$

where $\tilde D_\mu = \partial_\mu - i\tilde\omega_\mu$ is the covariant derivative of a fermion field Ψ in the scalar-dependent metric $\tilde g_{\mu\nu}$. The vielbein and spin connection associated with the matter metric $\tilde g_{\mu\nu}$ (a.k.a. Jordan frame) are related to those of the metric $g_{\mu\nu}$ (Einstein frame) as

$$\tilde e^\mu{}_a = A\, e^\mu{}_a\,, \quad \tilde\omega_\mu = \omega_\mu + \frac{1}{4}\sigma_{ab}(e^{\nu b}e^a{}_\mu - e^{\nu a}e^b{}_\mu)\partial_\nu\log A\,. \tag{6.97}$$

Noticing in addition that $\sqrt{-\tilde g} = A^4\sqrt{-g}$, one can perform a scalar-dependent field redefinition of the fermion, $\psi \equiv A^{3/2}\Psi$ (known as conformal dressing), such that any dependence of the

matter action on A is eliminated except in the mass term, leading to Eq. (6.28) with

$$m_*(\phi) = A(\phi)m\,. \tag{6.98}$$

This shows the equivalence of the two pictures when matter is composed of a free massive field. An equivalent derivation holds if there are more than one species.

At the level of the EOMs and the matter EOS, this equivalence can be seen by noting that the matter source term in the scalar EOM Eq. (6.5a) is just (working with $\phi = f\theta$)

$$\rho_s \frac{\partial m_*(\phi)}{\partial \phi} = T_\psi \frac{\partial \log A(\phi)}{\partial \phi}\,, \tag{6.99}$$

since $T_\psi = g^{\mu\nu}(T_\psi)_{\mu\nu} = \epsilon_\psi - 3p_\psi = m_*\rho_s$, which matches the source term of a conformally coupled scalar from Eq. (6.96). Furthermore, let us point out the fact that untilded (Einstein frame) quantities being functions of m_* and μ, *e.g.* $p_\psi = p_\psi(m_*(\phi), \mu)$, is consistent with the fact that the energy-momentum tensors in the Einstein and Jordan frames are related by $(T_\psi)_{\mu\nu} = A^2(\tilde{T}_\Psi)_{\mu\nu}$, thus $p_\psi = A^4\tilde{p}_\Psi$ with $\tilde{p}_\Psi = \tilde{p}_\Psi(m, \tilde{\mu})$ and $\tilde{\mu} = \mu/A$ (likewise $\tilde{k}_F = \sqrt{\tilde{\mu}^2 - m^2} = k_F/A$).

When the matter fields are not free, i.e. departing from the free Fermi gas limit, encoding all the interactions of a conformally coupled scalar as ϕ-dependent masses is certainly not enough. For instance, returning to the case of interest in which the fermion ψ is a nucleon, the introduction of pion-nucleon interactions in the presence of a conformally coupled scalar would require not only scalar-dependent pion masses, $m^2_{\pi*}(\phi) = A^2(\phi)m^2_\pi$, but a scalar-dependent pion decay constant as well, $f_{\pi*}(\phi) = A(\phi)f_\pi$.

This can also be understood by considering the interactions of a conformally coupled scalar above the QCD scale. While classically (neglecting quark masses for simplicity), the QCD action with conformally-dressed fields is a priori independent of ϕ, the trace anomaly gives rise to the interaction

$$\mathcal{L}_{G\phi} = -\log A(\phi)\frac{\beta(g_s)}{2g_s}G^2_{\mu\nu}\,, \tag{6.100}$$

where $G_{\mu\nu}$ is the gluon field strength, g_s the QCD coupling constant and β its beta function, $\beta(g_s) = \partial g_s/\partial \log\mu$. It is this interaction that leads to the ϕ-dependence of the low-energy parameters after QCD confinement, see *e.g.* [280–282].

This brings us to our final comment, which concerns the radiative stability of a light conformally coupled scalar. The trace anomaly is a manifestation of the fact that scale invariance is not a robust symmetry at the quantum level, with a non-vanishing beta function understood as an explicit breaking of the dilation symmetry. Such a symmetry would naturally ensure a hierarchically small mass for the scalar, if this were identified with a bona-fide dilaton, fixing $A(\phi) = e^{\phi/M_\phi}$, see e.g. [283] for a neat discussion. However, since the symmetry is explicitly broken, one should expect a contribution to the dilaton potential

$$\Delta V(\phi) \sim \frac{M^4_{\rm UV}}{16\pi^2}\frac{\beta}{g_s}\frac{\phi}{M_\phi}\,e^{4\phi/M_\phi}\,, \tag{6.101}$$

on top of the quartic potential allowed by scale invariance, $V \sim M^2_{\rm UV}M^2_\phi e^{4\phi/M_\phi}$, with $M_{\rm UV}$ the cutoff of the scalar effective field theory. If instead the function $A(\phi)$ corresponds to a generic conformally coupled scalar, one would expect $\Delta V \sim (M^2_{\rm UV}/4\pi)^2(\beta/g_s)\log A(\phi)$. In any case, the lightness of the scalar, required to yield appreciable effects in stars, is endangered by quantum effects, unless the cutoff is very low or tuning is invoked, see also App. C.4.

We finish this section with a brief comment on the previous literature. To our knowledge, most works on the configuration of NSs in scalar-tensor theories Eq. (6.95) have focussed in a regime where $M_\phi \sim M_{\rm P}$, see *e.g.* [268, 284–287] and [237] for a review. As we have discussed in Secs. 6.2.3 and 6.2.3, in this regime the effects of the scalar gradient cannot be neglected. In addition, for the functions $A(\phi)$ and $V(\phi)$ chosen in these works, the NGS of matter is either absent or it has not been identified. While it would be interesting to reasses these models in light of our new (microscopic) perspective on the scalarized matter EOS, we recall that the NGS is generically present in the so-called strongly scalarized scenario where $M_\phi \ll M_{\rm P}$, see Figs. 6.15 and 6.16.

6.2.5 Conclusions

In this work, we have presented a comprehensive and detailed study of the impact of scalarization on the configuration of NSs. This is a non-trivial back-reaction effect: a dense and large star can source the scalar field, which in turn alters the structure of the star. We have shown that at leading order the relevant (non-derivative) couplings of the scalar to matter can be encoded as a scalar-dependent nucleon mass. This allowed us to study in a straightforward way how the EOS of matter, modeled as a free Fermi gas, is affected by scalarization. In the infinite volume limit, we have shown that the total energy density and pressure of the system receives, beyond the Fermi gas contribution, a contribution from the scalar potential. It is the interplay between the change in the matter EOS due to a reduction of the nucleon mass and the scalar potential that determines the energetically preferred state of the system.

Our analysis has uncovered what can be considered one of the most salient effects of scalarization: the emergence of a new ground state of (nuclear) matter at some finite number density and zero pressure. The NGS emerges if the change in nucleon mass dominates over the scalar potential, leading to a larger binding energy per nucleon compared to well-separated nucleons. We have found that the NGS is quite generic and allowed by current constraints by exploring several scenarios beyond the SM with a light scalar: the QCD axion and lighter generalization thereof, generic pseudo-Nambu-Goldstone bosons (which we termed ALPs), and a simple scalar quadratically coupled to nucleons and with a quartic potential.

The phenomenological implications of scalarization, and in particular of the emergence of the NGS, are striking. Because a reduction of the nucleon mass leads to a stiffer EOS, NS masses far beyond the maximal mass predicted by the standard causal bounds can be reached. These stars are also much larger, such that their compactness is approximately the same as that of a free Fermi gas. On the other hand, the contribution of the scalar potential to the energy and pressure softens the EOS. When this effect dominates, we have found stars in a hybrid configuration, where a scalarized core coexists with the rest of the star in the standard phase. NSs with a phase transition within them are lighter yet unusually compact. In addition, because the standard phase of matter is in fact meta-stable yet (very) long-lived when the scalarized NGS exists, we have found that the M-R relation exhibits an instability gap in radii, in which no stars should be found. In connection to this fact, we have discovered that the new, absolutely stable branch extends down to small self-bound objects in the NGS, held together by the scalar force instead of by gravity. These SBOs have properties, such as mass and compactness, which greatly differ from those of standard stellar remnants.

We have provided analytic, semi-model-independent estimates of key quantities such as critical densities for scalarization, maximal mass of NSs and corresponding radius, as well as minimal and maximal sizes of SBOs. Whenever possible, we have also analytically determined the boundary of the parameter space where the NGS exists, as well as the new ground-state number

density of matter, for the different scalar scenarios under consideration. These estimates make the physics transparent, and we have checked all of them against numerical simulations. In this regard, we paid special attention to finite gradient effects, associated with the non-trivial profile of the scalar in finite volume systems, i.e. stars in our case. These contributions to the energy density and (anisotropic) pressure are important when the in-medium characteristic wavelength of the scalar field is of the order of the size of the object, and they lead to important departures, especially when the typical scale of the scalar f is close to $M_{\rm P}$.

We have also made explicit the connection between our analysis and the popular scalar-tensor theories, in the hope that our fresh perspective will contribute to elucidating their full dynamics and whole range of phenomenological implications.

Our results shed new light on the already clear importance of future electromagnetic and gravitational wave observations of compact stellar objects in general and NSs in particular. Indeed, observatories such as NICER and LIGO have the potential to discover signs, like very heavy NSs and gaps in radii, that could ideally be considered as smoking-gun signals of the scalarized NGS of matter. Certainly, many degeneracies are at play here, such as astrophysical uncertainties in the expected NS-BH mass gap along with the experimental difficulties in discerning between these two types of compact objects, large experimental errors in the determination of NS radii, or theoretical uncertainties in the EOS of NS matter. However, many of these constitute in principle a reducible background that could be greatly reduced thanks to the vigorous current and future experimental program in astrophysics. Besides, while a leap in our theoretical understanding of dense matter is not in foresight, for many of the scalar scenarios we considered, the relevant densities fall within perturbative control. Indeed, bounds on lighter QCD axions have already been derived from the effects of the NGS on the configuration of the much more dilute white dwarfs [14]. The uncertainty in the EOS is, unfortunately, most pronounced for the case of the QCD axion, where the possibility of scalarization itself is speculative. Furthermore, let us note that, with the exception of the linearly-coupled scalar, for all the other models we considered there is wide parameter space open to further experimental exploration. This in turn means these models can be tested with other, complementary probes: pulsar timing, stellar energy loss, long-range forces in binary mergers, or superradiance (see e.g. [76] for an overview of the status of (light) QCD axions).

We conclude with a summary of the directions that we believe deserve further investigation. An important question that we did not explore concerns the formation of stellar objects in the NGS, for which there are many non-trivial aspects to consider. Importantly, its answer is of no consequence to our findings, which concern the long-time, non-dynamical structure of stellar remnants. A related question concerns the cosmological evolution and phenomenological implications of the SBOs, which can be as small as the Compton wavelength of the scalar.

It would be interesting to extend our analysis to more realistic EOSs. We have found, using a free Fermi gas description, that pure neutron matter can be effectively self-bound at high densities due to the scalar dynamics. We expect that, by considering a more realistic EOS, this picture does not qualitatively change and asymmetric nuclear matter is self-bound as well. From our ongoing work we already have indications that this is the case when including nuclear interactions mediated by pion exchange, even incorporating the effects that scalarization has on the interactions themselves (e.g. a change in the mass of the pions); we have explicitly checked this for lighter QCD axions. Therefore, the emergence of a scalarized ground state of matter seems to be robust in the regime where we retain perturbative control.

Chapter 7

Phase Transitions from Stars

In this chapter, we study the potential detection of a transition between distinct vacua, specifically those initiated by dense compact objects such as stars.

To facilitate a lucid discussion of the underlying physics, we commence the first section of this chapter by considering a straightforward potential, following Coleman's framework (reference [288]). This potential involves a quartic of a single scalar field denoted as ϕ, incorporating a Z_2 symmetry, $\phi \to -\phi$, which is explicitly broken by a linear term. The potential of the scalar field is such that in vacuum it sits in the metastable minimum.

The existence of a barrier separating the two minima is argued to diminish with increasing density, motivated by known examples such as QCD. Consequently, for sufficiently high densities, the metastable minimum vanishes, resulting in the development of a non-trivial scalar profile within the dense system similar to as we have seen in Chap. 5 and Chap. 6. While in our previous models the scalar was in the true ground state of the theory in vacuum, in the scenario where it sits in a meta-stable minimum in vaccum, an instability can occur that can lead to the permeation of a bubble throughout the entire system. This is of course dependent on the density profile and evolution of the star under consideration. If triggered, these bubbles can escape and propagate indefinitely, driven by the scalar residing in the absolute minimum within the bubble which now extends far beyond the star. One can think of the star as a sort of catalyst for the scalar phase transition. These seeded phase transitions hold potential catastrophic implications for our universe.

Given our primary focus on classically allowed transitions to the true vacuum, they manifest as soon as sufficiently dense and large stars are formed. These late-phase transitions, occurring at redshifts approximately $z \sim 20$, give rise to a change in the vacuum energy relative to the value from measurements of the Cosmic Microwave Background (CMB). This enables us to constrain the parameters of the scalar potential, subject to the type of star that triggers the phase transition. However, if the energy difference between the two minima is sufficiently minute, these phase transitions might prove non-lethal and potentially observable through future cosmological and astrophysical observations.

In the second part of this chapter we introduce the Higgs hierarchy problem, which motivates models of dynamical relaxation such as the relaxion (see Ref. [10]), characterized by a scalar potential in the form of a tilted cosine. We discuss relaxion models in the third part of the chapter and apply our findings of part one to relaxion models. The magnitude of the relaxion potential is determined by the QCD quark condensate or the Higgs vacuum expectation value (VEV), both sensitive to baryonic densities found in stars. Consequently, the formation and subsequent escape of such bubbles yield stringent new constraints on the parameter space of these models.

All figures and substantial portions of the text presented in this chapter originate from references [12] and [13].

7.1 Density induced Vacuum Instabilities

This section is organized as follows. We present the simple scalar potential with two minima separated by a density dependent barrier in Sec. 7.3.1 and study its properties. The next section, Sec. 7.1.2, is devoted to the properties of compact objects relevant for classical bubble formation. This will be the topic of Sec. 7.1.3, where we continue with the determination of conditions that lead to the bubble escaping the star and have a look at the formation of bubble via quantum tunneling in the presence of a density background. After this we are left with the exploration of phenomenological consequences of star triggered late-time phase transitions in Sec. 7.1.8, in particular the constraints on the parameters of the model, that arise due to the change in vacuum energy. In App. D we show some simplifying approximations, the effect of ultra-high densities as well as the impact of gravitational forces on the bubble dynamics.

7.1.1 General Scalar Potential

The potential we consider is just the familiar quartic potential with a linear tilt,

$$V(\phi) = -\tfrac{1}{3\sqrt{3}}\,\Lambda_{\rm R}^4\,\frac{\phi}{f} + \tfrac{1}{8}\,\Lambda_{\rm B}^4\left(\frac{\phi^2}{f^2}-1\right)^2 . \tag{7.1}$$

$\Lambda_{\rm R}$ and $\Lambda_{\rm B}$ are the scales that control the size of what we denote as linear "rolling" and quartic "barrier" terms respectively (numerical factors are introduced for notational convenience), while f parametrizes the field distance between the two minima. The potential has two minima as long as

$$\delta^2 \equiv 1 - \frac{\Lambda_{\rm R}^4}{\Lambda_{\rm B}^4} > 0\,. \tag{7.2}$$

For $1-\delta^2 \ll 1$ the minima are located at $\phi_\pm \simeq \pm f$, and in particular the metastable minimum ϕ_- is a *deep* minimum. Instead, for $\delta^2 \ll 1$ the minima are at $\phi_- \simeq -f/\sqrt{3}$ and $\phi_+ \simeq 2f/\sqrt{3}$, and ϕ_- is *shallow*. The difference between these two types of metastable minima is evident from the mass of the scalar

$$m_\phi^2 \simeq \begin{cases} \sqrt{\frac{2}{3}}\frac{\Lambda_{\rm B}^4}{f^2}\delta\,, & \text{(shallow)} \\ \frac{\Lambda_{\rm B}^4}{f^2}\,. & \text{(deep)} \end{cases} \tag{7.3}$$

For a shallow minimum ($\delta^2 \ll 1$) the mass is parametrically suppressed with respect to the usual expectation, which is instead reproduced in the case of a deep minimum ($1-\delta^2 \ll 1$). Another quantity of phenomenological interest, which is very different between shallow and deep minima, is the height of the potential barrier,

$$\Delta V_{\rm top} \simeq \begin{cases} \frac{4}{27}\sqrt{\frac{2}{3}}\,\Lambda_{\rm B}^4\,\delta^3\,, & \text{(shallow)} \\ \frac{1}{8}\,\Lambda_{\rm B}^4\,. & \text{(deep)} \end{cases} \tag{7.4}$$

The suppression of the barrier in the case of minima with $\delta^2 \ll 1$ implies that even a small perturbation of the potential can easily destabilize the scalar field.

Let us note that while shallow metastable minima might naively be deemed as tuned, they naturally appear in relaxion models [10], where the barrier term is a periodic function of the

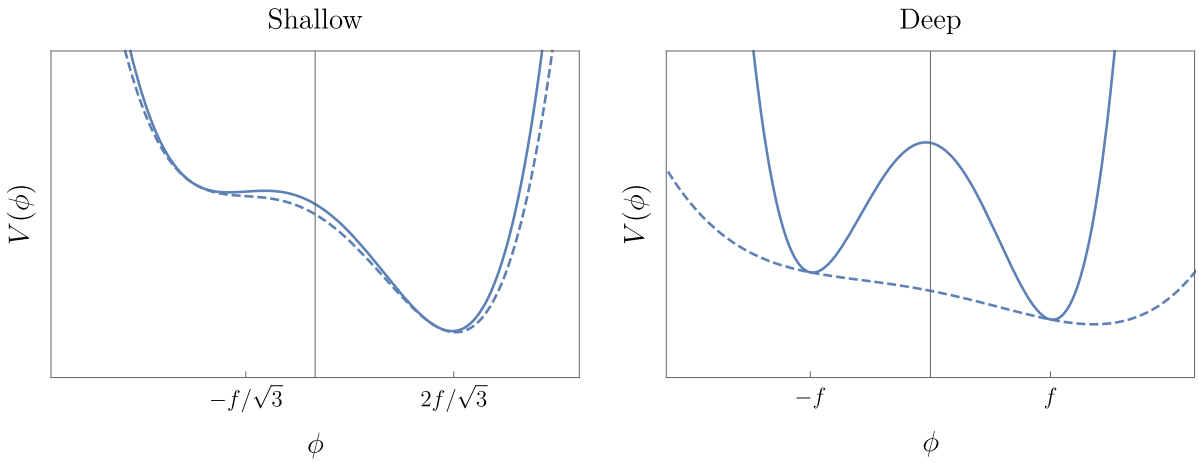

Figure 7.1: Potentials with shallow (left) and deep (right) minima in vacuum (solid) and in medium for a density ρ slightly larger than critical (dashed).

scalar field, e.g. $\cos(\phi/f)$, whose amplitude increases very slowly with each ϕ oscillation. There, the first minima of the potential are found when the barriers get just large enough, i.e. $\Lambda_{\rm B}^4 \approx \Lambda_{\rm R}^4$, or in our notation $\delta^2 \ll 1$. The quartic potential we have taken as a case study in Eq. (7.56) is a simplified version of the relaxion case.

Finite density

Finite density can impact a scalar potential in several ways, depending on how the scalar couples to the matter fields that constitute the dense system. In general, density corrections can be encoded as an additional term in the potential that explicitly depends on (number) density, ρ, and vanishes in vacuum, i.e. $\rho = 0$. For the sake of concreteness, in this section we focus on the scenario where these corrections can be entirely encoded as a non-trivial density dependence of the parameters of the potential Eq. (7.56). In particular, we consider the situation where the barrier $\Lambda_{\rm B}$ depends on density, and define the dimensionless quantity

$$\frac{\Lambda_{\rm B}^4(\rho)}{\Lambda_{\rm B}^4} \equiv 1 - \zeta(\rho)\,, \tag{7.5}$$

with $\zeta(\rho) \geqslant 0$ and $\zeta(0) = 0$. We want to stress that we have seen this exact behavior when discussing properties of the quark condensate at finite densities in Sec. 5.2.1. Note that the definitions of the above quantity differ slightly in the two sections, i.e. $\zeta_{\bar{q}q} \neq \zeta$ from Eq. (5.41).

This scenario is naturally realized when $\Lambda_{\rm B}$ itself is determined by the vacuum expectation value of an operator that is sensitive to finite density corrections. Perhaps the simplest example in the SM is provided by the QCD quark condensate, that is $\Lambda_{\rm B}^4 \propto \langle\bar{q}q\rangle \sim \Lambda_{\rm QCD}^3$, which is well-known to linearly decrease with (small) baryon number density $\rho_N = \langle N^\dagger N\rangle$ with ρ the baryon field [193]. In the notation of Eq. (7.5), this would imply, at leading order in density, that $\zeta(\rho_N) \propto \rho_N/\Lambda_{\rm QCD}^4$ in systems with a non-zero nucleon density, such as stars. The case of a $\Lambda_{\rm B}$ proportional to any other QCD condensate that is non-zero in vacuum and changes with baryon density, such as a gluon condensate, belongs to the same class. Within the realm of SM operators, the only other qualitatively different case is given by a barrier set by the Higgs VEV, that is $\Lambda_{\rm B}^4 \propto \langle h^2\rangle = v^2$. There, the coupling of the Higgs field to fermions, $y_\psi h\bar{\psi}\psi$, displaces its expectation value when in a (non-relativistic) ψ background, $\langle\bar{\psi}\psi\rangle \simeq \langle\psi^\dagger\psi\rangle \neq 0$. Considering

once again a system with a non-vanishing baryon density, the small displacement in the Higgs would lead, at leading order, to $\zeta(\rho_N) \propto \rho_N/m_h^2 v^2$. Let us note that $\Lambda_{\rm B}^4 \propto \langle \bar{q}q \rangle$ is realized by the QCD-axion [11,186], as well as by those models of relaxation of the electroweak scale where the relaxion is identified with the QCD-axion [10]. The case where the leading finite density effects are due to a shift of the Higgs field, $\Lambda_{\rm B}^4 \propto \langle h \rangle^2$, is found in non-QCD relaxion models [10], and it could arise as well in more general Higgs-portal models, e.g. [289]. A detailed discussion of finite density effects in these versions of the relaxion is found below. Going beyond the SM, we could, for instance, entertain the possibility that $\Lambda_{\rm B}$ originates from the confinement of a new QCD-like dynamics decoupled from the SM. Motivated by this case, we should further consider the existence of dark compact objects, a.k.a. dark stars [290–298], whose non-zero density can lead to a change of the scalar potential as in Eq. (7.5).

Because of the smaller barriers at finite density, the metastable minimum in vacuum is no longer a minimum in a dense system as soon as the condition Eq. (7.2), with $\Lambda_{\rm B}^4 \to \Lambda_{\rm B}^4(1-\zeta)$, is not satisfied. The critical value of ζ above which this destabilization occurs is

$$\zeta_c = 1 - \frac{\Lambda_{\rm R}^4}{\Lambda_{\rm B}^4} = \delta^2 \,. \tag{7.6}$$

It is evident from this expression that a shallow local minimum is more easily destabilized than a deep one, since $\zeta_c \ll 1$ for a shallow minimum while $\zeta_c \approx 1$ for a deep one. This is explicitly shown in Fig. 7.8.

We limit our discussion to $\zeta(\rho) \leqslant 1$, since otherwise the barrier term changes sign and the scalar potential is no longer bounded from below. This makes the analysis sensitive to higher-order terms in ϕ, which we have implicitly neglected; in other words, the scalar dynamics becomes UV sensitive and therefore no longer predictive. In addition, note that for what concerns the destabilization of the false vacuum, the relevant quantity is the ratio between the rolling and barrier scales. Therefore, we could just as well have considered a density dependent rolling term, $\Lambda_{\rm R}^4(\rho)$, as the source of the instability. However, as we show in Sec. 7.1.3, the formation of a scalar bubble inside a dense system of finite size, as well as its evolution, strongly depends on the magnitude of the rolling term. For this reason, in this Chapter we keep $\Lambda_{\rm R}$ density independent. Let us also point out that density is treated here a background field that eventually depends on space and time, see Sec. 7.1.2. Although we are phrasing our discussion of the fate of the metastable minimum in terms of a matter density, a priori other space-time dependent background fields could lead to similar effects on the scalar potential. An example where the role of density is played by a background electro-magnetic field will be presented for a relaxion model in Section 7.3.

As discussed above, for densities above the critical one, the scalar potential has a single minimum. We denote this minimum as $(\phi_+)_\rho$, such that it is clear that it is continuously connected, as the density is taken to zero, to the stable minimum in vacuum, ϕ_+. Let us note that close to criticality, i.e. for $\zeta(\rho) \simeq \zeta_c$, the in-density potential has the same form as a potential in vacuum with $\delta^2 \ll 1$, thus $\phi_{+\,\rho\simeq\rho_c} \simeq 2f/\sqrt{3}$. For the same reason, just before the critical density is reached, the in-medium metastable minimum is shallow and found at $-f/\sqrt{3}$, regardless of its value in vacuum ϕ_-. In contrast, far beyond the critical density, the single minimum of the potential is found at

$$\phi_{+\,\rho\gg\rho_c} \sim \left(\frac{1-\zeta_c}{1-\zeta(\rho)}\right)^{1/3} f \,, \tag{7.7}$$

which can be much larger than f if $\zeta \to 1$. Whenever the scalar potential has two minima, shallow or deep, at zero or non-zero density, the difference in the ground state energy between

them is given by

$$\Delta\Lambda \sim -\Lambda_{\rm R}^4\,, \tag{7.8}$$

up to an irrelevant $\mathcal{O}(1)$ factor.

We would like to emphasize that while in this Section we focus on a simple potential of the form Eq. (7.56), the analysis presented here is then applied in Sec. 7.3 to other types of potentials containing local minima separated by a density-dependent barrier. Furthermore, even though we pay particular attention to the fact that at finite density the scalar field can classically move to the true minimum of the potential, this is not the only case of interest; such a change of minimum could be classically forbidden at finite density as well, yet take place anyway due to a much shorter quantum-mechanical lifetime than in vacuum (see Sec. 7.1.7).

Let us comment here on the UV sensitivity of the scalar potential Eq. (7.56) and our assumptions on how it changes at finite density. Indeed, let us consider the case that $\Lambda_{\rm B}^4 = \alpha\langle h\rangle^2$, where α is just a proportionality factor. By closing the Higgs loop and cutting it off at a scale Λ_h, we obtain a contribution to the barrier term $\Delta\Lambda_{\rm B}^4 \sim \alpha(\Lambda_h/4\pi)^2$. We should then demand that this extra contribution does not erase the instability of the local minimum at finite density, which means $\Delta\Lambda_{\rm B}^4 \ll \Lambda_{\rm B}^4(\rho_c) \simeq \Lambda_{\rm R}^4$. This conditions translates into an upper bound on the cutoff of the scalar theory, $\Lambda_h \ll 4\pi\langle h\rangle\sqrt{1-\delta^2}$. Note this is larger for potentials with a shallow metastable minimum than for those with a deep minimum. Such a low cutoff does not endanger our analysis of the scalar field dynamics at finite density as long as $\Lambda_h \gg E_{\rm S}$, where $E_{\rm S}$ is the typical energy scale of the dense system. Similar conclusions apply to the other possible cases concerning the density dependence of $\Lambda_{\rm B}$, see the discussion below Eq. (7.5).[1] Besides, already from the quartic scalar interaction in Eq. (7.56), naturalness arguments indicate that new physics should appear at a scale $\Lambda_\phi \sim 4\pi f$ or below. Once again, we should demand that Λ_ϕ is significantly above $E_{\rm S}$.

7.1.2 Spherically Symmetric Dense Systems

In this section we study the properties of dense systems of finite size, in particular stars, relevant for the analysis in this section. We model the star as a spherically symmetric (non-rotating) object with a density profile that in general depends on radius and time, i.e. $\rho(r,t)$. The profile satisfies ($\rho' = d\rho/dr$),

$$\rho'(0,t) = 0\,, \qquad \rho(R_{\rm S}(t),t) = 0\,, \tag{7.9}$$

such that the density profile is differentiable at the origin, $r = 0$, and that the star ends at a finite radius, $r = R_{\rm S}$, respectively. In addition, we define a transition radius, $r = R_{\rm T}$, where the critical density is reached,

$$\rho(R_{\rm T}(t),t) = \rho_c\,. \tag{7.10}$$

We recall that at densities above critical, the local minimum of the potential is lost.

Since the scalar potential at finite density is minimized at a different value than in vacuum, minimization of the action forces the field to acquire a (spherically symmetric) non-trivial profile within and around the star, $\phi(r,t)$. This is determined by the classical EOM ($\dot\phi = d\phi/dt$, $\phi' = d\phi/dr$ and $V_{,\phi} = dV/d\phi$)

$$\ddot\phi - \phi'' - \frac{2}{r}\phi' = -V_{,\phi}\,, \tag{7.11}$$

[1] $\Lambda_{\rm B}$ is insensitive to the UV if e.g. the barrier term arises from the coupling of the scalar to the QCD topological charge, i.e. $\frac{1}{f}\phi G\tilde G$, which gives rise to a potential sensitive to $\Lambda_{\rm QCD}$ only. For instance, this is the case of the QCD-relaxion, where we recall that the corresponding scalar potential is of the form $\cos(\phi/f)$ instead of the simple quartic function we are considering.

where $V = V(\phi, \rho(r,t))$, with the boundary conditions

$$\phi'(0,t) = 0\,, \qquad \lim_{r\to\infty} \phi = \phi_-\,. \tag{7.12}$$

In order to solve Eq. (7.11) one needs to know the density profile of the star, which generically depends on non-trivial and in some cases not well-understood dynamics (e.g. the inner regions of NSs). If there is a large separation of scales in the problem, we can, as a first approximation, be agnostic of the details of the density profile, as we explain in the following. The characteristic scale controlling the classical evolution of the scalar profile, either in time or space, is determined by its potential. For the representative case that we are considering, Eq. (7.56), the EOM for the dimensionless field $\hat{\phi} \equiv \phi/f$ can be written as

$$\frac{\partial^2\hat{\phi}}{\partial\hat{t}^2} - \frac{\partial^2\hat{\phi}}{\partial\hat{r}^2} - \frac{2}{\hat{r}}\frac{\partial\hat{\phi}}{\partial\hat{r}} = 1 - \tfrac{3\sqrt{3}}{2}\frac{1-\zeta}{1-\zeta_c}(\hat{\phi}^2-1)\hat{\phi}\,, \tag{7.13}$$

where $\hat{r} = \mu r$, $\hat{t} = \mu t$, and

$$\mu^2 = \tfrac{1}{3\sqrt{3}}\frac{\Lambda_{\rm R}^4}{f^2} \sim \frac{\Lambda_{\rm R}^4}{f^2}\,. \tag{7.14}$$

For densities sufficiently above the critical one, such that $1-\zeta \ll 1-\zeta_c$, μ^{-1} sets the typical time and distance required for the scalar to move by $\Delta\hat{\phi} = \mathcal{O}(1)$. This is to be compared with the characteristic scales of the dense system.

Let us first discuss time evolution, i.e. the formation of the star. The dimensionless quantity $\mu T_{\rm S}$, where $T_{\rm S}$ is the characteristic time scale of the dense system, gives us a rough idea whether we can treat the evolution of the scalar field as effectively taking place in a nearly static, fixed system, or whether the time dependence of the scalar profile is comparable to (or much slower than) the typical time scale of the star. Indeed, for $\mu T_{\rm S} \gg 1$ the field reacts fast to changes in the background density profile, therefore we can describe the scalar dynamics as a *quasi-static* (or *adiabatic*) process, in which $\dot{\phi}$ and additional time derivatives can be neglected. On the other hand, for $\mu T_{\rm S} \ll 1$ the field reacts slow compared to the evolution of the star, in which case the evolution of the scalar profile can be described in a *sudden* (or *non-adiabatic*) approximation, where the formation of the star can be treated as an instantaneous change from vacuum to $\rho(r) \neq 0$ and ϕ starts "rolling" down the in-medium potential.

In the adiabatic limit, $\mu T_{\rm S} \gg 1$, the scalar profile can be found at any given time $t = \bar{t}$ during the formation of the star by solving its *time-independent* EOM, within a fixed background density $\rho(r) = \rho(r,\bar{t})$.[2] We shall consider simple density profiles that can be parametrized as

$$\rho(r) = \rho_o(\bar{t})\, g(r/R_{\rm S}(\bar{t}))\,, \tag{7.15}$$

where the function $g(x)$ fully encodes the radial dependence, with $g(0) = 1$ such that the density at the center is set by ρ_o, $g(R_{\rm T}/R_{\rm S}) = \rho_c/\rho_o$, and $g(1) = 0$. While obtaining the specific form of $\rho(r)$ at a given $\bar{t}$ is generically a complicated problem, the only quantities of qualitative relevance for our analysis are $R_{\rm T}$, the radius below which the critical density is surpassed, that is where the in-vacuo potential barrier disappears and the scalar can potentially be displaced by $O(f)$, and $\Delta R_{\rm T} = R_{\rm S} - R_{\rm T}$, the size of the transition region towards the end of the star, where the potential barrier reappears. We find that non-trivial dynamics take place when $\mu R_{\rm T} \sim 1$, and additionally when $\mu\Delta R_{\rm T} \sim 1$, see Sec. 7.3.2. The value of $R_{\rm T}$ depends on the value of the

[2] In practice, numerically calculating these static bounce-like solutions is challenging since it requires a finely-tuned boundary condition at the origin. More details on our numerical calculations can be found at the end of this section.

critical density, which in turn depends on how the scalar potential changes with density. For typical density profiles in which the central density is significantly larger than the critical one, one generically finds $R_{\rm T} \sim R_{\rm S}$ [104, 105]. This then implies that $\Delta R_{\rm T} \sim R_{\rm S}$ as well. In addition, since in practice each class of stars, e.g. NSs, WD stars, or main-sequence stars like the Sun, covers a range of radii, we also expect to find a range of values for $R_{\rm T}/R_{\rm S}$ and $\Delta R_{\rm T}/R_{\rm S}$, where generically both ratios are $\mathcal{O}(1)$.

In this paper we concentrate on the adiabatic limit just described. Since a non-trivial scalar profile develops when $\mu R_{\rm S} \sim 1$, we focus on stellar processes where the relevant time scale is $T_{\rm S} \gg R_{\rm S}$. The general properties of NSs has been extensively discussed in Sec. 3.2, however, not the dynamics. The birth of a NS follows from the gravitational collapse of the core of a massive star, which leads to a supernova (SN) explosion, see e.g. [299, 300]. While the details of this process are not completely understood, it has been reliably inferred that densities reach and surpass nuclear saturation in a time $T_{\rm S} = T_{\rm NS} \sim 1\,{\rm s}$. Within this time, the size of the core of the star in which densities have exceeded ρ_0 is an $\mathcal{O}(1)$ fraction of the total size of the final NS, i.e. $R_{\rm T} \sim R_{\rm S} = R_{\rm NS}$. Since the typical radius of a NS is $R_{\rm NS} \sim 10\,{\rm km}$, see Sec. 3.2, we find $R_{\rm NS} \ll T_{\rm S}$, justifying the quasi-static approximation. Similar conclusions can be reached for other types of stars, for instance WD stars, discussed in Sec. 3.1, or the Sun ($R_\odot \approx 7 \times 10^5\,{\rm km}$, $\rho_\odot \approx 7 \times 10^{-9}\,{\rm MeV}^3$). Note that the above-mentioned densities set the typical scales in the potential at which our mechanism is relevant. In any case, for completeness we briefly discuss the regime $\mu T_{\rm S} \ll 1$ in App. D.5.

For the reader's reference, the scale μ^{-1} is of order of the typical size of a NS for e.g. the potential parameters

$$\mu R_{\rm S} \sim 5 \left(\frac{R_{\rm S}}{10\,{\rm km}}\right) \left(\frac{\Lambda_{\rm R}}{10\,{\rm eV}}\right)^2 \left(\frac{1\,{\rm TeV}}{f}\right) . \tag{7.16}$$

Several additional comments are in order. First, in the special case that the (central) density happens to be very close to ρ_c, one naturally expects $R_{\rm T} \ll R_{\rm S}$, making the analysis more sensitive to the specifics of the density profile. Second, since the reaction time of the scalar gets suppressed by $\zeta - \zeta_c$, the adiabatic approximation naively fails at some arbitrarily small time interval around the time in which $\zeta \to \zeta_c$.[3] Lastly, our study neglects the effects of temperature altogether. This is a good approximation in most situations, yet for e.g. the Sun as well as in SN explosions, temperature could be as important as density, i.e. $T^3 \sim \rho$. Nevertheless, we note that for the motivated cases in which $\Lambda_{\rm B}^4 \sim \Lambda_{\rm QCD}^3$ or $\Lambda_{\rm B}^4 \sim v^2$, the effect of a finite temperature would generically go in the same destabilizing direction as density, i.e. decreasing the size of the potential barriers, reinforcing our conclusions regarding the formation and escape of a scalar bubble.

Let us conclude this section by briefly discussing our numerical analysis. In order to verify the theoretical results we present in Sec. 7.3.2, we have solved the *time-dependent* EOM presented in Eq. (7.13) numerically, assuming simple dependencies, e.g. $\zeta \propto \rho(r,t)$. The initial conditions for the scalar field are homogenous, i.e. $\phi(r,0) = \phi_-$ and $\dot\phi(r,0) = 0$. We implement a slow evolution of the density profile from $\rho(r,0) = 0$ to some final configuration Eq. (7.15) at $\bar t = T_{\rm S}$,

[3] In a spatially homogeneous situation, the local condition that determines if the scalar is able to follow the minimum of the potential can be expressed as $\dot\phi \gtrsim (d\phi_{\rm min}/d\rho)\,\dot\rho$, where $\phi_{\rm min} \simeq \phi_-$ as long the metastable minimum exists, and $(\phi_+)_\rho$ otherwise. However, if the system exhibits a non-trivial spatial dependence, that this condition is satisfied does not imply that the scalar actually follows the minimum; it becomes crucial to consider the gradient energy of the field, which impedes large field displacements. Besides, we note that right at the critical point, $\rho = \rho_c$, there is a discontinuous jump in $\phi_{\rm min}$ (from ϕ_- to $(\phi_+)_\rho$) and therefore $d\phi_{\rm min}/d\rho \to \infty$; equivalently, at the critical density $\mu \to 0$, since $\zeta = \zeta_c$, thus $\mu T_{\rm S} \to 0$. Time dependence can then become important, yet only if the system is large enough to render the gradient energy negligible compared to kinetic energy the field acquires rolling down the potential.

with $g(x) = 1-x^2$. Importantly, we fix $\mu T_{\rm S} \gg 1$, in agreement with the adiabatic limit. We verify that the quasi-static solutions we find have negligible amounts of kinetic energy compared to their gradient and potential energies. This quasi-static picture is maintained up until an instability takes place, i.e. until our numerical simulations display an expanding bubble that escapes from the star. Importantly, under our assumptions, the exact details of the star formation do not affect the quantitative scaling we present in the next section for the formation and escape of scalar bubbles.

7.1.3 Bubble Formation and Evolution

The formation of a non-trivial scalar profile induced by a star is effectively described, as justified in Sec. 7.1.2, by the quasi-static spherically-symmetric EOM for the scalar field, with a slowly-varying background density profile. The bubble-like solution $\phi(r)$ can be found numerically given a specific form for the density profile $\rho(r)$. The simple analytic results presented in this section have been explicitly verified by our numerical simulations.

A few simplifications allow us to analytically understand the dynamics of scalar bubbles at finite density. The field profile minimizes the total energy,

$$E(R) \simeq 4\pi \int_0^R \mathrm{d}r\, r^2 \left[\frac{1}{2}\phi'^2 + \Delta V(\phi,\rho)\right], \quad \Delta V(\phi,\rho) = V(\phi,\rho) - V(\phi_-,\rho)\,, \tag{7.17}$$

where we have cut the integral at a radius R as an approximation to the full infinite space, since the scalar field rapidly converges to its vacuum value ϕ_- for $r \gtrsim R$. Indeed, for radii larger than the transition radius, i.e. $r > R_{\rm T}$, densities are below critical and the potential is minimized at approximately the same metastable minimum as outside of the star. In the initial stages of the formation of the dense system, we expect the creation of a scalar *proto-bubble* with $R \simeq R_{\rm T}$, where the scalar field at its center, $\phi(0)$, has not yet reached ϕ_+, the value associated with the stable minimum of the in-vacuum potential, see Sec. 7.1.4. In other words, the field displacement, $\Delta\phi(0) \equiv \phi(0) - \phi_-$, satisfies $\Delta\phi(0) \lesssim \phi_+ - \phi_- \approx 2f$. This is because the star is too small, in particular the (mean) energy density in the field gradient that would correspond to a field displacement $\Delta\phi(0) \sim 2f$, which is $\frac{1}{2}\langle\phi'^2\rangle \sim (2f/R_{\rm T})^2$, is too large compared to the (mean) potential energy difference within the proto-bubble, $\epsilon = |\langle\Delta V\rangle|$. Only when the star, by which we mean $R_{\rm T}$, grows large enough, it becomes energetically favorable to reach $\phi(0) \sim \phi_+$. Therefore, only when

$$\left(\frac{2f}{R_{\rm T}}\right)^2 \lesssim \epsilon \tag{7.18}$$

can a scalar bubble *fully form*. Interestingly, once the condition Eq. (7.18) is satisfied, the equilibrium position $R \simeq R_{\rm T}$ can be lost, meaning the bubble can be pushed towards the outer region of the star, see Sec. 7.1.5. If such an instability takes place, the evolution of the bubble is no longer quasi-static, but rather the minimization of the energy of the system becomes a time-dependent problem that can be simply described by a time-dependent bubble radius, $R \to R(t)$, which quickly approaches relativistic speeds. Depending on how fast the potential barrier reappears with radius, the instability cannot be stopped and the bubble expands beyond the star. Specifically, we find that the bubble *escapes* if

$$\frac{\Delta\sigma}{\Delta R_{\rm T}} \lesssim \epsilon\,, \tag{7.19}$$

where $\Delta\sigma$ is the difference between the tension of bubble wall at $R \simeq R_{\rm T}$ and $R \gtrsim R_{\rm S}$. The fact that the wall tension changes as it propagates through the star is one of the unique aspects of

the bubble dynamics at finite density. In particular, it gives rise to an extra force that prevents the bubble from escaping the star unless ϵ is large enough. While for a bubble connecting to a shallow metastable minimum the condition Eq. (7.19) is readily satisfied (given Eq. (7.18) is), it is harder in the case of a deep minimum, because of the significant increase of the wall tension, being eventually dominated by the large barriers of the potential in vacuum. The discussion above is visualized in Fig. 7.2.

7.1.4 Formation: linear potential approximation

Let us start by considering the classical formation of a bubble in a star where the critical density is reached. In order not to unnecessarily complicate the discussion, let us assume that the in-density potential can be well approximated by the rolling term only, i.e. that due to the suppression of $\Lambda_{\rm B}^4(\rho) = \Lambda_{\rm B}^4(1-\zeta(\rho))$ we can neglect the barrier term,

$$V(\phi, \rho > \rho_c) \simeq -\mu^2 f \phi \,, \tag{7.20}$$

where recall that in Eq. (7.14) we have identified $\mu^2 \sim \Lambda_{\rm R}^4/f^2$ as the scale that characterizes the scalar profile. An exact solution to the scalar EOM with a linear potential is

$$\phi(r) = \frac{\mu^2 f}{6}(R_{\rm T}^2 - r^2) + \phi_- \,, \quad r \leqslant R_{\rm T} \,, \qquad \text{(proto-bubble)} \tag{7.21}$$

with boundary conditions $\phi'(0) = 0$ and $\phi(R_{\rm T}) = \phi_-$. We then simply take $\phi(r \geqslant R_{\rm T}) = \phi_-$. We find that the proto-bubble is of size $R = R_{\rm T}$ and the field displacement at its center, $\Delta\phi(0) \equiv \phi(0) - \phi_-$, is given by

$$\frac{\Delta\phi(0)}{f} = \frac{(\mu R_{\rm T})^2}{6} \,. \tag{7.22}$$

This situation is explicitly depicted in the second panel of Fig. 7.2. Eq. (7.21) constitutes a good a priori description of the scalar profile as long as the system is small enough that the in-density minimum, $(\phi_+)_\rho$, is not reached, i.e.

$$\frac{\Delta\phi(0)}{(\phi_+)_\rho - \phi_-} \lesssim 1 \,. \tag{7.23}$$

We recall that in general $(\phi_+)_\rho > \phi_+$, see the discussion around Eq. (7.7).

It is important to point out here that the quasi-static description of the proto-bubble can break down as soon as $\phi(0) \sim \phi_+$, as we discuss in Sec. 7.1.5. In this regard, Eq. (7.22) implies that any system, independently of its density profile or maximum density at its core, must have a minimum size in order for $\phi(0) \gtrsim \phi_+$, given by

$$R_{\rm T} \gtrsim \mu^{-1} \,, \tag{7.24}$$

where we have neglected $\mathcal{O}(1)$ factors.

The solution Eq. (7.21) can be extended to the situation in which the in-density minimum is reached somewhere inside the star, at $r = R_i < R_{\rm T}$. In that region the potential exhibits a minimum, and consequently the scalar field remains pinned at $(\phi_+)_\rho$. This is depicted in the third panel of Fig. 7.2, where we have chosen a core density such that $(\phi_+)_\rho$ is only slightly larger than ϕ_+. The scalar profile is well approximated by

$$\phi(r) = \begin{cases} (\phi_+)_\rho & r < R_i \\ -\frac{\mu^2 f}{6}(r - R_i)^2 + (\phi_+)_\rho & R_i < r < R_{\rm T} \\ \phi_- & r > R_{\rm T} \end{cases} \,, \qquad \text{(bubble)} \tag{7.25}$$

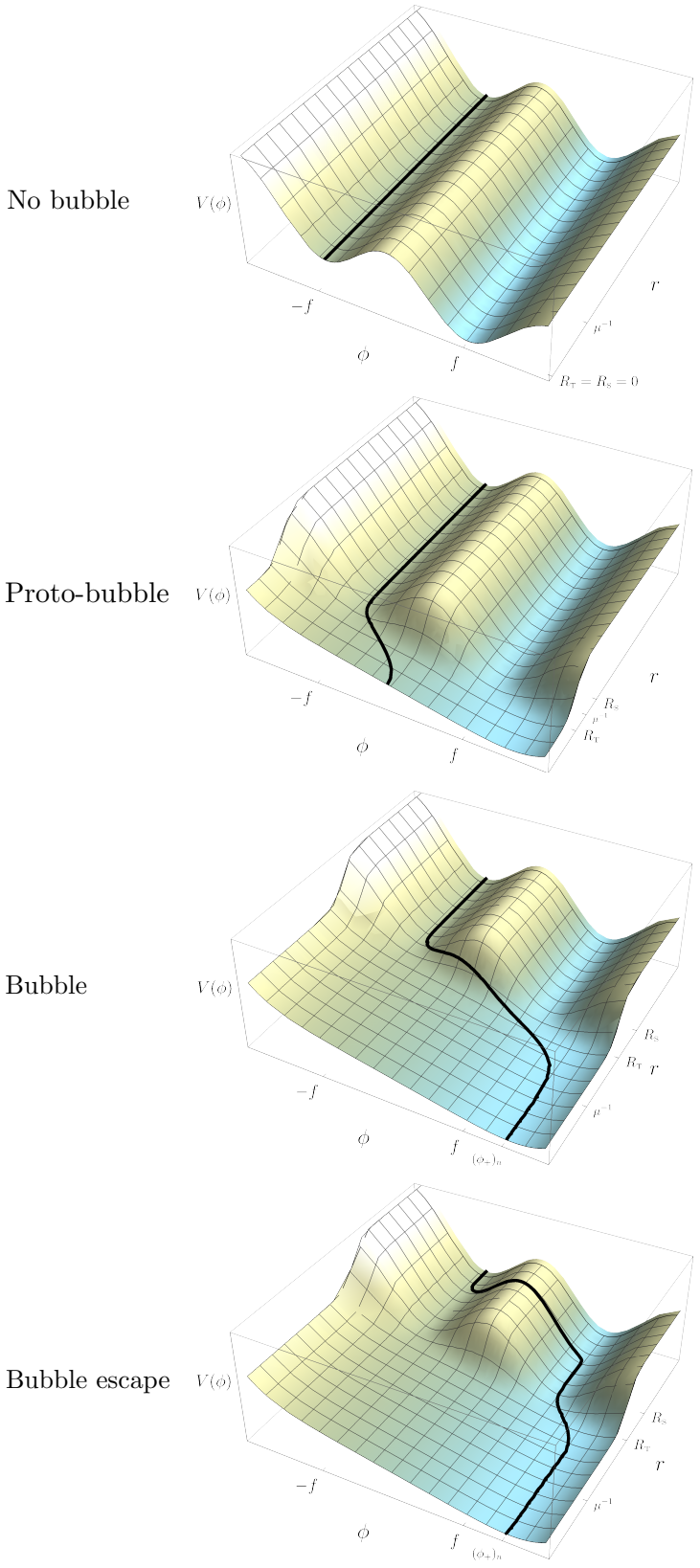

Figure 7.2: Quasi-static evolution of the in-density potential and scalar field profile, from no star to, as the star grows, the formation of the proto-bubble, complete formation of the bubble, and eventual bubble escape.

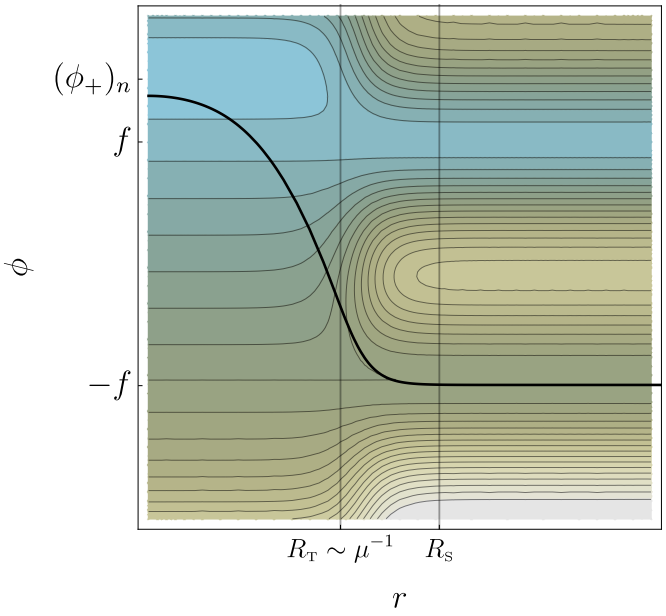

Figure 7.3: Scalar profile for $\mu R_\mathrm{T} \gtrsim 1$ on top of contours of the scalar potential.

where in the intermediate region, $r \in [R_i, R_\mathrm{T}]$, we have used the solution of the EOM with the linear potential Eq. (7.20), shifted it by $r \to r - R_i$, and required $\phi'(R_i) = 0$, $\phi(R_i) = (\phi_+)_\rho$; further matching to $\phi(R_\mathrm{T}) = \phi_-$ fixes the value of R_i, or equivalently the width of the bubble wall

$$x \equiv \frac{R_\mathrm{T} - R_i}{R_\mathrm{T}} \simeq \frac{\sqrt{6}}{\mu R_\mathrm{T}} \sqrt{\frac{(\phi_+)_\rho - \phi_-}{f}} \,. \tag{7.26}$$

Of course, in order for $R_i > 0$, R_T needs to be large enough as to allow the field to reach the minimum at finite density. In other words, the requirement that $x < 1$ implies

$$R_\mathrm{T} \gtrsim \frac{\sqrt{6}}{\mu} \sqrt{\frac{(\phi_+)_\rho - \phi_-}{f}} \,. \tag{7.27}$$

A scalar field profile for which this condition is satisfied is shown in Fig. 7.3, for a choice of central density not much larger than the critical density.

For an increasingly larger system, yet with with a core density fixed such that $(\phi_+)_\rho$ remains constant, the bubble wall becomes thinner, i.e. $x \ll 1$ when $\mu R_\mathrm{T} \gg 1$. In this thin-wall limit, the energy of the bubble, Eq. (7.17), can be approximated by a volume and a surface term [288],

$$E(R) \simeq -\frac{4\pi}{3} R^3 \, \epsilon + 4\pi R^2 \, \sigma \,, \tag{7.28}$$

where ϵ is the (potential) energy difference between the in-density and in-vacuo field values, while σ is the bubble-wall tension. For our simple scalar profile these read

$$\epsilon = \mu^2 f((\phi_+)_\rho - \phi_-) \gtrsim \Lambda_\mathrm{R}^4 \,, \tag{7.29}$$

$$\sigma = \tfrac{4}{3}\sqrt{\tfrac{2}{3}}((\phi_+)_\rho - \phi_-)\sqrt{\epsilon} \gtrsim \Lambda_\mathrm{R}^2 f \,. \tag{7.30}$$

In Eq. (7.28) we have traded $R_{\rm T}$ with R, since we are assuming that during the formation of the bubble its wall sits at $R \simeq R_{\rm T}$; in Sec. 7.1.5 we discuss under which circumstances such an equilibrium is lost, i.e. $R > R_{\rm T}$. Also, we have implicitly assumed that $(\phi_+)_\rho$ is constant below R_i, i.e. that the density does not significantly change for $r < R_i$. Both the inequalities in Eqs. (7.29), (7.30) follow from $(\phi_+)_\rho > \phi_+$, after neglecting $\mathcal{O}(1)$ factors. These correspond to the minimum values of the potential energy and tension of a fully formed bubble. As expected, we find $\epsilon \gtrsim |\Delta V(\phi_+, \rho)| = -\Delta\Lambda$, where recall that $\Delta\Lambda$ is the energy difference between the false and true ground states, Eq. (7.72). In addition, let us point out that the condition Eq. (7.27) can be understood from energy considerations, as the requirement that the (mean) field gradient is small enough, $\frac{1}{2}\langle\phi'^2\rangle \sim ((\phi_+)_\rho - \phi_-)^2/R_{\rm T}^2 \lesssim \epsilon$. In this regard, note also that the tension is dominated by the field displacement, $\sigma \sim ((\phi_+)_\rho - \phi_-)^2/(xR_{\rm T})$ [301].

In App. D.1 we reproduce the above scalings with a simpler linear profile approximation, where we do not need to assume that the potential is well described by a linear slope only. In particular, we can keep the subdominant barrier term and we find that, while leaving ϵ unchanged, it gives a corrections to the tension of the bubble wall that scales as

$$\frac{\Delta\sigma}{\sigma} \sim \frac{\Lambda_{\rm B}^4(\rho)}{\Lambda_{\rm R}^4} \simeq \frac{1-\zeta(\rho)}{1-\zeta_c}\,. \tag{7.31}$$

This becomes negligible when $\zeta \to 1$, that is also when $(\phi_+)_\rho \gg \phi_+$, see Eq. (7.7). On the other hand, when the density is not much above critical, the correction is parametrically $\mathcal{O}(1)$. Nevertheless, the most important effect of the potential barriers arises when we consider a bubble whose wall is beyond the transition radius, i.e. $R > R_{\rm T}$, as we discuss in the following.

7.1.5 Dynamics: escape vs equilibrium

In the previous discussion we worked under the assumption of a nearly-static bubble, which slowly grows with time only due to the increase in size of the star (or more accurately, due to the increase in size of the transition radius $R_{\rm T}$ where the critical density is reached). Here we show that in fact this adiabatic description can break down as soon as the star is dense and large enough that the field displacement inside it reaches the position of the true minimum in vacuum.

There are several ways to understand the origin of this instability. Qualitatively, for the potentials we are considering, finite density effects allow for the local minimum in vacuum to be continuously (i.e. classically) connected to the true minimum. This is because the in-vacuo potential barrier between them disappears in some region of the star ($r < R_{\rm T}$), see the right panel of Fig. 7.4. Once this region is large enough such that $\Delta\phi(0) \gtrsim \phi_+ - \phi_- \approx 2f$, it may become energetically favourable for the tail of the field profile, which extends outside the star, to be pushed over the potential barrier. This effectively leads to a first-order phase transition in the form of a bubble escaping the star. This is in contrast with other types of potentials with metastable minima, such as that shown in the left panel of Fig. 7.4, where even at finite density there is always a potential barrier between the two minima. This class of potentials does not allow for a classical path connecting them, and therefore leads to a smooth cross-over to a different in-density minimum.[4]

Let us note that the discussion is focussed on field displacements that are at least of the order of the field separation between the local and true minimum in vacuum. This is because, at

[4]Even with non-vanishing barriers, finite density effects could lead to a significant increase in the tunneling probability to the true minimum, thus seeding a quantum first-order phase transition. We discuss this possibility in Sec. 7.1.7 since it is of relevance as well for our potential whenever densities remain below critical, i.e. $\rho(r) < \rho_c\,\forall r$.

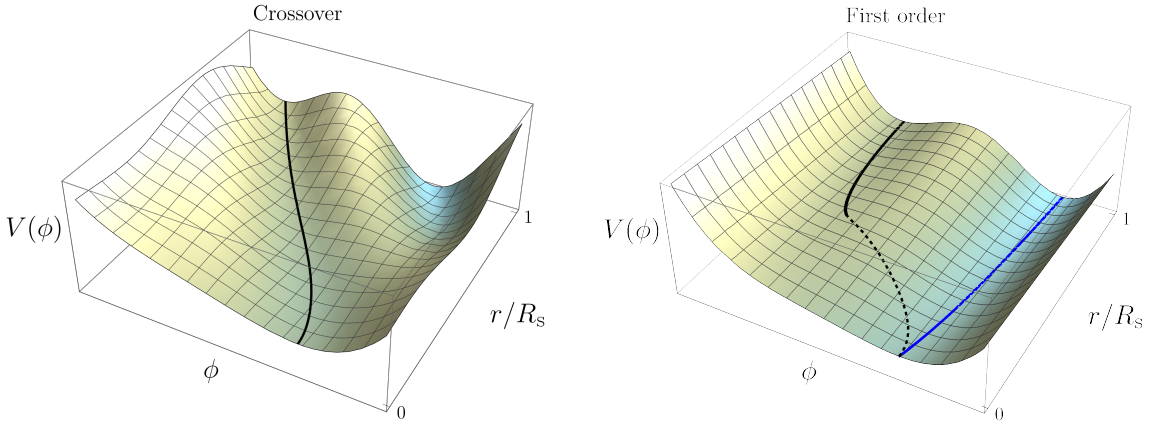

Figure 7.4: Crossover (left) versus first order phase transition (right) induced by a dense system (spherically symmetric and of finite size). For both cases the potential is shown as a function of radius, with $r/R_S = 0$ the center of the star. The black solid lines illustrate the scalar profile starting from a given in-vacuo ($r/R_S > 1$) minimum and following it inside the star. For a first-order phase transition, the black line stops where this minimum ceases to exist. The dashed line then illustrates the field profile that connects to the minimum within the star. The profile unavoidably passes through regions where $dV/d\phi \neq 0$, implying there are effective forces acting on the field. These forces give rise to the possibility that the initial scalar profile (black) classically changes to a new minimum in vacuum (blue).

least qualitatively, a bubble with $(\phi_+)_\rho \sim \phi_+$ captures all the non-trivial dynamics of the phase transition. In the following we focus on such a case, which corresponds to maximal densities of the order of the critical density. A discussion of the bubble dynamics for $(\phi_+)_\rho \gg \phi_+$, is deferred to App. D.4.

In order to quantitatively understand the dynamics of induced first-order phase transitions, we resort to the description of the scalar bubble wall as a particle in $d = 1 + 1$ dimensions. While this is a standard treatment when studying the dynamics of bubbles in vacuum or at finite temperature (see e.g. [302]), here we adapt it to the finite density environment, crucially including a position-dependent tension, $\sigma(R)$. The Lagrangian for the time-dependent bubble-wall position $R(t)$ is given by

$$\mathcal{L} = -\mathcal{M}(R)/\gamma - \mathcal{V}(R)\,, \tag{7.32}$$

where $\gamma = 1/\sqrt{1-\dot{R}^2}$. In the thin-wall approximation, $x \ll 1$, where the particle description best applies, we have

$$\mathcal{M}(R) = 4\pi \int_{R(1-x)}^{R} \mathrm{d}r\, r^2 \left[\frac{1}{2}\phi'^2 + \Delta V(\phi, \rho(r))\right] \equiv 4\pi R^2 \sigma(R)\,, \tag{7.33}$$

$$\mathcal{V}(R) = -\frac{4\pi}{3} R^3 \Delta\Lambda \equiv -\frac{4\pi}{3} R^3 \epsilon\,. \tag{7.34}$$

Several comments are in order regarding the bubble mass and potential at finite density. First, the bubble's energy given in Eq. (7.28) is precisely the Hamiltonian associated with Eq. (7.32) in the static limit $\dot{R} = 0$. Second, from the integral expression of $\mathcal{M}(R)$, it is clear that in the thin-wall limit the bubble wall is only sensitive to the density at $r = R$. Therefore, as the bubble moves through the star, its tension changes due to the changing density.[5] Since the bubble is

[5]We are implicitly assuming that the width of the wall is the smallest scale in the system. If this were not

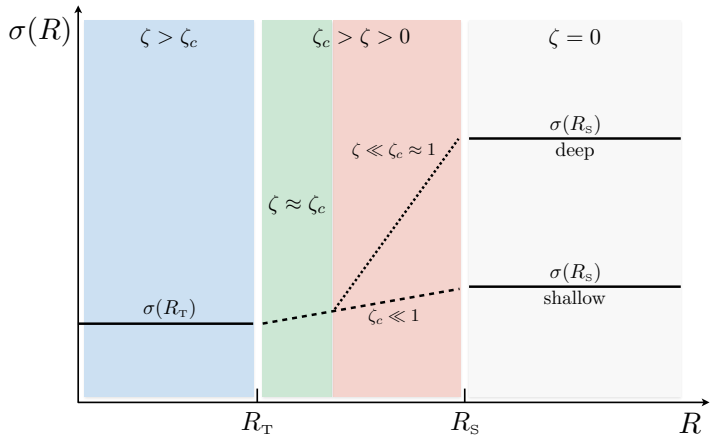

Figure 7.5: Sketch of the relevant regions of the star for what concerns the bubble-wall tension. Dashed and dotted lines do not necessarily represent the functional form of $\sigma(R)$. In the green region, the tension is dominated by the field displacement, while in the red region, the barriers come to dominate. Note that for $\zeta_c = \delta^2 \ll 1$ (i.e. shallow minimum), there is, in fact, no red region.

born with $R \simeq R_{\rm T}$, from Eq. (7.30) with $(\phi_+)_\rho \sim \phi_+$ we have

$$\sigma(R \simeq R_{\rm T}) \sim \Lambda_{\rm R}^2 f \,. \tag{7.35}$$

Recall that for the bubble to have been fully formed, $R_{\rm T}$ needs to satisfy Eq. (7.27), which for $(\phi_+)_\rho \sim \phi_+$ reads $R_{\rm T} \gtrsim \mu^{-1}$. Finally, $\mathcal{V}(R)$ is controlled by the potential energy difference between the two sides of the bubble wall, which from Eq. (7.29) with $(\phi_+)_\rho \sim \phi_+$ is given by

$$\epsilon \sim \Lambda_{\rm R}^4 \,. \tag{7.36}$$

The equation motion of the bubble wall reads

$$\sigma \ddot{R} \gamma^3 = \epsilon - \gamma \left(\frac{2\sigma}{R} + \sigma' \right) , \qquad \sigma' = \frac{d\sigma}{dR} \,. \tag{7.37}$$

Since we are mainly interested in the dynamics of the bubble right after its formation, we concentrate on the non-relativistic limit, i.e. we set $\gamma = 1$. The right-hand side of Eq. (7.37) is the sum of forces (pressures) acting on the bubble wall. The potential energy difference between the two sides of the wall pushes it outwards. The second and third terms are associated with the tension of the wall, both pushing it inwards. In particular, the change in tension σ' is positive, since densities decrease with R and in turn, the potential barriers, controlled by $\Lambda_{\rm B}^4(\rho)$, reappear and increase towards its vacuum value outside the star.

In order to understand the behavior of $\sigma(R)$, let us first recall that when the bubble is just formed, the tension is dominated by the field displacement, see Eq. (7.30). This implies that only the contribution to the tension from the barrier, estimated in Eq. (7.31), leads to increasing tension with R. For bubbles connecting shallow minima, $\delta^2 \ll 1$, this increase is small between $R_{\rm T}$ and $R_{\rm S}$,

$$\sigma(R_{\rm S}) - \sigma(R_{\rm T}) \sim f \Lambda_{\rm R}^2 \delta^2 \,. \qquad \text{(shallow)} \tag{7.38}$$

the case, we would expect finite-size effects in the form of e.g. deformations of the bubble. However, these would lead to at most $\mathcal{O}(1)$ corrections to our already approximate analytical results, leaving our qualitative conclusions unchanged.

In contrast, for deep minima, $\delta^2 \approx 1$, the tension goes from being displacement-dominated at $R \simeq R_{\rm T}$, to barrier-dominated towards the end as well as outside of the star $R \simeq R_{\rm S}$. There we can use the standard thin-wall approximation to compute the tension [288],

$$\sigma(r \simeq R_{\rm S}) \simeq \int_{-f}^{f} {\rm d}\phi \sqrt{2V(\phi)} \simeq \frac{2}{3}\Lambda_{\rm B}^2 f\,, \qquad \text{(deep)} \tag{7.39}$$

and $\sigma(R_{\rm S}) - \sigma(R_{\rm T}) \simeq \sigma(R_{\rm S})$. In addition, let us note that the bubble gets thinner when the barrier term dominates the tension. The bubble wall tension, as a function of its location, is schematically summarized in Fig. 7.5 for both the shallow and deep minimum cases.

Before moving to the detailed discussion of how the changing tension affects the dynamics of the bubble wall, let us note that in Eq. (7.37) we have ignored the effect of the gravitational force of the star on the bubble wall. In App. D.2 we discuss such a force, showing that while NSs it could be quantitatively relevant at some stage during the expansion, it does not qualitatively change the picture presented here.

Having established the behavior of the tension from $R_{\rm T}$ to $R_{\rm S}$, let us understand the dynamics of the bubble wall. Right after the formation of a thin-wall bubble at $R \simeq R_{\rm T} \gtrsim \mu^{-1}$, the particle description Eq. (7.37) applies. One then automatically finds $\ddot{R} > 0$ right before the transition region, since we can assume that σ' vanishes for $R < R_{\rm T}$, that is $\sigma'(R_{\rm T}^-) = 0$. The acceleration would remain positive in the limit that the force due to the change in tension vanished for any R, $\sigma' \to 0$; in this limit, the bubble would expand indefinitely, particularly beyond the star. In the opposite limit, in which σ' is very large just past the edge of the transition region, that is $\sigma'(R_{\rm T}^+) \to \infty$, the wall could not expand and therefore it would remain at an equilibrium radius $R = R_{\rm eq} = R_{\rm T}$ (and the bubble would only grows if $R_{\rm T}$ kept increasing). Clearly, a realistic situation lies in between these two limits, and it depends on how fast the density profile and thus the tension changes from $R_{\rm T}$ to the end of the star. This discussion gives us a qualitative understanding of why the bubble might generically be found in an equilibrium position at $R_{\rm S} > R > R_{\rm T}$. In a similar fashion, we can understand under which conditions the bubble escapes from the star. In the limit that the star has grown so large that the transition region starts at a radius much larger than the one needed to form the bubble, i.e. $R_{\rm T} \gg \mu^{-1}$, we have $\epsilon \gg 2\sigma(R_{\rm T})/R_{\rm T}$. Then, it follows from the equation of motion that the bubble wall would continue to accelerate for $R > R_{\rm T}$ as long as $\epsilon > \sigma'$. In the opposite limit, in which $R_{\rm T} \simeq \mu^{-1}$, we have $\epsilon \to 2\sigma(R_{\rm T})/R_{\rm T}$ and the additional force due to σ' would be enough to forbid its expansion. These different limits lead us to the conclusion that for a sufficiently large star, satisfying $R_{\rm T} \gtrsim \sigma(R_{\rm T})/[\epsilon - \sigma'(R_{\rm T})]$, the system is unstable and the bubble escapes if

$$\epsilon \gtrsim \kappa\, \sigma'_{\rm max}\,, \tag{7.40}$$

where $\sigma'_{\rm max}$ is the maximum value of σ' and $\kappa = \mathcal{O}(1)$. This condition is explicitly verified by our numerical simulations as well as in App. D.3, where we investigate Eq. (7.37) in the simplest case of a constant σ', finding $\kappa = 3$. Once again, (a version of) this condition can be expected to hold in general, on the basis that the standard force due to the surface tension becomes irrelevant at large R, leaving the variation of the tension as the only relevant force to determine if the bubble does or does not escape from the star.

7.1.6 Summary: formation and escape conditions

Given that the change in the wall tension is very different for a bubble connecting shallow or deep minima in vacuum, let us explicitly summarize for each case the conditions under which the bubble forms and escapes from the star.

For a shallow bubble, $\delta^2 \ll 1$, we find as formation and escape conditions, respectively

$$R_{\rm T} \gtrsim \frac{f}{\Lambda_{\rm R}^2} \quad \text{and} \quad \Delta R_{\rm T} \gtrsim \frac{f}{\Lambda_{\rm R}^2}\delta^2\,, \qquad \text{(shallow)} \tag{7.41}$$

up to irrelevant $\mathcal{O}(1)$ factors. Note that since σ' is suppressed by δ^2, as shown in Eq. (7.38), the escape condition is easier to satisfy than the condition for formation. This is unless, contrary to the expectation from generic density profiles, $\Delta R_{\rm T}$ is anomalously small. In terms of the mass of the scalar in vacuum, Eq. (7.3), these two conditions read as $m_\phi R_{\rm T} \gtrsim \sqrt{\delta}$ and $m_\phi \Delta R_{\rm T} \gtrsim \delta^{5/2}$.

For a bubble connecting deep minima, $\delta^2 \approx 1$, the rate of change of the tension is determined by the tension in vacuum, $\sigma' \sim \sigma(R_{\rm S})/\Delta R_{\rm T}$, as shown in Eq. (7.39). Therefore, we find the following conditions for the formation and escape of a deep bubble, respectively

$$R_{\rm T} \gtrsim \frac{f}{\Lambda_{\rm R}^2} \quad \text{and} \quad \Delta R_{\rm T} \gtrsim \frac{f}{\Lambda_{\rm R}^2}\frac{1}{\sqrt{1-\delta^2}}\,, \qquad \text{(deep)} \tag{7.42}$$

up to $\mathcal{O}(1)$ factors. As expected, it is generically much more difficult for a bubble connecting deep minima to transverse the transition region and expand beyond the star. Besides, while the condition for formation is formally the same as for shallow minima, let us recall that $\zeta_c = \delta^2 \approx 1$ generically implies that much larger densities are needed in this case. In terms of the mass of the scalar in vacuum, Eq. (7.3), the two conditions in Eq. (7.74) read as $m_\phi R_{\rm T} \gtrsim 1/\sqrt{1-\delta^2}$ and $m_\phi \Delta R_{\rm T} \gtrsim 1/(1-\delta^2)$.

7.1.7 Classical vs quantum

To conclude this section, we wish to investigate the possibility that, even when the system is not dense enough as to allow for a classical transition between the local and true minimum, finite density could still lead to a much shorter quantum-mechanical lifetime of the metastable minimum compared to the one in vacuum. This is reminiscent of the idea that black holes or compact objects can act as seeds for false vacuum decay, due to their strong gravitational fields, see e.g. [303–309].

Indeed, up until this point we did not care about the lifetime of the false vacuum, implicitly assuming that it was sufficiently large. The decay rate per unit volume is determined by the bounce action, $\Gamma/\mathcal{V} = Ae^{-S_{\rm B}}$ [288, 310]. By definition, in the case where the metastable minimum is deep, the thin-wall approximation holds. The action is well approximated by $S_{\rm B} \simeq (27/2)\pi^2\sigma^4/\epsilon^3$, which given the in-vacuo tension Eq. (7.39) and $\epsilon = -\Delta\Lambda \simeq \frac{2}{3\sqrt{3}}\Lambda_{\rm R}^4$, results in

$$S_{\rm B} \simeq 27\sqrt{3}\pi^2\left(\frac{f}{\Lambda_{\rm B}}\right)^4 \frac{1}{(1-\delta^2)^3}\,. \qquad \text{(deep)} \tag{7.43}$$

Since $\delta^2 \approx 1$ for a deep minimum, the bounce action is generically large and the decay rate extremely suppressed. For a shallow minimum, we can estimate the action by considering $\sigma \sim \Delta\phi^2/\Delta R$ with $\Delta R \sim \Delta\phi/\sqrt{\epsilon}$, which leads to $S_{\rm B} \sim \pi^2\Delta\phi^4/\epsilon$. We therefore find,[6]

$$S_{\rm B} \sim 24\pi^2\left(\frac{f}{\Lambda_{\rm B}}\right)^4\,. \qquad \text{(shallow)} \tag{7.44}$$

While for the same value of the ratio $f/\Lambda_{\rm B}$ the bounce action is smaller in the shallow than in the deep case, this is not the comparison we really care about. Instead, let us assume that

[6] More refined estimates can be easily derived for potentials where the barrier is negligible, see e.g. [311]. Nevertheless, our conclusions will not depend on such a refinement.

the local minimum is, for all practical purposes, stable in vacuum. This fact can dramatically change in a dense system only in the case of a deep minimum (even before a classical transition is allowed). This is clear since for a shallow minimum $S_{\rm B}(n<\rho_c)\simeq S_{\rm B}(0)$, while for a deep one

$$\frac{S_{\rm B}(n<\rho_c)}{S_{\rm B}(0)}\simeq\left[1-\zeta(\rho)\right]^2\,, \qquad \text{(deep)} \tag{7.45}$$

which is much smaller than one if $\zeta\approx 1$ (yet $\zeta<\zeta_c=\delta^2$). Generically, the decay rate can only be sufficiently fast compared to the lifetime of star if the bounce action is not very large, which drives us towards the non-perturbative regime for the scalar quartic coupling $\lambda\equiv(\Lambda_{\rm B}/f)^4$.[7] Nevertheless, this conclusion could well be specific to the type of false vacua we are taking as case study, thus one could imagine other scalar potentials where, being sensitive to finite density (either of SM degrees of freedom or beyond, e.g. dark matter), their local minima have much smaller lifetimes in a dense system. Additionally, let us note that the corresponding seeded nucleation of bubbles of the true ground state would generically not take place during the formation of the star. On the contrary, one would expect $1/\Gamma\gg T_{\rm S}$, while still being shorter than the the typical lifetime of the star, $1/\Gamma\ll\mathcal{T}$, such that the decay probability $\mathcal{T}\Gamma=\mathcal{O}(1)$, see footnote 7.1.7. This raises the possibility of a latent phase transition that could take place at any time.

Finally, let us point out that in the computation of the bounce action at finite density, we have assumed the system is large and homogeneous enough as for the effects of a non-trivial density profile or a spatial boundary to be negligible. We can phrase this as the requirement that $R_0\ll R_{\rm S}$, where $R_0=3\sigma/\epsilon$ is the radius of the nucleated bubble. For a deep minimum, this translates into $m_\phi R_{\rm S}\gg 1/(1-\delta^2)$, which coincides with the condition for the escape of a deep, classically formed, bubble, see Eq. (7.74). It would be interesting to further study, beyond these simple approximations, the process of quantum bubble nucleation in finite-size dense systems [312, 313].

7.1.8 Phenomenological implications

In this section we discuss the phenomenological consequences of the expansion, beyond the dense object, of a bubble of the true vacuum. The main model-independent signature of such a seeded phase transition is a change of the vacuum energy of the universe, Λ, or equivalently a change of the cosmological dark energy density, ε_Λ (with equation of state parameter $\omega=-1$).[8]

A particularly interesting trademark of these phase transitions is that they take place relatively late in the history of the universe. As explained in the previous section, the bubble

[7] Focussing on NSs as nucleation seeds, we can roughly estimate the requirement for an $\mathcal{O}(1)$ tunnelling probability by taking into account the volume of all NSs in the observable universe since the time of star formation until today (since such stars are stable in isolation). The volume of all NSs in the observable universe is roughly $\mathcal{V}_{\rm NS}\sim R_{\rm NS}^3 N_{\rm NS/G} N_{\rm G}\sim 10^{32}\,{\rm m}^3$, where $R_{\rm NS}\sim 10\,{\rm km}$ is the typical radius of a neutron star, $N_{\rm NS/G}\sim 10^9$ the number of NSs per galaxy (like ours) and $N_{\rm G}=10^{11}$ the number of galaxies. Since star formation happened relatively early, the relevant time scale is $\mathcal{T}\sim 1/H_0\sim 10^{17}\,{\rm s}$. Requiring that $\mathcal{T}\Gamma\sim\mathcal{O}(1)$ and using Eq. (7.43), we find

$$\frac{\lambda(1-\delta^2)^3}{(1-\zeta)^2}\sim\frac{27\sqrt{3}\pi^2}{\log(f^4\mathcal{T}\mathcal{V}_{\rm NS})}\gtrsim 1\,, \tag{7.46}$$

where the last inequality arises from assuming $f<M_{\rm P}$. Note that we also used the NDA estimation for the exponent coefficient $A\sim f^4$. In the best case scenario the metastable minimum is not very deep, e.g. $\delta\approx 0.8$. Demanding a mild reduction of the potential barrier in density, $\zeta\approx 0.5<\delta^2$, in order to catalyse the decay we need $\sqrt{\lambda}\gtrsim 2.3$, which is certainly not a weak coupling.

[8] In the following we exclude the possibility of an adjustment mechanism for the cosmological constant. Such a mechanism could interfere with the formation or escape of the bubble.

forms, expands and eventually escapes along with the formation of the star. Therefore, if a phase transition of this sort can happen, it took place at the onset of star formation. The first stars were born around the epoch of galaxy formation, thus at redshifts $z = z_{\rm S} \sim 10$ [314]. This then implies that the universe underwent a change of ε_Λ between recombination, $z \sim 10^3$, and the late universe, $z \lesssim 1$. Note that we are assuming that at redshifts $z \sim 1$ (associated with late-time cosmological measurements) the universe already transitioned successfully to the true ground state. The change in the dark energy content of the universe can thus best be probed by comparing CMB measurements versus local measurements (SNe, baryon acoustic oscillations or large-scale structure) of the expansion rate of the universe. Such a comparison depends on the fate of the bubbles, for instance if the phase transition proceeds via a single bubble or instead many bubbles are formed all over the universe (from as many stars) that subsequently collide and transfer at least an $\mathcal{O}(1)$ fraction of the kinetic energy of their walls into radiation. Providing a precise answer to this question is beyond the scope of this work. Instead, below we work out simple cosmological constraints on how much the energy budget of the universe can vary due to a late ($z \sim 10$) phase transition, to confirm our intuition that a change in the vacuum energy much larger than the current one is experimentally ruled out.

A too large change in vacuum energy leads to constraints on the parameters of the scalar potential. To make this point clear, let us note that the change in vacuum energy is given by $\Delta\Lambda = -\epsilon \sim -\Lambda_{\rm R}^4$, and the rolling scale enters both the conditions for formation and escape of a bubble of the true vacuum, see Eqs. (7.73), (7.74). Then, assuming the existence of stars with densities above critical, $n > \rho_c$, the condition for formation of a bubble with $R_{\rm T} \sim R_{\rm S}$, as expected for most stellar profiles, implies

$$-\Delta\Lambda \gtrsim \left(\frac{f}{R_{\rm S}}\right)^2 \approx \Lambda_0 \times 10^{15} \left(\frac{f}{10\,\text{TeV}}\right)^2 \left(\frac{10\,\text{km}}{R_{\rm S}}\right)^2 , \tag{7.47}$$

where $\Lambda_0 \approx (2.3\,\text{meV})^4$ is the value of the vacuum energy inferred from ΛCDM, and we have fixed $R_{\rm S}$ to the typical radius of a neutron star as an example. If such type of bubbles could have escaped from NSs, the corresponding change in the vacuum energy would be in gross contradiction with experimental data. Note that a similar region of parameter space is realized in e.g. relaxion models [10].

However, for much smaller values of f, or if we were to consider much larger astrophysical bodies (the largest stars known have $R_{\rm S} \sim 10^3 R_\odot$), astronomical structures, or even dense objects beyond the SM (such as dark stars), the change in the dark energy density could be much smaller. In particular, the very first stars to form ($z \sim 20-30$), the so-called Pop. III stars, are believed to have been supermassive $M \gtrsim 100\,M_\odot$ and as large as $R \sim 10^3\,R_\odot$, and therefore could be interesting candidates [315]. Likewise, the largest stars observed are red giants with radii up to $R \sim 10^3\,R_\odot$ and masses $M \sim 10\,M_\odot$. The corresponding nucleation of bubbles of the true vacuum and subsequent phase transition could then be an experimentally viable and very interesting phenomenon, which could be detected in the near future given the expected increase in precision of many current and planned cosmological observatories. Whether or not this type of phase transition could lead to interesting gravitational wave signatures is an interesting question, which we leave for future investigation along with the study of the corresponding cosmological dynamics.

Amusingly, if the phase transition proceeds via quantum tunneling, as we have argued in Sec. 7.1.7, a recent creation of a true vacuum bubble could lead to other, more direct, experimental signatures: since the bubble interacts with SM matter, gravitationally at the very least, the effects of a (non-percolated) bubble wall passing through Earth could potentially be detected [316, 317].

Let us finally point out that seeded phase transitions with $\Delta\Lambda \lesssim \Lambda_0$ could impact our understanding of the landscape solution to the cosmological constant problem. Originally connected with the requirement for galaxies and stars to form [318], the cosmological constant was predicted to lie within a range a couple of orders of magnitude larger than the value actually observed as dark energy. In light of our late-time phase transitions, taking place precisely because structures form, this discrepancy could well be an accident associated with the sensitivity to finite density effects of a scalar potential with metastable minima (potentially many of them as in [9]).

Cosmological constraints

While it is beyond the scope of this work to examine in detail the cosmological and astrophysical constraints arising from a phase transition at the dawn of galaxy/star formation, let us briefly comment on simple arguments why a large change in the energy content of the universe is not experimentally viable.

From local measurements of the (accelerated) expansion of the universe, we know it is dark energy dominated, and in particular $\varepsilon_r \ll \varepsilon_\Lambda$ at $z \lesssim 1$, where ρ_r is the energy density in radiation. If we assume that, at redshifts $z_{\rm S} \sim 10$, an $\mathcal{O}(1)$ fraction of the kinetic energy of the bubbles goes into radiation after they collide and percolate, then we find $\epsilon = \Delta\varepsilon_r(z_{\rm S}) \ll (1+z_{\rm S})^4\varepsilon_{\Lambda_0} \approx 10^4\varepsilon_{\Lambda_0}$, which is inconsistent with e.g. Eq. (7.47).

Still, it would be preferable to proceed with minimal assumptions regarding the fate of the bubble. One relatively robust assumption is that today our Hubble patch is in the true vacuum, while it was not prior to star formation, that is $\varepsilon_\Lambda(z > z_{\rm S}) \neq \varepsilon_{\Lambda_0}$. In this case, the most reliable test is to contrast late versus early universe measurements, something that has been actively pursued in recent years in light of the Hubble tension, the disparity between CMB and local determinations of the Hubble constant (see [319,320] for recent discussions). Of particular relevance is the study in [321], where constraints on the size of an early dark energy content of the universe at the time of recombination are derived. The bounds are given as a function of the critical redshift z_c where the dark energy starts to decay quickly, as $1/a^6$ (thus faster than radiation). Such a behaviour decreases the impact of this non-standard energy component at later times $z < z_c$, which we take as a good approximation towards independence from the fate of the bubble(s). Identifying $z_c = z_{\rm S}$, the bound $\varepsilon_\Lambda(z > z_{\rm S}) \gtrsim 10^2\varepsilon_{\Lambda_0}$ is derived, two order of magnitude stronger than the crude bound we derived before. Although we expect that a proper analysis of the fate of the bubbles and its impact on cosmological observables would yield even stronger bounds, in this work we will take

$$-\Delta\Lambda \lesssim 10^2 \times \Lambda_0 \tag{7.48}$$

to set constraints on the parameters of the scalar potential Eq. (7.56).

For the bound Eq. (7.48) to apply, the conditions for a bubble of the true ground state to form and escape from the dense system must be satisfied. Let us recall that the first of these conditions is that densities need to be above the critical density, i.e. $n > \rho_c$, or more specifically

$$\zeta(\rho) > 1 - \frac{\Lambda_{\rm R}^4}{\Lambda_{\rm B}^4}\,, \tag{7.49}$$

see Eqs. (7.2), (7.6). Since in this work we do not focus on any specific scenario for the function $\zeta(\rho)$,[9] we simply assume that stars exist with $n > \rho_c$, and note that denser stars are typically smaller. The other conditions concern the formation and escape of the bubble, which are different

[9] Constraints on relaxion models, where $\zeta(\rho)$ can be explicitly computed, are presented in [12].

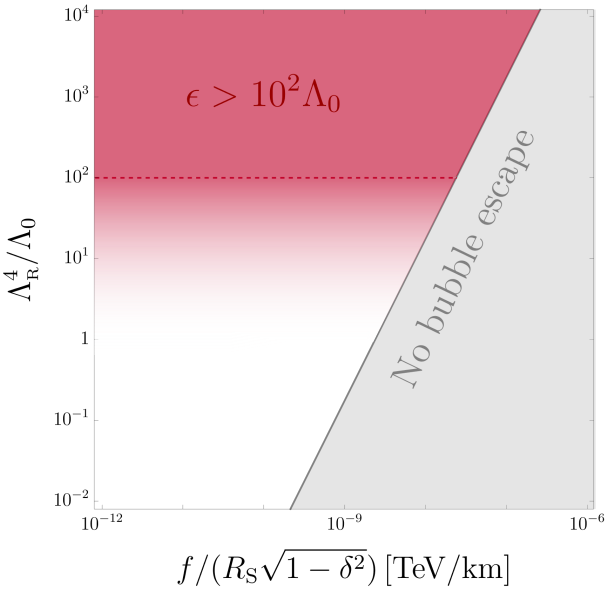

Figure 7.6: Region excluded by a density induced vacuum instability (shaded red) in the plane $(f/R_S\sqrt{1-\delta^2},\ \Lambda_R^4/\Lambda_0)$, where R_S is the typical radius of the (type of) star triggering the phase transition, i.e. where densities above critical are realized, $n > \rho_c$. The dashed line corresponds to the bound Eq. (7.48).

for a shallow metastable minimum than for a deep one, see Eq. (7.73) and Eq. (7.74), respectively. These depend on either R_T or $\Delta R_T = R_S - R_T$, which in turn depend on the density profile of the star. We will take $R_T \sim \Delta R_T \sim R_S$ as a generic expectation for stars where the core density is not very close to the critical one, as discussed in Sec. 7.1.2. Under this assumption, the strongest of the formation and escape conditions, for both shallow and deep minima, can be written as

$$\Lambda_R^4 \gtrsim \frac{f^2}{R_S^2}\frac{1}{1-\delta^2}\,. \tag{7.50}$$

We show the region of parameter space where this condition is satisfied in Fig. 7.6. Since a phase transition seeded by stars takes place in this region, the bound Eq. (7.48) applies, ruling out the corresponding part of it. Note that for a bubble connecting deep minima, Eq. (7.50) can be rewritten as $\Lambda_R^4 \gtrsim \Lambda_B^2 f/R_S$.

7.1.9 Conclusions

Could a phase transition have taken place in the universe due to the formation of stars? In this section, we explored this question by studying how false vacua change at finite density. Similar to the interactions with a thermal bath, the coupling of a scalar field to background matter can give rise to significant deformations of the scalar potential, to the point that a metastable minimum present in vacuum disappears at finite density. This leads to the formation of a non-trivial scalar profile, a.k.a. a scalar bubble, where the maximum field displacement within is controlled by the size of the dense system relative to the characteristic scale of the in-density potential; if the star gets large enough, a classical path to a deeper minimum of the potential becomes accessible. Interestingly, we found that when this occurs, the bubble, initially confined within the star, can become unstable and expand beyond the star and extend to infinity! By means of simple analytic arguments, we have shown that the bubble cannot be contained within

the star if the energy difference between the minima is large compared to how fast the potential barrier between them reappears towards the surface of the star. In other words, we have shown that if certain conditions regarding the properties of the metastable minimum and of the density profile are satisfied, stars can indeed act as seeds for a phase transition in the universe.

Our analysis of the fate of a false vacuum at finite density has been based on a tilted quartic potential, as in the classic work by Coleman [288]. This potential is characterized by the energy difference between the local and true minimum, the height of the potential barrier between them, and their separation in field space. Such a simple potential encodes the main features of local minima present in many scenarios beyond the SM. Specifically, the analysis performed in this section can be extended to the relaxion, a mechanism to explain the smallness of the electroweak scale that relies on a closely-packed landscape of local minima, with barriers between that depend on the value of Higgs field thus sensitive to SM matter densities [10]. This is the subject of Sec. 7.3. Other scenarios connected to the electroweak hierarchy problem or simply relying on the Higgs-portal, e.g. [289, 322–328], should be investigated as well in light of our findings. In this regard, while we have focussed on scenarios where density affects the size of the potential barrier between minima, the analysis where other scales are density-dependent is an interesting case to consider. We will see an example in Sec. 7.3, where instead of a decrease in the barrier, the increase of the tilt is the dominant effect leading to such phase transitions. Additionally, while we focused for concreteness on matter density, one should also consider other non-trivial backgrounds, such as an electromagnetic field, as sources for the instability of the false vacuum which we will also see in Sec. 7.3.

Phase transitions triggered by dense systems such as stars must confront the experimental constraints that arise from the change in the energy of the vacuum at late cosmological times, $z \sim 10$, when star formation begins. Indeed, on the one hand, the change in the ground state energy between the local and true vacuum is the key parameter that determines if a scalar bubble formed in a dense and large enough star is able to escape and propagate to infinity. On the other hand, early versus late cosmological measurements of the dark content of the universe constrain such a change. Nevertheless, we have shown that if the field distance between the minima is small enough or if the stars that can trigger the phase transition are very large, the phase transition could have taken place consistent with current cosmological data. Detailed cosmological and astrophysical constraints on these types of transitions, beyond the simple and likely too conservative bounds we have derived, deserves further investigation, in particular because of the relevance of scalar potentials with (many) false vacua for the electroweak hierarchy or the cosmological constant problems.

Finally, even though we focussed on classical transitions between minima, we have also shown how stars could act as a catalyzer where the tunneling probability of a false vacuum can be greatly enhanced. Although of a different, quantum-mechanical origin, once formed the dynamics of the corresponding scalar bubble would be described along similar lines as those presented here. The possibility of a seeded vacuum decay leaves us with another question: is it likely that a phase transition in the universe due to the formation of stars is soon to take place?

We continue this chapter with the formulation of the Higgs Hierarchy problem in Sec. 7.2 in order to motivate the relaxion model which we will investigate in Sec. 7.3 in light of our findings from from this section.

7.2 The Higgs Hierarchy Problem

In this section we introduce the Hierarchy problem in order to motivate the relaxion solution, which we discuss in Sec. 7.3 in light of our findings from Sec. 7.1.

In the context of the Hierarchy Problem, we draw inspiration from the discussion presented in [44], and for a broader perspective, we refer readers to recent articles on the topic [329, 330], as well as the original works [331–333].

At present, the SM stands as an effective field theory that remarkably describes nature within the scales we can experimentally probe, up to several TeV. However, as we approach the Planck scale, $E \sim 4\pi M_p$, gravity emerges as a strongly-coupled force, necessitating an extension of the SM at or before this energy regime. This does not rule out the possibility of earlier layers of UV completion, such as those accommodating neutrino masses, flavor, or electroweak symmetry breaking (EWSB).

Seen as an effective theory, aside from the gauge group $SU(3)\times SU(2)\times U(1)$, the SM reveals little. It presents itself as a series of local, gauge-invariant operators characterized by energy dimension d, with coefficients that, by dimensional analysis, scale as $\propto \Lambda_{\rm SM}^{4-d}$.

Let us begin with marginal operators of dimension $d = 4$ which are not sensitive to the cut-off scale $\Lambda_{\rm SM}$. They encompass almost all observable phenomena in nature, including the EW interactions, QCD, and quark and lepton masses. Together with the $d = 2$ and $d = 0$ operators, which we discuss later, these operators form the SM as a renormalizable theory. The considerable success of the SM arises from the accidental symmetries. These symmetries emerge without any underlying symmetry principle, only persisting at a given order because no operator breaking them at that order can coexist with the gauge symmetries. In particular, baryon and lepton family numbers stand as exact accidental symmetries within the SM.

Moving on to irrelevant operators i.e. $d > 4$. By NDA their contributions to low-energy observables are suppressed by $E^{d-4}/\Lambda_{\rm SM}^{4-d}$. Lepton number gets violated at $d = 5$ through the Weinberg operator [334],

$$\frac{1}{\Lambda_{\rm SM}} \left(\bar{L}_L H^c\right) \left(L_L^c H^c\right), \tag{7.51}$$

where L_L denotes the lepton doublet, H the Higgs doublet, and the superscript c stands for charge conjugation. Within one order of magnitude, this operator yields neutrino masses of approximately the right magnitude for $\Lambda_{\rm SM} \sim 10^{14}$GeV, i.e. $m_\nu \sim 0.1\,$eV and it stands as the unique dimension-five operator one can add to the SM.

Proceeding to the next higher dimension, $d = 6$, one finds that baryon number is violated. For coefficients of order one, the absence of proton decay implies $\Lambda_{\rm SM} \gtrsim 10^{16}$GeV.

From these considerations, it is entirely plausible that the SM remains valid up to very high scales, with $\Lambda_{\rm SM} \sim 10^{15}$GeV. Although the SM has certain other limitations, such as the non-generic flavor structure or the need to incorporate dark matter, none of these challenges are sufficiently strong to question the idea of heavy new physics. The only limitation capable of doing so is the Hierarchy Problem, which we will now explore.

Up to this point, we have not addressed the relevant operators of $d < 4$. There exist two such operators in the SM that need to be considered. These are at $d = 2$ the Higgs mass term $\sim \Lambda_{\rm SM}^2 H^\dagger H$ and at $d = 0$ the cosmological constant term $\sim \Lambda_{\rm SM}^4$. Unlike irrelevant operators which are suppressed by $\Lambda_{\rm SM}$, relevant operators are enhanced by it. For now, let us focus on the Higgs mass term. We know that the Higgs mass is measured to be $m_H = 125$GeV, implying that the mass parameter $\mu^2 = m_H^2/2 = (89\text{GeV})^2 \ll \Lambda_{\rm SM}^2$. Hence, the key question is, why does such an enormous hierarchy exist between the expected and measured parameter? The

fundamental aspect of the Hierarchy Problem lies in the significant disparity of these scales.

Let us have another look at the Higgs mass, assuming knowledge of the UV completion, we can express it as

$$m_H^2 = \int_0^\infty dE \frac{dm_H^2}{dE}(E;p), \tag{7.52}$$

where p represents the input parameters of the full theory. This integral sums up contributions to the Higgs mass from all energy scales. We can split the contributions into those where the SM remains a valid theory $E \leq \Lambda_{\text{SM}}$ and BSM contributions from above that energy threshold $E \geq \Lambda_{\text{SM}}$,

$$m_H^2 = \int_0^{\Lambda_{\text{SM}}} dE \frac{dm_H^2}{dE}(E;p) + \int_{\Lambda_{\text{SM}}}^\infty dE \frac{dm_H^2}{dE}(E;p) = \delta_{SM} m_H^2 + \delta_{BSM} m_H^2 \tag{7.53}$$

The SM contribution $m_H^2 \delta_{SM}$ can be computed, while the BSM contribution remains completely unknown. The low-energy contribution can be approximated by calculating one-loop contributions from the top quark, electroweak gauge bosons, and Higgs boson loops, as depicted in Fig. 7.7, resulting in

$$m_H^2 \delta_{SM} = \frac{\Lambda_{\text{SM}}^2}{(4\pi)^2} \left[6y_t^2 - \frac{3g_W^2}{2} \left(1 + \frac{1}{2\cos^2(\theta_W)} \right) - 6\lambda^2 \right], \tag{7.54}$$

where y_t is the top quark Yukawa coupling, g_W is the electroweak gauge coupling, and λ

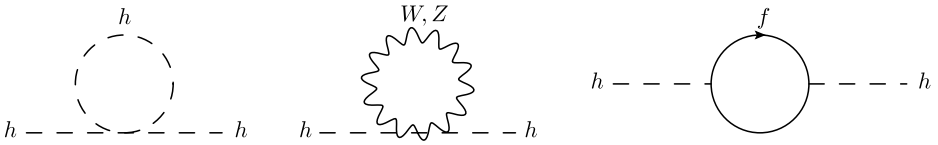

Figure 7.7: One loop contributions to the Higs mass from the top quark, electroweak gauge bosons and the Higgs self-coupling.

represents the Higgs self-coupling. These one-loop diagrams display quadratic sensitivity to the cutoff of the theory.

It becomes clear again that the Hierarchy Problem lies in the immense difference between the measured value of the Higgs mass and the expected order of magnitude from the IR contributions to it. The measured value necessitates that the completely unrelated BSM contributions $\delta_{BSM} m_H^2$ need to cancel the SM EFT contribution $\delta_{SM} m_H^2$ to extreme precision. This cancellation is captured by the tuning factor

$$\Delta_H = \left(\frac{\Lambda_{\text{SM}}}{m_H} \right)^2 \simeq \left(\frac{\Lambda_{\text{SM}}}{500\,\text{GeV}} \right)^2. \tag{7.55}$$

Requiring tuning of order one $\Delta_H \sim \mathcal{O}(1)$ needs new physics at the TeV scale while new physics at higher scales implies larger amount of tuning. This implies that even if we know the fundamental theory measurements with the precision equal to the amount of tuning is necessary to obtain a prediction for the Higgs mass.

Therefore, the severity of the Hierarchy Problem depends on the value of Δ_H, making the Higgs mass easier or harder to predict in the full theory. Only the experimental high-energy

frontier can shed light on the expected value of Δ_H, either by pushing $\Lambda_{\rm SM}$ to ever-higher scales or by revealing new physics that addresses the Hierarchy Problem.

In principle, the fundamental theory of nature could well be heavily tuned and that the solution to the hierarchy problem is something like anthropics. This is however counter-intuitive since physics seems to be natural more often than not and that the apparent tuning of parameters revealed some deeper reason, such as dynamic selection or symmetries. We therefore believe that it is worth while to study models in which the smallness of the EW scale comes about natural such as in models of dynamical relaxation, the topic of the next section.

7.3 Runaway Relaxion from Finite Density

This section is devoted to relaxion models, see Ref. [10]. We start in Sec. 7.3.1 with an introduction to the relaxion mechanism and general properties of the relaxion potential. We find that the relaxion potential naturally satisfies generic conditions needed to trigger the type of phase transitions we explored in Sec. 7.1. The relaxion in the late universe sits in a meta-stable minimum in vacuum and even more convenient all benchmark realizations of relaxion models are subject to density-dependent barriers. We explore the relaxion potential at finite densities in Sec. 7.3.2 and briefly review the conditions that lead to the formation and escape of relaxion bubbles, generally discussed and conveniently summarized previously in Sec. 7.1.6. In analogy to Sec. 7.1.8 we discuss the phenomenological implication of relaxion bubbles escaping from stars into our universe at late times in Sec. 7.3.3. We find that this puts novel constraints on benchmark relaxion models, which are briefly introduced and discussed. Finally we conclude and discuss our findings in Sec. 7.3.4.

7.3.1 The relaxion potential

The relaxion potential [10] is characterized by a washboard-like shape where the amplitude of the wiggles depends on the relaxion field ϕ itself,

$$V(\phi) = -\Lambda_{\rm R}^4 \frac{\phi}{f} - \tilde{\Lambda}_{\rm B}^4 F(\phi) \cos\frac{\phi}{f} \,. \tag{7.56}$$

$\Lambda_{\rm R}$ and $\tilde{\Lambda}_{\rm B}$ are the scales that control the size of the linear rolling and periodic back-reaction terms respectively, while $2\pi f$ parametrizes the field distance between adjacent minima. The monotonically increasing function $F(\phi)$ is of the form

$$F(\phi) = \left(\frac{\phi}{\phi_c} - 1\right)^{k/2} \Theta(\phi - \phi_{\rm c}) \,, \tag{7.57}$$

with $k = 1, 2$ and where ϕ_c is the field value where the periodic barriers turn on. This is taken such that the change in the size of the wiggles after a $2\pi f$ period is small, i.e. $\phi_c \gg f$, and therefore the landscape is densely populated over field ranges of order ϕ_c. The case $k = 0$ corresponds to Abbott's potential [9], where the size of the potential barriers is constant. The non-trivial behavior for $k = 1, 2$ arises from the dependence of the periodic term on the Higgs VEV, h, which in turn is determined by the scalar field ϕ.

Indeed, the Higgs potential, in particular the mass term, depends on the value of the relaxion,

$$V(h) = \tfrac{1}{2}(M^2 - g\phi M)h^2 + \tfrac{1}{4}\lambda h^4 \,, \tag{7.58}$$

where M is the cutoff and g is a small coupling that breaks the shift-symmetry associated with ϕ. Note that the periodic term in the relaxion potential, while breaking the continuous shift-symmetry, is still invariant under the discrete shift $\phi \to \phi + 2\pi f n$, $n \in \mathbb{Z}$. The coupling to the Higgs, as well as the linear term in the potential, break it completely, thus we expect

$$\frac{\Lambda_{\rm R}^4}{f} = c\, g M^3 \,, \tag{7.59}$$

where c is a parameter with the dimensions of an inverse coupling squared, therefore $c \sim 1/(4\pi)^2$ in a strongly coupled UV completion; in this work we take $c = 1$. Likewise, naive dimensional analysis yields $M \sim 4\pi f$; here we keep M and f independent and require that $f > M/4\pi$ ($f \gg M$ would correspond to a weakly coupled UV completion). As soon as the Higgs mass parameter turns negative, h acquires a VEV, given by

$$h^2 = \frac{M^2}{\lambda}\left(\frac{\phi}{\phi_c} - 1\right) \,, \quad \phi_c \equiv M/g \,, \tag{7.60}$$

where we have identified ϕ_c as given in Eq. (7.57).

One must now specify how the amplitude of the relaxion periodic term depends on the Higgs VEV. In Sec. 7.3.3 we discuss specific realizations of the relaxion, where such a dependence is either linear (QCD-relaxion), $\tilde{\Lambda}_{\rm B}^4 F(\phi) \equiv \Lambda_{\rm QCD}^4 h/v$ with $v \approx 246$GeV and $\Lambda_{\rm QCD}$ the QCD quark condensate, or quadratic (non-QCD-relaxion), $\tilde{\Lambda}_{\rm B}^4 F(\phi) \equiv \Lambda_{\rm C}(h/v)^2$, where $\Lambda_{\rm C}$ is the analogous of $\Lambda_{\rm QCD}$ for a new QCD-like confining dynamics. These two cases therefore correspond to $k = 1, 2$ in Eq. (7.57), respectively. More complicated functions, beyond Eq. (7.57), arise in the presence of extra light scanning scalars [335]. In any case, the change in the Higgs field between adjacent minima is

$$\Delta h^2 = \frac{2\pi}{\lambda}\frac{\Lambda_{\rm R}^4}{M^2} \,. \tag{7.61}$$

The requirement that $\phi_c \gg f$, which is correlated with the fact that the rolling term is hierarchically smaller than the cutoff of the theory, $\Lambda_{\rm R} \ll M$, see Eq. (7.59), ensures that the Higgs VEV varies slowly with every period of the potential.

Recall that in the relaxion mechanism, ϕ goes through a period of dynamical evolution, originally assumed to happen during a phase of cosmological inflation [10], where it rolls towards the minima of the landscape, generically stopping at one of the first (see below for a characterization of the minima). The parameters of the potential are adjusted, in a technically natural fashion, such that the Higgs VEV is of the right size at the minimum where the relaxion stops its evolution, that is $h = v$. Other proposals regarding the aforementioned time evolution of the relaxion have been put forward in e.g. [336–338] and [339]. In addition, already in [10] and subsequently in e.g. [335, 340], the potential itself was made to evolve during inflation, eventually leading to the relaxion resting in a minimum many periods beyond the first. In this section, we will not be concerned with the early cosmological dynamics of the relaxion. Instead, our analysis generally applies to whichever minimum the relaxion eventually stopped at, i.e. to the minimum where the relaxion is found when structures in the universe, particularly stars, start to form.

To ease the analysis of the landscape of relaxion minima, it is useful to redefine the scalar field as

$$\phi \equiv \phi_\ell(\theta) = (2\pi\ell + \theta)\, f \quad \text{with} \quad \ell \in \mathbb{N} \,, \quad \theta \in [0, 2\pi) \,, \tag{7.62}$$

where ℓ labels the period of the field. The local (metastable) minima of the potential are then denoted by $\phi_{\ell_*}(\theta_*)$, where the precise value of θ_* depends on the period ℓ_*. Minima are found as soon as the (ℓ_*-dependent) effective back-reaction grows large enough,

$$\Lambda_{\rm B}^4 \equiv \tilde{\Lambda}_{\rm B}^4 F(\phi_{\ell_*}(\pi/2)) > \Lambda_{\rm R}^4 \,. \tag{7.63}$$

In addition, we can conveniently choose to shift the origin of field space such that the minima start with $\ell_* = 1$, $\phi_\ell \to \phi_\ell + 2\pi f(\bar{\ell} - 1)$ with $\bar{\ell} = (\phi_c/2\pi f)\left[(\Lambda_{\rm R}^4/\tilde{\Lambda}_{\rm B}^4)^{2/k} + 1\right] + \xi$, where $\xi \in [0, 1)$ such that $\bar{\ell} \in \mathbb{N}$.

The relaxion landscape in Eq. (7.56) has two qualitatively different types of minima, depending on the relative size of the rolling and back-reaction terms, see Fig. 7.8. These can be parametrized by the variable δ

$$fV'(\phi_{\ell_*}(\pi/2)) \simeq -\Lambda_{\rm R}^4 + \Lambda_{\rm B}^4 \equiv \delta_{\ell_*}^2 \Lambda_{\rm B}^4 \,, \tag{7.64}$$

where V' is the derivative of the potential, here evaluated at the period ℓ_*. We note that δ_{ℓ_*} depends on the period, although to ease the notation we shall henceforth omit the subscript whenever unnecessary. For the first periods of the potential in which a minimum is present, the parameter δ is small. This implies that these minima are *shallow* [341]. Indeed, for $\delta^2 \ll 1$ the minimization condition $0 = fV'(\phi_{\ell_*}(\theta_*)) \simeq -\Lambda_{\rm R}^4 + \Lambda_{\rm B}^4 \sin(\theta_*)$ is satisfied at $\theta_* \simeq \pi/2 - \sqrt{2}\delta$, which is very close to the local maximum (found at $\theta \simeq \pi/2 + \sqrt{2}\delta$), see the lower-left panel of Fig. 7.8. The mass of the relaxion in these minima is given by

$$m_\phi^2 \simeq \frac{\Lambda_{\rm B}^4}{f^2}\sqrt{2}\delta \,, \qquad \text{(shallow)} \tag{7.65}$$

parametrically suppressed with respect to the usual expectation $m_\phi^2 \simeq \Lambda_{\rm B}^4/f^2$. In subsequent minima one finds $m_{\phi_{\ell_*}}^2 = \sqrt{\ell_*}\, m_{\phi_1}^2$, where the value of δ^2 corresponding to $\ell_* = 1$ is

$$\delta_{\ell_*=1}^2 \simeq \frac{k\pi f}{\phi_c}\left(\frac{\tilde{\Lambda}_{\rm B}^4}{\Lambda_{\rm R}^4}\right)^{2/k}\left(\tfrac{1}{4} + \xi\right) . \tag{7.66}$$

The other type of minima we are interested in corresponds to $\delta^2 \approx 1$. These are *deep* minima, since $\Lambda_{\rm B} \gg \Lambda_{\rm R}$, see the lower-right panel of Fig. 7.8. The minimization condition yields $\theta_* \simeq 1 - \delta^2 \ll 1$, and the relaxion mass is simply

$$m_\phi^2 \simeq \frac{\Lambda_{\rm B}^4}{f^2} \,. \qquad \text{(deep)} \tag{7.67}$$

Another quantity of phenomenological interest, which is markedly different between shallow and deep minima, is the height of the potential barrier,

$$\Delta V_{\rm top} \simeq \begin{cases} 4\sqrt{2}\Lambda_{\rm B}^4\delta^3 \,, & \text{(shallow)} \\ 2\Lambda_{\rm B}^4 \,. & \text{(deep)} \end{cases} \tag{7.68}$$

The suppression of the barrier in the case of minima with $\delta^2 \ll 1$ implies that even a small perturbation of the potential can easily destabilize the relaxion, displacing it towards lower energy minima.

This recovers the exact scaling as seen for the potential a la Coleman investigated in Eq. (7.3) and Eq. (7.4) and proves the point that relaxion models naturally give rise to the potentials studied in Sec. 7.1.

7.3.2 The relaxion at finite density

As we have seen in Sec. 7.3.1 when discussing the density dependence of the Coleman-like potential, depending on the parameters of the potential, the barrier separating the two minima

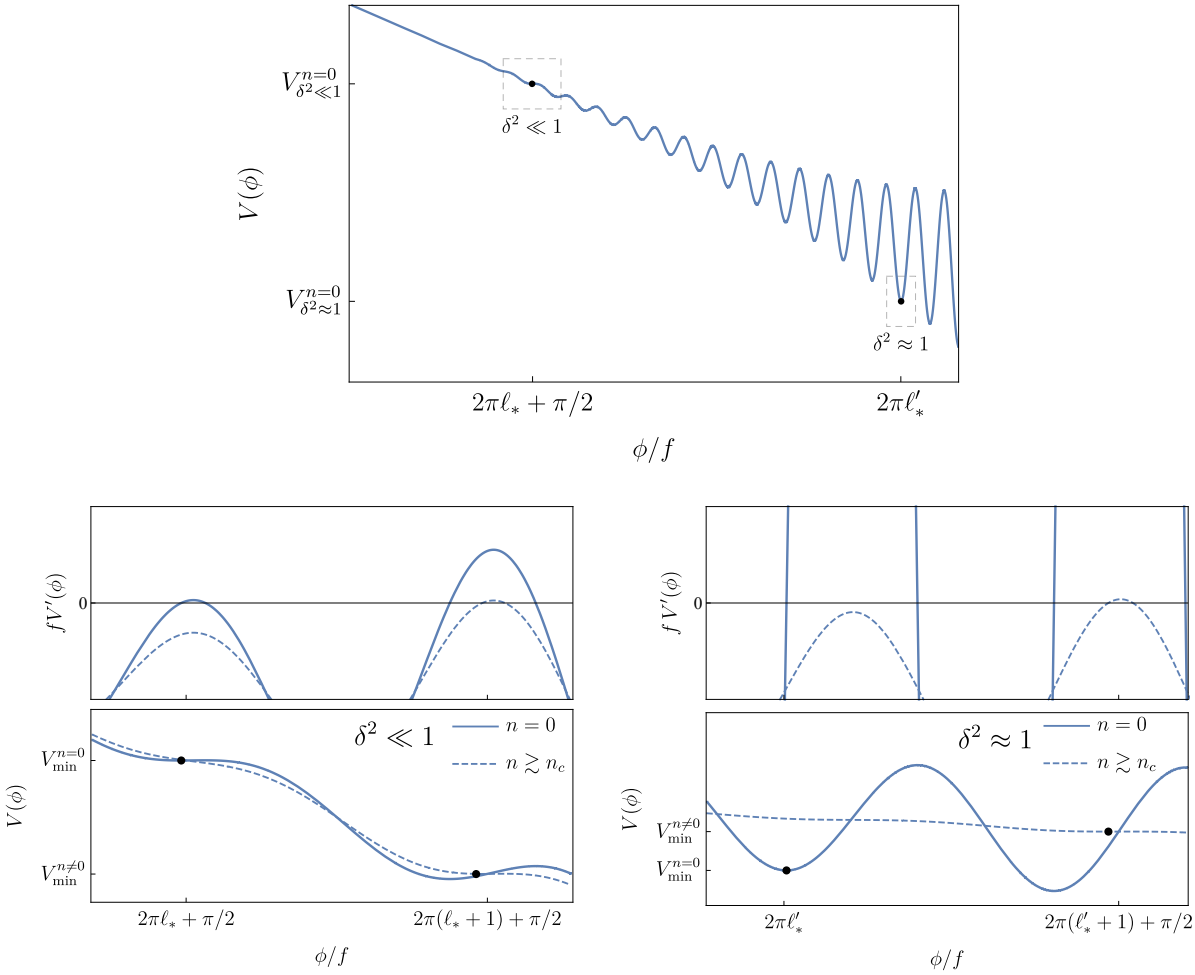

Figure 7.8: Global view of the relaxion potential (upper panel) and zoomed in regions with shallow (lower left) and deep (lower right) minima. Also plotted in the lower panels the in-density potential for ρ ($n = \rho$ in the plot) slightly larger than critical (dashed). The upper sub-panels show the derivative of the potential, both for $n = 0$ and $n \gtrsim \rho_c$. The first minima at finite density are always shallow.

can disappear in sufficiently dense systemt. In this section we analyse this behavior for the the relaxion potential Eq. (7.56).

As in Sec. 7.3.1 we mainly focus on a decrease of the back-reaction term, since for the relaxion this constitutes the leading deformation in most circumstances.[10] Indeed, in QCD-relaxion models, the size of the potential barriers is controlled by $\Lambda_{\rm QCD}$, which is known to linearly decreases with (small) baryon density [193, 210], a fact that has already been shown to affect the QCD axion [11, 186]. Alternatively, for non-QCD-relaxion models, we show in Sec. 7.3.3 that it is the change of the Higgs VEV with density that leads to a reduction of the potential barriers. In addition, in Sec. 7.3.3 we speculate about the possibility of dense systems made of the dark baryons, where the back-reaction term would decrease in a similar fashion as in QCD.

The scenario where the size of the potential barriers depends on density, ρ, has been recently

[10] In Sec. 7.3.3 we discuss a relaxion model in which the rolling term changes due to an electromagnetic background, as well as the modifications that this possibility introduces w.r.t. what we present in this section.

investigated in detail in [13]. Most of the discussion here parallels the one presented there. We summarize the main results and adapt the notation when necessary to match the relaxion potential.

In this section the dimensionless quantity ζ is redefined in complete analogy from Eq. (7.5) in Sec. 7.1 to parameterize the relative change in the back-reaction term at finite density

$$\zeta(\rho) \equiv 1 - \frac{\tilde{\Lambda}_{\rm B}^4(\rho)}{\tilde{\Lambda}_{\rm B}^4}\,, \tag{7.69}$$

with again $\zeta(\rho) \geqslant 0$ and $\zeta(0) = 0$. Let us now consider that in vacuum the relaxion sits at the minimum corresponding to some fixed period ℓ_*. One can then define a critical density, ρ_c, above which the effective back-reaction $\Lambda_{\rm B}$ at this minimum is no longer larger than the rolling term. This is implicitly given by

$$\zeta_c \equiv \zeta(\rho_c) = \delta_{\ell_*}^2\,, \tag{7.70}$$

where we recall that $\delta_{\ell_*}^2 = 1 - \Lambda_{\rm R}^4/\Lambda_{\rm B}^4$. When the critical density is reached, the local minimum associated with $\Lambda_{\rm B}$ ceases to exist. In other words, the relaxion minimum corresponding to the period ℓ_* (and obviously all the previous minima) is destabilized when $\zeta(\rho) > \delta_{\ell_*}^2$. Shallow minima, where $\delta^2 \ll 1$, are easily destabilized by density corrections, since $\zeta_c \ll 1$, while deep minima require $\zeta_c \approx 1$ in order to disappear, see Fig. 7.8. In the following, we restrict our discussion to $\zeta(\rho) \leq 1$, leaving the discussion of the case where the barriers change sign to App. D.7.

Hence at densities $\rho > \rho_c$ the minimum in which the relaxion resides in vacuum disappears. The number of periods between such a minimum and the first minimum of the in-medium potential is given by

$$N \equiv \ell_{*\,\rho} - \ell_* = \frac{\phi_c}{2\pi f}\left[\left(\frac{1-\zeta_c}{1-\zeta}\right)^{2/k} - 1\right]\left(\frac{\Lambda_{\rm R}^4/\tilde{\Lambda}_{\rm B}^4}{1-\zeta_c}\right)^{2/k} + \xi\,, \tag{7.71}$$

where $\xi \in [0,1)$ such that $N \in \mathbb{N}$. Independently of k ($k \neq 0$), ρ scales with the difference $\zeta - \zeta_c$. In addition, ρ scales with $\phi_c/f \gg 1$, thus as soon as ζ is above the critical value, the first in-density minimum is generically many periods beyond the one in vacuum. Additionally, the first minimum at finite density is always shallow: it lies at $\theta_{*\,n} \simeq \pi/2$, and the mass of the scalar as well as the potential barrier are suppressed beyond the naive expectations, much like for the shallow minima in vacuum.

The change in the ground state energy between consecutive minima, be these shallow or deep, at zero or non-zero density, is always

$$\Delta\Lambda \simeq -2\pi\Lambda_{\rm R}^4\,. \tag{7.72}$$

Formation and escape of a bubble

The disappearance of the in-vacuo minimum at supercritical densities leads to a non-trivial scalar profile, $\phi(r)$, developing within finite-size systems such as stars as we have seen in Sec. 7.1. The exact conditions for the formation and escape of such a bubble is summarized in Sec. 7.1.6 and can be readily applied to the relaxion potential Eq. (7.56).

For a shallow relaxion minimum ($\delta^2 \ll 1$), the change in the wall's tension is negligible, since already in vacuum the potential barrier separating the two adjacent minima is very small, Eq. (7.68). Therefore, when a shallow relaxion bubble forms, it generically escapes from the star as well. The condition for this to happen is

$$R_{\rm T} \gtrsim \frac{f}{\Lambda_{\rm R}^2}\,. \qquad \text{(shallow)} \tag{7.73}$$

Instead, for a deep relaxion minimum ($\delta^2 \approx 1$), the change in the wall's tension is significant, going from being dominated by the gradient energy at the core, to being dominated by the large potential barrier in vacuum. This implies that the escape condition is stronger than the condition for formation. The former reads

$$\Delta R_{\rm T} \gtrsim \frac{f}{\Lambda_{\rm R}^2} \frac{1}{\sqrt{1-\delta^2}} = \frac{f\Lambda_{\rm B}^2}{\Lambda_{\rm R}^4} \,. \qquad \text{(deep)} \tag{7.74}$$

As seen in Sec. 7.1, also for the relaxion potential it is generically much more difficult for a bubble connecting deep minima to escape from the star than for a shallow bubble. Furthermore, recall that in order to destabilize a deep minimum much larger densities are needed than in the shallow case. As also justified in Sec. 7.1, we take both the size of the core $R_{\rm T}$, and the size of the transition region from the core to the end of the star $\Delta R_{\rm T}$, to be of the same order as the whole size of the star, $R_{\rm S} \sim R_{\rm T} \sim \Delta R_{\rm T}$.

Note that we take into account WDs and NSs (see Chap. 3) and the Sun with typical density $\rho_\odot \approx 1.5\,{\rm g/cm^3} \times 1/m_p \approx 7 \times 10^{-9}\,{\rm MeV}^3$ and radius $R_\odot \approx 7 \times 10^5\,{\rm km}$.

Before moving to the phenomenological consequences of escaping bubbles for specific relaxion models, some additional comments are in order:

If the star grows very large compared to μ^{-1}, very large field displacements (w.r.t. where the relaxion resides in vacuum) are energetically allowed inside the bubble. Indeed, at a fixed core density such that ζ is not accidentally close to criticality, a very large core $R_{\rm T} \sim \sqrt{N}\mu^{-1} \gg \mu^{-1}$ allows for the relaxion to move by many periods $N \gg 1$, see Eq. (7.71). As explained in App. D.6, such a large relaxion bubble has the effect of helping the standard bubble connecting two adjacent minima (i.e. for which $\Delta\phi(0) \sim 2\pi f$) to escape from the star. In fact, such a bubble escapes independently of the density profile, regardless of how fast density decreases towards the outer edge of the star. In this case the conditions Eqs. (7.73), (7.74) read the same, only with $R_{\rm S}$ instead of $R_{\rm T}$ and $\Delta R_{\rm T}$; they simply encode the requirement for a standard relaxion bubble to expand once it is outside of the star, see Eqs. (D.24), (D.25). If one bubble is able to escape, the new relaxion minimum in vacuum becomes the one associated with the next period, i.e. $\ell_* + 1$. Interestingly, since $N = \ell_{*n} - \ell_* \gg 1$, such a new minimum is also unstable inside the dense system. This then implies that another bubble, within which this time the relaxion sits at the minimum $\ell_* + 2$, will generically be able to escape as well, and so on until the escape condition is no longer satisfied.

Finally, let us note that our whole discussion relies on the assumption that the density profile is treated as a background field that does not receive a large back-reaction from the formation and expansion of a relaxion bubble. In App. D.8 we discuss the interactions of the relaxion (non-trivial configurations) with the density profile, thereby justifying this treatment.

7.3.3 Bounds on relaxions

The relaxion bubbles are no different from our generic scalar bubbles in Sec. 7.1 and thus are born along with the stars that seed them. Therefore, if the conditions for the bubble to expand beyond the dense system are met, a phase transition in the universe to a new relaxion vacuum can occur whenever the right type of stars are formed.

As discussed in Sec. 7.1.8 such bubbles are forbidden if the change in the CC that comes along with them is too large, see Eq. (7.48).

Still, it is interesting to note that if we were to consider bubbles nucleated by the largest stars observed so far, with radii $R_{\rm S} \sim 10^3 R_\odot$, or by large non-standard astrophysical objects, associated for instance with some beyond the SM relic species, e.g. dark matter (see Sec. 7.3.3), then a phenomenologically viable late-time phase transition could have taken place. In this

regard, it would be interesting to perform a detailed assessment of the associated cosmological and astrophysical signatures.

Besides, in relaxion models, the change of minimum also implies a change in the Higgs VEV, for which there exist cosmological (and astrophysical) constraints as well. However, let us note right away that the relative change of the electroweak scale between minima is much smaller than the change in the vacuum energy: $(\Delta h^2/v^2)/(|\Delta\Lambda|/\Lambda_0) = \Lambda_0/\lambda c v^2 M^2 \ll 1$, where we have used Eq. (7.61). Nevertheless, since this is one of the trademarks of relaxion models compared to other landscapes, let us briefly review the bounds. There are significant constraints on a different value of the Higgs VEV during BBN, $|\Delta h/v| \lesssim 10^{-2}$ where $\Delta h = h - v$ [342]. In addition, it has been recently argued that SN explosions can only happen if h is below a factor of a few away from v [343]. While these constraints (the one from BBN in particular) could be violated if the universe underwent a change of relaxion minimum at star formation, as shown above, the associated change in vacuum energy always yields a more or equally stringent constraint.

In the remainder of this section, we work out the specifics of how a non-vanishing SM matter density (or an electromagnetic background) affects the potential of some benchmark relaxion models, and re-express the conditions for the formation and escape of bubbles in terms of their parameters.

QCD relaxion

The most economic origin of the relaxion periodic term is low-energy QCD dynamics, in which case we identify the relaxion with the QCD axion. The dependence on the Higgs VEV arises from the well-known dependence of the axion potential on the quark masses. This leads us to identify $\tilde{\Lambda}_{\rm B}$ in Eq. (7.56) as well as $\Lambda_{\rm B}$, the effective size of the periodic term at the minimum where the relaxion sits in vacuum, as

$$\tilde{\Lambda}_{\rm B}^4 = \Lambda_{\rm QCD}^4 \frac{M}{v\sqrt{\lambda}}\,, \quad \Lambda_{\rm B}^4 = \Lambda_{\rm QCD}^4 \frac{h}{v}\,. \tag{7.75}$$

Note that if a seeded phase transition took place, the relaxion would not sit at the same minimum today as right before star formation. Nevertheless, in the following we conservatively fix $h = v \approx 246\text{GeV}$, since any minimum before star formation with a smaller h would necessarily be shallower than the present one, making it easier for the transition to occur. The exponent of the function $F(\phi)$ in Eq. (7.57) is determined as well, $k = 1$, since the dependence of the back-reaction term on the Higgs VEV is linear. Note that the QCD(-axion) scale is $\Lambda_{\rm QCD}^4 \simeq m_\pi^2 f_\pi^2/4$. Finally, the value of δ, which determines if the relaxion minimum is shallow or deep, depends on the relative size of the rolling term, $\Lambda_{\rm R}^4 = gM^3 f$, according to Eq. (7.64),

$$\delta^2 = 1 - g\frac{M^3 f}{\Lambda_{\rm QCD}^4}\,. \tag{7.76}$$

In this regard, let us note that, as advanced, for the first minima of the potential δ is always a small parameter as long as the scanning of the Higgs VEV is sufficiently precise. At the first minimum,

$$\delta_{\ell_*=1}^2 \simeq \frac{\pi\Lambda_{\rm QCD}^4}{\lambda v^2 M^2}\left(\tfrac{1}{4} + \xi\right) \ll 1\,, \quad \xi \in [0,1)\,, \tag{7.77}$$

while for all the subsequent minima $\delta_{\ell_*}^2 = \ell_* \delta_1^2$. Since it has no actual significance, from now on we set $\xi = 0$.

Once all the relevant parameters of our potential have been identified, let us consider the fate of the relaxion bubbles, starting with shallow minima, $\delta^2 \ll 1$. This case should be primarily

considered as illustrative, since the value of the relaxion at the minimum is displaced from a multiple of $2\pi f$ by approximately $\pi/2$, thus the strong CP angle is also $\theta_{\rm QCD} \simeq \pi/2$, which is experimentally ruled out. Keeping this in mind, we can compute the dependence of the back-reaction term, or equivalently ζ in Eq. (7.69), on the baryon density ρ_N by means of the Hellmann-Feynman theorem, as explained in e.g. [11],

$$\zeta(\rho_N) \simeq \frac{\sigma_{\pi N}\rho_N}{m_\pi^2 f_\pi^2}\,. \tag{7.78}$$

This holds for densities below a few times nuclear saturation, and where $\sigma_{\pi N} \approx 45\,\text{MeV}$ is known as the pion-nucleon sigma term. In turn, since the critical value of ζ for which the relaxion can classically move is given by $\zeta_c = \delta^2$, we find that a proto-bubble can start forming if

$$\rho_N > \frac{\ell_*}{M^2}\frac{\pi\Lambda_{\rm QCD}^8}{\sigma_{\pi N}\lambda v^2} \approx 1\times 10^{-8}\,\text{MeV}^3\left(\frac{1\,\text{TeV}}{M/\sqrt{\ell_*}}\right)^2\,, \tag{7.79}$$

that is if densities are larger than $3\,\text{g/cm}^3 \times 1/m_p$. This is a very low critical density, found not only in NSs and WDs, but in the Sun as well. The densities reached in these systems then set the minimum value of $M/\sqrt{\ell_*}$ that is excluded if the bubble eventually fully forms and escapes the star. The corresponding condition is given in Eq. (7.73), which for the QCD-relaxion reads

$$R_{\rm S} \gtrsim \frac{f}{\Lambda_{\rm QCD}^2}\,, \tag{7.80}$$

where we have taken $R_{\rm T} \sim R_{\rm S}$ as argued in Sec. 7.3.2, and traded $\Lambda_{\rm R}$ with $\Lambda_{\rm QCD}$ given that $\delta^2 \ll 1$. Using typical radii and densities for the type of star under consideration, we arrive at the following excluded values for the relaxion decay constant and cutoff

$$\begin{aligned}
\text{NS}: &\quad f \lesssim 3\times 10^{-2} M_{\rm P}\,, &&\quad M/\sqrt{\ell_*} \gtrsim 1\times 10^{-4}\text{GeV}\,, \\
\text{WD}: &\quad f \lesssim 63\, M_{\rm P}\,, &&\quad M/\sqrt{\ell_*} \gtrsim 0.3\text{GeV}\,, \qquad \text{(QCD; shallow)} \\
\odot: &\quad f \lesssim 9\times 10^{3} M_{\rm P}\,, &&\quad M/\sqrt{\ell_*} \gtrsim 1.4\,\text{TeV}\,.
\end{aligned} \tag{7.81}$$

Therefore, while recalling that the shallow QCD relaxion is already ruled out by a too large $\theta_{\rm QCD}$, we find that classical rolling and escape would happen for nearly all values of f and $M/\sqrt{\ell_*}$. Note in fact that for both WDs and main-sequence stars the upper bounds on f are above $M_{\rm P}$, and that for NSs and WDs the lower bound on M is not larger than the electroweak scale.

The situation is markedly different for deep minima, particularly since we must require $\theta_{\rm QCD} \lesssim 10^{-10}$, which then fixes $1-\delta^2$ to be as small at the minimum in question. Since $\zeta_c = \delta^2$, this implies that the QCD barriers at finite density, $\Lambda_{\rm QCD}^4(1-\zeta(\rho))$, would need to nearly disappear for the relaxion to be able to classical move to the following minimum. Such large densities, if attainable at all inside NSs, are certainly beyond perturbative control, and thus the linear approximation used to derive Eq. (7.78) is not applicable. However, since in the cores of NSs densities could be higher than ten times nuclear saturation density [299], it has long been hypothesized that new phases of QCD, such as kaon condensation or color-superconductivity, could take place there, see Sec. 5 and [11] as well as references therein. As shown in that work, this raises the possibility that, while remaining finite, the periodic potential flips sign. As explained in App. D.7 (see also [254]), this would lead to relaxion condensation with $\Delta\phi(0) = \pi$, assuming a small rolling region. Such a type of bubble would remain confined inside the dense system.

Still, an exciting option remains that such a change of phase of strongly interacting matter, being controlled by QCD dynamics, happens very fast compared to the reaction time of the

relaxion. In the case of a deep minimum, this reaction time is prolonged compared to a shallow one, $\mu^{-1} = f/\Lambda_{\rm R}^2 = \theta_{\rm QCD}^{-1/2} f/\Lambda_{\rm QCD}^2$. Then, as discussed in Sec. 7.1, the kinetic energy that the field acquires after the sudden change of its potential could be enough to overcome the (flipped) barriers and to create a relaxion bubble with $\Delta\phi(0) \gg 2\pi f$. This facilitates the escape of a standard $2\pi f$ bubble, as discussed above (see also App. D.6). With our current knowledge of QCD at such extreme densities we cannot assert whether this is the right picture. Nevertheless, if it were, a phase transition would take place if the condition Eq. (D.25) is satisfied

$$f < \sqrt{\theta_{\rm QCD}}\Lambda_{\rm QCD}^2 R_{\rm NS} \approx 8 \times 10^{11}{\rm GeV} \left(\frac{\theta_{\rm QCD}}{10^{-10}}\right)^{1/2} . \qquad \text{(QCD; deep)} \tag{7.82}$$

Non-QCD relaxion

The correlation between the relaxion selection of the electroweak scale and of $\theta_{\rm QCD}$, i.e. between the electroweak hierarchy and the strong CP-problem, can be broken by positing that dynamics other than QCD is responsible for the generation of the periodic back-reaction term [10]. Such a non-QCD strong sector must still couple to the relaxion in such a way as for the amplitude of the barriers to depend on the Higgs VEV. Experimental constraints on new electroweak-charged degrees of freedom that get mass from electroweak symmetry breaking motivate that such a dependence is quadratic, instead of the linear dependence of the QCD scale (see however Sec. 7.3.3). Therefore, we identify our potential parameters in Eq. (7.56) as

$$\tilde{\Lambda}_{\rm B}^4 = \Lambda_{\rm C}^4 \frac{M^2}{\lambda v^2} , \quad \Lambda_{\rm B}^4 = \Lambda_{\rm C}^4 \frac{h^2}{v^2} , \quad k = 2 , \tag{7.83}$$

where $\Lambda_{\rm C}$ is the new confinement scale, analogous to $\Lambda_{\rm QCD}$ in Eq. (7.75). In order for the size of the barriers to be naturally dominated by the Higgs VEV squared, the condition $\Lambda_{\rm C}^2 \lesssim 4\pi v^2$ must be required [10, 335, 339, 344]. In parallel with the QCD-relaxion, the value of δ at a given minimum is determined by the relative size of the rolling term and $\Lambda_{\rm C}^4$, i.e. Eq. (7.76) with $\Lambda_{\rm QCD} \to \Lambda_{\rm C}$. The first minima of the landscape are always shallow, since $\delta_1^2 \simeq \pi\Lambda_{\rm C}^4/2\lambda v^2 M^2 \ll 1$ for $\Lambda_{\rm C}^2 \lesssim 4\pi v^2$ and $M \gg 4\pi v$.

The dependence of the back-reaction term on the (SM) matter density in this case is indirect, stemming from a change in the Higgs VEV. This is due to the coupling of the Higgs field to fermions, $\mathcal{L} \supset -\frac{1}{\sqrt{2}} y_\psi h \bar{\psi}\psi$, which in a (non-relativistic) ψ background, $\langle\bar{\psi}\psi\rangle \simeq \langle\bar{\psi}\gamma_0\psi\rangle = \rho_\psi$, displaces its VEV from its value in vacuum. The small relative displacement with respect to Eq. (7.60) is given, at leading order in ρ_ψ, by

$$\delta h^2(\rho_\psi) = \frac{y_\psi}{\sqrt{2}} \frac{\rho_\psi}{\lambda v^3} , \tag{7.84}$$

where we have evaluated $h = v$. The change $h^2 \to h^2(1 + \delta h^2)$ is then responsible for the density dependence of the relaxion potential. In this regard, note that both the rolling and back-reaction terms are affected, since both of them are in fact quadratic in the Higgs, see Eq. (7.58) and Eq. (7.83) respectively. Nevertheless, it is easy to see that the leading effect is associated with the latter since, while the Higgs contribution to the barriers is the leading piece, it is a subleading one for the linear slope as long as $v^2/M^2 \ll 1$.

The most relevant densities to consider, as in the case of the QCD-relaxion, are baryonic, since these are usually the largest (in particular in the cores of NSs) and the coupling of nucleons to the Higgs is significant $y_N = \sigma_{\pi N}/v$, where $N = n, p$. In NSs, besides neutrons and protons,

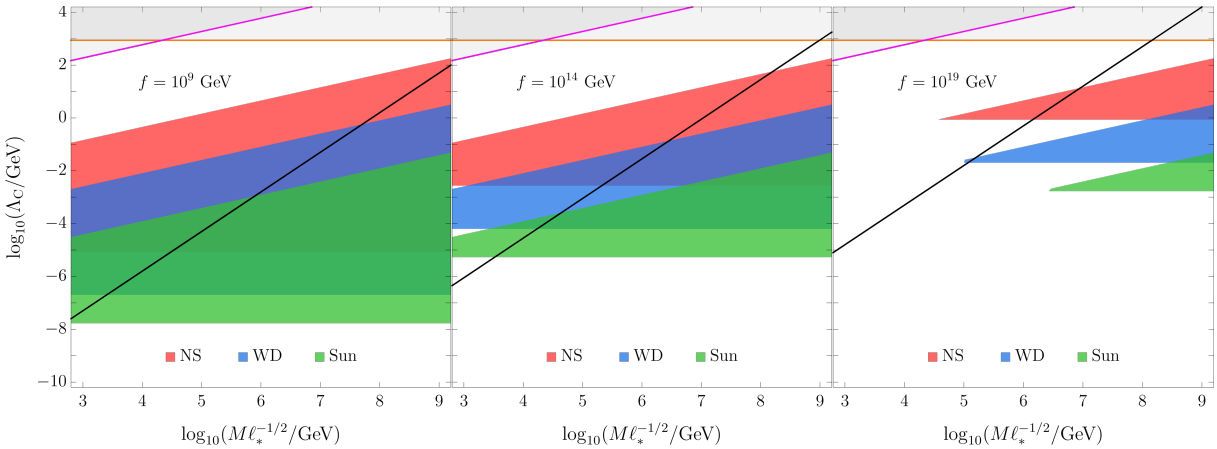

Figure 7.9: $(M/\sqrt{\ell_*}, \Lambda_C)$-regions excluded by the formation and escape of a non-QCD relaxion bubble induced by NSs (red), WDs (blue), and the Sun (green), in the case of shallow minima, $\delta^2 \ll 1$ or equivalently $\Lambda_R \simeq \Lambda_C$, and for $f = 10^9, 10^{14}, 10^{19}$GeV (left, middle, right panel, respectively). The grey, shaded region is excluded by the requirements $\Lambda_C^2 \lesssim 4\pi v^2$ (orange line) and $\Delta h^2 < v^2$ (magenta line), while the region of parameter space preferred by relaxation during inflation lies above the diagonal black line. Note that the latter line depends on a model-dependent period of dynamical evolution, which our constraints are independent of. The three lines are drawn taking $\ell_* = 1$.

leptons are present as well. Charge neutrality implies $\rho_p + \rho_e + \rho_\mu = 0$, where note that due to the highly energetic Fermi surface of the electron, β-equilibrium not only implies $\mu_n = \mu_p + \mu_e$ but $\mu_e = \mu_\mu$ as well, implying a non-vanishing muon density (for $\mu_\mu > m_\mu$). This is interesting since the coupling of muons to the Higgs, $y_\mu = m_\mu/v$, is twice as large as to nucleons. In the outer layers of NSs, in WDs and main-sequence stars, baryon densities become once again the most important, given the small coupling of electrons to the Higgs. We therefore focus on the effects of a non-vanishing ρ_N. Still working in the linear approximation, the decrease of the non-QCD barriers is encoded as

$$\zeta(\rho_N) \simeq \sqrt{2}\frac{\sigma_{\pi N}\rho_N}{m_h^2 v^2}\,, \tag{7.85}$$

where we have written it in terms of the physical Higgs mass, $m_h^2 = 2\lambda v^2$, to make apparent the similarity with Eq. (7.78). A relaxion bubble can then classically form if densities satisfy the following condition

$$\rho_N > \frac{\ell_* \Lambda_C^4}{M^2}\frac{\pi v^2}{\sqrt{2}\sigma_{\pi N}} \approx 3\times 10^{-3}\,\mathrm{MeV}^3 \left(\frac{1\,\mathrm{TeV}}{M/\sqrt{\ell_*}}\right)^2 \left(\frac{\Lambda_C \simeq \Lambda_R}{1\,\mathrm{MeV}}\right)^4 . \tag{7.86}$$

Even though finite density effects are relatively suppressed in the case of the non-QCD relaxion, the required critical densities are sufficiently small, for large cutoffs or small back-reactions, that they can be found from NSs to the Sun. Furthermore, relaxion bubbles will only form for shallow minima, $\zeta_c = \delta^2 \ll 1$, since values of $\zeta(\rho_N)$ close to unity, which are required to destabilize deep minima, can never be achieved (this would require exorbitant densities, of order $m_h^2 v^2/\sigma_{\pi N} \sim 10^{19}\,\mathrm{MeV}^3$).

The condition for a shallow bubble to fully form and escape the star simply reads

$$R_S \gtrsim \frac{f}{\Lambda_C^2}\,, \qquad \text{(non-QCD; shallow)} \tag{7.87}$$

where recall that for $\delta^2 \ll 1$ we have $\Lambda_{\rm R} \simeq \Lambda_{\rm C}$. The conditions in Eqs. (7.86), (7.87), which if satisfied imply a late-time phase transition at odds with experiment, give rise to non-trivial constraints on the parameter space of the non-QCD relaxion. These are qualitatively different and generically stronger than those dependent on the period of dynamical evolution; namely $\Lambda_{\rm R}^4 > M^6 f/\sqrt{12}\pi M_{\rm P}^3$ for relaxation during inflation, associated with the requirement of classical evolution of the field along with the energy density associated with the relaxion being a subdominant component [10,335,339,344]. A related but different discussion of chameleon effects relevant for dark matter direct detection experiments have been recently presented in [345]. We show our constraints in Figs. 7.9 and 7.10, in the planes $(M/\sqrt{\ell_*}, \Lambda_{\rm C})$, and (M, g) for $\ell_* = 1$, respectively. These are for three different values of the relaxion decay constant, $f = 10^9$, 10^{14}, 10^{19}GeV. In both planes, it is evident that the lower boundary of the excluded (shaded) regions extends to smaller values of either $\Lambda_{\rm C} \simeq \Lambda_{\rm R}$ or g as f is taken smaller, since it is easier for the relaxion bubble to fit inside a given type of star, Eq. (7.87). In turn, as f is taken larger, either $\Lambda_{\rm C}$ or g must be larger for the bubble to be able to form, which then requires higher densities, Eq. (7.86); this is why the constrains from less dense stars become comparatively weaker. Note that although the plots are cut at $M = 10^9$GeV, the constraints actually extend up to $M \lesssim 4\pi f$ in each case. Let us also point out that if the theoretical expectation that $f < M_{\rm P}$ is accepted, the constraints for $f = 10^{19}\text{GeV} \approx M_{\rm P}$ can be considered as absolute, meaning the corresponding parameter space is excluded for any (possible) value of the axion decay constant. Finally, considering larger stars with enough density would enlarge the excluded regions. In the case of the (green) region associated with main-sequence stars, once the inequality Eq. (7.48) is saturated, more refined experimental constraints on changes in the energy budget of the universe or from other observables, would be needed. For instance, the densities achieved in the largest stars ($\rho_N \sim 7 \times 10^{-17}\,\text{MeV}^3$, $R \sim 10^3 R_\odot$) are sufficiently high to destabilize the first minima of the non-QCD relaxion with $\Lambda_{\rm TC} \sim \Lambda_{\rm B} \sim \Lambda_0^{1/4}$, i.e. for which the change in the cosmological constant is currently experimentally allowed. This is, according to Eq. (7.86), true even for the smallest cutoff $M \sim 1\,\text{TeV}$. The investigation of the phenomenology of such phase transitions is beyond the scope of this work.

Technicolored relaxion

For the QCD and non-QCD relaxion models, the most essential density deformation of their respective landscapes is in the form of a smaller back-reaction term. Now we point out that in general, this is not the only possibility. In this section, we present a scenario in which the leading effect is due to a change in the rolling term. Furthermore, this change is induced not by background matter but by the electromagnetic fields surrounding a spinning neutron star.

Another variant of the relaxion model involves a technicolor-like sector which provides an additional source of electroweak symmetry breaking on top of the elementary Higgs. While this sector, irrespective of the relaxion, is severely constrained experimentally (by electroweak precision data, Higgs coupling measurements, and resonance searches at the LHC), it is not yet ruled out [346, 347]. Exactly like for the QCD axion, the coupling of the relaxion to the topological charge of this new confining sector gives rise to the periodic potential term [344], with the analog of $\Lambda_{\rm QCD}$ given by

$$\Lambda_{\rm TC}^4 \simeq 4\pi v'^3 m_U\,, \tag{7.88}$$

where v' is the electroweak-breaking order parameter of the technicolor (TC) sector. The electroweak scale is given by $v^2 = v'^2 + h^2$ and $m_U = y_U h/\sqrt{2}$ is the lightest techniquark mass, linearly proportional to the elementary Higgs VEV. The parameters of the relaxion potential are then identified as $\Lambda_{\rm R}^4 = gM^3 f$ (like in all the previous models), while $\tilde{\Lambda}_{\rm B}$ and $\Lambda_{\rm B}$ are similar

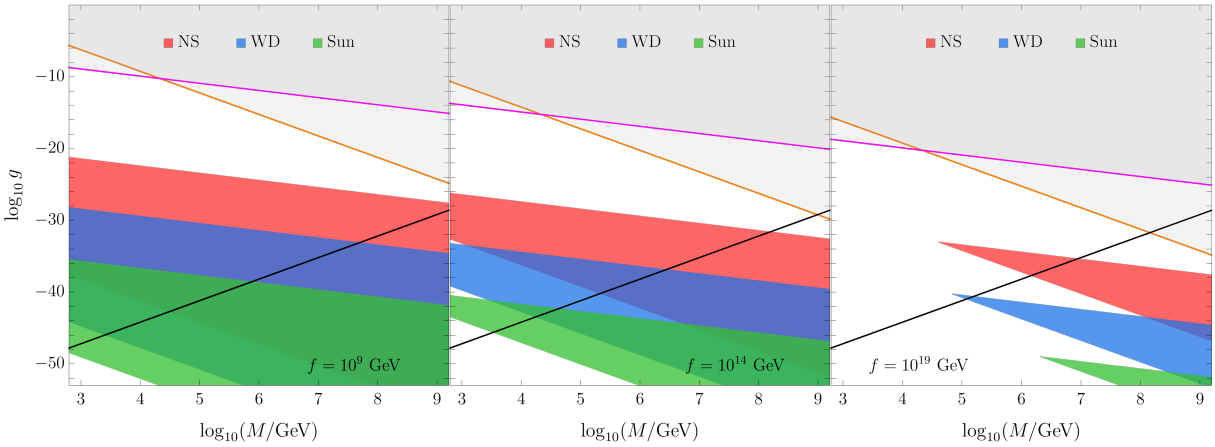

Figure 7.10: (M, g)-regions excluded by the formation and escape of a non-QCD relaxion bubble induced by NSs (red), WDs (blue), and the Sun (green), in the case of shallow minima, $\delta^2 \ll 1$ or equivalently $\Lambda_{\rm R} \simeq \Lambda_{\rm C}$, and for $f = 10^9, 10^{14}, 10^{19}$GeV (left, middle, right pannel). The grey, shaded region is excluded by the requirements $\Lambda_{\rm C}^2 \lesssim 4\pi v^2$ (orange line) and $\Delta h^2 < v^2$ (magenta line), while the region of parameter space preferred by relaxation during inflation lies above the diagonal black line. Note that the latter line depends on a model-dependent period of dynamical evolution, which our constraints are independent of. Recall that $g = \Lambda_{\rm R}^4/M^3 f$ and we have taken $\ell_* = 1$ in Eq. (7.86).

to the QCD relaxion, Eq. (7.75), with the following replacements

$$\Lambda_{\rm QCD} \to \Lambda_{\rm TC}\,, \quad v \to \sqrt{v^2 - v'^2}\,. \tag{7.89}$$

Due to the aforementioned experimental constraints, v' cannot be large, $v' \lesssim 70$GeV, nor very small either, since the masses of the TC resonances are expected below $4\pi v'$ [346].

It is crucial for our analysis that the relaxion in this model has a large coupling to photons. Just like for the QCD axion, this coupling is a consequence of the (model-independent) coupling to the technigluons as well as the (model-dependent) electromagnetic anomaly,

$$\frac{g_{\phi\gamma\gamma}}{4}\frac{\phi}{f}F_{\mu\nu}\tilde{F}^{\mu\nu}\,, \quad g_{\phi\gamma\gamma} = c\left(\frac{\alpha}{2\pi}\right)\,, \tag{7.90}$$

where c is a model-dependent constant. Such an interaction, which is not suppressed by the small shift-symmetry breaking parameter g, has significant implications for the fate of this relaxion model, in particular, because of the existence of strong electromagnetic fields surrounding rapidly rotating NSs (magnetars/pulsars).[11] Indeed, in such an environment the linear term in the relaxion potential receives an additional contribution, $\Lambda_{\rm R}^4 \to \Lambda_{\rm R}^4(1+\eta)$, where

$$\eta = \frac{g_{\phi\gamma\gamma}\boldsymbol{E}\cdot\boldsymbol{B}}{\Lambda_{\rm R}^4}\,. \tag{7.91}$$

The critical value of η at which the minimum in vacuum ceases to be a minimum in the electromagnetic background is given by $\eta_c = \delta^2/(1-\delta^2)$. This statement can be translated to a

[11] By considering a rotating star we are departing from our main assumptions concerning the characteristics of the system, as described in Sec. 7.1, in particular spherical symmetry and (near) time-independence. However, we expect such departures to neither have a large impact on our qualitative description nor to change the order of magnitude results we derive.

transition radius, $R_{\rm T}^{\rm EM}$, which is the maximal radius for which classical rolling is allowed (equivalent to the radius of the dense star core $R_{\rm T}$, see Sec. 7.1.3), and given by the solutions of $\eta(R_{\rm T}^{\rm EM}) = \eta_c$. It is also the position of the bubble wall at formation. The value of δ^2 at the ℓ_*-th shallow minimum is given, as in the QCD relaxion, by $\delta^2_{\ell_*} = \ell_* \delta_1^2$, where $\delta^2_{\ell_*=1}$ is as in Eq. (7.77) with $\Lambda_{\rm QCD} \to \Lambda_{\rm TC}$. The electric and magnetic fields depend on the intrinsic properties of the star as well as on space-time, in a similar fashion as the (baryonic) density profiles that were considered in our previous examples. However, in contrast to the case of a dense system of finite size, here the electromagnetic background extends to infinity (i.e. much beyond the surface of the star). This implies, for instance, that the radius at which classical rolling is allowed is potentially much larger than $R_{\rm S}$. As explained in Sec. 7.1.3 it is the size of this region compared to μ^{-1}, the typical length scale of the relaxion, that determines whether a bubble is formed or not. For a technicolored relaxion μ^{-1} is r-dependent,

$$\mu^{-1}(r) = \frac{f}{\Lambda_{\rm R}^2} \frac{1}{\sqrt{1+\eta(r)}} \,. \tag{7.92}$$

Let us then consider a simple model of the magnetosphere, in particular a rotating dipole in vacuum (see e.g. [227]),

$$\boldsymbol{E}\cdot\boldsymbol{B} = \frac{R_{\rm S}^6 B_{\rm S}^2 \Omega_{\rm S}}{4r^5} \sin\alpha \big(\cos\theta \sin\alpha + \sin\theta\cos\alpha \left[r\Omega_{\rm S} \cos\left(\lambda + r\Omega_{\rm S}\right) - \sin\left(\lambda + r\Omega_{\rm S}\right)\right] \big) \,, \tag{7.93}$$

with $B_{\rm S}$ the magnetic field at the stellar surface, $\Omega_{\rm S}$ the rotation frequency of the star, α the inclination angle of the dipole w.r.t. the rotation axis, and $\lambda = \phi - \Omega_{\rm S} t$ the co-rotating azimuthal angle. From here on we take $\alpha = \pi/4$ for simplicity. In addition, we average the dipole over one quadrant, that is $\theta \in [0, \pi/2]$ and $\phi \in [0, \pi]$, as well as over the relaxion time scale μ^{-1}. We identify two distinct limits, the first where the field reacts fast compared to the rotation frequency, $\mu \gg \Omega_{\rm S}$, and the second where it reacts slowly, $\mu \ll \Omega_{\rm S}$. Since the bubble dynamics, in particular if the bubble escapes or stays confined to the star, is a local statement governed by the position of the bubble wall at its formation, we take $\mu^{-1}(R_{\rm T}^{\rm EM})$ as the relevant time scale in both limits. Within the fast limit, in order to analytically determine $R_{\rm T}^{\rm EM}$ we perform an expansion both in $\Omega_{\rm S}/\mu \ll 1$ and $\Omega_{\rm S} r \ll 1$. For critical bubbles connecting shallow minima, the validity of the second approximation follows from the first along with Eq. (7.96). For critical bubbles connecting deep minima such an approximation is not valid in general, yet we verified a posteriori that it holds in the region of interest, i.e. where the bounds lie, see Fig. 7.11. In the limit where the field reacts slowly, we just perform an expansion in $\mu/\Omega_{\rm S} \ll 1$. After the dust settles, we end up with

$$\left\langle \boldsymbol{E}\cdot\boldsymbol{B} \right\rangle \simeq \frac{B_{\rm S}^2 R_{\rm S}^6 \Omega_{\rm S}}{4\pi^2 r^5} \begin{cases} (\pi - 2) \,, & \mu \gg \Omega_{\rm S} \,, \\ \pi \,, & \mu \ll \Omega_{\rm S} \,, \end{cases} \tag{7.94}$$

where we only kept the leading order terms. Note that the difference between the fast and slow limits is due to the time-dependent piece of the dipole, which is relevant only in the first case. For such a leading order averaged dipole, the transition radius is given by

$$R_{\rm T}^{\rm EM} = \left(\frac{\alpha}{8\pi^3} \frac{B_{\rm S}^2 R_{\rm S}^6 \Omega_{\rm S}}{\Lambda_{\rm TC}^4 \delta^2} \right)^{1/5} \begin{cases} (\pi - 2)^{1/5} \,, & \mu \gg \Omega_{\rm S} \,, \\ \pi^{1/5} \,, & \mu \ll \Omega_{\rm S} \,, \end{cases} \tag{7.95}$$

where we chose $c = 1$. Clearly, $R_{\rm T}^{\rm EM}$ is much larger for shallow minima ($\delta^2 \ll 1$) than for deep ones ($\delta^2 \approx 1$), since the size of the critical electromagnetic field is much smaller for the former

than for the latter. The condition that $R_{\rm T}^{\rm EM} > R_{\rm S}$, which is equivalent to the statement that the critical value of η is reached somewhere before the surface of the star, is certainly necessary for a bubble to form (equivalent to the condition $\zeta(\rho_N) > \zeta_c$ in the relaxion models previously discussed). However, since $\boldsymbol{E}\cdot\boldsymbol{B} = 0$ for $r < R_{\rm S}$, the conditions for the formation and expansion to infinity of the bubble sets a lower bound on the size of the region $R_{\rm T}^{\rm EM} - R_{\rm S}$ which is always more stringent than just $\eta(R_{\rm S}) > \eta_c$. For shallow minima, the condition for the formation of a $2\pi f$ bubble is roughly given by

$$R_{\rm T}^{\rm EM} - R_{\rm S} \gtrsim \frac{f}{\Lambda_{\rm R}^2} \simeq \frac{f}{\Lambda_{\rm TC}^2}\,. \qquad \text{(technicolor; shallow)} \tag{7.96}$$

This is the same condition leading to the escape of a bubble to infinity, since when $\delta^2 \ll 1$ the change in the potential from the inside to the outside of the transition region $r \sim R_{\rm T}^{\rm EM}$ is barely appreciable. We can explicitly verify that this is the case by considering the equation of motion of the bubble wall within the background electromagnetic field,

$$\sigma\ddot{R} = \epsilon - \frac{2\sigma}{R} - \sigma'\,, \qquad \epsilon(R) = 2\pi\Lambda_{\rm R}^4\left[1 + \frac{\delta^2}{1-\delta^2}\left(\frac{R_{\rm T}^{\rm EM}}{R}\right)^5\right]\,, \tag{7.97}$$

where ϵ is the energy density inside the bubble. Its R-dependence is due to the R-dependence of η. It is then clear that for a shallow minimum, where $\delta^2 \ll 1$ and therefore $\sigma' = d\sigma/dR \simeq 0$, the condition for the bubble to escape is, to good approximation, given by Eq. (7.96). Note that we have neglected $\mathcal{O}(1)$ factors as we did in Eqs. (7.73), (7.74), yet we expect them to be different here due to the non-spherical morphology of the system.

When the condition in Eq. (7.96) is satisfied, the phase transition implies a change in vacuum energy that is experimentally too large for $2\pi\Lambda_{\rm R}^4 \gtrsim 10^2\Lambda_0$, see Eq. (7.48). This allows us to exclude large regions of parameter space of the technicolored relaxion, as shown in the left panel of Fig. 7.11. To evaluate such a condition, we have taken as rotating neutron star properties, $R_{\rm S} = R_{\rm NS}$, and typical values for the surface angular velocity and magnetic fields of NSs,

$$\Omega_{\rm NS} \approx 10\,{\rm Hz}\,, \quad B_{\rm NS} \approx 10^{10}\,{\rm T}\,, \tag{7.98}$$

see e.g. [348]. The relaxion coupling to photons is given in Eq. (7.90), where we set $c = 1$ (and $\alpha \approx 1/137$); note that only if $c > 0$ the rolling term is larger than in vacuum ($c < 0$ would instead make the minimum deeper in the electromagnetic background). In Fig. 7.11 (left panel), the region to the right of a given labelled line is excluded, where each line corresponds to a different value of the relaxion decay constant (from $f = 10^{13}$ to 10^{19}GeV). Therefore, for a given f, large values of $M/\sqrt{\ell_*}$ are excluded depending on $\Lambda_{\rm R} \simeq \Lambda_{\rm TC}$. As $\Lambda_{\rm TC}$ increases, a certain critical value is reached where the size of the critical region quickly decreases and becomes smaller than $R_{\rm NS}$. The condition $R_{\rm T}^{\rm EM} \gtrsim R_{\rm NS}$ is independent of f, which is why all the excluded regions share the same upper boundary. The red band marks the region where the field neither reacts fast nor slowly compared to the rotation frequency, i.e. $\mu(R_{\rm T}^{\rm EM}) \sim \Omega_{\rm S}$. Given that $R_{\rm T}^{\rm EM}$ in Eq. (7.95) does not depend explicitly on f, the red band does not either. Within the band we expect $\mathcal{O}(1)$ deviations from the naive interpolation, shown as dashed lines in Fig. 7.11.

Interestingly, the presence of large electromagnetic fields around NSs would also lead to non-trivial constraints in the case of a bubble which connects deep minima. If the condition $\eta > \eta_c$ is satisfied, the condition for formation of a deep bubble is easily satisfied. This is because since $\eta_c \gg 1$, the slope of the potential is much larger in the region $r \lesssim R_{\rm T}^{\rm EM}$ than in vacuum. The relevant condition that leads to a phase transition is then the one concerning the escape of the bubble. We derive such a condition under the conservative simplification that past the transition

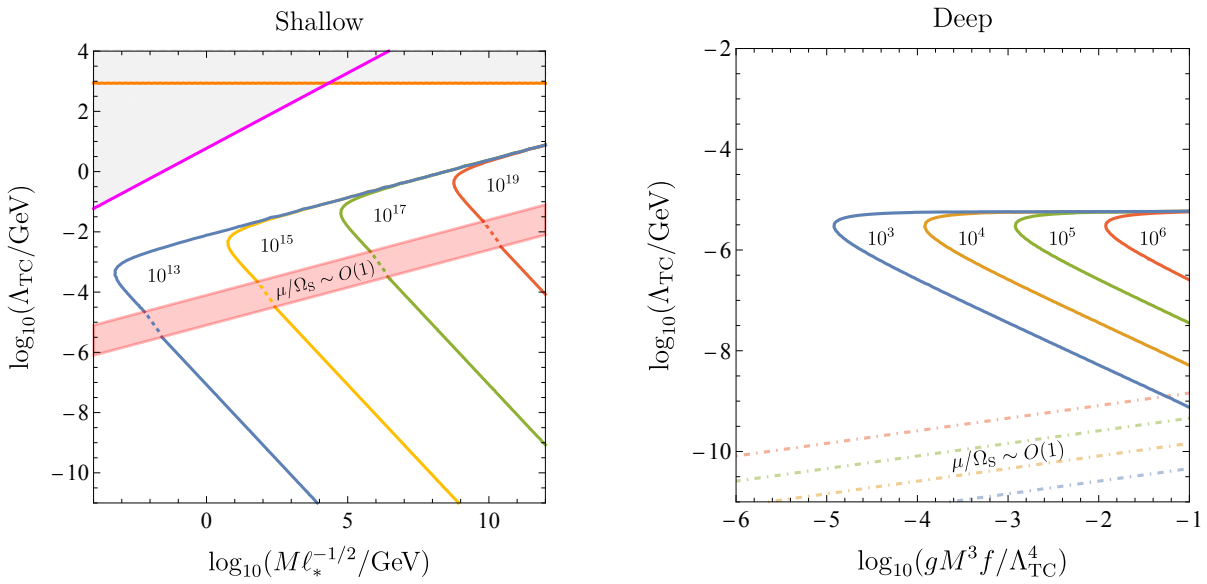

Figure 7.11: Regions excluded (inside labelled lines for several values of f[GeV]) by the formation and escape of a TC relaxion bubble induced by the electromagnetic fields generated by rotating NSs. Left panel: for a bubble connecting shallow minima, $\delta^2 \ll 1$ or equivalently $\Lambda_{\rm R} \simeq \Lambda_{\rm TC}$. The red band shows $\mu \sim \Omega_{\rm S}$ for a critical bubble. Right panel: for a bubble connecting deep minima, the depth parametrized by $gM^3f/\Lambda_{\rm TC}^4 = 1-\delta^2$. Dot-dashed lines show $\mu \sim \Omega_{\rm S}$ for the corresponding decay constant. Note the different range for $\Lambda_{\rm TC}$ (recall for shallow minima $\Lambda_{\rm TC} \simeq \Lambda_{\rm R}$) between the two plots.

radius the relaxion potential approximately returns to its in-vacuo form, i.e. $\eta(r > R_{\rm T}^{\rm EM}) = 0$. This is justified by the rapid decrease of $\boldsymbol{E}\cdot\boldsymbol{B}$, and therefore of η, with R, see Eq. (7.94). Then, our escape condition follows from requiring that $\ddot{R} > 0$ in Eq. (7.97), taking the minimal value of ϵ, that is $2\pi\Lambda_{\rm R}^4$, and the value of the tension force at the transition radius, that is $2\sigma/R_{\rm T}^{\rm EM}$, where note that due to our simplification we have $\sigma'(r > R_{\rm T}^{\rm EM}) = 0$. Then, a deep bubble escapes to infinity if

$$R_{\rm T}^{\rm EM} - R_{\rm S} \gtrsim \frac{f}{\Lambda_{\rm R}^2}\frac{1}{\sqrt{1-\delta^2}} \simeq \frac{\Lambda_{\rm TC}^2}{gM^3}\,, \qquad \text{(technicolor; deep)} \tag{7.99}$$

where we recall that $1-\delta^2 = \Lambda_{\rm R}^4/\Lambda_{\rm TC}^4 \ll 1$ and $\Lambda_{\rm R}^4 = gM^3f$. As in the case of relaxion bubbles seeded by baryon density, this condition implies that it is more difficult for a deep bubble to escape than a shallow one. The underlying reason is the same as well, in vacuum the bubble-wall tension is dominated by large potential barriers. Nevertheless, as shown in the right panel of Fig. 7.11, for not too small values of $\Lambda_{\rm R}^4/\Lambda_{\rm TC}^4$, a phase transition could still be induced between deep minima of the technicolored relaxion. As expected, the excluded regions, to the right of a given line, correspond to small values of the relaxion decay constant (up to $f \sim 10^6$GeV) and of the technicolor confinement scale. Dot-dashed lines show $\mu \sim \Omega_{\rm S}$ for a given f, and as can be seen the fast approximation holds where in the region of parameter space where the bounds lie. We checked explicitly that the expansion $\Omega_{\rm S} r \ll 1$ yields the correct results since $\Omega_{\rm S} R_{\rm T}^{\rm EM} \ll 1$ for the region of interest. We note that in this case of deep minima, the region we have excluded due to a phase transition with a too large change of the vacuum energy, is also ruled out from both CAST [349] and laboratory experiments, e.g. [350]. Still, for the allowed values $f \gtrsim 1.7\times10^7$GeV and $c = 1$, there would still be a non-trivial axion configuration around the neutron star, similar to [227].

Finally, we note that the lower bounds we derived on $\Lambda_{\rm TC}$ can be rephrased, given the collider constraints on v', as a lower bound on m_U in Eq. (7.88).

Dark compact objects

In this section we entertain the possibility that there are dark compact objects [290–298] in the universe. These dark stars, similar to standard stars, can induce the instability of a metastable vacuum. This would be particularly relevant when the periodic term in the landscape potential Eq. (7.56) arises from dark dynamics, as in the case of the non-QCD relaxion (especially if the scalar is sitting in a deep minimum, as in e.g. [335]) or in models where the barriers are Higgs independent [337, 338]. In addition, we show that this possibility opens the door to late-time phase transitions for which the associated change in vacuum energy is a priori experimentally allowed. As shown in Eq. (7.47), in the case of standard stars this can only happen for quite low values of f and if the bubbles are seeded solely by the largest stars known to date, with $R_{\rm S} \sim 10^3 R_\odot$.

Let us assume then a new species of fermion, which we refer to as dark baryon, whose relic abundance is non-negligible and which constitutes the main component of the dark stars (yet not necessarily making up all of the dark matter). Let us note right away that the existence of these stars requires non-trivial dynamics by which the dark fermion can dissipate their kinetic energy, accumulate and eventually form a compact object. If this is the case, the smaller dark stars will only be sustained by the Fermi degeneracy pressure associated with the dark baryon, thus, employing Eq. (3.4), with typical radii and densities

$$R_{\tilde{\rm S}} \sim \sqrt{8\pi}\frac{M_{\rm P}}{m_{\tilde{b}}^2}\,, \quad n_{\tilde{b}} \sim m_{\tilde{b}}^3\,, \tag{7.100}$$

where $m_{\tilde{b}}$ is the mass of the dark baryon.

Before moving on, we note that such a dark baryon is in fact motivated by the non-QCD relaxion, whose simplest UV realization crucially involves $N_{\tilde{f}}$ flavours of SM-neutral fermions, ρ, charged under a new confining $SU(N_{\tilde{\rm C}})$ gauge group. The associated IR scale, which controls the size of the relaxion barriers, is given by $\Lambda_{\rm C}^4 \simeq 4\pi f_{\tilde{\pi}}^3 m_N$ where $m_N = m_N(h^2) \ll 4\pi f_{\tilde{\pi}}$ is the mass of the dark quarks (taken degenerate for simplicity), whose dominant contribution is proportional to the square of the Higgs VEV, Eq. (7.60). The mass of the dark baryons, analogous to the QCD baryons, receives two contributions,

$$m_{\tilde{b}} = \tilde{m}_0 + \tilde{\sigma}(m_N)\,, \tag{7.101}$$

where $\tilde{m}_0$ is purely due to the dark strong dynamics while $\tilde{\sigma}$ is the analogue of the pion-nucleon sigma term of QCD. Likewise, at finite dark density, the barriers decrease according to $\Lambda_{\rm C}^4 \to \Lambda_{\rm C}^4(1-\zeta)$, where in the linear approximation,

$$\zeta(n_{\tilde{b}}) \simeq \frac{\tilde{\sigma} n_{\tilde{b}}}{\Lambda_{\rm C}^4} \sim \frac{m_{\tilde{b}}^3}{4\pi f_{\tilde{\pi}}^3}\,. \tag{7.102}$$

where in the last equality we have used Eq. (7.100) and the fact that $\tilde{\sigma} \simeq a m_N$ if $m_N \ll f_{\tilde{\pi}}$, where $a = \mathcal{O}(1)$ (yet note that in QCD the analogous coefficient is rather ≈ 10). Therefore, for a sufficiently large dark baryon mass, yet small enough to retain perturbative control, densities can be enough to seed the formation of a bubble. Finally, the condition that the system is large enough for the bubble to escape, assuming for simplicity that $\delta \sim 1$, and given that the size of

the dark neutron star is controlled by $m_{\tilde{b}}$, yields the condition

$$m_{\tilde{b}} \lesssim \Lambda_{\rm C} \sqrt{\frac{M_{\rm P}}{f}} \,. \tag{7.103}$$

Interestingly, the change in vacuum energy Eq. (7.72) associated with such a relaxion bubble is controlled by $m_{\tilde{b}}$ as well. Considering again for simplicity the case $\Lambda_{\rm R} \sim \Lambda_{\rm C}$,

$$-\Delta\Lambda \gtrsim m_{\tilde{b}}^4 \left(\frac{f}{M_{\rm P}}\right)^2 \approx 6 \times 10^{-3}\, \Lambda_0 \left(\frac{m_{\tilde{b}}}{10\,\text{keV}}\right)^4 \left(\frac{f}{10\,\text{TeV}}\right)^2 , \tag{7.104}$$

where the values of the dark mass and decay constant have been taken to illustrate that the change can be small enough as to avoid any trivial experimental inconsistency between the early and late universe. This gives rise to the exciting possibility that the change in the relaxion minimum could be detected with future cosmological measurements. In addition, if $m_{\tilde{b}}$ or f are small enough and the dark stars are dense and large enough to destabilize many relaxion minima (i.e. $N \gg 1$, see Eq. (7.71) and App. D.6), the effects of the continued phase transitions originating from the ongoing creation of relaxion bubbles interpolating between lower and lower pairs of consecutive minima could resemble the time evolution of a quintessence field as dark energy [316]. The dynamics of such a continued phase transition have been studied in [351].

Finally, we note that the in-vacuo relaxion mass, for the range of relaxion parameters where the change in vacuum energy is smaller than its current value, is

$$m_\phi \lesssim \frac{1}{f}\sqrt{\frac{\Lambda_0}{2\pi}} \approx 2 \times 10^{-16}\,\text{meV} \left(\frac{10\,\text{TeV}}{f}\right) , \tag{7.105}$$

which is, as expected, extremely small. Accordingly, the size of the dark compact object, $R_{\tilde{\rm S}} \sim 1/m_\phi$, is very large

$$R_{\tilde{\rm S}} \gtrsim f\sqrt{\frac{2\pi}{\Lambda_0}} \approx 1 \times 10^9\,\text{km} \left(\frac{f}{10\,\text{TeV}}\right) , \tag{7.106}$$

which for this value of f is roughly the size of the solar system.

7.3.4 Conclusions

The relaxion mechanism provides a solution to the electroweak hierarchy problem by postulating a landscape of vacua where the potential barriers between minima depend on the Higgs VEV, enabling vacuum selection with a small electroweak scale via a period of dynamical evolution. An immediate concern in postulating a multi-vacuum potential is whether the selected vacuum is stable on cosmological scales. While one usually considers vacuum transitions of quantum or finite temperature origin, in this section, we focused on the certainly less studied case of phase transition seeded by finite density objects such as stars. Using the results from Sec. 7.1, we were able to place new bounds on various relaxion models, ruling out regions of parameter space where such forbidden phase transitions would take place once stars are formed.

We showed that the connection of the relaxion with the Higgs is precisely what is behind the sensitivity of the relaxion vacua to finite density effects. In particular, in realizations where QCD dynamics generate the potential barriers, baryonic densities decrease the chiral symmetry breaking scale, leading to the possibility of QCD-relaxion bubbles. In realizations where instead new confining dynamics are responsible for the barriers, the change in the Higgs VEV due to the

background nucleons and muons, although small, is sufficient in some regions of parameter space to induce the formation of bubbles. Generically, we found that these bubbles easily escape from the stars where they are formed: NSs, WDs, or main-sequence stars, depending on how small the overall scale of the non-QCD relaxion potential is. We would also like to point out that our bounds have been recently investigated in light of stochastic relaxion models [352], which can open up large portions of previously believed unavailable relaxion parameter space given large enough inflation scales.

Notably, we discovered that not only matter density but an electromagnetic background can destabilize a metastable vacuum. This possibility is motivated by some constrained yet still viable realizations of the relaxion, in which the scalar field has large couplings to photons. We found that the large electric and magnetic fields of magnetars/pulsars destabilize the metastable minimum and lead to a phase transition that cannot be confined. Moreover, in this scenario, the transition can occur not only for shallow minima but also for metastable vacua in which there is a hierarchical separation between the energy difference and the potential barrier between the minima.

In general, relaxion phase transitions leading to a very small change in vacuum energy compared to its measured value could, in fact, have been induced by the formation of large dense objects in the universe. This is the case for very low relaxion decay constants and for the largest stars in the universe acting as seeds. We also considered the possibility that these naively harmless phase transitions may result from the formation of very large dark stars. Such stars would be sustained by the Fermi degeneracy pressure associated with the light stable dark baryons motivated by the non-QCD relaxion.

Finally, the new type of bound derived in this section for the relaxion landscape, namely vacuum instability induced by dense objects, could be relevant for other landscapes if subject to finite density deformations. These deformations are generically expected if the vacua are tied to the electroweak scale.

Chapter 8

Conclusions

Despite the solid and compelling theoretical and experimental indications that the Standard Model is incomplete, we have yet to detect new physics beyond its boundaries. The absence of any signals of BSM physics at the LHC has forced some extensions of the SM, such as composite Higgs and supersymmetry, into a fine-tuned region of the parameter space. While so far no detection has been observed, on the frontier of weakly coupled light scalar physics, there has been a notable increase in the innovation and construction of experiments aimed at detecting the QCD axion and ALPs. This thesis explored the extensive phenomenology of these weakly interacting light scalars, investigating their interactions with the Standard Model density.

In Chap. 2 we introduced the Strong $\mathcal{CP}$ Problem, i.e. the question of why the strong interactions preseve $\mathcal{CP}$ and the QCD axion solution as well as an ALP with lighter than expected mass. In particular, in Sec. 2.1, we reviewed the vacuum structure of Yang-Mills theories, where we saw that non-perturbative topological terms play an important role. In Sec. 2.2, we reviewed how these non-topological terms gave rise to experimentally measurable quantities in the presence of fermions. To understand this, we reviewed the axial anomaly in QCD, which naturally brought us to the formulation of the Strong $\mathcal{CP}$ Problem. Sec. 2.3 was concerned with the QCD axion solution to the Strong $\mathcal{CP}$ Problem, which employs the simple idea of promoting the $\bar{\theta}$-angle of QCD to a dynamical field. We discussed the UV dynamics of both the original Peccei-Quinn-Weinberg-Wilczek axion as well as two benchmark invisible axion models, the KSVZ and DSFZ axion. In Sec. 2.4, we derived the general model-dependent effective theory of the QCD axion in the IR, with the use of ChPT and precisely determined its couplings to SM matter. We focused on the couplings to nucleons. In order for the effective theory for nucleons to be valid, they had to be non-relativistic, which led us to introduce heavy baryon chiral perturbation theory with the QCD axion. In Sec. 2.5, we reviewed an ALP that behaved similarly to the QCD axion, except that its mass could be orders of magnitudes below the vanilla prediction. We concluded the chapter with a discussion on bounds on axions from astrophysical environments such as stellar remnants and supernovae in Sec. 2.6.

In Chap. 3, we reviewed the landscape of stellar remnants. In Sec. 3.1, we reviewed the physics of white dwarf stars and discussed various refinements of its equation of state, while Sec. 3.2 was devoted to neutron star physics. We saw that, while the equation of state of white dwarfs is quite well understood, the picture is very different for neutron stars. Since QCD becomes strongly coupled at the densities found in neutron stars perturbativity is lost. Furthermore, numerical advances are hampered by the fact that QCD at finite chemical potential suffers from an infamous fermion sign problem. In addition to that, we discussed that extrapolations of Standard Model equation of states including more degrees of freedom, such as mesons and hyperons generically soften the equation of state, which is clearly disfavored by the observation

of neutron stars with masses well above two solar masses.

In Chap. 4, we explored the effects of finite baryonic density on the QCD axion-nucleon coupling and found that they significantly change bounds on the QCD axion from supernovae and neutron star cooling. We started in Sec. 4.1 to review heavy baryon chiral perturbation theory at finite density by deriving the nucleon propagator in a finite density background using real-time thermal field theory. In Sec. 4.2, we calculated the density contributions to the QCD axion-nucleon vertex up to next-to-next-to-leading using the proper power counting scheme of chiral perturbation theory in this limit, discussed in App. A.6. With the density modified axion-nucleon vertex, we integrated the supernova luminosity for KSVZ and DSFZ models including systematic error bars for the first time. We discussed the implications on the bound derived from supernova 1987A.

In Chap. 5, we studied the possibility that the QCD axion developed a condensate at baryonic densities, such as found within neutron stars. We reviewed the basics of quantum field theories including a chemical potential, and the basics of meson condensation, and studied the QCD axion potential with $N_f = 2$ light flavors in the presence of a pion condensate in Sec. 5.1. We found that pion condensation for $N_f = 2$ light flavors can drive down the axion mass while at the same time increasing the neutral pion mass once in the proper mass eigenbasis, driven by the density dependent value of the pion condensate. In Sec. 5.2, we extended the study of the QCD axion potential at finite baryonic densities to $N_f = 3$ light flavors and studied the effects of kaon condensation on the QCD axion potential. Extrapolating to densities of around $3\rho_0$, we found that axion condensation can be triggered. In Sec. 5.3, we looked to asymptotic densities where QCD is in a color-flavor-locked phase and explored the potential of QCD axion in this phase. We found that even though instantons are generally suppressed in this phase, implying a smaller magnitude for the axion mass, axion condensation can be possible also in this regime.

In Chap. 6, we studied the effects of light scalars with non-derivative coupling to nucleons, generically present for *e.g.* the QCD axion, on the structure of stellar remnants. Such a coupling can in the most economic realizations be thought of as a scalar field-dependent nucleon, or more generally fermion, mass. We found that such light scalars can dramatically alter the stellar landscape. In Sec. 6.1, we saw how light QCD axions change the stellar composition of white dwarf stars. White dwarfs are very well understood since the relevant physics is mostly captured by the degeneracy pressure of electrons. Temperature, nuclear physics, and crystallization only play subdominant roles. Furthermore, there exist catalogs of a plentitude of observed properties of mass and radii as well as other properties, such as absorption lines, making them ideal laboratories to test the viability of new physics. We found that the axion led to a new ground state of nuclear matter within white dwarfs that implies the existence of a radius gap in their mass-radius curve. We performed numerically verified analytical estimates of the radius gap and found that confronting the modified mass-radius relation with observational data is incompatible with large parts of unexplored axion parameter space, allowing us to set stringent constraints. In Sec. 6.2, we showed how light scalar fields changed the stellar composition of neutron stars. Depending on the scalar self-interaction scale and the coupling to matter we found that either a new ground state or a coexistence region within the neutron star is accessible. While the new ground state led to dramatically stiffer equations of state, supporting more massive neutron stars, the coexistence region led to much softer hybrid star configurations with a first-order-phase-transition-like behavior. While we found that for the vanilla QCD axion hybrid star configurations are in principle possible, modulo the uncertainty of QCD at these densities, light QCD axions as well as linearly and quadratically coupled scalar fields can lead to new ground state phases. Therefore, we showed that BSM physics, if a new ground state is realized, can stiffen the equation of state of neutron stars, which is generally difficult within the Standard

Model. We also want to point out that a new ground state of nuclear matter implies the existence of absolutely stable self-bound objects, similar to strange quark matter. It was also shown that the theories under consideration are equivalent to certain theories of modified gravity, in particular theories of scalarization. While these theories are able to lead to heavier neutron stars, the existence of a new ground state of nuclear matter implying the existence of self-bound objects was so far overlooked in the literature. A future direction, which is currently work in progress, is to study the effect of light scalars coupled to electrons, muons, and other Standard Model matter fields.

In Chap. 7, we studied how stars can trigger phase transitions in the late universe if a light scalar field sits in a meta-stable minimum in vacuum. In Sec. 7.1, we considered a simple two-minimum potential with a $\mathcal{Z}_2$ symmetry $\phi \to -\phi$ that is explicitly broken by a linear term and derived the condition for bubble formation and escape. We found that if the energy difference between the true and the false vacuum is large compared to the increase of the barrier with decreasing density (we explicitly looked at the scenario where barriers decrease with increasing density), bubbles become unstable and are no longer confined to the star such that they permeate throughout the entire universe. We studied the phenomenology of such late-time phase transitions, namely at redshifts of star formation around $z \sim 10$. Since they come with a change of the Cosmological Constant at these times, we used early- vs late-time measurements of the Cosmological Constant to constrain these types of models. After formulating the Higgs Hierarchy problem in Sec. 7.2, we continued in Sec. 7.3 to apply our findings to relaxion models. Since relaxion models generally feature meta-stable minima in vacuum, they constituted the perfect conditions to apply our findings from Sec. 7.1. We determined the general conditions for a relaxion bubble to be released from a star and looked at typical benchmark relaxion models. For the QCD relaxion, which was previously ruled out from the prediction of an order-one QCD $\bar{\theta}$ angle, we found that our bubbles alone could have done the same job. For the non-QCD relaxion, we found that, depending on how far down the potential the relaxion relaxion stops, we can set stringent new constraints in previously unexplored parameter space. Interestingly, for technicolored relaxions with a coupling to photons, we found that the enhancement of the linear tilt in the potential triggered by photon background in neutron star magnetospheres leads to similar bounds. Lastly, we studied the scenario that dark compact objects trigger non-lethal phase transitions and their possible detection today.

The interplay of light scalar fields with Standard Model matter led to a rich phenomenology studied in this thesis. This is, however, not the end of the story since it also opens up many future directions. We are currently finalizing the implications of the density dependence of QCD axion-nucleon coupling, where we recently found that a model-independent bound can be set exceeding the current best model-independent bound by up to three orders of magnitude. Furthermore, we find that with our density-dependent coupling, a bound on the axion neutron coupling from neutron star cooling can be set for the first time.

Furthermore, we are actively investigating the implications of light scalar fields coupled to different matter fields such as electrons and muons, which by the compatibility with the observed stellar structure of white dwarfs and neutron stars, can lead to the most competitive bounds for these types of models.

Lastly, it is still ongoing work to find a mechanism that allows self-bound objects of axion-sourced nuclear matter, most likely in some dark sector, to constitute the dark matter. This would imply spectacular signatures since the QCD $\bar{\theta}$-angle would be changed once such a dark nugget overlaps with our Earth or in other Standard Model matter environments.

Acknowledgements

First of all, I want to thank my supervisor, Prof. Andreas Weiler, for providing me with the wonderful opportunity to do my doctoral studies in his research group. I am very grateful for his constant support, advice, and guidance and for pointing me toward interesting topics to work on. I am especially thankful for the many summer and winter schools, workshops, and conferences I attended, which broadened my knowledge and helped me to get in touch with the physics community. Lastly, I would like to thank him for the great atmosphere within the group and the many activities besides physics that made the time during my PhD even more fun! I could not have hoped for a better group or supervisor.

I thank Prof. Anson Hook and the entire theory group at Maryland University for their hospitality and kindness during my visit.

I thank Prof. Gilad Perez and the entire Weizmann theory group for the hospitality, great atmosphere, and the good times.

I especially thank Prof. Michael Geller from Tel-Aviv University for their hospitality, inspiring discussions, and the occasional bouldering session during my stay in Israel.

During my PhD I had the pleasure to collaborate and discuss with many excellent physicists, including Reuven Balkin, Javi Serra, Stefan Stelzl, Michael Geller, Abhishek Banerjee, Michael Stadlbauer, Kai Bartnick, and William DeRocco. I want to thank all of you for the many discussions and stimulating work atmosphere.

The time during my PhD would not have been as much fun if not for my amazing fellow office mates of T75 Reuven Balkin, Stefan Stelzl, Maximilian Ruhdorfer, Tobias Theil, Michael Stadlbauer, Dominik Haslehner, Emanuele Gendy, Pietro Baratella, Elena Venturini, Elena Kaiser, and Kai Bartnick. Thank you for being great colleagues and friends. I hope the Munich traditions, that is, the various summer and winter hikes as well as Christmas market crawls and excursions to Andechs, will be continued. Special thanks go to Stefan Stelzl, Kai Bartnick, Michael Stadlbauer, and Elena Kaiser for proofreading parts of this thesis. I would also like to thank the people from TUM and the MPP Gabriel Koole, Marius Wieseman, Lorenzo (quasi-bound state) DeRoss, Javier (flash) Reig Navarro, and Gael (tetris) Finauri for the occasional cold beverage (after work of course) and all the fun activities we did in the last years.

I thank all my friends for constantly being there for me and for your support during this time.

Denise, thank you for all your love, patience and understanding, and for coming with me.

Last but not least, I thank my mother, Beate, for her constant support, unconditional love, and encouragement. I am very grateful for your understanding in difficult times. Without you, none of this would have been possible.

Appendix A

Couplings of the QCD Axion to Nucleons at Finite Density

In this appendix we briefly summarize the standard construction of the effective axion chiral Lagrangian in HBChPT, invariant under charge conjugation (C) and parity (P) up to $\mathrm{N^2LO}$ and some selected pieces $\mathrm{N^3LO}$, necessary for renormalization. We start by writing down the relativistic pion axion nucleon Lagrangians and projecting to HBChPT. Relativistic corrections are also included. For reviews on the subject without the axion, see Refs. [41, 48, 49], as well as Ref. [353] for the HBChPT projection and Ref. [61] which considers the LO axion HBChPT Lagrangian and some selected terms at $\mathrm{N^2LO}$.

A.1 Chiral QCD Lagrangian

We analyse the transformation properties of external sources performing a spurion analysis. Starting point is the QCD Lagrangian with external isovector axial vector (a_μ), isoscalar axial vector (a_μ^s), scalar (s) and pseudo-scalar (p) sources. In absence of isovector and isoscalar vector sources ($v_\mu^{(s)} = 0$), which is the case for axion ChPT, we can write parity eigenstates in terms of left- and right handed fields, i.e. $r_\mu^{(s)} = a_\mu^{(s)}$ and $\ell_\mu^{(s)} = -a_\mu^{(s)}$. The QCD Lagrangian containing external sources then reads

$$\mathcal{L}_{\text{ext}} = \bar{q}_L \gamma^\mu \left(\ell_\mu + \ell_\mu^s\right) q_L + \bar{q}_R \gamma^\mu \left(r_\mu + r_\mu^s\right) q_R - \bar{q}_L \left(s - ip\right) q_R - \bar{q}_R \left(s + ip\right) q_L, \tag{A.1}$$

where $q_{L/R}$ are left- and right-handed quark fields. Isovector and isoscalar parts are associated with the $SU(2)$ and $U(1)$ parts of $U(2)$ respectively. The Lagrangian $\mathcal{L}_{\text{QCD}} = \mathcal{L}_{\text{QCD},0} + \mathcal{L}_{\text{ext}}$, with $\mathcal{L}_{\text{QCD},0}$ given by Eq. (2.55a), is invariant under local $U(2)_L \times U(2)_R$ transformations

$$q_{L/R} \to \exp\left(-i\frac{\theta_{L/R}(x)}{3}\right) V_{L/R}(x) q_{L/R}, \quad \theta_{L/R} \in U(1)_{L/R}, \quad V_{L/R} \in SU(2)_{L/R}, \tag{A.2}$$

as long as the external fields satisfy

$$\begin{aligned} r_\mu &\to V_R r_\mu V_R^\dagger + i V_R \partial_\mu V_R^\dagger, \\ \ell_\mu &\to V_L \ell_\mu V_L^\dagger + i V_L \partial_\mu V_L^\dagger, \\ \ell_\mu^s &\to \ell_\mu^s - \frac{1}{3}\partial_\mu \theta_L, \\ r_\mu^s &\to r_\mu^s - \frac{1}{3}\partial_\mu \theta_R, \\ (s-ip) &\to e^{-\frac{i}{3}(\theta_L-\theta_R)} V_L\,(s-ip)\,V_R^\dagger, \\ (s+ip) &\to e^{-\frac{i}{3}(\theta_R-\theta_L)} V_R\,(s+ip)\,V_L^\dagger. \end{aligned} \tag{A.3}$$

The derivative terms cancel analogous terms originating from the kinetic terms in the Lagrangian and are later used to construct covariant derivatives.

A.2 Effective Pion Lagrangian

In the broken phase, pions are described by the unitary flavor matrix U, see Eq. (2.67). It transforms linearly under chiral and axial $U(1)_A$ transformations

$$U \to e^{-\frac{i}{3}(\theta_R-\theta_L)} V_R U V_L^\dagger. \tag{A.4}$$

Since it collects the NGBs, associated with the broken generators of chiral symmetry breaking, it is charged under axial transformations only. Furthermore, under C and P transformations the NGBs and U transform as

$$\begin{aligned} \boldsymbol{\pi}(x) &\xrightarrow{\mathrm{C}} \boldsymbol{\pi}^T(x), \quad \boldsymbol{\pi}(x) \xrightarrow{\mathrm{P}} -\boldsymbol{\pi}(\mathcal{P}x) \\ U(x) &\xrightarrow{\mathrm{C}} U^T(x), \quad U(x) \xrightarrow{\mathrm{P}} U^\dagger(\mathcal{P}x). \end{aligned} \tag{A.5}$$

Hence, we find that the covariant derivative is given by the linear representation

$$\nabla_\mu U = \partial_\mu U - i\left(r_\mu + r_\mu^s\right) U + iU\left(\ell_\mu + \ell_\mu^s\right), \tag{A.6}$$

resulting in Eq. (2.68). Another spurion in the pion sector can be defined as

$$\chi = 2Bm_\phi^\dagger = 2B(s+ip), \tag{A.7}$$

see below Eq. (2.70b), which transforms as

$$\chi \to V_R \chi V_L^\dagger. \tag{A.8}$$

In the meson sector, the list of fundamental building blocks that we are interested in i.e. up to $O(p^2)$ is

$$U, \nabla_\mu U, \nabla_\mu \nabla_\nu U, \chi. \tag{A.9}$$

Out of these, the only non-trivial, hermitian, C and P invariant scalars under Lorentz are collected in the Lagrangian Eq. (2.70b). Higher order pion terms are not needed for our analysis, however, writing down the Lagrangian including the axion is straightforward.

A.3 Effective Baryon Lagrangian

The baryon field transforms non-linearly under chiral transformations

$$\Psi' = e^{-i\theta_V(x)} K(V_L(x), V_R(x), U(x))\Psi, \tag{A.10}$$

where $K(V_L, V_R, U)$ is the so-called compensator field and defines a non-linear $SU(N_f)$ valued function of U and V_L, V_R, defined by

$$U(x) = u^2(x), \quad u(x) \to u'(x) = \sqrt{V_R U V_L^\dagger} \equiv V_R u K^{-1}(V_L, V_R, U), \tag{A.11}$$

such that the explicit form of K is easily evaluated to

$$K(V_L, V_R, U) = (u')^{-1} V_R u = \left(\sqrt{V_R U V_L^\dagger}\right)^{-1} V_R \sqrt{U}. \tag{A.12}$$

Since Ψ is a singlet under the axial $U(1)_A$, the presence of an external axial source does not change its transformation behaviour,

$$\begin{aligned} D_\mu \Psi &= (\partial_\mu + \Gamma_\mu)\,\Psi, \\ \Gamma_\mu &= \frac{1}{2}\left[u^\dagger(\partial_\mu - i r_\mu)u + u(\partial_\mu - i\ell_\mu)u^\dagger\right], \end{aligned} \tag{A.13}$$

where Γ_μ is the chiral connection. Since Ψ is a singlet under $U(1)_A$, there is no term proportional to the axial isovector current in the covariant derivative, i.e. it is a pure vector quantity. Under parity and charge conjugation it transforms as

$$D_\mu \xrightarrow{\mathrm{P}} +\mathcal{P}_\mu{}^\nu D_\nu, \quad D_\mu \xrightarrow{\mathrm{C}} -D_\mu^T. \tag{A.14}$$

One can furthermore construct an hermitian, isovector, axial vector object containing one derivative, called the vielbein

$$u_\mu = i\left[u^\dagger(\partial_\mu - i r_\mu)u - u(\partial_\mu - i\ell_\mu)u^\dagger\right] = i u^\dagger\left(\partial_\mu U - i r_\mu U + i U \ell_\mu\right) u^\dagger. \tag{A.15}$$

The transformation behavior under $SU(2)_L \times SU(2)_R$, parity (P) and charge conjugation (C) is

$$u_\mu \overset{SU(2)_L \times SU(2)_R}{\longrightarrow} K u_\mu K^\dagger, \quad u_\mu \xrightarrow{\mathrm{P}} -\mathcal{P}_\mu{}^\nu u_\nu, \quad u_\mu \xrightarrow{\mathrm{C}} u_\mu^T. \tag{A.16}$$

u_μ sandwiched between a baryon bilinear stays invariant under local chiral gauge transformations. There exist two identities for the covariant derivative,

$$[D_\mu, D_\nu] = \frac{1}{4} u_\mu u_\nu, \tag{A.17a}$$

$$[D_\mu, u_\nu] = [D_\nu, u_\mu]\,. \tag{A.17b}$$

The first is known as curvature relation and shows that only completely symmetrized products of D_μ with itself as well as products of D_μ with u_μ have to be considered. The second relation shows in a similar way that covariant derivatives on the vielbein have to be taken into account in a completely symmetrized combination only. We can construct an analogous quantity to the vielbein from the isoscalar part of the linearly realized covariant derivative

$$\hat{u}_\mu = i u^\dagger\left(-i r_\mu^s U + i U \ell_\mu^s\right) u^\dagger = i u^\dagger(-2i a_\mu^s U) u^\dagger = 2 a_\mu^s, \tag{A.18}$$

which under parity and charge conjugation has exactly the same transformation properties as u_μ but only transforms under $U(1)_A$[1]

$$\hat{u}_\mu \xrightarrow{U(1)_A} \hat{u}_\mu - \partial_\mu \alpha_A, \quad \hat{u}_\mu \xrightarrow{\mathrm{P}} -\mathcal{P}_\mu{}^\nu \hat{u}_\nu, \quad \hat{u}_\mu \xrightarrow{\mathrm{C}} \hat{u}_\mu^T. \tag{A.19}$$

Furthermore we need a non-linearly transforming analog to the field χ, which we construct as hermitian and anti-hermitian combinations

$$\chi_\pm = u^\dagger \chi u^\dagger \pm u \chi^\dagger u, \tag{A.20}$$

with transformation properties

$$\chi_\pm \xrightarrow{SU(2)_L \times SU(2)_R} K \chi_\pm K^\dagger, \quad \chi_\pm \xrightarrow{\mathrm{P}} \pm \chi_\pm, \quad \chi_\pm \xrightarrow{\mathrm{C}} \chi_\pm^T. \tag{A.21}$$

For the construction of the chiral Lagrangian it will be useful to separate every field into isovector and isoscalar components. Therefore we define

$$\tilde{X} = X - \frac{1}{2} \langle X \rangle , \tag{A.22}$$

where $\langle \cdot \rangle$ denotes the flavor trace such that $\tilde{X}$ projects out the isovector part of X. The basic building blocks in this form are therefore $u_\mu, \hat{u}_\mu, \tilde{\chi}_\pm, \langle \chi_\pm \rangle$. Note that, in the special case of $SU(2)$ one can show that

$$\langle XY \rangle = \{X, Y\} . \tag{A.23}$$

We are now in the position to construct the chiral nucleon Lagrangian containing the axion. In the following we, write down the minimal set of operators for which we closely follow Ref. [353]. Invariant monomials take the generic form

$$\bar{\Psi} A^{\mu\nu\cdots} \Theta_{\mu\nu\ldots} \Psi + \text{h.c.} \, . \tag{A.24}$$

The operator $A^{\mu\nu\cdots}$ is a product of pion and/or external fields and their covariant derivatives, all of course in the non-linear representation. $\Theta_{\mu\nu\ldots}$ is a product of Clifford algebra elements $\Gamma_{\mu\nu\ldots}$ and the symmetrized product of n covariant derivatives $D^n_{\alpha\beta\ldots} = \{D_\alpha, \{D_\beta, \{\ldots, D_\omega\}\}\}$ acting on the nucleon field.

$\Gamma_{\mu\nu\ldots}$ contains Clifford algebra elements which are understood to be expanded in the basis $(\mathbb{1}, \gamma_5, \gamma_\mu, \gamma_5\gamma_\mu, \sigma_{\mu\nu})$ and the metric $\eta_{\mu\nu}$ as well as Levi-Civita symbols $\varepsilon_{\mu\nu\alpha\beta}$. Eq. (A.24) is not the most general form. The fact that $\Theta_{\mu\nu\ldots}$ contains only the totally symmetrized product of covariant derivatives acting on Ψ is due to the curvature relation, see Eq. (A.17a). Another property, namely that no two indices of $\Theta_{\mu\nu\ldots}$ are contracted (except for Levi-Civita symbols) is due the fact that at a given chiral order $\not{D}\Psi$ can always be replaced by $-im_N\Psi$. This explains why a couple of Clifford algebra structures do not need to be considered, *e.g.* the LHS of $\bar{\Psi} A^{\alpha\beta\ldots}\gamma^\lambda D^n_{\lambda\alpha\beta\ldots}\Psi + \text{h.c.} = -im_N \bar{\Psi} A^{\alpha\beta\ldots} D^{n-1}_{\alpha\beta\ldots}\Psi$ is replaced by the RHS. More such

[1]Note, that if we were to construct only one such axial vector type object associated with the full $U(2)_L \times U(2)_R$ we would effectively end up with the same structure. However, this would collect both isovector and isoscalar components in a single building block to which one would naively associate only one constant in the effective Lagrangian. This would not be the most general approach because the isovector and isoscalar symmetries are completely independent from each other, *e.g.* one can only do a, say, $U(1)_A$ transformation while leaving the isovector part completely untouched. So if one started with only one building block one would have to break it up again into isovector and isoscalar parts to describe this scenario.

eliminations due to the use of the EOM can me made and the minimal set is shown, ordered by ascending chiral power, given in Ref. [353] to be

$$\begin{aligned} &\mathbb{1}, \\ &\gamma_5\gamma_\mu, D_\mu, \\ &\eta_{\mu\nu}, \sigma_{\mu\nu}, \gamma_5\gamma_\mu D_\nu, D_{\mu\nu}, \end{aligned} \tag{A.25}$$

where $D_{\mu\nu} = \{D_\mu, D_\nu\}$.

For the operator $A^{\mu\nu\cdots}$ one writes down combinations of fields in every ordering. The number of Lorentz indices gives the chiral power. Furthermore, it is instructive to write them in terms of isovector and isoscalar parts. For $SU(2)$ this is equivalent to write every product as commutator, or as an anticommutator, respectively. This has the advantage to obtain simple transformation properties for charge conjugation and parity. The transformation behaviour of the Clifford algebra elements under parity-, charge- and hermitian conjugation in the form

$$\begin{aligned} &\Gamma^p_{\mu\nu\ldots} = (\pm 1)\mathcal{P}_\mu{}^\alpha \mathcal{P}_\nu{}^\beta \ldots \Gamma_{\alpha\beta\ldots}, \quad \Gamma^c_{\mu\nu\ldots} = (\pm 1)\Gamma_{\mu\nu\ldots}, \\ &\Gamma^\dagger_{\mu\nu\ldots} = (\pm 1)^{\gamma_\dagger}\gamma_0\Gamma_{\mu\nu\ldots}\gamma_0 \end{aligned} \tag{A.26}$$

and the chiral order (including the metric and the Levi-Civita) are shown in Table A.1. Note that the full transformation behavior of $\bar\Psi\Theta_{\mu\nu\ldots\alpha\beta\ldots}\Psi = \bar\Psi\Gamma_{\mu\nu\ldots}D^n_{\alpha\beta\ldots}\Psi$ may include an additional sign due to integration by parts, but is included in Table A.1. All relevant operators from the minimal list of $\Theta_{\mu\nu\ldots}$ are shown, see Eq. (A.25). The transformation behaviour of the fields

$\Theta_{\mu\nu\ldots}$	$\mathbb{1}$	γ_5	γ_μ	$\gamma_5\gamma_\mu$	$\sigma_{\mu\nu}$	$\eta_{\mu\nu}$	$\epsilon_{\mu\nu\lambda\rho}$	D_μ	$\gamma_5\gamma_\mu D_\nu$	$D_{\mu\nu}$
$O(p^n)$	$O(1)$	$O(p)$	$O(1)$	$O(1)$	$O(1)$	$O(1)$	$O(1)$	$O(1)$	$O(1)$	$O(1)$
P	$+$	$-$	$+$	$-$	$+$	$+$	$-$	$+$	$-$	$+$
C	$+$	$+$	$-$	$+$	$-$	$+$	$+$	$-$	$-$	$+$
$\dagger$	$+$	$-$	$+$	$+$	$+$	$+$	$+$	$-$	$-$	$+$

Table A.1: Transformation properties of $\Theta_{\mu\nu\ldots}$.

$A^{\mu\nu\cdots}$ under parity, charge and hermitian conjugation in the form

$$A^p_{\mu\nu\ldots} = (\pm 1)^{a_p}\mathcal{P}_\mu{}^\alpha\mathcal{P}_\nu{}^\beta\ldots A_{\alpha\beta\ldots} \quad A^c_{\mu\nu\ldots} = (\pm 1)^{a_c}A^T_{\mu\nu\ldots} \quad A^\dagger_{\mu\nu\ldots} = (\pm 1)^{a_\dagger}A_{\mu\nu\ldots} \tag{A.27}$$

as well as the chiral order (including the metric and Levi-Civita) and the combinations of covariant derivatives acting on nucleons are shown in Table A.2. With the transformation properties at hand we can write down all operators invariant under parity, charge conjugation and hermitian conjugation at a given chiral order. At first chiral order $O(p)$ we find the relativistic pion nucleon Lagrangian, including the axion

$$\mathcal{L}^{(1)}_{\pi N} = \bar\Psi\left(i\not{D} - m_N + \frac{g_A}{2}\not{u}\gamma_5 + \frac{g_0}{2}\not{\hat u}\gamma_5\right)\Psi, \tag{A.28}$$

given in Eq. (2.78). At the next higher chiral order $O(p^2)$ we find the most general Lagrangian to be

$$\begin{aligned} \mathcal{L}^{(2)}_{\pi N} = \bar\Psi\Bigg[&c_1\langle\chi_+\rangle - \left(\frac{c_2}{8m_N^2}\langle u_\mu u_\nu\rangle D^{\mu\nu} + \text{h.c.}\right) + \frac{c_3}{2}u\cdot u + c_4\frac{i}{4}[u_\mu, u_\nu]\sigma^{\mu\nu} \\ &+c_5\tilde\chi_+ - \left(\frac{c_8}{8m_N^2}\langle\hat u_\mu u_\nu\rangle D^{\mu\nu} + \text{h.c.}\right) + \frac{c_9}{2}\hat u\cdot u\Bigg]\Psi. \end{aligned} \tag{A.29}$$

$A_{\mu\nu\ldots}$	P	C	†
$O(p)$			
u_μ	$-$	$+$	$+$
$\hat{u}_\mu$	$-$	$+$	$+$
$O(p^2)$			
$\tilde{\chi}_+$	$+$	$+$	$+$
$\langle\chi_+\rangle$	$+$	$+$	$+$
$\tilde{\chi}_-$	$-$	$+$	$-$
$\langle\chi_-\rangle$	$-$	$+$	$-$
$[u_\mu, u_\nu]$	$+$	$-$	$-$
$\langle u_\mu u_\nu\rangle$	$+$	$+$	$+$
$\langle\hat{u}_\mu u_\nu\rangle$	$+$	$+$	$+$
$\langle\hat{u}_\mu\hat{u}_\nu\rangle$	$+$	$+$	$+$
$[D_\mu, u_\nu]$	$-$	$+$	$+$
$[D_\mu, \hat{u}_\nu]$	$-$	$+$	$+$

Table A.2: Transformation properties of $A_{\mu\nu\ldots}$.

Note that we dropped all $1/f_\phi^2$ terms, all terms $\propto [\hat{u}_\mu, u_\nu] \sim \partial_\mu a \partial_\nu \pi^a \, [\mathbb{1}, \tau^a] = 0$, as well as terms $\propto [\hat{u}, \hat{u}] = 0$. Note that $c_{6,7}$ are terms proportional to the field strength tensor, which we do not include here.

Next we treat the nucleons in the HBChPT limit, as described in Sec. 2.4.3. We define projection operators according

$$P_{v\pm} = \frac{1 \pm \not{v}}{2}, \tag{A.30}$$

and introduce velocity dependent fields, i.e. velocity eigenstates, N_v and H_v

$$N_v \equiv e^{im_N v\cdot x} P_{v+}\Psi, \quad H_v \equiv e^{im_N v\cdot x} P_{v-}\Psi, \tag{A.31}$$

satisfying

$$\not{v} N_v = +N_v, \quad \not{v} H_v = -H_v. \tag{A.32}$$

Note that we drop the subscript in the main text however it should also there be understood as velocity dependent. Therefore the nucleon field is decomposed as

$$\Psi(x) = e^{-im_N v\cdot x} \left[N_v(x) + H_v(x)\right]. \tag{A.33}$$

Let us consider a positive plane wave solution to the free Dirac equation with momentum $\boldsymbol{p}$

$$\psi_{\boldsymbol{p}}^{(+)(\alpha)}(\boldsymbol{x}, t) = u^{(\alpha)}(\boldsymbol{p}) e^{-ip\cdot x}, \tag{A.34}$$

$$u^{(\alpha)}(\boldsymbol{p}) = \sqrt{E(\boldsymbol{p}) + m_N} \begin{pmatrix} \chi^{(\alpha)} \\ \frac{\boldsymbol{\sigma}\cdot\boldsymbol{p}}{E(\boldsymbol{p})+m_N}\chi^{(\alpha)} \end{pmatrix} \tag{A.35}$$

where $E(\boldsymbol{p}) = p^0 = \sqrt{\boldsymbol{p}^2 + m_N^2}$ and with our choice of v^μ, they are given by

$$P_{v+} = \begin{pmatrix} \mathbb{1}_{2\times2} & 0_{2\times2} \\ 0_{2\times2} & 0_{2\times2} \end{pmatrix}, \quad P_{v-} = \begin{pmatrix} 0_{2\times2} & 0_{2\times2} \\ 0_{2\times2} & \mathbb{1}_{2\times2} \end{pmatrix}. \tag{A.36}$$

Therefore, the velocity eigenstates take the form

$$N_v^{(\alpha)}(x) = \sqrt{E(\boldsymbol{p}) + m_N} \begin{pmatrix} \chi^{(\alpha)} \\ 0_{2\times1} \end{pmatrix} e^{-i[E(\boldsymbol{p})-m_N]t + i\boldsymbol{p}\cdot\boldsymbol{x}}, \tag{A.37}$$

$$H_v^{(\alpha)}(x) = \sqrt{E(\boldsymbol{p}) + m_N} \begin{pmatrix} 0_{2\times 1} \\ \frac{\boldsymbol{\sigma}\cdot\boldsymbol{p}}{E(\boldsymbol{p})+m_N}\chi^{(\alpha)} \end{pmatrix} e^{-i[E(\boldsymbol{p})-m_N]t + i\boldsymbol{p}\cdot\boldsymbol{x}}. \tag{A.38}$$

Next, we integrate out the heavy component. We plug the decomposed nucleon field, Eq. (A.33) into the leading order EOM from Eq. (2.78) and get rid of the phase. Then we project out P_{v+} and P_{v-} components, solve one formally for H_v using the definitions

$$A_\perp^\mu = A^\mu - v\cdot A v^\mu, \quad v\cdot A_\perp = 0, \quad \not{A}_\perp = A_\perp^\mu \gamma_\mu. \tag{A.39}$$

and plug it into the remaining equation, which leads to the following Lagrangian

$$\begin{aligned} \hat{\mathcal{L}} = &\bar{N}_v \left(iv\cdot D + \frac{g_A}{2}\not{u}_\perp\gamma_5 + \frac{g_0}{2}\not{\hat{u}}_\perp\gamma_5 \right) N_v + \bar{N}_v \left(i\not{D}_\perp + \frac{g_A}{2} v\cdot u\gamma_5 + \frac{g_0}{2} v\cdot\hat{u}\gamma_5 \right) \\ &\times \left(2m_N + iv\cdot D - \frac{g_A}{2}\not{u}_\perp\gamma_5 - \frac{g_0}{2}\not{\hat{u}}_\perp\gamma_5 \right)^{-1} \left(i\not{D}_\perp - \frac{g_A}{2} v\cdot u\gamma_5 - \frac{g_0}{2} v\cdot\hat{u}\gamma_5 \right) N_v. \end{aligned} \tag{A.40}$$

Now we define the velocity dependent spin operator

$$S_v^\mu \equiv \frac{i}{2}\gamma_5\sigma^{\mu\nu}v_\nu = -\frac{1}{2}\left(\gamma^\mu \not{v} - v^\mu\right), \quad (S_v^\mu)^\dagger = \gamma_0 S_v^\mu \gamma_0, \tag{A.41}$$

where again we drop the v sub- or superscript in the main text and which in 4-dim has the properties

$$v\cdot S_v = 0, \quad \{S_v^\mu, S_v^\nu\} = \frac{1}{2}\left(v^\mu v^\nu - \eta^{\mu\nu}\right), \quad [S_v^\mu, S_v^\nu] = i\epsilon^{\mu\nu\rho\sigma} v_\rho S_\sigma^v. \tag{A.42}$$

This definition is very useful since we can trade the 6 different Dirac structures that appear in Eq. (A.40) with two 4×4 matrices, $\mathbb{1}_{4\times4}$ and S_v. To that end we use the relations

$$\bar{N}_v \mathbb{1}_{4\times4} N_v = \bar{N}_v \mathbb{1}_{4\times4} N_v, \tag{A.43a}$$
$$\bar{N}_v \gamma_5 N_v = 0, \tag{A.43b}$$
$$\bar{N}_v \gamma^\mu N_v = v^\mu \bar{N}_v N_v, \tag{A.43c}$$
$$\bar{N}_v \gamma^\mu\gamma_5 N_v = 2\bar{N}_v S_v^\mu N_v, \tag{A.43d}$$
$$\bar{N}_v \sigma^{\mu\nu} N_v = 2\epsilon^{\mu\nu\sigma\rho} v_\rho \bar{N}_v S_\sigma^v N_v, \tag{A.43e}$$
$$\bar{N}_v \sigma^{\mu\nu}\gamma_5 N_v = 2i\left(v^\mu \bar{N}_v S_v^\nu N_v - v^\nu \bar{N}_v S_v^\mu N_v \right). \tag{A.43f}$$

We expand the second bracket in the last term of Eq. (A.40) in orders of $1/m_N^n$ and write

$$\hat{\mathcal{L}} = \hat{\mathcal{L}}_{\pi N}^{(1)} + \sum_{n=1}^{\infty} \frac{1}{(2m_N)^n} \hat{\mathcal{L}}^{(n)}, \tag{A.44}$$

where the first term is exactly given by

$$\hat{\mathcal{L}}_{\pi N}^{(1)} = \bar{N}_v \left(iv\cdot D + g_A S_v\cdot u + g_0 S\cdot\hat{u} \right) N_v, \tag{A.45}$$

which we recognize as the leading pion nucleon HBChPT Lagrangian including the axion, see Eq. (2.82). The first term in the sum leads to relativistic corrections at chiral order $O(p^2)$.

Despite relativistic corrections contributing at chiral order $O(p^2)$ to $\hat{\mathcal{L}}_{\pi N}^{(2)}$ from integrating out the heavy component at leading chiral order, the obvious contribution comes from integrating out the heavy component from the relativistic Lagrangian at $O(p^2)$, Eq. (A.29) and we write

$$\hat{\mathcal{L}}_{\pi N}^{(2)} = \hat{\mathcal{L}}_{\pi N, c_i}^{(2)} + \hat{\mathcal{L}}_{\pi N, 1/m_N}^{(2)}. \tag{A.46}$$

Note that relativistic corrections from integrating out H_v from the EOM of $\mathcal{L}^{(2)}_{\pi N}$ will enter at $O(p^3)$, which we do not need for our analysis in full generality. Therefore, it is sufficient to consider the P_{v+} projection of the $O(p^2)$ EOM and only keep the term proportional to the light component N_v, since the term $\propto H_v$ will only generate relativistic $1/m_N^2$ corrections of chiral order $O(p^3)$. Then, using the relations Eq. (A.43), one finds

$$\begin{aligned}\hat{\mathcal{L}}^{(2)}_{\pi N,c_i} =&\bar{N}_v\Big(c_1\langle\chi_+\rangle + \frac{c_2}{2}(v\cdot u)^2 + c_3\,(u\cdot u) + c_4\,[S^\mu,S^\nu]\,u_\mu u_\nu + c_5\widetilde{\chi}_+ + \\ &+\frac{c_8}{4}(v\cdot u)(v\cdot\hat{u}) + c_9\,(u\cdot\hat{u})\Big)N_v.\end{aligned} \tag{A.47}$$

The relativistic corrections come from the first term in the sum of Eq. (A.44), namely

$$\begin{aligned}\hat{\mathcal{L}}^{(2)}_{\pi N,1/m_N} &= \frac{1}{2m_N}\hat{\mathcal{L}}^{(1)}\\ &\simeq \frac{1}{2m_N}\bar{N}_v\left(i\not{D}_\perp + \frac{g_A}{2}v\cdot u\gamma_5 + \frac{g_0}{2}v\cdot\hat{u}\gamma_5\right)\left(i\not{D}_\perp - \frac{g_A}{2}v\cdot u\gamma_5 - \frac{g_0}{2}v\cdot\hat{u}\gamma_5\right)N_v\\ &= \frac{1}{2m_N}\bar{N}_v\Big[-D^2 + (v\cdot D)^2 - ig_A\,\{D\cdot S_v, v\cdot u\} - ig_0\,\{D\cdot S_v, v\cdot\hat{u}\}\\ &\quad - \frac{g_A^2}{4}(v\cdot u)^2 - \frac{g_0^2}{4}(v\cdot\hat{u})^2 - \frac{g_Ag_0}{2}(v\cdot u)(v\cdot\hat{u}) + \frac{i}{4}\epsilon^{\mu\nu\rho\sigma}\,[u_\mu,u_\nu]\,v_\rho S^v_\sigma\Big]N_v,\end{aligned} \tag{A.48}$$

where we used

$$\not{D}_\perp\not{D}_\perp = D^2 - (v\cdot D)^2 - \frac{i}{4}\epsilon^{\mu\nu\rho\sigma}\,[u_\mu,u_\nu]\,v_\rho S^v_\sigma, \tag{A.49a}$$

$$\not{D}_\perp\gamma_5 = 2D\cdot S_v. \tag{A.49b}$$

The result is therefore

$$\begin{aligned}\hat{\mathcal{L}}^{(2)}_{\pi N} =&\hat{\mathcal{L}}^{(2)}_{\pi N,c_i} + \hat{\mathcal{L}}^{(2)}_{\pi N,1/m_N} =\\ =&\bar{N}_v\left[-\frac{1}{2m_N}\left(D^2 - (v\cdot D)^2 + ig_A\,\{S_v\cdot D, v\cdot u\} + ig_0\,\{S_v\cdot D, v\cdot\hat{u}\}\right)\right.\\ &+\hat{c}_1\langle\chi_+\rangle + \frac{\hat{c}_2}{2}(v\cdot u)^2 + \hat{c}_3\,(u\cdot u) + \frac{\hat{c}_4}{2}i\epsilon^{\mu\nu\rho\sigma}\,[u_\mu,u_\nu]\,v_\rho S^v_\sigma\\ &\left.+\,\hat{c}_5\tilde{\chi}_+ + \frac{\hat{c}_8}{4}(v\cdot u)(v\cdot\hat{u}) + \hat{c}_9\,(u\cdot\hat{u})\right]N_v,\end{aligned} \tag{A.50}$$

where $\hat{c}_i$ include relativistic $1/m_N$ corrections,

$$\begin{aligned}&\hat{c}_1 = c_1, \quad \hat{c}_2 = c_2 - \frac{g_A^2}{4m_N}, \quad \hat{c}_3 = c_3, \quad \hat{c}_4 = c_4 + \frac{1}{4m_N},\\ &\hat{c}_5 = c_5, \quad \hat{c}_8 = c_8 - \frac{g_Ag_0}{m_N}, \quad \hat{c}_9 = c_9.\end{aligned} \tag{A.51}$$

Now there are still terms in $\hat{\mathcal{L}}^{(2)}_{\pi N,1/m_N}$ that can be eliminated by appropriate field re-definitions. One can for instance eliminate terms $\propto (v\cdot D)^2$. However, since this term does not contribute to our process in practice we do without a field redefinition. For completeness, we define

$$N_v \to \left[1 + \frac{iv\cdot D}{4m_N} - \frac{g_AS_v\cdot u}{4m_N} - \frac{g_0S_v\cdot\hat{u}}{4m_N}\right]N_v, \tag{A.52}$$

and insert it into Eq. (2.82) gives, up to total derivatives,

$$\begin{aligned}\hat{\mathcal{L}}^{(1)}_{\pi N} &\to \hat{\mathcal{L}}^{(1)}_{\pi N} + \Delta\hat{\mathcal{L}}^{(2)}_{\pi N} \\ &= \hat{\mathcal{L}}^{(1)}_{\pi N} + \frac{1}{2m_N}\bar{N}_v\Big[-(v\cdot D)^2 - \frac{g_A^2}{4}i\epsilon^{\mu\nu\rho\sigma}\left[u_\mu,u_\nu\right]v_\rho S^v_\sigma - \frac{g_A^2}{2}\left(v\cdot u\right)^2 \\ &\quad + \frac{g_A^2}{4}\left(u\cdot u\right) - \frac{g_A g_0}{4}\left\{v\cdot u, v\cdot\hat{u}\right\} + g_A g_0\left(u\cdot\hat{u}\right)\Big]N_v,\end{aligned} \tag{A.53}$$

and we neglected terms $O(1/m_N^2, 1/f_\phi^2)$. The first term cancels the EOM term in Eq. (A.48), while the remaining terms shift the constants in Eq. (A.47). In total, we find the HBChPT Lagrangian at chiral order $O(p^2)$ as the sum $\hat{\mathcal{L}}^{(2)}_{\pi N,c_i} + \hat{\mathcal{L}}^{(2)}_{\pi N,1/m_N} + \Delta\hat{\mathcal{L}}^{(2)}_{\pi N}$ to be

$$\begin{aligned}&\hat{\mathcal{L}}^{(2)}_{\pi N,c_i} + \hat{\mathcal{L}}^{(2)}_{\pi N,1/m_N} + \Delta\hat{\mathcal{L}}^{(2)}_{\pi N} \\ &= \bar{N}_v\Big[-\frac{1}{2m_N}\left(D^2 + ig_A\left\{S_v\cdot D, v\cdot u\right\} + ig_0\left\{S_v\cdot D, v\cdot\hat{u}\right\}\right) \\ &\quad + \frac{a_1}{m_N}\left\langle\chi_+\right\rangle + \frac{a_2}{2m_N}\left(v\cdot u\right)^2 + \frac{a_3}{m_N}\left(u\cdot u\right) + \frac{a_4}{2m_N}i\epsilon^{\mu\nu\rho\sigma}\left[u_\mu,u_\nu\right]v_\rho S^v_\sigma \\ &\quad + \frac{a_5}{m_N}\tilde{\chi}_+ + \frac{a_8}{8m_N}\left\{v\cdot u, v\cdot\hat{u}\right\} + \frac{a_9}{m_N}\left(u\cdot\hat{u}\right)\Big]N_v\end{aligned} \tag{A.54}$$

where

$$\begin{aligned}&\frac{a_1}{m_N} = c_1, \quad \frac{a_2}{m_N} = c_2 - \frac{g_A^2}{8m_N}, \quad \frac{a_3}{m_N} = c_3 + \frac{g_A^2}{8m_N}, \quad \frac{a_4}{m_N} = c_4 + \frac{1-g_A^2}{4m_N}, \\ &\frac{a_5}{m_N} = c_5, \quad \frac{a_8}{m_N} = c_8 - \frac{g_A g_0}{2m_N}, \quad \frac{a_9}{m_N} = c_9 + \frac{g_A g_0}{2m_N}.\end{aligned} \tag{A.55}$$

A.4 Discrete Symmetries

Let us start with parity transformations. First we recall that under a Lorentz transformation Λ, implemented by the unitary operator $U(\Lambda)$, a Dirac field transforms as

$$U(\Lambda)^{-1}\Psi(x)U(\Lambda) = D(\Lambda)\Psi(\Lambda^{-1}x). \tag{A.56}$$

A parity transformation is defined as

$$\mathcal{P}^\mu{}_\nu = (\mathcal{P}^{-1})^\mu{}_\nu = \mathrm{Diag}(+1,-1,-1,-1), \quad \mathcal{P}\equiv U(\mathcal{P}), \quad \mathcal{P}_\mu{}^\nu\mathcal{P}^\mu{}_\nu = \mathbb{1}, \tag{A.57}$$

such that we find

$$\begin{aligned}\Psi(x) &\xrightarrow{\mathcal{P}} \mathcal{P}^{-1}\Psi(x)\mathcal{P} = i\gamma_0\Psi(\mathcal{P}x), \\ \bar{\Psi}(x) &\xrightarrow{\mathcal{P}} \mathcal{P}^{-1}\bar{\Psi}(x)\mathcal{P} = -i\bar{\Psi}(\mathcal{P}x)\gamma_0\end{aligned} \tag{A.58}$$

For Weyl fields, comprising a Dirac field, parity therefore exchanges left- and right-handed fields

$$\mathcal{P}^{-1}\Psi_{L/R}(x)\mathcal{P} = i\Psi_{R/L}(\mathcal{P}x). \tag{A.59}$$

For fermion bilinears $\bar{\Psi}A\Psi$, where A is some combination of gamma matrices satisfying $\bar{A} = A$, $\bar{A} = \gamma_0 A^\dagger\gamma_0$, such that $\bar{\Psi}A\Psi$ is hermitian, we let the spinors transform under parity,

$$\left(\mathcal{P}^{-1}\bar{\Psi}\mathcal{P}\right)A\left(\mathcal{P}^{-1}\Psi\mathcal{P}\right) = \bar{\Psi}\gamma_0 A\gamma_0\Psi, \tag{A.60}$$

which gives the transformation behaviour of A by identifying $A^p \equiv \mathcal{P}^{-1}A\mathcal{P} = \gamma_0 A \gamma_0$ under parity

$$\mathcal{P}^{-1}A\mathcal{P} = \gamma_0 A \gamma_0. \tag{A.61}$$

Therefore, if we let both, the spinors and A, transform under parity, the result will be invariant. For basis elements of the Clifford algebra sandwiched between two spinors we therefore find

$$\begin{aligned}
\mathcal{P}^{-1}\mathbb{1}\mathcal{P} &= +\mathbb{1}, \\
\mathcal{P}^{-1}\gamma_5\mathcal{P} &= -\gamma_5, \\
\mathcal{P}^{-1}\gamma^\mu\mathcal{P} &= +\mathcal{P}^\mu{}_\nu\gamma^\nu, \\
\mathcal{P}^{-1}\gamma^\mu\gamma_5\mathcal{P} &= -\mathcal{P}^\mu{}_\nu\gamma^\nu\gamma_5, \\
\mathcal{P}^{-1}\sigma^{\mu\nu}\mathcal{P} &= +\mathcal{P}^\mu{}_\alpha\mathcal{P}^\nu{}_\beta\sigma^{\alpha\beta},
\end{aligned} \tag{A.62}$$

which we now use to determine transformation properties of the external fields and the derivative, which couples to γ^μ, under parity

$$\begin{aligned}
\mathcal{P}^{-1}s\mathcal{P} &= +s, \\
\mathcal{P}^{-1}p\mathcal{P} &= -p, \\
\mathcal{P}^{-1}\left\{v_\mu, v_\mu^{(s)}\right\}\mathcal{P} &= +\mathcal{P}_\mu{}^\nu\left\{v_\nu, v_\nu^{(s)}\right\}, \\
\mathcal{P}^{-1}\left\{a_\mu, a_\mu^{(s)}\right\}\mathcal{P} &= -\mathcal{P}_\mu{}^\nu\left\{a_\nu, a_\nu^{(s)}\right\}.
\end{aligned} \tag{A.63}$$

We are also interested in the transformation behaviour of the four derivative under parity. Similarly to γ^μ, we want the spatial components to transform with a minus, while the zero component should be invariant. We do not want a global minus since it couples to γ^μ and require the product to be invariant. This is simply achieved by

$$\mathcal{P}^{-1}\partial_\mu\mathcal{P} = +\mathcal{P}_\mu{}^\nu\partial_\nu. \tag{A.64}$$

Next we similarly consider charge conjugation. Dirac fields transform as

$$\begin{aligned}
&\mathcal{C}^{-1}\Psi(x)\mathcal{C} = \mathcal{C}\bar{\Psi}^T, \\
&\mathcal{C}^{-1}\bar{\Psi}(x)\mathcal{C} = \Psi^T\mathcal{C}, \quad \text{with} \quad \mathcal{C} = i\gamma_2\gamma_0.
\end{aligned} \tag{A.65}$$

Dirac bilinears $\bar{\Psi}A\Psi$ transform under charge conjugation as

$$\mathcal{C}^{-1}\left(\bar{\Psi}A\Psi\right)\mathcal{C} = (\mathcal{C}^{-1}\bar{\Psi}\mathcal{C})(\mathcal{C}^{-1}A\mathcal{C})(\mathcal{C}^{-1}\Psi\mathcal{C}) = \Psi^T\mathcal{C}A^c\mathcal{C}\bar{\Psi}^T = -\bar{\Psi}\mathcal{C}^T(A^c)^T\mathcal{C}^T\Psi = \bar{\Psi}\left(\mathcal{C}^{-1}(A^c)^T\mathcal{C}\right)\Psi, \tag{A.66}$$

where we made use of $\mathcal{C}^T = \mathcal{C}^{-1} = -\mathcal{C}$ and defined $A^c = \mathcal{C}^{-1}A\mathcal{C}$. Requiring invariance of the full expression we find the transformation property of A under charge conjugation

$$A = \mathcal{C}^{-1}(A^c)^T\mathcal{C} \quad \Rightarrow \quad A^c = \mathcal{C}^{-1}A^T\mathcal{C} \tag{A.67}$$

Going through the list of Clifford algebra elements we find

$$\begin{aligned}
\mathcal{C}^{-1}\mathbb{1}\mathcal{C} &= +\mathbb{1}, \\
\mathcal{C}^{-1}\gamma_5\mathcal{C} &= +\gamma_5, \\
\mathcal{C}^{-1}\gamma^\mu\mathcal{C} &= -\gamma^\mu, \\
\mathcal{C}^{-1}\gamma^\mu\gamma_5\mathcal{C} &= +\gamma^\mu\gamma_5, \\
\mathcal{C}^{-1}\sigma^{\mu\nu}\mathcal{C} &= -\sigma^{\mu\nu}.
\end{aligned} \tag{A.68}$$

Therefore, external fields transform under charge conjugation as

$$\begin{aligned}
\mathcal{C}^{-1} s \mathcal{C} &= +s^T, \\
\mathcal{C}^{-1} p \mathcal{C} &= +p^T, \\
\mathcal{C}^{-1} \left\{ v_\mu, v_\mu^{(s)} \right\} \mathcal{C} &= - \left\{ v_\mu^T, (v_\mu^{(s)})^T \right\}, \\
\mathcal{C}^{-1} \left\{ a_\mu, a_\mu^{(s)} \right\} \mathcal{C} &= \left\{ a_\mu^T, (a_\mu^{(s)})^T \right\}. \\
\mathcal{C}^{-1} \partial_\mu \mathcal{C} &= -\partial_\mu^T
\end{aligned} \tag{A.69}$$

Note that the transpose for the four derivative is the transpose of a unit matrix in flavor space. With this knowledge we can continue to the construction of the effective Lagrangian.

In this appendix we show explicitly how certain quantities transform under parity and charge conjugation

Four derivative

The transformation behaviour of the four derivative under charge conjugation is shown explicitly. We let the spinors transform as usual

$$\begin{aligned}
(\mathcal{C}^{-1} \bar{\Psi} \mathcal{C}) \partial_\mu (\mathcal{C}^{-1} \Psi \mathcal{C}) &= \Psi^T \mathcal{C} \partial_\mu \mathcal{C} \bar{\Psi}^T \\
&= -\bar{\Psi} \mathcal{C}^T \overleftarrow{\partial}_\mu \mathcal{C}^T \Psi \\
&= \bar{\Psi} \mathcal{C}^{-1} \overleftarrow{\partial}_\mu \mathcal{C} \Psi \\
&= \bar{\Psi} \overleftarrow{\partial}_\mu \Psi \overset{\text{i.b.p}}{=} -\bar{\Psi} \partial_\mu \Psi,
\end{aligned} \tag{A.70}$$

where we neglected the transpose, the minus in the second line is from the exchange of two fermions, and used in the last step that $\mathcal{C}$ commutes with ∂_μ. Therefore, the four derivative transforms under charge conjugation as

$$\mathcal{C}^{-1} \partial_\mu \mathcal{C} = -\partial_\mu, \tag{A.71}$$

and is understood to act on the operator on its right. It is however instructive to keep the transpose in the end such that we define

$$\partial_\mu^c = -\partial_\mu^T. \tag{A.72}$$

Covariant derivatives

The covariant derivative in the non-linear representation acting on nucleon field transforms under charge conjugation as

$$\begin{aligned}
D_\mu^c &= \partial_\mu^c + \frac{1}{2} \left[u^* \left(\partial_\mu^c + i \ell_\mu^T \right) u^T + u^T \left(\partial_\mu^c + i r_\mu^T \right) u^* \right] + 2i (a_\mu^s)^T \\
&= \left[-\partial_\mu - \Gamma_\mu + 2i (a_\mu^s) \right]^T \\
&= -D_\mu^T
\end{aligned} \tag{A.73}$$

and under parity it is trivial to show that $D_\mu^p = \mathcal{P}_\mu{}^\nu D_\nu$. Furthermore, with the above, we find that the anti-commutator of two covariant derivatives $D_{\mu\nu} = \{D_\mu, D_\nu\}$ transforms as

$$\begin{aligned}
D_{\mu\nu}^c &= \left\{ -D_\mu^T, -D_\nu^T \right\} = \left\{ D_\nu, D_\mu^T \right\}^T = +D_{\mu\nu}^T \\
D_{\mu\nu}^p &= +\mathcal{P}_\mu{}^\alpha \mathcal{P}_\mu{}^\beta D_{\alpha\beta}.
\end{aligned} \tag{A.74}$$

For the covariant derivative in the linear representation acting on the meson field we find under charge conjugation

$$\begin{aligned}
[\nabla_\mu U]^c &= 2u^T\partial_\mu^c u^T + i\ell_\mu^T U^T - iU^T r_\mu^T - 2i(a_\mu^s)^T U^T \\
&= \left[-2u\overleftarrow{\partial_\mu}u - ir_\mu U + iU\ell_\mu - 2ia_\mu^s U\right]^T \\
&\overset{\text{i.b.p}}{=} \left[2u\partial_\mu u - ir_\mu U + iU\ell_\mu - 2ia_\mu^s U\right]^T \\
&= \left[\partial_\mu U - ir_\mu U + iU\ell_\mu - 2ia_\mu^s U\right]^T \\
&= +\left[\nabla_\mu U\right]^T,
\end{aligned} \tag{A.75}$$

while under parity we find

$$\begin{aligned}
[\nabla_\mu U]^p &= \mathcal{P}_\mu{}^\nu\left(\partial_\nu U^\dagger - i\ell_\nu U^\dagger + iU^\dagger r_\nu + 2ia_\nu^s U^\dagger\right) \\
&= +\left[\mathcal{P}_\mu{}^\nu\nabla_\nu U\right]^\dagger.
\end{aligned} \tag{A.76}$$

Note that r_μ, ℓ_μ, a_μ^s are hermitian.

Isoscalar and isovector vielbein

The transformation behaviour under charge conjugation is

$$u_\mu^c = i\left[u^*(-\partial_\mu^T + i\ell_\mu^T)u^T - u^T(-\partial_\mu^T + ir_\mu^T)u^*\right] = u_\mu^T, \tag{A.77}$$

$$\hat{u}_\mu^c = (2a_\mu^s)^c = \hat{u}_\mu^T. \tag{A.78}$$

while under parity

$$u_\mu^p = -\mathcal{P}_\mu{}^\nu u_\nu, \tag{A.79}$$

$$\hat{u}_\mu^c = -\mathcal{P}_\mu{}^\nu \hat{u}_\nu. \tag{A.80}$$

It is also straight forward to show that u_μ is hermitian

$$\begin{aligned}
u_\mu^\dagger &= -i\left[u^\dagger\left(\overleftarrow{\partial}_\mu + ir_\mu\right)u - u\left(\overleftarrow{\partial}_\mu + i\ell_\mu\right)u^\dagger\right] \\
&= -i\left[u^\dagger\left(-\partial_\mu + ir_\mu\right)u - u\left(-\partial_\mu + i\ell_\mu\right)u^\dagger\right] \\
&= u_\mu.
\end{aligned} \tag{A.81}$$

Since a_μ^s is hermitian so is $\hat{u}_\mu$.

Commutators of vielbeins

First, note that two commutators are zero as can be easily seen from $[u_\mu, \hat{u}_\nu] = [\hat{u}_\mu, u_\nu] \propto [\tau^a, \mathbb{1}] = 0$ and $[\hat{u}_\mu, \hat{u}_\nu] \propto [\mathbb{1}, \mathbb{1}] = 0$. The transformation behaviour under charge conjugation is

$$[u_\mu, u_\nu]^c = \left[u_\mu^T, u_\nu^T\right] = [u_\nu, u_\mu]^T = -\left[u_\mu, u_\nu\right]^T, \tag{A.82}$$

$$\{u_\mu, u_\nu\}^c = \left\{u_\mu^T, u_\nu^T\right\} = \{u_\nu, u_\mu\}^T = +\left\{u_\mu, u_\nu\right\}^T, \tag{A.83}$$

$$\{\hat{u}_\mu, \hat{u}_\nu\}^c = \left\{\hat{u}_\mu^T, \hat{u}_\nu^T\right\} = \{\hat{u}_\nu, \hat{u}_\mu\}^T = +\left\{\hat{u}_\mu, \hat{u}_\nu\right\}^T, \tag{A.84}$$

$$\{\hat{u}_\mu, u_\nu\}^c = \left\{\hat{u}_\mu^T, u_\nu^T\right\} = \{u_\nu, \hat{u}_\mu\}^T = +\{\hat{u}_\mu, u_\nu\}^T\,, \tag{A.85}$$
$$\{u_\mu, \hat{u}_\nu\}^c = \left\{u_\mu^T, \hat{u}_\nu^T\right\} = \{\hat{u}_\nu, u_\mu\}^T = +\{u_\mu, \hat{u}_\nu\}^T\,. \tag{A.86}$$
$$\tag{A.87}$$

Under parity

$$[u_\mu, u_\nu]^p = \left[-\mathcal{P}_\mu{}^\alpha u_\alpha, -\mathcal{P}_\nu{}^\beta u_\beta\right] = +\mathcal{P}_\mu{}^\alpha \mathcal{P}_\mu{}^\beta\,[u_\alpha, u_\beta]\,, \tag{A.88}$$
$$\{u_\mu, u_\nu\}^p = +\mathcal{P}_\mu{}^\alpha \mathcal{P}_\mu{}^\beta\,\{u_\alpha, u_\beta\}\,, \tag{A.89}$$
$$\{\hat{u}_\mu, \hat{u}_\nu\}^p = +\mathcal{P}_\mu{}^\alpha \mathcal{P}_\mu{}^\beta\,\{\hat{u}_\alpha, \hat{u}_\beta\}\,, \tag{A.90}$$
$$\{\hat{u}_\mu, u_\nu\}^p = +\mathcal{P}_\mu{}^\alpha \mathcal{P}_\mu{}^\beta\,\{\hat{u}_\alpha, u_\beta\}\,, \tag{A.91}$$
$$\{u_\mu, \hat{u}_\nu\}^p = +\mathcal{P}_\mu{}^\alpha \mathcal{P}_\mu{}^\beta\,\{u_\alpha, \hat{u}_\beta\}\,. \tag{A.92}$$
$$\tag{A.93}$$

Under hermitian conjugation we get

$$[u_\mu, u_\nu]^\dagger = \left[u_\nu^\dagger, u_\mu^\dagger\right] = -\,[u_\mu, u_\nu]\,, \tag{A.94}$$
$$\{u_\mu, u_\nu\}^\dagger = \left\{u_\nu^\dagger, u_\mu^\dagger\right\} = +\,\{u_\mu, u_\nu\}\,, \tag{A.95}$$
$$\{\hat{u}_\mu, \hat{u}_\nu\}^\dagger = \left\{\hat{u}_\nu^\dagger, \hat{u}_\mu^\dagger\right\} = +\,\{\hat{u}_\mu, \hat{u}_\nu\}\,, \tag{A.96}$$
$$\{\hat{u}_\mu, u_\nu\}^\dagger = \left\{u_\nu^\dagger, \hat{u}_\mu^\dagger\right\} = +\,\{\hat{u}_\mu, u_\nu\}\,, \tag{A.97}$$
$$\{u_\mu, \hat{u}_\nu\}^\dagger = \left\{\hat{u}_\nu^\dagger, u_\mu^\dagger\right\} = +\,\{u_\mu, \hat{u}_\nu\}\,. \tag{A.98}$$

Covariant derivative of vielbeins

Under charge conjugation we find

$$\begin{aligned}[D_\mu, u_\nu]^c &= \left[-D_\mu^T, u_\nu^T\right] = -\,[u_\nu, D_\nu]^T = +\,[D_\mu, u_\nu]^T\,.\\ [D_\mu, \hat{u}_\nu]^c &= \left[-D_\mu^T, \hat{u}_\nu^T\right] = -\,[\hat{u}_\nu, D_\nu]^T = +\,[D_\mu, \hat{u}_\nu]^T\,,\end{aligned} \tag{A.99}$$

while under parity we find

$$\begin{aligned}[D_\mu, u_\nu]^p &= -\mathcal{P}_\mu{}^\alpha \mathcal{P}_\mu{}^\beta\,[D_\alpha, u_\beta]\,,\\ [D_\mu, \hat{u}_\nu]^p &= -\mathcal{P}_\mu{}^\alpha \mathcal{P}_\mu{}^\beta\,[D_\alpha, \hat{u}_\beta]\,.\end{aligned} \tag{A.100}$$

Under hermitian conjugation we find

$$\begin{aligned}&[D_\mu, u_\nu]^\dagger = \left(D_\mu u_\nu - u_\nu \overleftarrow{D}_\mu\right)^\dagger = u_\nu^\dagger \overleftarrow{D}_\mu^\dagger - D_\mu^\dagger u_\nu^\dagger = D_\mu u_\nu - u_\nu \overleftarrow{D}_\nu = +\,[D_\mu, u_\nu]\,,\\ &[D_\mu, \hat{u}_\nu]^\dagger = +\,[D_\mu, \hat{u}_\nu]\,.\end{aligned} \tag{A.101}$$

Scalar and pseudo scalar fields

$\chi = 2B(s - ip)$ transforms under charge conjugation and parity as

$$\begin{aligned}\chi^c &= 2B(s^T - ip^T) = \chi^T,\\ \chi^p &= 2B(s + ip) = \chi^\dagger.\end{aligned} \tag{A.102}$$

For the non-linear version of the above, $\chi_\pm = u^\dagger \chi u^\dagger \pm u \chi^\dagger u$, we find under charge and parity

$$\begin{aligned} \chi_\pm^c &= u^* \chi^T u^* \pm u^T \chi^* u^T = \chi_\pm^T \\ \chi_\pm^p &= u \chi^\dagger u \pm u^\dagger \chi u^\dagger = \pm \chi_\pm . \end{aligned} \tag{A.103}$$

Therefore also the isovector and isoscalar components transform as

$$\begin{aligned} \langle \chi_\pm \rangle^c &= + \langle \chi_\pm \rangle , \\ \langle \chi_\pm \rangle^p &= \pm \langle \chi_\pm \rangle , \\ \tilde{\chi}_\pm^c &= + \tilde{\chi}_\pm^T , \\ \tilde{\chi}_\pm^p &= \pm \tilde{\chi}_\pm . \end{aligned} \tag{A.104}$$

A.5 Construction of the nucleon contact interactions

While the pure nucleon contact terms are well known, we now aim to construct all possible two-nucleon contact terms which include either the field u_μ or $\hat{u}_\mu$. Those are the only fields with chiral dimension one from table A.2. We start with the ones including u_μ. The only terms one can construct to fulfil the right transformation properties are

$$\bar{N} S^\mu N \bar{N} u_\mu N, \quad \bar{N} N \bar{N} S^\mu u_\mu N, \quad \epsilon^{abc} \epsilon^{\mu\nu\rho\sigma} v_\sigma \bar{N} S_\nu \tau^b N \bar{N} S_\rho \tau^c N u_\mu^a . \tag{A.105}$$

It can easily be shown that taking the non-relativistic limit and applying Fierz and other basic identities these are in fact not independent of each other. The explicit relations are $\bar{N} S^\mu N \bar{N} u_\mu N = -\bar{N} N \bar{N} S^\mu u_\mu N$ and $8 \bar{N} S^\mu N \bar{N} u_\mu N = \epsilon^{abc} \epsilon^{\mu\nu\rho\sigma} v_\sigma \bar{N} S_\nu \tau^b N \bar{N} S_\rho \tau^c N u_\mu^a$. Therefore we only need one of them in the Lagrangian which following the literature (e.g. [354]) we write as

$$\mathcal{L}_{\pi NN} \supset \frac{c_D}{2 f_\pi^2 \Lambda_\chi} (\bar{N} N) \left(\bar{N} S^\mu u_\mu N \right) . \tag{A.106}$$

For the terms involving $\hat{u}_\mu$ things are even simpler because $\hat{u}_\mu$ is proportional to the identity matrix in isospin space. There are only two possible combinations satisfying the transformation properties given by

$$\bar{N} N \bar{N} S^\mu \hat{u}_\mu N, \quad \bar{N} \tau^a N \bar{N} S^\mu \hat{u}_\mu \tau^a N . \tag{A.107}$$

Again, it can easily be seen that $\bar{N} \tau^a N \bar{N} S^\mu \hat{u}_\mu \tau^a N = -3 \bar{N} N \bar{N} S^\mu \hat{u}_\mu N$ and so we find for the Lagrangian

$$\mathcal{L}_{\pi NN} \supset \frac{\tilde{c}_D}{2 f_\pi^2 \Lambda_\chi} (\bar{N} N) \left(\bar{N} S^\mu \hat{u}_\mu N \right) . \tag{A.108}$$

This concludes the construction of all terms of the Lagrangian necessary to calculate the corrections to the axion-nucleon coupling.

A.6 Power Counting in Heavy Baryon Chiral Perturbation Theory

We already saw the result of the power counting in Eq. (2.81) which is relevant since we want to systematically calculate diagrams to a given process up to some fixed chiral oder and therefore need to organize them by relevance which is called power counting. Here we derive explicitly this result. Power counting in ChPT but also effective theories in general, was first established by Weinberg see [50–53], for a more recent discussion see als Refs. [49, 355, 356]. We expand

the theory in powers of momentum over mass scale, in this case in powers of $(k/\Lambda_\chi)^\nu$, where $\Lambda_\chi \simeq 770$ MeV is the the mass of the ρ meson and k the momentum involved in the process. A generic Feynman diagram can always be mapped to the general expression

$$\delta^{(4)}(k)^C \int \left(d^4q\right)^L \frac{1}{(q^2)^{I_p}} \frac{1}{q_0^{I_n}} \prod_i \left(q^{d_i}\right)^{V_i}, \tag{A.109}$$

where L is the number of loops, I_n (I_p) is the number of internal nucleon (pion) lines, d_i is the number of derivatives or pion mass insertions on the i-th vertex, appearing V_i times in the diagram under consideration. C counts the number of disconnected subdiagrams. Therefore a generic diagram is of chiral order ν given by

$$\nu = 4 - 4C + 4L - 2I_p - I_n + \sum_i V_i d_i \tag{A.110}$$

We can use now the identities

$$\begin{aligned} \sum_i V_i n_i &= 2I_n + E_n, \\ \sum_i V_i p_i &= 2I_p + E_p, \end{aligned} \tag{A.111}$$

as well as the topological identity

$$L - C = I_p + I_n - \sum_i V_i, \tag{A.112}$$

to simplify this expression. Here E_n (E_p) is the number of external nucleon (pion) lines in the diagram, n_i (p_i) is the number of nucleon (pion) lines attached to each vertex with index i. We can use Eq. (A.111) to write equation Eq. (A.112) as

$$2(L - C) = -E_n - E_p + \sum_i V_i (n_i + p_i - 2). \tag{A.113}$$

Using this as well as $I_n = \sum_i V_i \frac{n_i}{2} - \frac{E_n}{2}$ we find

$$\nu = 4 + 2(L - C) - \frac{E_n}{2} + \sum_i V_i \left(d_i + \frac{n_i}{2} - 2\right). \tag{A.114}$$

As discussed in *e.g.* Ref. [356], due to the different normalization of the multi-particle states, the addition of spectator nucleons changes the power counting. This annoyance can be prevented by adapting the counting and we thus redefine $\nu \to \nu + \frac{3}{2}E_n - 4$ and fix the number of connected diagrams $C = 1$ to find

$$\nu = E_n + 2(L - C) + \sum_i V_i \Delta_i, \qquad \Delta_i = d_i + \frac{1}{2} n_i - 2. \tag{A.115}$$

Since we are eventually only interested in calculating vertex corrections to the axion-nucleon Bremsstrahlungs process involving one connected diagram ($C = 1$) and two external nucleons ($E_n = 2$) the relevant power counting scheme becomes

$$\nu = 2L + \sum_i V_i \Delta_i, \qquad \Delta_i = d_i + \frac{1}{2} n_i - 2, \tag{A.116}$$

exactly recovering Eq. (2.81) Note that in HBChPT we effectively perform a double expansion in powers of k/m_N and k/Λ_χ. In the following we will treat them on the same footing i.e. $k/m_N \sim k/\Lambda_\chi$ even though $m_N > \Lambda_\chi$, which implies that corrections $\sim 1/\Lambda_\chi$ slightly dominate.

To include the axion in the power counting we first notice that the axion decay constant f_ϕ is much larger than any other scale in the problem. Eventually we will be interested in processes with one external axion which implies that the amplitude will at least be suppressed by $\sim (1/f_\phi)$. All amplitudes including additional internal axion are further suppressed and hence completely negligible.

Let us compare the axion momenta to pion and residual nucleon momenta. Because of the splitting of the nucleon momenta in Eq. (2.80) the residual momentum of the pion and the nucleon enjoy the relation

$$v \cdot k \sim \frac{\boldsymbol{k}^2}{2m_N}, \tag{A.117}$$

which implies that for pions or nucleons any vertex leading to the scaling $v \cdot k$ will be suppressed. However, for the axion this is not the case. Since its mass is negligible $m_\phi^2 \simeq 0$, it follows that

$$(p_\phi^0)^2 = (\boldsymbol{p}_\phi)^2. \tag{A.118}$$

Therefore we find that for the power counting it does not matter if the axion couples as $v \cdot p_\phi$ or like $S \cdot p_\phi$ as can be seen from

$$\begin{aligned} v \cdot p_\phi &\sim p_\phi^0 \sim \frac{\boldsymbol{p}_\phi^2}{2m_N} \sim \frac{k}{m_N} k, \\ S \cdot p_\phi &\sim \boldsymbol{\sigma} \cdot \boldsymbol{p}_\phi \sim |\boldsymbol{p}_\phi| \sim p_\phi^0 \sim \frac{k}{m_N} k, \end{aligned} \tag{A.119}$$

where k is a typical momentum involved.

With the proper power counting at hand we can go ahead and systematically calculate

A.7 Sample Calculation of V_1

In this part of the Appendix, we want to show an explicit finite density loop calculation. We focus on the vertex correction $\mathbf{V_1}$. The two different contributions are

$$\begin{aligned} \mathbf{V_1} = \int \frac{d^4k}{(2\pi)^4}(-1) &\left[-\frac{g_A}{2f_\pi}\boldsymbol{\sigma}\cdot(\boldsymbol{k}-\boldsymbol{p})\tau^a\right]\left[\frac{i}{k^0} - 2\pi\delta(k^0)\theta(k_F - |\boldsymbol{k}|)\right]\left[\frac{c_i}{2f_\phi}\boldsymbol{\sigma}\cdot\boldsymbol{p}_\phi\right]\times \\ \times &\left[\frac{i}{k^0+p_\phi^0} - 2\pi\delta(k^0+p_\phi^0)\theta(k_F - |\boldsymbol{k}+\boldsymbol{p}_\phi|)\right]\left[\frac{g_A}{2f_\pi}\boldsymbol{\sigma}\cdot(\boldsymbol{k}-\boldsymbol{p})\tau^b\right]\left[\frac{-i\delta^{ab}}{m_\pi^2-(k-p)^2}\right]. \end{aligned} \tag{A.120}$$

Note that for any diagram, we need to take care of the spin and isospin structure separately. Only then we can evaluate the full integration. We only consider the density dependent part. Due to the δ functions, the dk^0 are trivial and we get after cancelling some minus signs

$$\begin{aligned} \mathbf{V_1} = \int \frac{d^3k}{(2\pi)^3} \Bigg\{ &\left[\frac{g_A}{2f_\pi}\boldsymbol{\sigma}\cdot(\boldsymbol{k}-\boldsymbol{p})\tau^a\right]\left[\frac{c_i}{2f_\phi}\boldsymbol{\sigma}\cdot\boldsymbol{p}_\phi\right]\left[\frac{g_A}{2f_\pi}\boldsymbol{\sigma}\cdot(\boldsymbol{k}-\boldsymbol{p})\tau^a\right]\times \\ &\times\frac{1}{p_\phi^0}\theta(k_F-|\boldsymbol{k}+\boldsymbol{p}_\phi|)\left[\frac{1}{m_\pi^2-(k-p)^2}\right] - \left[\frac{g_A}{2f_\pi}\boldsymbol{\sigma}\cdot(\boldsymbol{k}-\boldsymbol{p})\tau^a\right]\left[\frac{c_i}{2f_\phi}\boldsymbol{\sigma}\cdot\boldsymbol{p}_\phi\right]\times \\ &\times\frac{1}{p_\phi^0}\theta(k_F-|\boldsymbol{k}|)\left[\frac{g_A}{2f_\pi}\boldsymbol{\sigma}\cdot(\boldsymbol{k}-\boldsymbol{p})\tau^a\right]\left[\frac{1}{m_\pi^2-(k-p)^2}\right]\Bigg\}. \end{aligned} \tag{A.121}$$

We now simple properties of the pauli matrices to find

$$\begin{aligned}[\boldsymbol{\sigma}\cdot(\boldsymbol{k}-\boldsymbol{p})]\,[\boldsymbol{\sigma}\cdot\boldsymbol{p}_\phi]\,[\boldsymbol{\sigma}\cdot(\boldsymbol{k}-\boldsymbol{p})] &= \frac{1}{2}\left(\sigma_i\sigma_j\sigma_k+\sigma_k\sigma_j\sigma_i\right)(k-p)_i(p_\phi)_j(k-p)_k = \\ &= 2\,[\boldsymbol{p}_\phi\cdot(\boldsymbol{k}-\boldsymbol{p})]\,[\boldsymbol{\sigma}\cdot(\boldsymbol{k}-\boldsymbol{p})]-[\boldsymbol{\sigma}\cdot\boldsymbol{p}_\phi]\,(\boldsymbol{k}-\boldsymbol{p})^2\end{aligned} \tag{A.122}$$

Now plugging this back in, we find

$$\begin{aligned}\mathbf{V_1} = &\left(\frac{g_A}{2f_\pi}\right)^2\frac{1}{p_\phi^0}\tau^a\frac{c_i}{2f_\phi}\tau^a\times \\ &\int\frac{d^3k}{(2\pi)^3}\left\{\theta(k_F-|\boldsymbol{k}+\boldsymbol{p}_\phi|)\frac{2\,[\boldsymbol{p}_\phi\cdot(\boldsymbol{k}-\boldsymbol{p})]\,[\boldsymbol{\sigma}\cdot(\boldsymbol{k}-\boldsymbol{p})]-[\boldsymbol{\sigma}\cdot\boldsymbol{p}_\phi]\,(\boldsymbol{k}-\boldsymbol{p})^2}{\tilde{m}_\pi^2+(\boldsymbol{k}-\boldsymbol{p})^2}+\right. \\ &\left.-\,\theta(k_F-|\boldsymbol{k}|)\frac{2\,[\boldsymbol{p}_\phi\cdot(\boldsymbol{k}-\boldsymbol{p})]\,[\boldsymbol{\sigma}\cdot(\boldsymbol{k}-\boldsymbol{p})]-[\boldsymbol{\sigma}\cdot\boldsymbol{p}_\phi]\,(\boldsymbol{k}-\boldsymbol{p})^2}{m_\pi^2+(\boldsymbol{k}-\boldsymbol{p})^2}\right\},\end{aligned} \tag{A.123}$$

where we used $m_\pi^2-(k-p_\phi)^2=m_\pi^2-(k_0^2+2k_0p_\phi^0+p_{a0}^2)+(\boldsymbol{k}-\boldsymbol{p}_\phi)^2=\tilde{m}_\pi^2+(\boldsymbol{k}-\boldsymbol{p}_\phi)^2$ with $k_0\sim\frac{Q^2}{2m}\ll Q$ negligible and we called $\tilde{m}_\pi^2=m_\pi^2-p_\phi^2$. Now we shift one of the integrals by $-\boldsymbol{p}_\phi$, such that we find

$$\begin{aligned}\mathbf{V_1} = &\left(\frac{g_A}{2f_\pi}\right)^2\frac{1}{p_\phi^0}\tau^a\frac{c_i}{2f_\phi}\tau^a\times \\ &\int_{|k|<k_F}\frac{d^3k}{(2\pi)^3}\left\{\frac{2\,[\boldsymbol{p}_\phi\cdot(\boldsymbol{k}-\boldsymbol{p}-\boldsymbol{p}_\phi)]\,[\boldsymbol{\sigma}\cdot(\boldsymbol{k}-\boldsymbol{p}-\boldsymbol{p}_\phi)]-[\boldsymbol{\sigma}\cdot\boldsymbol{p}_\phi]\,(\boldsymbol{k}-\boldsymbol{p}-\boldsymbol{p}_\phi)^2}{\tilde{m}_\pi^2+(\boldsymbol{k}-\boldsymbol{p}-\boldsymbol{p}_\phi)^2}+\right. \\ &\left.-\,\frac{2\,[\boldsymbol{p}_\phi\cdot(\boldsymbol{k}-\boldsymbol{p})]\,[\boldsymbol{\sigma}\cdot(\boldsymbol{k}-\boldsymbol{p})]-[\boldsymbol{\sigma}\cdot\boldsymbol{p}_\phi]\,(\boldsymbol{k}-\boldsymbol{p})^2}{m_\pi^2+(\boldsymbol{k}-\boldsymbol{p})^2}\right\}.\end{aligned} \tag{A.124}$$

We can now write this in term of integrals defined below as

$$\begin{aligned}\mathbf{V_1} = &\left(\frac{g_A}{2f_\pi}\right)^2\frac{1}{p_\phi^0}\tau^a\frac{c_i}{2f_\phi}\tau^a\left[2\left(I_1(\tilde{m}_\pi,\boldsymbol{p},\boldsymbol{p}_\phi)-I_1(m_\pi,\boldsymbol{p}+\boldsymbol{p}_\phi,\boldsymbol{p}_\phi)\right)+\right. \\ &\left.-\,\boldsymbol{\sigma}\cdot\boldsymbol{p}_\phi\left(I_2(\tilde{m}_\pi,\boldsymbol{p}+\boldsymbol{p}_\phi)-I_2(m_\pi,\boldsymbol{p})\right)\right].\end{aligned} \tag{A.125}$$

A.8 Explicit loop calculations

A.8.1 1-loop corrections

Following the nomenclature of Fig. 2.2 we calculate the two non-vanishing one loop diagrams, (e_1) and (e_2), and give the results in terms of the standard integrals defined in App. A.9 and as in the main text we define

$$\omega_p\equiv -v\cdot p,\quad \omega_a\equiv -v\cdot(p+p_\phi). \tag{A.126}$$

We split the calculation up in parts since for the same vertex multiple LECs contribute. For the diagram with the c_3 vertex we find

$$\begin{aligned}(e_1)_1 &= \left(\frac{2g_Ac_3c_{u-d}}{f_\pi^2f_\phi\Lambda}\right)\tau^3p_\phi^\mu S^\nu\left(\frac{1}{i}\right)\int\frac{d^4k}{(2\pi)^4}\frac{k_\mu k_\nu}{(k^2-m_\pi^2)(\omega_a-v\cdot k)} \\ &= -\left(\frac{g_Ac_3c_{u-d}}{f_\pi^2f_\phi\Lambda}\right)\tau^3\boldsymbol{\sigma}\cdot\boldsymbol{p}_\phi J_2(\omega_a),\end{aligned} \tag{A.127a}$$

as well as

$$(e_2)_1 = -\left(\frac{g_A c_3 c_{u-d}}{f_\pi^2 f_\phi \Lambda}\right) \tau^3 \boldsymbol{\sigma}\cdot\boldsymbol{p}_\phi J_2(\omega_p). \tag{A.128}$$

For the c_9 vertex we find

$$\begin{aligned}(e_1)_2 &= \left(\frac{3g_A c_9 c_{u+d}}{f_\pi^2 f_\phi \Lambda}\right) S^\mu p_\phi^\nu \left(\frac{1}{i}\right) \int \frac{d^4k}{(2\pi)^4} \frac{k_\mu k_\nu}{(k^2-m_\pi^2)(\omega_a - v\cdot k)} \\ &= -\left(\frac{3g_A c_9 c_{u+d}}{2f_\pi^2 f_\phi \Lambda}\right) \boldsymbol{\sigma}\cdot\boldsymbol{p}_\phi J_2(\omega_a),\end{aligned}$$

and

$$(e_2)_2 = -\left(\frac{3g_A c_9 c_{u+d}}{2f_\pi^2 f_\phi \Lambda}\right) \boldsymbol{\sigma}\cdot\boldsymbol{p}_\phi J_2(\omega_p). \tag{A.129}$$

For the last diagram with the c_4 vertex we find

$$\begin{aligned}(e_1)_3 &= \left(-\frac{2g_A c_4 c_{u-d}}{f_\pi^2 f_\phi \Lambda}\right) \tau^3 \left(\frac{1}{i}\right) \int \frac{d^4k}{(2\pi)^4} \frac{(S\cdot k)(\boldsymbol{p}_\phi\cdot\boldsymbol{k}) - (S\cdot p_\phi)\boldsymbol{k}^2}{(k^2-m_\pi^2)(\omega_a - v\cdot k)} \\ &= 2\tau^3 \left(\frac{g_A c_4 c_{u-d}}{f_\pi^2 f_\phi \Lambda}\right) \boldsymbol{\sigma}\cdot\boldsymbol{p}_\phi J_2(\omega_a),\end{aligned}$$

as well as

$$(e_2)_3 = 2\tau^3 \left(\frac{g_A c_4 c_{u-d}}{f_\pi^2 f_\phi \Lambda}\right) \boldsymbol{\sigma}\cdot\boldsymbol{p}_\phi J_2(\omega_p). \tag{A.130}$$

Summing up all the contributions leads to

$$\begin{aligned}(e_1)+(e_2) &= (e_1)_1 + (e_1)_2 + (e_1)_3 + (e_2)_1 + (e_2)_2 + (e_2)_3 \\ &= \frac{g_A}{f_\phi f_\pi^2}\left[(2\hat{c}_3 - 4\hat{c}_4)\, c_{u-d}\tau^3 + 3\hat{c}_9 c_{u+d}\right]\left[J_2(\omega_a) + J_2(\omega_p)\right] S\cdot p_a \\ &= \frac{g_A}{3f_\phi f_\pi^2}\left[(2\hat{c}_3 - 4\hat{c}_4)\, c_{u-d}\tau^3 + 3\hat{c}_9 c_{u+d}\right]\left\{\frac{1}{16\pi^2}\left[m_\pi^2(\omega_a+\omega_p) - \left(\omega_a^3+\omega_p^3\right)\right.\right. \\ &-4\left(m_\pi^2-\omega_a^2\right)^{3/2}\cos^{-1}\left(\frac{-\omega_a}{m_\pi}\right) - 4\left(m_\pi^2-\omega_p^2\right)^{3/2}\cos^{-1}\left(\frac{-\omega_p}{m_\pi}\right)\Big] \\ &\left.\left.-\Lambda(\lambda)\left(6m_\pi^2(\omega_a+\omega_p) - 4\left(\omega_a^3+\omega_p^3\right)\right)\right\} S\cdot p_a.\end{aligned} \tag{A.131}$$

Here $\Lambda(\lambda)$ is a function collecting the scale dependent and divergent pieces in dimensional regularization given by

$$\Lambda(\lambda) = L(\lambda) + \frac{1}{16\pi^2}\log\frac{m_\pi}{\lambda}. \tag{A.132}$$

A.8.2 Density insertions

The relevant vertex diagrams at 1-loop finite density are given in figure Figs. A.1 and A.2. We calculate them explicitly in the following and give the results in terms of the standard integrals defined in A.9.

The diagrams contributing at order $\nu = 0$ evaluate to

$$\textbf{(1a)} = -i\left(\frac{g_A c_{u-d} p_\phi^0}{4f_\pi^2 f_\phi}\right)\epsilon_{3ab}\tau^a\tau^b \int_0^{k_F} \frac{d^3k}{(2\pi)^3}\left[\frac{\boldsymbol{\sigma}\cdot(\boldsymbol{k}-\boldsymbol{p}-\boldsymbol{p}_\phi)}{\tilde{m}_\pi^2 + (\boldsymbol{k}-\boldsymbol{p}-\boldsymbol{p}_\phi)^2}\right]$$

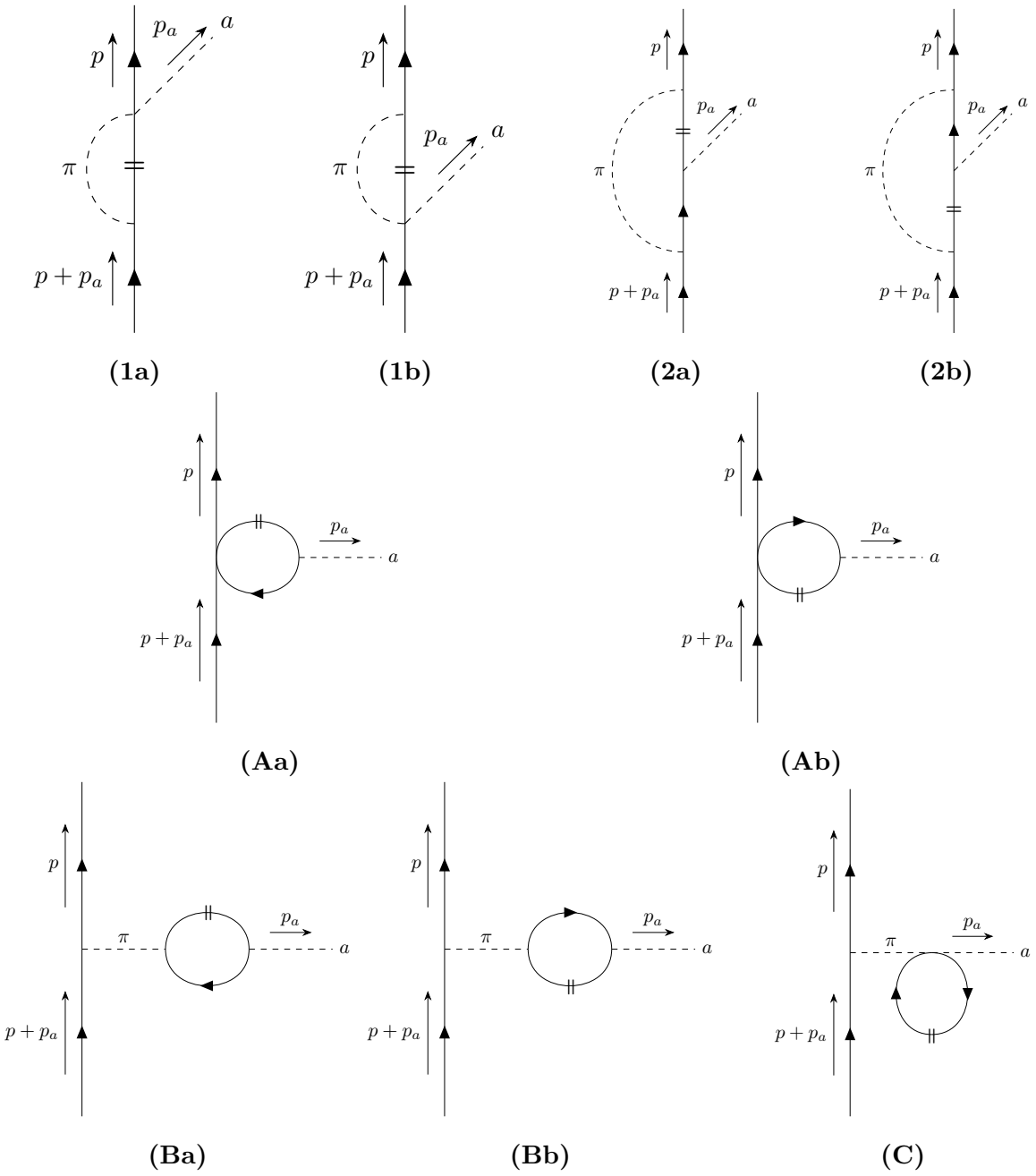

Figure A.1: 1-loop finite density diagrams contributing at chiral order $\nu = 0$

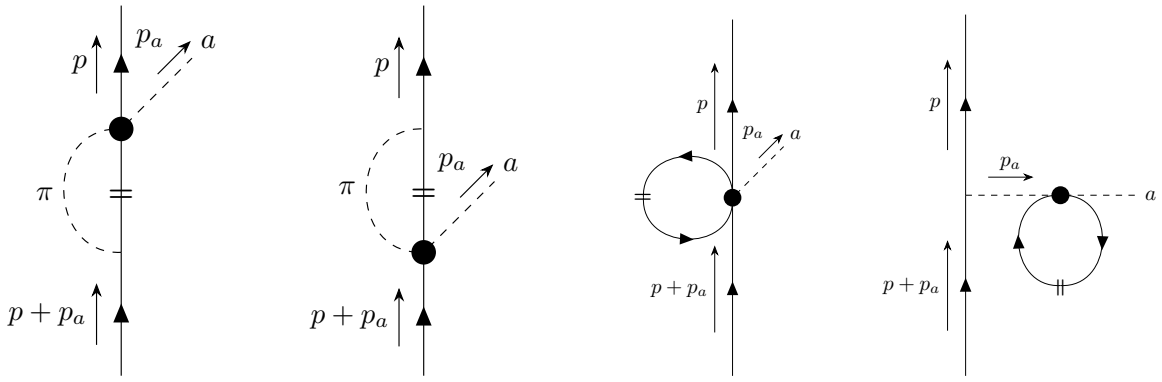

Figure A.2: 1-loop finite density diagrams contributing at chiral order $\nu = 1$

$$= -\frac{c_{u-d} g_A p_\phi^0}{2 f_\pi^2 f_\phi} \tau^3 I_3(\tilde{m}_\pi, p + p_\phi), \tag{A.133a}$$

$$\textbf{(1b)} = -\frac{c_{u-d} g_A p_\phi^0}{2 f_\pi^2 f_\phi} \tau^3 I_3(m_\pi, p), \tag{A.133b}$$

as well as

$$\begin{aligned}\textbf{(2a)} &= -\left(\frac{g_A^2 \hat{c}_N}{8 f_\pi^2 f_\phi}\right) \frac{1}{p_\phi^0} \int_0^{k_F} \frac{d^3k}{(2\pi)^3} \left[\frac{2\boldsymbol{\sigma}\cdot(\boldsymbol{k}-\boldsymbol{p}-\boldsymbol{p}_\phi)\boldsymbol{p}_\phi\cdot(\boldsymbol{k}-\boldsymbol{p}-\boldsymbol{p}_\phi) - \boldsymbol{\sigma}\cdot\boldsymbol{p}_\phi(\boldsymbol{k}-\boldsymbol{p}-\boldsymbol{p}_\phi)^2}{\tilde{m}_\pi^2 + (\boldsymbol{k}-\boldsymbol{p}-\boldsymbol{p}_\phi)^2}\right] \\ &= -\left(\frac{g_A^2 \hat{c}_N}{8 f_\pi^2 f_\phi}\right) \frac{1}{|\boldsymbol{p}_\phi|} \left[2 I_1(\tilde{m}_\pi, p + p_\phi, p_\phi) - \boldsymbol{\sigma}\cdot\boldsymbol{p}_\phi I_2(\tilde{m}_\pi, p + p_\phi)\right], \end{aligned} \tag{A.134a}$$

$$\textbf{(2b)} = \left(\frac{g_A^2 \hat{c}_N}{8 f_\pi^2 f_\phi}\right) \frac{1}{|\boldsymbol{p}_\phi|} \left[2 I_1(m_\pi, p, p_\phi) - \boldsymbol{\sigma}\cdot\boldsymbol{p}_\phi I_2(m_\pi, p)\right]. \tag{A.134b}$$

For the diagrams at $\nu = 1$ we have different vertices contributing to the same diagram. Therefore we split up the calculation for the diagram into parts. For diagram **(4)** we find

$$\begin{aligned}\textbf{(4a)}_1 &= \left(\frac{g_A c_{u-d} c_3}{f_\pi^2 f_\phi \Lambda_\chi}\right) \tau^3 \int_0^{k_F} \frac{d^3k}{(2\pi)^3} \left[\frac{\boldsymbol{\sigma}\cdot(\boldsymbol{k}-\boldsymbol{p}-\boldsymbol{p}_\phi)(\boldsymbol{p}_\phi\cdot(\boldsymbol{k}-\boldsymbol{p}-\boldsymbol{p}_\phi) + \boldsymbol{p}_\phi^2)}{\tilde{m}_\pi^2 + (\boldsymbol{k}-\boldsymbol{p}-\boldsymbol{p}_\phi)^2}\right] \\ &= \left(\frac{g_A c_{u-d} c_3}{f_\pi^2 f_\phi \Lambda_\chi}\right) \tau^3 \left[I_1(\tilde{m}_\pi, p + p_\phi, p_\phi) - |\boldsymbol{p}_\phi|^2 I_3(\tilde{m}_\pi, p + p_\phi)\right], \end{aligned} \tag{A.135a}$$

$$\begin{aligned}\textbf{(4a)}_2 &= \frac{3}{2}\left(\frac{g_A c_9 c_{u+d}}{f_\pi^2 f_\phi \Lambda_\chi}\right) \int_0^{k_F} \frac{d^3k}{(2\pi)^3} \left[\frac{\boldsymbol{\sigma}\cdot(\boldsymbol{k}-\boldsymbol{p}-\boldsymbol{p}_\phi)(\boldsymbol{p}_\phi\cdot(\boldsymbol{k}-\boldsymbol{p}-\boldsymbol{p}_\phi) + \boldsymbol{p}_\phi^2)}{\tilde{m}_\pi^2 + (\boldsymbol{k}-\boldsymbol{p}-\boldsymbol{p}_\phi)^2}\right] \\ &= \left(\frac{3 g_A c_9 c_{u+d}}{2 f_\pi^2 f_\phi \Lambda_\chi}\right) \left[I_1(\tilde{m}_\pi, p + p_\phi, p_\phi) - |\boldsymbol{p}_\phi|^2 I_3(\tilde{m}_\pi, p + p_\phi)\right], \end{aligned} \tag{A.135b}$$

$$\begin{aligned}\textbf{(4a)}_3 &= -\left(\frac{g_A c_{u-d} c_4}{f_\pi^2 f_\phi \Lambda_\chi}\right) \tau^3 \int_0^{k_F} \frac{d^3k}{(2\pi)^3} \left[\frac{\boldsymbol{\sigma}\cdot\boldsymbol{p}_\phi(\boldsymbol{k}-\boldsymbol{p}-\boldsymbol{p}_\phi)^2 - \boldsymbol{\sigma}\cdot(\boldsymbol{k}-\boldsymbol{p}-\boldsymbol{p}_\phi)\boldsymbol{p}_\phi\cdot(\boldsymbol{k}-\boldsymbol{p}-\boldsymbol{p}_\phi)}{\tilde{m}_\pi^2 + (\boldsymbol{k}-\boldsymbol{p}-\boldsymbol{p}_\phi)^2}\right] \\ &= \left(\frac{g_A c_{u-d} c_4}{f_\pi^2 f_\phi \Lambda_\chi}\right) \tau^3 \left[I_1(\tilde{m}_\pi, p + p_\phi, p_\phi) - (\boldsymbol{\sigma}\cdot\boldsymbol{p}_\phi) I_2(\tilde{m}_\pi, p + p_\phi)\right], \end{aligned} \tag{A.135c}$$

$$\begin{aligned}(\mathbf{4a})_4 &= \left(\frac{6g_A c_5 m_\phi^2 f_\phi}{f_\pi^4 \Lambda_\chi}\right) \int_0^{k_F} \frac{d^3k}{(2\pi)^3} \left[\frac{\boldsymbol{\sigma}\cdot(\boldsymbol{k}-\boldsymbol{p}-\boldsymbol{p}_\phi)}{\tilde{m}_\pi^2+(\boldsymbol{k}-\boldsymbol{p}-\boldsymbol{p}_\phi)^2}\right] \\ &= -\left(\frac{6g_A c_5 m_\phi^2 f_\phi}{f_\pi^4 \Lambda_\chi}\right) I_3(\tilde{m}_\pi, p+p_\phi),\end{aligned} \tag{A.135d}$$

and

$$(\mathbf{4b})_1 = \left(\frac{g_A c_{u-d} c_3}{f_\pi^2 f_\phi \Lambda_\chi}\right) \tau^3 I_1\left(m_\pi, p, p_\phi\right), \tag{A.136a}$$

$$(\mathbf{4b})_2 = \left(\frac{3g_A c_9 c_{u+d}}{2f_\pi^2 f_\phi \Lambda_\chi}\right) I_1\left(m_\pi, p, p_\phi\right), \tag{A.136b}$$

$$(\mathbf{4b})_3 = \left(\frac{g_A c_{u-d} c_4}{f_\pi^2 f_\phi \Lambda_\chi}\right) \tau^3 \left[I_1(m_\pi, p, p_\phi) - (\boldsymbol{\sigma}\cdot\boldsymbol{p}_\phi) I_2(m_\pi, p)\right], \tag{A.136c}$$

$$(\mathbf{4b})_4 = \left(\frac{6g_A c_5 m_\phi^2 f_\phi}{f_\pi^4 \Lambda_\chi}\right) I_3(m_\pi, p). \tag{A.136d}$$

The calculation of diagram **(5)** is straight forward and we find

$$\begin{aligned}(\mathbf{5}) =& \frac{1}{2f_\pi^2 f_\phi \Lambda_\chi}\left(c_D c_{u-d}\tau^3 + \tilde{c}_D c_{u+d}\right)(\boldsymbol{\sigma}\cdot\boldsymbol{p}_\phi)\int_0^{k_F}\frac{d^3k}{(2\pi)^3} \\ =& \frac{k_F^3}{12\pi^2 f_\pi^2 f_\phi \Lambda_\chi}\left(c_D c_{u-d}\tau^3 + \tilde{c}_D c_{u+d}\right)(\boldsymbol{\sigma}\cdot\boldsymbol{p}_\phi).\end{aligned} \tag{A.137}$$

Moving on to diagram **(D)** we find that the only non vanishing part comes from the vertex with the coupling c_3 and evaluates to

$$\begin{aligned}(\mathbf{D}) &= 4\tau^3\left(\frac{g_A c_{u-d} c_3}{f_\pi^2 f_\phi \Lambda_\chi}\right)(\boldsymbol{\sigma}\cdot\boldsymbol{p}_\phi)\frac{p_\phi^2}{m_\pi^2-p_\phi^2}\int_0^{k_F}\frac{d^3k}{(2\pi)^3} \\ &= \tau^3\left(\frac{2k_F^3 g_A c_{u-d} c_3}{3\pi^2 f_\pi^2 f_\phi \Lambda_\chi}\right)(\boldsymbol{\sigma}\cdot\boldsymbol{p}_\phi)\frac{p_\phi^2}{m_\pi^2-p_\phi^2} \sim 0,\end{aligned} \tag{A.138}$$

goes to zero for $m_\phi \to 0$.

As discussed in Sec. 4.2, for an arbitrary matter configuration, one needs to repeat the calculation with the modified propagator Eq. (4.33). For the above diagrams, one finds

$$(\mathbf{1}) \to \left(\frac{c_{u-d} g_A}{2f_\pi^2 f_\phi}\right)|\boldsymbol{p}_\phi|\left[I_3(m_\pi, p) + I_3(\tilde{m}_\pi, p+p_\phi)\right]. \tag{A.139}$$

$$(\mathbf{2}) \to -\left(\frac{g_A^2 \tilde{g}_a}{8f_\pi^2 f_\phi}\right)\frac{1}{p_\phi^0}\left[2\left(I_1(\tilde{m}_\pi, p+p_\phi, p_\phi) - I_1(m_\pi, p, p_\phi)\right) - (\boldsymbol{\sigma}\cdot\boldsymbol{p}_\phi)\left(I_2(\tilde{m}_\pi, p+p_\phi) - I_2(m_\pi, p)\right)\right]. \tag{A.140}$$

$$(\mathbf{4a})_1 \to \left(\frac{g_A c_{u-d} c_3}{f_\pi^2 f_\phi \Lambda_\chi}\right)\left[I_1\left(\tilde{m}_\pi, p+p_\phi, p_\phi\right) - |\boldsymbol{p}_\phi|^2 I_3(\tilde{m}_\pi, p+p_\phi)\right] \tag{A.141a}$$

$$(\mathbf{4a})_2 \to -\left(\frac{g_A c_9 c_{u+d}}{2f_\pi^2 f_\phi \Lambda_\chi}\right)\tau^3\left[I_1\left(\tilde{m}_\pi, p+p_\phi, p_\phi\right) - |\boldsymbol{p}_\phi|^2 I_3(\tilde{m}_\pi, p+p_\phi)\right] \tag{A.141b}$$

$$\textbf{(4a)}_3 \to -\left(\frac{g_A c_{u-d} c_4}{f_\pi^2 f_\phi \Lambda_\chi}\right)\left[I_1(\tilde{m}_\pi, p+p_\phi, p_\phi) - (\boldsymbol{\sigma}\cdot\boldsymbol{p}_\phi) I_2(\tilde{m}_\pi, p+p_\phi)\right] \tag{A.141c}$$

$$\textbf{(4a)}_4 \to +\left(\frac{6 g_A c_5 m_\phi^2 f_\phi}{f_\pi^4 \Lambda_\chi}\right)\tau^3 I_3(\tilde{m}_\pi, p+p_\phi) \tag{A.141d}$$

$$\textbf{(4b)}_1 \to \left(\frac{g_A c_{u-d} c_3}{f_\pi^2 f_\phi \Lambda_\chi}\right) I_1\left(m_\pi, p, p_\phi\right) \tag{A.142a}$$

$$\textbf{(4b)}_2 \to -\left(\frac{g_A c_9 c_{u+d}}{2 f_\pi^2 f_\phi \Lambda_\chi}\right)\tau^3 I_1\left(m_\pi, p, p_\phi\right) \tag{A.142b}$$

$$\textbf{(4b)}_3 \to -\left(\frac{g_A c_{u-d} c_4}{f_\pi^2 f_\phi \Lambda_\chi}\right)\left[I_1(m_\pi, p, p_\phi) - \boldsymbol{\sigma}\cdot\boldsymbol{p}_\phi I_2(m_\pi, p)\right] \tag{A.142c}$$

$$\textbf{(4b)}_4 \to -\left(\frac{6 g_A c_5 m_\phi^2 f_\phi}{f_\pi^4 \Lambda_\chi}\right)\tau^3 I_3(m_\pi, p) \tag{A.142d}$$

$$\textbf{(5)} \to \frac{k_F^3}{12\pi^2 f_\pi^2 f_\phi \Lambda_\chi}\left(c_D c_{u-d} + \tilde{c}_D c_{u+d}\tau^3\right)(\boldsymbol{\sigma}\cdot\boldsymbol{p}_\phi) \tag{A.143}$$

For diagram **(D)**, the non-vanishing vertices change: c_5 and c_9 both contribute. We find

$$\textbf{(D)} \to \begin{cases} c_5: & \left(\frac{4k_F^3 g_A c_5 f_\phi m_\phi^2}{3\pi^2 m_\pi^2 f_\pi^4 \Lambda_\chi}\right)\tau^3(\boldsymbol{\sigma}\cdot\boldsymbol{p}_\phi), \\ c_9: & \left(\frac{k_F^3 g_A c_{u+d} c_9}{3\pi^2 f_\pi^2 f_\phi \Lambda_\chi}\right)\tau^3(\boldsymbol{\sigma}\cdot\boldsymbol{p}_\phi)\frac{p_\phi^2}{m_\pi^2 - p_\phi^2} \quad \sim 0. \end{cases} \tag{A.144}$$

We find that both contributions go to zero in the limit $m_\phi \to 0$.

A.9 Useful Integrals

For the vacuum loops, the following standard integrals also defined in [49] are useful

$$\Delta_\pi = -\frac{1}{i}\int \frac{\mathrm{d}^d k}{(2\pi)^d}\frac{1}{k^2 - m_\pi^2 + i\eta} = 2m_\pi^2\left(L(\lambda) + \frac{1}{(4\pi)^2}\ln\frac{m_\pi}{\lambda}\right) + \mathcal{O}(d-4), \tag{A.145}$$

$$\frac{1}{i}\int \frac{\mathrm{d}^d k}{(2\pi)^d}\frac{\{1, k_\mu, k_\mu k_\nu\}}{\left(k^2 - m_\pi^2 + i\eta\right)\left(\omega - v\cdot k + i\eta\right)} = \left\{J_0(\omega), v_\mu J_1(\omega), g_{\mu\nu} J_2(\omega) + v_\mu v_\nu J_3(\omega)\right\}, \tag{A.146}$$

$$L(\lambda) = \frac{\lambda^{d-4}}{(4\pi)^2}\left(\frac{1}{d-4} - \frac{1}{2}\left[\ln(4\pi) + \Gamma'(1) + 1\right]\right), \tag{A.147}$$

where

$$\begin{aligned} J_0(\omega) &= -4\omega L + \frac{2\omega}{(4\pi)^2}\left(1 - 2\ln\frac{m_\pi}{\lambda}\right) - \frac{1}{4\pi^2}\sqrt{m_\pi^2 - \omega^2}\arccos\frac{-\omega}{m_\pi} + \mathcal{O}(d-4), \\ J_1(\omega) &= w J_0(\omega) + \Delta_\pi, \\ J_2(\omega) &= \frac{1}{d-1}\left[\left(m_\pi^2 - \omega^2\right) J_0(\omega) - \omega\Delta_\pi\right], \\ J_3(\omega) &= w J_1(\omega) - J_2(\omega). \end{aligned} \tag{A.148}$$

At finite density, the relevant standard integrals, also given in [357, 358], read

$$\Gamma_0(m_\pi, p) = \int_0^{k_F} dk \int_{-1}^{1} dx \frac{k^2}{m_\pi^2 + p^2 + k^2 + 2pkx}, \tag{A.149a}$$

$$\Gamma_1(m_\pi,p)=\int_0^{k_F}dk\int_{-1}^{1}dx\frac{k^3x/p}{m_\pi^2+p^2+k^2+2pkx}, \tag{A.149b}$$

$$\Gamma_2(m_\pi,p)=\int_0^{k_F}dk\int_{-1}^{1}dx\frac{k^4\left(1-x^2\right)/2}{m_\pi^2+p^2+k^2+2pkx}, \tag{A.149c}$$

$$\Gamma_3(m_\pi,p)=\int_0^{k_F}dk\int_{-1}^{1}dx\frac{k^4\left(3x^2-1\right)/\left(2p^2\right)}{m_\pi^2+p^2+k^2+2pkx}. \tag{A.149d}$$

For the calculation provided in section 4.2 it additionally turns out to be useful to define

$$\begin{aligned} I_1\left(m_\pi,p,q\right)&=\int_0^{k_F}\frac{d^3k}{(2\pi)^3}\frac{\boldsymbol{\sigma}\cdot(\boldsymbol{k}+\boldsymbol{p})\boldsymbol{q}\cdot(\boldsymbol{k}+\boldsymbol{p})}{m_\pi^2+(\boldsymbol{k}+\boldsymbol{p})^2}\\ &=\frac{1}{4\pi^2}\left[(\boldsymbol{\sigma}\cdot\boldsymbol{q})\,\Gamma_2(m_\pi,p)+(\boldsymbol{\sigma}\cdot\boldsymbol{p})\,(\boldsymbol{q}\cdot\boldsymbol{p})\,(\Gamma_0(m_\pi,p)+2\Gamma_1(m_\pi,p)+\Gamma_3(m_\pi,p))\right], \end{aligned} \tag{A.150a}$$

$$I_2\left(m_\pi,p\right)=\int_0^{k_F}\frac{d^3k}{(2\pi)^3}\frac{(\boldsymbol{k}+\boldsymbol{p})\cdot(\boldsymbol{k}+\boldsymbol{p})}{m_\pi^2+(\boldsymbol{k}+\boldsymbol{p})^2}=\frac{1}{4\pi^2}\left(\frac{2k_F^3}{3}-m_\pi^2\Gamma_0(m_\pi,p)\right), \tag{A.150b}$$

$$I_3\left(m_\pi,p\right)=\int_0^{k_F}\frac{d^3k}{(2\pi)^3}\frac{\boldsymbol{\sigma}\cdot(\boldsymbol{k}+\boldsymbol{p})}{m_\pi^2+(\boldsymbol{k}+\boldsymbol{p})^2}=(\boldsymbol{\sigma}\cdot\boldsymbol{p})\frac{1}{4\pi^2}\left(\Gamma_1(m_\pi,p)+\Gamma_0(m_\pi,p)\right). \tag{A.150c}$$

The functions $F_i(p,k_F^{p/n},p_\phi)$ used in the main text are as cumbersome as uninsightful to write down and will explicitly be given in a supplementary mathematica file in [16].

Appendix B

The QCD Axion at Finite Density

B.1 Axion mass calculation with instantons

We calculate the axion mass by integrating out the neutral pions $\{\pi_0, \eta, \eta'\}$ in the $N_f = 3$ chiral Lagrangian, from the potential

$$V_0 = b(\mathrm{Tr}[U^\dagger M_\phi] + \mathrm{h.c.}) - c(e^{-i(\phi/f_\phi + \eta'/f_{\eta'})} + \mathrm{h.c.})\,, \tag{B.1}$$

where in vacuum, b is

$$b = \frac{m_\pi^2 f_\pi^2}{2(m_u + m_d)}, \tag{B.2}$$

and effectively $c \to \infty$, while $b = -A_3\Delta_3^2$ and $c = \Delta_3^6/\Lambda^2$ in the CFL phase when instantons dominate. Note that the η' is normalized differently in the CFL phase. This procedure produces the correct leading order result for the axion mass but neglects (some of) the subleading corrections. In the generic basis of Eq. (2.54), the potential then reads

$$\begin{aligned} V =& 2bm_u \cos\left(\frac{Q_u\phi}{f_\phi} - \frac{\frac{\eta}{\sqrt{3}} + \pi_0}{f_\pi} - \frac{\eta'}{3f_{\eta'}}\right) + 2bm_d \cos\left(\frac{Q_d\phi}{f_\phi} + \frac{\pi_0 - \frac{\eta}{\sqrt{3}}}{f_\pi} - \frac{\eta'}{3f_{\eta'}}\right) \\ &+ 2bm_s \cos\left(\frac{Q_s\phi}{f_\phi} + \frac{2\eta}{\sqrt{3}f_\pi} - \frac{\eta'}{3f_{\eta'}}\right) - 2c\cos\left(\frac{\eta'}{f_{\eta'}} - \frac{(\mathrm{Tr}[Q_\phi] - 1)\,\phi}{f_\phi}\right), \end{aligned} \tag{B.3}$$

with $Q_\phi = \mathrm{Diag}[Q_u, Q_d, Q_s]$. We integrate π_0 out by using its equation of motion at linear order in the fields

$$\pi_0 = \frac{(m_u Q_u - m_d Q_d)}{(m_d + m_u)}\left(\frac{f_\pi}{f_\phi}\phi\right) + \frac{(m_d - m_u)}{3\,(m_d + m_u)}\left(\sqrt{3}\eta + \frac{f_\pi}{f_{\eta'}}\eta'\right). \tag{B.4}$$

Next, we similarly integrate η out

$$\begin{aligned} \eta =& \frac{\sqrt{3}\,(-m_d m_s Q_s + m_d m_u\,(Q_d + Q_u) - m_s m_u Q_s)}{2\,(m_d m_s + m_u m_d + m_s m_u)}\left(\frac{f_\pi}{f_\phi}\phi\right) \\ &+ \frac{(m_d\,(m_s - 2m_u) + m_s m_u)}{2\sqrt{3}\,(m_d m_s + m_u m_d + m_s m_u)}\left(\frac{f_\pi}{f_{\eta'}}\eta'\right). \end{aligned} \tag{B.5}$$

Finally, we integrate out η'

$$\eta' = \frac{-bm_d m_s m_u \mathrm{Tr}[Q_\phi] + c\,(m_d m_s + m_u m_d + m_s m_u)\,(\mathrm{Tr}[Q_\phi] - 1)}{-bm_d m_s m_u + c\,(m_d m_s + m_u m_d + m_s m_u)}\left(\frac{f_{\eta'}}{f_\phi}\phi\right). \tag{B.6}$$

The potential is minimized around $\langle\phi\rangle = \langle\pi_0\rangle = \langle\eta\rangle = \langle\eta'\rangle = 0$ and we find the following axion mass

$$m_\phi^2 = \frac{-2bc\, m_u m_d}{f_\phi^2 (m_u+m_d)\left(c\left[1+\frac{m_u m_d}{m_s(m_u+m_d)}\right] - b\left[\frac{m_d m_u}{m_u+m_d}\right]\right)}\,. \tag{B.7}$$

Once we have diagonalized the mass matrix, one could be concerned with the effect of the $O(f_\pi/f_\phi)$ kinetic mixing, which is generically induced by the derivative couplings of the axion. Let us explicitly show that this does not affect the leading order results for the axion mass. Our starting point, without loss of generality, is the following Lagrangian

$$\mathcal{L} = \frac{1}{2} m_\pi^2 \begin{pmatrix} \boldsymbol{\pi} & \phi \end{pmatrix} \begin{pmatrix} b & 0 \\ 0 & c\xi^2 \end{pmatrix} \begin{pmatrix} \boldsymbol{\pi} \\ \phi \end{pmatrix} + \frac{1}{2} \begin{pmatrix} \partial_\mu \boldsymbol{\pi} & \partial_\mu \phi \end{pmatrix} \begin{pmatrix} 1 & \xi \boldsymbol{d} \\ \xi \boldsymbol{d}^T & 1 \end{pmatrix} \begin{pmatrix} \partial^\mu \boldsymbol{\pi} \\ \partial^\mu \phi \end{pmatrix}, \tag{B.8}$$

where $b = \mathrm{Diag}[b_1, .., b_n]$ is an $n \times n$ diagonal matrix of $\mathcal{O}(1)$ numbers, $\boldsymbol{d}$ is a vector of n $\mathcal{O}(1)$ numbers, c is an $\mathcal{O}(1)$ number, and $\xi \equiv f_\pi/f_\phi$ is our expansion parameter. Let's start by performing the orthogonal rotation R_1 in the meson subspace, such that

$$R_1 \boldsymbol{d} = (0, \ldots, |d|). \tag{B.9}$$

We rewrite the Lagrangian in this basis

$$\mathcal{L} = \frac{1}{2} m_\pi^2 \begin{pmatrix} \boldsymbol{\pi} & \phi \end{pmatrix} \begin{pmatrix} R_1 b R_1^T & 0 \\ 0 & c\xi^2 \end{pmatrix} \begin{pmatrix} \boldsymbol{\pi} \\ \phi \end{pmatrix} + \frac{1}{2} \begin{pmatrix} \partial_\mu \pi_1 & \ldots & \partial_\mu \pi_n & \partial_\mu \phi \end{pmatrix} \begin{pmatrix} 1 & & & \\ & \ddots & & \\ & & 1 & |d|\xi \\ & & |d|\xi & 1 \end{pmatrix} \begin{pmatrix} \partial^\mu \pi_1 \\ \vdots \\ \partial^\mu \pi_n \\ \partial^\mu \phi \end{pmatrix}. \tag{B.10}$$

We diagonalize and canonically normalize the lower 2×2 block in the second term by rotating and rescaling the fields

$$\begin{pmatrix} \pi_n \\ \phi \end{pmatrix} = \underbrace{\frac{1}{\sqrt{2}} \begin{pmatrix} 1 & 1 \\ -1 & 1 \end{pmatrix}}_{\equiv R_2} \underbrace{\begin{pmatrix} \frac{1}{\sqrt{1-|d|\xi}} & 0 \\ 0 & \frac{1}{\sqrt{1+|d|\xi}} \end{pmatrix}}_{\equiv T} \begin{pmatrix} \bar{\pi}_n \\ \bar{\phi} \end{pmatrix}. \tag{B.11}$$

Our mass matrix in the new basis now reads

$$m_\pi^2 T R_2^T \begin{pmatrix} \left[R_1 b R_1^T\right]_{nn} & 0 \\ 0 & c\xi^2 \end{pmatrix} R_2 T\,. \tag{B.12}$$

T can be expanded $T = \mathbb{1} + \frac{1}{2}|d|\xi\sigma_3 + \mathcal{O}(\xi^2)$. At leading order $T = \mathbb{1}$ and the mass matrix can be re-diagonalized by performing the inverse orthogonal rotation R_2^{-1}, bringing it back to the diagonal form of Eq. (B.8). One concludes that the axion mass receives no leading order correction due to the kinetic mixing.

B.2 Baryon-ChPT with non-trivial vacuum alignment

We generalize the $N_f = 3$ chiral Lagrangian with baryons for a non-trivial ground state orientation, $U_0 \neq 1$ with $U_0^\dagger U_0 = \mathbb{1}_3$, e.g. in the kaon-condensed phase

$$U_0(\theta) = \begin{pmatrix} \cos\theta & 0 & i\sin\theta \\ 0 & 1 & 0 \\ i\sin\theta & 0 & \cos\theta \end{pmatrix}. \tag{B.13}$$

We denote $U_0(\theta/2) \equiv \xi_0(\theta)$ (such that $\xi_0^2 = U_0$) and drop for brevity the explicit θ-dependence. The standard $SU(3)_L \times SU(3)_R$ generators are given by the Gell-Mann matrices

$$T_L^a = \lambda^a\,, \quad T_R^a = \lambda^a\,. \tag{B.14}$$

It should be understood that the L and R operators act on different indices and therefore commute. We define the following rotated generators

$$(T_L^a)_\theta = \xi_0(T_L^a)\xi_0^\dagger\,, \quad (T_R^a)_\theta = \xi_0^\dagger(T_R^a)\xi_0\,, \tag{B.15}$$

The broken and unbroken generators are given by

$$X^a = (T_L^a)_\theta - (T_R^a)_\theta\,, \quad T^a = (T_L^a)_\theta + (T_R^a)_\theta\,, \tag{B.16}$$

respectively. The fluctuation around the vacuum are parametrized by the Goldstone matrices

$$\xi_L = e^{i\frac{\pi^a}{2f_\pi}(T_L^a)_\theta} = \xi_0 \exp\left[\frac{i\pi^a\lambda^a}{2f_\pi}\right]\xi_0^\dagger\,, \quad \xi_R = e^{-i\frac{\pi^a}{2f_\pi}(T_R^a)_\theta} = \xi_0^\dagger \exp\left[-\frac{i\pi^a\lambda^a}{2f_\pi}\right]\xi_0\,, \tag{B.17}$$

with transformation properties

$$\xi_L \to L\xi_L V_\theta^\dagger\,, \quad \xi_R = R\xi_R V_\theta^\dagger\,, \tag{B.18}$$

with V_θ a NGB-dependent transformation under the unbroken $SU(3)$ subgroup of $SU(3)_L \times SU(3)_R$, the transformations under the latter denoted by L and R respectively. As usual, it is convenient to construct

$$\Sigma = \xi_L U_0 \xi_R^\dagger = \xi_0 \exp\left[\frac{i\pi^a\lambda^a}{f_\pi}\right]\xi_0\,, \tag{B.19}$$

which transforms as $\Sigma \to L\Sigma R^\dagger$. Following standard notation,

$$\pi^a\lambda^a = \sqrt{2}\begin{pmatrix} \frac{\pi_0}{\sqrt{2}} + \frac{\eta}{\sqrt{6}} & \pi^+ & K^+ \\ \pi^- & -\frac{\pi_0}{\sqrt{2}} + \frac{\eta}{\sqrt{6}} & K_0 \\ K^- & \bar{K}_0 & -\sqrt{\frac{2}{3}}\eta \end{pmatrix}. \tag{B.20}$$

We introduce the (θ-rotated) baryon octet as linearly-transforming fields, $\hat{B}^\theta_{L,R}$,

$$\hat{B}^\theta_L \to L\hat{B}^\theta_L L^\dagger\,, \quad \hat{B}^\theta_R = R\hat{B}^\theta_R R^\dagger\,, \tag{B.21}$$

where we use the θ-superscript because the finite-density backgrounds we consider consist of a non-vanishing ensemble of the standard (non-rotated) baryons, given by

$$\hat{B}_L = \xi_0^\dagger \hat{B}^\theta_L \xi_0\,, \quad \hat{B}_R = \xi_0 \hat{B}^\theta_R \xi_0^\dagger\,, \tag{B.22}$$

with the usual parameterization

$$B_{L,R} = \begin{pmatrix} \frac{\Sigma_0}{\sqrt{2}} + \frac{\Lambda}{\sqrt{6}} & \Sigma^+ & p \\ \Sigma^- & -\frac{U_0}{\sqrt{2}} + \frac{\Lambda}{\sqrt{6}} & n \\ \Xi^- & \Xi_0 & -\sqrt{\frac{2}{3}}\Lambda \end{pmatrix}_{L,R}. \tag{B.23}$$

The Lagrangian in this basis is given by

$$\mathcal{L} = \mathcal{L}_U^0 + \mathcal{L}_B^0 + \mathcal{L}_M + \mathcal{L}_\ell^0 \,, \tag{B.24}$$

$$\mathcal{L}_U^0 = \frac{f_\pi^2}{4}\mathrm{Tr}[\partial_\mu U^\dagger \partial^\mu U] \,, \tag{B.25}$$

$$\mathcal{L}_B^0 = i\mathrm{Tr}[\bar{\hat{B}}_L^\theta \gamma^\mu \partial_\mu \hat{B}_L^\theta] + i\mathrm{Tr}[\bar{\hat{B}}_R^\theta \gamma^\mu \partial_\mu \hat{B}_R^\theta] - M_B \mathrm{Tr}[\bar{\hat{B}}_L^\theta U \hat{B}_R^\theta U^\dagger + \text{h.c.}] \,, \tag{B.26}$$

$$\begin{aligned}\mathcal{L}_M = &-\frac{\langle \bar{q}q\rangle_0}{2}\mathrm{Tr}[U^\dagger M] \\ &+ a_1 \mathrm{Tr}[\bar{\hat{B}}_L^\theta M \hat{B}_R^\theta U^\dagger] + \bar{a}_1 \mathrm{Tr}[\bar{\hat{B}}_R^\theta U^\dagger M U^\dagger \hat{B}_L^\theta U] \\ &+ a_2 \mathrm{Tr}[\bar{\hat{B}}_R^\theta U^\dagger \hat{B}_L^\theta M] + \bar{a}_2 \mathrm{Tr}[\bar{\hat{B}}_L^\theta U \hat{B}_R^\theta U^\dagger M U^\dagger] \\ &+ a_3 \mathrm{Tr}[\bar{\hat{B}}_L^\theta U \hat{B}_R^\theta \Sigma^\dagger + \bar{\hat{B}}_R^\theta U^\dagger \hat{B}_L^\theta U]\mathrm{Tr}[U^\dagger M] + \text{h.c.} \,,\end{aligned} \tag{B.27}$$

$$\mathcal{L}_\ell^0 = \sum_{\ell=e,\mu} \bar{\ell}(i\gamma^\mu \partial_\mu - m_\ell)\ell \,. \tag{B.28}$$

where we recall the quark mass matrix spurion transforms as $M \to LMR^\dagger$, we dropped some terms at the same order in derivatives (acting on the U matrices) that are irrelevant for our discussion, and we included leptons.

B.2.1 Adding chemical potential

We add chemical potentials for the three mutually commuting abelian symmetries associated with neutron and proton numbers and electric charge (from here on, we neglect the other baryons). Under $U(1)_{n,p}$, $\psi \to e^{i\alpha}\psi$ for $\psi = n, p$ respectively, while under $U(1)_{\text{EM}}$ electromagnetism,

$$\hat{B}_{L,R} \to e^{i\alpha Q_e}\hat{B}_{L,R}e^{-i\alpha Q_e} \,, \;\; U \to e^{i\alpha Q_e} U e^{-i\alpha Q_e} \,, \;\; \ell \to e^{-i\alpha}\ell \,, \tag{B.29}$$

with

$$Q_e = \frac{1}{3}\begin{pmatrix} 2 & & \\ & -1 & \\ & & -1 \end{pmatrix} . \tag{B.30}$$

Chemical potentials are introduced following the prescription in Eq. (5.2), i.e. by, modifying temporal derivatives as

$$\partial_0 U \to \partial_0 U + i[\hat{\mu}, U] \,, \tag{B.31}$$

$$\partial_0 \hat{B}_{L,R} \to \partial_0 \hat{B}_{L,R} + i[\hat{\mu}, \hat{B}_{L,R}] + i\hat{\mu}_{n,p}\hat{B}_{L,R} \,, \tag{B.32}$$

$$\partial_0 \ell \to \partial_0 \ell - i\mu\ell \,, \tag{B.33}$$

where we denoted

$$\hat{\mu} = \mu\, Q_e \,, \quad \hat{\mu}_{n,p} = \mathrm{Diag}[\mu_p - \mu, \mu_n, 0] \,. \tag{B.34}$$

We then get the following additional terms to the Lagrangian (B.24)

$$\mathcal{L}_U^\mu = \mathcal{L}_U^0 + \frac{f_\pi^2}{4}\left(\mathrm{Tr}[2i\partial_0 U[\hat{\mu}, U^\dagger]] - \mathrm{Tr}[[\hat{\mu}, U][\hat{\mu}, U^\dagger]]\right) \,, \tag{B.35}$$

$$\mathcal{L}_B^\mu = \mathcal{L}_B^0 - \left(\mathrm{Tr}[\bar{\hat{B}}_L^\theta \gamma^0 [\hat{\mu}, \hat{B}_L^\theta]] + \mathrm{Tr}[\bar{\hat{B}}_R^\theta \gamma^0 [\hat{\mu}, \hat{B}_R^\theta]]\right)$$

$$- \left(\mathrm{Tr}[\bar{\hat{B}}^\theta_L \gamma^0 \hat{\mu}_{n,p} \hat{B}^\theta_L] + \mathrm{Tr}[\bar{\hat{B}}^\theta_R \gamma^0 \hat{\mu}_{n,p} \hat{B}^\theta_R] \right) , \tag{B.36}$$

$$\mathcal{L}^\mu_\ell = \mathcal{L}^0_\ell + \mu \sum_{\ell=e,\mu} \bar{\ell} \gamma^0 \ell \, . \tag{B.37}$$

B.2.2 Non-linear field basis

It is usually most convenient to work in a field basis for the baryons in which these only transform under the non-linearly realized unbroken $SU(3)$ subgroup of $SU(3)_L \times SU(3)_R$,

$$B^\theta_L \to V_\theta B^\theta_L V^\dagger_\theta \, , \quad B^\theta_R = V_\theta B^\theta_R V^\dagger_\theta \, , \tag{B.38}$$

with the dressed fields

$$B^\theta_R = \xi^\dagger_R \hat{B}^\theta_R \xi_R \, , \quad B^\theta_L = \xi^\dagger_L \hat{B}^\theta_L \xi_L \, . \tag{B.39}$$

In this basis there are no non-derivative interactions of the mesons with the baryons from the mass terms in Eq. (B.27). Besides, in complete analogy to Eq. (B.22), the standard (non-rotated) baryons are given by

$$B_L = \xi^\dagger_0 B^\theta_L \xi_0 \, , \quad B_R = \xi_0 B^\theta_R \xi^\dagger_0 \, . \tag{B.40}$$

In terms of such fields, which we recall make up the finite-density background, the baryon Lagrangian is given by

$$\mathcal{L}^\mu_B = i\mathrm{Tr}[\bar{B}\gamma^\mu D_\mu B] - M_B \mathrm{Tr}[\bar{B}B] - \mu \mathrm{Tr}[\bar{B}\gamma^0 [\hat{Q}_e, B]] - \mathrm{Tr}[\bar{B}\gamma^0 \hat{\mu}_{u,d} B] \, , \tag{B.41}$$

where the baryon covariant derivative is given by $D_\mu B = \partial_\mu B + [e_\mu, B]$, with

$$e_\mu \equiv \frac{1}{2} \left(\xi^\dagger_0 (e_L)_\mu \xi_0 + \xi_0 (e_R)_\mu \xi^\dagger_0 \right) , \quad (e_L)_\mu \equiv i \xi^\dagger_L \partial_\mu \xi_L \, , \;\; (e_R)_\mu \equiv i \xi^\dagger_R \partial_\mu \xi_R \, , \tag{B.42}$$

and

$$\hat{Q}_e \equiv \frac{1}{2} \left(\xi^\dagger_0 \xi^\dagger_L Q_e \xi_L \xi_0 + \xi_0 \xi^\dagger_R Q_e \xi_R \xi^\dagger_0 \right) , \tag{B.43}$$

reproducing Eq. (5.54). The part of the Lagragian proportional to the quark mass matrix reads

$$\begin{aligned} \mathcal{L}_M = & -\frac{\langle \bar{q}q \rangle_0}{2} \mathrm{Tr}[\hat{M}] + a_1 \mathrm{Tr}[\bar{B}_L \hat{M} B_R] + \bar{a}_1 \mathrm{Tr}[\bar{B}_R \hat{M} B_L] \\ & + a_2 \mathrm{Tr}[\bar{B}_R B_L \hat{M}] + \bar{a}_2 \mathrm{Tr}[\bar{B}_L B_R \hat{M}] + a_3 \mathrm{Tr}[\bar{B}_L B_R + \bar{B}_R B_L] \mathrm{Tr}[\hat{M}] + \mathrm{h.c.} \, . \end{aligned}$$

where we defined the dressed mass matrix

$$\hat{M} \equiv \xi^\dagger_0 \xi^\dagger_L M \xi_R \xi^\dagger_0 \, , \tag{B.44}$$

as in Eq. (5.30). From $\mathcal{L}_M$ in this form it becomes apparent that the $L \leftrightarrow R$ exchange symmetry of QCD implies $a_{1,2} = \bar{a}_{1,2}$, which allows us to write

$$\mathcal{L}_M = -\frac{1}{2} \mathrm{Tr}[\langle \bar{q}q \rangle_n (\hat{M} + \hat{M}^\dagger)] \, , \tag{B.45}$$

$$\langle \bar{q}q \rangle_n \equiv \langle \bar{q}q \rangle_0 \mathbb{1}_3 - 2a_1 B\bar{B} - 2a_2 \bar{B}B - 2a_3 \mathrm{Tr}[\bar{B}B] \mathbb{1}_3 \, . \tag{B.46}$$

From this expression one can derive the density-dependent quark condensate of Eq. (5.41), since in the non-relativistic limit $\bar{B}B = \bar{B}\gamma_0 B$ and in the mean-field approximation we can treat the baryons as fixed classical background fields, thus

$$\bar{p}p = \bar{p}\gamma_0 p \to \langle \bar{p}\gamma_0 p \rangle = n_p \tag{B.47}$$

and likewise for the neutron. Besides, note that the baryon masses m_n and m_p are given in terms of $\{\sigma_{\pi N}, \tilde{\sigma}_{\pi N}, \sigma_s\}$ in Eqs. (5.39), (5.40) respectively. One can then relate the coefficients $\{a_1, a_2, a_3\}$ of the baryon chiral Lagrangian to the sigma terms

$$\sigma_{\pi N} = -2\bar{m}(a_1 + 2a_3)\,, \tag{B.48}$$

$$\tilde{\sigma}_{\pi N} = 2\Delta m\, a_1\,, \tag{B.49}$$

$$\sigma_s = -2m_s(a_2 + a_3)\,. \tag{B.50}$$

Finally, we recall that at zero temperature all the states with $E(p) = \sqrt{p^2 + m_\psi^2} < \mu_\psi$ are occupied, such that

$$n_\psi = \langle \bar{\psi}(x)\gamma_0\psi(x)\rangle = g_\psi \int_0^{E(p)<\mu_\psi} \frac{\mathrm{d}^3 p}{(2\pi)^3} = \frac{g_\psi}{6\pi^2}(\mu_\psi^2 - m_\psi^2)^{3/2}\,, \tag{B.51}$$

with g_ψ counting the internal degrees of freedom, e.g. $g_\psi = 2$ for a fermion. In Sec. 5.2.1 we fixed the values of $\{n, n_p\}$ by implicitly fixing the values of $\{\mu_p, \mu_n\}$

$$\mu_p = \sqrt{(3\pi^2 n_p)^{2/3} + m_p^2}\,, \tag{B.52}$$

$$\mu_n = \sqrt{(3\pi^2 n_n)^{2/3} + m_n^2}\,. \tag{B.53}$$

Note that one can fix $\{n, n_p\}$ while still keeping the charge chemical potential μ free by choosing the appropriate value of μ_p, namely if $\mu \to \mu + \delta\mu$, then $\mu_p \to \mu_p - \delta\mu$.

B.3 Axion mass in Kaon-condensed phase

Tree-level mixing with the mesons in the kaon-condensed phase are removed when the matrix Q_ϕ satisfies the following condition

$$\{\langle \bar{q}q\rangle_n, \xi_0 M Q_\phi \xi_0 + \xi_0^\dagger M Q_\phi \xi_0^\dagger\} \propto \mathbb{1}_3\,. \tag{B.54}$$

If $\mathrm{Re}(U_0)$ is a diagonal matrix, such that $[\mathrm{Re}(U_0), \langle \bar{q}q\rangle_n] = 0$, the Q_ϕ matrix given by

$$(Q_\phi)_n^\theta = \frac{X_n^\theta}{\mathrm{Tr} X_n^\theta}\,, \quad X_n^\theta = M^{-1}\left(\xi_0 \frac{\langle \bar{q}q\rangle_n^{-1}}{\mathrm{Re}(U_0)}\xi_0^\dagger + \xi_0^\dagger \frac{\langle \bar{q}q\rangle_n^{-1}}{\mathrm{Re}(U_0)}\xi_0\right)\,, \tag{B.55}$$

satisfies B.54. Plugging Eq. (B.55) in Eq. (5.30), we find the axion mass

$$(m_\phi^2)_{\theta,n} = -\frac{1}{2f_\phi^2}\mathrm{Tr}\left[\langle \bar{q}q\rangle_n \left(\xi_0 M (Q_a^\theta)^2 \xi_0 + \xi_0^\dagger M (Q_a^\theta)^2 \xi_0^\dagger\right)\right]\,. \tag{B.56}$$

Appendix C

Heavy Neutron Stars from Light Scalars

C.1 Derivation of the TOV equations coupled to a scalar field

The Lagrangian under consideration, including gravity is, see Eq. (6.28)

$$\mathcal{L}_{\psi\phi} = \sqrt{-g}\left[\bar{\psi}\left(ie^{\mu}{}_{a}\gamma^{a}D_{\mu} - m_{*}(\phi)\right)\psi + \frac{1}{2}g^{\mu\nu}(\partial_{\mu}\phi)(\partial_{\nu}\phi) - U(\phi)\right], \tag{C.1}$$

where the metric $g_{\mu\nu}$ is

$$ds^2 = e^{\nu(r)}dt^2 - e^{\sigma(r)}dr^2 - r^2d\theta^2 - r^2\sin^2\theta d\phi^2. \tag{C.2}$$

We assume that the energy momentum tensor is the one of a perfect fluid with $\epsilon(\mu,\phi) = \epsilon_m(\mu, m_*(\phi)) + U(\phi)$ and $p(\mu,\phi) = p_m(\mu, m_*(\phi)) - U(\phi)$ given by Eq. (6.34). In addition we get a contribution from the scalar gradient

$$T^{\phi}_{\mu\nu} = \partial_{\mu}\phi\partial_{\nu}\phi - \frac{1}{2}g_{\mu\nu}g_{\alpha\beta}\partial^{\alpha}\phi\partial^{\beta}\phi. \tag{C.3}$$

The full energy momentum tensor is

$$\begin{aligned} T_{\mu\nu} &= (\epsilon + p)\,u_{\mu}u_{\nu} - g_{\mu\nu}p + \partial_{\mu}\phi\partial_{\nu}\phi - \frac{1}{2}g_{\mu\nu}g_{\alpha\beta}\partial^{\alpha}\phi\partial^{\beta}\phi \\ &= (\epsilon_m + p_m)\,u_{\mu}u_{\nu} - g_{\mu\nu}p_m + \partial_{\mu}\phi\partial_{\nu}\phi - \frac{1}{2}g_{\mu\nu}\left(g_{\alpha\beta}\partial^{\alpha}\phi\partial^{\beta}\phi - 2U(\phi)\right) \end{aligned} \tag{C.4}$$

where $u^{\mu} = (1/\sqrt{g_{00}}, 0, 0, 0)$ is the 4-velocity of the fluid, satisfying $g_{\mu\nu}u^{\mu}u^{\nu} = +1$. The trace is

$$\begin{aligned} T &= \epsilon - 3p - g_{\mu\nu}\partial^{\mu}\phi\partial^{\nu}\phi \\ &= \epsilon_m - 3p_m - g_{\mu\nu}\partial^{\mu}\phi\partial^{\nu}\phi + 4U(\phi) \end{aligned} \tag{C.5}$$

The scalar field equation of motion is obtained by varying the action w.r.t ϕ

$$\begin{aligned} \delta S = 0 &= -intd^4x\sqrt{-g}\left[-g_{\mu\nu}\partial^{\nu}\left(\delta\phi\right)\partial^{\mu}\phi + \frac{dV}{d\phi}\delta\phi\right] \\ &= -intd^4x\sqrt{-g}\left[g_{\mu\nu}\partial^{\nu}\partial^{\mu}\phi + \frac{1}{\sqrt{-g}}\partial^{\mu}\left(\sqrt{-g}g_{\mu\nu}\right)\partial^{\nu}\phi + \frac{dV}{d\phi}\right]\delta\phi, \end{aligned} \tag{C.6}$$

with

$$\nabla^\mu \nabla_\mu \phi \equiv \frac{1}{\sqrt{-g}} \partial_\mu \left(\sqrt{-g} g^{\mu\nu} \partial_\nu \phi \right) \tag{C.7}$$

and

$$V(\phi) = U(\phi) - \bar{\psi}\psi \left[F(\phi) - F(\phi_0) \right] \tag{C.8}$$

we get

$$\nabla^2 \phi = -e^{-\sigma} \left[\phi'' + \left(\frac{2}{r} + \frac{\nu' - \sigma'}{2} \right) \phi' \right] = -\frac{dV}{d\phi}. \tag{C.9}$$

Varying the action w.r.t the metric gives the Einstein equations

$$R_{\mu\nu} = \kappa \left(T_{\mu\nu} - \frac{1}{2} g_{\mu\nu} T \right), \tag{C.10}$$

with $\kappa = 8\pi G$. The non-trivial Christoffel symbols are

$$\begin{aligned}
\Gamma^r_{rr} &= \frac{\sigma'}{2}, & \Gamma^r_{\theta\theta} &= -re^{-\sigma}, \\
\Gamma^r_{\phi\phi} &= -e^{-\sigma} r \sin^2\theta, & \Gamma^r_{tt} &= \frac{\nu'}{2} e^{\nu - \sigma}, \\
\Gamma^\theta_{r\theta} &= \frac{1}{r}, & \Gamma^\theta_{\phi\phi} &= -\sin\theta\cos\theta, \\
\Gamma^\phi_{r\phi} &= \frac{1}{r}, & \Gamma^\phi_{\theta\phi} &= \cot\theta, \\
\Gamma^r_{rt} &= \frac{\nu'}{2}.
\end{aligned} \tag{C.11}$$

These lead to non-trivial components of the Ricci tensor

$$\begin{aligned}
R_{tt} &= \frac{e^{\nu-\sigma}}{4r} \left[\nu' \left(4 - r\sigma' \right) + r\nu'^2 + 2r\nu'' \right], \\
R_{rr} &= \frac{1}{4} \left(\nu'\sigma' - \nu'^2 - 2\nu'' \right) + \frac{\sigma'}{r}, \\
R_{\theta\theta} &= R_{\phi\phi} \sin^{-2}\theta = \frac{1}{2} e^{-\sigma} \left(-r\nu' + r\sigma' + 2e^\sigma - 2 \right).
\end{aligned} \tag{C.12}$$

We can write component wise

$$\begin{aligned}
tt: &\quad \frac{e^{\nu-\sigma}}{4r} \left[\nu' \left(4 - r\sigma' \right) + r\nu'^2 + 2r\nu'' \right] = \kappa \frac{e^\nu}{2} \left[\epsilon + 3p \right], \\
rr: &\quad \frac{1}{4} \left[\nu'\sigma' - \nu'^2 - 2\nu'' \right] + \frac{\sigma'}{r} = \kappa \frac{e^\sigma}{2} \left[\epsilon - p + 2e^{-\sigma} (\phi')^2 \right], \\
\theta\theta: &\quad \frac{1}{2} e^{-\sigma} \left[-r\nu' + r\sigma' + 2e^\sigma - 2 \right] = \kappa \frac{r^2}{2} \left[\epsilon - p \right],
\end{aligned} \tag{C.13}$$

which gives

$$\begin{aligned}
tt: &\quad -\sigma'\nu' + (\nu')^2 + 2\nu'' + \frac{4\nu'}{r} = 2\kappa e^\sigma \left[\epsilon + 3p \right], \\
rr: &\quad -\sigma'\nu' + (\nu')^2 + 2\nu'' - \frac{4\sigma'}{r} = -2\kappa e^\sigma \left[\epsilon - p + 2e^{-\sigma} (\phi')^2 \right], \\
\theta\theta: &\quad 2 + r\nu' - r\sigma' = 2e^\sigma \left[-\frac{\kappa r^2}{2} \left(\epsilon - p \right) + 1 \right],
\end{aligned} \tag{C.14}$$

which gives

$$\begin{aligned} tt: &\quad -\sigma'\nu' + (\nu')^2 + 2\nu'' + \frac{4\nu'}{r} = 2\kappa e^{\sigma}\left[\epsilon + 3p\right], \\ rr: &\quad \nu' + \sigma' = \kappa r e^{\sigma}\left[\epsilon + p + e^{-\sigma}(\phi')^2\right], \\ \theta\theta: &\quad \nu' - \sigma' = \frac{2e^{\sigma}}{r}\left[-\frac{\kappa r^2}{2}(\epsilon - p) + 1 - e^{-\sigma}\right], \end{aligned} \tag{C.15}$$

which gives

$$\begin{aligned} tt: &\quad -\sigma'\nu' + (\nu')^2 + 2\nu'' + \frac{4\nu'}{r} = 2\kappa e^{\sigma}\left[\epsilon + 3p\right], \\ rr: &\quad \nu' = \kappa r e^{\sigma}\left[p + \frac{e^{-\sigma}}{2}\left(\phi'\right)^2\right] + \frac{e^{\sigma} - 1}{r}, \\ \theta\theta: &\quad \sigma' = \kappa r e^{\sigma}\left[\epsilon + \frac{e^{-\sigma}}{2}\left(\phi'\right)^2\right] - \frac{e^{\sigma} - 1}{r}. \end{aligned} \tag{C.16}$$

In the limit $\phi = 0$ for all r one can integrate the $\theta\theta$ component and obtain the usual result

$$e^{-\sigma}\left(r\sigma' - 1\right) = \partial_r\left(re^{-\sigma}\right) = 1 - \kappa r^2\epsilon \quad \rightarrow \quad e^{-\sigma(r)} = 1 - \frac{2GM(r)}{r}, \tag{C.17}$$

with $M(r) = 4\pi\int_0^r dx\, x^2\,\epsilon(x)$ the enclosed mass. We take the derivative of the rr component and, using the equation for σ', obtain

$$\begin{aligned} \nu'' &= \kappa e^{\sigma}\left[\left(1 + r\sigma'\right)p + rp' + \frac{e^{-\sigma}}{2}\left(\left(\phi'\right)^2 + 2r\phi'\phi''\right)\right] + \frac{e^{\sigma}}{r}\left[\sigma' - \frac{1}{r} + \frac{e^{-\sigma}}{r}\right] \\ &= \kappa e^{\sigma}\left[\left\{2 - e^{\sigma} + \kappa r^2 e^{\sigma}\left(\epsilon + \frac{e^{-\sigma}}{2}(\phi')^2\right)\right\}p + rp' + \frac{e^{-\sigma}}{2}\phi'\left(\phi' + 2r\phi''\right) + e^{\sigma}\left(\epsilon + \frac{e^{-\sigma}}{2}(\phi')^2\right)\right] - \frac{e^{2\sigma} - 1}{r^2}. \end{aligned} \tag{C.18}$$

Using the expression for ν' and ν'' in the tt component and solving for p', we end up with

$$\begin{aligned} p' &= -\frac{(\epsilon + p)\,e^{\sigma}}{2r}\left[1 - e^{-\sigma} + \kappa r^2 p\right] - \frac{(\phi')^2}{r}\left[1 + e^{-\sigma} - \frac{\kappa r^2}{4}(\epsilon - 3p)\right] - e^{-\sigma}\phi'\phi'', \\ \nu' &= \kappa r e^{\sigma}\left[p + \frac{e^{-\sigma}}{2}\left(\phi'\right)^2\right] + \frac{e^{\sigma} - 1}{r}, \\ \sigma' &= \kappa r e^{\sigma}\left[\epsilon + \frac{e^{-\sigma}}{2}\left(\phi'\right)^2\right] - \frac{e^{\sigma} - 1}{r}. \end{aligned} \tag{C.19}$$

At this point we notice that we have a set of three coupled differential equations which can be integrated numerically, by assigning an equation of state $\epsilon = \epsilon(p(r), \phi(r))$ namely

$$\begin{aligned} p' &= -\frac{(\epsilon + p)\,e^{\sigma}}{2r}\left[1 - e^{-\sigma} + \kappa r^2 p\right] - \frac{(\phi')^2}{r}\left[1 + e^{-\sigma} - \frac{\kappa r^2}{4}(\epsilon - 3p)\right] - e^{-\sigma}\phi'\phi'', \\ \sigma' &= \kappa r e^{\sigma}\left[\epsilon + \frac{e^{-\sigma}}{2}\left(\phi'\right)^2\right] - \frac{e^{\sigma} - 1}{r}, \\ \phi'' &+ \frac{2}{r}\left[\frac{1 + e^{\sigma}}{2} + \frac{\kappa r^2 e^{\sigma}}{4}\left(p - \epsilon\right)\right]\phi' = e^{\sigma}\frac{dV}{d\phi}. \end{aligned} \tag{C.20}$$

Using the expression for ϕ'' in the first equation we finally end up with

$$\begin{aligned} p' + \phi'\left(\frac{dV}{d\phi}\right) &= -\frac{(\epsilon+p)\,e^{\sigma}}{2r}\left[1 - e^{-\sigma} + \kappa r^2\left(p + \frac{e^{-\sigma}}{2}(\phi')^2\right)\right], \\ \sigma' &= \kappa r e^{\sigma}\left[\epsilon + \frac{e^{-\sigma}}{2}\left(\phi'\right)^2\right] - \frac{e^{\sigma}-1}{r}, \\ \phi'' + \frac{2}{r}\left[\frac{1+e^{\sigma}}{2} + \frac{\kappa r^2 e^{\sigma}}{4}\left(p-\epsilon\right)\right]\phi' &= e^{\sigma}\frac{dV}{d\phi}. \end{aligned} \tag{C.21}$$

As a sanity check we take the limit $\phi = \phi' = \phi'' = 0$ and obtain

$$\begin{aligned} p' &= -\frac{\epsilon+p}{2r}\left[1 - e^{-\sigma} + \kappa r^2 p\right] e^{\sigma}, \\ \sigma' &= \frac{1}{r}\left[1 - e^{\sigma}\left(1 - \kappa r^2 \epsilon\right)\right], \end{aligned} \tag{C.22}$$

which we recognize as the regular TOV equations (simply $e^{\sigma} = (1 - 2GM/r)^{-1}$). Taking instead $\kappa \to 0$ (with $e^{\sigma} \to 1$ as $\kappa \to 0$) we end up with

$$p' = -\phi'\left(\frac{2}{r}\phi' + \phi''\right) = -\phi'\frac{dV}{d\phi}, \tag{C.23}$$

or in terms of p_m, together with the equation of motion

$$\begin{aligned} p_m' &= -\phi'\left(\frac{dV}{d\phi} - \frac{\partial U}{\partial \phi}\right) = -\left\langle\bar{\psi}\psi\right\rangle\left(\frac{\partial F(\phi)}{\partial \phi}\right)\phi', \\ \phi'' + \frac{2}{r}\phi' = \frac{\partial V}{\partial \phi} &= -\frac{\partial U(\phi)}{\partial \phi} + \left\langle\bar{\psi}\psi\right\rangle\left(\frac{\partial F(\phi)}{\partial \phi}\right), \end{aligned} \tag{C.24}$$

gives the equations we know from finite flat space.

C.2 Dimensional analysis and negligible gradient limit

It is useful to rewrite the EOMs Eq. (3.1) in terms of dimensionless quantities, which we define as

$$\begin{aligned} &\hat{p} \equiv p/m^4\,, \quad \hat{\varepsilon} \equiv \varepsilon/m^4\,, \quad \hat{r} = r/\alpha\,, \quad \hat{M} = M/(\alpha^3 m^4)\,, \\ &\hat{V} \equiv V/\Lambda^4\,, \quad \hat{m}_*(\theta) \equiv m_*(\theta)/m\,, \quad \hat{\rho}_s \equiv (m\rho_s)/\Lambda^4\,, \end{aligned} \tag{C.25}$$

where $\Lambda^4 \sim m_\phi^2 f^2$ is the typical scale associated with the scalar potential. The EOMs are then given by

$$\theta''\left(1 - \frac{2c_1\hat{M}}{\hat{r}}\right) + \frac{2}{\hat{r}}\theta'\left(1 - \frac{c_1\hat{M}}{\hat{r}} - 2\pi c_1 \hat{r}^2\left(\hat{\varepsilon} - \hat{p}\right)\right) = c_3\left(\frac{\partial \hat{V}}{\partial\theta} + \hat{\rho}_s\frac{\partial \hat{m}_*(\theta)}{\partial\theta}\right), \tag{C.26a}$$

$$\begin{aligned} \hat{p}' = &-\frac{c_1\hat{M}\hat{\varepsilon}}{\hat{r}^2}\left[1 + \frac{\hat{p}}{\hat{\varepsilon}}\right]\left[1 - \frac{2c_1\hat{M}}{\hat{r}}\right]^{-1}\left[1 + \frac{4\pi\hat{r}^3}{\hat{M}}\left(\hat{p} + \frac{1}{2}c_2\theta'^2\left\{1 - \frac{2c_1\hat{M}}{\hat{r}}\right\}\right)\right] \\ &- c_2 c_3\theta'\left(\frac{\partial \hat{V}}{\partial\theta} + \hat{\rho}_s\frac{\partial \hat{m}_*}{\partial\theta}\right), \end{aligned} \tag{C.26b}$$

$$\hat{M}' = 4\pi\hat{r}^2\left(\hat{\varepsilon} + \frac{1}{2}c_2\theta'^2\left[1 - \frac{2c_1\hat{M}}{\hat{r}}\right]\right), \tag{C.26c}$$

where we identify three relevant dimensionless coefficients

$$c_1 \equiv \frac{\alpha^2 m^4}{M_{\rm P}^2}\,, \quad c_2 \equiv \frac{f^2}{\alpha^2 m^4}\,, \quad c_3 \equiv \frac{\alpha^2\Lambda^4}{f^2}\,. \tag{C.27}$$

α is an arbitrary length scale, to be chosen at convenience. For instance, the typical size of a gravitationally-bound star is determined by the condition $c_1(\alpha = R) = 1$, which implies $R = M_{\rm P}/m^2$. On the other hand, the typical scale associated with the scalar field is given by the condition $c_3\mathrm{Max}\{1, \hat{\rho}_s\}(\alpha = \lambda_\phi) \sim 1$, which strictly speaking is a locally defined property since $\hat{\rho}_s$ depends on $\hat{r}$. This typical scale of the scalar field, which changes with density, is what we refer to as the wavelength of the field.

The negligible gradient approximation and in-medium wavelength

To understand the negligible gradient approximation, let us focus on Eq. (C.26a),

$$\theta'' + \frac{2}{\hat{r}}\theta' = c_3\left(\frac{\partial\hat{V}}{\partial\theta} + \hat{\rho}_s\frac{\partial\hat{m}_*}{\partial\theta}\right), \tag{C.28}$$

where we neglected the $O(1)$ deformation of the scalar derivatives due to gravity, as they do not play a significant role in the following discussion. Over a region of size $\hat{r}_2 - \hat{r}_1 \equiv \Delta\hat{r}$, around the mean position $\frac{1}{2}(\hat{r}_2 + \hat{r}_1) \equiv \hat{r}_c$ where θ changes by $\Delta\theta$, the LHS scales as $\sim \frac{\Delta\theta}{(\Delta\hat{r})^2}$. This is true both in the case where the transition occurs when $\hat{r}_c \gg \Delta\hat{r}$, in which case the θ' term is $O(\Delta\hat{r}/\hat{r}_c)$ suppressed w.r.t to the θ'' term, or when the transition happens for $\hat{r}_c \sim \Delta\hat{r}$, in which case the θ' and θ'' term scale the same.

Consider then the scalar profile $\theta(r)$ derived from the EOS Eq. (6.36), where $\rho_s = \rho_s(r)$ as follows from the solution of Eq. (3.1). By construction this ensures that the RHS of Eq. (C.28) vanishes. This is a good approximation to the full coupled system of EOMs if the corrections due to the scalar field derivatives $\theta'(r)$ and $\theta''(r)$ in Eq. (C.26) can be considered small, in which case the EOMs reduce indeed to Eq. (6.36) and Eq. (3.1). Let us assess the validity of this approximation by separating the discussion into two qualitatively different cases depending on the behavior of $\theta(r)$, (1) θ varies continuously in a finite region and (2) θ is discontinuous, i.e. jumps from one value to another, forming a so-called bubble wall. In both of these regions, we argue that while θ' and θ'' do not vanish, $\theta(r)$ can nonetheless be considered a good approximate solution overall under certain conditions. We shall derive an upper bound on f which ensures these conditions are satisfied, with the strongest bound coming from the condition for the formation of the bubble wall.

We start with the case where $\theta(r)$ is continuous. This is typical in linearly coupled models ($n = 1$ in Eq. (6.27), see Sec. 6.2.3), at least at small enough densities. While it is easier to characterize the gradient corrections in this region, as we show below it typically provides a weaker bound on f when both (1) and (2) behaviors of θ can happen within the same scalar theory. Consider a region where $\theta(r)$ undergoes an $O(1)$ change in its value from θ_0 to θ_∞ such that $\bar{\theta} \equiv (\theta_\infty + \theta_0)/2 \sim \Delta\theta \equiv \theta_\infty - \theta_0 = O(1)$, within a region of size $\Delta\hat{r}$. The LHS of Eq. (C.28) scales like $\Delta\theta/\Delta\hat{r}^2$, as previously explained. Since the RHS vanishes at leading order by construction, it is sensible to Taylor expand it and evaluate it at $\bar{\theta}$. By demanding that

the change in θ takes place within the confines of a star, i.e. $\Delta\hat{r} \lesssim 1$ in units $\alpha = R$, and that deviations from the assumed profile are at most of order $\Delta\theta$, we arrive at the condition

$$R^2 \gg \frac{1}{m_\phi^2(\bar{\theta})} \quad \text{where} \quad m_\phi^2(\bar{\theta}) f^2 \equiv \frac{\partial}{\partial\theta}\left(\frac{\partial V(\theta)}{\partial\theta} + \rho_s \frac{\partial m_*}{\partial\theta}\right)\Big|_{\theta=\bar{\theta}} . \tag{C.29}$$

This condition can also be interpreted as an energy requirement, identifying f^2/R^2 as the gradient energy density associated with the smooth change of the scalar field, and $m_\phi^2(\bar{\theta})f^2$ at the gain in effective potential energy. Note that these types of continuous transitions also occur in models where the θ_∞ phase is ultra-relativistic, which is the common case in the models in Sec. 6.2.3, as well as in part of the parameter space of the models in Sec. 6.2.3.

A different condition associated with the negligible gradient approximation, typically leading to a stronger upper bound on f, corresponds to the case in which $\theta(r)$ exhibits a discontinuity. This happens for instance in quadratically coupled models ($n = 2$ in Eq. (6.27)) just above the critical density for scalarization. The gradient energy density associated with such a jump in θ is naively infinite, since θ' and θ'' are singular. Clearly, this is not a sensible result, and indeed the bubble wall is not infinitely thin but it has a finite size, determined by the in-medium wavelength of the scalar field, λ_ϕ. Since in the transition region (i.e. inside the wall), $\theta(r)$ solving Eq. (6.36) is not a good approximation, we return to Eq. (C.28) and set the units to $\alpha = \lambda_\phi$. We then find that at low densities, the wavelength can be estimated as

$$\lambda_\phi^{\text{low}} \equiv \frac{\sqrt{\Delta\theta} f}{\sqrt{(\partial V/\partial\theta)|_{\theta=\bar{\theta}}}} , \tag{C.30}$$

where $\Delta\theta \equiv \theta_\infty - \theta_0$ is the jump in θ and $\bar{\theta} \equiv (\theta_\infty + \theta_0)/2$, and as before we generically consider $\Delta\theta \sim \bar{\theta} = O(1)$. By using this definition, as opposed to the vacuum Compton wavelength defined as $m_\phi^{-1} \equiv f/\sqrt{(\partial^2 V/\partial\theta^2)|_{\theta=\theta_0}}$, we avoid potentially misidentifying the relevant scaling of the RHS of Eq. (C.28), which can be dominated by higher order terms in the potential once θ is sufficiently far away from θ_0. This can occur for scalar potentials that feature more than one scale, like in the quadratic coupling model discussed in Sec. 6.2.3, where the potential can be dominated by the quartic term. This effect, which admittedly requires some fine-tuning in the potential, is nonetheless captured by the definition in Eq. (C.30). In natural potentials defined by a single scale, i.e. $f_\phi \sim f$, $\lambda_\phi^{\text{low}}$ reduces to m_ϕ^{-1} as expected, like in the models discussed in Sec. 6.2.3.

We emphasize however that $\lambda_\phi^{\text{low}}$ does not actually play an important role in determining the upper bound on f from the requirement of negligible gradient energy, but rather the in-medium or high-density effective wavelength, identified as

$$\lambda_\phi \equiv \frac{\sqrt{\Delta\theta} f}{\sqrt{\bar{\rho}_s |\partial m_*/\partial\theta||_{\theta=\bar{\theta}}}} , \tag{C.31}$$

where $\bar{\rho}_s$ is the typical scalar density at the internal edge of the transition region, i.e. roughly the scalar density at the lowest pressure of the internal phase. The fact that λ_ϕ, rather than $\lambda_\phi^{\text{low}}$, is what determines the relevant size of the scalar bubble stems from the requirement that, for the scalar field to be significantly sourced, a sufficiently large scalar density is needed, in particular $m\rho_s \gtrsim m_\phi^2 f^2 (M_\phi/f)^n$, following the discussion after Eq. (6.36) and using Eq. (6.27). Still, $\lambda_\phi^{\text{low}}$ is interesting in cases where $\lambda_\phi^{\text{low}} \gtrsim R$ (while $\lambda_\phi < \lambda_\phi^{\text{low}}$). In this case, the scalar profile extends to the region outside the star, resulting in a scalar halo and potentially interesting effects like long-range forces between stars [186].

Having determined λ_ϕ, note that the gradient energy density associated with a bubble wall is typically larger than that of a continuous scalar profile discussed above, given that the former scales as f^2/λ_ϕ^2, thus enhanced w.r.t. the latter by $(R/\lambda_\phi)^2$. Nevertheless, the condition

$$\lambda_\phi \ll R\,, \tag{C.32}$$

is the correct one to ensure first that the scalar can be sourced when $\theta(r)$ solving Eq. (6.36) is discontinuous, and second that its contribution to the TOV equations Eq. (C.26b) and Eq. (C.26c) is subleading. For $\lambda_\phi \gg R$, the formation of the bubble is not energetically favorable, leading to the trivial $\theta = \theta_0$ solution. This regime can be understood as a decoupling limit $f/M_{\rm P} \gg 1$, given the scaling with f of Eq. (C.31) and that $R \sim M_{\rm P}/m^2$. For $\lambda_\phi \sim R$, the effects of the gradient energy are no longer negligible and the full coupled system of Eq. (C.26) must be solved (also when $1/m_\phi(\bar\theta) \sim R$ in Eq. (C.29)). Therefore, only when Eq. (C.32) holds the bubble can be formed, and its contribution to the total energy (mass) of the star be safely neglected, given that it is localized to a thin region much smaller than the total size of the star.

C.3 Analytic discussion of constant density objects

In this appendix, we derive the main results presented in Sec. 6.2.2. In models that allow a NGS, the total core pressure for all configurations on the stable branch balances two distinct contributions,

$$p(0) \equiv p_0 = \Delta p_{\rm grav.} + \Delta p_{\rm grad.}\,. \tag{C.33}$$

with

$$\Delta p_{\rm grad.} = -\int_0^R {\rm d}r\, \theta' \left(\frac{\partial V}{\partial \theta} + \rho_s \frac{\partial m_*}{\partial \theta}\right)\,, \tag{C.34}$$

$$\Delta p_{\rm grav.} \simeq -\int_0^R {\rm d}r\, \frac{M(r)\varepsilon(r)}{M_{\rm P}^2 r^2}\,, \tag{C.35}$$

where we took for simplicity the Newtonian limit of the TOV equations, which, as discussed below, suffices for the estimations in this section.

Self-bound objects (SBOs) are such that $\Delta p_{\rm grav.} \ll \Delta p_{\rm grad.}$, they are composed of matter in the NGS and are held together by the gradient pressure of the scalar field. The opposite limit, $\Delta p_{\rm grav.} \gg \Delta p_{\rm grad.}$, corresponds to stars. The smallest possible configurations on the stable branch are of size $R \sim \lambda_\phi$, and both gravitational and gradient pressures are spread across the object, thus $\Delta p_{\rm grav.}$ and $\Delta p_{\rm grad.}$ must be calculated by summing up the contributions from $r = R$ until the core. For a given f, these smallest configurations can either be self- or gravitationally-bound.

In order to analytically characterize, up to $O(1)$ factors, these objects in different regimes, we make the following simplifying assumptions. First, we consider large systems, $R \gg \lambda_\phi$, in which $p'_{\rm grad.}$ is localized at the boundary of the object where the transition occurs. Second, we assume a simple linear energy density profile from the core $\varepsilon(0) \equiv x_0 \varepsilon_{\rm NGS}$ to the edge of the object $\varepsilon(R) \equiv x_R \varepsilon_{\rm NGS}$,

$$\varepsilon(r)/\varepsilon_{\rm NGS} = (x_0 - x_R)(1 - r/R) + x_R\,. \tag{C.36}$$

Next, we calculate the gravitational pressure using the Newtonian limit of the TOV equations, neglecting $O(1)$ general relativistic corrections as well as the contribution of the localized gradient

energy to the energy density. Lastly, for simplicity, we assume the NGS phase is non-relativistic. This approximation is typically applicable when $m_*(\theta)$ is bounded, in which case the NGS can be anything between non- and ultra-relativistic. For an ultra-relativistic NGS phase, a similar derivation is straightforward. When $m_*(\theta)$ is unbounded, the NGS is typically ultra-relativistic and has a fixed ρ_s. Also in this case, a similar derivation is straightforward.

Under these assumptions, we can approximate the internal pressure as

$$p_0 \simeq \underbrace{\frac{R^2\varepsilon_{\rm NGS}^2 x_0^2}{M_{\rm P}^2}}_{\Delta p_{\rm grav.}} + \underbrace{\frac{f\sqrt{\varepsilon_{\rm NGS} x_R}}{R}\sqrt{\frac{\delta m_*}{1-\delta m_*}}}_{\Delta p_{\rm grad.}} \simeq \frac{\varepsilon_{\rm NGS}^{5/3}(x_0^{5/3}-1)}{m_*^{8/3}}\,, \tag{C.37}$$

where $\Delta p_{\rm grad.}$ is calculated over a small transition region from R to $R+\lambda_\phi$, approximating the scalar profile as a linear transition, i.e. $\theta' \sim 1/\lambda_\phi = \text{const.}$, and taking the leading order term in the $\lambda_\phi/R \ll 1$ expansion. We also approximated $\frac{\partial m_*}{\partial\theta} \sim m\,\delta m_*$. For simplicity, we assume in the following that $\delta m_* \ll 1$. This assumption can be relaxed by rescaling $\delta m_* \to \delta m_*/(1-\delta m_*)$ in all the expressions below. Finally, the last equality in Eq. (C.37) is a self-consistency condition due to the assumed non-relativistic EOS at the core, i.e. $p_0 = p(\varepsilon(0))$.

Self-bound objects: $\Delta p_{\rm grav.} \ll \Delta p_{\rm grad.}$

An interesting prediction for finite f is the existence of SBOs, for which gravity does not a play role, and therefore their pressure, energy density, and scalar field profiles can be computed by solving the $M_{\rm P} \to \infty$ limit of the coupled TOV equations, Eq. (6.45). In the $R \gg \lambda_\phi$ limit, they are well-described by constant profiles. They are held together by the gradient pressure exerted at the edge of the object, where the transition occurs in the form of a scalar bubble wall of size λ_ϕ that "traps" the matter inside and prevents it from expanding.

We apply the simple model of Eq. (C.37) by taking $x_0 = x_R \equiv x_{\rm SBO} \gtrsim 1$, which describes a constant energy density system. This allows us to write the SBO radius as a function of its core energy density (or equivalently, in this approximation, its core number density)

$$R_{\rm SBO}(x_{\rm SBO}) \simeq \frac{m_*^{8/3}\delta m_*^{1/2} f}{\varepsilon_{\rm NGS}^{7/6}}\frac{x_{\rm SBO}^{1/2}}{x_{\rm SBO}^{5/3}-1}\,, \tag{C.38}$$

where $\Delta p_{\rm grav.}$ was neglected. From Eq. (C.38), it is clear that SBOs become smaller (larger) as the central density, i.e. $x_{\rm SBO}$, increases (decreases). Their total mass is given by

$$M_{\rm SBO}(x_{\rm SBO}) = \frac{4\pi}{3}x_{\rm SBO}\varepsilon_{\rm NGS}R_{\rm SBO}^3(x_{\rm SBO}) \simeq \frac{4\pi}{3}\frac{f^3\delta m_*^{3/2}m_*^8}{\varepsilon_{\rm NGS}^{5/2}}\frac{x_{\rm SBO}^{5/2}}{(x_{\rm SBO}^{5/3}-1)^3}\,. \tag{C.39}$$

For finite f, SBOs are bounded in size both from above and from below. The smallest object possible would have $R_{\rm SBO}^{\rm min} \sim \lambda_\phi$, for which the approximation $R \gg \lambda_\phi$ breaks down. This also implicitly defines the maximal possible density of the self-bound object. For very low densities the object becomes large, reaching the point where $\Delta p_{\rm grav.}$ can no longer be neglected. We then define the maximal SBO radius at the equilibrium point $\Delta p_{\rm grav.} \simeq \Delta p_{\rm grad.}$. Using Eq. (C.37), we can analytically estimate it in two limiting cases

$$R_{\rm SBO}^{\rm max} \sim \begin{cases} \left(\frac{fM_{\rm P}^2\delta m_*^{1/2}}{\varepsilon_{\rm NGS}^{3/2}}\right)^{1/3} & \delta m_*^{1/2}\left(\frac{m_*^4}{\varepsilon_{\rm NGS}}\right)\left(\frac{f}{M_{\rm P}}\right) \ll 1 \\ \left(\frac{M_{\rm P}^7}{\delta m_*^{1/2}m_*^{12}f}\right)^{1/6} & \delta m_*^{1/2}\left(\frac{m_*^4}{\varepsilon_{\rm NGS}}\right)\left(\frac{f}{M_{\rm P}}\right) \gg 1 \end{cases}. \tag{C.40}$$

The first case corresponds to $x_{\rm SBO} \simeq 1$, in which the equilibrium happens when the SBO is close to its ground state density. The second case corresponds to $x_{\rm SBO} \gg 1$, in which the equilibrium happens when the SBO is much denser than its ground state density, and thus the maximal radius is independent of the NGS properties.

Constant energy density gravitationally-bound objects: $\Delta p_{\rm grav.} \gg \Delta p_{\rm grad.}$

As the core pressure increases, gravity pressure becomes the dominant component. We return to our simple model of Eq. (C.37), and note that, in the absence of a sizeable gradient pressure, vanishing Fermi pressure at $r = R$ requires us to set $x_R \simeq 1$, while we have $x_0 \gtrsim 1$, finding

$$R(x_0) \sim \left(\frac{M_{\rm P}^2 (x_0^{5/3} - 1)}{m_*^{8/3} \varepsilon_{\rm NGS}^{1/3} x_0^2} \right)^{1/2} . \tag{C.41}$$

Around $x_0 \simeq 1$, the radius increases with increasing core energy density, in contrast to the SBOs which exhibited the opposite behavior. Still, in the limit, $\delta m_*^{1/2} (m_*^4/\varepsilon_{\rm NGS})(f/M_{\rm P}) \ll 1$, these smallest gravitationally-bound systems can also be approximated as of constant energy density since although their pressure drops away from the core, it is sufficiently low that the EOS is always close to $\varepsilon \simeq \varepsilon_{\rm NGS}$. At large enough core pressures, the constant energy density approximation breaks down, and any further increase in core pressure leads to a decrease in radius, which is the typical behavior for gravitationally-bound objects described by a Fermi gas; indeed, the radius Eq. (C.41) decreases with increasing core energy density for $x_0 \gg 1$.

Finally, recall that for $\delta m_*^{1/2} (m_*^4/\varepsilon_{\rm NGS})(f/M_{\rm P}) \gg 1$, the most massive and largest SBOs have $\varepsilon \gg \varepsilon_{\rm NGS}$ (i.e. $x_{\rm SBO} \gg 1$). Therefore, any increase in pressure would lead to a swift breakdown of the constant energy approximation as follows from the EOS, and a return to the typical radius decrease with increasing core pressure. As a result, the maximal mass of the gravitationally-bound stars in the NGB coincides with that of the SBOs in this limit.

To conclude, we can approximate the maximal star radius, up to $O(1)$ factors, as

$$R^{\rm max} \sim \begin{cases} \left(\frac{M_{\rm P}^2}{m_*^{8/3} \varepsilon_{\rm NGS}^{1/3}} \right)^{1/2} = \left(\frac{\delta m_*^{1/2} m_*^4 f}{\varepsilon_{\rm NGS} M_{\rm P}} \right)^{-1/3} R_{\rm SBO}^{\rm max} & \delta m_*^{1/2} \left(\frac{m_*^4}{\varepsilon_{\rm NGS}} \right) \left(\frac{f}{M_{\rm P}} \right) \ll 1 \\ \left(\frac{M_{\rm P}^7}{\delta m_*^{1/2} m_*^{12} f} \right)^{1/6} = R_{\rm SBO}^{\rm max} & \delta m_*^{1/2} \left(\frac{m_*^4}{\varepsilon_{\rm NGS}} \right) \left(\frac{f}{M_{\rm P}} \right) \gg 1 \end{cases} , \tag{C.42}$$

which are the analytic estimates used in the main text in Eq. (6.48).

Comparison with numerical results of BM1 ALP model

Let us check our analytical estimates with the numerical results we presented for the BM1 benchmark in Sec. 6.2.3. For this purpose, it is useful to zoom in on the right panel of Fig. 6.14 at low masses and small radii, see Fig. C.1. Our numerical results agree with our estimates for $R_{\rm min}^{\rm SBO}$ given in Eq. (6.78) and are indeed well-described at low pressures by the curve defined by Eq. (6.79) independently of f. The visible deviations from the line at low radii is a finite gradient effect explained by our modeling of the SBOs described in this appendix. The smallest SBOs can have a central number and energy densities which can be a few times larger than $\rho_{\rm NGS}$ and $\varepsilon_{\rm NGS}$, respectively. Therefore, the energy density can be larger than $\varepsilon_{\rm NGS}$, leading to configurations that lie above the curve defined by Eq. (6.79). For the smallest objects, with $R \simeq R_{\rm min}^{\rm SBO}$, the size of the transition region becomes comparable to the size of the object, and the assumptions of constant pressure and number density, on which our description depends on,

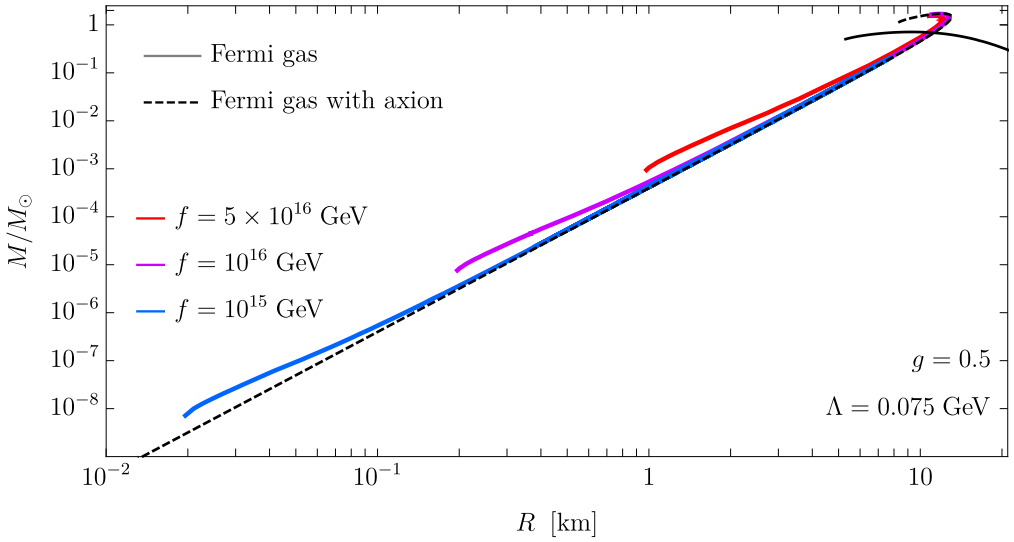

Figure C.1: The low-mass and small-radius region of the M-R curves of the benchmark BM1 in the ALP model of Sec. 6.2.3. The free Fermi gas without axion (solid black), the negligible gradient limit (dashed black), and including finite gradient effects for $f = \{5\times10^{16}, 10^{16}, 10^{15}\}$GeV in red, purple, and blue respectively.

are no longer valid. Note that the dashed line describing the M-R curve in the negligible gradient limit ($f/M_{\rm P} \to 0$) describes gravitationally-bound constant-density objects since gravity is the only force in this limit. However, as long as the object is dilute enough, i.e. $\rho \simeq \rho_{\rm NGS}$, it has constant energy density $\varepsilon_{\rm NGS}$ and Eq. (6.79) is valid, regardless of whether it is a self- or gravitationally-bound object. Note also that for the most massive NGS stars, the effects of the gradient pressure at the edge of the star is increasingly negligible, making the properties of the gravitationally-bound stars essentially f-independent, clearly visible in the right panel of Fig. 6.14.

As shown in Fig. C.2, the numerical solutions agree with our simple modelling of the SBOs given above. The smallest SBOs are the densest and exhibit the highest internal pressure. These properties are in fact f-independent, *e.g.* the maximal pressure is given in this case by

$$p_{\rm max}^{\rm SBO} \simeq g m_N \rho_{\rm NGS} \approx \varepsilon_0/2\,. \tag{C.43}$$

for the BM1 benchmark. The maximal density can be found by solving $\Delta p_{\rm grad.} = p_{\rm max}^{\rm SBO}$ numerically, which results in $\rho_{\rm max} \approx 10\rho_{\rm NGS}$. These results match, up to $O(1)$ factors, the numerical results shown in Fig. C.2, confirming the f-independent behavior of the smallest SBOs in number density (left panel) and pressure (right panel). Note that the smallest SBOs are the least compatible with the underlying assumptions of our modeling of SBOs, namely constant density and small transition region. Fig. C.2 also confirms our f-dependent predictions, i.e. the minimal and maximal size of the SBOs. The qualitative behavior of the curves follows the description given above; the smallest SBOs with $R \simeq R_{\rm min}^{\rm SBO}$ are the densest and have the highest pressures. As the number density decreases and ρ approaches $\rho_{\rm NGS}$, the object becomes larger, more dilute and the internal pressure decreases. This continues until $R \simeq R_{\rm max}^{\rm SBO}$, where gravity becomes important and matter must be added inside in order to counter the increasing gravitational pressure. From this point on, the mass and radius increase as the central number density and

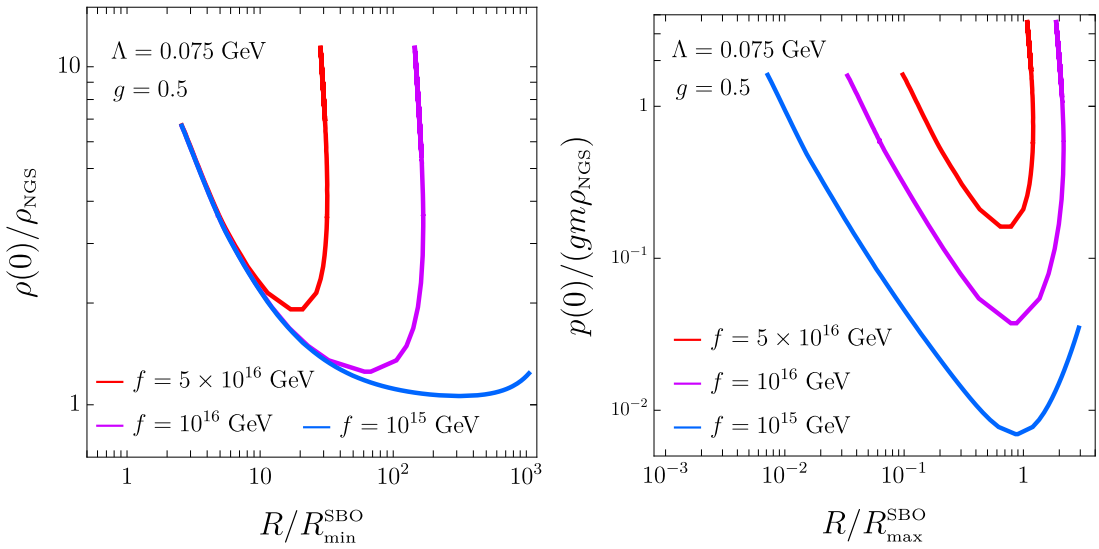

Figure C.2: Left panel: The NGS configurations in the $\{\rho(0), R\}$ plane, where $\rho(0)$ is the central number density. $\rho(0)$ is shown in units of the (f-independent) NGS number density given in Eq. (6.77), while the radius is given in units of the (f-dependent) minimal radius expected for the SBOs, given in Eq. (6.78) . The numerical results agree with the analytical estimates of the maximal density and minimal size up to $O(1)$ factors. Right panel: The NGS configurations in the $\{p(0), R\}$ plane, where $p(0)$ is the central pressure. $p(0)$ is plotted in units of the (f-independent) maximal pressure given in Eq. (C.43), while the radius is given in units of the (f-dependent) maximal radius expected for the SBOs, given in Eq. (6.78). The numerical results agree with the analytical estimates of the maximal pressure and size up to $O(1)$ factors.

pressure increase. For both $f = 5 \times 10^{16}$GeV and $f = 10^{16}$GeV, we find that the maximal size of the gravitationally-bound stars coincides with $R_{\rm max}^{\rm SBO}$, consistent with the analytic estimates in Eq. (C.42).

C.4 Large nucleon mass reduction in $f(\phi)G_{\mu\nu}^2$ models

Prompted by Eq. (6.100), we present here a simple model that can lead to a large reduction of the nucleon mass, thus populating most of the parameter space of Fig. 6.11, albeit at the cost of some tuning. Above the QCD scale, we consider the following Lagrangian

$$\mathcal{L}_\phi = \frac{1}{2}(\partial_\mu \phi)^2 - g f(\phi) \frac{\beta(g_s)}{2g_s} G^{\mu\nu} G_{\mu\nu} - \epsilon \frac{\beta(g_s)}{g_s} \frac{M_{\rm UV}^4}{32\pi^2} g f(\phi)\,, \tag{C.44}$$

where $f(\phi)$ is a dimensionless function of the scalar field ϕ such that $f(0) = 0$, and g is a dimensionless coefficient (introduced in analogy to the ALP g factor in Eq. (6.67)). The last term in Eq. (C.44) is the UV contribution to the potential, naturally expected from closing a gluon loop at leading order in $gf(\phi)$, where $M_{\rm UV}$ is the cutoff of the scalar theory and we allowed for tuning in the UV by introducing the parameter $\epsilon < 1$. Note that Eq. (C.44) could be generalized by adding interaction terms with the light quarks $\sum_{q=u,d,s} f_q(\phi) m_q \bar{q} q$. As seen for the QCD axion in Sec. 2.3, these interactions lead to a comparatively smaller coupling to nucleons, and we disregard them, along with quark masses, in the following.

Below the QCD scale, we use the well-known fact that the divergence of the dilatation current can be used to obtain the matrix element [280–282]

$$\langle N | \frac{\beta(g_s)}{2g_s} G^{\mu\nu} G_{\mu\nu} | N \rangle = m_0\,, \tag{C.45}$$

where $m_0 \approx 869.5\,\text{MeV}$ [359] is the nucleon mass in the chiral limit. This allows to match the theory in Eq. (C.44) to

$$\mathcal{L}_\phi^{\rm IR} \supset -m_N \bar{N} N \left[1 - \frac{g}{g_*} f(\phi)\right] - \left(\epsilon \frac{\beta}{g_s} \frac{M_{\rm UV}^4}{32\pi^2} + c\Lambda_{\rm QCD}^4\right) g f(\phi)\,, \tag{C.46}$$

at leading order in $gf(\phi)$ and neglecting the difference in β/g_s between the scale at which Eq. (C.44) is defined and the QCD scale, $\Lambda_{\rm QCD}$. Note that $g_* = m_N/m_0 \approx 1.08$, yet since we are neglecting quark masses we will consistently take $g_* = 1$. We also added an IR contribution to the scalar potential in Eq. (C.46), generated by the interaction of ϕ with the gluons and proportional to QCD contribution to the cosmological constant, which we have estimated as

$$\langle 0 | \frac{\beta(g_s)}{2g_s} G^{\mu\nu} G_{\mu\nu} | 0 \rangle = c\Lambda_{\rm QCD}^4\,, \tag{C.47}$$

with $c = O(1)$.

At this point, we can map the function $f(\phi)$ to either the ALP model of Sec. 6.2.3, with $f(\phi) = (1 - \cos\phi/f)/2$, or to the linearly and quadratically coupled models of Secs. 6.2.3 and 6.2.3, with $gf(\phi) = \phi/M_\phi$ and $gf(\phi) = (\phi/M_\phi)^2$, respectively. Let us note that in deriving Eq. (C.46) we kept only the leading order term in $gf(\phi)$, while a large (in-medium) reduction of the nucleon mass requires $gf(\phi) \sim 1$. As a result, for small values of $m_*(\theta_\infty)$ (recall θ_∞ is the high-density limiting value of ϕ/f), control over such non-linear terms is required.

Finally, evaluating the scalar potential in Eq. (C.46) at θ_∞, we find

$$V(\theta_\infty) = \left(\epsilon \frac{\beta}{g_s} \frac{M_{\rm UV}^4}{32\pi^2} + c\Lambda_{\rm QCD}^4\right)\left(1 - \frac{m_*(\theta_\infty)}{m_N}\right) \equiv V_0(\theta_\infty)\left(1 - \frac{m_*(\theta_\infty)}{m_N}\right) . \tag{C.48}$$

By canceling the UV and QCD contributions to the potential, a significant fraction of the parameter space of Fig. 6.11 is populated. In particular, note that the larger the degree of tuning, the smaller $V(\theta_\infty)$ can be, which is the regime where larger departures (*e.g.* in the mass and radius of NSs) are found w.r.t. the standard GR prediction. In Fig. 6.11, the blue curve correspond to Eq. (C.48) with $V_0(\theta_\infty) \sim (0.17\text{GeV})^4$.

Appendix D

Density Induced Instabilities

In this appendix we give some additional analytic estimates that back up some of the approximations used in Sec. 7.

D.1 Linear Profile Approximation

The parametric dependence of the results in Sec. 7.1.4 can be reproduced by considering a simpler, linear approximation for the scalar profile (recall $\Delta\phi(0) \equiv \phi(0) - \phi_-$)

$$\phi(r) = \begin{cases} \phi(0) & r < R_i \\ \phi(0) - \frac{\Delta\phi(0)}{R_{\rm T}-R_i}(r - R_i) & R_i < r < R_{\rm T} \\ \phi_- & r > R_{\rm T} \end{cases}, \qquad \text{(bubble; linear)} \tag{D.1}$$

and treating both $\phi(0)$ and R_i as variational parameters determined by the minimization of the energy of the bubble $E(\phi(0), R_i)$, i.e. Eq. (7.17) with $R = R_{\rm T}$. Expressing it in terms of $\Delta\phi(0)$ and the width $x = 1 - R_i/R_{\rm T}$, the energy is given by

$$E(\Delta\phi(0), x) = -E_0 \frac{\Delta\phi(0)}{f}\left[1 - \tfrac{3}{2}x + x^2 - \tfrac{1}{4}x^3 - \tfrac{3}{8}\frac{\alpha\Delta\phi(0)}{fx}\left(1 - x + \tfrac{1}{3}x^2\right)\right], \tag{D.2}$$

where $E_0 = \frac{4\pi}{3}\mu^2 f^2 R_{\rm T}^3$ and we have defined

$$\alpha \equiv \frac{4}{(\mu R_{\rm T})^2}\,. \tag{D.3}$$

During the formation of the system, $R_{\rm T}$ is small and therefore $\alpha \gg 1$. Minimization of the energy with respect to both $\Delta\phi(0)$ and x yields $x = 1$ and

$$\frac{\Delta\phi(0)}{f} = \frac{1}{\alpha}\,. \tag{D.4}$$

Therefore, we find a proto-bubble ($R_i = 0$) in which the field displacement at the origin is $\Delta\phi(0)/f \sim (\mu R_{\rm T})^2$, which is the result of an optimal balance between the gradient and potential energies. Parametrically, this matches the result in Eq. (7.22), albeit with a different numerical coefficient. As soon as the slowly-growing star is large enough that the in-density minimum $(\phi_+)_\rho$ can be reached, which happens when $\alpha \leqslant f/((\phi_+)_\rho - \phi_-)$, it should be energetically

favorable for the profile to develop a core where the scalar value is fixed to $\phi(0) = (\phi_+)_\rho$. Then, minimization of the energy with respect to x leads to

$$x = \frac{1}{2}\sqrt{\frac{\alpha((\phi_+)_\rho - \phi_-)}{f}} + O(\alpha)\,, \tag{D.5}$$

This matches the result in Eq. (7.26), except for a numerical factor. Likewise, the energy of the bubble in the thin-wall limit $\alpha \ll f/((\phi_+)_\rho - \phi_-)$ is given by Eq. (7.28) where ϵ and σ scale as in Eqs. (7.29), (7.30) respectively, $\epsilon = \mu^2 f((\phi_+)_\rho - \phi_-)$ and $\sigma = ((\phi_+)_\rho - \phi_-)\sqrt{\epsilon}$.

The linear profile Eq. (D.1) has the advantage that it is simple to estimate the importance of departures from the approximation of a linear potential, Eq. (7.56), we have worked under in the main text. In particular, we can compute the effects of including the barrier term in Eq. (7.56) at finite density, i.e. with $\Lambda_{\rm B} \to \Lambda_{\rm B}(n)$. While ϵ remains unchanged in the thin-wall limit, the tension receives a correction

$$\frac{\Delta\sigma}{\sigma} = \frac{\sqrt{3}}{10}\frac{\Lambda_{\rm B}^4(n)}{\Lambda_{\rm R}^4}\,, \tag{D.6}$$

where we have assumed that the bubble is thin enough as to probe a fixed density.

D.2 Gravitational Force

In the equation of motion of the bubble, Eq. (7.37), we have neglected the gravitational force that the star exerts on the wall. While this does not change the conclusions we derived in the main text, it can lead to $O(1)$ numerical changes of the bubble's escape condition, at least for the densest stars, i.e. neutron stars.

In the non-relativistic and weak-field limits, the gravitational force of the star on the bubble wall per unit area (i.e. the pressure), is given by

$$F_{\rm G}(R) = -\frac{1}{8\pi M_{\rm P}^2}\frac{m(R)\sigma}{R^2}\,, \tag{D.7}$$

where $m(R)$ is the enclosed mass of the star and σ the wall tension. Using a simple estimate for the neutron star number density $n \sim m_n^3$ and radius $R_{\rm NS} \sim \sqrt{8\pi}M_{\rm P}/m_n^2$, obtained by equating (Fermi-degeneracy) kinetic and gravitational energy densities and where m_n is the neutron mass, we find $m(R) \sim 8\pi M_{\rm P}^2 R^3/R_{\rm NS}^2$. Therefore, for a neutron star

$$\text{NS}: \quad F_{\rm G}(R) \sim \frac{\sigma R}{R_{\rm NS}^2}\,, \tag{D.8}$$

while for less dense stars the gravitational force is much smaller, i.e. for white dwarfs it is suppressed by m_e/m_p. This additional force leads to a modification of the bubble wall equation of motion, in the non-relativistic limit (weak-field) and for $R \leqslant R_{\rm NS}$

$$\sigma\ddot{R} \simeq \epsilon - \frac{2\sigma}{R}\left(1 + \frac{R^2}{2R_{\rm NS}^2}\right) - \sigma'\,, \tag{D.9}$$

which is subleading to the tension force except for $R \sim R_{\rm NS}$. Likewise, once if the bubble leaves the star, the enclosed mass is the total mass of star and therefore for $R \geqslant R_{\rm NS}$

$$\sigma\ddot{R} \simeq \epsilon - \frac{2\sigma}{R}\left(1 + \frac{R_{\rm NS}}{2R}\right)\,, \tag{D.10}$$

which once again introduces an $O(1)$ change only when $R \sim R_{\rm NS}$.

D.3 Linear Tension Approximation

The simplest modelling of $\sigma(R)$, that is a constant σ', allows us to analytically derive the condition Eq. (7.40). Let us then consider a linear increase of the tension with R, starting at $R_{\rm T}$ and ending at $R_{\rm S} = R_{\rm T} + \Delta R_{\rm T}$, thus with $\sigma' = [\sigma(R_{\rm S}) - \sigma(R_{\rm T})]/\Delta R_{\rm T}$ constant. The equilibrium position of the bubble wall is determined by $\ddot{R}(R = R_{\rm eq}) = 0$, and reads

$$R_{\rm eq} = \frac{2[\sigma' R_{\rm T} - \sigma(R_{\rm T})]}{3\sigma' - \epsilon}\,, \qquad R_{\rm T} > \sigma(R_{\rm T})/\sigma' \quad \text{and} \quad 3\sigma' > \epsilon\,, \tag{D.11}$$

where the inequalities ensure that this is indeed an equilibrium position, i.e. with $E''(R_{\rm eq}) > 0$, where $E(R)$ is the energy of the bubble (note that $\ddot{R} \propto -E'$). For consistency, we should also require $R_{\rm eq} \geqslant R_{\rm T}$, since that means that the bubble can in fact enter the transition region, where $\sigma' \neq 0$. This happens only if the star has grown large enough

$$R_{\rm T} > \frac{2\sigma(R_{\rm T})}{\epsilon - \sigma'}\,. \qquad \text{(entry transition region)} \tag{D.12}$$

This condition is equivalent to the requirement $\ddot{R}(R_{\rm T}) \not< 0$,[1] and it only makes sense for $\epsilon > \sigma'$. If the condition Eq. (D.12) is not satisfied, it just means that $R_{\rm eq} = R_{\rm T}$ and the bubble is trapped inside the star. In addition, note that whenever the bubble is able to enter the transition region but the conditions in Eq. (D.11) are not satisfied, then the bubble automatically escapes the star, since there is no stable radius $R > R_{\rm T}$ for which $\ddot{R} = 0$ and $E'' > 0$. If instead the conditions in Eqs. (D.11), (D.12) are satisfied, then there is indeed an equilibrium position at $R_{\rm eq} > R_{\rm T}$, which increases as the star gets larger. This last fact generically leads to a smaller force from the term $2\sigma/R$ in Eq. (7.37). Eventually, the equilibrium condition is lost when the position of the wall reaches the outer edge of the star, i.e. $R_{\rm eq} \geqslant R_{\rm S}$. This takes place when

$$R_{\rm T} > \frac{3\sigma(R_{\rm S}) - \sigma(R_{\rm T}) - \epsilon\Delta R_{\rm T}}{\epsilon - \sigma'}\,. \qquad \text{(exit transition region)} \tag{D.13}$$

With the linear approximation for $\sigma(R)$ we then conclude that, as long as the volume energy of the bubble is larger than the rate of change of the tension, there is a minimum transition radius such that the bubble can permeate through the transition region, Eq. (D.12), and another for which the bubble can reach the surface of the star, Eq. (D.13). From that point outwards the bubble expands throughout the whole universe, since $\ddot{R}(R > R_{\rm S}) > 0$. Moreover, we also learn that if $\epsilon > 3\sigma'$, the only equilibrium position is $R_{\rm eq} = R_{\rm T}$, and this is lost as soon as the star is large enough as to satisfy Eq. (D.12). Importantly, let us note that when $\epsilon > 3\sigma'$, Eq. (D.12) is in fact approximately the same as the condition for the formation of the bubble, Eq. (D.4), thus in this case the formation and escape of the bubble take place simultaneously.

D.4 Ultra-high Densities

In Sec. 7.1.5 we centered our discussion of the bubble dynamics on the case where densities in the core of the star, while above critical, are not much larger than n_c. This is because a fully formed bubble for which the field at its center is $(\phi_+)_\rho \sim \phi_+$ already allows for the possibility of a classical phase transition to the true vacuum.

[1] This requirement does not depend on σ' being constant, and the condition on $R_{\rm T}$ in Eq. (D.12) holds in general with $\sigma' \to \sigma'(R_{\rm T})$, under our approximation that σ' turns on at $R_{\rm T}$.

In this appendix we extend our analysis to the case of ultra-high densities, by which we mean $\zeta \to 1$. In this situation, the only minimum of the in-medium potential is found at $(\phi_+)_\rho \gg \phi_+$, see Eq. (7.7). As we explain in the following, we find that the escape of a bubble of the true vacuum can take place regardless of the scalar inside the star reaching the in-density minimum of the potential, i.e. $\phi(0) < (\phi_+)_\rho$, but it is enough that the field displacement is at least $\Delta\phi(0) \gtrsim \phi_+ - \phi_-$. As a matter of fact, if the star is large enough as to allow $\phi(0) \gg \phi_+$, the correspondingly large field displacement inside the (proto)-bubble makes it easier for a bubble to escape from the star.

The key point is that, for what concerns the possibility of a bubble of the true vacuum escaping from the star, one only needs to focus on a "sub-bubble" with a field displacement $\Delta\phi_{\rm sub} = \phi_+ - \phi_- \approx 2f$. The energy density of such a sub-bubble is simply $\epsilon_{\rm sub} \sim \Lambda_{\rm R}^4$, while its tension scales as

$$\sigma_{\rm sub}(R_{\rm T}) \sim \sqrt{\Delta\phi(0) f}\,\Lambda_{\rm R}^2\,. \tag{D.14}$$

The latter is enhanced by a factor $(\Delta\phi(0)/\Delta\phi_{\rm sub})^{1/2}$ with respect to the naive expectation, due to the higher potential energy difference of the large (proto-)bubble that contains the sub-bubble, $|\langle\Delta V\rangle| \sim \Delta\phi(0)\Lambda_{\rm R}^4/f$. This simple estimate holds as well if we assume that the in-density minimum is reached, i.e. $\phi(0) = (\phi_+)_\rho$.

Such an enhancement of the tension facilitates the escape of the sub-bubble, since it decreases the contracting force associated with σ' in Eq. (7.37). In particular, we now have $\sigma'_{\rm sub} \sim [\sigma(R_{\rm S}) - \sigma_{\rm sub}(R_{\rm T})]/\Delta R_{\rm T}$, which is smaller than when $\phi(0) \sim \phi_+$, see Eqs. (7.38), (7.39); in fact it could even be negative. Notice that instead the force associated with the surface tension of the wall at the transition radius, $2\sigma_{\rm sub}(R_{\rm T})/R_{\rm T}$, remains constant, since $R_{\rm T} \sim \sqrt{\Delta\phi(0)/f}\mu^{-1}$. Therefore, the net result is that it is much easier for the escape condition Eq. (7.40) to be satisfied. The larger (proto-)bubble supporting the sub-bubble helps the latter permeate through the entire star. The proper condition that determines if the sub-bubble of true vacuum expands throughout the whole universe is then

$$R_{\rm S} \gtrsim \frac{2\sigma(R_{\rm S})}{\epsilon}\,. \tag{D.15}$$

We have explicitly verified this result via our numerical simulations. For a bubble connecting shallow minima, $\delta^2 \ll 1$, this condition translates into

$$R_{\rm S} \gtrsim \frac{f}{\Lambda_{\rm R}^2}\,, \qquad \text{(sub-bubble; shallow)} \tag{D.16}$$

a requirement that is automatically satisfied given that $R_{\rm S} > R_{\rm T}$. For a bubble connecting deep minima, $\delta^2 \approx 1$, we find instead

$$R_{\rm S} \gtrsim \frac{f}{\Lambda_{\rm R}^2}\frac{1}{\sqrt{1-\delta^2}}\,. \qquad \text{(sub-bubble; deep)} \tag{D.17}$$

This is similar to the escape condition for a deep bubble, Eq. (7.74), yet on $R_{\rm S}$ instead of $\Delta R_{\rm T}$.

D.5 Sudden Approximation

We have been assuming that the bubble, during either its formation or expansion through the star, is always found in a nearly-static ($\dot{R} = 0$) equilibrium position, with its radius evolving slowly only because $R_{\rm T} = R_{\rm T}(\bar{t})$ does, as the star is being formed. Only at the point where equilibrium is lost, $\ddot{R} > 0$ and the bubble is free to gain kinetic energy. This was justified in

Sec. 7.1.2 on the basis that the characteristic reaction time of the scalar field, μ^{-1}, is much shorter than the evolution time of the star $T_{\rm S}$. In this section we wish to comment on the opposite situation, where $\mu T_{\rm S} \ll 1$.

In this limit, the star is formed instantaneously, with a large region $r < R_{\rm T}$ where the in-density potential allows for the scalar field to start classically rolling. If such a region was of infinite extent, i.e. if the system was spatially homogeneous, the field would roll, accelerate, and finally oscillate around the true minimum. However, in a finite-size system, one needs to crucially take into account the contribution of the spatial gradient to the energy of the field configuration. Indeed, ϕ moves in an effective potential $V(\phi) + \frac{1}{2}\phi'^2$ that becomes large towards the transition region, where the field must return to its vacuum value ϕ_-. Therefore, the sudden formation of the star and the corresponding gain of kinetic energy $\frac{1}{2}\dot{\phi}^2$ does not automatically imply that a first order phase transition will proceed via the escape of a scalar bubble from the dense system. As a matter of in fact, the situation is not much different that in the quasi-static case, as we now explain.

Concerning the formation of the bubble, the main difference with respect to our discussion in Sec. 7.1.4 can be phrased in terms of the maximal value that $\Delta\phi(0) = \phi(0) - \phi_-$, the field displacement at the center of the star, can take. Indeed, because of the kinetic energy the field acquires by rolling down the in-medium potential, $\Delta\phi(0)$ will generically be larger than what found in Eq. (7.22) for the same $R_{\rm T}$, yet oscillating in time. Accordingly, the whole scalar profile will necessarily oscillate in time as well. Then, if the size of star, specifically $R_{\rm T}$, is still not large enough for $\phi(0)$ to reach ϕ_+, the field value corresponding to the true minimum of the scalar potential in vacuum, then such an oscillating scalar profile remains trapped within the star, in a sort of oscillon that, even after eventually losing its kinetic energy,[2] remains as a confined static bubble (see e.g. [360] for a recent discussion of such type of field configurations in vacuum).

Otherwise, if $\Delta\phi(0) \gtrsim 2f$, then whether the scalar bubble remains confined to the dense region or escapes to infinity follows from the same analysis as in Sec. 7.1.5, yet with the properties of the bubble, i.e. the potential energy difference between the two sides of the bubble wall and the tension, now oscillating in time.

We stress again that the main difference between the quasi-static and sudden scenarios concerns the value of $R_{\rm T}$ for which a given field displacement is attained. Another way to interpret this fact is to compare, for the same value of $R_{\rm T}$, the dynamics of the bubble wall between the two scenarios. Because of the larger field displacement in the sudden case, the maximum values of $\epsilon(t)$ and $\sigma(R,t)$ will both be larger, while $\sigma'(R,t)$ will be smaller, than in the quasi-static case. This situation resembles the quasi-static evolution of a bubble in the limit that $n \gg n_c$, discussed in App. D.4. Therefore, we could similarly conclude that in the sudden approximation and for $R_{\rm T} \gg \mu^{-1}$, the condition that determines if the bubble expands indefinitely is

$$R_{\rm S} \gtrsim \frac{2\sigma(R_{\rm S})}{\epsilon}\,. \tag{D.18}$$

D.6 Formation and Escape of $N \gg 1$ Bubbles

In the main text we have concentrated on bubbles interpolating between two consecutive relaxion minima, located at the period ℓ_* outside the bubble and at ℓ_*+1 inside it. However, the relaxion displacement at the core of the star could be much larger than $2\pi f$, in particular $\Delta\phi(0) \sim 2\pi f N$ with $N \gg 1$ is expected to naturally occur for relaxion bubbles at densities significantly above the critical one, see Eq. (7.71). In this appendix we provide a discussion of the fate of the

[2] This could proceed via radiation of ϕ quanta, or because of the interactions of ϕ with the environment.

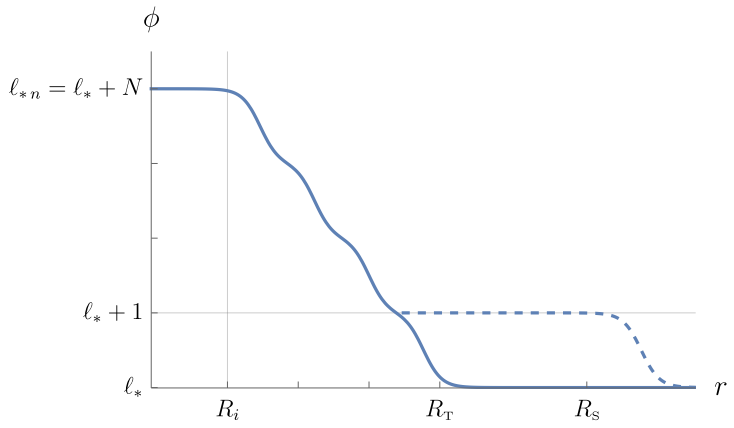

Figure D.1: $N \gg 1$ bubble in equilibrium at $R \sim R_{\rm T}$ (solid) and sub-bubble that has already escaped from the star (dashed).

relaxion bubbles in such a situation, following closely [13] while avoiding the detailed derivation presented there.

For the first in-density minimum to be reached, the energy in the in the field's gradient, $\sim (2\pi f N/R_{\rm T})^2$, needs to be compensated by the gain in potential energy inside the bubble, $\sim 2\pi\Lambda_{\rm R}^4 N$. This can only happen if the core of the star is large enough

$$R_{\rm T} \gtrsim \frac{\sqrt{N}}{\mu}\,, \tag{D.19}$$

where we recall that $\mu = \Lambda_{\rm R}^2/f$. If this is the case, a large bubble with a field displacement of $\Delta\phi(0) \sim 2\pi f N$ is fully formed. The properties of such a bubble, that is its volume energy density and tension can be simply estimated as,

$$\epsilon \sim \mu^2 f \Delta\phi(0) \sim 2\pi\Lambda_{\rm R}^4 N\,, \tag{D.20}$$

$$\sigma \sim \Delta\phi(0)\sqrt{\epsilon} \sim \Lambda_{\rm R}^2 f (2\pi N)^{3/2}\,. \tag{D.21}$$

This large relaxion bubble can be thought as made of a series of N sub-bubbles, each corresponding to a field displacement w.r.t. to the next of $2\pi f$, see Fig. D.1. This is motivated by the fact that in vacuum each relaxion minimum is separated by a potential barrier, so the escape of relaxion bubbles from the star takes place in discrete steps, starting with the outermost bubble, within which the relaxion sits just one period away, i.e. at $\ell_* + 1$, from its in-vacuo value. This sub-bubble has then a volume energy density and tension

$$\epsilon_{\rm sub} \sim 2\pi\Lambda_{\rm R}^4\,, \tag{D.22}$$

$$\sigma_{\rm sub}(R_{\rm T}) \sim \Lambda_{\rm R}^2 f (2\pi N)^{1/2}\,. \tag{D.23}$$

Note in particular that the wall tension is enhanced by a factor $\sqrt{N}$ w.r.t. the one of a standard relaxion bubble. It is this enhancement that facilitates the sub-bubble escape from the star. Indeed, the characteristic contracting force of bubbles propagating through a star, $\sigma' \sim \Delta\sigma/\Delta R_{\rm T}$ associated with a radius-dependent tension, is mitigated because $\Delta\sigma \sim \sigma_{\rm sub}(R_{\rm S}) - \sigma_{\rm sub}(R_{\rm T})$ decreases (or could even become negative) at large N. We have explicitly verified this effect via numerical simulations of the sub-bubble's dynamics.

The condition for the expansion, beyond the confines of the star and towards infinity, of this $2\pi f$ bubble then coincides with the condition that the bubble does not contract in vacuum,

$\epsilon_{\rm sub} \gtrsim 2\sigma_{\rm sub}(R_{\rm S})/R_{\rm S}$, where $\sigma_{\rm sub}(R_{\rm S})$ is the tension of the wall in vacuum. For shallow minima, since the potential barrier Eq. (7.68) is very small, this tension is simply $\sigma_{\rm sub}(R_{\rm S}) \sim 2\pi f\sqrt{\epsilon_{\rm sub}}$. Therefore, the condition reads

$$R_{\rm S} \gtrsim \frac{f}{\Lambda_{\rm R}^2}\,, \qquad \text{(sub-bubble; shallow)} \tag{D.24}$$

which is automatically satisfied given that $R_{\rm S} > R_{\rm T}$ and Eq. (D.19). Instead, for deep minima we can use the thin-wall approximation to compute the wall's tension $\sigma_{\rm sub}(R_{\rm S}) \simeq 8f\Lambda_{\rm B}^2$, and the correct condition is then

$$R_{\rm S} \gtrsim \frac{f}{\Lambda_{\rm R}^2}\frac{1}{\sqrt{1-\delta^2}}\,. \qquad \text{(sub-bubble; deep)} \tag{D.25}$$

Finally, let us note that if the conditions for a sub-bubble to escape are satisfied, this will also be the case for subsequent sub-bubbles (with $N \to N-1$), up until N becomes so small that the enhancement in the sub-bubble tension $\sigma_{\rm sub}$ is not enough to guarantee that $\epsilon \gtrsim \sigma'$, that is that the outwards pressure due to the gain in ground state energy is not enough to overcome the tension's gradient.

D.7 Opposite-sign Back-reaction

The discussion in the main text has been restricted to densities that, while allowing for the field to classically move inside the star, i.e. $\zeta(n) > \zeta_c = \delta^2$, are still such that the back-reaction term in the potential is non-vanishing, even if negligibly small. In this section we want to consider instead the possibility that $\zeta(n) > 1$, such that the wiggles not only vanish but change sign in some region inside the star.

In this situation, we can identify another inner core radius $R'_{\rm T}$, such that for $r < R'_{\rm T}$, minima of the in-density potential reappear due to opposite-sign barriers. This is fixed by $\zeta(R'_{\rm T}) = 2-\delta^2$, where δ is defined, as in vacuum, as the difference between the size of the rolling and back-reaction terms at the minimum of interest, see Eq. (7.64). Because of the different sign of the back-reaction term, the minima are now shifted by π with respect to those for $\zeta < 1$, i.e. they are located at $(2\pi\ell_{*\,n} + \theta_{*\,n} + \pi)f$. The field displacement, or equivalently the value of $\ell_{*\,n}$ where the relaxion sits for $r < R'_{\rm T}$, is determined by the size of the region between the two core radii, $\Delta R'_{\rm T} \equiv R_{\rm T} - R'_{\rm T}$. This difference sets, in the same fashion as Eq. (D.19), the field displacement from the in-vacuo value, $\Delta\phi(R'_{\rm T})/f \sim (\mu\Delta R'_{\rm T})^2$. From this point on, the fate of the bubble (or sub-bubble) is not much different than what already discussed in Sec. 7.3.2 and App. D.6. In particular, if $\Delta R'_{\rm T} \gg \mu^{-1}$, the relevant dynamics is that of a $2\pi f$ sub-bubble, for which the condition Eq. (D.24) determines if it escapes the star and expands to infinity. The only subtlety arises for $\Delta\phi(R'_{\rm T}) = \pi f$. In this case the potential energy density of the bubble receives a contribution from the back-reaction term in addition to the rolling term. We find $\epsilon \simeq \pi\Lambda_{\rm R}^4 + 2(\zeta-1)\Lambda_{\rm B}^4$, where we recall that we are dealing with densities such that $\zeta > 1$. While for sufficiently large ζ this extra contribution naively helps the bubble expand, as soon as the bubble wall goes through the outer transition region of the star, $r > R_{\rm T}$, ϵ decreases because the relaxion value inside the bubble, $(2\pi\ell_* + \pi)f$, is not a minimum of the potential in vacuum. This eventually prevents the bubble from escaping. This type of confined bubble (yet with $\Lambda_{\rm R} = 0$) has been found to be a plausible consequence of the QCD axion [11], or special deformations thereof [186], in neutron stars.

D.8 Bubble Interactions with the Environment

In the main text we have treated the density profile as a non-dynamical classical background field, upon which a non-trivial scalar field develops. In this appendix we study in some more detail the interactions of the scalar bubble with the dense environment.

Let us discuss first the force exerted by individual nucleons, N, on the bubble wall. We focus on the case of the QCD relaxion, since the interactions of non-QCD relaxions with protons and neutrons are much weaker, being mediated by Higgs exchange. The interaction with nucleons is of the form $\sim \sigma_{\pi N} \bar{N} N \cos(\phi/f)$. This constitutes a contribution to their mass that depends on the relaxion field, and therefore on space-time, $m_{\pi N}(r) \sim \sigma_{\pi N} \cos(\phi(r)/f)$. Recall that most of the mass of a nucleon comes from a term independent of the quark masses and thus independent of ϕ, $m_N = M_B + m_{\pi N}$ with $M_B \gg m_{\pi N}$. It is precisely this interaction of the relaxion with nucleons that gives rise to the leading linear correction to the back-reaction term in the limit of small baryonic densities, after substituting $\bar{N}N \to n_b$, as given in Eq. (7.78). Note however that for this treatment to hold, one is implicitly assuming that the scalar field interacts classically with the density profile, or in other words that single nucleons are able to penetrate the bubble wall with negligible quantum-mechanical reflection.

Let us have a look then at the one-dimensional quantum mechanics of a nucleon in the potential associated with its space-time dependent mass, $m_{\pi N}(r)$. This follows the discussion in [254], with some important modifications. Before proceeding, let us note there are two qualitatively different types of potentials depending on the relaxion profile. For bubbles in which the scalar field displacement is $\Delta\phi(0) = 2\pi f$ (our focus in the main text) the overall change of the nucleon mass between inside and outside the bubble vanishes, while at the center of the bubble wall, where $\Delta\phi = \pi/2$, $m_{\pi N} \sim -\sigma_{\pi N}$; the potential thus resembles a well. If instead the field displacement is $\Delta\phi(0) = \pi f$ (briefly discussed in App. D.7), we have that the change from outside to inside the bubble $\Delta m_N \sim -2\sigma_{\pi N}$, and the potential is a downwards step. In any of these cases, in order to properly compute the force that the nucleons exert on the bubble wall, it is important to realize that the relevant scales of the problem are the thickness of the wall, of order $\mu^{-1} \sim f/\Lambda_{\rm R}^2$, and the nucleon wavelength, given by $\lambda_N \sim 1/m_N v$, where v is the relative velocity of the nucleons with respect to the wall, which we expect to be non-negligible (either because of their Fermi momentum, temperature, or the initial yet small velocity that the bubble acquires when it forms). We therefore expect $\lambda_N \mu \ll 1$, which already indicates that the nucleons interact with the potential classically. Focussing for concreteness on the step-like potential, we can go further and split it in J small patches, each of them of size λ_N, where quantum mechanical effects become important. In each step the nucleon mass decreases by an amount $\delta m_N = |\Delta m_N|/J \sim 2\sigma_{\pi N}/J$. Therefore, for each step the quantum-mechanical reflection coefficient is given by

$$\mathbb{R}_1 = \frac{(k-k')^2}{(k+k')^2} \simeq \frac{\delta m_N^2}{4 m_N^2 v^4}\,, \tag{D.26}$$

where k is the momentum of the nucleon before traversing the wall, and k' its momentum once inside the bubble. In the second equality we have taken the non-relativistic limit, $k \simeq mv$ and $k' \simeq \sqrt{k^2 + 2 m_N \delta m_N}$, and expanded in δm_N. Taking into account all the J barriers, the total reflection coefficient is bounded by

$$\mathbb{R} \lesssim J \mathbb{R}_1 \simeq \frac{\Delta m_N^2}{4 m_N^2 v^4 J}\,, \tag{D.27}$$

which vanishes in the limit $J \gg 1$. This agrees then with the naive expectation that for $\lambda_N \mu \ll 1$ the system behaves classically, without reflection. In fact, one can also compute the total force

on the bubble wall associated with the gain in momentum of the nucleons as they pass through it. For a single nucleon, after going down all the J steps, the force is $f_N = J(k' - k)\mathbb{T} \simeq |\Delta m_N|/v$. Therefore, for an ensemble of nucleons with density n_b, the total force reads

$$F_N = n_b v f_N \sim 2\sigma_{\pi N} n_b \,. \tag{D.28}$$

This precisely matches the piece of the volume force associated with the change of the potential barriers derived in App. D.7 (opposite-sign back-reaction), $\sim 2\zeta\Lambda_{\rm B}^4 \sim 2\sigma_{\pi N} n_b$. For the potential-well case (i.e. for $2\pi f$ bubbles), with this quantum-mechanical treatment we find, as expected, $F_N = 0$. However, given that the wall appears to the individual nucleons as a classical potential well, these tend to accumulate at the wall, i.e. the density (as well as temperature) increases at the wall; this in turn means that the wall gets thicker. Therefore, it appears that as the bubble expands through the star, it carries with it a local (of size μ^{-1}) increase in density. However, for most of the star the density profile remains unaltered.

Bibliography

[1] ATLAS collaboration, *Observation of a new particle in the search for the Standard Model Higgs boson with the ATLAS detector at the LHC*, *Phys. Lett. B* **716** (2012) 1 [arXiv:1207.7214].

[2] CMS collaboration, *Observation of a New Boson at a Mass of 125 GeV with the CMS Experiment at the LHC*, *Phys. Lett. B* **716** (2012) 30 [arXiv:1207.7235].

[3] B.W. Lee, C. Quigg and H.B. Thacker, *Weak interactions at very high energies: The role of the higgs-boson mass*, *Phys. Rev. D* **16** (1977) 1519.

[4] C. Abel et al., *Measurement of the Permanent Electric Dipole Moment of the Neutron*, *Phys. Rev. Lett.* **124** (2020) 081803 [arXiv:2001.11966].

[5] R. Peccei and H.R. Quinn, *CP Conservation in the Presence of Instantons*, *Phys. Rev. Lett.* **38** (1977) 1440.

[6] R. Peccei and H.R. Quinn, *Constraints Imposed by CP Conservation in the Presence of Instantons*, *Phys. Rev. D* **16** (1977) 1791.

[7] S. Weinberg, *A New Light Boson?*, *Phys. Rev. Lett.* **40** (1978) 223.

[8] F. Wilczek, *Problem of Strong P and T Invariance in the Presence of Instantons*, *Phys. Rev. Lett.* **40** (1978) 279.

[9] L. Abbott, *A Mechanism for Reducing the Value of the Cosmological Constant*, *Phys. Lett. B* **150** (1985) 427.

[10] P.W. Graham, D.E. Kaplan and S. Rajendran, *Cosmological Relaxation of the Electroweak Scale*, *Phys. Rev. Lett.* **115** (2015) 221801 [arXiv:1504.07551].

[11] R. Balkin, J. Serra, K. Springmann and A. Weiler, *The QCD axion at finite density*, *JHEP* **07** (2020) 221 [arXiv:2003.04903].

[12] R. Balkin, J. Serra, K. Springmann, S. Stelzl and A. Weiler, *Runaway relaxion from finite density*, *JHEP* **06** (2022) 023 [arXiv:2106.11320].

[13] R. Balkin, J. Serra, K. Springmann, S. Stelzl and A. Weiler, *Density induced vacuum instability*, *SciPost Phys.* **14** (2023) 071 [arXiv:2105.13354].

[14] R. Balkin, J. Serra, K. Springmann, S. Stelzl and A. Weiler, *White dwarfs as a probe of light QCD axions*, arXiv:2211.02661.

[15] R. Balkin, J. Serra, K. Springmann, S. Stelzl and A. Weiler, *Heavy neutron stars from light scalars*, arXiv:2307.14418.

[16] K. Springmann, M. Stadlbauer, S. Stelzl and A. Weiler, "QCD Axion Couplings at Finite Density." in preparation.

[17] R. Balkin, K. Bartnick, F. Jung, K. Springmann, S. Stelzl and A. Weiler, "Stellar Remnants as a Probe of Non-Derivatively Coupled Scalars." in preparation.

[18] A. Belavin, A.M. Polyakov, A. Schwartz and Y. Tyupkin, *Pseudoparticle Solutions of the Yang-Mills Equations*, *Phys. Lett. B* **59** (1975) 85.

[19] R. Jackiw and C. Rebbi, *Vacuum Periodicity in a Yang-Mills Quantum Theory*, *Phys. Rev. Lett.* **37** (1976) 172.

[20] J. Callan, Curtis G., R. Dashen and D.J. Gross, *The Structure of the Gauge Theory Vacuum*, *Phys. Lett. B* **63** (1976) 334.

[21] V. Rubakov, *Classical theory of gauge fields*, Princeton Univ. Press, Princeton, NJ, USA (2002).

[22] S.L. Adler, *Axial vector vertex in spinor electrodynamics*, *Phys. Rev.* **177** (1969) 2426.

[23] J.S. Bell and R. Jackiw, *A PCAC puzzle: $\pi^0 \to \gamma\gamma$ in the σ model*, *Nuovo Cim. A* **60** (1969) 47.

[24] G. 't Hooft, *How Instantons Solve the U(1) Problem*, *Phys. Rept.* **142** (1986) 357.

[25] K. Fujikawa, *Path Integral Measure for Gauge Invariant Fermion Theories*, *Phys. Rev. Lett.* **42** (1979) 1195.

[26] V. Baluni, *CP Violating Effects in QCD*, *Phys. Rev. D* **19** (1979) 2227.

[27] J.E. Kim and G. Carosi, *Axions and the Strong CP Problem*, *Rev. Mod. Phys.* **82** (2010) 557 [arXiv:0807.3125].

[28] A. Hook, *TASI Lectures on the Strong CP Problem and Axions*, *PoS* **TASI2018** (2019) 004 [arXiv:1812.02669].

[29] L. Di Luzio, M. Giannotti, E. Nardi and L. Visinelli, *The landscape of QCD axion models*, *Phys. Rept.* **870** (2020) 1 [arXiv:2003.01100].

[30] M. Pospelov and A. Ritz, *Theta vacua, QCD sum rules, and the neutron electric dipole moment*, *Nucl. Phys. B* **573** (2000) 177 [arXiv:hep-ph/9908508].

[31] Particle Data Group collaboration, *Review of particle physics*, *Phys. Rev. D* **98** (2018) 030001.

[32] G. Grilli di Cortona, E. Hardy, J. Pardo Vega and G. Villadoro, *The QCD axion, precisely*, *JHEP* **01** (2016) 034 [arXiv:1511.02867].

[33] S. Coleman, *Aspects of Symmetry: Selected Erice Lectures*, Cambridge University Press (1985), 10.1017/CBO9780511565045.

[34] C. Vafa and E. Witten, *Parity Conservation in QCD*, *Phys. Rev. Lett.* **53** (1984) 535.

[35] A. Zhitnitsky, *On Possible Suppression of the Axion Hadron Interactions. (In Russian)*, *Sov. J. Nucl. Phys.* **31** (1980) 260.

[36] M. Dine, W. Fischler and M. Srednicki, *A Simple Solution to the Strong CP Problem with a Harmless Axion*, *Phys. Lett. B* **104** (1981) 199.

[37] J.E. Kim, *Weak Interaction Singlet and Strong CP Invariance*, *Phys. Rev. Lett.* **43** (1979) 103.

[38] M.A. Shifman, A. Vainshtein and V.I. Zakharov, *Can Confinement Ensure Natural CP Invariance of Strong Interactions?*, *Nucl. Phys. B* **166** (1980) 493.

[39] J. Gasser and H. Leutwyler, *Chiral Perturbation Theory to One Loop*, *Annals Phys.* **158** (1984) 142.

[40] A. Krause, *Baryon Matrix Elements of the Vector Current in Chiral Perturbation Theory*, *Helv. Phys. Acta* **63** (1990) 3.

[41] E. Epelbaum, H.-W. Hammer and U.-G. Meissner, *Modern Theory of Nuclear Forces*, *Rev. Mod. Phys.* **81** (2009) 1773 [arXiv:0811.1338].

[42] S.R. Coleman, J. Wess and B. Zumino, *Structure of phenomenological Lagrangians. 1.*, *Phys. Rev.* **177** (1969) 2239.

[43] C.G. Callan, Jr., S.R. Coleman, J. Wess and B. Zumino, *Structure of phenomenological Lagrangians. 2.*, *Phys. Rev.* **177** (1969) 2247.

[44] G. Panico and A. Wulzer, *The Composite Nambu-Goldstone Higgs*, vol. 913, Springer (2016), 10.1007/978-3-319-22617-0, [arXiv:1506.01961].

[45] S. Weinberg, *Nonlinear realizations of chiral symmetry*, *Phys. Rev.* **166** (1968) 1568.

[46] P. Langacker and H. Pagels, *Chiral perturbation theory*, *Phys. Rev. D* **8** (1973) 4595.

[47] J. Gasser, M.E. Sainio and A. Svarc, *Nucleons with Chiral Loops*, *Nucl. Phys. B* **307** (1988) 779.

[48] V. Bernard, N. Kaiser and U.-G. Meissner, *Chiral dynamics in nucleons and nuclei*, *Int. J. Mod. Phys. E* **4** (1995) 193 [arXiv:hep-ph/9501384].

[49] S. Scherer, *Introduction to chiral perturbation theory*, *Adv. Nucl. Phys.* **27** (2003) 277 [arXiv:hep-ph/0210398].

[50] S. Weinberg, *Phenomenological Lagrangians*, *Physica A* **96** (1979) 327.

[51] S. Weinberg, *Nuclear forces from chiral Lagrangians*, *Phys. Lett. B* **251** (1990) 288.

[52] S. Weinberg, *Effective chiral Lagrangians for nucleon - pion interactions and nuclear forces*, *Nucl. Phys. B* **363** (1991) 3.

[53] S. Weinberg, *Three body interactions among nucleons and pions*, *Phys. Lett. B* **295** (1992) 114 [arXiv:hep-ph/9209257].

[54] H. Georgi, *An Effective Field Theory for Heavy Quarks at Low-energies*, *Phys. Lett. B* **240** (1990) 447.

[55] E.E. Jenkins and A.V. Manohar, *Baryon chiral perturbation theory using a heavy fermion Lagrangian*, *Phys. Lett. B* **255** (1991) 558.

[56] E.E. Jenkins and A.V. Manohar, *Chiral corrections to the baryon axial currents*, *Phys. Lett. B* **259** (1991) 353.

[57] P. Carenza, T. Fischer, M. Giannotti, G. Guo, G. Martínez-Pinedo and A. Mirizzi, *Improved axion emissivity from a supernova via nucleon-nucleon bremsstrahlung*, *JCAP* **10** (2019) 016 [arXiv:1906.11844].

[58] L.B. Leinson, *Impact of axions on the Cassiopea A neutron star cooling*, *JCAP* **09** (2021) 001 [arXiv:2105.14745].

[59] L.B. Leinson, *Axion mass limit from observations of the neutron star in Cassiopeia A*, *JCAP* **08** (2014) 031 [arXiv:1405.6873].

[60] Particle Data Group collaboration, *Review of Particle Physics*, *PTEP* **2022** (2022) 083C01.

[61] T. Vonk, F.-K. Guo and U.-G. Meißner, *Precision calculation of the axion-nucleon coupling in chiral perturbation theory*, *JHEP* **03** (2020) 138 [arXiv:2001.05327].

[62] D. Siemens, V. Bernard, E. Epelbaum, A.M. Gasparyan, H. Krebs and U.-G. Meißner, *Elastic and inelastic pion-nucleon scattering to fourth order in chiral perturbation theory*, *Phys. Rev. C* **96** (2017) 055205 [arXiv:1704.08988].

[63] V. Bernard, N. Kaiser and U.-G. Meissner, *Aspects of chiral pion - nucleon physics*, *Nucl. Phys. A* **615** (1997) 483 [arXiv:hep-ph/9611253].

[64] P. Gysbers et al., *Discrepancy between experimental and theoretical β-decay rates resolved from first principles*, *Nature Phys.* **15** (2019) 428 [arXiv:1903.00047].

[65] U.-G. Meissner, G. Muller and S. Steininger, *Renormalization of the chiral pion - nucleon Lagrangian beyond next-to-leading order*, *Annals Phys.* **279** (2000) 1 [arXiv:hep-ph/9809446].

[66] N. Fettes, U.-G. Meissner and S. Steininger, *Pion - nucleon scattering in chiral perturbation theory. 1. Isospin symmetric case*, *Nucl. Phys. A* **640** (1998) 199 [arXiv:hep-ph/9803266].

[67] M. Hoferichter, J. Ruiz de Elvira, B. Kubis and U.-G. Meißner, *Matching pion-nucleon Roy-Steiner equations to chiral perturbation theory*, *Phys. Rev. Lett.* **115** (2015) 192301 [arXiv:1507.07552].

[68] H.M. Georgi, L.J. Hall and M.B. Wise, *Grand Unified Models With an Automatic Peccei-Quinn Symmetry*, *Nucl. Phys. B* **192** (1981) 409.

[69] M. Dine and N. Seiberg, *String Theory and the Strong CP Problem*, *Nucl. Phys. B* **273** (1986) 109.

[70] S.M. Barr and D. Seckel, *Planck scale corrections to axion models*, *Phys. Rev. D* **46** (1992) 539.

[71] M. Kamionkowski and J. March-Russell, *Planck scale physics and the Peccei-Quinn mechanism*, *Phys. Lett. B* **282** (1992) 137 [arXiv:hep-th/9202003].

[72] K.R. Dienes, E. Dudas and T. Gherghetta, *Invisible axions and large radius compactifications*, *Phys. Rev. D* **62** (2000) 105023 [arXiv:hep-ph/9912455].

[73] A. Hook, *Solving the Hierarchy Problem Discretely*, *Phys. Rev. Lett.* **120** (2018) 261802 [arXiv:1802.10093].

[74] L. Di Luzio, B. Gavela, P. Quilez and A. Ringwald, *An even lighter QCD axion*, *JHEP* **05** (2021) 184 [arXiv:2102.00012].

[75] L. Di Luzio, B. Gavela, P. Quilez and A. Ringwald, *Dark matter from an even lighter QCD axion: trapped misalignment*, *JCAP* **10** (2021) 001 [arXiv:2102.01082].

[76] C. O'Hare, "cajohare/axionlimits: Axionlimits." https://cajohare.github.io/AxionLimits/, July, 2020. 10.5281/zenodo.3932430.

[77] G.G. Raffelt, *Axion Constraints From White Dwarf Cooling Times*, *Phys. Lett. B* **166** (1986) 402.

[78] G.G. Raffelt, *Astrophysical methods to constrain axions and other novel particle phenomena*, *Phys. Rept.* **198** (1990) 1.

[79] F. Capozzi and G. Raffelt, *Axion and neutrino bounds improved with new calibrations of the tip of the red-giant branch using geometric distance determinations*, *Phys. Rev. D* **102** (2020) 083007 [arXiv:2007.03694].

[80] O. Straniero, C. Pallanca, E. Dalessandro, I. Dominguez, F.R. Ferraro, M. Giannotti et al., *The RGB tip of galactic globular clusters and the revision of the axion-electron coupling bound*, *Astron. Astrophys.* **644** (2020) A166 [arXiv:2010.03833].

[81] G.G. Raffelt, *Stars as laboratories for fundamental physics: The astrophysics of neutrinos, axions, and other weakly interacting particles* (5, 1996).

[82] G. Raffelt and D. Seckel, *Bounds on Exotic Particle Interactions from SN 1987a*, *Phys. Rev. Lett.* **60** (1988) 1793.

[83] M.S. Turner, *Axions from SN 1987a*, *Phys. Rev. Lett.* **60** (1988) 1797.

[84] A. Burrows, M.S. Turner and R.P. Brinkmann, *Axions and SN 1987a*, *Phys. Rev. D* **39** (1989) 1020.

[85] H.-T. Janka, *Explosion Mechanisms of Core-Collapse Supernovae*, *Ann. Rev. Nucl. Part. Sci.* **62** (2012) 407 [arXiv:1206.2503].

[86] R.P. Brinkmann and M.S. Turner, *Numerical Rates for Nucleon-Nucleon Axion Bremsstrahlung*, *Phys. Rev. D* **38** (1988) 2338.

[87] G.G. Raffelt, *Astrophysical axion bounds*, *Lect. Notes Phys.* **741** (2008) 51 [arXiv:hep-ph/0611350].

[88] L. Di Luzio, F. Mescia, E. Nardi, P. Panci and R. Ziegler, *Astrophobic Axions*, *Phys. Rev. Lett.* **120** (2018) 261803 [arXiv:1712.04940].

[89] G. Lucente, L. Mastrototaro, P. Carenza, L. Di Luzio, M. Giannotti and A. Mirizzi, *Axion signatures from supernova explosions through the nucleon electric-dipole portal*, *Phys. Rev. D* **105** (2022) 123020 [arXiv:2203.15812].

[90] M. Pospelov and A. Ritz, *Theta induced electric dipole moment of the neutron via QCD sum rules*, *Phys. Rev. Lett.* **83** (1999) 2526 [arXiv:hep-ph/9904483].

[91] J. Keller and A. Sedrakian, *Axions from cooling compact stars*, *Nucl. Phys. A* **897** (2013) 62 [arXiv:1205.6940].

[92] A. Sedrakian, *Axion cooling of neutron stars*, *Phys. Rev. D* **93** (2016) 065044 [arXiv:1512.07828].

[93] K. Hamaguchi, N. Nagata, K. Yanagi and J. Zheng, *Limit on the Axion Decay Constant from the Cooling Neutron Star in Cassiopeia A*, *Phys. Rev. D* **98** (2018) 103015 [arXiv:1806.07151].

[94] M.V. Beznogov, E. Rrapaj, D. Page and S. Reddy, *Constraints on Axion-like Particles and Nucleon Pairing in Dense Matter from the Hot Neutron Star in HESS J1731-347*, *Phys. Rev. C* **98** (2018) 035802 [arXiv:1806.07991].

[95] A. Sedrakian, *Axion cooling of neutron stars. II. Beyond hadronic axions*, *Phys. Rev. D* **99** (2019) 043011 [arXiv:1810.00190].

[96] Particle Data Group collaboration, *Axions and other similar particles*, *PTEP* **2020** (2020) 083C01.

[97] D. Page, M. Prakash, J.M. Lattimer and A.W. Steiner, *Rapid Cooling of the Neutron Star in Cassiopeia A Triggered by Neutron Superfluidity in Dense Matter*, *Phys. Rev. Lett.* **106** (2011) 081101 [arXiv:1011.6142].

[98] P.S. Shternin, D.G. Yakovlev, C.O. Heinke, W.C. Ho and D.J. Patnaude, *Cooling neutron star in the cassiopeia a supernova remnant: evidence for superfluidity in the core*, *Monthly Notices of the Royal Astronomical Society: Letters* **412** (2011) L108.

[99] L.B. Leinson, *Superfluid phases of triplet pairing and rapid cooling of the neutron star in Cassiopeia A*, *Phys. Lett. B* **741** (2015) 87 [arXiv:1411.6833].

[100] R. Bollig, N. Yadav, D. Kresse, H.T. Janka, B. Müller and A. Heger, *Self-consistent 3D Supernova Models From −7 Minutes to +7 s: A 1-bethe Explosion of a ∼19 $M_\odot$ Progenitor*, *Astrophys. J.* **915** (2021) 28 [arXiv:2010.10506].

[101] J.M. Lattimer, *The nuclear equation of state and neutron star masses*, *Ann. Rev. Nucl. Part. Sci.* **62** (2012) 485 [arXiv:1305.3510].

[102] G. Baym, T. Hatsuda, T. Kojo, P.D. Powell, Y. Song and T. Takatsuka, *From hadrons to quarks in neutron stars: a review*, *Rept. Prog. Phys.* **81** (2018) 056902 [arXiv:1707.04966].

[103] S. Weinberg, *Gravitation and Cosmology: Principles and Applications of the General Theory of Relativity*, John Wiley and Sons, New York (1972).

[104] S. Shapiro and S. Teukolsky, *Black holes, white dwarfs, and neutron stars: The physics of compact objects* (1983).

[105] N.K. Glendenning, *Compact stars: Nuclear physics, particle physics, and general relativity*, Springer New York (1997).

[106] S. Chandrasekhar, *The Maximum Mass of Ideal White Dwarfs*, *American Physical Society* **74** (1931) 81.

[107] A. Bédard, P. Bergeron and G. Fontaine, *Measurements of Physical Parameters of White Dwarfs: A Test of the Mass–Radius Relation*, *The Astrophysical Journal* **848** (2017) 11.

[108] P.-E. Tremblay, N. Gentile-Fusillo, R. Raddi, S. Jordan, C. Besson, B.T. Gänsicke et al., *The Gaia DR1 mass–radius relation for white dwarfs*, *Monthly Notices of the Royal Astronomical Society* **465** (2016) 2849.

[109] S.R.G. Joyce, M.A. Barstow, S.L. Casewell, M.R. Burleigh, J.B. Holberg and H.E. Bond, *Testing the white dwarf mass-radius relation and comparing optical and far-UV spectroscopic results with Gaia DR2, HST, and FUSE*, *Monthly Notices of the Royal Astronomical Society* **479** (2018) 1612.

[110] H.E. Bond, R.L. Gilliland, G.H. Schaefer, P. Demarque, T.M. Girard, J.B. Holberg et al., *Hubble Space Telescope Astrometry of the Procyon System*, *The Astrophysical Journal* **813** (2015) 106.

[111] H.E. Bond, G.H. Schaefer, R.L. Gilliland, J.B. Holberg, B.D. Mason, I.W. Lindenblad et al., *The Sirius System and Its Astrophysical Puzzles: Hubble Space Telescope and Ground-based Astrometry*, *The Astrophysical Journal* **840** (2017) 70.

[112] S.G. Parsons, B.T. Gänsicke, T.R. Marsh, R.P. Ashley, M.C.P. Bours, E. Breedt et al., *Testing the white dwarf mass–radius relationship with eclipsing binaries*, *Monthly Notices of the Royal Astronomical Society* **470** (2017) 4473 [arXiv:https://academic.oup.com/mnras/article-pdf/470/4/4473/19179437/stx1522.pdf].

[113] W.R. Brown, M. Kilic, A. Kosakowski, J.J. Andrews, C.O. Heinke, M.A. Agüeros et al., *The ELM survey. VIII. ninety-eight double white dwarf binaries*, *The Astrophysical Journal* **889** (2020) 49.

[114] S.i.P. Nunes, J.D.V. Arbañil and M. Malheiro, *The Structure and Stability of Massive Hot White Dwarfs*, *Astrophys. J.* **921** (2021) 138 [arXiv:2108.08238].

[115] S.M. de Carvalho, M. Rotondo, J.A. Rueda and R. Ruffini, *Relativistic Feynman-Metropolis-Teller treatment at finite temperatures*, *Phys. Rev. C* **89** (2014) 015801.

[116] D. Koester, *Convective Mixing and Accretion in White Dwarfs*, *aap* **52** (1976) 415.

[117] R. Kippenhahn, A. Weigert and A. Weiss, *Stellar structure and evolution*, Astronomy and Astrophysics Library, Springer (8, 2012), 10.1007/978-3-642-30304-3.

[118] N.P.G. Fusillo, P.-E. Tremblay, E. Cukanovaite, A. Vorontseva, R. Lallement, M. Hollands et al., *A catalogue of white dwarfs in Gaia EDR3*, *Monthly Notices of the Royal Astronomical Society* **508** (2021) 3877.

[119] Madej, J., Nalezyty, M. and Althaus, L. G., *Mass distribution of DA white dwarfs in the First Data Release of the Sloan Digital Sky Survey*, *A&A* **419** (2004) L5.

[120] Nalezyty, M. and Madej, J., *A catalogue of isolated massive white dwarfs*, *A&A* **420** (2004) 507.

[121] Koester, D. and Kepler, S. O., *Carbon-rich (DQ) white dwarfs in the Sloan Digital Sky Survey*, *A&A* **628** (2019) A102.

[122] F.M. Jiménez-Esteban, S. Torres, A. Rebassa-Mansergas, G. Skorobogatov, E. Solano, C. Cantero et al., *A white dwarf catalogue from Gaia-DR2 and the Virtual Observatory*, *Monthly Notices of the Royal Astronomical Society* **480** (2018) 4505 [arXiv:1807.02559].

[123] P. Bergeron, P. Dufour, G. Fontaine, S. Coutu, S. Blouin, C. Genest-Beaulieu et al., *On the measurement of fundamental parameters of white dwarfs in the Gaia era*, *The Astrophysical Journal* **876** (2019) 67.

[124] C. Genest-Beaulieu and P. Bergeron, *A comprehensive spectroscopic and photometric analysis of DA and DB white dwarfs from SDSS and Gaia*, *The Astrophysical Journal* **871** (2019) 169.

[125] P. de Forcrand, *Simulating QCD at finite density*, *PoS* **LAT2009** (2009) 010 [arXiv:1005.0539].

[126] NANOGrav collaboration, *Relativistic Shapiro delay measurements of an extremely massive millisecond pulsar*, *Nature Astron.* **4** (2019) 72 [arXiv:1904.06759].

[127] A.B. Migdal, *Pion Fields in Nuclear Matter*, *Rev. Mod. Phys.* **50** (1978) 107.

[128] M. Mannarelli, *Meson condensation*, *Particles* **2** (2019) 411 [arXiv:1908.02042].

[129] N.K. Glendenning, *THE HYPERON COMPOSITION OF NEUTRON STARS*, *Phys. Lett. B* **114** (1982) 392.

[130] D. Chatterjee and I. Vidaña, *Do hyperons exist in the interior of neutron stars?*, *Eur. Phys. J. A* **52** (2016) 29 [arXiv:1510.06306].

[131] U. Lombardo and H.J. Schulze, *Superfluidity in neutron star matter*, *Lect. Notes Phys.* **578** (2001) 30 [arXiv:astro-ph/0012209].

[132] N.K. Glendenning, *Phase transitions and crystalline structures in neutron star cores*, *Phys. Rept.* **342** (2001) 393.

[133] K. Chatziioannou and S. Han, *Studying strong phase transitions in neutron stars with gravitational waves*, *Phys. Rev. D* **101** (2020) 044019 [arXiv:1911.07091].

[134] A. Bauswein, N.-U.F. Bastian, D.B. Blaschke, K. Chatziioannou, J.A. Clark, T. Fischer et al., *Identifying a first-order phase transition in neutron star mergers through gravitational waves*, *Phys. Rev. Lett.* **122** (2019) 061102 [arXiv:1809.01116].

[135] F. Özel and P. Freire, *Masses, Radii, and the Equation of State of Neutron Stars*, *Ann. Rev. Astron. Astrophys.* **54** (2016) 401 [arXiv:1603.02698].

[136] LIGO Scientific, Virgo collaboration, *GW170817: Observation of Gravitational Waves from a Binary Neutron Star Inspiral*, *Phys. Rev. Lett.* **119** (2017) 161101 [arXiv:1710.05832].

[137] LIGO Scientific, Virgo, Fermi-GBM, INTEGRAL collaboration, *Gravitational Waves and Gamma-rays from a Binary Neutron Star Merger: GW170817 and GRB 170817A*, *Astrophys. J. Lett.* **848** (2017) L13 [arXiv:1710.05834].

[138] LIGO Scientific, Virgo collaboration, *GW170817: Measurements of neutron star radii and equation of state*, *Phys. Rev. Lett.* **121** (2018) 161101 [arXiv:1805.11581].

[139] B. Margalit and B.D. Metzger, *Constraining the Maximum Mass of Neutron Stars From Multi-Messenger Observations of GW170817*, *Astrophys. J. Lett.* **850** (2017) L19 [arXiv:1710.05938].

[140] E. Annala, T. Gorda, A. Kurkela and A. Vuorinen, *Gravitational-wave constraints on the neutron-star-matter Equation of State*, *Phys. Rev. Lett.* **120** (2018) 172703 [arXiv:1711.02644].

[141] M. Shibata, E. Zhou, K. Kiuchi and S. Fujibayashi, *Constraint on the maximum mass of neutron stars using GW170817 event*, *Phys. Rev. D* **100** (2019) 023015 [arXiv:1905.03656].

[142] KAGRA, LIGO Scientific, Virgo, VIRGO collaboration, *Prospects for observing and localizing gravitational-wave transients with Advanced LIGO, Advanced Virgo and KAGRA*, *Living Rev. Rel.* **21** (2018) 3 [arXiv:1304.0670].

[143] LIGO Scientific, Virgo collaboration, *GWTC-1: A Gravitational-Wave Transient Catalog of Compact Binary Mergers Observed by LIGO and Virgo during the First and Second Observing Runs*, *Phys. Rev. X* **9** (2019) 031040 [arXiv:1811.12907].

[144] LIGO Scientific, Virgo collaboration, *GWTC-2: Compact Binary Coalescences Observed by LIGO and Virgo During the First Half of the Third Observing Run*, *Phys. Rev. X* **11** (2021) 021053 [arXiv:2010.14527].

[145] LIGO Scientific, VIRGO, KAGRA collaboration, *GWTC-3: Compact Binary Coalescences Observed by LIGO and Virgo During the Second Part of the Third Observing Run*, arXiv:2111.03606.

[146] M. Punturo et al., *The Einstein Telescope: A third-generation gravitational wave observatory*, *Class. Quant. Grav.* **27** (2010) 194002.

[147] D. Reitze et al., *Cosmic Explorer: The U.S. Contribution to Gravitational-Wave Astronomy beyond LIGO*, *Bull. Am. Astron. Soc.* **51** (2019) 035 [arXiv:1907.04833].

[148] LIGO Scientific, Virgo collaboration, *GW190814: Gravitational Waves from the Coalescence of a 23 Solar Mass Black Hole with a 2.6 Solar Mass Compact Object*, *Astrophys. J. Lett.* **896** (2020) L44 [arXiv:2006.12611].

[149] S.M. Brown, C.D. Capano and B. Krishnan, *Using Gravitational Waves to Distinguish between Neutron Stars and Black Holes in Compact Binary Mergers*, *Astrophys. J.* **941** (2022) 98 [arXiv:2105.03485].

[150] J.F. Coupechoux, A. Arbey, R. Chierici, H. Hansen, J. Margueron and V. Sordini, *Discriminating same-mass neutron stars and black holes gravitational waveforms*, *Phys. Rev. D* **105** (2022) 064063 [arXiv:2106.05805].

[151] I. Bednarek, P. Haensel, J.L. Zdunik, M. Bejger and R. Manka, *Hyperons in neutron-star cores and two-solar-mass pulsar*, *Astron. Astrophys.* **543** (2012) A157 [arXiv:1111.6942].

[152] M. Oertel, M. Hempel, T. Klähn and S. Typel, *Equations of state for supernovae and compact stars*, *Rev. Mod. Phys.* **89** (2017) 015007 [arXiv:1610.03361].

[153] I. Bombaci, *The Hyperon Puzzle in Neutron Stars*, *JPS Conf. Proc.* **17** (2017) 101002 [arXiv:1601.05339].

[154] J.M. Lattimer, *Neutron Stars and the Nuclear Matter Equation of State*, *Ann. Rev. Nucl. Part. Sci.* **71** (2021) 433.

[155] A. Nathanail, E.R. Most and L. Rezzolla, *GW170817 and GW190814: tension on the maximum mass*, *Astrophys. J. Lett.* **908** (2021) L28 [arXiv:2101.01735].

[156] C.D. Bailyn, R.K. Jain, P. Coppi and J.A. Orosz, *The Mass distribution of stellar black holes*, *Astrophys. J.* **499** (1998) 367 [arXiv:astro-ph/9708032].

[157] C.L. Fryer and V. Kalogera, *Theoretical black hole mass distributions*, *Astrophys. J.* **554** (2001) 548 [arXiv:astro-ph/9911312].

[158] F. Ozel, D. Psaltis, R. Narayan and J.E. McClintock, *The Black Hole Mass Distribution in the Galaxy*, *Astrophys. J.* **725** (2010) 1918 [arXiv:1006.2834].

[159] J. Antoniadis et al., *A Massive Pulsar in a Compact Relativistic Binary*, *Science* **340** (2013) 6131 [arXiv:1304.6875].

[160] F. Crawford, M.S.E. Roberts, J.W.T. Hessels, S.M. Ransom, M. Livingstone, C.R. Tam et al., *A Survey of 56 Mid-latitude EGRET Error Boxes for Radio Pulsars*, *Astrophys. J.* **652** (2006) 1499 [arXiv:astro-ph/0608225].

[161] M. Linares, T. Shahbaz and J. Casares, *Peering into the dark side: Magnesium lines establish a massive neutron star in PSR J2215+5135*, *Astrophys. J.* **859** (2018) 54 [arXiv:1805.08799].

[162] R. Gamba, J.S. Read and L.E. Wade, *The impact of the crust equation of state on the analysis of GW170817*, *Class. Quant. Grav.* **37** (2020) 025008 [arXiv:1902.04616].

[163] J.M. Lattimer and B.F. Schutz, *Constraining the equation of state with moment of inertia measurements*, *Astrophys. J.* **629** (2005) 979 [arXiv:astro-ph/0411470].

[164] K.C. Gendreau, Z. Arzoumanian, P.W. Adkins, C.L. Albert, J.F. Anders, A.T. Aylward et al., *The Neutron star Interior Composition Explorer (NICER): design and development*, in *Space Telescopes and Instrumentation 2016: Ultraviolet to Gamma Ray*, J.-W.A. den Herder, T. Takahashi and M. Bautz, eds., vol. 9905 of *Society of Photo-Optical Instrumentation Engineers (SPIE) Conference Series*, p. 99051H, July, 2016, DOI.

[165] K.Y. Ekşi, C. Güngör and M.M. Türkoğlu, *What does a measurement of mass and/or radius of a neutron star constrain: Equation of state or gravity?*, *Phys. Rev. D* **89** (2014) 063003 [arXiv:1402.0488].

[166] M.C. Miller and J.M. Miller, *The Masses and Spins of Neutron Stars and Stellar-Mass Black Holes*, *Phys. Rept.* **548** (2014) 1 [arXiv:1408.4145].

[167] D. Psaltis, F. Özel and D. Chakrabarty, *Prospects for Measuring Neutron-Star Masses and Radii with X-Ray Pulse Profile Modeling*, *Astrophys. J.* **787** (2014) 136 [arXiv:1311.1571].

[168] C.A. Raithel, F. Ozel and D. Psaltis, *Model-Independent Inference of Neutron Star Radii from Moment of Inertia Measurements*, *Phys. Rev. C* **93** (2016) 032801 [arXiv:1603.06594].

[169] A. Bauswein, O. Just, H.-T. Janka and N. Stergioulas, *Neutron-star radius constraints from GW170817 and future detections*, *Astrophys. J. Lett.* **850** (2017) L34 [arXiv:1710.06843].

[170] M. Ruiz, S.L. Shapiro and A. Tsokaros, *GW170817, General Relativistic Magnetohydrodynamic Simulations, and the Neutron Star Maximum Mass*, *Phys. Rev. D* **97** (2018) 021501 [arXiv:1711.00473].

[171] LIGO Scientific, Virgo collaboration, *Properties of the binary neutron star merger GW170817*, *Phys. Rev. X* **9** (2019) 011001 [arXiv:1805.11579].

[172] R. Essick, P. Landry and D.E. Holz, *Nonparametric Inference of Neutron Star Composition, Equation of State, and Maximum Mass with GW170817*, *Phys. Rev. D* **101** (2020) 063007 [arXiv:1910.09740].

[173] N. Kaiser, S. Fritsch and W. Weise, *Chiral dynamics and nuclear matter*, *Nucl. Phys. A* **697** (2002) 255 [arXiv:nucl-th/0105057].

[174] N. Kaiser, S. Fritsch and W. Weise, *Nuclear mean field from chiral pion nucleon dynamics*, *Nucl. Phys. A* **700** (2002) 343 [arXiv:nucl-th/0108010].

[175] N.P. Landsman and C.G. van Weert, *Real and Imaginary Time Field Theory at Finite Temperature and Density*, *Phys. Rept.* **145** (1987) 141.

[176] J. Menendez, D. Gazit and A. Schwenk, *Chiral two-body currents in nuclei: Gamow-Teller transitions and neutrinoless double-beta decay*, *Phys. Rev. Lett.* **107** (2011) 062501 [arXiv:1103.3622].

[177] R.J. Furnstahl and B.D. Serot, *Covariant Feynman rules at finite temperature: Time-path formulation*, *Phys. Rev. C* **44** (1991) 2141.

[178] J.W. Holt, M. Rho and W. Weise, *Chiral symmetry and effective field theories for hadronic, nuclear and stellar matter*, *Phys. Rept.* **621** (2016) 2 [arXiv:1411.6681].

[179] M. Quiros, *Finite temperature field theory and phase transitions*, in *ICTP Summer School in High-Energy Physics and Cosmology*, pp. 187–259, 1, 1999 [arXiv:hep-ph/9901312].

[180] M.S. Turner, *Dirac neutrinos and SN1987A*, *Phys. Rev. D* **45** (1992) 1066.

[181] G. Raffelt and D. Seckel, *A selfconsistent approach to neutral current processes in supernova cores*, *Phys. Rev. D* **52** (1995) 1780 [arXiv:astro-ph/9312019].

[182] W. Keil, H.-T. Janka, D.N. Schramm, G. Sigl, M.S. Turner and J.R. Ellis, *A Fresh look at axions and SN-1987A*, *Phys. Rev. D* **56** (1997) 2419 [arXiv:astro-ph/9612222].

[183] P. Carenza, B. Fore, M. Giannotti, A. Mirizzi and S. Reddy, *Enhanced Supernova Axion Emission and its Implications*, *Phys. Rev. Lett.* **126** (2021) 071102 [arXiv:2010.02943].

[184] H.-T. Janka, "The garching core-collapse supernova archive." https://wwwmpa.mpa-garching.mpg.de/ccsnarchive/.

[185] R. Bollig, W. DeRocco, P.W. Graham and H.-T. Janka, *Muons in Supernovae: Implications for the Axion-Muon Coupling*, *Phys. Rev. Lett.* **125** (2020) 051104 [arXiv:2005.07141].

[186] A. Hook and J. Huang, *Probing axions with neutron star inspirals and other stellar processes*, *JHEP* **06** (2018) 036 [arXiv:1708.08464].

[187] J.I. Kapusta and C. Gale, *Finite-temperature field theory: Principles and applications*, Cambridge Monographs on Mathematical Physics, Cambridge University Press (2011), 10.1017/CBO9780511535130.

[188] H.E. Haber and H.A. Weldon, *Thermodynamics of an Ultrarelativistic Bose Gas*, *Phys. Rev. Lett.* **46** (1981) 1497.

[189] J.I. Kapusta, *Bose-Einstein Condensation, Spontaneous Symmetry Breaking, and Gauge Theories*, *Phys. Rev.* **D24** (1981) 426.

[190] D.T. Son and M.A. Stephanov, *QCD at finite isospin density*, *Phys. Rev. Lett.* **86** (2001) 592 [arXiv:hep-ph/0005225].

[191] J.B. Kogut and D. Toublan, *QCD at small nonzero quark chemical potentials*, *Phys. Rev.* **D64** (2001) 034007 [arXiv:hep-ph/0103271].

[192] A. Mammarella and M. Mannarelli, *Intriguing aspects of meson condensation*, *Phys. Rev.* **D92** (2015) 085025 [arXiv:1507.02934].

[193] T.D. Cohen, R. Furnstahl and D.K. Griegel, *Quark and gluon condensates in nuclear matter*, *Phys. Rev. C* **45** (1992) 1881.

[194] P. Gubler and D. Satow, *Recent Progress in QCD Condensate Evaluations and Sum Rules*, *Prog. Part. Nucl. Phys.* **106** (2019) 1 [arXiv:1812.00385].

[195] U.G. Meissner, J.A. Oller and A. Wirzba, *In-medium chiral perturbation theory beyond the mean field approximation*, *Annals Phys.* **297** (2002) 27 [arXiv:nucl-th/0109026].

[196] N. Kaiser, P. de Homont and W. Weise, *In-medium chiral condensate beyond linear density approximation*, *Phys. Rev.* **C77** (2008) 025204 [arXiv:0711.3154].

[197] S. Goda and D. Jido, *Chiral condensate at finite density using the chiral Ward identity*, *Phys. Rev.* **C88** (2013) 065204 [arXiv:1308.2660].

[198] N. Kaiser and W. Weise, *Chiral condensate in neutron matter*, *Phys. Lett.* **B671** (2009) 25 [arXiv:0808.0856].

[199] T. Krger, I. Tews, B. Friman, K. Hebeler and A. Schwenk, *The chiral condensate in neutron matter*, *Phys. Lett.* **B726** (2013) 412 [arXiv:1307.2110].

[200] W. Weise, *Dense Baryonic Matter and Strangeness in Neutron Stars*, in *8th International Conference on Quarks and Nuclear Physics (QNP2018) Tsukuba, Japan, November 13-17, 2018*, 2019 [arXiv:1905.03955].

[201] D.B. Kaplan and A.E. Nelson, *Kaon Condensation in Dense Matter*, *Nucl. Phys. A* **479** (1988) 273c.

[202] V. Thorsson, M. Prakash and J.M. Lattimer, *Composition, structure and evolution of neutron stars with kaon condensates*, *Nucl. Phys.* **A572** (1994) 693 [arXiv:nucl-th/9305006].

[203] A. Ramos, J. Schaffner-Bielich and J. Wambach, *Kaon condensation in neutron stars*, *Lect. Notes Phys.* **578** (2001) 175 [arXiv:nucl-th/0011003].

[204] N.K. Glendenning and J. Schaffner-Bielich, *First order kaon condensate*, *Phys. Rev.* **C60** (1999) 025803 [arXiv:astro-ph/9810290].

[205] H.T. Cromartie et al., *Relativistic Shapiro delay measurements of an extremely massive millisecond pulsar*, *Nat. Astron.* **4** (2019) 72 [arXiv:1904.06759].

[206] H. Djapo, B.-J. Schaefer and J. Wambach, *On the appearance of hyperons in neutron stars*, *Phys. Rev.* **C81** (2010) 035803 [arXiv:0811.2939].

[207] T. Muto and T. Tatsumi, *Theoretical aspects of kaon condensation in neutron matter*, *Phys. Lett.* **B283** (1992) 165.

[208] J. Polchinski, *Effective field theory and the Fermi surface*, in *Proceedings, Theoretical Advanced Study Institute (TASI 92): From Black Holes and Strings to Particles: Boulder, USA, June 1-26, 1992*, pp. 0235–276, 1992 [arXiv:hep-th/9210046].

[209] D.B. Kaplan, *Five lectures on effective field theory*, arXiv:nucl-th/0510023.

[210] M.G. Alford, K. Rajagopal and F. Wilczek, *QCD at finite baryon density: Nucleon droplets and color superconductivity*, *Phys. Lett. B* **422** (1998) 247 [arXiv:hep-ph/9711395].

[211] R. Rapp, T. Schäfer, E.V. Shuryak and M. Velkovsky, *Diquark bose condensates in high density matter and instantons*, *Phys.Rev.Lett.* **81** (1998) 53 [arXiv:hep-ph/9711396].

[212] M.G. Alford, K. Rajagopal and F. Wilczek, *Color flavor locking and chiral symmetry breaking in high density QCD*, *Nucl. Phys.* **B537** (1999) 443 [arXiv:hep-ph/9804403].

[213] D.T. Son, *Superconductivity by long range color magnetic interaction in high density quark matter*, *Phys. Rev.* **D59** (1999) 094019 [arXiv:hep-ph/9812287].

[214] M.G. Alford, A. Schmitt, K. Rajagopal and T. Schäfer, *Color superconductivity in dense quark matter*, *Rev. Mod. Phys.* **80** (2008) 1455 [arXiv:0709.4635].

[215] D.K. Hong, *An Effective field theory of QCD at high density*, *Phys. Lett.* **B473** (2000) 118 [arXiv:hep-ph/9812510].

[216] D.T. Son and M.A. Stephanov, *Inverse meson mass ordering in color flavor locking phase of high density QCD*, *Phys. Rev.* **D61** (2000) 074012 [arXiv:hep-ph/9910491].

[217] D.T. Son and M.A. Stephanov, *Inverse meson mass ordering in color flavor locking phase of high density QCD: Erratum*, *Phys. Rev.* **D62** (2000) 059902 [arXiv:hep-ph/0004095].

[218] R. Casalbuoni and R. Gatto, *Effective theory for color flavor locking in high density QCD*, *Phys. Lett.* **B464** (1999) 111 [arXiv:hep-ph/9908227].

[219] P.F. Bedaque and T. Schäfer, *High density quark matter under stress*, *Nucl. Phys.* **A697** (2002) 802 [arXiv:hep-ph/0105150].

[220] T. Schäfer, *Mass terms in effective theories of high density quark matter*, *Phys. Rev.* **D65** (2002) 074006 [arXiv:hep-ph/0109052].

[221] T. Schäfer, *Patterns of symmetry breaking in QCD at high baryon density*, *Nucl. Phys.* **B575** (2000) 269 [arXiv:hep-ph/9909574].

[222] A. Kryjevski, D.B. Kaplan and T. Schäfer, *New phases in CFL quark matter*, *Phys. Rev.* **D71** (2005) 034004 [arXiv:hep-ph/0404290].

[223] T. Schäfer, *Instanton effects in QCD at high baryon density*, *Phys. Rev.* **D65** (2002) 094033 [arXiv:hep-ph/0201189].

[224] K. Rajagopal and E. Shuster, *On the applicability of weak coupling results in high density QCD*, *Phys. Rev.* **D62** (2000) 085007 [arXiv:hep-ph/0004074].

[225] B. Bellazzini, C. Csaki, J. Hubisz, J. Serra and J. Terning, *Cosmological and Astrophysical Probes of Vacuum Energy*, *JHEP* **06** (2016) 104 [arXiv:1502.04702].

[226] C. Csáki, C. Eröncel, J. Hubisz, G. Rigo and J. Terning, *Neutron Star Mergers Chirp About Vacuum Energy*, *JHEP* **09** (2018) 087 [arXiv:1802.04813].

[227] B. Garbrecht and J. McDonald, *Axion configurations around pulsars*, *JCAP* **07** (2018) 044 [arXiv:1804.04224].

[228] J.-F. Fortin and K. Sinha, *Constraining Axion-Like-Particles with Hard X-ray Emission from Magnetars*, *JHEP* **06** (2018) 048 [arXiv:1804.01992].

[229] F.V. Day and J.I. McDonald, *Axion superradiance in rotating neutron stars*, *JCAP* **1910** (2019) 051 [arXiv:1904.08341].

[230] M. Buschmann, R.T. Co, C. Dessert and B.R. Safdi, *X-ray Search for Axions from Nearby Isolated Neutron Stars*, arXiv:1910.04164.

[231] J. Huang, M.C. Johnson, L. Sagunski, M. Sakellariadou and J. Zhang, *Prospects for axion searches with Advanced LIGO through binary mergers*, *Phys. Rev.* **D99** (2019) 063013 [arXiv:1807.02133].

[232] E. Witten, *Cosmic Separation of Phases*, *Phys. Rev. D* **30** (1984) 272.

[233] D. Koester and G. Chanmugam, *REVIEW: Physics of white dwarf stars*, *Reports on Progress in Physics* **53** (1990) 837.

[234] L. Ubaldi, *Effects of theta on the deuteron binding energy and the triple-alpha process*, *Phys. Rev. D* **81** (2010) 025011 [arXiv:0811.1599].

[235] J. Zhang, Z. Lyu, J. Huang, M.C. Johnson, L. Sagunski, M. Sakellariadou et al., *First Constraints on Nuclear Coupling of Axionlike Particles from the Binary Neutron Star Gravitational Wave Event GW170817*, *Phys. Rev. Lett.* **127** (2021) 161101 [arXiv:2105.13963].

[236] A. Arvanitaki, M. Baryakhtar and X. Huang, *Discovering the QCD Axion with Black Holes and Gravitational Waves*, *Phys. Rev. D* **91** (2015) 084011 [arXiv:1411.2263].

[237] D.D. Doneva, F.M. Ramazanoğlu, H.O. Silva, T.P. Sotiriou and S.S. Yazadjiev, *Scalarization*, arXiv:2211.01766.

[238] J.R. Ellis, S. Kalara, K.A. Olive and C. Wetterich, *Density Dependent Couplings and Astrophysical Bounds on Light Scalar Particles*, *Phys. Lett. B* **228** (1989) 264.

[239] M. Nauenberg and J. Chapline, George, *Determination of Properties of Cold Stars in General Relativity by a Variational Method*, *Astrophys. J.* **179** (1973) 277.

[240] C.E. Rhoades, Jr. and R. Ruffini, *Maximum mass of a neutron star*, *Phys. Rev. Lett.* **32** (1974) 324.

[241] V. Kalogera and G. Baym, *The maximum mass of a neutron star*, *Astrophys. J. Lett.* **470** (1996) L61 [arXiv:astro-ph/9608059].

[242] T. Damour and G. Esposito-Farese, *Nonperturbative strong field effects in tensor - scalar theories of gravitation*, *Phys. Rev. Lett.* **70** (1993) 2220.

[243] J. Khoury and A. Weltman, *Chameleon fields: Awaiting surprises for tests of gravity in space*, *Phys. Rev. Lett.* **93** (2004) 171104 [arXiv:astro-ph/0309300].

[244] N. Blinov, S.A.R. Ellis and A. Hook, *Consequences of Fine-Tuning for Fifth Force Searches*, *JHEP* **11** (2018) 029 [arXiv:1807.11508].

[245] T. Damour and A.M. Polyakov, *The String dilaton and a least coupling principle*, *Nucl. Phys. B* **423** (1994) 532 [arXiv:hep-th/9401069].

[246] N. Yunes and F. Pretorius, *Dynamical Chern-Simons Modified Gravity. I. Spinning Black Holes in the Slow-Rotation Approximation*, *Phys. Rev. D* **79** (2009) 084043 [arXiv:0902.4669].

[247] T.P. Sotiriou and S.-Y. Zhou, *Black hole hair in generalized scalar-tensor gravity*, *Phys. Rev. Lett.* **112** (2014) 251102 [arXiv:1312.3622].

[248] H.O. Silva, J. Sakstein, L. Gualtieri, T.P. Sotiriou and E. Berti, *Spontaneous scalarization of black holes and compact stars from a Gauss-Bonnet coupling*, *Phys. Rev. Lett.* **120** (2018) 131104 [arXiv:1711.02080].

[249] F. Serra, J. Serra, E. Trincherini and L.G. Trombetta, *Causality constraints on black holes beyond GR*, *JHEP* **08** (2022) 157 [arXiv:2205.08551].

[250] D.-Y. Hong, Z.-H. Wang and S.-Y. Zhou, *Causality bounds on scalar-tensor EFTs*, arXiv:2304.01259.

[251] J.R. Oppenheimer and G.M. Volkoff, *On Massive neutron cores*, *Phys. Rev.* **55** (1939) 374.

[252] R.C. Tolman, *Static solutions of Einstein's field equations for spheres of fluid*, *Phys. Rev.* **55** (1939) 364.

[253] S.R. Coleman, *The Uses of Instantons*, *Subnucl. Ser.* **15** (1979) 805.

[254] A. Hook and J. Huang, *Searches for other vacua. Part I. Bubbles in our universe*, *JHEP* **08** (2019) 148 [arXiv:1904.00020].

[255] E. Farhi and R.L. Jaffe, *Strange Matter*, *Phys. Rev. D* **30** (1984) 2379.

[256] C. Alcock, E. Farhi and A. Olinto, *Strange stars*, *Astrophys. J.* **310** (1986) 261.

[257] C. Gao and A. Stebbins, *Structure of Stellar Remnants with Coupling to a Light Scalar*, arXiv:2110.07012.

[258] S. Koranda, N. Stergioulas and J.L. Friedman, *Upper limit set by causality on the rotation and mass of uniformly rotating relativistic stars*, *Astrophys. J.* **488** (1997) 799 [arXiv:astro-ph/9608179].

[259] L. Lindblom, *Limits on the gravitational redshift form neutron stars*, *Astrophys. J.* **278** (1984) 364.

[260] P. Haensel, J.P. Lasota and J.L. Zdunik, *On the minimum period of uniformly rotating meutron stars*, arXiv:astro-ph/9901118.

[261] H.A. Buchdahl, *General Relativistic Fluid Spheres*, *Phys. Rev.* **116** (1959) 1027.

[262] J.W.T. Hessels, S.M. Ransom, I.H. Stairs, P.C.C. Freire, V.M. Kaspi and F. Camilo, *A radio pulsar spinning at 716-hz*, *Science* **311** (2006) 1901 [arXiv:astro-ph/0601337].

[263] P. Haensel, J.L. Zdunik, M. Bejger and J.M. Lattimer, *Keplerian frequency of uniformly rotating neutron stars and strange stars*, *Astron. Astrophys.* **502** (2009) 605 [arXiv:0901.1268].

[264] J.B. Hartle, *Slowly rotating relativistic stars. 1. Equations of structure*, *Astrophys. J.* **150** (1967) 1005.

[265] J.B. Hartle and K.S. Thorne, *Slowly Rotating Relativistic Stars. II. Models for Neutron Stars and Supermassive Stars*, *Astrophys. J.* **153** (1968) 807.

[266] P. Pani and E. Berti, *Slowly rotating neutron stars in scalar-tensor theories*, *Phys. Rev. D* **90** (2014) 024025 [arXiv:1405.4547].

[267] D.D. Doneva, S.S. Yazadjiev, K.V. Staykov and K.D. Kokkotas, *Universal I-Q relations for rapidly rotating neutron and strange stars in scalar-tensor theories*, *Phys. Rev. D* **90** (2014) 104021 [arXiv:1408.1641].

[268] D.D. Doneva and S.S. Yazadjiev, *Rapidly rotating neutron stars with a massive scalar field—structure and universal relations*, *JCAP* **11** (2016) 019 [arXiv:1607.03299].

[269] D. Popchev, K.V. Staykov, D.D. Doneva and S.S. Yazadjiev, *Moment of inertia–mass universal relations for neutron stars in scalar-tensor theory with self-interacting massive scalar field*, *Eur. Phys. J. C* **79** (2019) 178 [arXiv:1812.00347].

[270] K. Yagi and N. Yunes, *I-Love-Q*, *Science* **341** (2013) 365 [arXiv:1302.4499].

[271] K. Yagi and N. Yunes, *I-Love-Q Relations in Neutron Stars and their Applications to Astrophysics, Gravitational Waves and Fundamental Physics*, *Phys. Rev. D* **88** (2013) 023009 [arXiv:1303.1528].

[272] E.E. Flanagan and T. Hinderer, *Constraining neutron star tidal Love numbers with gravitational wave detectors*, *Phys. Rev. D* **77** (2008) 021502 [arXiv:0709.1915].

[273] S. Postnikov, M. Prakash and J.M. Lattimer, *Tidal Love Numbers of Neutron and Self-Bound Quark Stars*, *Phys. Rev. D* **82** (2010) 024016 [arXiv:1004.5098].

[274] K. Yagi and N. Yunes, *Approximate Universal Relations for Neutron Stars and Quark Stars*, *Phys. Rept.* **681** (2017) 1 [arXiv:1608.02582].

[275] L. Caloni, M. Gerbino, M. Lattanzi and L. Visinelli, *Novel cosmological bounds on thermally-produced axion-like particles*, *JCAP* **09** (2022) 021 [arXiv:2205.01637].

[276] C.A.J. O'Hare and E. Vitagliano, *Cornering the axion with CP-violating interactions*, *Phys. Rev. D* **102** (2020) 115026 [arXiv:2010.03889].

[277] P. Brax, S. Fichet and G. Pignol, *Bounding Quantum Dark Forces*, *Phys. Rev. D* **97** (2018) 115034 [arXiv:1710.00850].

[278] K.A. Olive and M. Pospelov, *Environmental dependence of masses and coupling constants*, *Phys. Rev. D* **77** (2008) 043524 [arXiv:0709.3825].

[279] L. Del Grosso, G. Franciolini, P. Pani and A. Urbano, *Fermion soliton stars*, arXiv:2301.08709.

[280] M.A. Shifman, A.I. Vainshtein and V.I. Zakharov, *Remarks on Higgs Boson Interactions with Nucleons*, *Phys. Lett. B* **78** (1978) 443.

[281] D.B. Kaplan and M.B. Wise, *Couplings of a light dilaton and violations of the equivalence principle*, *JHEP* **08** (2000) 037 [arXiv:hep-ph/0008116].

[282] T. Damour and J.F. Donoghue, *Equivalence Principle Violations and Couplings of a Light Dilaton*, *Phys. Rev. D* **82** (2010) 084033 [arXiv:1007.2792].

[283] R. Sundrum, *Gravity's scalar cousin*, arXiv:hep-th/0312212.

[284] F.M. Ramazanoğlu and F. Pretorius, *Spontaneous Scalarization with Massive Fields*, *Phys. Rev. D* **93** (2016) 064005 [arXiv:1601.07475].

[285] P. Brax, A.-C. Davis and R. Jha, *Neutron Stars in Screened Modified Gravity: Chameleon vs Dilaton*, *Phys. Rev. D* **95** (2017) 083514 [arXiv:1702.02983].

[286] S. Morisaki and T. Suyama, *Spontaneous scalarization with an extremely massive field and heavy neutron stars*, *Phys. Rev. D* **96** (2017) 084026 [arXiv:1707.02809].

[287] K.V. Staykov, D. Popchev, D.D. Doneva and S.S. Yazadjiev, *Static and slowly rotating neutron stars in scalar–tensor theory with self-interacting massive scalar field*, *Eur. Phys. J. C* **78** (2018) 586 [arXiv:1805.07818].

[288] S.R. Coleman, *The Fate of the False Vacuum. 1. Semiclassical Theory*, *Phys. Rev. D* **15** (1977) 2929.

[289] P. Brax and C. Burrage, *Screening the Higgs portal*, arXiv:2101.10693.

[290] R. Foot, *Have mirror stars been observed?*, *Phys. Lett. B* **452** (1999) 83 [arXiv:astro-ph/9902065].

[291] G. Narain, J. Schaffner-Bielich and I.N. Mishustin, *Compact stars made of fermionic dark matter*, *Phys. Rev. D* **74** (2006) 063003 [arXiv:astro-ph/0605724].

[292] D. Spolyar, K. Freese and P. Gondolo, *Dark matter and the first stars: a new phase of stellar evolution*, *Phys. Rev. Lett.* **100** (2008) 051101 [arXiv:0705.0521].

[293] F. Sandin and P. Ciarcelluti, *Effects of mirror dark matter on neutron stars*, *Astropart. Phys.* **32** (2009) 278 [arXiv:0809.2942].

[294] C. Kouvaris and N.G. Nielsen, *Asymmetric Dark Matter Stars*, *Phys. Rev. D* **92** (2015) 063526 [arXiv:1507.00959].

[295] M.I. Gresham and K.M. Zurek, *Asymmetric Dark Stars and Neutron Star Stability*, *Phys. Rev. D* **99** (2019) 083008 [arXiv:1809.08254].

[296] D. Curtin and J. Setford, *Signatures of Mirror Stars*, *JHEP* **03** (2020) 041 [arXiv:1909.04072].

[297] D. Curtin and J. Setford, *How To Discover Mirror Stars*, *Phys. Lett. B* **804** (2020) 135391 [arXiv:1909.04071].

[298] M. Hippert, J. Setford, H. Tan, D. Curtin, J. Noronha-Hostler and N. Yunes, *Mirror Neutron Stars*, arXiv:2103.01965.

[299] J. Lattimer and M. Prakash, *The physics of neutron stars*, *Science* **304** (2004) 536 [arXiv:astro-ph/0405262].

[300] J. Pons, S. Reddy, M. Prakash, J. Lattimer and J. Miralles, *Evolution of protoneutron stars*, *Astrophys. J.* **513** (1999) 780 [arXiv:astro-ph/9807040].

[301] G.W. Anderson and L.J. Hall, *The Electroweak phase transition and baryogenesis*, *Phys. Rev. D* **45** (1992) 2685.

[302] E.J. Weinberg, *Classical solutions in quantum field theory: Solitons and Instantons in High Energy Physics*, Cambridge Monographs on Mathematical Physics, Cambridge University Press (9, 2012), 10.1017/CBO9781139017787.

[303] W.A. Hiscock, *Can Black Holes Nucleate Vacuum Phase Transitions?*, *Phys. Rev. D* **35** (1987) 1161.

[304] D.R. Green, E. Silverstein and D. Starr, *Attractor explosions and catalyzed vacuum decay*, *Phys. Rev. D* **74** (2006) 024004 [arXiv:hep-th/0605047].

[305] R. Gregory, I.G. Moss and B. Withers, *Black holes as bubble nucleation sites*, *JHEP* **03** (2014) 081 [arXiv:1401.0017].

[306] K. Mukaida and M. Yamada, *False Vacuum Decay Catalyzed by Black Holes*, *Phys. Rev. D* **96** (2017) 103514 [arXiv:1706.04523].

[307] N. Oshita, M. Yamada and M. Yamaguchi, *Compact objects as the catalysts for vacuum decays*, *Phys. Lett. B* **791** (2019) 149 [arXiv:1808.01382].

[308] A. Shkerin and S. Sibiryakov, *Black hole induced false vacuum decay from first principles*, *JHEP* **11** (2021) 197 [arXiv:2105.09331].

[309] A. Shkerin and S. Sibiryakov, *Black hole induced false vacuum decay: The role of greybody factors*, arXiv:2111.08017.

[310] J. Callan, Curtis G. and S.R. Coleman, *The Fate of the False Vacuum. 2. First Quantum Corrections*, *Phys. Rev. D* **16** (1977) 1762.

[311] K.-M. Lee and E.J. Weinberg, *Tunneling without barriers*, *Nucl. Phys. B* **267** (1986) 181.

[312] I.K. Affleck and F. De Luccia, *Induced Vacuum Decay*, *Phys. Rev. D* **20** (1979) 3168.

[313] B. Grinstein and C.W. Murphy, *Semiclassical Approach to Heterogeneous Vacuum Decay*, *JHEP* **12** (2015) 063 [arXiv:1509.05405].

[314] P. Madau and M. Dickinson, *Cosmic Star Formation History*, *Ann. Rev. Astron. Astrophys.* **52** (2014) 415 [arXiv:1403.0007].

[315] V. Bromm and R.B. Larson, *The First stars*, *Ann. Rev. Astron. Astrophys.* **42** (2004) 79 [arXiv:astro-ph/0311019].

[316] J. Garriga and A. Vilenkin, *Solutions to the cosmological constant problems*, *Phys. Rev. D* **64** (2001) 023517 [arXiv:hep-th/0011262].

[317] M. Pospelov, S. Pustelny, M. Ledbetter, D. Jackson Kimball, W. Gawlik and D. Budker, *Detecting Domain Walls of Axionlike Models Using Terrestrial Experiments*, *Phys. Rev. Lett.* **110** (2013) 021803 [arXiv:1205.6260].

[318] S. Weinberg, *Anthropic Bound on the Cosmological Constant*, *Phys. Rev. Lett.* **59** (1987) 2607.

[319] L. Verde, T. Treu and A. Riess, *Tensions between the Early and the Late Universe*, 7, 2019, DOI [arXiv:1907.10625].

[320] L. Knox and M. Millea, *Hubble constant hunter's guide*, *Phys. Rev. D* **101** (2020) 043533 [arXiv:1908.03663].

[321] T. Karwal and M. Kamionkowski, *Dark energy at early times, the Hubble parameter, and the string axiverse*, *Phys. Rev. D* **94** (2016) 103523 [arXiv:1608.01309].

[322] A. Arvanitaki, S. Dimopoulos, V. Gorbenko, J. Huang and K. Van Tilburg, *A small weak scale from a small cosmological constant*, *JHEP* **05** (2017) 071 [arXiv:1609.06320].

[323] T.C. Bachlechner, K. Eckerle, O. Janssen and M. Kleban, *Multiple-axion framework*, *Phys. Rev. D* **98** (2018) 061301 [arXiv:1703.00453].

[324] A. Strumia and D. Teresi, *Relaxing the Higgs mass and its vacuum energy by living at the top of the potential*, *Phys. Rev. D* **101** (2020) 115002 [arXiv:2002.02463].

[325] N. Arkani-Hamed, R.T. D'Agnolo and H.D. Kim, *The Weak Scale as a Trigger*, arXiv:2012.04652.

[326] R. Tito D'Agnolo and D. Teresi, *Sliding naturalness: cosmological selection of the weak scale*, *JHEP* **02** (2022) 023 [arXiv:2109.13249].

[327] R. Tito D'Agnolo and D. Teresi, *Sliding Naturalness: New Solution to the Strong-CP and Electroweak-Hierarchy Problems*, *Phys. Rev. Lett.* **128** (2022) 021803 [arXiv:2106.04591].

[328] G.F. Giudice, M. McCullough and T. You, *Self-organised localisation*, *JHEP* **10** (2021) 093 [arXiv:2105.08617].

[329] R. Barbieri, *Electroweak theory after the first Large Hadron Collider phase*, *Phys. Scripta T* **158** (2013) 014006 [arXiv:1309.3473].

[330] G.F. Giudice, *Naturally Speaking: The Naturalness Criterion and Physics at the LHC*, arXiv:0801.2562.

[331] G. 't Hooft, *Naturalness, chiral symmetry, and spontaneous chiral symmetry breaking*, *NATO Sci. Ser. B* **59** (1980) 135.

[332] S. Dimopoulos and L. Susskind, *Mass Without Scalars*, .

[333] L. Susskind, *Dynamics of Spontaneous Symmetry Breaking in the Weinberg-Salam Theory*, *Phys. Rev. D* **20** (1979) 2619.

[334] S. Weinberg, *Baryon and Lepton Nonconserving Processes*, *Phys. Rev. Lett.* **43** (1979) 1566.

[335] J. Espinosa, C. Grojean, G. Panico, A. Pomarol, O. Pujolàs and G. Servant, *Cosmological Higgs-Axion Interplay for a Naturally Small Electroweak Scale*, *Phys. Rev. Lett.* **115** (2015) 251803 [arXiv:1506.09217].

[336] E. Hardy, *Electroweak relaxation from finite temperature*, *JHEP* **11** (2015) 077 [arXiv:1507.07525].

[337] A. Hook and G. Marques-Tavares, *Relaxation from particle production*, *JHEP* **12** (2016) 101 [arXiv:1607.01786].

[338] N. Fonseca, E. Morgante and G. Servant, *Higgs relaxation after inflation*, *JHEP* **10** (2018) 020 [arXiv:1805.04543].

[339] N. Fonseca, E. Morgante, R. Sato and G. Servant, *Relaxion Fluctuations (Self-stopping Relaxion) and Overview of Relaxion Stopping Mechanisms*, *JHEP* **05** (2020) 080 [arXiv:1911.08473].

[340] A. Nelson and C. Prescod-Weinstein, *Relaxion: A Landscape Without Anthropics*, *Phys. Rev.* **D96** (2017) 113007 [arXiv:1708.00010].

[341] A. Banerjee, H. Kim, O. Matsedonskyi, G. Perez and M.S. Safronova, *Probing the Relaxed Relaxion at the Luminosity and Precision Frontiers*, *JHEP* **07** (2020) 153 [arXiv:2004.02899].

[342] J. Yoo and R.J. Scherrer, *Big bang nucleosynthesis and cosmic microwave background constraints on the time variation of the Higgs vacuum expectation value*, *Phys. Rev.* **D67** (2003) 043517 [arXiv:astro-ph/0211545].

[343] G. D'Amico, A. Strumia, A. Urbano and W. Xue, *Direct anthropic bound on the weak scale from supernovæ explosions*, *Phys. Rev. D* **100** (2019) 083013 [arXiv:1906.00986].

[344] T. Flacke, C. Frugiuele, E. Fuchs, R.S. Gupta and G. Perez, *Phenomenology of relaxion-Higgs mixing*, *JHEP* **06** (2017) 050 [arXiv:1610.02025].

[345] R. Budnik, H. Kim, O. Matsedonskyi, G. Perez and Y. Soreq, *Probing the relaxed relaxion and Higgs-portal with S1 \& S2*, arXiv:2006.14568.

[346] S. Chang, J. Galloway, M. Luty, E. Salvioni and Y. Tsai, *Phenomenology of Induced Electroweak Symmetry Breaking*, *JHEP* **03** (2015) 017 [arXiv:1411.6023].

[347] R. Harnik, K. Howe and J. Kearney, *Tadpole-Induced Electroweak Symmetry Breaking and pNGB Higgs Models*, *JHEP* **03** (2017) 111 [arXiv:1603.03772].

[348] A.K. Harding, *The Neutron Star Zoo*, *Front. Phys. (Beijing)* **8** (2013) 679 [arXiv:1302.0869].

[349] CAST collaboration, *New CAST Limit on the Axion-Photon Interaction*, *Nature Phys.* **13** (2017) 584 [arXiv:1705.02290].

[350] OSQAR collaboration, *New exclusion limits on scalar and pseudoscalar axionlike particles from light shining through a wall*, *Phys. Rev. D* **92** (2015) 092002 [arXiv:1506.08082].

[351] R. Easther, J.T. Giblin, Jr, L. Hui and E.A. Lim, *A New Mechanism for Bubble Nucleation: Classical Transitions*, *Phys. Rev. D* **80** (2009) 123519 [arXiv:0907.3234].

[352] A. Chatrchyan and G. Servant, *The stochastic relaxion*, *JHEP* **06** (2023) 107 [arXiv:2210.01148].

[353] N. Fettes, U.-G. Meissner, M. Mojzis and S. Steininger, *The Chiral effective pion nucleon Lagrangian of order p**4*, *Annals Phys.* **283** (2000) 273 [arXiv:hep-ph/0001308].

[354] E. Epelbaum, A. Nogga, W. Gloeckle, H. Kamada, U.G. Meissner and H. Witala, *Three nucleon forces from chiral effective field theory*, *Phys. Rev. C* **66** (2002) 064001 [arXiv:nucl-th/0208023].

[355] H. Krebs, *Nuclear Currents in Chiral Effective Field Theory*, *Eur. Phys. J. A* **56** (2020) 234 [arXiv:2008.00974].

[356] E. Epelbaum, *Four-nucleon force using the method of unitary transformation*, *Eur. Phys. J. A* **34** (2007) 197 [arXiv:0710.4250].

[357] J.W. Holt, N. Kaiser and W. Weise, *Density-dependent effective nucleon-nucleon interaction from chiral three-nucleon forces*, *Phys. Rev. C* **81** (2010) 024002 [arXiv:0910.1249].

[358] J.W. Holt, M. Kawaguchi and N. Kaiser, *Implementing chiral three-body forces in terms of medium-dependent two-body forces*, *Front. in Phys.* **8** (2020) 100 [arXiv:1912.06055].

[359] M. Hoferichter, J. Ruiz de Elvira, B. Kubis and U.-G. Meißner, *Roy–Steiner-equation analysis of pion–nucleon scattering*, *Phys. Rept.* **625** (2016) 1 [arXiv:1510.06039].

[360] J. Ollé, O. Pujolàs and F. Rompineve, *Oscillons and Dark Matter*, *JCAP* **02** (2020) 006 [arXiv:1906.06352].